

UTILIZING THE INDENOFUORENE SCAFFOLD TO ACCESS STABLE AND
TUNABLE DIRADICALS

by

JUSTIN JAY DRESSLER

A DISSERTATION

Presented to the Department of Chemistry and Biochemistry
and the Graduate School of the University of Oregon
in partial fulfillment of the requirements
for the degree of
Doctor of Philosophy

June 2020

DISSERTATION APPROVAL PAGE

Student: Justin Jay Dressler

Title: Utilizing the Indenofluorene Scaffold to Access Stable and Tunable Diradicals

This dissertation has been accepted and approved in partial fulfillment of the requirements for the Doctor of Chemistry degree in the Department of Chemistry and Biochemistry by:

Mike Pluth	Chairperson
Michael Haley	Advisor
Ramesh Jasti	Core Member
Hans Dreyer	Institutional Representative

and

Kate Mondloch	Interim Vice Provost and Dean of the Graduate School
---------------	--

Original approval signatures are on file with the University of Oregon Graduate School.

Degree awarded June 2020

© 2020 Justin Jay Dressler

DISSERTATION ABSTRACT

Justin Jay Dressler

Doctor of Philosophy

Department of Chemistry and Biochemistry

June 2020

Title: Utilizing the Indenofluorene Scaffold to Access Stable and Tunable Diradicals

The concept of an organic molecule that possess two distinct radical centers yet is stable enough to be isolated and studied has intrigued chemists since the first reported diradical compound in 1904. In the last ten years the research of open-shell molecules has undergone a renaissance as chemists strive to get a fundamental understanding of the inherent electronic and magnetic properties that diradical polycyclic hydrocarbons (PCHs) display. The recent surge in reports of diradical PCHs is accredited to the development of new synthetic methods and spectroscopic techniques to fully characterize these unusual compounds. Although there has been an increase in the number of new diradicaloids there are very few reports in which structural modifications are made to a known diradical scaffold to tailor the properties towards the potential needs of industry. In this thesis I present studies in which we aim to produce series of open-shell compounds with moderate to good stability, with which we discover structure property connections to incrementally fine tune the singlet-triplet energy gap of a series of diradicals.

In Chapter I the Haley lab's first foray into the field of diradicals along with a short introduction of diradical character is presented. The mentality and direction behind our groups work on diradicals in the last five years is also discussed. Chapter II describes the discovery of the second ever diradical reported by the Haley lab which possess a unique

ground state triplet. Chapter III examines the synthesis of an uncommon open-shell compound named indenoindenodibenzothiophene (IIDBT) that was coined as a persistent singlet diradical. Chapter IV expands on the work done in the previous chapter and the singlet-triplet energy gap (ΔE_{ST}) is altered through molecule isomerism. Chapter V builds on the original synthesis of diindenoanthracene (DIAn) and a series of diradicals based on DIAn is synthesized to fine tune diradical character and ΔE_{ST} based on changes in bond order. In Chapter VI, late stage modification is used to modify the antiaromaticity and diradical character of indacenodibenzothiophenes (IDBT) and IIDBT derivatives, to impart meaningful change with less synthetic effort.

This dissertation contains previously published and unpublished coauthored material.

CURRICULUM VITAE

NAME OF AUTHOR: Justin Jay Dressler

GRADUATE AND UNDERGRADUATE SCHOOLS ATTENDED:

University of Oregon, Eugene
University of Wisconsin Eau Claire, Eau Claire

DEGREES AWARDED:

Doctor of Philosophy, Chemistry, 2020, University of Oregon
Masters of Science, Chemistry, 2017, University of Oregon
Bachelor of Science, Chemistry, 2015, University of Wisconsin-Eau Claire

AREAS OF SPECIAL INTEREST:

Synthetic Organic Chemistry
Physical Organic Chemistry

PROFESSIONAL EXPERIENCE:

Research Assistant, University of Oregon, 2015-2020
Research Assistant, University of Wisconsin Eau Claire, 2013-2015
Visiting Scholar, University of Albany, 2017
Visiting Scholar, Universidad de Valencia, Spain, 2019
Teaching Fellow, University of Oregon, 2015-2020

GRANTS, AWARDS, AND HONORS:

Poster Prize, From Carbon-Rich to Carbon-Based Materials Fusion Conference,
Tuning Diradical Character in Diindenoanthracene Fused Diradicals, 2018
The Chair's Achievement Award, University of Wisconsin Eau Claire, 2015
ACS Senior Organic Chemistry Student Award, University of Wisconsin Eau
Claire, 2015

Outstanding Senior Award, University of Wisconsin Eau Claire, 2015

Dr. Jack Pladziewicz Research Scholarship, University of Wisconsin Eau Claire, 2015

Outstanding College Chemistry Student of 2014 – Central Wisconsin Section of the ACS, University of Wisconsin Eau Claire, 2015

Marie and Floy Krause Scholarship, University of Wisconsin Eau Claire, 2013

PUBLICATIONS:

Dressler, J. J.; Barker, J. E.; Hashimoto, H. E.; Karas, L. J.; Kishi, R.; Zakharov, L. N.; MacMillan, S. N.; Gomez-Garcia, C. J.; Nakano, M.; Wu, J. I.; Haley, M. M. Late-stage Modification of Electronic Properties of Antiaromatic and Diradicaloid Indeno[1,2-*b*]fluorene Analogues via Sulfur Oxidation. *Submitted J. Am. Chem. Soc.* **2020**.

Dressler, J. J.; Valdivia, A. C.; Kishi, R.; Rudebusch, G. E.; Ventura, A. M.; Chastain, B. E.; Gomez-Garcia, C. J.; Zakharov, L. N.; Nakano, M.; Casado, J.; Haley, M. M. Diindenoanthracene Diradicaloids Enable Rational, Incremental Tuning of their Singlet-Triplet Energy Gaps. *Chem*, **2020**, *6*, 1-16.

Barker, J. E.; Dressler, J. J.; Valdivia, A. C.; Kishi, R.; Strand, E. T.; Zakharov, L. N.; MacMillan, S. N.; Gomez-Garcia, C. J.; Nakano, M.; Casado, J.; Haley, M. M. Molecule Isomerism Modulates the Diradical Properties of Stable Singlet Diradicaloids. *J. Am. Chem. Soc.* **2020**, *3*, 1548-1555.

Zeidell, A. M.; Jennings, L.; Frederickson, C. K.; Ai, Q.; Dressler, J. J.; Zakharov, L. N.; Risko, C.; Haley, M. M.; Jurchescu, O. D. Organic Semiconductors Derived from Dinaphtho-Fused-*s*-Indacenes: How Molecular Structure and Film Morphology Influence Thin-Film Transistor Performance. *Chem. Mater.* **2019**, *31*, 6962-6970.

Dressler, J. J.; Mitsuru, T.; Espejo, G. L.; Kishi, R.; Takauku, S.; Gomez-Garcia, C. J.; Zakharov, L. N.; Nakano, M.; Casado, J.; Haley, M. M. Thiophene and its sulfur inhibit indenoindenodibenzothiophene diradicals from low-energy lying thermal triplets. *Nat. Chem.* **2018**, *10*, 1134-1140.

Frederickson, C. K.; Barker, J. E.; Dressler, J. J.; Zhou, Z.; Hanks, E. R.; Bard, J. P.; Zakharov, L. N.; Petrukhnina, M. A.; Haley, M. M. Synthesis and Characterization of a Fluorescent Dianthracenoindacene. *Synlett* **2018**, *29*, 2562-2566.

Dressler J. J.; Zhou, Z.; Marshall, J. L.; Kishi, R.; Takamuku, S.; Zhang, Z.; Spisak, S. N.; Nakano, M.; Petrukhina, M. A.; Haley, M. M. Synthesis of 7,12-Dimesitylindeno[1,2-*a*]fluorene, the Sole Unknown Indenofluorene Regioisomer, and Crystallographic Characterization via Its Dianion. *Angew. Chem. Int. Ed.* **2017**, *56*, 15167-15469.

Dressler, J. J.; Miller, S. A.; Meeuwseen, B. T.; Riel, A. M.; Dahl, B. J. Synthesis of dilactone bridged terphenyls with crankshaft architectures. *Tetrahedron* **2015**, *71*, 283-292.

ACKNOWLEDGMENTS

First, I would like to thank Professor Mike Haley, my advisor, for his support, invaluable guidance and his genuine excitement for research. I appreciate the direct and honest feedback, along with the with the spirited personality I could count on through my entire graduate career. The lab environment and culture that we have developed in the last five years is second to none, and the results/success that we have produced over my time in the lab have been more than I think either of us could have asked for.

Additionally, I would like to thank Mike for the many wonderful opportunities I have had to travel the world, they are life experiences that I will never forget and will cherish.

I would like to thank the chemistry front office staff, the instrument support staff and my committee. Thank you to Mike Pluth and Ramesh Jasti for their support and insights. Thank you, Ramesh, for your words of encouragement through my years at UO.

I would also like to thank all of my labmates for making my time in the lab more enjoyable and keeping me sane. Specifically, Dr. Gabe Rudebusch, Dr. Jon Marshall, Dr. Conerd Frederickson, Dr. Chun-Lin Deng, Josh Barker, Jeremy Bard, and Gabrielle Warren. I will never forget how quickly Gabe, Jon, Conerd (and Annie) made me feel at home in the Haley lab and how it made the transition to Eugene easier. I am endlessly grateful for all of the invites during my first summer here. Additionally, I would like to extend a special thank you to Josh Barker for being the other main graduate student on the IF project and for his war-tested friendship. Josh was an excellent labmate, who always made it easy to discuss our work and was the voice of reason when I would be upset about this or that and always gave solid advice on how to proceed. (Bonus shout out to Dr. Brittany White for our many discussions about professional advice and dealing

with troublesome situations). A special thanks to all three of my rotation mentors who each taught me valuable lessons in technique and critical thinking and I strongly believe they helped me build a foundation from which to succeed, Dr. Gabe Rudebusch, Dr. Dan Seidenkranz and Dr. Evan Darzi. I would also like to thank Dr. Jeff Van Raden for being a great friend and a source of advice in my more senior years. Working with undergraduate student Brian Chastain was an incredible opportunity and I would like to thank him for his efforts. Thank you to all other mentees for helping me learn to teach and for dealing with my shortcomings as a mentor: Austin Ventura, Josh Barker, Claire Ottenon, Emily Wearing, and Hannah Hashimoto. I would like to thank Eric Strand for being an awesome undergrad. Without my eye-opening research experience as an undergraduate I would not be here, I thank Prof. Bart Dahl for his support and lunches.

I would like to extend a major thank you to Erik Leonhardt, Dani Hamann, Matt Cerda, Kira Egelhofer for being an amazing cohort and helping me both academically and personally get through my first year of graduate school, without you all I would not have made it. Erik, thanks for struggling through first year with me and for your friendship. Thank you to all my friends above and those I have not covered in any of the categories above: Jenna Mancuso, Dr. Mike Nellist, Turner Newton, Dr. Toby Sherbow, Andy Hicks, Thais de Faria, Cheers to the countless drinks and great fun we had.

Thank you, my partner Lizzie Cochran, for the endless love and unwavering support/help though the end of my graduate career I couldn't have done it without you. I look forward to our future together. I am grateful to my parents, Jay and Becky and the rest of my family for their support. Thank you to my best friends, Ryan Smith and Lyle Paukner for providing a constant escape from the expectations of graduate school.

Dedicated to my parents, and grandparents, my friends and wonderful pets.

TABLE OF CONTENTS

Chapter	Page
I. INTRODUCTION TO DIRADICALS: LEARNING HOW TO TUNE	
DIRADICAL PROPERTIES BY STRUCTURAL REFINEMENT	1
1.1 Authorship Statement.....	1
1.2 Introduction.....	1
1.3 What is Diradical Character?	2
1.4 Project Motivations	5
1.5 First Steps Towards π -Expansion	5
1.6 Inaugural Diradical Studies.....	6
1.7 Blueprint for Stable and Tunable Diradicals	9
1.8 Bridge to Chapter II	11
II.SYNTHESIS OF 7,12-DIMESITYLINDENO[1,2-a]FLUORENE, THE SOLE UNKNOWN INDENOFUORENE REGIOISOMER AND CRYSTALLOGRAPHIC CHARACTERIZATION VIA ITS DIANION.....	
2.1 Authorship Statement and Abstract	12
2.2 Introduction.....	12
2.3 Results and Discussion	15
2.4 Conclusions.....	20
2.5 Experimental Section	20
2.5.1 General Experimental Details	20
2.5.2 Synthetic Details	20
2.5.3 Cs Reduction Details.....	22
2.6 Bridge to Chapter III.....	23

Chapter	Page
III. THIOPHENE AND ITS SULFUR INHIBIT INDENOINDENODIBENZO- THIOPHENE (IIDBT) FROM LOW-ENERGY LYING THERMAL TRIPLETS....	25
3.1 Authorship Statement and Abstract	25
3.2 Introduction.....	26
3.3 Results and Discussion	29
3.4 Conclusions.....	36
3.5 Experimental Section	37
3.5.1 General Experimental Details	37
3.5.2 Synthetic Details	37
3.6 Bridge to Chapter IV.....	41
IV. MOLECULE ISOMERISM MODULATES THE DIRADICAL PROPERTIES OF STABLE SINGLET DIRADICALOIDS.....	42
4.1 Authorship Statement and Abstract	42
4.2 Introduction.....	42
4.3 Results and Discussion	46
4.4 Conclusions.....	54
4.5 Experimental Section	54
4.5.1 General Experimental Details	54
4.5.2 Synthetic Details	55
4.6 Bridge to Chapter V	58
V. DIINDENOANTHRACENE DIRADICALS ENABLE RATIONAL INCREMENTAL TUNING OF THEIR SINGLET-TRIPLET ENERGY GAPS	59
5.1 Authorship Statement and Abstract	59
5.2 Introduction.....	59

Chapter	Page
5.3 Results and Discussion	63
5.4 Conclusions.....	75
5.5 Experimental Section	76
5.5.1 General Experimental Details	76
5.5.2 Synthetic Details	76
5.6 Bridge to Chapter VI.....	89
VI. LATE-STAGE MODIFICATION OF ELECTRONIC PROPERTIES OF ANTIAROMATIC AND DIRADICALOID INDENO[1,2- <i>b</i>]FLUORENE ANALOGUES VIA SULFUR OXIDATION	90
6.1 Authorship Statement and Abstract	90
6.2 Introduction.....	90
6.3 Results and Discussion	93
6.4 Conclusions.....	106
6.5 Experimental Section	106
6.5.1 General Experimental Details	106
6.5.2 Synthetic Details	107
6.6 Bridge to Chapter VII	111
VII. CONCLUSIONS AND OUTLOOK.....	112
APPENDICES	113
A. CHAPTER II SUPPLEMENTARY INFORMATION	113
B. CHAPTER III SUPPLEMENTARY INFORMATION	128
C. CHAPTER IV SUPPLEMENTARY INFORMATION	143

Chapter	Page
D. CHAPTER V SUPPLEMENTARY INFORMATION	159
E. CHAPTER VI SUPPLEMENTARY INFORMATION	207
REFERENCES CITED.....	238

LIST OF FIGURES

Figure	Page
1.1 The electronic structure of Tschitschibabin's hydrocarbon where the ground state is composed of a mixture of the closed shell (1a) and open shell resonance structures (1b). The contribution of the open shell form is described by the diradical character index y . The energy difference between the singlet ground (1b) and triplet excited state (1c) is defined as ΔE_{ST}	3
1.2 Typical examples of recently reported diradicaloids (2-6), drawn in the closed shell resonance form	4
1.3 Molecules synthesized in the Haley lab based on the indeno[1,2- <i>b</i>]fluorene scaffold. Compounds 7 , 8 , 10 , 12 , and 14 do not display diradical character, while compounds 9 , 11 and 13 have been tuned to display pronounced diradical character.....	4
1.4 The blueprint for stable organic diradicals base on the diindenoanthracene scaffold. There are two areas of potential modification (i) altering the core length (shown in blue) and/or (ii) outer arene exchange (shown in orange).	9
1.5 Representative set of molecules that have used diindeno fusion as a method for the production of stable diradicals.	11
2.1 The five regioisomers (1-5) of the indenofluorene family including when isolable derivatives were first reported and calculated y values (PUHF /6-311G*//SF-CL-TDDFT B3LYP/6-311G*) of the parent hydrocarbon.....	13
2.2 NICS(1) (left) and ACID (right) calculations of [1,2- <i>a</i>]IF 6 at the UB3LYP/6-311G* level	16
2.3 Electronic absorption spectrum of [1,2- <i>a</i>]IF 6 in CH ₂ Cl ₂ ; (inset) vertical expansion of the low-energy region of the spectrum.....	18
2.4 (a) ORTEP of the 6 ²⁻ core; thermal ellipsoids at the 40% probability level. (b) Ball-and-stick model of the independent unit of [Cs ₂ ²⁺ (THF) ₂ (6 ²⁻)].....	19
3.1 PAHs with open-shell character a , The electronic structure of open shell PAHs is described by the diradical character index, y , and the energy difference between the singlet ground state and first triplet excited state, $\Delta E(S_0-T_1)$. b , Two recently published examples of OS singlet diradicaloids with thermally accessible triplet states, SHZ 4 and DIAn 5 . c , Complementary strategies used for tuning the diradical character in quinoidal PAHs.	27
3.2 Theoretical assessment of IIDBT. a , Comparison of the spatial distributions of	

Figure	Page
the HOMO and LUMO wave functions for 7 and 10 calculated at the tuned-LC-RBLYP/6-311G(d) level of theory; isosurface value of 0.01 a.u. b , Depiction of the two canonical OS resonance forms between the thiophenes for IIDBT 10	31
3.3 Synthesis of IIDBT and trapping as the dihydro/dideuterio adducts 10cH ₂ /10cD ₂ . Benzothiophene fragments are appended to 12 by a Suzuki-Miyaura reaction to give 13 , followed by saponification and Friedel-Crafts acylation to yield dione 14 . Nucleophilic addition of aryl groups followed by a reductive dearomatization furnishes 10 . If the aryl groups do not provide sufficient steric protection, then the radical centers react to give the dihydro/dideuterio adduct. ..	32
3.4 SQUID magnetic, solid-state and optoelectronic properties of IIDBT. a , Thermal variation of the $\chi_m T$ product of compound 10a in the solid state in the temperature range 100-800 K from SQUID measurements. Solid line is the best fit to the model. b , ORTEP image of 10a with selected bond distances (Å) within the hexacyclic core and thermal ellipsoids drawn with 35% probability level, hydrogens are omitted for clarity. c , Comparison of the electronic absorption spectrum of 5 (green), 7 (black), 9 (red) and 10a (blue) in CH ₂ Cl ₂ . d , Room temperature solid-state 785 nm Raman spectra of 9 (red), 10a (blue), and 10cH₂ (black).	33
4.1 Chemical structures of <i>anti</i> -IIDBT (1) and <i>syn</i> -IIDBT (2). All canonical forms possess 2,6-naphtho conjugation (bold bonds). In boxes, linear conjugation (left, Li and Lk) vs cross conjugation (right, Ci and Ck) dispositions of the labeled <i>ijkl</i> atoms where delocalization of the radical centers to the <i>k</i> atoms disrupts thiophene aromaticity	43
4.2 Diradical resonance forms of the hydrocarbon core of the two known dibenzoheptazethrene regioisomers	45
4.3 <i>Anti</i> and <i>syn</i> IIDBT derivatives studied in this work.....	46
4.4 Odd-electron density maps for 1a (left) and 2a (right) with contour value 0.0005 au calculated at the tuned-LC-RBLYP-CASCI(2,2)/6-311G* level. Mulliken population analysis for the odd-electron density on the relevant carbon and sulfur atoms of the linear and cross-conjugated paths is shown on top.....	47
4.5 (a) Molecular packing of 2b with the ellipsoids drawn with 50% probability level; hydrogens are omitted for clarity. (b) Experimental (black) bond lengths for the core motifs of 2b and 1a along with the calculated (blue) values for 2a and 1a	49
4.6 Bisphenylenyl-fused indacene (6) and indenoindene (7) for comparison	50

Figure	Page
4.7 Electronic absorption (in CH ₂ Cl ₂ , top) and Raman spectra (in the solid state with 1064 nm laser excitation, bottom) of 1a (red) and 2a (blue). Raman spectrum of aromatized 2cH2 is in black.	51
4.8 (Top) Variable-temperature ¹ H NMR spectra (in 1,2-C ₆ D ₄ Cl ₂) of 2a . (Bottom) SQUID magnetometry data of 1a,1b and 2a,2b ; for 1b and 2b the data for the heating and cooling curves are denoted by squares and circles, respectively.	52
5.1 Examples of Known Diradicaloid Molecules (A) The first two reported carbon-centered diradicaloids in the literature, Theile's (1) and Tschitschibabin's (2) hydrocarbons, drawn in the closed-shell resonance form. (B) Representative examples of recently reported diradicaloids (3–8), drawn in the closed-shell resonance form (Mes = 2,4,6-trimethylphenyl).	61
5.2 Diradicaloid Molecules Based on the diindeno[1,2-b:1',2'-g]anthracene Scaffold (A) Target DIAn compounds 9–13 illustrate how incremental changes to the diradical scaffold can result in significant changes to the overall magnetic properties of each molecule.(B) Closed shell (left), open shell singlet (center), and open shell triplet (right) forms of a DIAn derivative with generic fused aryl groups; the 2,6-anthraceno conjugation of the two radical centers is shown by the bolded bonds.	62
5.3 Odd Electron Density Maps and NICS(1) Values of Models 9'–13'. Odd-electron densities were calculated at the tuned-LC-RBLYP CASCI(2,2)/6-311G* level.Magnetic response calculations were performed at the LC-UBLYP/6-311G* level where the same range-separating parameters as those for the estimation of physical parameters were employed (for details, see Appendix D). Yellow surface of odd-electron density map represents the isosurface with the contour value of 0.0005 a.u. NICS(1) values are in ppm.	65
5.4 Variable temperature NMR spectroscopy studies of 12. VT ¹ H NMR spectra of the aromatic region of <i>anti</i> -dibenzoDIAn 12 in CDCl ₃ showing thermal depopulation of the paramagnetic triplet state at low temperatures.	69
5.5 X-ray crystallographic analysis of 9–13. X-ray structures of DIAn derivatives 10-13 with selected bond lengths (Å; experimental values in black, calculated values in blue) along with the previously published data for DIAn 9 ; ellipsoids drawn at the 50% probability level. Experimental values for 12 and 13 are the average of the bond lengths found for the three and two symmetrically independent molecules, respectively.	70
5.6 Spectroscopy and magnetometry Data of 9–13. (A) Electronic absorption spectra of DIAn derivatives 9-13 in CHCl ₃ solution at room temperature.	

Figure	Page
(B) Raman spectra of 9-12 and comparison with the dihydroDIAn precursors 25 and 28 . (C) Raman spectra of 13 and comparison with 9 and the naphthalene core analogue 5 . (D) SQUID data of 9-13 in the solid state (empty circles) along with the corresponding Bleaney-Bowers fits (solid lines).	72
6.1 New IDBTs 1 and 2 , known IIDBTs 3 and 4 , their sulfone analogues 5-8 , and decomposition product 9	92
6.2 (Top) Proton NMR spectra of the aromatic region of IDBTs 1 and 2 and the corresponding sulfones 5 and 6 . The central proton (*) displayed in bold in the structures on the left can be used as to roughly assess antiaromaticity. (Bottom) NICS-XY scans for IDBTs 1 and 2 and sulfones 5 and 6 along with the scan for the parent <i>s</i> -indacene, in order of most to least paratropic; for clarity the ring labels are shown above in the structure of 5	96
6.3 Selected resonance forms for the hydrocarbon dianion reference analogues of (a) <i>syn</i> -IDBT 2 and (b) <i>anti</i> -IDBT 1 ; boxed structures are the dominant resonance forms recognized by NBO.	97
6.4 Natural population analyses (NPA) charges for <i>s</i> -indacene	97
6.5 Electronic absorption spectra of the three stable sulfones 5 , 6 , and 8 and their parent thiophenes 1 , 2 , and 4 in CHCl ₃ at room temperature. The spectrum of each sulfone is a similar color to the parent compound, with the sulfone having the lighter hue	99
6.6 Cyclic voltammograms of 5 , 6 and 8	101
6.7 X-ray structures of (left to right) sulfone derivatives 5-Mes , 6 , and 8 and decomposition product 9 with selected bond lengths (Å; experimental values in black, calculated values in blue); ellipsoids drawn at the 50% probability level. Experimental numbers for 6 represent the average value from two crystallographically independent molecules.	102
6.8 Generalized structures displaying the “normal” bonding pattern observed in most indeno[1,2- <i>b</i>]fluorene-based molecules and the “flipped” bonding pattern observed for sulfones 5 , 6 and 8 . (Bottom) NICS-XY scans of both <i>anti</i> -IDBT- <i>S</i> geometries where 5 is the observed bond-flipped orientation and 5* is the normally observed bonding pattern.....	103
6.9 (Top) Variable temperature ¹ H NMR spectra of the aromatic region of 8 in 1,1,2,2-tetrachloroethane- <i>d</i> ₂ . (Bottom) SQUID magnetometry data for 8 in the solid state (circles) along with the corresponding Bleaney-Bower fits (solidlines).....	105

LIST OF TABLES

Table	Page
6.1 Cyclic voltammetry data for thiophenes 1 , 2 and 4 and sulfones 5 , 6 and 8	101
A1. Diradical character indices γ for the five parent IF regioisomers 1-5 calculated at the PUHF/6-311G*//SF-CL-TDDFT B3LYP/6-311G* level of approximation.	117
A2. C –C bond lengths (Å) of dimesityl[1,2- <i>a</i>]IF 6 optimized for the singlet (S) And triplet (T) states at several levels along with numbering scheme.	118
A3. Excitation properties (excitation wavelength λ and oscillator strength f) of Triplet 6 calculated at the TD-UB3LYP/6-311G* level.	121
B1. Theoretically Estimated γ and ΔE_{S-T} Values of Compounds 6-11. Zero-point vibration energy correction was estimated from the frequency analysis at the R(U)B3LYP/6-311G* level of approximation.	135
B2. Physical Parameters calculated by the CASCI (2,2) method using the MOs obtained by tuned-LC-RBLYP/6-311G(d) calculation.	135
B3. Comparison of bond lengths (Å) of selected bond lengths between 6 and 9	136
B4. Comparison of bond lengths (Å) of selected bond lengths between 7 and 10	137
B5. Comparison of bond lengths (Å) of selected bond lengths between 8 and 11	137
B6. Singlet–Triplet gap (ΔE_{S-T}) and Each Physical Parameter Calculated by the CASCI(2,2) Method Using the UNOs Obtained by UHF/6-311G(d) calculation.	139
C1. Summary of calculations results for 1a and 1s	149
D1. Summary of calculation results for compounds 9-13 when R = H.	176
D2. Summary of calculation results for compounds 9-13 when R = CCSiMe ₃	177
D3. Summary of calculations for bisphenylenyl fused derivatives (BPLA)..	179
D4. Redox potentials (V) for compounds 9-13 analyzed by cyclic voltammetry and the corresponding CV and optically-determined energy gaps (eV).	204
E1. Calculated optical data and HOMO-LUMO energy gaps for compounds 1-8	217

Table	Page
E2. Summary of calculation results for γ and singlet-triplet energy gap.	225

LIST OF SCHEMES

Scheme	Page
1.1 Synthetic route used to reach DIAn (9) on the gram scale	7
2.1 Synthesis of indeno[1,2- <i>a</i>]fluorene 6 and formation of the dianion-based complex [Cs ₂ ²⁺ (THF) ₂ (6 ²⁻)] (see Figure 2.4 for its complete structure).	17
4.1 Synthesis of <i>syn</i> -IIDBTs 2 including dihydro-products.	48
5.1 Synthesis of diindeno[1,2- <i>b:l'</i> ,2'- <i>g</i>]anthracenes 9–13 (A) Friedel-Crafts acylation route to prepare 9 , 12 , and 13 , which has been successfully executed with the cross-coupling partners on the bottom left of the scheme. (B) Friedel-Crafts alkylation route to prepare 10 and 11	67
6.1 Synthesis of IDBTs 1 , 2 and IIDBT 3 , 4 and their conversion to the respective sulfones 5-8 along with formation of decomposition product 9	94

CHAPTER I

INTRODUCTION TO DIRADICALS: LEARNING HOW TO TUNE DIRADICAL PROPERTIES BY STRUCTURAL REFINEMENT

1.1 Authorship Statement

This chapter includes soon to be submitted for publication and co-authored material from: Dressler, J. J.; Haley, M. M. Learning How to tune diradical properties by structural refinement. *J. Phys. Org. Chem.* To be submitted: **2020**. Further permission related to the use of the material excerpted in this chapter should be directed to Wiley-VCH (assuming publication). This manuscript was written solely by myself and editorial assistance was provided by Prof. Mike Haley.

1.2 Introduction

Graduate students and weathered professors alike lament that there is a great deal of luck and serendipity involved in the success and direction of their research. This cliché, while trite to some, is still very much true and can shape the directionality of many scientists' careers. Unsurprisingly, serendipity has played a large role in the Haley lab's entrance into and now detailed involvement in the field of stable organic diradicals. In 2016 when we reported the first stable organic diradical from our lab based on the diindenoanthracene (DIAn) scaffold,^[1] searching for novel ways to make durable diradicals was not the motivation behind synthesizing DIAn. In fact, when the ultimately successful synthetic route was conceived in late 2014, there was no real intention of becoming a player in the challenging and intellectually stimulating field of organic diradicals. In reality the motivation behind the project stemmed from a simple question that would further the research interests of the lab at the time: "What would happen to a molecule's optoelectronic properties if the benzene core of indeno[1,2-*b*]fluorene ([1,2-*b*]IF, **7**) was π -expanded to naphthalene and/or anthracene?". Having explored a substantial degree of chemical space around the benzene-cored indenofluorene family,^[2] this question seemed to provide an interesting and potentially productive avenue of research to delve into. But before beginning a discussion on the Haley lab's entry into the

field of diradicals, we must first define and understand the unique properties of diradicals.

1.3 What is Diradical Character?

While there is some disagreement in the literature on the exact definition of a diradical molecule, we define a diradical based on the criterion put forth by Abe:^[3] *a molecule in which there are two unpaired electrons (radicals), in which these radicals have a dipole-dipole interaction large enough to produce two spin states, namely, singlet and triplet states (spin states), due to the small interaction distance between the radicals.* If the electron exchange interaction between the two unpaired electrons is negligible because of a large distance between the two electrons, then the compound is instead defined as a biradical.^[3] The unique nature of diradical compounds comes as a function of the uncommon open-shell and closed-shell resonance structures that these molecules possess in their ground state.^[3,4] This concept can be better understood by examining one of the first reported diradicals, a molecule commonly known as Tschitschibabin's hydrocarbon^[5] (**1**, Figure 1.1). Hydrocarbon **1** can exist either in the closed-shell resonance form **1a** or in the open-shell resonance form **1b**, where both resonance forms contribute to the overall nature and properties of the ground state. The switching between resonance structures results in breaking of the exocyclic π -bonds and leads to the formation of two aromatic benzene rings. This process is commonly described as a recovery of aromatic Clar sextets^[6] and is often used to rationalize the drive for diradical compounds to exist in the open-shell form.^[7] To describe the contribution of the open shell resonance form to the overall ground state of the diradical, the diradical character index (y) is used. This term, simply put, expresses how diradical a compound is. The diradical character index is a computational value based on the natural orbital occupation number (NOON) analysis of the lowest unoccupied natural orbital.^[8] The index y can range in value between 0 and 1, where a value of $y=1$ is a purely open-shell/diradical compound and a value of $y=0$ is completely closed shell. In practice, most reported diradicals have a y value somewhere between 0.5 and 0.99, and molecules that have y indices below 0.4 often display few if any properties associated with diradical character.

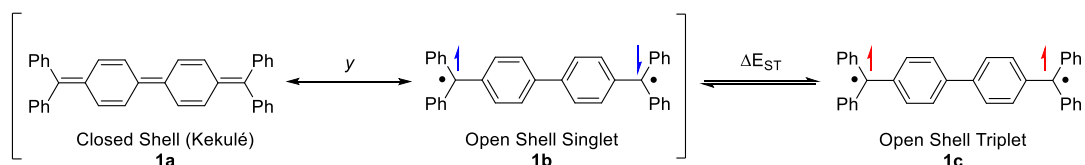


Figure 1.1 The electronic structure of Tschitschibabin's hydrocarbon where the ground state is composed of a mixture of the closed shell (**1a**) and open shell resonance structures (**1b**). The contribution of the open shell form is described by the diradical character index y . The energy difference between the singlet ground (**1b**) and triplet excited state (**1c**) is defined as ΔE_{ST} .

To add to the complexity, when a compound displays diradical character the two electrons can exist either in a spin paired singlet state (**1b**) or a spin parallel triplet state (**1c**), and the energy it takes to go from the singlet to triplet state is known as the singlet-triplet energy gap (ΔE_{ST}). Due to the double-spin polarization effect,^[9] the vast majority of diradicals possess a ground state singlet with a thermally accessible triplet state;^[3] however, there is a only small number of ground state triplet diradicaloids.^[10] Furthermore, there is a qualitative relationship that exists between diradical character and the singlet-triplet energy gap, in that as the diradical character of a compound increases the ΔE_{ST} decreases. While this rule of thumb applies for most diradicals, this relationship is only strictly quantitative in the case of a molecule with a y value equal to 1, where the ΔE_{ST} gap is equal to zero.^[11]

Fueled by a fundamental interest in their unique ground and magnetic states and a desire to understand these fickle compounds better, there have been many classes of carbon-based diradicaloids (Figure 1.2) developed/explored in the last 12-15 years, including but not limited to zethrenes^[7a,12] (**2**), anthenes^[13] (**3**), bisphenalenyls^[14] (**4**), extended quinodimethanes^[15] (**5**), higher-order acenes^[16] (**6**), indenofluorenes^[10a,17] and related diindenoacenes,^[1,11,18] the last of which are the focus of this dissertation (see Figure 1.3). The diagnostic properties of diradicals, which arise from the unique combination of closed- and open-shell resonance forms, can include: narrow HOMO-LUMO energy gaps,^[7c,19] low-energy electronic absorptions due a low-lying doubly excited electronic configuration,^[20] redox amphoterism,^[14c,19a] electron spin resonance (ESR) signals and/or a magnetic response in a superconducting quantum interference device (SQUID) magnetometer,^[18d] multicenter bonding,^[14a,21] substantial two-photon absorption cross-sections^[22] and peak broadening or sharpening in the proton NMR

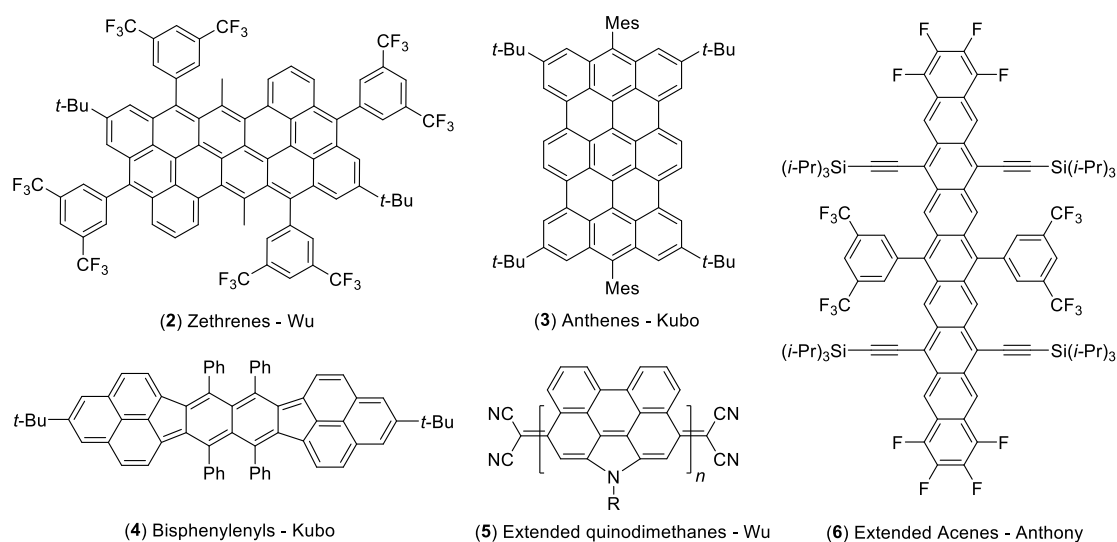


Figure 1.2 Typical examples of recently reported diradicaloids (**2-6**), drawn in the closed shell resonance form.

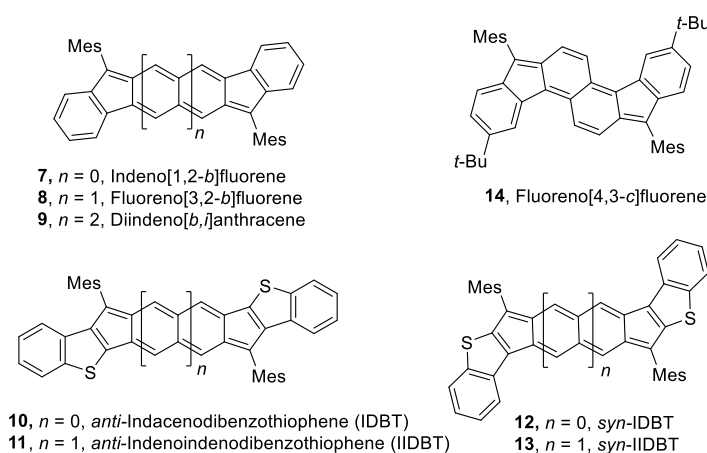


Figure 1.3 Molecules synthesized in the Haley lab based on the indeno[1,2-*b*]fluorene scaffold. Compounds **7**, **8**, **10**, **12**, and **14** do not display diradical character, while compounds **9**, **11** and **13** have been tuned to display pronounced diradical character.

spectrum due to the thermal equilibrium of the spin states. Because of these unusual properties, the diradical hydrocarbons listed above have been earmarked for various applications such as molecular electronics^[3] and spintronics,^[23] lithium-ion batteries,^[24] nonlinear optics,^[25] and singlet fission.^[26] Plagued by the high reactivity and low modularity of currently available diradicals, their full potential in materials applications has yet to be realized, despite the many posited breakthrough uses. Nonetheless, there

have been some preliminary device applications of diradicals^[25d] in areas such as organic field effect transistors (OFETs),^[27] near-infrared absorption dyes,^[28] and singlet fission applications.^[29] These latter examples provide a beacon of hope for the eventual widespread implementation of diradicals into materials.

1.4 Project Motivations

When we entered the field of organic diradicals, there was a clear abundance of interest in discovering new examples; however, we realized that, while there was this booming increase in the number of reported carbon-based diradicals, there were very few cases in which subsequent structural modification was made to the originally reported scaffold aimed at altering its optical and magnetic properties. This lack of systematic modification of the diradical character and singlet-triplet energy gap set the stage for our group's mentality and efforts in the area of diradical research. We wanted to gain a fundamental understanding of the inherent electronic and magnetic properties of open shell compounds. We felt that in order to harness the full potential of diradicals in meaningful application, specifically those applications wishing to exploit the unique spin-states that diradicals possess, the ability to control and manipulate the diradical character and the related ΔE_{ST} gap with precision would be paramount. This key guiding principle of learning to fine-tune molecule properties in a systematic way has been the unifying theme of the Haley lab's research on diradicals for the last five years.

1.5 First Steps Towards π -Expansion

For our initial attempts at answering the question, "What would happen to the optoelectronic properties if the core of [1,2-*b*]IF (**7**) was π -expanded?", we prepared in 2012 our first fluorenofluorene (FF) derivative, which is based on a central naphthalene.^[30] Starting from a known dione, addition of mesityllithium followed by a SnCl₂-mediated reductive dearomatization afforded deep blue fluoreno[4,3-*c*]fluorene **14**. Importantly, this result showed that we could successfully synthesize π -expanded systems in a manner analogous to the [1,2-*b*]IFs.^[31] Despite its S-shaped geometry, the absorption spectrum of [4,3-*c*]FF was strikingly similar to the "parent" [1,2-*b*]IF, albeit with the expected red-shift of the low energy absorptions (515 nm in **7** to 649 nm in **14**) due to the

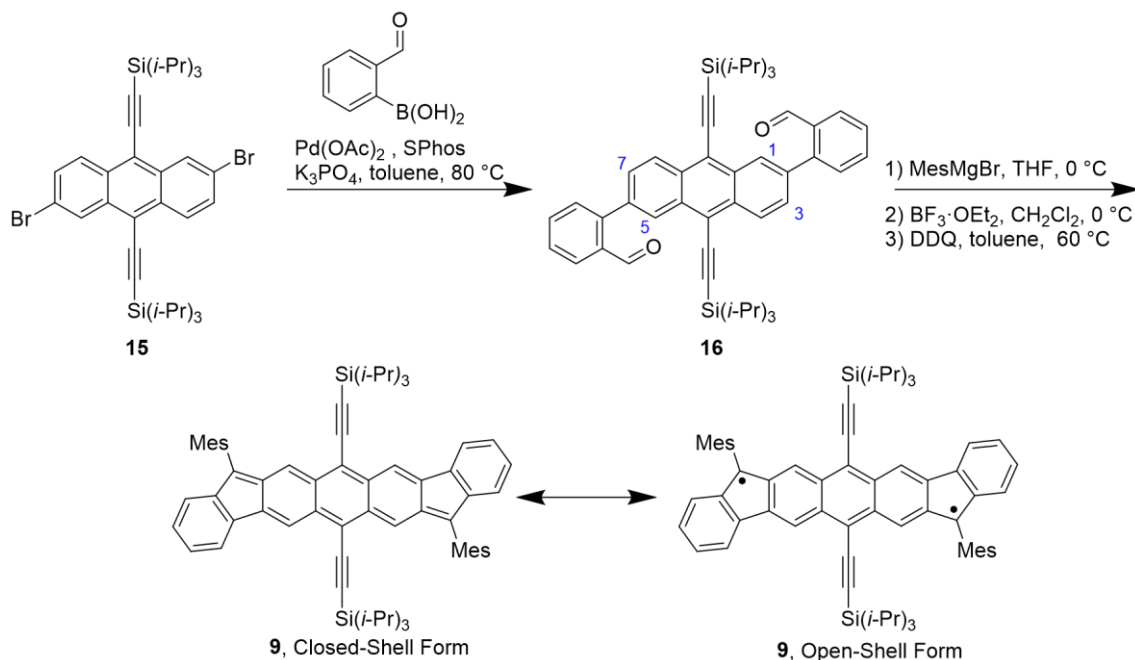
expanded nature of the π -system. The CV data showed that **14** displayed redox amphoterism like [1,2-*b*]IF **7**,^[31] with a narrow electrochemical energy gap of 1.69 eV (vs. 2.22 eV for **7**).^[30] As we noted at the time, despite its structural similarity to compounds displaying open-shell character, a lack of line broadening in the variable temperature (VT) proton NMR spectrum (up to 160 °C) and the lack of an EPR signal of the powder and solution sample established the closed-shell nature of fluoreno[4,3-*c*]fluorene.

As a quick aside, aided by the disclosure of a key bistriflate intermediate by the McCulloch group,^[32] we recently returned to the fluorenofluorene arena and successfully prepared the linearly-fused, π -expanded [1,2-*b*]IF analogue, fluoreno[3,2-*b*]fluorene **8**.^[33] Despite the different mode of fusion of the indene units to the central naphthalene, this work led to the same conclusions experimentally and computationally as the [4,3-*c*]FF study, in that the observed structural and optical properties of [3,2-*b*]FF **8** were consistent with a quinoidal core, i.e., a closed-shell molecule. Given that the changes to molecule properties were relatively modest for **8** and **14**, we were curious whether an anthracene as the core motif would have a greater effect on the overall properties. Fortuitously, we unearthed profound changes to the properties of the anthracene-cored analogue of [1,2-*b*]IF and along with it a new research direction of stable diradical hydrocarbons.

1.6 Inaugural Diradical Studies

The breakthrough result was the isolation and characterization of a diindeno[*b,i*]anthracene (DIAn) derivative, as the open-shell molecule that combined moderate diradical character ($y = 0.62$) with high chemical stability (half-life ~2 months in solution and indefinitely stable in the solid state).^[1] Admittedly, we had started work on the molecule in late 2012 but it took until 2016 to bring this to fruition. As was the problem with linear [3,2-*b*]FF **8**, creating an anthracene derivative with the requisite 2,3,6,7-substitution pattern is non-trivial. To add to the complexity, for a successful synthesis, the 2,6-substituents (e.g., halogens/triflates for cross-coupling) must be different from those on the 3,7-positions (e.g., aldehydes/esters/acids for subsequent Friedel-Crafts reactions). Graduate student Gabe Rudebusch took on this challenge in fall 2014 and devised the synthetic route in Scheme 1.1. Gabe identified the need for kinetic

stabilization at the areas of high spin density (primarily the apical carbons in the five-membered rings) by using bulky mesityl groups orthogonally oriented to the conjugated scaffold and bulky triisopropylsilyl (TIPS) groups on carbons 9 and 10 to enhance the solubility of the large polycyclic hydrocarbon (PCH) as well as to inhibit endoperoxide formation across the anthracene core which very often leads to decomposition pathways.



Scheme 1.1 Synthetic route used to reach DIAn **9** on the gram scale.

Starting from known dibromide **15** (Scheme 1.1), Suzuki cross-coupling gave dialdehyde **16** that was then treated with mesitylmagnesium bromide to furnish an intermediate diol (not shown). To his credit, Gabe recognized that the steric bulk of the TIPS and mesityl groups were paramount in the directionality of the Friedel-Crafts alkylation reaction, as the steric clash blocked the undesired ring closure at the electronically favored 1/5-positions of the anthracene core and instead led to closure at electronically disfavored carbons 3 and 7 (blue numbers Scheme 1.1). We know that steric clash is key in this step as replacement of the mesityl group with smaller phenyl rings does give 1,5-ring closure (determined by x-ray), whereas use of the electron-poor pentafluorophenyl motif shuts down Friedel-Crafts reactivity altogether.^[34] Oxidation

with DDQ furnished DIAn **9** as deep violet crystals. Notably, these reactions could be performed on the gram scale with no need for column chromatography.

With an ample supply of **9** in hand, we performed a variety of spectroscopic experiments that can suggest the presence of an open-shell resonance contribution to the molecule. The low energy absorption in the UV-Vis spectrum was significantly red shifted ($\lambda_{\text{max}} \sim 700$ nm) due to the π -extended nature of the core. Additionally, a weak shoulder appeared 775 nm that extends to the near-IR region, which is indicative of the symmetry-forbidden transition typical of diradical compounds. Cyclic voltammetry (CV) displayed two reversible oxidation and reduction peaks, indicative of the amphoteric redox character that DIAn possess. Moreover, the CV data gave rise to a narrow HOMO-LUMO energy gap of 1.45 eV, which is very small for a PCH with no electron withdrawing units, hinting at diradical behavior. Examination of the x-ray crystal structure of DIAn revealed that the bond length from the apical carbon (sp^2 center) of the five-membered ring to the central anthracene core was 1.406 Å, which is roughly the mean value of the analogous bond lengths in closed-shell [1,2-*b*]IF (1.381 Å) and open-shell [2,1-*b*]IF (1.437 Å).^[17] This bond length suggests that the open-shell resonance structure is contributing to the overall ground state of DIAn, as the open-shell form has single bond character in this key position, elongating the bond length.

To cement the diradical nature of DIAn, we turned to experiments that would confirm its magnetic properties. The room temperature proton NMR spectrum of **9** showed relatively well resolved aromatic signals that further sharpened upon cooling to –25 °C due to depopulation of the triplet state. On the other hand, heating the sample broadened the aromatic proton resonances, which by 150 °C had essentially disappeared into the base line. Importantly, the aromatic resonances return upon cooling back to room temperature, with no evidence of decomposition. To experimentally measure the singlet-triplet energy gap, we utilized SQUID magnetometry, where a powder sample of DIAn was heated from 4 to 400K while monitoring the magnetic response of the sample. SQUID allowed us to experimentally track the small change in magnetism that arises from switching from the singlet to triplet state. Fitting the raw data using the Bleaney-Bowers equation^[35] gave an experimentally determined ΔE_{ST} of –4.2 kcal mol⁻¹, which was in good agreement with the calculated value of –4.9 kcal mol⁻¹.^[36]

1.7 Blueprint for Stable and Tunable Diradicals

After reporting DIAn in 2016, we realized we had a unique opportunity to push the boundaries of organic diradicals in a systematic way. Looking at its construction, the DIAn scaffold provided both a relatively easy to modify system and, just as importantly, a blueprint for stable diradicals with two customizable positions: (i) the size of the acene core and (ii) exchange of the outer benzenes with other fused arenes (Figure 1.4).

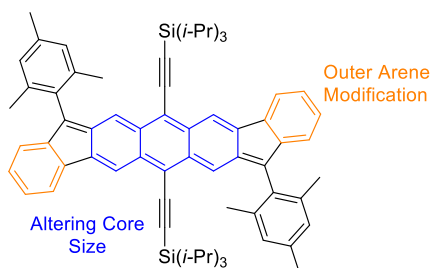


Figure 1.4 The blueprint for stable organic diradicals base on the diindenoanthracene scaffold. There are two areas of potential modification (i) altering the core length (shown in blue) and/or (ii) outer arene exchange (shown in orange).

Fortunately, in our original pursuit of π -expanding the [1,2-*b*]IF core we had already inadvertently performed a study on how changing the conjugation pathway between the radical centers affected the diradical character index and the singlet-triplet energy gap. What we observed were overall large-scale changes in y and ΔE_{ST} . As you increase the size of the acene core (point (i) above) from benzene (**7**, $y = 0.24$, $\Delta E_{ST} = -19.4$ kcal mol⁻¹) to naphthalene (**8**, $y = 0.49$, $\Delta E_{ST} = -10.3$ kcal mol⁻¹) up to anthracene (**9**, $y = 0.62$, $\Delta E_{ST} = -4.7$ kcal mol⁻¹), the diradical character of the molecule increases to the point of being experimentally observable and the singlet-triplet energy gap decreases, as experimentally determined by SQUID. Gratifyingly, these results match other groups studies on altering the conjugation distance between the two distinct radical centers in other PCH diradicals such as zethrenes,^[12a] bisphenalenyls^[4a] and the indeno[2,1-*b*]fluorene analogues.^[17,18b] While this trend of increased core size leads to enhanced diradical character is a fundamentally important steppingstone, it only provides the ability to perform a “course shim” on the overall properties of the diradicals. With both the FF and DIAn scaffolds, we also have the ability to alter potential diradical properties through

outer arene exchange, as judicious choice of these external arenes should enable a systematic study where we can perform a “fine shim” in adjusting y and ΔE_{ST} .

It is important to point out that the purposeful choice of using indene (or “indeno”) units as the fused groups on DIAn has led to the discovery of another design principle for stable organic diradicals. While we were one of the first groups to do so, diindeno-fusion on either side of a pro-aromatic core, in our case an anthracene, has become a popular strategy towards producing diradical PCH that are robust enough to be isolated and further studied (Figure 1.5). In the last five years there have been reports of diindenopicyrenes (**17**)^[37] diindeopyrenes (**18**)^[38], diidenobischrysenes (**19**)^[39], diindenophenanthrenes (**20**)^[40], and diindenocorannulenes(**21**)^[41], all of which possess diradical character once the central π -system has been capped with two indeno units. Interestingly enough, recently reported diindenophenanthrene (DIPh) is actually a constitutional isomer of DIAn, where the fusion pattern of the three central benzenes is the main structural difference between the two diradicals. The change in the way that the benzenes are linked through the core does not lead to a significant difference in how diradical DIPh is when compared to DIAn; however, the singlet-triplet energy gap was reduced to $-1.43 \text{ kcal mol}^{-1}$ for DIPh, as found experimentally by ESR. Furthermore, in the recent disclosure of diindeocorannulene (DIC), the Cao group reported two different DIC isomers (DIC-1 and DIC-2) with which they were able to tune the diradical character and ΔE_{ST} through molecule isomerism, a strategy that we have employed ourselves as seen in Chapter IV where we compared *anti* and *syn*-IIDBT, compounds **11** and **13**, respectively. The aim of this thesis is to perform the “fine shim” adjusting of the diradical character and the closely related singlet-triplet energy gap utilizing the blueprint for stable diradicals that DIAn provides (Figure 1.4). The various methods for fine tuning the diradical character and ΔE_{ST} in our systems, such as: heteroatom incorporation, molecule isomerism, judicious outer arene exchange and post-synthetic modification can be further explored by reading Chapters II–VI, a sampling of the molecules used to carry out these studies can be seen in Figure 1.3.

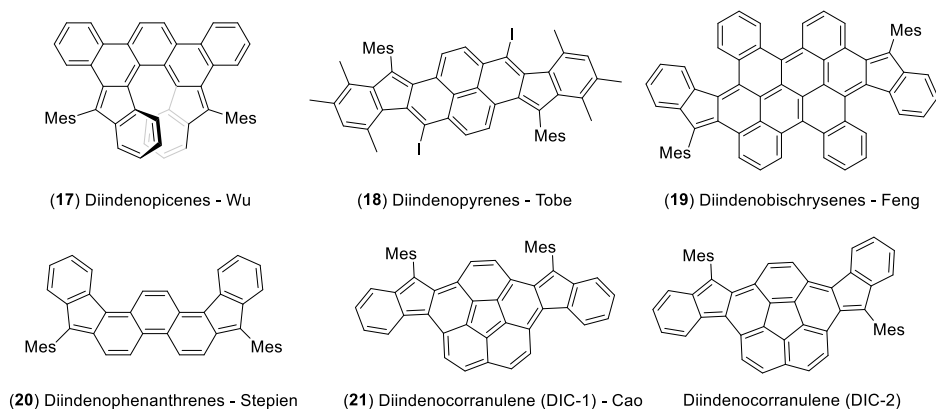


Figure 1.5 Representative set of molecules that have used diindeno fusion as a method for the production of stable diradicals.

1.8 Bridge to Chapter II

The work in this chapter was a summary of the Haley research group's introduction and early progress in the field of organic diradicals. The discovery of diindenoanthracene opened the doors to many projects involving diradicals in the Haley lab. The work highlighted in this chapter is a summation of the Haley group's contributions to organic diradical before I joined the lab in 2016. The next chapter and all the subsequent chapters will focus on the work that I have done to expand upon the understanding and potential usefulness of organic diradicals throughout my own graduate career.

CHAPTER II

SYNTHESIS OF 7,12-DIMESITYLINDENO[1,2-*a*]FLUORENE, THE SOLE UNKNOWN INDENOFUORENE REGIOISOMER AND CRYSTALLOGRAPHIC CHARACTERIZATION VIA ITS DIANION.

2.1 Authorship Statement and Abstract

This chapter includes previously published and co-authored material from: Dressler, J. J.; Zhou, Z.; Marshall, J. L.; Kishi, R.; Takamuku, S.; Wei, Z.; Spisak, S. N.; Nakano, M.; Petrukhina, M. A.; Haley, M. M. *Angew. Chem. Int. Ed.* **2017**, *56*, 15167-15469. Further permissions related to the use of the material excerpted in this chapter should be directed to Wiley-VCH. This manuscript was written by myself with editorial assistance from Prof. Mike Haley, Prof. Marina Petrukhina and Dr. Jon Marshall. The experimental work presented in this chapter was carried out by myself, Zheng Zhou and Dr. Jon Marshall.

Of the five possible indenofluorene regioisomers, examples of a fully conjugated [1,2-*a*]IF scaffold have so far remained elusive. This work reports the preparation and characterization of 7,12-dimesitylindeno[1,2-*a*]fluorene as a highly reactive species. Experimental and computational data support the notion of a molecule with pronounced diradical character that exists in a triplet ground state. As such, both NICS and ACID calculations suggest that the [1,2-*a*]IF scaffold is weakly Baird aromatic. Reduction of the unstable red solid with Cs metal produces the dianion of the title compound, from which single crystals could be obtained and X-ray data acquired, fully corroborating the proposed indeno[1,2-*a*]fluorene hydrocarbon core.

2.2 Introduction

The past decade has seen a resurgence of interest in polycyclic antiaromatic hydrocarbons (PAAHs) as potential small molecule semiconductors for use in organic electronics.^[1] Compared with the more commonly studied polycyclic aromatic hydrocarbons (PAHs),^[2] the inherently low HOMO/LUMO energy levels and small energy gaps of PAAHs make them ideal complements for acenes in materials

applications.^[3] Since 2010 our group^[4] and others^[5,6] have investigated a class of PAAHs based on the fully conjugated indenofluorene (IF) scaffold (**1-5**, Figure 2.1). Inclusion of the two five-membered rings within the conjugated skeleton has shown promise as a method to stabilize against oxidative and photolytic degradation. Additionally, their inclusion enhances the electron-accepting capabilities of the molecules,^[7] leading to the examination of IFs and their congeners as possible n-type or ambipolar organic semiconductors.^[6e,f,8] The overall $4n$ π -electron count (making the molecules formally antiaromatic) and the potential to form an open-shell diradical resonance structure (inherent to all IFs) have also fueled interest in these compounds and their derivatives from a basic science standpoint.^[8b,c,9]

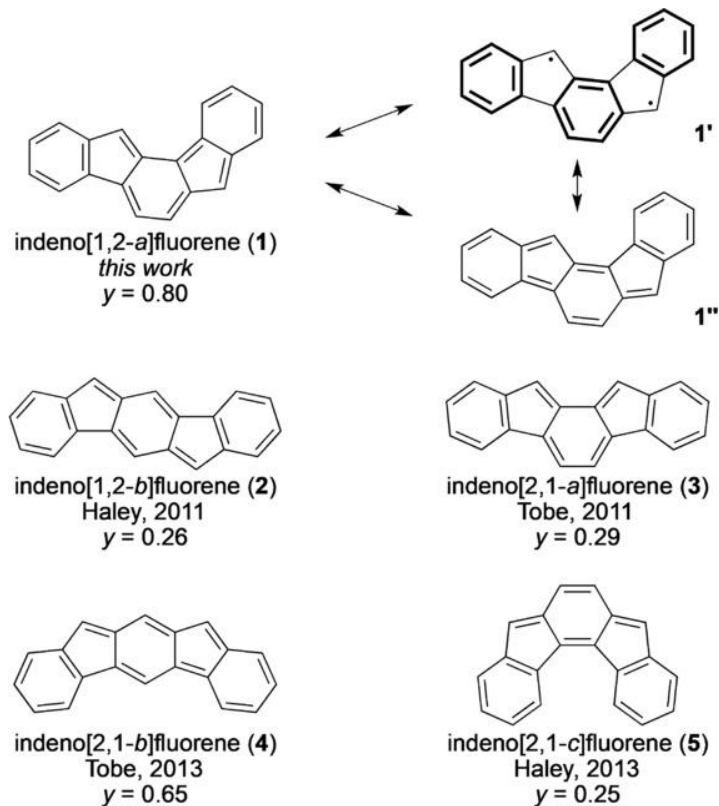


Figure 2.1 The five regioisomers (**1-5**) of the indenofluorene family including when isolable derivatives were first reported and calculated y values (PUHF/6-311G**//SF-CL-TDDFT B3LYP/6-311G*) of the parent hydrocarbon.

Recently the synthesis and study of diradical compounds has garnered renewed attention as these species could be useful as promising materials in molecular spintronics, non-linear optics, and singlet fission.^[10] The contribution of the open-shell form to the

ground state structure is described by the diradical character index,^[11] y , with $y = 1$ defining a pure open-shell (OS) system and $y = 0$ describing a pure closed-shell (CS) system.^[9b,k] With the potential to re-aromatize the quinoidal motif (e.g., **1**, **1'**) to a diradical structure (e.g., **1''**), indenofluorenes make an interesting case study. The five IF regioisomers^[12] result in a wide range of computed diradical character values from $y = 0.25$ for indeno[2,1-*c*]fluorene **5** to as large as $y = 0.80$ for indeno[1,2-*a*]fluorene **1** (Figure 2.1 and Table A1 in Appendix A).^[13]

The large differences in y values for the IF regioisomers can be rationalized by examining the number of Clar sextets^[14] in the OS and CS resonance structures, along with the orientation of the radicals in relation to the central benzene unit in the OS form. IFs with two Clar sextets in the CS form and three in the OS resonance structure exhibit only a modest gain in stability of one additional Clar sextet in the OS form, resulting in IFs with low diradical character (**2**, **3**, **5**). These three isomers also have either an *ortho*- or *para*-quinodimethane subunit at the central six-membered ring, permitting easy return to the CS form.^[12a,b,d] In contrast, IFs with only one Clar sextet in the CS state (**1** and **4**) gain two additional aromatic Clar sextets by converting to the OS form, which provides a significant driving force to exist in the OS state and thus leads to much larger y values.^[12c] Additionally, the increased diradical character in **1** and **4** compared to the other regioisomers is in part due to the *meta*-quinodimethane subunit present in the IF core, which makes the return to the CS state challenging. Despite intensive research efforts directed toward the IF family over the last seven years, a fully conjugated indeno[1,2-*a*]fluorene has yet to be reported.^[15] This is very likely due to the large diradical character of **1** which, based on many studies, suggests that **1** and its derivatives may only be ephemeral compounds because of their presumed reactivity. In this work we report the preparation and characterization of indeno[1,2-*a*]fluorene **6** as a highly reactive diradicaloid species. Reduction of **6** with elemental Cs tames this reactive compound as its dianion and provides definitive structural proof via X-ray diffraction analysis for the once missing [1,2-*a*]IF regioisomer.

2.3 Results and Discussion

Geometry optimization for the parent [1,2-*a*]IF in the singlet state at the RB3LYP/6-311G* level^[16] reveals two local minima, the geometries of which are similar to those of the CS forms of **1** and **1'** in their bond length alternation patterns (Table A2), while one local minimum corresponding to the **1'** OS form is found by UB3LYP/6-311G* calculation. To examine the relative stabilities of these local minima in the singlet state, spin-flip non-collinear time-dependent density functional theory (SF-NC-TDDFT)^[17] single point calculations with the PBE50 functional and the 6-311G* basis set were performed.^[18a] The UB3LYP optimized **1'** singlet structure is 2.08 and 2.25 kcal mol⁻¹ more stable than the RB3LYP optimized **1** and **1'** structures, respectively (Figure A.9). The *y* value of the OS **1'** structure is estimated to be 0.97, which indicates that the molecule would exhibit almost pure diradical nature. Further exploration of the singlet potential energy surface by using the SF-collinear (SF-CL-)TDDFT BHandHLYP/6-311G* method^[18b] provides a local minimum 2.24 kcal mol⁻¹ lower than the UB3LYP optimized **1'** singlet structure. From the bond length alternation patterns, the SF-CL-TDDFT optimized singlet geometry is in between the **1** and **1'** singlet forms (Table A2). Indeed, the *y* value of the SF-CL-TDDFT optimized singlet structure is estimated to be 0.80, which is slightly smaller than that of the UB3LYP optimized **1'** form. Geometry optimization for the triplet state was also performed at both the UB3LYP/6-311G* and SF-CL-TDDFT BHandHLYP/6-311G* levels. In contrast to the singlet state, the triplet state optimized structures are close to each other (Table A2). Adiabatic singlet-triplet (S-T) energy gaps calculated at the SF-NC-TDDFT PBE50/6-311G* level are 5.75 kcal mol⁻¹ for the UB3LYP optimized **1'**-like structure, and 5.96 kcal mol⁻¹ for the SF-CL-TDDFT optimized structure, which implies that the triplet state is predicted to be lower than the singlet state. Further examination of adiabatic S-T energy gap of the [1,2-*a*]IF with mesityl groups, **6**, by using the UB3LYP optimized structures (Table A2), also supports that **6** is a ground state triplet (see Supporting Appendix A).

With 20 conjugated π -electrons and predictions of a triplet ground state, IF **6** fits the criteria required for a Baird aromatic molecule.^[19] Essentially the inverse of Hückel aromaticity, Baird aromaticity has become a topic of interest in recent years.^[20] To probe the tropicity of **6**, we performed both nucleus independent chemical shift (NICS)^[21] and

anisotropy of the induced current density (ACID)^[22] computations. As shown in Figure 2.2, the NICS(1) values suggest that the outer benzenes are strongly aromatic (> -10 ppm) while the inner rings have weak but distinctly diatropic ring currents (-3.6 to -4.2 ppm). The ACID plot supports the presence of strongly diatropic outer benzenes and a much weaker diatropic ring current in the tricyclic indacene perimeter, which would be weakly Baird aromatic.

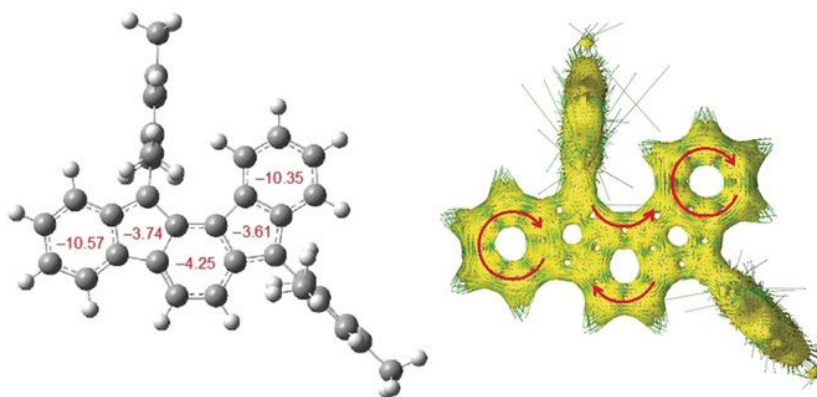
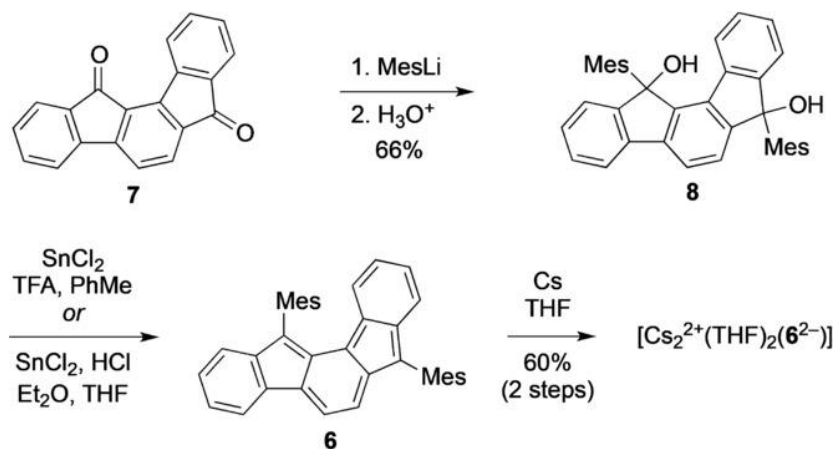


Figure 2.2 NICS(1) (left) and ACID (right) calculations of [1,2-*a*]IF **6** at the UB3LYP/6-311G* level.

Treatment of known dione **7**^[23] with mesityllithium cleanly furnished diol **8** as chromatographically separable diastereomers (Scheme 2.1). Reduction of either diastereomer of **8** using SnCl₂ in rigorously degassed toluene afforded a deep crimson solution that was chromatographed on silica. Upon exposure to air and/or prolonged storage as a solid, the isolated material (single spot by TLC) decomposed to multiple new spots, indicating that the compound was quite unstable, an observation consistent for a molecule with pronounced open-shell character. Use of prudent air-free techniques did permit limited solution-based spectroscopic characterization of the red solid presumed to be **6**. The proton NMR spectrum of the crimson solution shows very broad signals in the aromatic region at room temperature. Interestingly, cooling the sample to -88 °C resulted in the disappearance of these peaks, while heating the sample to 100 °C resulted in slightly sharpened signals in the aromatic region (Figure A.14). The appearance of new proton signals at elevated temperatures supports the notion that **6** exists as a triplet ground state, causing NMR silence until the singlet state is thermally populated. To further explore the ground state triplet nature of **6**, EPR spectra were obtained. At room

temperature there is a broad signal around $g = 2$ that is most likely due to a monoradical impurity,^[12c] whereas the intensity of a new signal with triplet-like features increases upon decreasing the temperature to 5 K (Figure A.15). While these qualitative observations seem to support the predicted triplet ground state in **6**, the low quality EPR data set precluded further analysis.



Scheme 2.1 Synthesis of indeno[1,2-*a*]fluorene **6** and formation of the dianion-based complex [Cs₂²⁺(THF)₂(**6**²⁻)] (see Figure 2.4 for its complete structure).

The electronic absorption spectrum of [1,2-*a*]IF **6** (Figure 2.3) shows a strong transition from 330 to 425 nm and smaller absorptions with apparent vibrational fine structure at 520 and 559 nm. These values, which are replicated well in the calculated spectrum (Figure A.12 and Table A3), are consistent with the λ_{max} observed for other IF-related structures.^[12] Furthermore, the spectrum shows multiple weaker bands from 600 to 1000 nm (Figure 2.3, inset). These broad low-energy absorbances, which equate to an optically-determined E_{gap} of ~ 1.3 eV, are similar to those observed for indeno[2,1-*b*]fluorene^[12c] and are indicative of a structure with a significant diradical contribution to the ground state. The cyclic voltammogram (Figure A.16) of **6** shows a symmetric trace with a reversible reduction at -0.67 V and a reversible oxidation at 0.74 V (both vs. SCE). The electro-chemically determined SUMO is -3.82 eV and the SOMO is -5.29 eV, giving an E_{gap} of 1.46 eV. This value (calculated $E_{\text{gap}} = 1.82$ eV, Figure A.13) is smaller than expected for a CS hydro-carbon yet agrees well with the electrochemically-determined E_{gap} for [2,1-*b*]IF (1.26 eV),^[12c] the other known OS IF structure.

The mounting experimental data and the logical outcome of the synthetic route strongly suggest that the unstable red solid is most likely IF isomer **6**. Unfortunately, attempts to form single crystals for definitive structural proof were fruitless. However, prior studies have shown that IF derivatives can be reduced easily to monoanion and dianion states and crystallographic data secured.^[9b,d] Importantly, such reductions do not alter the carbon skeleton; therefore, X-ray crystallography of the reduced product would reveal the molecule's carbon connectivity and provide the structural confirmation that **6** is the missing IF regioisomer.

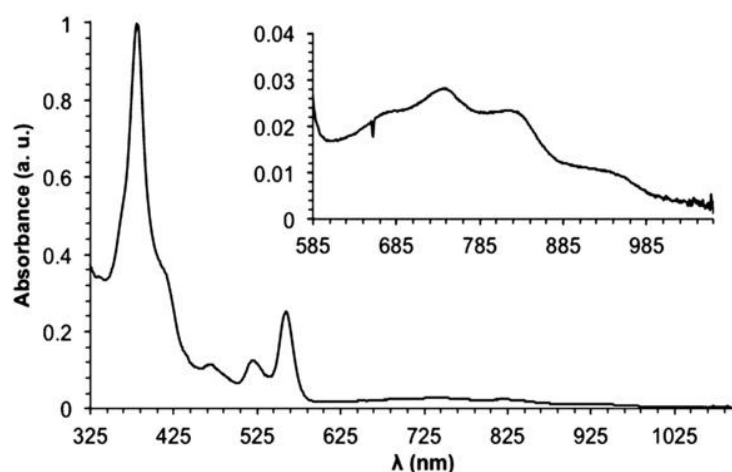


Figure 2.3 Electronic absorption spectrum of [1,2-*a*]IF **6** in CH₂Cl₂; (inset) vertical expansion of the low-energy region of the spectrum.

To reach the target dianion, freshly prepared **6** (using SnCl₂ with etherial HCl) was reacted with an excess of metallic Cs in THF solution under strictly anaerobic conditions. The resulting product was crystallized as orange blocks from THF upon slow diffusion of hexanes (see Section 2.5.3 for details). X-ray structural characterization, reveals the expected indeno[1,2-*a*]fluorene hydrocarbon core (Figure 2.4a) and provides the first geometrical parameters for its dianion.^[24] As might be expected, reduction of **6** generates a cyclopentadiene-like aromatic anion in each five-membered ring.^[9d] The C–C bond lengths of **6**²⁻ suggest that the molecule could be viewed as two indene anions bridged by an isolated ethene unit (short C3–C4 bond length of 1.361 Å). The bond length alternation pattern of [Cs₂²⁺(THF)₂(**6**²⁻)] is in relatively good agreement with that of the geometry for **6**²⁻ optimized at the RB3LYP/6-311+G* level. While there are slight

discrepancies in some bond lengths, these are probably due to the presence of counterionic species.

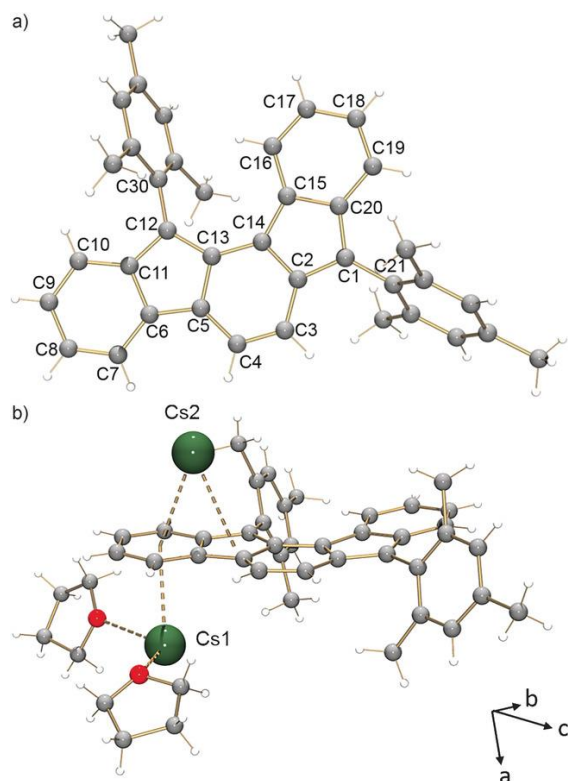


Figure 2.4 (a) ORTEP of the 6^{2-} core; thermal ellipsoids at the 40% probability level. (b) Ball-and-stick model of the independent unit of $[\text{Cs}_2^{2+}(\text{THF})_2(6^{2-})]$.

In the molecular structure, where the asymmetric unit contains one ligand and two Cs ions along with two THF molecules (Figure 2.4b), Cs1 coordinates the terminal six-membered ring of 6^{2-} with Cs...C bond distances ranging over 3.424(6)–3.519(7) Å (distance to ring centroid is 3.173(6) Å). The Cs1 ion has two THF molecules bound with Cs...O bond distances of 2.932(18) and 3.184(5) Å. In contrast, the Cs2 ion interacts with both six- and five-membered rings of the dianion with Cs...C bond distances ranging over 3.104(6)–4.000(6) Å and 3.104(6)–3.849(6) Å, respectively. The corresponding distances to the ring centroids are 3.295(6) and 3.287(6) Å, similar to previously reported values.^[25] Through the open side, both Cs1 and Cs2 ions coordinate the neighboring dianion (the distances to the ring centroids are 3.272(6) for Cs1; 3.052(6) and 3.672(6) Å for five- and six-membered rings for Cs2), thus forming an extended 2D ribbon (Figure A.18).

2.4 Conclusions

In conclusion, we report the synthesis and characterization of indeno[1,2-*a*]fluorene **6**, the last unknown IF regioisomer. The molecule is predicted to be a triplet in the ground state; both its reactivity and temperature-dependent NMR and EPR spectroscopic characteristics support this notion. The UV-vis and CV data suggest formation of a low E_{gap} material (1.3-1.4 eV). X-ray analysis of the dianion of **6** provides definitive structural proof of the pentacyclic IF core. Future studies will focus on more stable indeno[1,2-*a*]fluorenes as well as on additional IF analogues predicted to possess significant diradical character.

2.5 Experimental Sections

2.5.1 General Experimental Details

All air-sensitive manipulations were carried out under an inert atmosphere using either standard Schlenk technique or an N₂-filled drybox. For air-sensitive reactions, THF and toluene were refluxed with Na benzophenone ketyl for 24 h prior to distillation and use. For all manipulations performed in an N₂-filled drybox, THF and toluene were refluxed with Na benzophenone ketyl for 24 h prior to distillation and then degassed via freeze-pump-thaw cycles. For column chromatography, silica gel (240-300 mesh) was used. For air sensitive reactions, silica gel was heated at 150 °C overnight under vacuum and then stored in an N₂-filled drybox. All other reagents were used as received without further purification. NMR spectra were recorded on Bruker Avance III HD 600 equipped with a Prodigy multinuclear cryoprobe (¹H: 600 MHz, ¹³C: 151 MHz) NMR spectrometer. ¹H and ¹³C chemical shifts (δ) are expressed in ppm relative to the residual CHCl₃ (¹H: 7.26 ppm, ¹³C: 77.16 ppm) and CH₂Cl₂, (¹H: 5.32 ppm, ¹³C: 54.00 ppm) reference. UV-Vis spectra were recorded on an Agilent Technologies Cary 60 UV-Vis spectrometer in HPLC grade CH₂Cl₂.

2.5.2 Synthetic Details

Indeno[1,2-*a*]fluorene-7,12-dione (7). Dione **7** was prepared according to the literature,^[1] isolated as a bright yellow powder. Given the age of the procedure, NMR

data are previously unreported and are included here for completeness. ^1H NMR (600 MHz, CDCl_3) δ 8.91 (d, $J = 7.6$ Hz, 1H), 7.82 (d, $J = 7.3$ Hz, 1H), 7.77 (d, $J = 7.4$ Hz, 1H), 7.75 (d, $J = 7.3$ Hz, 1H), 7.67–7.61 (m, 2H), 7.58 (d, $J = 7.4$ Hz, 1H), 7.49 (d, $J = 7.3$ Hz, 1H), 7.47–7.40 (m, 2H). ^{13}C NMR (151 MHz, CDCl_3) δ 193.00, 192.62, 149.88, 143.49, 143.44, 142.56, 136.20, 135.41, 135.24, 135.12, 134.90, 130.89, 130.43, 129.94, 128.98, 127.60, 124.64, 124.09, 121.16, 120.04.

7,12-Dimesitylindeno[1,2-a]fluorene-7,12-diol (8). In an oven-dried flask, 2-bromomesitylene (0.32 mL, 2.12 mmol) was dissolved in dry THF (50 mL), cooled to -78 °C under a N_2 atmosphere, and BuLi (2.5 M in hexanes, 0.78 mL, 1.95 mmol) was added dropwise. This mixture was stirred at -78 °C for 1 h after which it was transferred via cannula to another oven-dried flask containing dione **7** (100 mg, 0.354 mmol,) in dry THF (50 mL), also cooled to -78 °C under a N_2 atmosphere. This reaction mixture was slowly warmed to rt with stirring overnight. The reaction was then quenched under Ar with a saturated aq. NH_4Cl solution (Ar sparged) and extracted with Et_2O (3x). The combined organic layer was washed with brine (3x), dried (MgSO_4) and concentrated in vacuo. The resulting crude oil was purified via flash chromatography (4:1 hexanes/ EtOAc) to yield the diastereomeric diols as yellow solids. First diastereomer of **8** (93.5 mg, 51%), mp 230–232 °C. ^1H NMR (600 MHz, CD_2Cl_2) δ 7.69 (d, $J = 7.5$ Hz, 1H), 7.59 (d, $J = 7.6$ Hz, 1H), 7.42 (d, $J = 7.5$ Hz, 1H), 7.38 (td, $J = 7.5, 1.1$ Hz, 1H), 7.32 (d, $J = 7.6$ Hz, 1H), 7.30–7.24 (m, 2H), 7.16 (d, $J = 7.4$ Hz, 1H), 7.12 (td, $J = 7.4, 1.3$ Hz, 1H), 7.10–7.04 (m, 2H), 6.98 (s, 1H), 6.59 (s, 1H), 6.56 (s, 1H), 3.10 (s, 3H), 2.92 (s, 3H), 2.41 (s, 1H), 2.25–2.19 (m, 7H), 1.36 (s, 3H), 1.19 (s, 3H). ^{13}C NMR (151 MHz, CD_2Cl_2) δ 152.65, 152.09, 149.60, 146.90, 141.40, 139.73, 139.32, 138.70, 138.45, 136.91, 136.73, 136.51, 135.82, 135.45, 133.32, 132.88, 131.64, 131.30, 129.72, 129.28, 129.10, 128.94, 126.02, 125.30, 125.04, 124.13, 120.82, 120.60, 87.03, 86.40, 26.35, 26.07, 22.21, 21.71, 20.79, 20.76. Second diastereomer of **8** (28.2 mg, 15%), mp 156–158 °C. ^1H NMR (600 MHz, CD_2Cl_2) δ 7.69 (d, $J = 7.7$ Hz, 1H), 7.61 (d, $J = 7.6$ Hz, 1H), 7.41–7.36 (m, 2H), 7.31 (d, $J = 7.6$ Hz, 1H), 7.27 (td, $J = 7.4, 1.1$ Hz, 1H), 7.23 (d, $J = 7.7$ Hz, 1H), 7.16 (d, $J = 7.4$ Hz, 1H), 7.13 (td, $J = 7.4, 1.1$ Hz, 1H), 7.10 (s, 1H), 7.06 (td, $J = 7.5, 1.4$ Hz, 1H), 7.00 (s, 1H), 6.62 (s, 1H), 6.54 (s, 1H), 3.10 (s, 3H), 2.92 (s, 3H), 2.50 (s, 1H), 2.24 (s, 3H), 2.23 (s, 3H), 2.22 (s, 1H), 1.35 (s, 3H), 1.31 (s, 3H). ^{13}C

NMR (151 MHz, CD₂Cl₂) δ 152.61, 152.25, 149.70, 147.06, 141.47, 139.74, 139.44, 138.64, 138.34, 136.88, 136.79, 136.40, 136.33, 135.78, 135.60, 135.54, 133.34, 132.94, 131.42, 131.19, 129.67, 129.24, 129.17, 128.94, 125.86, 125.21, 124.99, 124.06, 120.98, 120.56, 87.25, 86.54, 26.39, 26.12, 22.37, 21.77, 20.80, 20.77. HRMS (ESI) for C₃₈H₃₄O₂ [M+Na]⁺: calcd 545.2457, found 545.2482.

7,12-Dimesitylindeno[1,2-*a*]fluorene (6) [Method #1]. In an N₂-filled dry box, diol **8** (25.0 mg, 0.48 mmol) was dissolved in dry degassed toluene (2 mL) and anhydrous SnCl₂ (36.2 mg, 0.191 mmol) and trifluoroacetic acid (0.07 mL, 0.90 mmol) were added. The flask was removed from the N₂-filled dry box and the mixture was further degassed via 3 freeze-pump-thaw cycles. The reaction mixture was then vigorously stirred at room temperature and monitored via TLC (aliquots for TLC analysis were obtained via a N₂-purged syringe, 4:1 hexanes/CH₂Cl₂). When complete (typically 2-4 h), the mixture was returned to the N₂-filled dry box and immediately filtered through a plug of dried silica gel, and concentrated *in vacuo*. The crude product was purified via flash chromatography (4:1 hexanes/CH₂Cl₂). The fractions obtained from this reaction initially showed one spot via TLC analysis. If the solution was left to stand, multiple new spots developed after 1-2 h while no trace of the original spot remained. If a fraction was concentrated *in vacuo* and then immediately dissolved, multiple new spots began to appear. This degradation was observed regardless of whether the compound was isolated and purified in the drybox or on the bench top. The NMR, UV-vis, CV, and EPR data were obtained directly on the isolated pure fractions without concentration.

2.5.3 Cs Reduction Details

General. All manipulations were carried out using break-and-seal^[4] and glovebox techniques under an atmosphere of Ar. Cesium metal (99.9 %) was purchased from Sigma Aldrich. Solvents (THF and hexanes) were dried over Na/benzophenone and distilled prior to use. THF-*d*₈ was dried over NaK₂ alloy and vacuum-transferred. The NMR spectra were measured on a Bruker AC-400 spectrometer at 400 MHz for ¹H and 52.5 MHz for ¹³³Cs and were referenced to the solvent signals for ¹H and 0.1M CsNO₃ in D₂O for ¹³³Cs.

7,12-Dimesitylindeno[1,2-*a*]fluorene (6) [Method #2]. Diol **8** (10 mg, 0.038 mmol) and SnCl₂ (30 mg, 8 equiv.) were added into the system. The mixture was dissolved in dry THF (5 mL) followed by the addition of HCl in Et₂O (0.2 mL, 2.0 M). The color changed from yellow to deep red in 1 min. After 3 h stirring at 25 °C, the mixture was passed through a long plug of Al₂O₃ under Ar flow. An anhydrous mixture of isopentane:Et₂O (95:5, ~20 mL) was used to elute product off the plug. The solvent was removed under reduced pressure to give **6** as a red solid. The reaction flask containing this solid was quickly sealed under vacuum and transferred into the glove box for immediate use in the reduction step.

Preparation of [Cs₂²⁺(THF)₂(6²⁻)]. One drop of cesium (excess) and 7,12-dimesitylindeno-[1,2-*a*]fluorene (**6**, freshly prepared as above) were quickly added into the system in the glove box, following by addition of anhydrous THF (1.5 mL). Under an Ar atmosphere, the mixture was stirred at 25 °C for 24 h to complete the reaction. The initial color was red but it changed to red brown after 15 min and remained the same color before the reaction was stopped. The mixture was filtered to give a red brown solution, from which the product was precipitated by addition of hexanes (5 mL). The mixture was filtered and the orange-brown solid was washed twice with hexanes and then dried under reduced pressure for 10 min. The solid was then dissolved in THF (1 mL) and that solution was layered with hexanes (1 mL) and cooled to 5 °C. Orange blocks of [Cs₂²⁺(THF)₂(6²⁻)] (9 mg, 60%) were collected after 5 d. ¹H NMR (400 MHz, THF-*d*₈): δ 7.73 (d, *J* = 9.2 Hz, 1H), 7.71 (d, *J* = 9.2 Hz, 1H), 6.94 (s, 2H), 6.89 (s, 2H), 6.82–6.71 (m, 3H), 6.63 (t, *J* = 6.7 Hz, 1H), 6.54–6.43 (m, 3H), 6.03 (t, *J* = 8.0 Hz, 1H), 2.41 (s, 3H), 2.31 (s, 3H), 2.10 (s, 3H), 2.00 (s, 3H). ¹³³Cs NMR (THF-*d*₈): δ –88.1 ppm.

2.6 Bridge to Chapter III

This work highlights our lab's ability to produce and characterize new diradical compounds, even those with a rare triplet ground state. In the second ever reported diradical from our lab, the appearance of diradical character resulted from changing the path of radical conjugation through the core between the radical centers. In the case of the IF derivative we work with the most (and will for the rest of the studies in this dissertation), indeno[1,2-*b*]fluorene, the path of radical conjugation, puts the radicals in

an *para* relationship to each other. However in the case indeno[1,2-*a*]fluorene the radicals were placed in an *ortho* orientation to each other across the benzene core. While changing the path of radical conjugation does lead to large scale and exciting changes in the γ value and singlet/triplet ground state, the next study focuses on exchanging the external benzene units for benzothiophenes, so that the conjugation pathway between the two radicals remains the same across a series of molecules, enabling a more stepwise and systematic study.

CHAPTER III

THIOPHENE AND ITS SULFUR INHIBIT INDENOINDENO-DIBENZOTHIOPHENE (IIDBT) DIRADICALS FROM LOW-ENERGY LYING THERMAL TRIPLETS

3.1 Authorship Statement and Abstract

This chapter includes previously published an co-authored material from: Dressler, J. J.; Teraoka, M.; Espejo, G. L.; Kishi, R.; Takauku, S.; Gomez-Garia, C. J.; Zakharov, L. N.; Nakano, M.; Casado, J.; Haley, M. M. Thiophene and its sulfur inhibit indenoindenodibenzothiophene diradicals from low-energy lying thermal triplets. *Nat. Chem.* **2018**, *10*, 1134-1140. Further permissions related to the use of the material excerpted in this chapter should be directed to SpringerNature. This manuscript was written by myself with editorial assistance from Prof. Mike Haley, Prof. Nakano and Prof. Juan Casado. The experimental work in this chapter was performed by myself and Mitsuru Teraoka.

Many qualitative structure-property correlations between diradical character and emerging molecular properties are known. For example, the increase of diradical character further decreases the singlet-triplet energy gap. Here we show that inclusion of thiophenes within a quinoidal polycyclic hydrocarbon imparts appreciable diradical character yet retains the large singlet-triplet energy gap, a phenomenon that has no precedent in the literature. The low aromatic character of thiophene and its electron-rich nature are the key properties that lead to these unique findings. A new indenoindenodibenzothiophene scaffold has been prepared and fully characterized by several spectroscopies, magnetic measurements, solid state x-ray and state-of-the-art quantum chemical calculations, all corroborating this unique dichotomy between the diradical input and the emerging magnetic properties. New structure-property relationships such as these are not only extremely important in the field of diradical chemistry and organic electronics but also supply new insights into the versatility of π -electron chemical bonding.

3.2 Introduction

Diradical polycyclic aromatic hydrocarbons (PAHs) have attracted considerable attention in recent years because of possible uses as organic electronic materials. Even though open shell PAHs have been known for over a century now¹, their study still offers new insights on the fundamental nature of the π bond as well as new avenues of research on chemical reactivity and unique electronic and magnetic properties in π -expanded systems. Diradicaloids often display narrow HOMO-LUMO energy gaps², low energy electronic absorptions due to a low-lying doubly-excited electronic configuration³, redox amphoterism and multicenter bonding⁴, and ESR signal(s) and peak broadening in the proton NMR spectrum². These unique electronic and magnetic characteristics have sparked interest in potential applications such as molecular electronics and spintronics⁵, lithium-ion batteries⁶, nonlinear optics⁷⁻⁹ and singlet fission materials¹⁰⁻¹². In line with the many applications and fundamental questions facing open shell PAHs, many classes of diradical molecules have been examined in recent years, such as zethrenes¹³⁻¹⁶, anthenes^{17,18}, bisphenalenyls¹⁹⁻²¹, indenofluorenes (IFs) and analogues²²⁻²⁸, extended quinodimethanes²⁹⁻³¹ and higher order acenes³²⁻³⁴. Unfortunately, the diradical nature of these compounds, which makes them of great interest, very often imparts high reactivity that can present a significant challenge in their synthesis. Using bulky substituents (e.g., mesityl (Mes, 2,4,6-trimethylphenyl) groups) at the sites of high radical density can provide kinetic stabilization and is often the key to successful isolation of diradicaloids.

The unique nature of diradical compounds arises from the uncommon open shell and closed shell resonance structures that these molecules possess³⁵⁻³⁸. *para*-Quinodimethane, one of the most simple pro-aromatic diradicals^{7,29,39}, can exist either in the quinoidal closed shell (CS) form **1** or in the open shell (OS) form **2** with two distinct radical centers (Fig. 3.1a). Interconversion between the two resonance structures results in cleavage of the exocyclic π bonds to yield a central aromatic benzene unit, recovering a Clar sextet, which is thought to be an energetic driving force to exist in the OS state^{15,40}. The weight of the OS resonance form in the overall ground state of a diradicaloid can be estimated with y , the diradical character index, a computational value based on natural orbital occupation number (NOON) of the lowest unoccupied natural orbital⁴¹. An index of $y = 1$ is purely diradical and an index of $y = 0$ is closed shell. The energy difference

(ΔE_{S-T}) between spin-paired singlet state (**2**) and spin-parallel triplet state (**3**) determines the extent to which the triplet state is thermally populated³⁷. The vast majority of OS PAHs have a thermally accessible triplet state. Two notable examples of such compounds are super-heptazethrene (SHZ, **4**, Fig. 3.1b)¹⁴ and diindenoanthracene (DIAn, **5**)⁴. Both compounds (**1**) have significant diradical character ($y > 0.6$), (**2**) possess a thermally accessible triplet state with an experimental ΔE_{S-T} gap of -0.94 and -4.18 kcal mol⁻¹, respectively, (**3**) show peak broadening in their proton NMR spectra and (**4**) exhibit thermal dependent magnetic susceptibility in SQUID measurements. The two compounds are also bookend examples for diradical stability, having half-lives of 4.3 hours and 64 days for **4** and **5**, respectively.

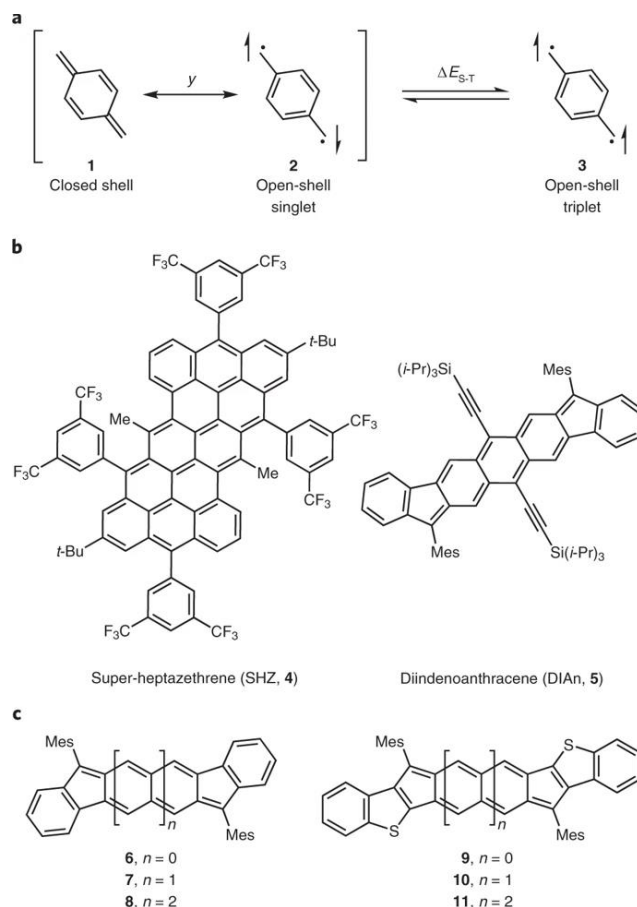


Figure 3.1 PAHs with open-shell character. **a**, The electronic structure of open shell PAHs is described by the diradical character index, y , and the energy difference between the singlet ground state and first triplet excited state, $\Delta E(S_0-T_1)$. **b**, Two recently published examples of OS singlet diradicaloids with thermally accessible triplet states, SHZ **4** and DIAn **5**. **c**, Complementary strategies used for tuning the diradical character in quinoidal PAHs.

Far less common in the literature are examples of diradicaloids that do not exhibit a thermally accessible triplet state yet still display pronounced diradical character, molecules we describe as persistent singlet diradicaloids. This might be counterintuitive as one qualitatively associates large diradical character with a small ΔE_{S-T} energy gap; however, this is a connection that is strictly quantitative in the case of full diradical character ($y = 1$) where the ΔE_{S-T} gap nearly vanishes if the exchange interaction (K_{ab}) is negligible (see eq. (1) and (2) below). For systems where $0 < y < 1$, the quantitative y - ΔE_{S-T} relationship depends on the particular molecular scaffold, explaining why two diradicals with similar y values might display different ΔE_{S-T} gaps. Theoretically, a persistent singlet diradicaloid must have a moderate/large ΔE_{S-T} energy gap and an intermediate/large computed y index value. Phenomenologically, such a molecule must possess radical reactivity, should show notable elongation of the double bond connected to the radical center in its x-ray structure, might display softened vibrational Raman frequencies, exhibit well-resolved signals in its proton NMR spectrum, etc. The requirements listed above for a persistent singlet state diradicaloid are interrelated, yet are not completely fulfilled in a vast majority of known examples of diradicaloids in the literature, e.g., molecules that show radical reactivity and/or large ΔE_{S-T} gap but low y index values⁴², low-energy UV-Vis absorptions but distinct quinoidal bond lengths in the x-ray analysis, etc^{15,43}. Furthermore, a recent theoretical and experimental study has clarified that contrary to intuition, a high optically-allowed first excitation energy could be achieved even in compounds with large y values²⁷. While the discovery of a singlet state PAH diradicaloid with all these features existing concurrently has so far been elusive, herein we show a unique case of the dichotomy between y and ΔE_{S-T} , leading to such a molecule. Through this study, we seek to understand the basic reasons that modulate diradical character in connection with some of the emerging diradical properties mentioned above (e.g., ΔE_{S-T} gap).

To this end, we have been pursuing two complementary strategies for tailoring the diradical character as a basis of tuning the electronic properties of quinoidal PAHs²². First has been elongating the central core while maintaining the same fused outer ring (e.g., **6**→**7**→**8**, Fig. 3.1c)^{4,28}. More recently we have pursued altering the bond order of the fused outer ring while retaining the same core motif (e.g., **6**→**9**, **7**→**10**, Fig. 3.1c)^{25,26}.

While the former strategy did not yield appreciably OS molecules until the anthracene core in **5/8**, we posited that this latter strategy, using the increased double bond character of the fused benzothiophenes, could lead to unique diradicaloid structures. Herein we report the preparation of three indenoindenodi(benzo-thiophene) (IIDBT) derivatives (**10**), open-shell singlet ground electronic state molecules that possess moderately strong diradical character and unusually large singlet-triplet energy gaps. In this work the diradical singlet state of IIDBT is supported experimentally by spectroscopy (NMR, SQUID, Raman, electronic absorption), X-ray analysis, and chemical reactivity; only at elevated temperatures (>450 K) do we obtain spectroscopic evidence (SQUID) for the diradical triplet state.

3.3 Results and Discussion

We firstly compare the theoretically estimated y and ΔE_{S-T} values of **6-8** with those of **9-11**. Geometry optimizations for singlet **6-11** were performed at the RB3LYP/6-311G(d) level of approximation⁴⁴, the use of which has been reported to reproduce well the experimental geometries of diradical PAHs involving five-membered rings⁴⁵. Indeed, selected C-C bond lengths of the RB3LYP geometries for the present compounds are in good agreement with the experimentally available results (Supplementary Tables B3-B5). Interestingly, the lengths of bond 1 of **9-11** (1.41-1.42 Å, Supplementary Tables B3-B5) are elongated compared to those of **6-8** (1.38-1.39 Å), thus indicating that the contribution of the diradical form becomes larger in thiophene-containing **9-11** than in the purely hydrocarbon counterparts **6-8**.

The y values calculated at the PUHF/6-311G(d) level are summarized in Table B1. For both series (**6-8** and **9-11**), the y values increase with elongation of the central core. Concomitantly to the bond 1 lengthening behavior, compounds **9-11** have larger y values than **6-8**. We also performed geometry optimizations for triplet **6-11** at the UB3LYP/6-311G(d) level, and the adiabatic ΔE_{S-T} gaps were estimated at the spin-flip non-collinear time-dependent density functional theory (SF-NC-TDDFT)^{46,47} with PBE50 functional using 6-311G(d) basis set (Table B1). As expected, ΔE_{S-T} decreases with the increase of y with all the examined compounds possessing singlet ground states.

Comparison of compounds **7** and **10**, both with the same dicyclopentanaphthalene core yet with dissimilar fused outer arene rings, illustrates the fundamental role of the thiophene. In the two-electron diradical model^{8,9,38}, the ΔE_{S-T} gap as a function of y is expressed as:

$$\Delta E_{S-T} = \frac{U}{2} \left[1 - \frac{1}{\sqrt{y(2-y)}} \right] + 2K_{ab} = \frac{U}{2} f_{ST}(y) + 2K_{ab} \quad (1)$$

with:

$$y = 1 - \frac{1}{\sqrt{1 + \left(\frac{U}{4t_{ab}}\right)^2}} \quad (2)$$

where U is the difference between on- and inter-site Coulomb repulsions, K_{ab} is the direct exchange integral, t_{ab} is the transfer integral and $f_{ST}(y)$ is the square brackets part in eq. (1), all defined between the electrons in the localized natural orbitals a and b . Note here that K_{ab} is positive, while $f_{ST}(y)$ increases from a large negative value to 0 with increasing y from ~ 0 to 1. This implies that a non-magnetic molecule takes a singlet ground state ($\Delta E_{S-T} < 0$) and the $|\Delta E_{S-T}|$ becomes small as increasing y if the U value is a constant, while if a molecule has a larger U with retaining y , $|\Delta E_{S-T}|$ could become large even at the same y . U and t_{ab} are related respectively to the spatial overlap and the energy gap between the bonding HOMO and anti-bonding LUMO (Supplementary Appendix B).

Theoretically in Table B1, **7** and **10** are diradicals with $y(\mathbf{7}) < y(\mathbf{10})$, which is a result of the fact that $|t_{ab}|(\mathbf{7}) > |t_{ab}|(\mathbf{10})$ and $U(\mathbf{7}) < U(\mathbf{10})$ according to Table B2 and Eq. (2). These differences are explained by the fact that (i) the HOMO-LUMO gap is smaller in **10** than in **7** owing to the larger π -conjugation offered by the benzothiophene motif compared to benzene; and (ii) the electron-rich sulfur atom offers a stronger repulsion environment (i.e., U) nearby the radical center than the benzene units alone. This nicely shows the dual electronic role of thiophenes, either as electron polarizable rings (i.e., low aromaticity, π -conjugation enabler) and as electron-rich donor sites, and both effects are favorable for the increase of the diradical character (see Supplementary Appendix B for an interpretation in terms of the natural orbitals). Interestingly, the thiophene rings in the diradical configurations also act as π -delocalization limits (little to no electronic extension onto the peripheral benzenes in **10** in contrast to **7** in Fig. 3.2a), which

concentrates and greatly stabilizes the electron and spin density between them. This is also related with the fact that the low aromaticity and larger π -conjugation of thiophene (which reduces the energy required to break a double bond) allow additional diradical resonance forms in **10** than in **7** (Fig. 3.2b).

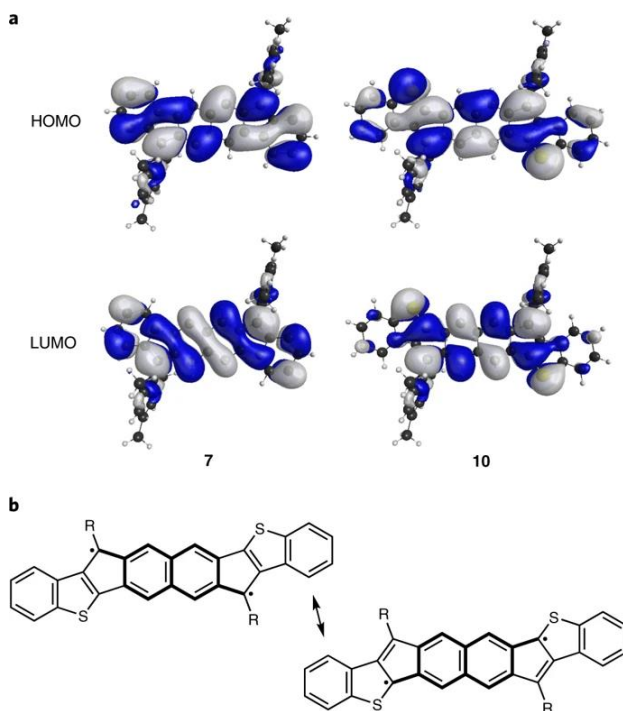


Figure 3.2 Theoretical assessment of IIDBT. **a**, Comparison of the spatial distributions of the HOMO and LUMO wave functions for **7** and **10** calculated at the tuned-LC-RBLYP/6-311G(d) level of theory; isosurface value of 0.01 a.u. **b**, Depiction of the two canonical OS resonance forms between the thiophenes for IIDBT **10**.

Given that K_{ab} is negligibly small (Table B2) in both compounds, the ΔE_{S-T} is determined by the first addend which depends exclusively on U and y and that gives rise to $|\Delta E_{S-T}(\mathbf{7})| > |\Delta E_{S-T}(\mathbf{10})|$ by Eq. (1). By comparing **7** and **10**, both U and y have significant weight in the final ΔE_{S-T} outcome. From **10** to **11**, U is increased while $|t_{ab}|$ is decreased due to the larger anthracene π -core in **11**, resulting in an increase of y and consequently, $|\Delta E_{S-T}(\mathbf{11})| < |\Delta E_{S-T}(\mathbf{10})|$. In other words, the theoretical scenario is that **10** has medium-large diradical character ($y = 0.61$) that gives a moderate-large $|\Delta E_{S-T}|$ gap, representing a molecular platform where diradical properties might be extensively expressed and yet preserved from the interference of low-energy lying magnetically

active triplets (and thus triplet reactivity). To provide experimental evidence of the unexpected role that thiophene plays for the divergence between γ and ΔE_{S-T} , the preparation of derivatives **10a-c** and the characterization of their diradical properties is next described.

The facile synthesis of IIDBTs **10** was achieved utilizing a bistriflate intermediate (**12**, Fig. 3.3) recently reported by Knall *et al.*⁴⁸ Suzuki cross-coupling of **12** with benzothiophene 2-pinacolate ester⁴⁹ gave the desired naphthalene **13** in 88% yield. Saponification of diester **13** followed by intramolecular Friedel-Craft acylation furnished poorly soluble dione **14** in 77% yield. Addition of mesityllithium to **14** generated an intermediate diol, which then was reduced using SnCl₂ in rigorously anaerobic and anhydrous reaction conditions to afford the fully conjugated mesityl-substituted IIDBT **10a** as a vibrant deep purple solid in 62% yield. Repetition of this sequence with triisopropylphenyllithium gave the corresponding IIDBT **10b**, albeit in reduced yield because of the difficulty of adding the bulky nucleophile to the electrophilic dione.

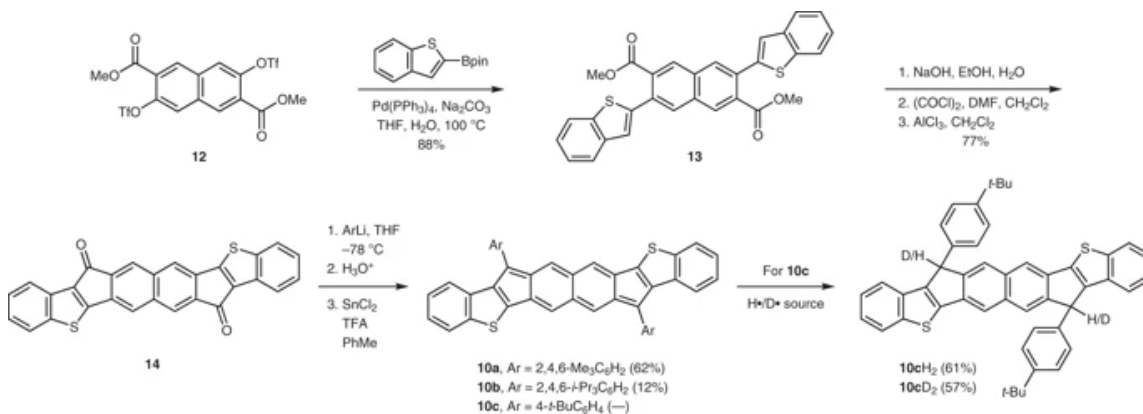


Figure 3.3 Synthesis of IIDBT and trapping as the dihydro/dideuterio adducts **10cH₂**/**10cD₂**. Benzothiophene fragments are appended to **12** by a Suzuki-Miyaura reaction to give **13**, followed by saponification and Friedel-Crafts acylation to yield dione **14**. Nucleophilic addition of aryl groups followed by a reductive dearomatization furnishes **10**. If the aryl groups do not provide sufficient steric protection, then the radical centers react to give the dihydro/dideuterio adduct.

Interestingly, the ¹H NMR spectra of **10a-b** at room temperature displayed well-resolved signals. This result is somewhat surprising compared to the proton spectrum of DIAn **5**, which clearly showed broadened signals at room temperature⁴. Heating a sample

of **10a** in 1,1,2,2-tetrachloroethane- d_2 to 125 °C did not result in appreciable peak broadening (Fig. B.18), whereas **5** at the same temperature showed only broad, featureless humps in its proton spectrum. The disparity between the NMR data sets, with both molecules possessing nearly identical diradical character values (~ 0.6), could be indicative for **10a** of a diradical species with a large, thermally prohibitive ΔE_{S-T} gap in this range of temperatures. This possibility is corroborated by the calculated ΔE_{S-T} values of -4.9 and -8.8 kcal mol $^{-1}$ for **5**⁴ and **10**, respectively, as well as by ESR and SQUID experiments, which were silent for possible triplet species up to 400 K for **10a**, whereas analogous experiments clearly showed a triplet state for **5**.

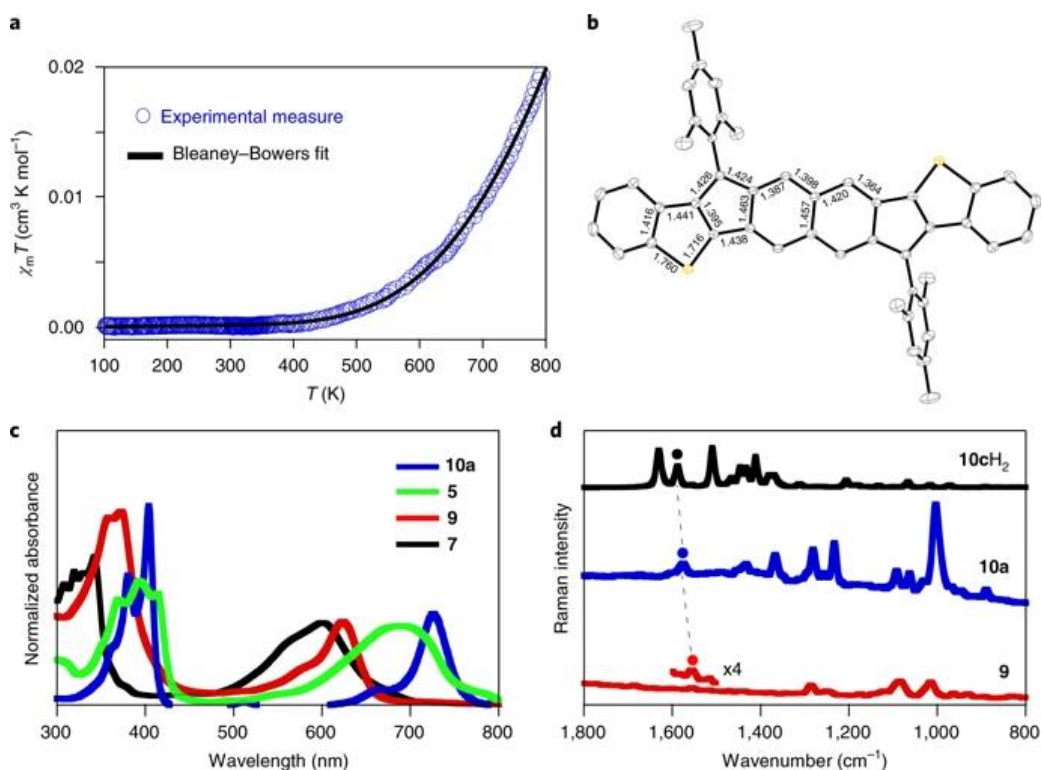


Figure 3.4 SQUID magnetic, solid-state and optoelectronic properties of IIDBT. a, Thermal variation of the $\chi_m T$ product of compound **10a** in the solid state in the temperature range 100-800 K from SQUID measurements. Solid line is the best fit to the model. **b,** ORTEP image of **10a** with selected bond distances (Å) within the hexacyclic core and thermal ellipsoids drawn with 35% probability level, hydrogens are omitted for clarity. **c,** Comparison of the electronic absorption spectrum of **5** (green), **7** (black), **9** (red) and **10a** (blue) in CH_2Cl_2 . **d,** Room temperature solid-state 785 nm Raman spectra of **9** (red), **10a** (blue), and **10cH₂** (black).

Magnetic measurements with SQUID and ESR on the vast majority of diradical molecules in the literature typically do not go higher than 400-500 K, an insufficient range to experimentally evaluate ΔE_{S-T} values in our IIDBT derivatives. Consequently, we performed SQUID measurements for **10a** with a sample space oven capable of reaching temperatures up to 800 K inserted into the instrument. Fig. 3.4a reveals a continuous increase of the magnetic molar susceptibility after *ca.* 450 K. Fitting the data to the Bleaney-Bowers equation affords a low to high-spin energy gap, ΔE_{S-T} , of -8.0 kcal mol⁻¹. This experimental value is in very good agreement with the adiabatic ΔE_{S-T} value from calculations, -8.8 kcal mol⁻¹ for **10**. Given the different spin multiplicity of the state transition, the free energy variation at 298.15 K was calculated at the same level of theory, resulting in a value of -7.9 kcal mol⁻¹, also in excellent accordance with the experiment. Differential scanning calorimetry (DSC) data (Fig. B.19) confirmed the stability of **10a** at these high temperatures.

Attempts to generate IIDBT **10c** afforded instead the “hydrogenated” product **10cH₂**, confirmed by mass spectrometry (MS) and by the appearance of a new singlet at 5.22 ppm in the ¹H NMR spectrum. This singlet disappeared when the reaction was spiked with D₂O (also confirmed by ²D NMR and MS). Whereas the methyl/isopropyl groups of **10a-b** provide steric protection of the carbon centers with high radical character, this clearly is not the case in **10c**, which allows the radical centers the opportunity to scavenge hydrogen atoms. To prove that **10cH₂/10cD₂** resulted from radical reactivity, repetition of the SnCl₂ reaction in the presence of Bu₃SnD, a deuterium source known to proceed via a radical mechanism, furnished **10cD₂** as the sole isolable product.

Deep blue crystals of **10a** suitable for X-ray diffraction were obtained by layering CH₃CN over a concentrated solution of the IIDBT in CHCl₃ (Fig. 3.4b). The resultant X-ray structure revealed that the carbon-carbon bond length from the apical carbon to the naphthalene core (the aforementioned bond 1) is 1.424 Å, which is much longer than the analogous bond length in DIAn **5** (1.406 Å). This longer bond is indicative of diradical character as known open shell structures have significantly reduced double bond character in this position. For example, the analogous bond lengths in indeno[2,1-*b*]fluorene and fluoreno[2,3-*b*]fluorene, molecules with pronounced diradical character

and a thermally accessible triplet state, are both 1.437 Å^{24,27}. In contrast, the analogous bond lengths in indacenedi(benzothiophene) (IDBT) **9** and IF **6** are 1.409 and 1.380 Å^{23,25}, respectively, reflecting their reduced diradical character, further supporting the notion that **10** is an open-shell singlet diradicaloid.

Comparison of the UV-Vis absorption profile (Fig. 3.4c) of IIDBT **10a** (blue) to fluorenofluorene **7**²⁸ (black) and to its IDBT analogue **9** (red) shows that the wavelength maxima of **10** are red-shifted compared to those of the all-hydrocarbon counterpart, in line with the increase of π -conjugation in the thiophene derivative as theoretically demonstrated above (i.e., see discussion of t_{ab}). Additionally, there is a low energy absorption at ca. 725 nm that is indicative of a narrow HOMO-LUMO gap and a low energy shoulder at 750 nm that is associated with the one-photon activation of the two-photon absorption band arisen from the large diradical contribution to the ground electronic state. TDDFT calculations at the UB3LYP/6-311G(d) level predict that the first absorption bands of **7** and **10** are at 618 nm ($f = 0.734$) and 722 nm ($f = 0.628$), both of which are assigned as a one-electron HOMO-LUMO transition. HOMO-LUMO energy gaps of **7** and **10** are estimated to be 1.92 eV and 1.57 eV, respectively, at the RB3LYP/6-311G(d) level. The computational results are in good agreement with the experimental λ_{max} values (600 and 725 nm, respectively) and optical energy gaps (1.82 and 1.55 eV, respectively). Comparison of DIAn **5** (green) with IIDBT shows that **10** has a more well defined absorbance profile; however, both molecules have low energy absorbances characteristic of diradical character.

The 785 nm resonance Raman spectrum of **10a** is shown in Fig. 3.4d together with the spectra of reference compounds **9** and **10cH₂**. Emergence of bands in the range of 1600-1570 cm⁻¹ is typical of aromatic acenes, which is relevant in the context of the current discussion as the conversion between the closed shell and the open shell resonance structures would result in an aromatization of the naphthalene core of **10**^{16,30}. The spectrum of IDBT **9** is characterized by the near-absence of the band in the 1600-1570 cm⁻¹ region, while **10a** displays a new band at 1576 cm⁻¹, indicating the aromatization of the naphthalene core and therefore supporting the diradical nature of the ground electronic state of **10a**. In comparison, the position of this band is very near that of **10cH₂** (1587 cm⁻¹), a molecule that possesses a fully aromatized naphthalene core.

To further confirm the re-aromatization of the central core, nucleus-independent chemical shift (NICS(1)) calculations on fluorenofluorene (FF) **7**, IDBT **9**, and IIDBT **10** were performed at the U(R)B3LYP/6-311G(d) level and are shown in Supplementary Fig. B.15⁵⁰. As previously disclosed, the central core of IDBT **9** exhibits strong antiaromatic character (7.24)²⁶, while the aromaticity of the central unit is modestly recovered in IIDBT **10** (−1.30) when the core is elongated from benzene to naphthalene; a similar result is obtained in FF **7** (−1.59). This tendency shows a good correlation with the result of diradical character and spectroscopic properties. In addition, the aromaticity in terminal benzene rings in IDBT **9** (−9.89) and IIDBT **10** (−10.1) is larger than in FF **7** (−7.49), even comparable to benzene itself (−10.1), whereas the antiaromaticity of five-membered carbocycles is more intensified in **9** (12.1) and **10** (2.96) than in **7** (0.32). These features suggest that the aromatization effect by the terminal benzene rings on the five-membered carbocycles in FF **7** is significantly reduced in IDBT **9** and IIDBT **10** by inserting fused benzothiophenes, in agreement with the rupture of aromaticity on the thiophenes (see Fig. 3.2b) and with the role of the sulfur atoms as electron donors towards the radical centers. This latter point is nicely represented by the odd-electron density distribution, which indicates the spatial contribution of unpaired electrons to the diradical character (Fig. B.16).

3.4 Conclusions

In conclusion, IIDBTs **10a-b** were synthesized and fully characterized using a variety of spectroscopic techniques and x-ray diffraction analysis. Due to a large ΔE_{S-T} gap (−8.0 kcal mol^{−1}) and a moderately large diradical character index (0.61), the indenoindenodi(benzothiophene) scaffold is posited to be an open-shell singlet that does not exhibit a low-energy lying thermally accessible triplet state up to 125 °C/400 K. X-ray bond length analysis, UV-Vis absorption and vibrational Raman spectroscopies, and unique chemical reactivity seen in the IIDBT system all support the existence of a persistent singlet diradicaloid. Importantly, IIDBT is an extremely rare example of a PAH that exists predominantly as an open-shell singlet with a seemingly large singlet-triplet gap, where only above 175 °C/450 K can the triplet state be accessed, as confirmed by SQUID studies. The fine balance between benzene and thiophene aromaticities and the

role of electron-donating sulfur atoms are the origins of these uncommon findings. The rationalization of the electronic structure of IIDBT contributes to understanding the structure-properties relationships that will open the window to designing new diradicals with tailorable singlet-triplet gaps and subsequent optical and magnetic properties. Further investigation into additional structurally-related open-shell singlet PAHs is currently underway in our laboratories, to further expand on the knowledge of such important molecules.

3.5 Experimental Section

3.5.1 General Experimental Details

All air-sensitive manipulations were carried out under an inert atmosphere using standard Schlenk technique. For moisture sensitive reactions, THF and toluene were refluxed with Na benzophenone ketyl for 24 h prior to distillation and use. For column chromatography, silica gel (240-300 mesh) was used. All other reagents were purchased and used as received without further purification. NMR spectra were recorded on a Bruker Avance III HD 500 equipped with a Prodigy multinuclear cryoprobe (^1H : 500 MHz, ^2D : 77 MHz) or Bruker Avance III HD 600 equipped with a Prodigy multinuclear cryoprobe (^1H : 600 MHz, ^{13}C : 151 MHz) NMR spectrometer at room temperature (unless otherwise noted). ^1H and ^{13}C NMR chemical shifts (δ) are expressed in ppm relative to the residual non-deuterated solvent reference (CDCl_3 : ^1H 7.26 ppm, ^{13}C 77.16 ppm; CD_2Cl_2 : ^1H 5.32 ppm, ^{13}C 53.84 ppm; $\text{DMSO}-d_6$: ^1H 2.50 ppm, ^{13}C 39.52 ppm). UV-Vis spectra were recorded on an Agilent Technologies Cary 60 UV-Vis spectrometer in HPLC grade CH_2Cl_2 . Compound **12**¹ and 2-(4,4,5,5-tetramethyl-1,3,2-dioxaborolan-2-yl)benzo[b]thiophene² were prepared according to literature procedures. In several instances, the poor solubility of the IIDBT derivatives hindered acquisition of good NMR spectra, thus greatly exaggerating impurities present in the samples from our Schlenk line.

3.5.2 Synthetic Details

Synthesis of diester 13. A three-neck round-bottom flask fitted with a condenser was charged with bistriflate **12** (3.50 g, 9.2 mmol, 1 equiv.), benzothiophene 2-pinacolate

ester (5.75 g, 22.1 mmol, 2.4 equiv.), Na₂CO₃ (12.08 g, 36.8 mmol, 4.4 equiv.), THF (80 ml), and H₂O (40 ml). After bubbling N₂ through this mixture for 1 hour, Pd(PPh₃)₄ (0.0413 g, 0.184 mmol, 0.02 equiv.) was added and the reaction vessel was purged for an additional 10 minutes. After refluxing overnight and cooling to room temperature, the reaction was quenched with H₂O and poured over filter paper. The precipitate was washed with H₂O and MeOH to yield diester **13** as a yellow solid (4.12 g, 88%); ¹H NMR (500 MHz, CDCl₃, 25 °C) δ (ppm) 8.35 (s, 2H), 8.12 (s, 2H), 7.88 (d, *J* = 7.5 Hz, 2H), 7.83 (d, *J* = 7.5 Hz, 2H), 7.42-7.35 (m, 4H), 7.36 (s, 2H) 3.81 (s, 6H); ¹³C NMR (151 MHz, CDCl₃, 25 °C) δ (ppm) 168.52, 141.96, 140.54, 140.23, 132.67, 132.33, 132.17, 131.30, 130.51, 124.72, 124.67, 123.96, 123.42, 122.31, 52.84; high-resolution mass spectroscopy (HRMS) (ES⁺) (*m/z*), calculated for C₃₀H₂₀O₄S₂ (M)⁺ 508.0803, found 508.0809.

Synthesis of dione 14. A single neck round bottomed flask fitted with a condenser was charged with diester **13** (0.476 g, 0.936 mmol, 1 equiv.), NaOH (0.60 g, 15.0 mmol, 16 equiv.), EtOH (15 ml), and H₂O (4.5 ml). After refluxing the flask overnight, the reaction was cooled and the EtOH evaporated. Concentrated HCl was slowly added to the aqueous solution and a precipitate formed, which was isolated and washed sequentially with cold H₂O and cold MeOH to yield the diacid intermediate as a yellow solid (0.373 g, 83%); ¹H NMR (600 MHz, DMSO-*d*₆, 25 °C) δ (ppm) 13.37 (s, 2H), 8.48 (s, 2H), 8.36 (s, 2H), 8.03 (d, *J* = 7.7 Hz, 2H), 7.92 (d, *J* = 7.2 Hz, 2H), 7.54 (s, 2H), 7.44-7.38 (m, 4H); ¹³C NMR (151 MHz, DMSO-*d*₆, 25 °C) δ (ppm) 169.03, 141.58, 139.92, 139.61, 133.16, 131.99, 130.93, 130.52, 129.30, 124.73, 124.65, 123.88, 123.25, 122.29. HRMS (ES⁺) (*m/z*), calculated for C₂₈H₁₇O₄S₂ (M+H)⁺ 481.0568, found 481.0569. To a suspension of the diacid (0.476 g, 0.991 mmol, 1 equiv.) in CH₂Cl₂ (20 ml) was added 3 drops of DMF followed by oxalyl chloride (0.34 ml, 3.96 mmol, 3.0 equiv.). After 1 hour, the volatiles were removed under reduced pressure. The crude acid chloride was dissolved in CH₂Cl₂ (20 ml) and solid AlCl₃ (0.661 g, 4.95 mmol, 5 equiv.) was added to the flask. The reaction was stirred overnight and then poured into an HCl-ice mixture, precipitating the dione. The solid was filtered and washed successively with H₂O, CH₂Cl₂ and MeOH to afford dione **14** as a purple solid that was too poorly soluble

to obtain NMR spectra (0.41 g, 93%); HRMS (ES⁺) (*m/z*), calculated for C₂₈H₁₂O₂S₂ (M)⁺ 444.0279, found 444.0297.

Synthesis of IIDBT 10a. In an oven-dried round bottom flask, a suspension of dione **14** (0.219 g, 0.493 mmol, 1 equiv.) in dry THF (25 ml) was cooled to -78 °C under a N₂ atmosphere. In a separate oven-dried round bottom flask, 2-bromomesitylene (0.6 ml, 3.94 mmol, 8 equiv.) was dissolved in dry THF (25 ml), cooled to -78 °C under a N₂ atmosphere, and *n*-BuLi (2.5 M in hexanes, 1.47 ml, 3.69 mmol, 7.5 equiv.) was added dropwise. After stirring the mixture at -78 °C for 1 hour, the aryl lithiate was transferred via cannula to the flask containing the dione. This reaction mixture was slowly warmed to room temperature overnight with stirring. The reaction was then quenched with a saturated aq. NH₄Cl solution and extracted with Et₂O (3×). The combined organic layer was washed with brine, dried (MgSO₄) and concentrated in vacuo. The resulting crude oil was passed through a silica plug eluting with hexanes, followed by a CH₂Cl₂ wash, to provide the desired diol that was carried onto the reductive dearomatization step without further purification. In a single-neck round-bottom flask the crude diol (0.05 g, 0.073 mmol, 1 equiv.) and anhydrous SnCl₂ (33 mg, 0.175 mmol, 4 equiv.) were dissolved in dry degassed toluene (15 ml). Trifluoroacetic acid (catalytic) was added and this mixture was then vigorously stirred. The reaction was monitored via TLC (9:1 hexanes/CH₂Cl₂). After 3 hours, the mixture was poured over a silica plug and washed with hexanes. Switching to 1:1 hexanes/CH₂Cl₂ eluted the product. The solvent was evaporated and the solid was washed with cold MeCN to remove trace impurities. The remaining solid was redissolved in CHCl₃ and MeCN was layered over the solution to furnish IIDBT **10a** as deep purple crystals (0.199 g, 62% from **14**); ¹H NMR (500 MHz, CDCl₃, 25 °C) δ (ppm) 7.62 (d, *J* = 8.0 Hz, 2H), 7.17 (s, 2H), 7.16 (t, *J* = 8.1 Hz, 2H), 7.08 (t, *J* = 7.6 Hz, 2H), 7.03 (s, 4H), 6.91 (d, *J* = 7.7 Hz, 2H), 6.84 (s, 2H), 2.41 (s, 6H), 2.20 (s, 12H); ¹³C NMR (151 MHz, CDCl₃, 25 °C) δ (ppm) 148.22, 147.56, 145.45, 141.61, 141.07, 140.60, 139.95, 135.80, 134.75, 133.71, 133.29, 133.09, 131.43, 130.27, 128.60, 128.29, 126.89, 125.00, 32.81, 23.59; HRMS (ES⁺) (*m/z*), calculated for C₄₆H₃₅S₂ (M+H)⁺ 651.2180, found 651.2184.

Synthesis of IIDBT 10b. Following the procedure for **10a**, dione **14** (0.130 g, 0.292 mmol, 1 equiv.) and 1-bromo-2,4,6-triisopropylbenzene (0.59 ml, 2.34 mmol, 8

equiv.) were reacted to yield crude diol. Diol (0.062 g, 0.073 mmol, 1 equiv.) and SnCl₂ (55 mg, 0.291 mmol, 4 equiv) were reacted. After 4 hours, the mixture was poured over a silica plug and washed with hexanes. Switching to 1:1 hexanes/CH₂Cl₂ eluted the product. The solvent was evaporated and the solid was washed with cold MeCN to remove trace impurities. The remaining solid was redissolved in CHCl₃ and MeCN was layered over the solution to furnish IIDBT **10b** as deep blue crystals (0.024 g, 12% from **9**); ¹H NMR (500 MHz, CDCl₃, 25 °C) δ (ppm) 7.60 (d, *J* = 8.1 Hz, 2H), 7.21 (s, 2H), 7.15-7.12 (m, 6H), 7.04 (t, *J* = 7.1 Hz, 2H), 6.89 (s, 2H), 6.82 (d, *J* = 7.9 Hz, 2H), 3.06-2.99 (m, 6H), 1.37 (d, *J* = 6.9 Hz, 12H), 1.13 (d, *J* = 6.8 Hz, 12H), 1.01 (d, *J* = 6.8 Hz, 12H); ¹³C NMR (151 MHz, CDCl₃, 25 °C) δ (ppm) 148.96, 147.70, 146.12, 144.62, 141.74, 139.73, 138.45, 132.74, 131.26, 130.53, 129.91, 128.09, 127.42, 125.09, 124.94, 123.70, 122.05, 120.75, 34.28, 31.30, 24.81, 24.14, 24.09; HRMS (ES⁺) (*m/z*) calculated for C₅₈H₅₉S₂ (M+H)⁺ 819.4058, found 819.4086.

Synthesis of dihydro-IIDBT 10cH₂. Following the procedure for **10a**, dione **9** (0.130 g, 0.292 mmol, 1 equiv.) and 1-bromo-4-*tert*-butylbenzene (0.40 ml, 2.336 mmol, 8 equiv.) were reacted to yield the crude diol. Diol (0.025 g, 0.035 mmol, 1 equiv.) and SnCl₂ (30 mg, 0.140 mmol, 4 equiv) were reacted at 70 °C. After 4 hours, the mixture was poured over a silica plug and washed with hexanes. Switching to 4:1 hexanes/CH₂Cl₂ eluted the product. The dihydro product was further purified using flash column chromatography using 7:3 hexanes/CH₂Cl₂ as eluent to furnish **10cH₂** as a tan solid (121 mg, 61% from **9**); ¹H NMR (500 MHz, CD₂Cl₂, 25 °C) δ (ppm) 7.89 (d, *J* = 7.8 Hz, 2H), 7.83 (s, 2H), 7.72 (s, 2H), 7.43 (d, *J* = 7.4 Hz, 2H), 7.32 (d, *J* = 8.3 Hz, 4H), 7.29–7.21 (m, 4H), 7.13 (d, *J* = 8.4 Hz, 4H), 5.22 (s, 2H), 1.28 (s, 18H); ¹³C NMR (151 MHz, CD₂Cl₂, 25 °C) δ (ppm) 150.45, 150.29, 146.79, 144.85, 143.27, 137.31, 136.84, 135.09, 132.76, 127.99, 126.17, 125.07, 124.73, 124.27, 124.12, 122.29, 118.01, 51.20, 34.77, 31.48; HRMS (ES⁺) (*m/z*) calculated for C₄₈H₄₀S₂ (M+H)⁺ 680.2572, found 680.2539.

Synthesis of dideutero-IIDBT 10cD₂. Following the procedure for **10a**, dione **9** (0.130 g, 0.292 mmol, 1 equiv.) and 1-bromo-4-*tert*-butylbenzene (0.40 ml, 2.336 mmol, 8 equiv.) were reacted to yield the crude diol. Diol (0.025 g, 0.035 mmol, 1 equiv.), SnCl₂ (30 mg, 0.140 mmol, 4 equiv) and 0.1 ml of D₂O were reacted at 70 °C. After 4 hours, the mixture was poured over a silica plug and washed with hexanes. Switching to 4:1

hexanes/CH₂Cl₂ eluted the product. The dideutero product was further purified using flash column chromatography using 7:3 hexanes/CH₂Cl₂ as eluent to furnish **10cD₂** as an off yellow solid (113 mg, 57% from **9**); ¹H NMR (600 MHz, CD₂Cl₂, 25 °C) δ (ppm) 7.89 (d, *J* = 7.9 Hz, 2H), 7.82 (s, 2H), 7.70 (s, 2H), 7.42 (d, *J* = 7.8 Hz, 2H), 7.31 (d, *J* = 8.1 Hz, 4H), 7.28 (t, *J* = 7.1 Hz, 2H), 7.24 (t, *J* = 7.2 Hz, 2H), 7.12 (d, *J* = 8.0 Hz, 4H), 1.29 (s, 18H); ²D NMR (77 MHz, CDCl₃, 25 °C) δ (ppm) 5.16 (s); ¹³C NMR (151 MHz, CD₂Cl₂, 25 °C) δ (ppm) 150.42, 150.21, 146.74, 144.84, 143.30, 137.32, 136.83, 135.09, 132.74, 127.99, 126.15, 125.05, 124.71, 124.25, 124.09, 122.27, 117.98, 51.17, 34.76, 31.53; HRMS (EI⁺) (*m/z*) calculated for C₄₈H₃₈D₂S₂ 682.2697, found 682.2704.

3.6 Bridge to Chapter IV

The work in this chapter focuses on changing the properties of our naphthalene cored indeno[1,2-*b*]fluorene analogues to show detectable and experimentally measurable diradical character. Diradical character was “activated” in IIDBT by the exchange of a benzene for a benzothiophene, increasing the antiaromaticity of the core and leading to an enhanced tendency to exist in the open shell form. Excitingly IIDBT has the unexpected bonus of possessing an unprecedentedly high singlet-triplet energy gap, allowing us to coin and report the first ever persistent singlet diradical. The next chapter focuses on tuning the properties of persistent singlet diradicals through molecule isomerism, switching the orientating of the benzothiophene units in relation to the core.

CHAPTER IV

MOLECULE ISOMERISM MODULATES THE DIRADICALS PROPERTIES OF STABLE SINGLET DIRADICALOIDS

4.1 Authorship Statement and Abstract

This chapter includes previously published and co-authored material from: Barker, J. E.; Dressler, J. J.; Valdivia, A. C.; Kishi, R.; Strand, E. T.; Zakharov, L. N.; MacMillan, S. N.; Gomez-Garcia, C. J.; Nakano, M.; Casado, J.; Haley, M. M. Molecule Isomerism Modulates the Diradical Properties of Stable Singlet Diradicaloids. *J. Am. Chem. Soc.* **2020**, *3*, 1548-1555. Further permissions related to the use of the material excerpted in this chapter should be directed to the American Chemical Society. This manuscript was co-wrote between myself and Josh Barker. Editorial assistance was provided by Prof. Mike Haley, Prof. Juan Casado and Prof Nakano. The experimental work was performed by myself, Josh Barker, Eric Strand and Abel Valdivia.

Inclusion of quinoidal cores in conjugated hydrocarbons is a common strategy to modulate the properties of diradicaloids formed by aromaticity recovery within the quinoidal unit. Here we describe an alternative approach of tuning of diradical properties in indenoindenodibenzothiophenes upon *anti*→*syn* isomerism of the benzothiophene motif. This alters the relationship of the S atom with the radical center from linear to cross conjugation yet retains the same 2,6-naphtho conjugation pattern of the rearomatized core. We conduct a full comparison between the *anti* and *syn* derivatives based on structural, spectroscopic, theoretical and magnetic measurements, showing that these systems are stable open-shell singlet diradicaloids that only access their triplet state at elevated temperatures.

4.2 Introduction

The subject of open-shell character and its interplay with the fundamental properties in polycyclic hydrocarbons¹ is a topic of high relevance to organic electronics.² Among molecules possessing open-shell character, diradicals³ in particular have garnered substantial attention as they have been proposed as candidates for a variety of materials

applications, such as ambipolar organic field effect transistors, singlet fission in organic photovoltaics, organic spintronics, etc.⁴ The design of Kekuléan diradicals is mainly based on a quinoidal core that upon recovery of aromaticity stabilizes the open-shell form (Figure 4.1).⁵ Depending upon the length of the quinoidal motif, the diradical character index (γ)⁶ and its closely related observable property, the singlet-triplet energy gap (ΔE_{ST}), can be broadly modulated. Though there are other structural features, such as the presence of donor and acceptor groups,⁷ the flexibility of the rearomatized core,⁸ etc., this quinoidal strategy represents the first and simplest method for tuning the electronic and magnetic properties of diradicaloids and has resulted in a wide range of ΔE_{ST} values in the literature.⁵ Adherence to this strategy has resulted in a shotgun approach focused on the synthesis of diversiform quinoidal topologies for the design of Kekuléan diradicaloids.⁵ A more deliberate tactic for tuning ΔE_{ST} requires consideration of additional electronic factors that could provide further improvement of the broader quinoidal strategy. We posit that a “*structure refinement approach*”, based on subtle/minor alteration of molecular geometry yet with retention of the same quinoidal/diradical core might allow a more rational modulation of ΔE_{ST} .

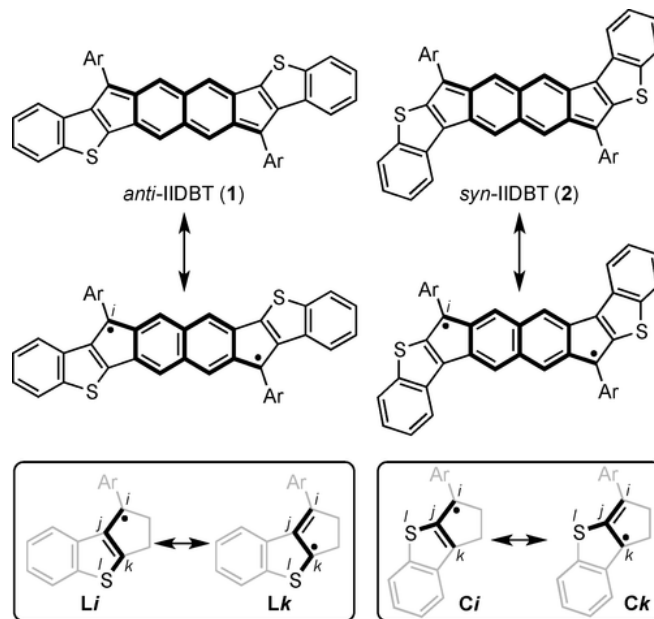


Figure 4.1 Chemical structures of *anti*-IIDBT (1) and *syn*-IIDBT (2). All canonical forms possess 2,6-naphtho conjugation (bold bonds). In boxes, linear conjugation (left, **Li** and **Lk**) vs cross conjugation (right, **Ci** and **Ck**) dispositions of the labeled *ijkl* atoms where delocalization of the radical centers to the *k* atoms disrupts thiophene aromaticity.

We recently reported the *anti*-indenoindenodibenzothiophene diradicaloid **1** (*anti*-IIDBT, Figure 4.1)⁹ with a medium-large y value (0.61; PUHF/6-311G* level of theory) and a large ΔE_{ST} (-8.0 kcal mol⁻¹; experimental magnetic susceptibility measurements). Theoretical examination of the molecular parameters involved in the y - ΔE_{ST} connection found that the position of the sulfur atom (i.e., its lone π -electron pair) relative to the radical center plays a key role increasing ΔE_{ST} at constant y . Analysis of the *syn*-IIDBT (**2**) regioisomer therefore became necessary to confirm the theoretical conclusions. In the IIDBTs *anti*- and *syn*- denote the position of the sulfur atom relative to the apical carbon (carbon i , Figure 4.1) of the 5-membered ring, where the radical can delocalize from i to atom k in each isomer (canonical forms **Li**–**Lk** and **Ci**–**Ck**). It is important to note that the 2,6-naphtho conjugation path of the radicals is consistent in both **1** and **2** enabling direct comparison of the effects of the sulfur positioning. Linear conjugation of the sulfur and the radical along the path $ijkl$ (**Li** and **Lk**) in **1** is in contrast to cross-conjugation along ijk in **2** (**Ci** and **Ck**), and in forms **Lk** and **Ck** the thiophene aromaticity is broken, all of which highlight the changing role of the sulfur to act electronically on the radical centers. As a result, this scenario could offer the desired “tuning” of ΔE_{ST} consisting of: (i) the relative through-bond separation between the sulfur and the radical center that are three and one atoms apart in **Li** and **Lk** (Figure 4.1, **1**) compared to two atoms apart in **Ci** and **Ck** (Figure 4.1, **2**) and (ii) the change in the conjugation mode (linear vs. cross) between the S lone pair and the radical as discussed above.

Previously reported carbon-based diradicaloid regioisomers have illustrated stark differences in properties that result from making small geometric changes to a molecule; however, in most of these existing cases, structural isomerism concomitantly changes the conjugation pattern, thus altering the diradical character based on the quinoidal character of the molecule.¹⁰ For instance, the known dibenzoheptazethrene isomers (Figure 4.2) exhibit a marked difference in magnetic properties: whereas the 5,6:13,14-regioisomer displays pronounced open shell character, the 1,2:9,10-isomer is closed shell.^{10d} This difference is exacerbated in the indenofluorene family^{11,12} as there is the possibility of either para, meta, or ortho conjugation between the radical centers (Figure C10), which imparts significant changes in the magnetic structure to the extent that, from one isomer to another, the ground electronic state can even change from singlet to triplet.^{11e,13}

Furthermore, substituent type and placement on the hydrocarbon backbone very often varies within the isomer series, thus diminishing meaningful comparison of molecule electronic and magnetic properties.^{10d,f,i} Structural isomerism in nitrogen- (verdazyl) and oxygen-based (nitroxide) diradicals has also been reported, but in these cases there is little effect on magnetic properties as the radical centers are not conjugated to the backbone.¹⁴

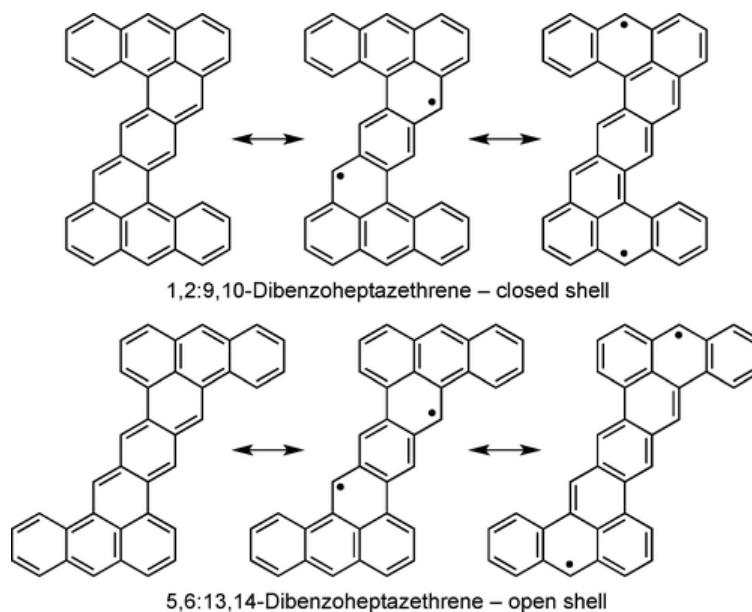


Figure 4.2 Diradical resonance forms of the hydrocarbon core of the two known dibenzoheptazethrene regioisomers

Unlike previous examples, the relationship of the radical centers in this current study, namely 2,6-conjugation, as well as the bond of benzothiophene fusion (*jk* in Figure 4.1) are identical in both **1** and **2**, thus meaning that only a single parameter that could influence magnetic properties is altered. Herein we report the synthesis of the *syn*-IIDBT isomers **2a**, **2b** and **2cH₂** as well as new *anti*-IIDBT **1b** (Figure 4.3) and computationally and experimentally corroborate that varying the benzothiophene subunit from *anti* to *syn* orientation in the IIDBT scaffold is an efficient strategy to modulate ΔE_{ST} .⁶ In addition, we demonstrate that these molecules are stable singlet diradicaloids at room temperature and only access the triplet state at elevated temperatures, where they are stable upwards of 375-400 °C.

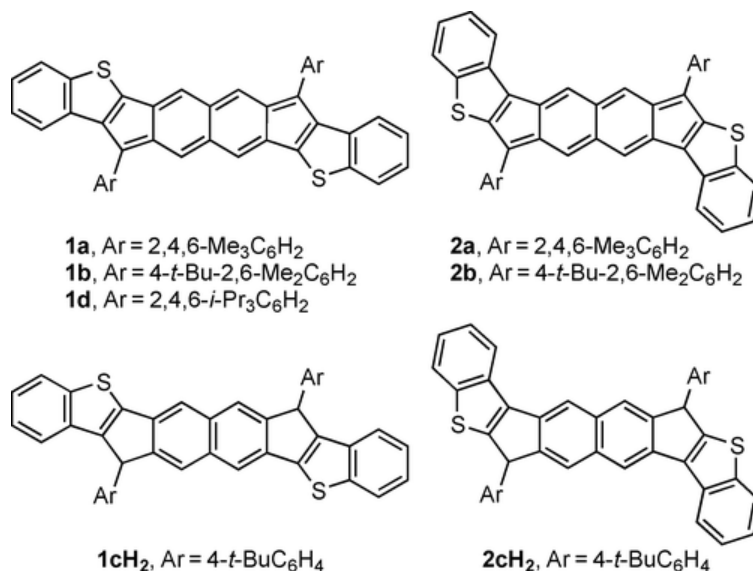


Figure 4.3 *Anti* and *syn* IIBDT derivatives studied in this work.

4.3 Results and Discussion

Quantum chemical calculations have been performed to explore the validity of our hypothesis. Equation 1 provides, in the two-electron diradical model, the dependence of ΔE_{ST} on y (defined by Equation 2) in terms of U (the difference between on- and inter-site Coulomb repulsions), t_{ab} (the transfer integral) and K_{ab} (direct exchange integral), where a and b define the electrons in the localized natural orbitals. Table C1 summarizes the main theoretical data for both **1** and **2** (see Appendix C for additional details in Table C1).

$$\Delta E_{ST} = \frac{U}{2} \left[1 - \frac{1}{\sqrt{y(2-y)}} \right] + 2K_{ab} = \frac{U}{2} f_{ST}(y) + 2K_{ab} \quad (1)$$

$$y = 1 - \frac{1}{\sqrt{1 + \left(\frac{U}{4t_{ab}}\right)^2}} \quad (2)$$

The computational results reveal that *anti*→*syn* isomerism slightly increases y and decreases ΔE_{ST} , the mechanism of which can be discussed by evaluating the integral parameters (see Table C1 for details of the integral evaluations). For proper disjoint orbitals, such as in our case, $K_{ab} \ll \frac{U}{2} f_{ST}(y)$; hence, according to the values in Table C1, the term containing U and t_{ab} is the dominant factor as far as ΔE_{ST} is concerned. Thus, the

increase in U/t_{ab} in **2** (3.10) compared to U/t_{ab} in **1** (3.03) anticipates a moderate increase of γ in the *syn* isomer and a concomitant decrease in ΔE_{ST} . The $U_{syn} < U_{anti}$ reveals that the repulsive terms between the radical and the sulfur decrease in **2**, which can be explained by the location of the radical center relative to the sulfur in cross conjugation compared to linear conjugation in **1** (see bold paths in the boxes of Figure 4.1). In addition, $t_{ab-syn} < t_{ab-anti}$ is due to enlargement of the interaction distance between the two radicals in the delocalized forms **Lk** and **Ck**. Form **Ck** is possible in **2** because of the same cross conjugation effect, while in the case of **1**, this delocalized form is less feasible due to geminal repulsion between the radical and the sulfur. To further corroborate this description, Figure 4.4 shows the odd-electron density maps for **1** and **2**, which indicate very little amplitude on the S atom of **2** yet rather large amplitude in the same heteroatom in **1** (see Figure C.11) for the HONO/LUNO orbitals and Figure C.12 for the Mulliken population analysis). This illustrates the effect of the cross-conjugation mode in the *syn* isomer, which isolates the sulfur from the radical conjugation paths. All these factors contribute to a suitable modulation of ΔE_{ST} , thus fulfilling our purposes in this study.

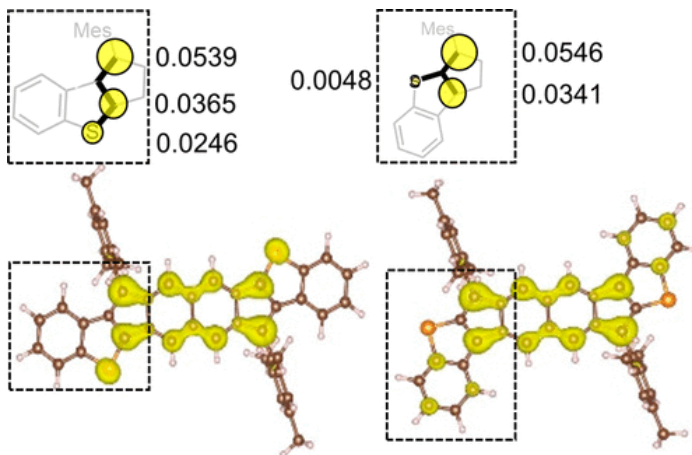
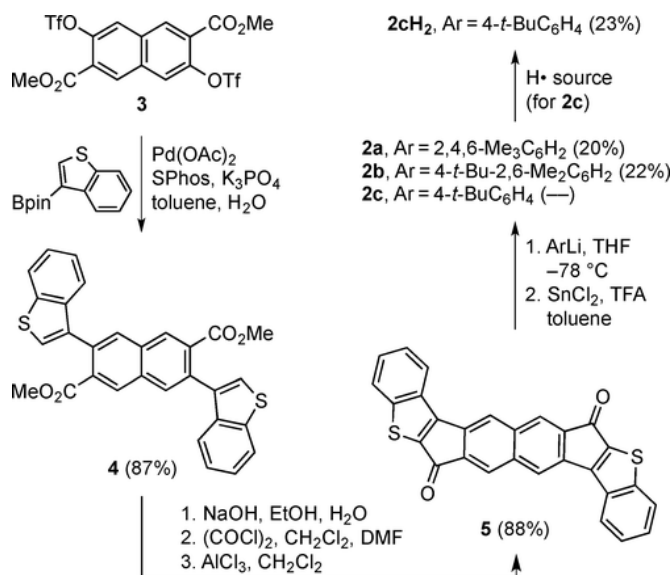


Figure 4.4 Odd-electron density maps for **1a** (left) and **2a** (right) with contour value 0.0005 au calculated at the tuned-LC-RBLYP-CASCI(2,2)/6-311G* level. Mulliken population analysis for the odd-electron density on the relevant carbon and sulfur atoms of the linear and cross-conjugated paths is shown on top.

In solid state physics, the Hubbard model¹⁵ successfully accounts for the electronic properties of conductive and semiconducting π -conjugated materials in which two basic electronic parameters are considered among the interacting electrons, namely the transfer integral, t , and the repulsion term U . One prediction of the model is that the

semiconducting energy gap increases with increasing U and decreases with increasing t (a nice case of this U versus t balance is the Mott metal-insulator transition¹⁶). This description is very similar to that employed in the two-electron model for our case. Here, though t_{ab} is not equal for both isomers, the increase of electronic repulsion U in **1** compared to **2** enlarges the observed magnetic ΔE_{ST} gap on **2** \rightarrow **1**. This comparison nicely discloses the close correspondence between solid-state physics and molecular physics to address closely related phenomena.



Scheme 4.1 Synthesis of *syn*-IIDBTs **2** including dihydro-products.

Encouraged by the promising theoretical predictions, the *syn*-IIDBTs **2** were prepared via a similar synthetic route used for **1**. Starting from known bistriflate **3**¹⁷ (Scheme 4.1), Suzuki-Miyaura cross-coupling with benzothiophene 3-boronpinacolate ester¹⁸ furnished diester **4** in an 88% yield. Saponification of **4** followed by acyl chloride formation and then intramolecular Friedel-Crafts acylation yielded essentially insoluble dione **5**. Reaction of **5** with mesityllithium at -78°C gave the penultimate diol, which is then reductively dearomatized using SnCl_2 in rigorously anaerobic and anhydrous reaction conditions to afford fully conjugated, deep green **2a** in modest yield. Use instead of 2,6-dimethyl-4-*t*-butylphenyllithium or 4-*t*-butylphenyllithium gave *syn*-IIDBTs **2b** and **2cH₂**, respectively, with the latter structure gaining two hydrogen atoms because of the reduced steric protection of the radical centers, in analogy to formation of **1cH₂**.⁹

Additionally, treatment of the known *anti*-IIDBT dione⁹ with 2,6-dimethyl-4-*t*-butylphenyllithium followed by SnCl₂ furnished the new *anti*-IIDBT **1b**.

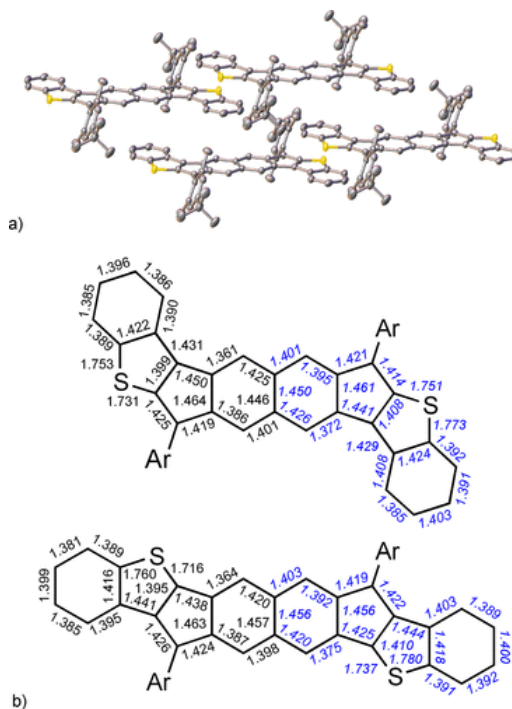


Figure 4.5 (a) Molecular packing of **2b** with the ellipsoids drawn with 50% probability level; hydrogens are omitted for clarity. (b) Experimental (black) bond lengths for the core motifs of **2b** and **1a** along with the calculated (blue) values for **2a** and **1a**.

Dark green crystals suitable for X-ray diffraction were obtained by slow evaporation of a solution of **2b** in a 10:1 mixture of CHCl₃ and CH₃CN. The resultant X-ray structure along with the relevant experimentally- and computationally-determined bond lengths for **1** and **2** are given in Figure 4.5. The X-ray data revealed that the carbon-carbon bond length from the apical carbon to the naphthalene core is 1.419(4) Å, which is comparable in length to the analogous bond in the crystal structures of **1a** (1.424(4) Å)⁹ and **1d** (1.426(5) Å; see Figure C.20 in Appendix C). All three values are roughly the same within experimental error and suggest a pronounced open-shell character of the IIDBT scaffold. In contrast, the analogous CC bond in closed-shell molecules is usually in the range of 1.38-1.40 Å.^{11a,c,12b} Interestingly, these ~1.42 Å values also show that the steric bulk of the aryl group attached to the apical carbon has little to no effect on this bond length (e.g., **1d**), as might be expected given their orthogonality with respect to the

plane of the IIDBT framework. The biggest disparity between the structures of **1a/d** and **2b** resides in the thiophene rings, where there is a marked difference in the C–S bond lengths—1.731/1.753 Å for **2b** vs. 1.716/1.760 Å for **1a**, reflecting the differences in S orientation, i.e., the linear conjugation vs. cross conjugation arguments. The computational bond lengths do an excellent job replicating the aforementioned trends (Figures 4.5 and C.13).

In the crystal lattice, **2b** packs as dimeric pairs where one of the outer benzene ring overlaps with the same ring of its nearest neighbor with intermolecular π – π distances of 3.47–3.51 Å. Although the odd-electron density map in Figure 4.4 does show some spin density on three of the benzene carbons of **2a**, these particular carbons overlap with the three benzene carbons that have no spin density; thus, the likelihood of magnetic interactions between neighboring molecules in the solid state is minimal. This result is in sharp contrast with Kubo’s related bisphenalenyl-fused indacene (**6**)¹⁹ and indenoindene (**7**)²⁰ molecules that do display multiple close π – π contacts between carbons of high spin density of the phenalenyl groups (e.g., 3.10–3.23 Å for **7**), suggestive of strong π -dimer formation in the solid state (Figure 4.6) In the case of **1a** there are only two close π – π contacts (3.49 and 3.53 Å), whereas in **1d** the analogous distances are all >3.7 Å; however, the outer benzenes possess no spin density (Figure 4.4), indicating no intermolecular magnetic interactions are present within these IIDBT scaffolds in the solid state.

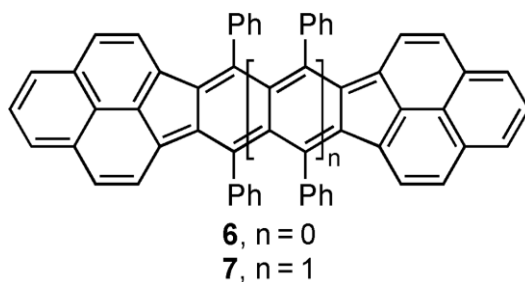


Figure 4.6 Bisphenylenyl-fused indacene (**6**) and indenoindene (**7**) for comparison.

The electronic absorption spectra (Figure 4.7, top) depict a redshift of +25 nm from 724 to 749 nm going from **1a** to **2a**, indicating a reduction of the optical gap even though the two compounds are compositionally identical. Quantum chemical calculations

(TD-UB3LYP/ 6-311G* level) also predict a similar redshift from 703 nm for **1a** to 741 nm for **2a** of the main lowest energy lying theoretical excitation, which corresponds to a HOMO-LUMO transition. In the lowest energy part of these strong absorptions, weak shoulders can also be observed that are typical of diradical molecules and are associated with double excitations. This is related with the $t_{ab-syn} < t_{ab-anti}$ discussion above and, as such, it is explained in terms of an extended conjugational path in **2** between the two radical centers due to cross conjugation, which limits the effect of the sulfurs on it.

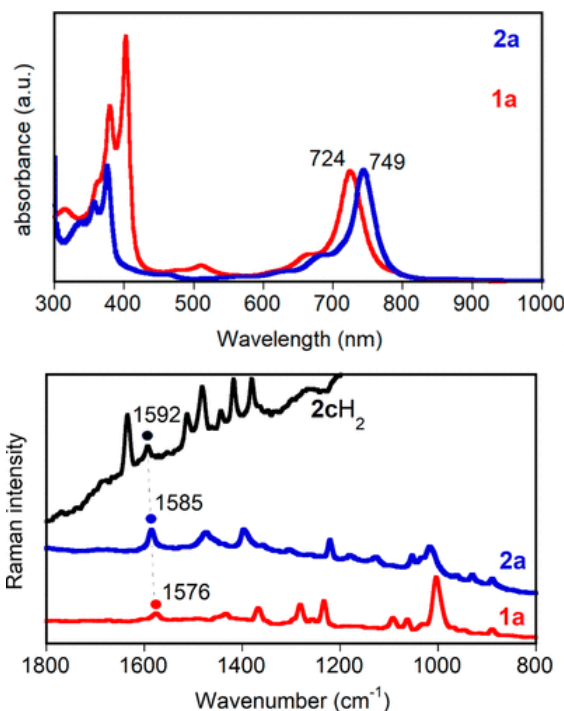


Figure 4.7 Electronic absorption (in CH_2Cl_2 , top) and Raman spectra (in the solid state with 1064 nm laser excitation, bottom) of **1a** (red) and **2a** (blue). Raman spectrum of aromatized **2cH2** is in black.

The solid-state Raman spectra of **1a** and **2a** at room temperature are shown in Figure 4.7 (bottom). The characteristic C=C stretching mode of the central naphthalene unit in **1a** appears at 1576 cm^{-1} and is representative of a transitional structure from quinoidal to aromatic for this core. This is in agreement with a medium diradical index of $y=0.61$, confirming that aromaticity recovery is the main driving force for diradical formation, although it is not fully completed.^{5c,9} In the case of **2a** ($y=0.66$), the same yet more intense Raman band emerges at 1585 cm^{-1} , upshifted by $+9\text{ cm}^{-1}$, indicating an

additional gain of aromatization of the naphthalene core in this isomer. In addition, this band is only $+7\text{ cm}^{-1}$ away from the same stretching mode in **2cH₂** (1592 cm^{-1}), a molecule that contains a fully aromatized naphthalene (note that in **1a** \rightarrow **1cH₂** the upshift is $+11\text{ cm}^{-1}$). The emerging interpretation is that the contribution of the 2,6-naphthoquinoidal conjugation to ΔE_{ST} does not arise separately from cross-conjugation of the sulfur lone pair and the radical, but there is a synergy between the two. We mean that delocalization of the radical to *k* in form **Ck** of Figure 4.1 enlarges/weakens the distance/interaction between the two radicals which simultaneously reinforces the aromatic character of the central naphthalene.

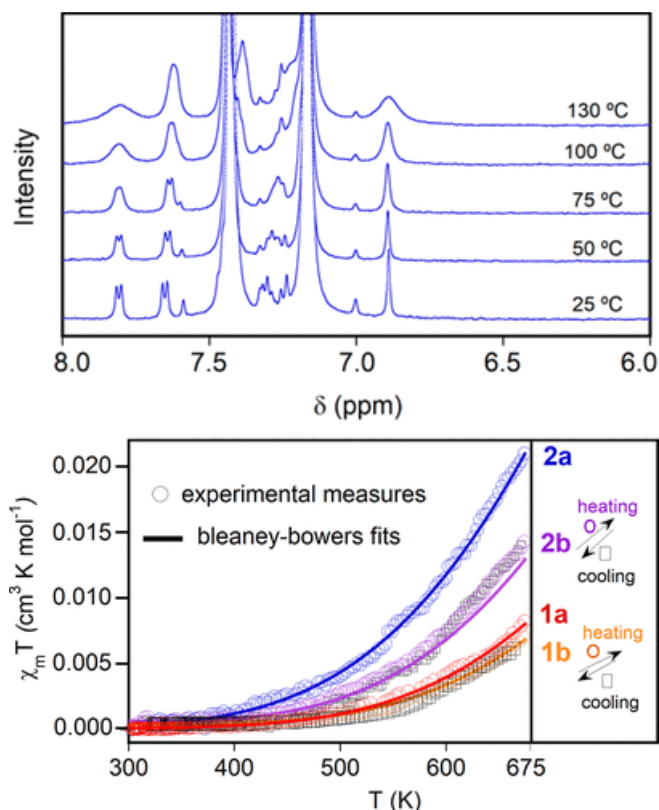


Figure 4.8 (Top) Variable-temperature ^1H NMR spectra (in $1,2\text{-C}_6\text{D}_4\text{Cl}_2$) of **2a**. (Bottom) SQUID magnetometry data of **1a,1b** and **2a,2b**; for **1b** and **2b** the data for the heating and cooling curves are denoted by squares and circles, respectively.

The ^1H NMR spectra of **2a** as a function of the temperature are shown in Figure 4.8 (top). At room temperature, the spectrum is clearly resolved with all peaks assignable to the structure of **2a**. At higher temperatures these peaks have broadened as is clearly observed at $130\text{ }^\circ\text{C}$. While this behavior was observed for **1a**, the onset of peak

broadening in **2a** occurs at a considerably lower temperature (75 °C) compared to that for **1a** (125 °C), suggesting a smaller singlet-triplet energy gap.

In the solid state, SQUID measurements for **2a** (Figure 4.8, bottom) show a clear increase of the molar susceptibility from low to high temperature that is typical behavior of singlet low-spin ground electronic state from which a high-spin triplet excited state is populated thermally. Fitting the data to the Bleany-Bowers equation²¹ yields a singlet-triplet energy gap of $-6.9 \text{ kcal mol}^{-1}$, which agrees well with the ΔE_{ST} predicted from calculations ($-8.06 \text{ kcal mol}^{-1}$). Furthermore, the matching of the experimental data to a Bleany-Bowers dimer model confirms the rather small spin-spin intermolecular interaction in the solid such as revealed by the large π - π distances in the X-ray data. This $\sim 1 \text{ kcal mol}^{-1}$ modulation of ΔE_{ST} in **2a** demonstrates the finer tuning of ΔE_{ST} in the closely related IIDBT regioisomers. This result stands in contrast to the much larger range of ΔE_{ST} values that result from variation of the size of the acene diradical core (i.e., the number of fused rings). For example, in the family of bis-phenalenyl-fused molecules, ΔE_{ST} varies from $-7.2 \text{ kcal mol}^{-1}$ for **6** to $-4.5 \text{ kcal mol}^{-1}$ for **7** and $-2.9 \text{ kcal mol}^{-1}$ for the analogue possessing an anthracene core.²²

One of the unique attributes of the IIDBTs is the need for pronounced heating in order to populate the triplet state, which then raises the question of the thermal stability of the scaffold. Thermogravimetric analysis (TGA, Figure C.16-C.19) of both sets of isomers reveals that the onset of decomposition is $\sim 375 \text{ °C}$ with significant mass loss above 400 °C . Examination of the data for **1a** indicates that the first two events are sequential loss of the mesityl groups followed by decomposition of the conjugated core at higher temperatures ($>450 \text{ °C}$). Heating samples of **1b** and **2b** in the SQUID up to 675-700 K and then cooling back to room temperature (Figures 4.8 and C.14 & 15) afford ΔE_{ST} values (**1b**: H -8.2 /C $-8.4 \text{ kcal mol}^{-1}$; **2b**: H -7.2 /C $-7.0 \text{ kcal mol}^{-1}$) that are in very good agreement with those obtained by only heating SQUID samples of **1a** and **2a** (-8.0 and $-6.9 \text{ kcal mol}^{-1}$, respectively), further corroborating the thermal stability of the IIDBT family of diradicaloids.

4.4 Conclusions

In summary, we have demonstrated a finer, rational adjustment of ΔE_{ST} by *anti* \rightarrow *syn* isomerism of the IIDBT framework. The two constitutional isomers have a common 2,6-naphtho core that contributes the greater amount to ΔE_{ST} whereas *anti/syn* flip modulates this value within ~ 1 kcal mol⁻¹, which we attribute to the combination of change in the relative position of the radical and of the S atom together with the change from linear to cross conjugation. Importantly, we have shown that IIDBTs **1** and **2** are stable singlet diradicaloids at room temperature and only access the triplet state at elevated temperatures, where they are stable upwards of 375-400 °C as revealed by TGA analysis as well as by the reversibility of the high temperature SQUID measurements.

With this study we have posited the question of the necessary fine control of ΔE_{ST} in a stable diradical as the way to design tailored open-shell molecules with control of their emerging properties. While most published studies employ a more qualitative approach to varying ΔE_{ST} without much emphasis on the actual ΔE_{ST} outcome, knowledge of how to subtly tune the singlet-triplet energy gap as well as understanding of what diradical parameter one is altering will be essential for future design and use of diradicals in materials applications. Practical diradicals are those with intermediate diradical character (i.e., greater stability, efficient non-linear optical response, capability of photonic control, etc.) where the tailored design of ΔE_{ST} becomes mandatory. Additional efforts to accomplish this tailoring via a “structural refinement approach” will be the subject of future studies.

4.5. Experimental Section

4.5.1 General Experimental Details

All air-sensitive manipulations were carried out under an inert atmosphere using standard Schlenk technique. For moisture sensitive reactions, THF and toluene were refluxed with Na benzophenone ketyl for 24 h prior to distillation and use. Silica gel (240-300 mesh) was used for column chromatography. All other reagents were purchased and used as received. NMR spectra were recorded on a Bruker Avance III HD 500 equipped with a Prodigy multinuclear cryoprobe (¹H: 500 MHz, ²D: 77 MHz) or Bruker Avance III HD 600 equipped with a Prodigy multinuclear cryoprobe (¹H: 600 MHz, ¹³C:

151 MHz) NMR spectrometer at room temperature (unless otherwise noted). ^1H and ^{13}C NMR chemical shifts (δ) are expressed in ppm relative to the residual non-deuterated solvent reference (CDCl_3 : ^1H 7.26 ppm, ^{13}C 77.16 ppm; CD_2Cl_2 : ^1H 5.32 ppm, ^{13}C 53.84 ppm; $\text{DMSO-}d_6$: ^1H 2.50 ppm, ^{13}C 39.52 ppm). UV-Vis spectra were recorded on an Agilent Technologies Cary 60 UV-Vis spectrometer in HPLC grade CH_2Cl_2 . *anti*-Dione,⁸ compound **3**⁹ and 3-(4,4,5,5-tetramethyl-1,3,2-dioxaborolan-2-yl)benzo[*b*]thiophene¹⁰ were prepared according to literature procedures.

4.5.2 Synthetic Details

Diester 4. A two-neck round-bottom flask fitted with a condenser was charged with bistriflate **3**⁹ (0.500 g, 0.925 mmol, 1 equiv.), benzothiophene 3-boronpinacolate ester¹⁰ (0.601 g, 2.31 mmol, 2.5 equiv.), K_3PO_4 (0.589 g, 2.78 mmol, 3 equiv.), $\text{Pd}(\text{OAc})_2$ (8.3 mg, 0.037 mmol, 0.04 equiv.), and SPhos (30.4 mg, 0.074 mmol, 0.08 equiv.). These solids were then placed under N_2 atmosphere and dissolved in toluene (40 mL) and H_2O (1 mL) that had been sparged with N_2 for 1.5 h. After refluxing overnight and cooling to room temperature, the reaction was quenched with H_2O and poured over filter paper. The precipitate was washed with H_2O and MeOH to yield diester **4** (409 mg, 87%) as a yellow solid. ^1H NMR (500 MHz, CDCl_3 , 25 °C) δ 8.54 (s, 2H), 8.09 (s, 2H), 7.94 (d, J = 8.0 Hz, 2H), 7.51 (d, J = 7.8 Hz, 2H), 7.46 (s, 2H), 7.39 (t, J = 7.3 Hz, 2H), 7.35 (t, J = 7.4 Hz, 2H), 3.53 (s, 6H); ^{13}C NMR (151 MHz, CDCl_3 , 25 °C) δ (ppm) 168.02, 139.82, 139.21, 136.80, 133.61, 133.24, 132.05, 131.58, 131.07, 124.58, 123.93, 123.02, 122.32, 52.50; HRMS (ES^+) (m/z), calculated for $\text{C}_{30}\text{H}_{20}\text{O}_4\text{NaS}_2$ ($\text{M}+\text{Na}$)⁺ 531.0701, found 531.0654.

***syn*-Dione 5.** A round-bottom flask fitted with a condenser was charged with diester **3** (0.400 g, 0.786 mmol, 1 equiv.), KOH (0.706 g, 12.6 mmol, 16 equiv.), EtOH (60 mL), and H_2O (15 mL). After refluxing the flask overnight, the reaction was cooled and the EtOH evaporated. Concentrated HCl was slowly added to the aqueous solution and a precipitate formed, which was isolated and washed with H_2O to yield the diacid intermediate as a yellow solid that was carried on without further purification.

To a suspension of the diacid (0.345 g, 0.718 mmol, 1 equiv.) in CH_2Cl_2 (40 mL) was added 3 drops of DMF followed by oxalyl chloride (0.24 ml, 2.87 mmol, 4.0 equiv.).

After 12 h, the volatiles were removed under reduced pressure. The crude acid chloride was dissolved in CH₂Cl₂ (40 mL) and solid AlCl₃ (0.479 g, 3.59 mmol, 5 equiv.) was added to the flask. The reaction was stirred overnight and then poured into an HCl-ice mixture, precipitating the dione. The solid was filtered and washed successively with H₂O, CH₂Cl₂ and acetone to afford dione **5** as a purple solid (0.302 g, 88%) that was too insoluble to obtain NMR spectra. HRMS (ES⁺) (*m/z*), calculated for C₂₈H₁₃O₂S₂ (M+H)⁺ 445.0351, found 445.0352.

syn-IIDBT 2a. In an oven-dried round bottom flask, a suspension of dione **5** (0.195 g, 0.439 mmol, 1 equiv.) in dry THF (20 mL) was cooled to -78 °C under a N₂ atmosphere. In a separate oven-dried round bottom flask, 2-bromomesitylene (0.537 mL, 3.51 mmol, 8 equiv.) was dissolved in dry THF (20 mL), cooled to -78 °C under a N₂ atmosphere, and *n*-BuLi (2.5 M in hexanes, 1.32 mL, 3.29 mmol, 7.5 equiv.) was added dropwise. After stirring the mixture at -78 °C for 1 h, the aryl lithiate was transferred via cannula to the flask containing the dione. This reaction mixture was stirred for 4 h at -78 °C, then slowly warmed to room temperature overnight with stirring. The reaction was then quenched with a saturated aq. NH₄Cl solution and extracted with CH₂Cl₂ (3×). The combined organic layer was washed with brine, dried (MgSO₄) and concentrated in vacuo. The resulting crude residue was passed through a silica plug eluting with hexanes, followed by a CH₂Cl₂ wash, to provide the desired diol that was carried onto the reductive dearomatization step without further purification.

In a single-neck round-bottom flask the crude diol (0.140 g, 0.204 mmol, 1 equiv.) and anhydrous SnCl₂ (0.154 g, 0.84 mmol, 4 equiv.) were dissolved in dry degassed toluene (60 mL). Trifluoroacetic acid (5 drops) was added and this mixture was then vigorously stirred. The reaction was monitored via TLC (9:1 hexanes/CH₂Cl₂). After 3 h, the solvent was evaporated and the solid was washed with cold MeCN to remove trace impurities. The remaining solid was redissolved in CHCl₃ and MeCN was layered over the solution to furnish *syn*-IIDBT **2a** as a deep green solid (0.055 mg, 20% from **5**). Unfortunately, **2a** proved to be poorly soluble so that only its proton NMR spectra could be obtained. ¹H NMR (500 MHz, CDCl₃, 25 °C) δ (ppm) 7.71 (d, *J* = 7.9 Hz, 2H), 7.55 (d, *J* = 8.0 Hz, 2H), 7.24 (m, 2H), 7.17–7.13 (m, 4H), 6.99 (s, 4H), 6.64 (s, 2H), 2.37 (s,

6H), 2.28 (s, 12H); HRMS (ES⁺) (*m/z*), calculated for C₄₆H₃₅S₂ (M+H)⁺ 651.2175, found 651.2174.

***syn*-IIDBT 2b.** Following the procedure described above for **2a**, dione **5** (0.115 g, 0.26 mmol, 1 equiv.), 2-bromo-5-*t*-butyl-1,3-dimethylbenzene (0.625 g, 2.59 mmol, 10 equiv.), and *n*-BuLi (2.5 M in hexanes, 0.984 mL, 2.46 mmol, 9.5 equiv.) were reacted to give the crude diol. Dearomatization of the crude diol (0.130 g, 0.17 mmol, 1 equiv.) with anhydrous SnCl₂ (0.125 g, 0.68 mmol, 4 equiv.) gave a deep green solution which was reacted for 4 h and then filtered through a pad of celite. The filtrate was concentrated, triturated with MeCN, and filtered to yield *syn*-IIDBT **2b** as a deep green solid (40 mg, 22% from **5**). ¹H NMR (600 MHz, CD₂Cl₂, 25 °C) δ 7.74 (d, *J* = 6.8 Hz, 2H), 7.58 (d, *J* = 8.0 Hz, 2H), 7.30–7.26 (m, 2H), 7.23–7.16 (m, 8H), 6.67 (s, 2H), 2.31 (s, 12H), 1.38 (s, 18H); ¹³C NMR (126 MHz, CD₂Cl₂, 25 °C) δ (ppm) 151.20, 147.70, 146.77, 140.84, 140.04, 138.98, 136.47, 133.37, 132.35, 131.93, 129.76, 129.22, 128.29, 125.57, 125.35, 124.70, 123.99, 122.21, 34.36, 31.09, 20.56; HRMS (ASAP) (*m/z*) calculated for C₅₂H₄₇S₂ (M+H)⁺ 735.3119, found 735.3119.

DihydroIIDBT 2cH₂. Following the procedure described above for **2a**, dione **5** (0.1 g, 0.225 mmol, 1 equiv.) and 1-bromo-4-*tert*-butylbenzene (0.39 mL, 2.25 mmol, 10 equiv.), and *n*-BuLi (1.6 M in hexanes, 1.34 mL, 2.14 mmol, 9.5 equiv.) were reacted to yield the crude diol. The diol (0.1 g, 0.14 mmol, 1 equiv.) and SnCl₂ (0.107 g, 0.56 mmol, 4 equiv.) were reacted at 70 °C. After 4 h, the mixture was poured over a silica plug and washed with hexanes. Switching to 3:1 hexanes/CH₂Cl₂ eluted the crude product. The dihydro product was further purified using preparative TLC using 2:1 hexanes/CH₂Cl₂ as eluent to furnish **2cH₂** (21 mg, 23% from **5**) as a pale yellow solid. ¹H NMR (500 MHz, CD₂Cl₂, 25 °C) δ (ppm) 8.29 (d, *J* = 7.9 Hz, 2H), 8.15 (s, 2H), 7.90 (d, *J* = 7.9 Hz, 2H), 7.82 (s, 2H), 7.55 (t, *J* = 7.6 Hz, 2H), 7.41 (t, *J* = 7.6 Hz, 2H), 7.36 (d, *J* = 7.9 Hz, 4H), 7.17 (d, *J* = 7.9 Hz, 4H), 5.36 (s, 2H), 1.31 (s, 18H); ¹³C NMR (126 MHz, CD₂Cl₂, 25 °C) δ (ppm) 152.32, 150.37, 149.92, 145.22, 139.70, 137.68, 136.40, 132.90, 131.54, 127.47, 125.86, 124.98, 124.32, 123.85, 123.68, 122.24, 116.91, 53.85, 53.63, 53.41, 53.20, 52.98, 51.91, 34.40, 31.07, 29.68; HRMS (ASAP) (*m/z*) calculated for C₄₈H₄₀S₂ (M+H)⁺ 680.2572, found 680.2539.

anti-IIDBT 1b. Following the procedure described above for **2a**, *anti*-dione⁸ (0.140 g, 0.32 mmol, 1 equiv.) and 2-bromo-5-*t*-butyl-1,3-dimethylbenzene (0.608 g, 2.52 mmol, 8 equiv.), and *n*-BuLi (1.6 M in hexanes, 1.50 mL, 2.36 mmol, 7.5 equiv.) were reacted to give the crude diol. Dearomatization of the crude diol (0.201 g, 0.261 mmol, 1 equiv.) with anhydrous SnCl₂ (0.198 g, 1.05 mmol, 4 equiv.) gave a deep green solution which was reacted for 4 h and then filtered through a pad of celite. The filtrate was concentrated, triturated with MeCN, and filtered to yield *syn*-IIDBT **1b** (0.074 g, 42% from *anti*-dione) as a deep green solid. ¹H NMR (500 MHz, CD₂Cl₂, 25 °C) δ (ppm) 7.61 (d, $J = 7.7$ Hz, 2H), 7.24–7.13 (m, overlapping singlets and a triplet, 8H), 7.08 (s, 2H), 6.92 (d, $J = 7.8$ Hz, 2H), 6.86 (s, 2H), 2.23 (s, 12H), 1.41 (s, 18H); ¹³C NMR (126 MHz, CD₂Cl₂, 25 °C) δ (ppm) 150.94, 145.30, 144.75, 142.54, 138.76, 138.25, 136.66, 133.00, 131.87, 130.93, 130.59, 130.18, 127.59, 125.54, 125.21, 124.64, 123.88, 122.07, 34.65, 31.62, 20.96; HRMS (ASAP) (m/z) calculated for C₅₂H₄₇S₂ (M+H)⁺ 735.3119, found 735.3076.

4.6 Bridge to Chapter V

The work discussed in Chapter IV is focused on the ability to fine-tune the characteristic properties of diradicaloids, namely the diradical character index (γ) and the singlet-triplet energy gap (ΔE_{ST}). These properties were altered through molecule isomerism and specifically looking to change the electron repulsion factor (U), by changing the interaction pathway and distance between the radical centers of the diradical and the lone pair on the sulfur atom. Importantly through changing the sulfur location we were able to change the singlet-triplet energy gap between molecules to be a difference of approximately 1 kcal mol⁻¹. It is known that the ability to fine-tune the singlet-triplet energy gap will lead to more magnetic applications of diradicals. Modulating the ΔE_{ST} within a 1 kcal mol⁻¹ range is a step in the right direction. The work presented here laid the foundation for the work presented in the next chapter in which we fine-tuned the singlet-triplet energy gap in a series of five different molecules to be within 1.6 kcal mol⁻¹ of each other.

CHAPTER V

DIINDENOANTHRACENE DIRADICALS ENABLE RATIONAL, INCREMENTAL TUNING OF THEIR SINGLET-TRIPLET ENERGY GAPS

5.1 Authorship Statement and Abstract

This chapter includes previously published and co-authored material from:: Dressler, J. J.;_Valdivia, A. C.; Kishi, R.; Rudebusch, G. E.; Ventura, A. M.; Chastain, B. E.; Gomez-Garcia, C. J.; Zakharov, L. N.; Nakano, M.; Casado, J.; Haley, M. M. Diindenoanthracene Diradicaloids Enable Rational, Incremental Tuning of their Singlet-Triplet Energy Gaps. *Chem*, **2020**, 6, 1-16. Further permissions related to the use of the materials excerpted in this chapter should be directed to Cell. This manuscript was written by myself. Editorial assistance was provided by Prof. Mike Haley and Prof. Juan Casado. The experimental work in this chapter was performed by myself, Dr. Gabe Rudebusch, Brian Chastain, and Abel Valdivia.

A fundamental understanding of the inherent electronic and magnetic properties of open-shell diradicaloids is essential so that these properties can be modified to create molecules that meet the potential needs of industry. However, there have been very few attempts to date to systematically accomplish this in diradicaloid compounds. Herein, we present the synthetic, spectroscopic and computational investigation of a series of molecules based on the diindeno[1,2-*b*:1',2'-*g*]anthracene framework. Calculations suggest that by altering the transfer integral term, t_{ab} , we are able to manipulate the diradical character and thus ΔE_{ST} within this series of molecules. Experimentally determined values by SQUID magnetometry show that we can effectively “tune” ΔE_{ST} of the five derivatives within a narrow 1.6 kcal mol⁻¹ range.

5.2 Introduction

Interest in polycyclic aromatic hydrocarbons (PAHs) possessing diradical character has undergone a strong resurgence in recent years. The increase in reports of carbon-based diradicaloids has been fueled by both the inherent novelty of these molecules as well as their promise as organic electronic and magnetic materials.¹ Because

of the different magnetic states that these molecules can possess, diradicaloid hydrocarbons have been posited to be useful in applications such as molecular electronics and spintronics², lithium-ion batteries³, nonlinear optics⁴⁻⁷ and singlet fission.⁸⁻¹⁰ To date, however, their application still remains to be realized, though there have been some preliminary attempts.^{7,11,12} Since the first reports of carbon-centered diradicaloids, namely Thiele's hydrocarbon (**1**, Figure 5.1A) in 1904¹³ and Tschitschibabin's hydrocarbon (**2**) in 1907,¹⁴ the study of this broad class of compounds has offered new insights on the fundamental nature of the π bond as well as on unusual electronic and magnetic properties in π -expanded systems.¹⁵ The desire to explore this chemical space and fully understand these molecules has led to the synthesis of many classes of organic diradicaloids (Figure 5.1B) including but not limited to bisphenalenyls (**3**),¹⁶⁻¹⁹ extended quinodimethanes (**4**),²⁰⁻²² indeno-fluorenes²³⁻²⁶ and related diindenoacenes (**5**)²⁶⁻³³, zethrenes (**6**),³⁴⁻³⁷ anthenes (**7**),^{38,39} and higher-order acenes (**8**).⁴⁰⁻⁴² Arguably the biggest challenge in discovering new diradicaloid PAHs, and thereby limiting our understanding of this class of compounds, is that the diradical character that makes these systems potentially interesting also makes their synthesis demanding. As shown in Figure 5.1B, strategic placement of large steric protecting groups near the areas of high radical density permits more stable derivatives to be characterized successfully. Diradicaloid molecules exhibit a number of less common properties,⁴³⁻⁴⁵ such as a narrow HOMO–LUMO energy gap,¹ low-energy electronic absorptions attributable to a low-lying doubly excited electronic configuration,^{46,47} multicenter bonding,^{16,17} redox amphoterism,^{19,28} electron spin resonance (ESR) signal(s), and peak broadening in the proton NMR spectrum.⁴⁸

To date two basic strategies have been used in diradicaloid PAHs to modify the diradical character index (y) and its closely related observable property, the singlet-triplet energy gap (ΔE_{ST}):¹ (1) altering the length of the π -conjugated core^{21,30,34,38,43} or (2) varying the orientation of the radical centers attached to the core.^{23-25,36,49} While logical series of diradicaloid scaffolds have been reported that rely on one of these two strategies to modulate such properties, the observed variations were often large in magnitude and did not lead to the ability to fine-tune ΔE_{ST} and y in a precise way. The study closest to accomplishing a fine-tuning of ΔE_{ST} was an elegant series of oligorylene ribbons reported by Wu in 2017 with four derivatives within a 2.0 kcal mol⁻¹ range,⁵⁰ however, the work

did not provide insight as to what electronic factors were being affected and there was only modest agreement between the experimental ΔE_{ST} and the calculated values along with limited stability of the longer oligomers. Although concepts such as aromaticity recovery/number of Clar sextets and molecule twisting/nonplanarity provide a straightforward way to qualitatively interpret open shell structures, a fundamental, quantitative knowledge of how to manipulate the underlying physical properties that affect diradical character is lacking. To that end, we seek to rationally design molecules with finely tuned diradical character γ based on the two fundamental quantum chemical quantities that control it,⁵¹ namely an electron-electron repulsion term (U) and an energy resonance term or transfer integral (t_{ab}) that gives account of the electron delocalization. As noted in a recent publication, “The ability to tune the S–T gap would provide materials based on diradicaloid hydrocarbons with accessible bulk magnetic moments and therefore plays a central role in design of materials with conducting and magnetic properties.”⁴⁶

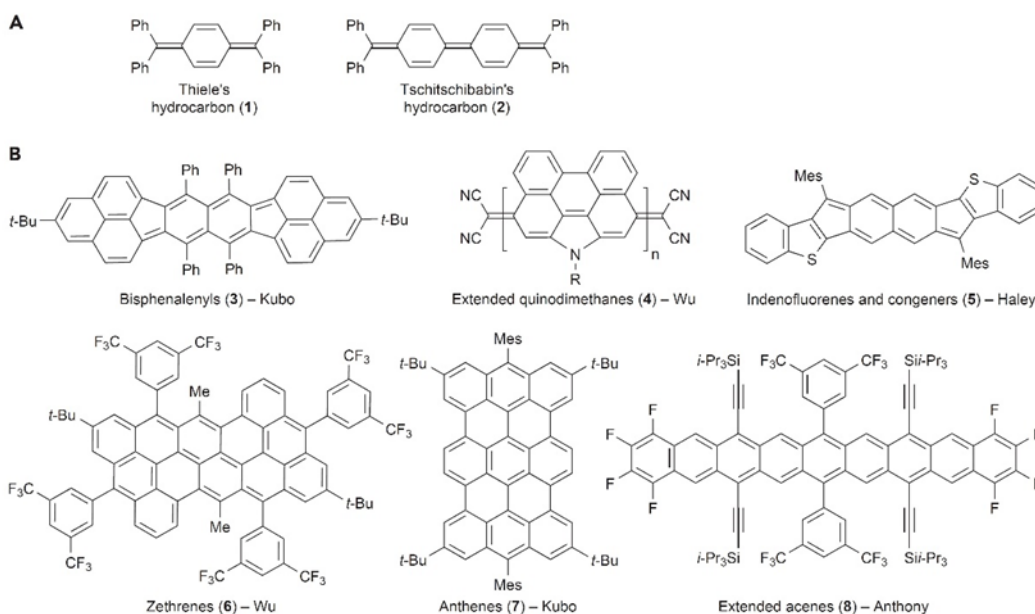


Figure 5.1 Examples of Known Diradicaloid Molecules (A) The first two reported carbon-centered diradicaloids in the literature, Thiele's (1) and Tschitschibabin's (2) hydrocarbons, drawn in the closed-shell resonance form. (B) Representative examples of recently reported diradicaloids (3–8), drawn in the closed-shell resonance form (Mes = 2,4,6-trimethylphenyl).

Though the global analysis of the electronic structure of diradicals is contained in the U vs. t_{ab} balance, an experimental local parameter directly connected with the diradical character is the bond order (BO) of the outer rings fused to the indacene core. In 2016 we reported a series of indeno[1,2-*b*]fluorenes where the change of bond order dramatically affected the strength of the paratropicity within the indacene core.⁵²

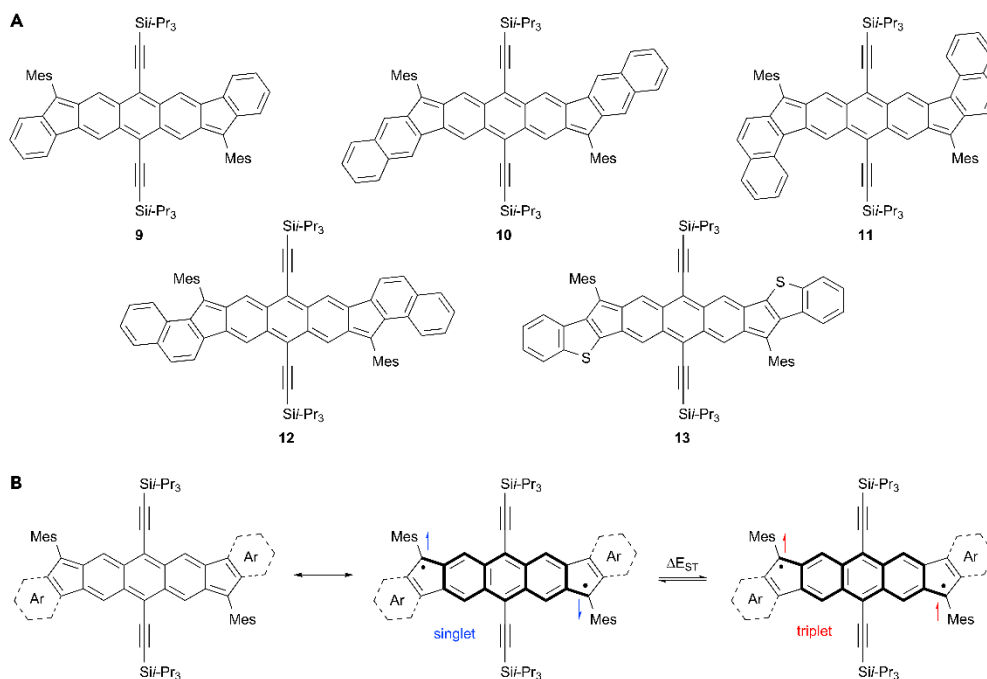


Figure 5.2 Diradicaloid Molecules Based on the diindeno[1,2-*b*:1',2'-*g*]anthracene Scaffold (A) Target DIAn compounds **9–13** illustrate how incremental changes to the diradical scaffold can result in significant changes to the overall magnetic properties of each molecule. (B) Closed shell (left), open shell singlet (center), and open shell triplet (right) forms of a DIAn derivative with generic fused aryl groups; the 2,6-anthraceno conjugation of the two radical centers is shown by the bolded bonds.

Whereas benzothiophene fusion ($BO = 2$) afforded compounds that were nearly as antiaromatic as *s*-indacene itself,²⁹ linear fusion of anthracene ($BO = 1.25$) quenched indacene paratropicity.³² Given the known relationship between antiaromaticity and diradical character,^{45,53} we hypothesize that using the same bond order alteration strategy within the diindeno[1,2-*b*:1',2'-*g*]anthracene scaffold (DIAn, **9**, Figure 5.2A), a stable molecule with significant diradicaloid character,²⁷ would allow us to craft a series of

structurally similar molecules (**10-13**, Figure 5.2A). This “*structure refinement approach*”, based on subtle alteration of molecular geometry yet with retention of the same 2,6-anthraceno π -conjugated quinoidal/diradical core (Figure 5.2B), would enable a systematic, quantitative study examining incremental change in the diradical character y , the ΔE_{ST} energy gap and the overall electronic properties of a closely related series of stable diradicaloids. We recently reported that thiophene isomerism in derivatives of **5** permits rational modification of the repulsion term U and thus a ~ 1 kcal mol⁻¹ change in ΔE_{ST} .⁵⁴ Herein we disclose the preparation of DIAn derivatives **10-13** as well as a new synthesis of **9**, and examine the trend of systematically increasing diradical behavior by variable temperature NMR and Raman spectroscopy, electronic absorbance spectroscopy, and bond length analysis of their solid-state structures. Additionally, in our continuing efforts towards fine-tuning the ΔE_{ST} energy gap in new diradicaloids and in the interest of full understanding of the molecular and electronic-based reasons of such a tuning, we probe ΔE_{ST} experimentally utilizing SQUID magnetometry. In conjunction, quantum chemical calculations are used to rationalize the key electronic factors that lead to such modulation, i.e., the transfer integral t_{ab} .

5.3 Results and Discussion

Calculations: To corroborate the “local” bond order hypothesis as well as the “global” U vs. t_{ab} fine balance in the definition of the diradical properties, quantum chemical calculations on model structures **9’-13’** were performed both without (Table D1) and with the two (trialkylsilyl)ethynyl groups (Table D2). The relevant theoretical diradical index values (y , that takes values of “0” or pure closed-shell molecules and “1” for pure diradicals) calculated at the spin-projected (P)UHF/6-311G* level together with the ΔE_{ST} gaps at the spin-flip time-dependent density functional theory (SF-TDDFT)^{55,56} level are given in Tables D1 and D2, along with the experimentally determined ΔE_{ST} values. A nice correspondence between the experimental and theoretical ΔE_{ST} gaps is observed, which allows us to use the 2 electrons in 2 sites model of diradicals to obtain the main physical parameters (also shown in Tables D1 and D2) dictating their unique diradical structures at the CASCI(2,2)/6-311G* level using the tuned-LC-RBLYP Kohn-Sham orbitals.^{57,58} Note that even though the y and ΔE_{ST} values by the two-electron

model tend to under- and over-estimate the results at the PUHF and SF-TDDFT levels, respectively, the trends of the results by benzo-fusion are well reproduced. These values are all condensed in equations (1) and (2) of this model:

$$\Delta E_{S-T} = \frac{U}{2} \left[1 - \frac{1}{\sqrt{y(2-y)}} \right] + 2K_{ab} = \frac{U}{2} f_{ST}(y) + 2K_{ab} \quad (1)$$

with:

$$y = 1 - \frac{1}{\sqrt{1 + \left(\frac{U}{4t_{ab}}\right)^2}} \quad (2)$$

Here, K_{ab} indicates a direct exchange integral. The increase of the chain length from DIAn (**9'**) to dibenzoDIAns (**10'**, **11'** and **12'**) always decreases t_{ab} (i.e., enhances delocalization over the terminal parts), which is seen by the appearance of odd electron density partially delocalized into the terminal rings (i.e., arrows next to E rings in Figure 5.3; see Figure D.44 for structural depiction of the possible resonance forms). The rationale for this is that the aromatic character of the outer benzenes in DIAn (rings D in Figure 5.3) is slightly stronger than in the equivalent benzenes in the angular-fused dibenzoDIAn derivatives, which is confirmed by the reduced amplitudes of the nucleus independent chemical shift (NICS(1)) values in **11'** and **12'** in Figures 5.3 and D.33. On the other hand, the NICS(1) value on ring D of **10'** is slightly larger than that in **9'**, which accounts for the smaller change in t_{ab} on **9'** → **10'** than in **9'** → **11'**, **12'**. From Equation 2 we see that smaller t_{ab} , such as in the case of dibenzoDIAns compared to DIAn, increases the diradical character in Table D2 because the change in U is relatively small (see the Supplemental Appendix D for further discussion of integrals U and t). Finally, the evolution of the t_{ab} in the dibenzoDIAn series is also in agreement with the overall shift of the low energy absorption bands of the UV/Vis-NIR spectra of **9'** → **10'**/**11'**/**12'** (*vide infra*).

Additional fusion of a six-membered ring onto the bay region of rings C/D/E of **12'** gives rise to the known bisphenalenyl-fused anthracene derivative¹⁸ (BPLA; its structure and computational data are given in Figure D.37 and Table D3). Results for BPLA show a much smaller t_{ab} compared to **12'** (0.467 a.u. in BPLA vs 0.781 a.u. in **12'**) and a larger diradical character y (0.883 in BPLA vs. 0.711 in **12'** at the PUHF level), highlighting the impact of greater delocalization of the odd electron density (Figures

D.38–D.43) in the terminal rings and reduced aromaticity in the common benzenes in BPLA (–5.30/–7.65 ppm in BPLA vs. –7.09/–10.01 ppm in **12'**).

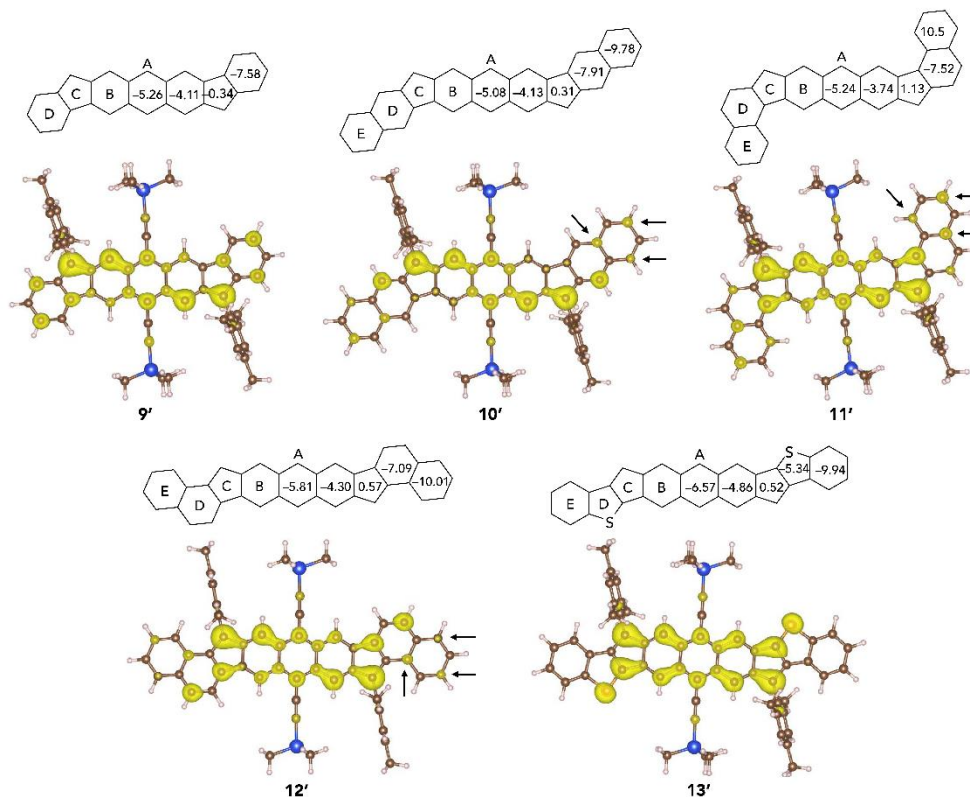


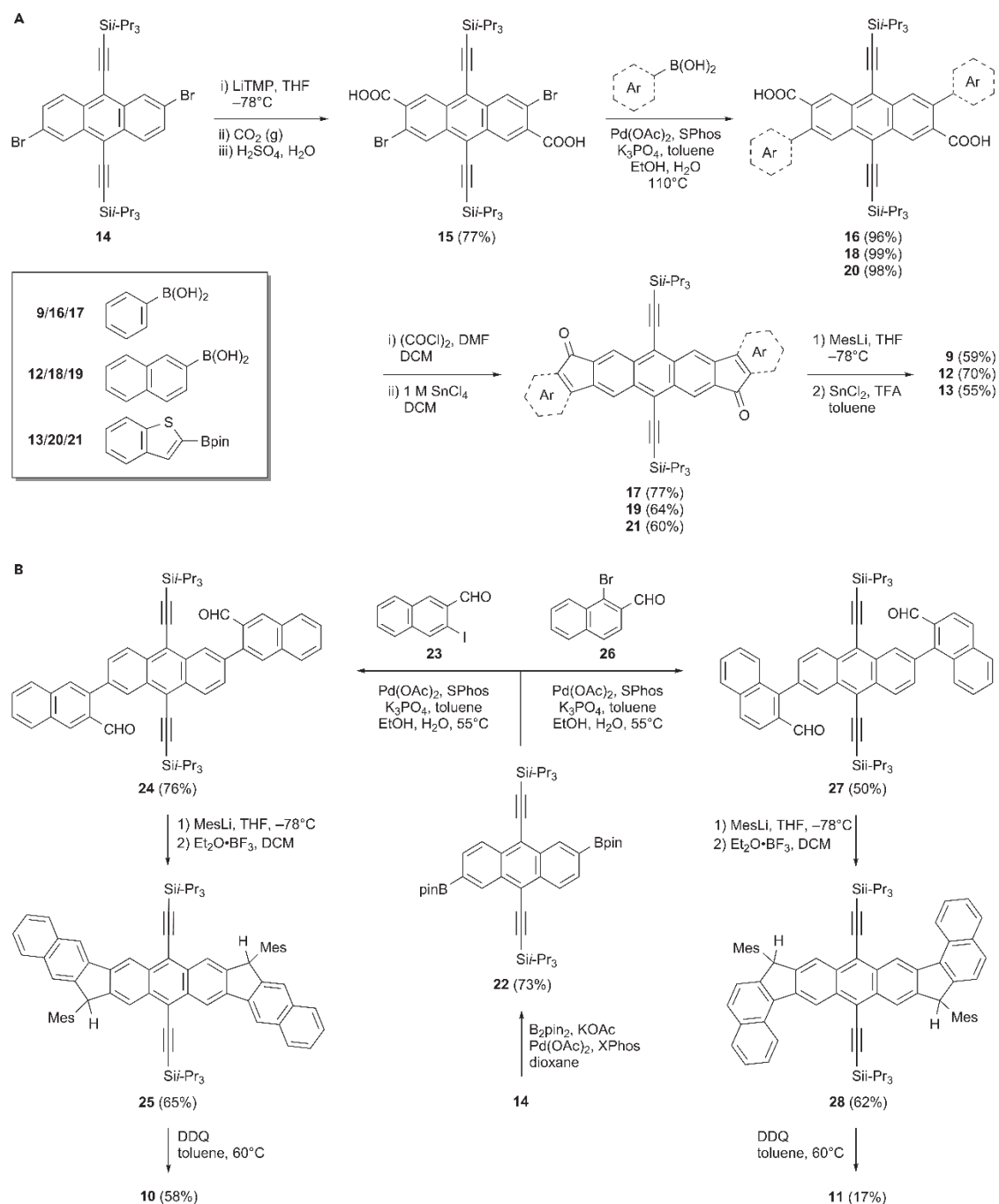
Figure 5.3 Odd Electron Density Maps and NICS(1) Values of Models **9'**–**13'**. Odd-electron densities were calculated at the tuned-LC-RBLYP CASCI(2,2)/6-311G* level. Magnetic response calculations were performed at the LC-UBLYP/6-311G* level where the same range-separating parameters as those for the estimation of physical parameters were employed (for details, see Supplemental Appendix D). Yellow surface of odd-electron density map represents the isosurface with the contour value of 0.0005 a.u. NICS(1) values are in ppm.

The inter-site repulsion term U , the other key electronic factor, decreases from **9'** → **10'**/**11'**/**12'**, but the magnitude of this change is smaller than that in t_{ab} , which results in the increase of y as explained above. However, U , conversely to t_{ab} , increases on **10'** → **11'**/**12'** which might indicate a better repulsion screening in the terminal moiety of **10'**. Even though there is a balance between the $U/2$ and $f(y)$ in ΔE_{ST} , the reduction of U and t_{ab} for **9'** → **10'** results in a slight increase of the ΔE_{ST} as observed experimentally and predicted by calculations. Results of $U/2$ for **10'**, **11'** and **12'** (1.348, 1.378, and 1.377 a.u., respectively) are close to that of phenalenyl analogue BPLA (1.385 a.u.), illustrating

that the major change in the diradical features between the dibenzoDIAn and BPLA primarily comes from the role of t_{ab} .

For the PAHs under study, the t_{ab} term shows the greater difference from compound to compound, meaning that the two unpaired electrons are progressively less coupled or less bonded (larger degree of delocalization) on $\mathbf{10}' \rightarrow \mathbf{11}'/\mathbf{12}'$ and is what primarily determines the variation of y and of the ΔE_{ST} gaps, although the results are determined by the subtle balance of several terms. Conversely, we have recently shown that $y/\Delta E_{ST}$ can be modulated by considering suitable chemical structures that mainly modify U keeping t_{ab} almost constant, for instance, by introducing sulfur atoms within the full PAH structure.^{33,54} As a part of this study, compound **13** with a common anthracene core and terminal benzothiophene-based moieties is also reported. The molecule is isostructural with dibenzoDIAn **12**, where the (CH=CH) motif opposite the apical carbon has been replaced with an isoelectronic S atom. In this case t_{ab} only slightly changes from **12'** (0.781 a.u.) to **13'** (0.774 a.u.), whereas $U/2$ significantly increases from 1.377 a.u. in **12'** to 1.572 a.u. in **13'** and thus justifies the larger diradical character (0.711 in **12'** and 0.815 in **13'**) in spite of a similar ΔE_{ST} (calculated as -3.45 kcal mol⁻¹ in **12'** and -3.41 kcal mol⁻¹ in **13'**, which is primarily due to the reduction of $U/2$ term.⁵⁴

Synthesis: To prepare a family of modified DIAn derivatives, we sought a more modular synthetic route. As with the original preparation of **9**, steric protection at the sites of high radical density with mesityl (2,4,6-trimethylphenyl) groups will kinetically shield the reactive sites, and the large mesityl and (triisopropylsilyl)ethynyl groups should provide resistance to degradation pathways and enhance solubility. Starting from known dibromoanthracene **14**⁵⁹ (Scheme 5.1A), selective deprotonation at the 3- and 7-positions using LiTMP, followed by careful addition of gaseous CO₂ and then protonation with dilute aqueous acid afforded diacid **15** as the key intermediate to which a variety of aryl groups could be attached via Suzuki-Miyaura cross-coupling. Using DIAn itself as a test case, cross-coupling **15** with phenylboronic acid provided



Scheme 5.1. Synthesis of diindeno[1,2-*b:l'*,2'-*g*]anthracenes 9–13 (A) Friedel-Crafts acylation route to prepare 9, 12, and 13, which has been successfully executed with the cross-coupling partners on the bottom left of the scheme. (B) Friedel-Crafts alkylation route to prepare 10 and 11.

diaryldiacid **16** in 96% yield, which was subjected to Friedel-Crafts acylation conditions to form the heptacyclic core of DIAn-dione **17** in very good yield (confirmed by x-ray analysis; see Figure D.65). Nucleophilic attack on **17** by mesityllithium afforded the intermediate diol (not shown), which was then treated with SnCl₂ and catalytic TFA to furnish the fully conjugated core of DIAn **9**, whose spectral data were identical with those previously reported.²⁷ Repetition of this synthetic sequence using either 2-naphthylboronic acid or benzothiophene 2-boronpinacolate ester⁶⁰ gave diacids **18** and **20**, respectively, that were converted into diones **19** and **21**, then ultimately into new DIAn derivatives **12** and **13** isolated as blue and blue-black solids, respectively.

Given the propensity of naphthalene to undergo electrophilic aromatic substitution at the 1/4/5/8-positions, the preparation of the *syn* and *linear* dibenzoDIAn derivatives required a return to the original DIAn synthetic route. Starting again from **14**, Pd-mediated double Miyaura borylation with B₂pin₂ afforded bis(boronate ester) **22** (Scheme 5.1B). Cross-coupling this molecule with two equivalents of iodoaldehyde **23** (see the Supplemental Appendix D for its preparation) gave dialdehyde **24**, which was then reacted with excess MesLi followed by Friedel-Crafts alkylation using BF₃•OEt₂ to furnish dihydroDIAn **25**. Oxidation with DDQ provided the *linear* dibenzoDIAn **10** as an emerald green solid in good overall yield. Repetition of this sequence using bromoaldehyde **26** gave dial **27**, which was turned into dihydro intermediate **28** and then *syn* dibenzoDIAn **11** (army green solid) in an analogous manner. As with the original synthesis of **9**, selective ring closure occurs exclusively at the C3 and C7 positions of the anthracene core as a result of the steric clash between the bulky mesityl and TIPS groups. Careful handling and storage of all the diarenoDIAn derivatives is required once synthesized as these molecules begin to degrade at room temperature if exposed to air for extended periods of time. Unlike the parent system **9**, which has a half-life in solution of 64 days,²⁷ the half-lives of the diarenoDIAns in solution range from ~20 days for **10** to as little as 4.5 days for **13** (Figures D.59-D.62); therefore, as the diradicaloid character of a molecule increases, its stability correspondingly decreases.

To gather more evidence of the diradical nature of these compounds, variable temperature (VT) ¹H NMR spectroscopy was performed with each derivative. Typical of molecules with pronounced open-shell character, the aromatic region of the proton NMR

spectra of **11–13** at room temperature showed either broad, unresolved peaks or a completely flat baseline, as illustrated for **12** in Figure 5.4 (see also Figure D.48 and D.48-D.51). Cooling of the samples in the spectrometer did result in the appearance of discernable peaks around -15 to -30 °C with the peaks continuing to grow until the experimental cut-off of -55 °C, where the aromatic signals never gain full resolution. Importantly, when the instrument was warmed back to room temperature, the new spectrum resembles the original room temperature spectrum, confirming that **11–13** do not undergo a reaction/decomposition during the VT NMR experiments. Attempts to obtain fully resolved spectra of a sample of **12** dissolved in THF- d_8 and cooled to -100 °C were only modestly successful (Figures D.49-D.50) as compound **12** was also less soluble in THF- d_8 than in CDCl_3 .⁶¹ Nonetheless, this experiment suggests that a thermally accessible, magnetically active species is responsible for broadening the aromatic signals and that even at -100 °C the magnetic species is still somewhat populated, justifying the lack of full-resolution.

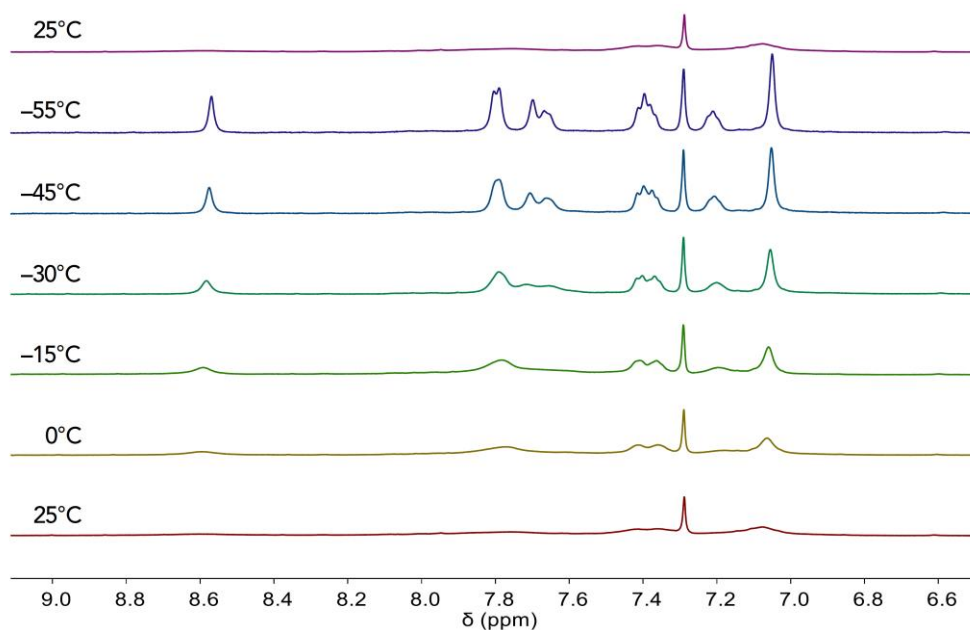


Figure 5.4 Variable temperature NMR spectroscopy studies of **12**. VT ^1H NMR spectra of the aromatic region of *anti*-dibenzoDIAn **12** in CDCl_3 showing thermal depopulation of the paramagnetic triplet state at low temperatures.

In contrast to **11–13**, the VT ^1H NMR spectra collected for *linear* dibenzoDIAn **10** exhibited very little to no peak broadening. At room temperature the aromatic region displayed relatively well-defined aromatic signals and cooling to $-55\text{ }^\circ\text{C}$ resulted in full resolution of the aromatic signals, suggesting the magnetic species was minimally populated at room temperature and below (Figures D.55-D.56). Upon heating a $(\text{CDCl}_3)_2$ solution of **10** to $140\text{ }^\circ\text{C}$, thermal broadening of the aromatic signals only begins to occur at the experimental cut-off (Figures D.57-D.58). The behavior of **10** in the high temperature NMR experiments matches more closely to that of DIAn **9** (onset of broadening at $50\text{ }^\circ\text{C}$),²⁷ with a higher onset point, indicative of the larger singlet-triplet energy gap that **10** possesses.

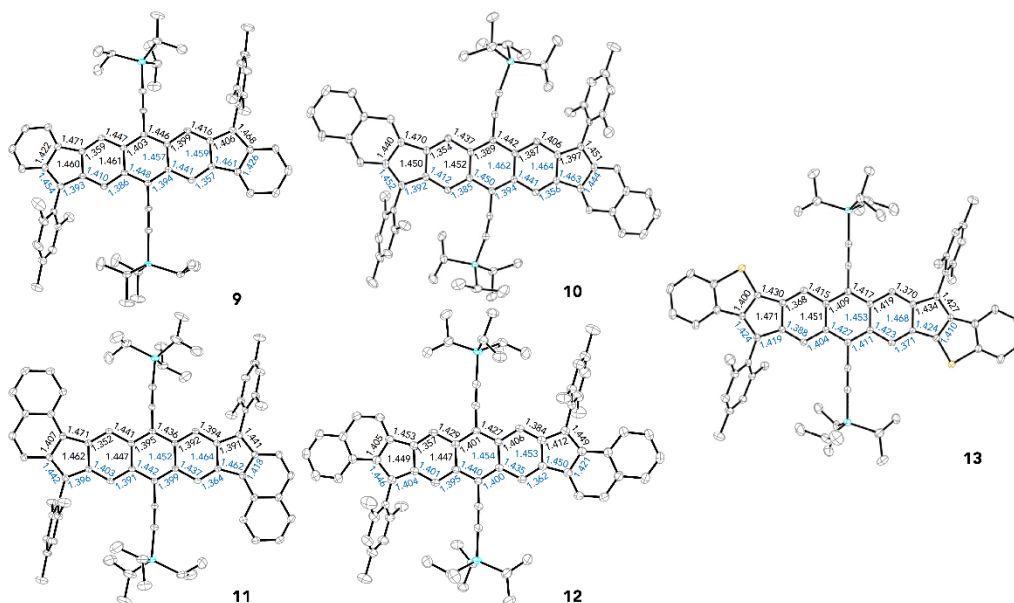


Figure 5.5 X-ray crystallographic analysis of **9–13**. X-ray structures of DIAn derivatives **10–13** with selected bond lengths (Å; experimental values in black, calculated values in blue) along with the previously published data for DIAn **9**; ellipsoids drawn at the 50% probability level. Experimental values for **12** and **13** are the average of the bond lengths found for the three and two symmetrically independent molecules, respectively.

To gain insight into the ground-state molecular structure of diradicaloid PAHs, single-crystal X-ray diffraction (XRD) and bond length analysis of the resultant structures has been used as a rough guideline to compare diradical character experimentally. Fortuitously, crystals that were suitable for XRD were grown by slow diffusion of CH_3CN into CHCl_3 for all four new DIAn derivatives and their structures

secured (Figure 5.5). Similar to **9**, DIAnS **10-13** are centrosymmetric. Molecules **10**, **12** and **13** pack roughly as 1D stacks, whereas **11** appears like a 2D brickwork patterns. There are no short C \cdots C contacts (<3.8 Å) in the structures of **10** or **11**. DibenzodiAn **12** contains two close C \cdots C contacts (~ 3.45 Å) between ring D and the same ring of its nearest neighbor. Compound **13** has close C \cdots C (3.43 Å) and C \cdots S contacts (3.53 Å), also between neighboring D rings. These distances are considerably longer than those for Kubo's related bisphenalenyl-fused arenes (3.1–3.2 Å), which exhibit strong π -dimer formation in the solid state;^{16,17} thus, the likelihood of magnetic interactions between neighboring molecules of **12** and **13** in the solid state is minimal.

The outer naphthalene units of compounds **10-12** have bond lengths typical of a naphthalene motif, pointing to the aromatic character of the outer rings (also supported by the NICS(1) calculations). For benzothiophene-fused **13**, there is a distinct asymmetry in the C–S bond lengths (1.717 and 1.761 Å), similar to what was found for **5** (1.716 and 1.760 Å), which is due to the increased conjugation from the linear arrangement of the *anti*-fused S atom to the radical center versus a cross-conjugation arrangement if the thiophene was fused in a *syn*-fashion.⁵⁴

Examination of the quinoidal core of **10-13** shows that the molecules possess bond lengths similar to those in the core of **9** (as might be expected) that range from 1.352 to 1.471 Å, with several of the quinoidal C=C bond lengths near 1.4 Å. In particular, the bond length from the apical carbon of the five-membered ring carbon to the anthracene core is of great interest, as this can provide a first approximation of how open shell a molecule is. This bond length in structurally analogous mesityl-substituted indenofluorene isomers can be as short as 1.380 Å in the closed shell indeno[1,2-*b*]fluorene²³ and as long as 1.437 Å for proven open-shell indeno[2,1-*b*]fluorene,²⁴ which in the latter is accredited to the open shell resonance form contributing more single bond character to this position as the diradical resonance form gains favor. In the case of PAHs **9-12**, these values run between 1.391–1.412 Å, and is as large as 1.434 Å in **13**, suggesting that there are contributions from both the open-shell and closed-shell resonance structures, corroborating the open-shell nature of these compounds. One might expect a trend of increasing bond length as the diradical character increases (**13** > **12** > **11** > **9** \approx **10**). While this expectation is supported by the calculated bond lengths as well as

by the experimental values for four of the diarenoDIANs, isomer **11** is a notable exception, as it is the shortest of them all (1.391 Å) yet is calculated to be longer and more diradical than **9** or **10**.⁶² It should be noted that the differences in the apical carbon bond lengths between **9-13** are close to the statistical margin of error of the XRD measurements, indicating that although a useful tool to gauge roughly how diradical a compound may be, this comparison is a “local” marker of the diradical character that does not consider the effect globally and is likely insufficient to account for small molecule-to-molecule variations in order to distinguish compounds with very similar diradical characters (e.g., **11** vs. **12**).

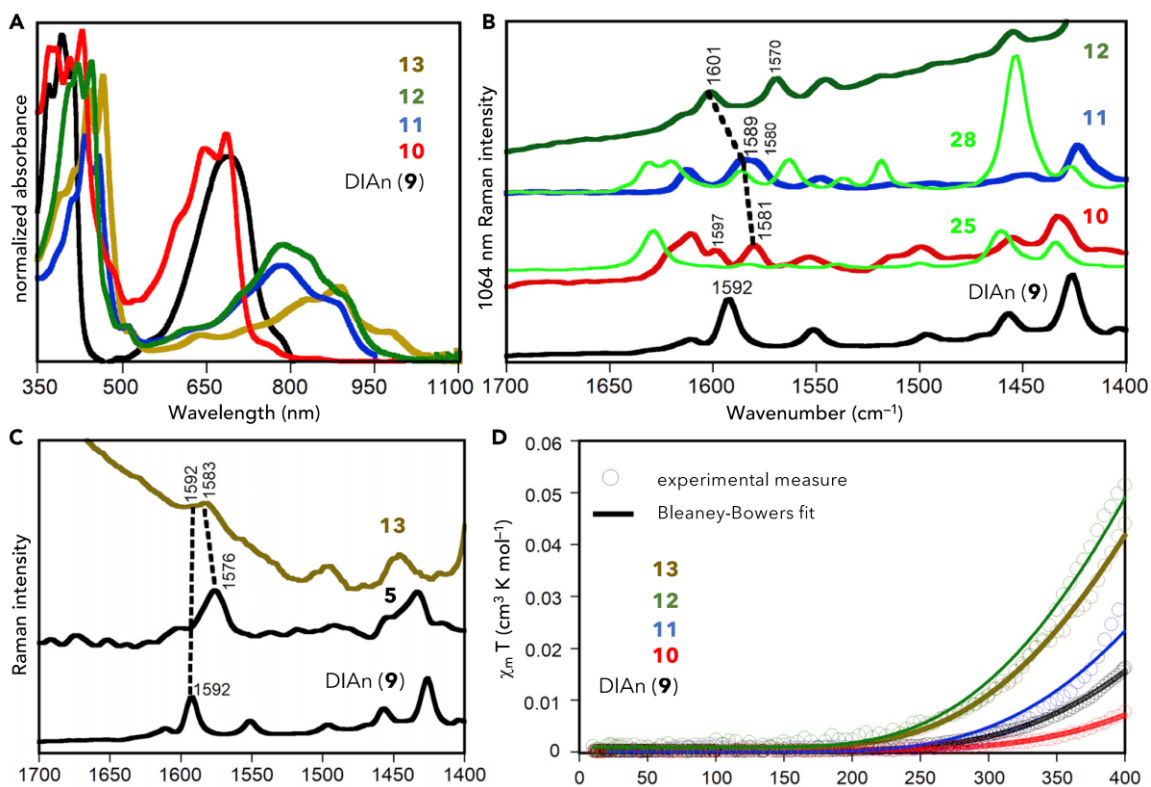


Figure 5.6 Spectroscopy and magnetometry Data of **9-13**. (A) Electronic absorption spectra of DIAN derivatives **9-13** in CHCl_3 solution at room temperature. (B) Raman spectra of **9-12** and comparison with the dihydroDIAN precursors **25** and **28**. (C) Raman spectra of **13** and comparison with **9** and the naphthalene core analogue **5**. (D) SQUID data of **9-13** in the solid state (empty circles) along with the corresponding Bleaney-Bowers fits (solid lines).

The diarenoDIAn derivatives **10-13** exhibit UV-Vis-NIR electronic absorption spectra very similar to other related quinoidal polycyclic hydrocarbons and to the parent DIAn **9** (Figures 5.6A and D.63). In addition, these spectra were recorded at low temperature (i.e., 80 K) in order to deal with those of the singlet ground electronic states clean from triplet interference at 300 K. Each spectrum displays characteristic absorptions of anthracene-based compounds showing electronic absorption in the range of 340-470 nm. Interestingly, in the low energy region linear-**10** displays a slight blue-shifted absorption (700 nm) when compared to DIAn **9** (711 nm); however, there is a marked redshift on going from **10** to *syn*-**11** (803 nm), *anti*-**12** (839 nm), and **13** (955 nm), which is in agreement with the rather small change of the t_{ab} term on **9** → **10** and with the pronounced decrease of t_{ab} on going from **10** to **11/12** (see Table D2 and discussion thereof). The rich blue/green colors of **10-13** can be accredited to these low energy absorptions that tail off into the near IR region (850-1050 nm), due to the narrow HOMO-LUMO gap of these derivatives and are indicative of the large diradical contribution to the ground state. In addition, at lower energies, well defined bands are recorded at 791 nm in **9**, 759 nm in **10**, 892 nm in **11**, 902 nm in **12**, and 1044 nm in **13**, which behave in parallel to the main ones and that are explained as electronic absorptions arising from a low-lying doubly excited electronic configuration⁴⁶⁻⁴⁸. Interestingly, these bands, which usually appear as shoulders at room temperature, are clearly distinguished at 80 K. For completeness of the study, Figure D.64 and Table D4 disclose the cyclic voltammetry electrochemical data also in comparison with that reported for DIAn (**9**), which reveal very good agreement between the optically- and electrochemically determined HOMO-LUMO energy gaps (1.13-1.41 eV) of **9-13**.

To further track the changes in molecule structure from the closed-shell to open-shell resonance structures, Raman spectroscopy (Figure 5.6B) was performed on the three dibenzoDIAn derivatives and compared to the parent **9**. In regard of the interpretation of the significant variation of t_{ab} in this diradical series related with the tuned bonding of the two unpaired electrons through the central common anthracene spacer, the Raman spectra provide evidence of the vibrational structure of this central anthracene core. In the 1550-1600 cm^{-1} vibrational region in particular, the Raman bands associated with the collective C=C stretches of these central anthracene moieties appear, i.e., $\nu_{\text{anth}}(\text{C}=\text{C})$. In

Figures D.45 and D.46, theoretical Raman spectra are discussed whereas Figure D.47 shows the vibrational normal modes on which the assignment of the main Raman bands is based (see additional discussion Supplemental Appendix D). In Figure 5.6B we also show the Raman spectra of the dihydrogenated precursors of **10** and **11**, compounds **25** and **28**, respectively, which undoubtedly possess complete aromatic character in their anthracenes. On **25** \rightarrow **10** and **28** \rightarrow **11**, we observe downshifts of the $\nu_{\text{anth}}(\text{C}=\text{C})$ wavenumber in agreement with the effect of partial quinoidization of these anthracenes (quinoidization always produces wavenumber downshifts).²⁰ According to this, the change between **28** and **11** ($\Delta\nu = 9 \text{ cm}^{-1}$) is smaller than between **25** and **10** ($\Delta\nu = 18 \text{ cm}^{-1}$) as a result of the larger diradical character (i.e., smaller quinoidal character) in **11**. For the series of diradical compounds under analysis we observe that: (i) the $\nu_{\text{anth}}(\text{C}=\text{C})$ wavenumber values of these bands are different from molecule to molecule and simultaneously, all these differ from that of DIAn **9**. (ii) Among **10/11/12**, **10** appears at 1581 cm^{-1} , the lowest wavenumber, revealing that of the three, this molecule keeps the larger degree of quinoidal character (i.e., consistent with the larger ΔE_{ST}). (iii) From **11** to **12**, the difference of 12 cm^{-1} from 1589 to 1601 cm^{-1} is seemingly large but qualitatively consistent with $\Delta E_{\text{ST}}(\mathbf{11}) > \Delta E_{\text{ST}}(\mathbf{12})$. At the same time, this result is in agreement with the smaller $\nu_{\text{anth}}(\text{C}=\text{C})$ differences between **28** and **11**, highlighting that the degree of aromaticity in the central anthracene in **12** is the largest among the three isomers and further corroborated by the smallest ΔE_{ST} found (*vide infra*).

Figure 5.6C also displays the Raman spectra of **13** compared with that of DIAn **9** and with the analogous benzothiophene-fused compound with a central naphthalene, i.e., molecule **5**. An upshift from **5** to **13** of the Raman band associated with the central moieties is detected, showing the larger overall aromaticity gained on the anthracene unit. On the other hand, comparing **13** and **9** we observe the same $\nu_{\text{anth}}(\text{C}=\text{C})$ wavenumber bands at 1592 cm^{-1} , despite $y(\mathbf{9}) \neq y(\mathbf{13})$, which is accounted by the particular U increasing role of the sulfur atoms, an electronic effect that in **9/13** does not essentially alter neither the bond length alternation pattern nor the vibrational pattern of the corresponding anthracenes.

To experimentally examine the magnetic properties of this family of molecules with different computed singlet-triplet energy gaps, superconducting quantum

interference device (SQUID) magnetometry was carried out. The magnetic behaviors up to 400 K were measured and the signal subjected to a Bleaney-Bowers fitting⁶¹ (Figure 5.6D) that only considers a dimer (low spin and high spin states) model. From these adjustments the ΔE_{ST} gaps were obtained and can be compared with the theoretically determined gaps in Table D2. The magnetic measurement is fully reversible and the same curve can be reproduced in the cooling direction back to room temperature (changes smaller than 5% of the total molar magnetic susceptibility before and after one cycle of heating-cooling), indicative of thermally resistant molecules. The absence of hysteresis in the heating/cooling curves shows that the routes for the population and depopulation of the high spin state do not differ. The resulting data also indicate that the ground electronic state is a singlet and the thermally excited state is a triplet, typical of molecules in which the diradical character is expressed by the correlation between the quinoidal and aromatic resonance forms. All of the newly determined ΔE_{ST} gaps are <10% variance from their calculated values. For example, the largest and smallest energy gaps are correctly measured and calculated for **10** ($\Delta E_{ST(\text{exp})} = -4.8$, $\Delta E_{ST(\text{calc})} = -5.09$ kcal mol⁻¹) and **12** ($\Delta E_{ST(\text{exp})} = -3.2$, $\Delta E_{ST(\text{calc})} = -3.45$ kcal mol⁻¹), respectively. Compounds **9**, **11** and **13** also show very good agreement (Tables D1 and D2). This narrow range of 1.6 kcal mol⁻¹ for the experimental ΔE_{ST} values of the five molecules clearly supports our hypothesis of “fine tuning” magnetic properties using a “*structure refinement approach*”.

5.4 Conclusions

In conclusion, a new set of diradicaloid molecules based on the diindeno[1,2-*b*:1',2'-*g*]anthracene motif has been prepared. A complete study addressing their spectroscopic and magnetic characterization together with model quantum chemical calculations has been carried out. Based on the 2 electron / 2 sites model, the diradical character is dictated by two electronic parameters, the repulsion term U and the transfer integral, t_{ab} . Herein, we have shown how to design new diradicaloids based on the fine tuning of the transfer integral term using structure refinement (altering external rings D and E in Figure 5.3) of a series of molecules containing a common 2,6-anthraceno conjugation of the two radical centers. Most notably, by making what might seem to be minor changes to the fusion “bond order” of the outer rings, we are able to incrementally

and rationally tune the singlet-triplet energy gap of the diarenoDIAn series over a narrow 1.6 kcal mol⁻¹ range. As demonstrated by this study, we are aiming to produce real, synthesizable compounds illustrating how to exploit electronic structure concepts such as *U* and *t*_{ab}. These structure-property connections and their complete understanding are mandatory for the rational design of diradicaloid molecules, i.e., diradicals with tailored singlet-triplet energy gaps for specific organic electronic applications.

5.5 Experimental Section

5.5.1 General Experimental Details

All air-sensitive manipulations were carried out under dry nitrogen gas using standard Schlenk techniques. For moisture sensitive reactions, THF and toluene were refluxed with Na benzophenone ketyl for 24 h prior to distillation and use. Silica gel (240-300 mesh) was used for column chromatography. All other reagents were purchased and used as received. NMR spectra were recorded on a Bruker Avance III HD 500 equipped with a Prodigy multinuclear cryoprobe (¹H: 500 MHz, ²D: 77 MHz) or Bruker Avance III HD 600 equipped with a Prodigy multinuclear cryoprobe (¹H: 600 MHz, ¹³C: 151 MHz) NMR spectrometer at room temperature (unless otherwise noted). ¹H and ¹³C NMR chemical shifts (δ) are expressed in ppm relative to the residual non-deuterated solvent reference (CDCl₃: ¹H 7.26 ppm, ¹³C 77.16 ppm; DMSO-*d*₆: ¹H 2.50 ppm, ¹³C 39.52 ppm). UV-Vis spectra were recorded on an Agilent Technologies Cary 60 UV-Vis spectrometer in HPLC grade CH₂Cl₂. In select instances, the poor solubility of the DB-DIAn derivatives hindered acquisition of good ¹³C NMR spectra. Additionally, because of the diradical nature of the fully conjugated DB-DIAn compounds, complete assignment of peaks is not possible due to thermal broadening. Dibromoanthracene **14**¹ and benzothiophene 2-boronpinacolate ester² were prepared as previously described. All other reagents were commercially available and used as received.

5.5.2 Synthetic Details

9,10-Bis(triisopropylsilyl)ethynyl-3,7-dibromo-2,6-anthracenedicarboxylic acid (15). A three-neck round-bottom flask fitted with an addition funnel and a 24/40 Schlenk line adaptor was flame dried and charged with 2,2,6,6-tetramethylpiperidine

(2.93 mL, 17.22 mmol, 6 equiv.) and THF (80 mL). The reaction flask was chilled to 0 °C where *n*-BuLi (8.97 mL, 14.35 mmol, 5 equiv.) was added dropwise and then stirred for 30 min. After cooling the reaction flask to –78 °C, the addition funnel was charged with a solution of dibromoanthracene **14** (2.00 g, 2.87 mmol, 1 equiv.) in THF (80 mL) which was then added dropwise over 5 h. Next, a flame dried flask with excess solid CO₂ was connected to the Schlenk adaptor and CO₂ gas was transferred to the reaction mixture for approximately 30 min. The excess CO₂ gas was vented from the flask through a bubbler for 15 min. The reaction was then quenched with 20% H₂SO₄ solution (40 mL) and stirred at –78 °C for 15 min, then warmed slowly to room temperature. The organic layer was extracted thrice (EtOAc) and the combined organics were washed with water and brine, dried (MgSO₄) and concentrated *in vacuo*. The solid was dissolved in Et₂O and concentrated to 5 mL where *n*-hexanes was added and left in the freezer overnight. The precipitate was collected and washed with cold hexanes to give **15** (1.73 g, 77%) as a yellow solid. ¹H NMR (600 MHz, DMSO-*d*₆, 25 °C) δ (ppm) 9.02 (s, 2H), 8.81 (s, 2H), 1.33–1.26 (m, 6H), 1.23 (d, *J* = 7.0 Hz, 36 H). ¹³C NMR (151 MHz, DMSO-*d*₆, 75 °C) δ (ppm) 165.82, 132.66, 132.47, 131.31, 130.36, 130.01, 118.94, 117.94, 107.89, 100.77, 18.20, 10.58. High-resolution mass spectroscopy HRMS (ES⁺) (*m/z*), calculated for C₃₈H₄₈Br₂O₄Si₂ (M)⁺ 783.1536 found 783.1521.

9,10-Bis(triisopropylsilyl)ethynyl-3,7-diphenyl-2,6-anthracenedicarboxylic acid (16). A three-neck round-bottom flask equipped with a condenser was charged with dibromodiacid **15** (0.750 g, 0.96 mmol, 1 equiv.), phenylboronic acid (0.581 g, 4.77 mmol, 5 equiv.), and K₃PO₄ (1.01 g, 4.77 mmol, 5 equiv.), then the reaction flask was evacuated and back-filled three times with nitrogen. Toluene (32 mL), EtOH (32 mL), and H₂O (3.2 mL) were added to the flask and the solution was sparged for 1.5 h. PdOAc₂ (9 mg, 0.038 mmol, 0.04 equiv.) and SPhos (32 mg, 0.076 mmol, 0.08 equiv.) were then added followed by 20 min of sparging. The reaction was placed under N₂ and heated at 105 °C for 24 h. The reaction was cooled, diluted with EtOH, and filtered to remove the palladium solids. The organics were removed, then Et₂O was added to the flask which resulted in a suspension. The precipitate was collected and washed with cold Et₂O and H₂O to give **16** (0.713 g, 96%) as a bright yellow solid. ¹H NMR (600 MHz, DMSO-*d*₆) δ 8.43 (s, 2H), 8.41 (s, 2H), 7.66 (d, *J* = 7.4 Hz, 4H), 7.38 (t, *J* = 7.4 Hz, 4H),

7.33 (t, $J = 7.3$ Hz, 2H), 1.27–1.18 (m, 42H). ^{13}C NMR (151 MHz, $\text{DMSO-}d_6$) δ 171.57, 142.12, 139.47, 131.40, 131.26, 128.76, 128.40, 128.21, 127.30, 126.71, 126.70, 116.79, 104.54, 103.89, 19.21, 11.40. HRMS (TOF) (m/z), calculated for $\text{C}_{50}\text{H}_{59}\text{O}_4\text{Si}_2$ ($\text{M}+\text{H}$) $^+$ 779.3946 found 779.3945.

DIAn Dione 17. Compound **16** (0.317 g, 0.41 mmol, 1 equiv.) was added to a flame-dried single-neck round-bottom flask. Dry DCM (25 mL) was added to the flask followed by oxalyl chloride (0.14 mL, 1.63 mmol, 4 equiv.) and dry DMF (0.06 mL, 0.81 mmol, 2 equiv.). This was stirred at room temperature for 1 h. The organics were then removed utilizing a secondary trap and the solid acid chloride was redissolved in dry DCM (50 mL), followed by the dropwise addition of 1 M SnCl_4 in DCM (1.63 mL, 1.63 mmol, 4 equiv.). A reflux condenser was quickly switched onto the flask and the reaction was heated to reflux for 4 h. The reaction was cooled to room temperature and quenched with H_2O , followed by the addition of 1M NaOH. The resultant mixture was poured into a Büchner funnel and the isolated solid was washed with H_2O and EtOH to give **17** (0.309 g, 77%) as a vibrant orange solid powder. ^1H NMR (600 MHz, CDCl_3) δ 8.97 (s, 2H), 8.71 (s, 2H), 7.83 (d, $J = 7.4$ Hz, 2H), 7.75 (d, $J = 7.5$ Hz, 2H), 7.64 (t, $J = 7.4$ Hz, 2H), 7.43 (t, $J = 7.4$ Hz, 2H), 1.44–1.27 (m, 42H). ^{13}C NMR (151 MHz, CDCl_3) δ 192.06, 144.51, 138.78, 136.90, 135.52, 135.39, 134.80, 134.24, 129.90, 125.16, 124.65, 123.19, 121.46, 118.32, 107.28, 102.11, 18.94, 11.57. HRMS (TOF) (m/z), calculated for $\text{C}_{50}\text{H}_{55}\text{O}_2\text{Si}_2$ ($\text{M}+\text{H}$) $^+$ 743.3735 found 743.3702.

DIAn 9. In an oven-dried round bottom flask, a suspension of dione **17** (0.100 g, 0.13 mmol, 1 equiv.) in dry THF (10 mL) was cooled to -78 °C under a N_2 atmosphere. In a separate oven-dried round bottom flask, 2-bromomesitylene (0.18 mL, 1.04 mmol, 8 equiv.) was dissolved in dry THF (5 mL), cooled to -78 °C under a N_2 atmosphere, and n -BuLi (1.6 M in hexanes, 0.61 mL, 0.98 mmol, 7.5 equiv.) was added dropwise. After stirring the mixture at -78 °C for 1 h, the aryl lithiate was transferred via cannula to the flask containing the dione. This reaction mixture was slowly warmed to room temperature overnight with stirring. The reaction was then quenched with a saturated aq. NH_4Cl solution and extracted thrice with DCM. The combined organic layer was washed with brine (3 \times), dried (MgSO_4) and concentrated in vacuo. The resulting crude oil was passed through a silica plug eluting with hexanes, followed by 1:2 DCM/hexanes to elute

one diastereomer and 3:1 DCM/hexanes to elute the other. The desired diol was carried onto the reductive dearomatization step without further purification.

In a single-neck round-bottom flask the diol (0.116 g, 0.12 mmol, 1 equiv.) and anhydrous SnCl₂ (88 mg, 0.46 mmol, 4 equiv.) were dissolved in dry degassed toluene (20 mL). Trifluoroacetic acid (catalytic) was added and this mixture was then vigorously stirred while monitoring via TLC (9:1 hexanes/CH₂Cl₂). After 4 h, the solvent was removed *in vacuo*, the solid was passed through a silica plug eluting first with hexanes followed by hexanes/DCM (3:1) to remove the product. The organics were removed, and the resultant solid was dissolved in minimal CHCl₃. MeCN was layered over the solution and then cooled at -20 °C overnight to furnish DIAn **9** (74 mg, 59% over two steps) as deep violet crystals. The spectroscopic data were identical to those previously reported.³

9,10-Bis(triisopropylsilyl)ethynyl-3,7-di-2-naphthalenyl-2,6-anthracenedicarboxylic acid (18). A two-neck round-bottom flask was charged with dibromodiacid **15** (0.750 g, 0.96 mmol, 1 equiv.), 2-naphthaleneboronic acid (0.822 g, 4.78 mmol, 5 equiv.), and K₃PO₄ (1.01 g, 4.78 mmol, 5 equiv.), then the reaction flask was evacuated and back-filled three times with nitrogen. Toluene (38 mL), EtOH (38 mL), and H₂O (3.8 mL) were added to the flask and the solution was sparged for 2 h. PdOAc₂ (9 mg, 0.038 mmol, 0.04 equiv.) and SPhos (32 mg, 0.076 mmol, 0.08 equiv.) were then added followed by 20 min of sparging. The reaction was placed under N₂ and heated at 95 °C overnight. The reaction was cooled, diluted with EtOH, and filtered to remove the palladium solids. The volatiles were removed, then Et₂O was added to the flask which was left in the freezer overnight. The precipitate was collected and washed with cold Et₂O to give **18** (0.842 g, 99%) as a yellow-orange solid. ¹H NMR (600 MHz, DMSO-*d*₆) δ 8.56 (s, 2H), 8.48 (s, 2H), 8.12 (s, 2H), 7.97–7.82 (m, 8H), 7.58–7.50 (m, 4H), 1.29–1.13 (m, 42H). ¹³C NMR (151 MHz, DMSO-*d*₆) δ 171.76, 145.57, 140.30, 139.69, 133.48, 132.60, 131.49, 131.42, 128.32, 127.88, 127.24, 126.97, 126.73, 126.43, 126.19, 126.17, 123.93, 116.84, 104.54, 104.03, 19.22, 11.41. HRMS (TOF) (*m/z*), calculated for C₅₈H₆₃O₄Si₂ (M+H)⁺ 879.4259 found 879.4211.

anti-Dione 19. A single-neck round-bottom flask was charged with diacid **18** (0.84 g, 0.95 mmol, 1 equiv.) and dry DCM (40 mL). Oxalyl chloride (0.33 mL, 3.82 mmol, 4 equiv.) and DMF (0.15 mL, 1.91 mmol, 2 equiv.) were added to the flask and

the reaction stirred for 1 h. The volatiles were then removed and the crude acid chloride was redissolved in DCM (80 mL). SnCl₄ (1 M in DCM, 3.8 mL, 3.82 mmol, 4 equiv.) was added dropwise and then the reaction was refluxed for 4 h. Upon completion the reaction was quenched by the addition of H₂O, followed by 1 M NaOH solution. The resultant mixture was poured into a Büchner funnel and the isolated solid was washed with H₂O and EtOH to give **19** (0.513 g, 64%) as a bright orange powder. Due to the insolubility of **19**, ¹H and ¹³C NMR data were not attainable. HRMS (ASAP) (*m/z*), calculated for C₅₈H₅₉O₂Si₂ (M+H)⁺ 843.4054, found 843.4066.

anti-DB-DIAN 12. In an oven-dried round bottom flask, a suspension of dione **19** (0.513 g, 0.608 mmol, 1 equiv.) in dry THF (56 mL) was cooled to -78 °C under a N₂ atmosphere. In a separate oven-dried round bottom flask, 2-bromomesitylene (0.74 mL, 4.87 mmol, 8 equiv.) was dissolved in dry THF (28 mL), cooled to -78 °C under a N₂ atmosphere, and *n*-BuLi (1.6 M in hexanes, 2.85 mL, 4.56 mmol, 7.5 equiv.) was added dropwise. After stirring the mixture at -78 °C for 1 h, the aryl lithiate was transferred via cannula to the flask containing the dione. This reaction mixture was slowly warmed to room temperature overnight with stirring. The reaction was then quenched with a saturated aq. NH₄Cl solution and extracted thrice with DCM. The combined organic layer was washed with brine (3×), dried (MgSO₄) and concentrated in vacuo. The resulting crude oil was passed through a silica plug eluting with hexanes, followed by 1:2 DCM/hexanes to elute one diastereomer and 3:2 DCM/hexanes to elute the other. The desired diol was carried onto the reductive dearomatization step without further purification.

In a single-neck round-bottom flask the diol (0.175 g, 0.16 mmol, 1 equiv.) and anhydrous SnCl₂ (122 mg, 0.646 mmol, 4 equiv.) were dissolved in dry degassed toluene (30 mL). Trifluoroacetic acid (catalytic) was added and this mixture was then vigorously stirred while monitoring via TLC (9:1 hexanes/CH₂Cl₂). After 4 h, the solvent was removed *in vacuo*, the solid was passed through a silica plug eluting first with hexanes followed by hexanes/DCM (3:1) to remove the product. The organics were removed and the resultant solid was dissolved in minimal CHCl₃. MeCN was layered over the solution and then cooled at -20 °C overnight to furnish **anti-DB-DIAN 12** (121 mg, 70%) as deep blue crystals. ¹H NMR (500 MHz, CDCl₃, -35 °C) δ 8.54 (s, 2H), 7.81–7.72 (m, 4H),

7.71–7.60 (m, 4H), 7.41–7.31 (m, 4H), 7.18 (m, 2H), 7.02 (s, 4H), 2.43 (s, 6H), 2.06 (s, 12H), 1.09 (d, $J = 6.6$ Hz, 42H). ^{13}C NMR (151 MHz, CDCl_3 , -35 °C) δ 142.3, 139.20, 137.75, 137.42, 136.69, 136.31, 135.83, 134.45, 132.46, 131.54, 129.92, 129.75, 129.12, 128.56, 128.03, 127.20, 126.05, 125.13, 124.00, 123.84, 123.20, 119.83, 105.88, 102.67, 21.67, 20.60, 18.93, 11.27. UV-Vis (CH_2Cl_2) λ_{max} (ϵ) 420 (73,570), 445 (74,730), 705 (sh, 16,520), 785 (30,580), 903 (sh, 15,710) nm. HRMS (ES^+) (m/z), calculated for $\text{C}_{76}\text{H}_{81}\text{Si}_2$ ($\text{M}+\text{H}$) $^+$ 1049.5822, found 1049.5821.

9,10-Bis(triisopropylsilyl)ethynyl-3,7-di-2-benzo[*b*]thienyl-2,6-anthracenedicarboxylic acid (20). A two-neck round-bottom flask was charged with dibromodiacid **15** (1.00 g, 1.27 mmol, 1 equiv.), benzothiophene 2-pinacolate ester (0.800 g, 3.06 mmol, 2.4 equiv.), and K_3PO_4 (1.19 g, 5.61 mmol, 4.4 equiv.), and the reaction flask was evacuated and back-filled three times with nitrogen. Toluene (25 mL), EtOH (25 mL), and H_2O (2.5 mL) were added to the flask and the solution was sparged for 2 h. PdOAc_2 (12 mg, 0.051 mmol, 0.04 equiv.) and SPhos (42 mg, 0.10 mmol, 0.08 equiv.) were then added followed by 20 min of sparging. The reaction was placed under N_2 and heated at 95 °C overnight. The reaction was cooled, diluted with EtOH, and filtered to remove the palladium solids. The volatiles were removed, then Et_2O was added to the flask which was left in the freezer overnight. The precipitate was collected and washed with cold acetone and H_2O to give **20** (1.12 g, 98%) as an orange-yellow solid. ^1H NMR (600 MHz, $\text{DMSO}-d_6$, 75 °C) δ 8.72 (s, 2H), 8.55 (s, 2H), 7.94 (d, $J = 7.5$ Hz, 2H), 7.92 (s, 2H), 7.85 (d, $J = 7.5$ Hz, 2H), 7.41–7.37 (m, 4H), 1.38–1.18 (m, 42H). ^{13}C NMR (151 MHz, $\text{DMSO}-d_6$, 75 °C) δ 169.85, 142.29, 140.05, 139.02, 131.18, 131.02, 130.73, 126.54, 124.12, 124.08, 123.40, 123.25, 121.53, 116.79, 105.26, 102.45, 18.39, 10.72. HRMS (TOF) (m/z), calculated for $\text{C}_{54}\text{H}_{59}\text{O}_4\text{Si}_2\text{S}_2$ ($\text{M}+\text{H}$) $^+$ 891.3387 found 891.3353.

BT-Dione 21. A single-neck round-bottom flask was charged with diacid **20** (0.66 g, 0.74 mmol, 1 equiv.) and dry DCM (35 mL). Oxalyl chloride (0.26 mL, 2.96 mmol, 4 equiv.) and DMF (0.12 mL, 1.48 mmol, 2 equiv.) were added to the flask and the reaction stirred for 1 h. The volatiles were then removed and the crude acid chloride was redissolved in DCM (70 mL). SnCl_4 (1 M in DCM, 3.0 mL, 2.96 mmol, 4 equiv.) was added dropwise and then the reaction was refluxed for 4 h. Upon completion the reaction

was quenched by the addition of H₂O, followed by 1 M NaOH solution. The resultant mixture was poured over a Büchner funnel and the isolated solid was washed with H₂O and cold hexanes to give **21** (0.380 g, 60%) as a bright orange powder. Due to the insolubility of **21**, ¹H and ¹³C NMR data were not attainable. HRMS (ASAP) (*m/z*), calculated for C₅₄H₅₅O₂S₂Si₂ (M+H)⁺ 855.3176 found 855.3143.

BT-DIAN 13. In an oven-dried round bottom flask, a suspension of dione **19** (0.350 g, 0.41 mmol, 1 equiv.) in dry THF (20 mL) was cooled to -78 °C under a N₂ atmosphere. In a separate oven-dried round bottom flask, 2-bromomesitylene (0.50 mL, 3.28 mmol, 8 equiv.) was dissolved in dry THF (10 mL), cooled to -78 °C under a N₂ atmosphere, and *n*-BuLi (1.6 M in hexanes, 1.92 mL, 3.07 mmol, 7.5 equiv.) was added dropwise. After stirring the mixture at -78 °C for 1 h, the aryl lithiate was transferred via cannula to the flask containing the dione. This reaction mixture was slowly warmed to room temperature overnight with stirring. The reaction was then quenched with a saturated aq. NH₄Cl solution and extracted thrice with DCM. The combined organic layer was washed with brine (3×), dried (MgSO₄) and concentrated in vacuo. The resulting crude oil was passed through a silica plug eluting with hexanes, followed by 25% DCM/hexanes to elute one diastereomer and 40% DCM/hexanes to elute the other. The desired diol was carried onto the reductive dearomatization step without further purification.

In a single-neck round-bottom flask the diol (0.150 g, 0.14 mmol, 1 equiv.) and anhydrous SnCl₂ (107 mg, 0.57 mmol, 4 equiv.) were dissolved in dry degassed toluene (15 mL). trifluoroacetic acid (catalytic) was added and this mixture was then vigorously stirred while monitoring via TLC (9:1 hexanes/CH₂Cl₂). After 4 h, the reaction mixture was passed through a silica plug eluting first with hexanes to removed non-polar impurities, followed by hexanes/DCM (3:1) to remove the product. The organics were removed, and the leftover solids were dried on the vacuum for 1 h. Cold acetonitrile was then added to the flask and the solids were scrapped from the walls and collected by vacuum filtration to furnish a dark blue, almost black powder, **BT-DIAN 13**. (80 mg, 55% from diol). Due to the open-shell nature of **BT-DIAN** not all peaks are assignable; the alkyl peaks however are assignable. ¹H NMR (600 MHz, CDCl₃, -35 °C) δ 8.33 (br s, 2H), 7.96–7.83 (br s, 2H), 7.73 (d, *J* = 7.9 Hz, 2 H), 7.20–7.10 (m, 6H), 7.00 (s, 2H), 2.40

(s, 6H), 2.15 (s, 12H), 1.15–1.03 (m, 42H). ^{13}C NMR (600 MHz, CDCl_3 , $-35\text{ }^\circ\text{C}$) δ 146.78, 145.31, 139.31, 137.40, 136.98, 134.83, 132.78, 132.28, 130.29, 129.34, 129.23, 128.48, 128.27, 126.66, 125.87, 125.59, 125.45, 124.10, 122.68, 106.22, 102.30, 102.14, 21.57, 20.86, 18.83, 11.34. UV-Vis (CH_2Cl_2) λ_{max} (ϵ) 441 (75,750), 465 (87,700), 828 (sh, 17,280), 887 (20,880), 976 (sh, 8,130) nm. HRMS (ES^+) (m/z), calculated for $\text{C}_{72}\text{H}_{77}\text{S}_2\text{Si}_2$ ($\text{M}+\text{H}$) $^+$ 1061.5005 found 1061.5056.

9,10-Bis(triisopropylsilyl)ethynyl-2,6-bis(pinacolatoboron)anthracene (22). A regulated pressure vessel was charged with dibromide **14** (1.00 g, 1.44 mmol, 1 equiv), B_2Pin_2 (2.187 g, 8.61 mmol, 6 equiv.), KOAc (0.845 g, 8.61 mmol, 6 equiv.), PdOAc_2 (13 mg, 0.057 mmol, 0.04 equiv.), XPhos (55 mg, 0.12 mmol, 0.08 equiv.) and then evacuated and backfilled five times. Dry, deoxygenated dioxane was added to the pressure vessel which was then sealed and stirred overnight at $110\text{ }^\circ\text{C}$. After cooling, the reaction mixture was poured into MeCN and stirred for 1 h. The mixture was then poured over a Büchner funnel to collect both the product and left-over palladium junk, which was then washed with cold ACN. The product was then collected by washing with DCM and concentrated. The product chromatographed on silica gel (3:2 hexanes/DCM) to give **22** (0.828 g, 73%) as an orange solid. ^1H NMR (600 MHz, CDCl_3) δ 9.25 (s, 2H), 8.59 (dd, $J = 8.6, 1.2$ Hz, 2H), 7.91 (dd, $J = 8.6, 1.2$ Hz, 2H), 1.39 (s, 12H), 1.36–1.28 (m, 42H). ^{13}C NMR (151 MHz, CDCl_3) δ 136.41, 133.43, 132.35, 130.60, 126.28, 119.42, 105.21, 103.31, 83.92, 25.01, 18.94, 11.58; HRMS (ASAP) (m/z), calculated for $\text{C}_{48}\text{H}_{73}\text{B}_2\text{O}_4\text{Si}_2$ ($\text{M}+\text{H}$) $^+$ 791.5233, found 791.5225.

Dialdehyde 24. A two-neck round-bottom flask was charged with **22** (0.627 g, 0.79 mmol, 1 equiv.), 3-iodo-2-naphthaldehyde (**23**) (0.525 g, 1.86 mmol, 2.2 equiv.), and K_3PO_4 (0.539 g, 2.54 mmol, 3 equiv.) and the flask was evacuated and backfill five times. Toluene (35 mL), EtOH (35 mL) and H_2O (3.5 mL) were added to the flask and the solution sparged for 2 h. PdOAc_2 (8 mg, 0.034 mmol, 0.04 equiv.) and SPhos (28 mg, 0.068 mmol, 0.08 equiv.) were then added followed by 20 min of sparging. The reaction was refluxed overnight at $60\text{ }^\circ\text{C}$. After cooling to room temperature, the reaction was quenched with H_2O and then the organics extracted thrice with DCM. The organics were washed with H_2O and brine and then dried (MgSO_4) and the solvent was removed. The crude solid was taken up in DCM (5 mL) and then EtOH (50 mL) was added. This

mixture was sonicated and then left in the freezer overnight. The precipitate was collected and washed with cold EtOH to give **24** (0.51 g, 76%) as a yellow solid. ^1H NMR (500 MHz, CDCl_3 , 25 °C) δ 10.31 (s, 2H), 8.88 (s, 2H), 8.75 (d, $J = 8.7$ Hz, 2H), 8.66 (s, 2H), 8.12–8.09 (m, 4H), 7.95 (d, $J = 8.3$ Hz, 2H), 7.76 (d, $J = 8.8$ Hz, 2H), 7.70 (t, $J = 8.5$ Hz, 2H), 7.63 (t, $J = 8.5$ Hz, 2H), 1.35–1.20 (m, 42H). ^{13}C NMR (151 MHz, CDCl_3) δ 192.01, 140.01, 137.07, 135.64, 132.52, 131.96, 131.88, 131.75, 130.77, 130.39, 129.79, 129.66, 129.27, 128.33, 127.91, 127.34, 127.13, 119.02, 105.91, 102.83, 18.92, 11.42. HRMS (ASAP) (m/z) calculated for $\text{C}_{58}\text{H}_{63}\text{O}_2\text{Si}_2$ ($\text{M}+\text{H}$) $^+$ 847.4408, found 847.4398.

Dihydro-linear-DB-DIAn 25. In a flame-dried round bottom flask, a solution of **24** (0.508 g, 0.600 mmol, 1 equiv.) in dry THF (50 mL) was cooled to -78 °C under a N_2 atmosphere. In a separate oven-dried round bottom flask, a solution of 2-bromomesitylene (0.55 mL, 3.60 mmol, 6 equiv.) in dry THF (25 mL) was cooled to -78 °C under a N_2 atmosphere, and *n*-BuLi (1.6 M in hexanes, 2.07 mL, 3.30 mmol, 5.5 equiv.) was added dropwise. After stirring the mixture at -78 °C for 1 h, the aryl lithiate was transferred via cannula to the flask containing dialdehyde **24**. The reaction was stirred at -78 °C for 1 h, then warmed to room temperature over 1 h. The reaction was then quenched with a saturated aq. NH_4Cl solution and extracted thrice with Et_2O . The combined organic layer was washed with brine, dried (MgSO_4) and concentrated in vacuo. The resulting crude oil was passed through a silica plug eluting with hexanes, followed by 1:2 DCM/hexanes to elute one diastereomer and 3:1 DCM/hexanes to elute the other. This diol was carried onto the Friedel-Crafts alkylation with no additional purification.

A flame dried single-neck round bottom flask was charged with the crude diol and dry DCM (55 mL) was added. After cooling to 0 °C, $\text{BF}_3 \cdot \text{OEt}_2$ (0.31 mL, 2.56 mmol, 4 equiv.) was added dropwise and the solution changed to a deep red color. After stirring for 10 min, the reaction was quenched with sat. aq. NaHCO_3 solution. The mixture was extracted thrice with DCM and the organics were washed with H_2O and brine. The organic layer was dried (MgSO_4) and concentrated to a solid. A small amount of DCM was added to dissolve the solid and EtOH was added to the solution. This was sonicated and left in the freezer overnight. A precipitate was isolated and washed with cold EtOH. The remainder of the title compound was isolated from the filtrate by column

chromatography. Eluting with hexanes/DCM (7:1) afforded **25** (0.410 g, 65%) as a yellow-brown solid (the compound is a *syn/anti* mixture of mesityl isomers that are not separated before oxidation). ¹H NMR (500 MHz, CDCl₃) δ 9.19 (s, 2H), 8.40 (s, 2H), 8.39 (s, 2H), 7.96 (d, *J* = 8.4 Hz, 2H), 7.76 (d, *J* = 7.8 Hz, 2H), 7.70 (s, 2H), 7.51–7.43 (m (overlapping t), 4H), 7.08 (s, 2H), 6.67 (s, 2H), 6.02 (s, 2H), 2.78 (s, 6H), 2.32 (s, 6H), 1.45–1.40 (m, 6H) 1.24–1.19 (m, 36H), 1.16 (s, 6H). ¹³C NMR (151 MHz, CDCl₃) δ 147.15, 146.03, 140.25, 138.79, 137.75, 137.46, 136.34, 135.03, 134.19, 133.17, 132.88, 132.35, 130.68, 128.52, 127.96, 126.01, 125.63, 122.70, 121.60, 119.77, 118.44, 118.00, 104.55, 104.08, 48.85, 21.81, 20.94, 19.67, 19.11, 18.91, 11.70, 11.59. HRMS (ES⁺) (*m/z*) calculated for C₇₆H₈₃Si₂ (M+H)⁺ 1051.6033, found 1051.5974.

linear-DB-DIAn 10. Compound **25** (0.100 g, 0.095 mmol, 1 equiv.) was added to a flame-dried flask which was then evacuated and backfilled five times with nitrogen Dry toluene (27 mL) was added to the flask and the solution was sparged for 10 min. The solution was heated to 60 °C and then a solution of DDQ (0.033 g, 0.143 mmol, 1.5 equiv.) in dry toluene (3 mL) was added dropwise. The reaction turned a teal blue color and was heated at 60 °C for 3 h. After cooling, the crude mixture was absorbed onto silica and a silica plug was run using hexanes/DCM (9:1). The eluent was concentrated in vacuo and the residue dissolved in a small amount of CHCl₃ and mixed with ten times the amount of MeCN. After cooling overnight at –20 °C, the precipitate was collected to give **10** (58 mg, 58%) as a dark blue solid. ¹H NMR (600 MHz, CDCl₃, –35 °C) δ 8.82 (s, 2H), 8.20 (s, 2H), 8.09 (d, *J* = 7.7 Hz, 2H), 7.56 (t, *J* = 7.6 Hz, 2H), 7.46 (d, *J* = 7.7 Hz, 2H), 7.37 (t, *J* = 7.5 Hz, 2H), 7.28 (s, 2H), 7.26 (s, 2H, hidden below solvent), 7.00 (s, 4H), 2.38 (s, 6H), 2.08 (s, 12H), 1.23–1.08 (m, 42H). ¹³C NMR (151 MHz, CDCl₃, –35 °C) δ 182.75, 157.16, 142.00, 138.77, 138.22, 137.83, 134.93, 134.83, 133.88, 133.39, 133.35, 133.21, 132.79, 129.61, 129.52, 128.95, 128.61, 128.09, 124.20, 121.66, 120.86, 119.87, 106.35, 102.59, 21.69, 20.26, 18.91, 11.28. UV-Vis (CH₂Cl₂) λ_{max} (ε) 429 (48,820), 599 (sh, 20,870), 645 (31,460), 685 (33,580), 768 (sh, 2,150) nm. HRMS (ASAP) (*m/z*) calculated for C₇₆H₈₀Si₂ (M+H)⁺ 1049.5825, found 1049.5853.

Dialdehyde 27. A two-neck round-bottom flask was charged with **22** (0.801 g, 1.01 mmol, 1 equiv.), 1-bromo-2-naphthaldehyde (**26**, 0.500 g, 2.12 mmol, 2.1 equiv.), and K₃PO₄ (0.644 g, 3.03 mmol, 3 equiv.). The flask was evacuated and backfill five

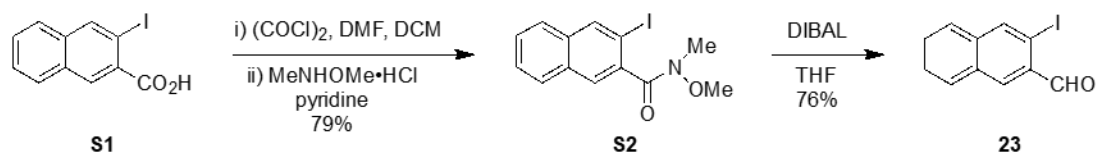
times. Toluene (40 mL), EtOH (40 mL) and H₂O (4 mL) were added to the flask and the mixture sparged with N₂ for 2 h. PdOAc₂ (9 mg, 0.040 mmol, 0.04 equiv.) and SPhos (33 mg, 0.068 mmol, 0.081 equiv.) were then added followed by 20 min of sparging. The reaction was stirred overnight at 60 °C. After cooling to room temperature, the mixture was quenched with H₂O and then extracted thrice with DCM. The organic layer was washed with H₂O and brine and then dried (MgSO₄) and the solvent was removed. The crude solid was dissolved in DCM (5 mL) and then EtOH (50 mL) was added. This mixture was sonicated and then left in the freezer overnight. The precipitate was collected and washed with cold EtOH to give **27** (0.429 g, 50%) as a yellow solid. The NMR data are consistent with a mixture of rotamers. ¹H NMR (500 MHz, CDCl₃) δ 10.08 (s, 2H), 8.83–8.79 (m, 4H), 8.19 (dd, *J* = 8.6, 2.2 Hz, 2H), 8.05 (d, *J* = 8.7 Hz, 2H), 8.02 (d, *J* = 8.2 Hz, 2H), 7.85 (d, *J* = 8.5, 2H), 7.77 (d, *J* = 8.8 Hz, 2H), 7.69 (t, *J* = 7.5 Hz, 2H), 7.52 (t, *J* = 7.5 Hz, 2H), 1.23–1.09 (m, 42H). ¹³C NMR (151 MHz, CDCl₃) δ 192.32, 192.23, 145.80, 136.18, 136.17, 134.10, 132.29, 132.24, 132.23, 132.15, 131.48, 131.42, 130.41, 130.40, 130.30, 128.88, 128.81, 128.76, 128.75, 128.39, 128.35, 127.75, 127.68, 127.39, 127.15, 127.08, 122.37, 122.29, 119.32, 106.63, 102.54, 77.23, 77.02, 76.81, 19.01, 18.73, 18.72, 11.35. HRMS (ASAP) (*m/z*) calculated for C₅₈H₆₃O₂Si₂ (M+H)⁺ 847.4348, found 847.4343.

Dihydro-syn-DB-DIAn 28. In a flame-dried round bottom flask, a solution of **27** (0.819 g, 0.97 mmol, 1 equiv.) in dry THF (50 mL) was cooled to –78 °C under a N₂ atmosphere. In a separate oven-dried round bottom flask, a solution of 2-bromomesitylene (0.88 mL, 5.80 mmol, 6 equiv.) in dry THF (25 mL) was cooled to –78 °C under a N₂ atmosphere, and *n*-BuLi (1.6 M in hexanes, 3.32 ml, 5.32 mmol, 5.5 equiv.) was added dropwise. After stirring the mixture at –78 °C for 1 h, the aryl lithiate was transferred via cannula to the flask containing the dialdehyde. The reaction was stirred at –78 °C for 1 h, then warmed to room temperature over 1 h. The reaction was then quenched with a saturated aq. NH₄Cl solution and extracted thrice with Et₂O. The combined organic layer was washed with brine, dried (MgSO₄) and concentrated in vacuo. The resulting crude oil was passed through a silica plug eluting with hexanes, followed by EtOAc to furnish both diol diastereomers. This diol was carried onto the Friedel-Crafts alkylation with no additional purification.

A flame dried single-neck round bottom flask was charged with the crude diol and dry DCM (75 mL). After the mixture was cooled to 0 °C, BF₃·OEt₂ (0.47 mL, 3.87 mmol, 4 equiv.) was added dropwise and the solution changed to a deep red color. After stirring for 10 min, the mixture was quenched with sat. aq. HCO₃ solution. The mixture was extracted thrice with DCM (a precipitate formed in the organic layer and was found to be a portion of the title compound) and the organics were washed with H₂O and brine. The organic layer was dried (MgSO₄) and concentrated in vacuo. The resultant solid was dissolved in a small amount of DCM and EtOH was added to the solution. This mixture was sonicated and left in the freezer overnight. The precipitate was isolated and washed with cold EtOH. The remainder of the title compound was isolated from the filtrate by column chromatography eluting with hexanes/DCM (9:1) to afforded the **28** (0.631g, 62%) as a yellow-brownish solid (the compound is a *syn/anti* mixture of mesityl isomers that are not separated before oxidation). ¹H NMR (600 MHz, CDCl₃) δ 9.61 (s, 2H), 9.08 (d, *J* = 8.4 Hz, 2H), 8.53 (s, 2H), 8.00 (d, *J* = 8.0 Hz, 2H), 7.85 (d, *J* = 8.2 Hz, 2H), 7.72 (t, *J* = 7.5 Hz, 2H), 7.60 (t, *J* = 7.4 Hz, 2H), 7.41 (d, *J* = 8.1 Hz, 2H), 7.09 (s, 2H), 6.66 (s, 2H), 5.88 (s, 2H), 2.78 (s, 6H), 2.32 (s, 6H), 1.33–1.22 (m, *J* = 6.4 Hz, 42H), 1.13 (s, 6H). ¹³C NMR (151 MHz, CDCl₃) δ 147.96, 147.48, 141.64, 137.88, 137.66, 136.29, 134.24, 133.76, 133.58, 132.39, 131.82, 130.61, 129.98, 129.81, 129.39, 128.92, 127.06, 124.14, 122.49, 121.07, 120.22, 118.17, 104.51, 104.30, 49.71, 21.91, 20.86, 18.97, 11.41. HRMS (ES⁺) (*m/z*) calculated for C₇₆H₈₃Si₂ (M+H)⁺ 1051.6033 found 1051.5970.

***syn*-DB-DIA_n 11.** Compound **28** (0.100 g, 0.095 mmol, 1 equiv.) was added to a flame-dried single neck round bottom flask and the reaction flask was evacuated and backfilled five times with N₂. Dry toluene (27 mL) was added to the flask and the solution was sparged for 10 min. The solution was heated to 60 °C and a solution of DDQ (0.033 g, 0.143 mmol, 1.5 equiv.) in dry toluene (3 mL) was added dropwise. The reaction turned a deep army green color and was then stirred at 60 °C for 3 h. To purify the title compound the reaction mixture was absorbed onto silica and a plug was run using 1:20 DCM/hexanes to isolate the deep green compound. The organics from the plug were pumped down and dissolved in a small amount of CHCl₃ and mixed with ten times the amount of CH₃CN. After cooling in the freezer overnight, the precipitate was collected via vacuum filtration to give **12** (0.017 g, 17%) as a dark army green solid. ¹H

NMR (600 MHz, CDCl₃, -35 °C) δ 8.95 (s, 2H), 8.58 (d, J = 8.3 Hz, 2H), 7.78–7.71 (m, 4H), 7.54 (d, J = 8.5 Hz, 2H), 7.48 (t, J = 7.6 Hz, 2H), 7.38 (t, J = 7.4 Hz, 2H), 7.05 (d, J = 8.4 Hz, 2H), 7.01 (s, 4H), 2.40 (s, 6H), 2.10 (s, 12H), 1.24–0.95 (m, 42H). ¹³C NMR data could not be collected due to the poor solubility of *syn*-DB-DIAN. UV-Vis (CH₂Cl₂) λ_{max} (ϵ) 435 (33,310), 459 (30,350), 705 (sh, 8,750), 785 (14,200), 883 (sh, 8,670) nm. HRMS (ASAP) (m/z) calculated for C₇₆H₈₁Si₂ (M+H)⁺ 1049.5825, found 1049.5853.



Weinreb Amide S2. 3-Amino-2-naphthoic acid was converted to 3-iodo-2-naphthoic acid (**S1**) following the procedure of Quideau et al.⁴ To a flame-dried single-neck round-bottom flask with a Claisen head was successively added **S1** (2.87 g, 9.63 mmol, 1 equiv.), dry DCM (30 mL), oxalyl chloride (1.65 mL, 19.26 mmol, 2 equiv.) and catalytic DMF (0.3 mL). After stirring for 2 h, the volatiles were removed using a secondary trap and the crude acid chloride was then re-dissolved in dry DCM (30 mL). The reaction flask was cooled to 0 °C and then pyridine (1.9 mL, 23.59 mmol, 2.45 equiv.) and *N,O*-dimethylhydroxylamine hydrochloride (1.13 g, 11.55 mmol, 1.2 equiv.) were added to the flask. The reaction was warmed to room temperature and stirred overnight. The mixture was diluted with EtOAc and then washed with a sat. aq. CuSO₄ solution. The organics were then extracted thrice with EtOAc and then washed with brine, dried (MgSO₄) and concentrated in vacuo. The crude solid was then absorbed onto silica and purified by column chromatography eluting with hexanes/EtOAc (2:1) to give **S2** (2.57 g, 79%) as an off-white solid. ¹H NMR (600 MHz, CDCl₃) δ 8.36 (s, 1H), 7.83–7.78 (m, 1H), 7.76–7.71 (m, 1H), 7.75 (s, 1H), 7.55–7.51 (m, 2H), 3.46 (br s, 6H). ¹³C NMR (151 MHz, CDCl₃) δ 170.64, 138.76, 138.17, 134.45, 131.67, 127.95, 127.40, 127.04, 126.60, 126.09, 88.94, 61.28, 32.66. HRMS (ASAP) (m/z) calculated for C₁₃H₁₃INO₂ (M+H)⁺ 341.9991, found 342.0014.

3-Iodo-2-naphthaldehyde (23). A single-neck round-bottom flask charged with **S2** (2.45 g, 7.18 mmol, 1 equiv.) and dry THF (60 mL) was cooled to $-78\text{ }^{\circ}\text{C}$, where DIBAL-H (1 M solution in hexanes, 21.5 mL, 21.54 mmol, 3 equiv.) was added dropwise. After stirring at $-78\text{ }^{\circ}\text{C}$ for 2 h, the reaction was quenched at $-78\text{ }^{\circ}\text{C}$ using sat. aq. NH_4Cl solution. After an additional 5 min of stirring at $-78\text{ }^{\circ}\text{C}$, the reaction was slowly warmed to room temperature over 90 min. The mixture was extracted thrice with EtOAc and the combined organics were washed with brine, dried (MgSO_4) and concentrated in vacuo. The crude solid was absorbed onto silica and a plug was run first with hexanes and then hexanes/DCM (2:1) to elute the product (1.655 g, 81%) that was obtained as a fluffy off-white powder. ^1H NMR (600 MHz, CDCl_3) δ 10.23 (s, 1H), 8.42 (s, 1H), 8.37 (s, 1H), 7.93 (d, $J = 8.1$ Hz, 1H), 7.74 (d, $J = 8.1$ Hz, 1H), 7.62 (t, $J = 7.5$ Hz, 1H), 7.56 (t, $J = 7.5$ Hz, 1H). ^{13}C NMR (151 MHz, CDCl_3) δ 195.87, 140.29, 137.72, 132.40, 132.29, 131.59, 130.26, 130.10, 127.96, 127.05, 93.16. HRMS (ASAP) (m/z) calculated for $\text{C}_{11}\text{H}_8\text{IO}$ ($\text{M}+\text{H}$) $^+$ 282.9648, found 282.9620.

5.6 Bridge to Chapter VI

In this work we wanted to show the ability to make very small but important changes to the diradical character and singlet-triplet energy gap in a series of closely related organic diradicals based on the diindenoanthracene scaffold. In this work we were importantly able to keep the conjugation pathway between the radical centers the same and only modulate the external arenes. In this way we were able to trace any property changes back to the synthetic alteration of the external aryl units. Through changing the external arenes, we changed the antiaromaticity of the pi-expanded *s*-indacene core which lead to trackable changes in y and ΔE_{ST} . This work was extremely gratifying in that the experimental results matched calculations very well and we were able to show a control and fine-tuning of the singlet-triplet energy gap that the diradical community has been waiting for. While this work was very rewarding and important the structural changes were synthetic taxing and thus the work in the Chapter VI looks to make incremental step-wise changes to antiaromaticity, diradical character and the singlet-triplet energy gap through post-synthetic modification to avoid such arduous synthetic routes.

CHAPTER VI

LATE-STAGE MODIFICATION OF ELECTRONIC PROPERTIES OF ANTIAROMATIC AND DIRADICALOID INDENO[1,2-*b*]FLUORENE ANALOGUES VIA SULFUR OXIDATION

6.1 Authorship Statement and Abstract

This chapter includes submitted for publication and co-authored material from: Dressler, J. J.; Barker, J. E.; Hashimoto, H. E.; Karas, L. J.; Kishi, R.; Zakharov, L. N.; MacMillan, S. N.; Gomez-Garcia, C. J.; Nakano, M.; Wu, J. I.; Haley, M. M. Late-stage Modification of Electronic Properties of Antiaromatic and Diradicaloid Indeno[1,2-*b*]fluorene Analogues via Sulfur Oxidation. Submitted; *J. Am. Chem. Soc.* **2020**. Any permissions related to the use of the material excerpted in this chapter should be directed to the American Chemical Society (assuming publication). This manuscript was written by myself with editorial assistance from Prof. Mike Haley and Josh Barker. The experimental work in this chapter was performed by myself, Josh Barker and Hannah Hashimoto.

The ability to alter optoelectronic and magnetic properties of molecules at a late stage in their preparation is in general a non-trivial feat. Here we report the late-stage oxidation of benzothiophene-fused indacenes and dicyclopentanaphthalenes to their corresponding sulfone derivatives. We find that while such modifications increase the HOMO-LUMO energy gap to a small degree, other properties such as HOMO and LUMO energy levels, molecule paratropicity, bonding patterns within the molecular geometry, and singlet-triplet energy gaps are influenced to a much greater degree. Computations corroborate the experimental findings and offer possible explanations for these profound changes in molecule properties.

6.2 Introduction

Recently there has been resurgent interest in polycyclic conjugated hydrocarbons (PCHs) that possess unique properties for application in organic electronics. The earliest and most promising PCH targets were acenes;¹⁻⁴ however, these compounds are prone to

oxidative degradation.^{3,5,6} In an attempt to develop suitable acene alternatives with decreased aromaticity and yet retain the π -conjugation integral to the high charge carrier mobility of acenes, PCHs that possess antiaromatic character have become fruitful avenues of research.⁷ Defined as cyclic, planar, fully conjugated systems with $(4n)$ π -electrons,⁸ antiaromatic molecules often display properties such as decreased delocalization, narrow HOMO-LUMO energy gaps,⁹⁻¹¹ paratropic proton NMR chemical shifts, as well as concomitant large positive nucleus independent chemical shift (NICS) values.^{9,12,13} A common strategy to generate antiaromatic hydrocarbons that are closely related to acenes is to replace one or more six-membered ring with either a four- or five-membered carbonaceous ring. This approach over the past decade has resulted in a wide range of antiaromatic compounds based mainly on pentalenes,¹⁴⁻²² cyclobutadienes,²³⁻²⁶ and indacenes,²⁷⁻³³ among others. The research on such molecules was in part fueled by the Breslow group's hypothesis that reduced aromaticity/ antiaromaticity has the potential to increase molecular conductivity.³⁴⁻³⁷ Very recent studies support this notion, as organic field effect transistors (OFETs) with antiaromatic molecules as the semiconducting layer can now exhibit average hole-mobilities that are greater than or equal to $1 \text{ cm}^2 \text{ V}^{-1} \text{ s}^{-1}$.^{23,25,38,39}

Another group of PCHs accruing interest are those that display diradical character. The recent increase in reports of carbon-based diradicaloids has also been driven by their potential applications both in organic electronics^{40,41} and as magnetic materials.⁴²⁻⁴⁵ The desire to gain a better fundamental understanding of these compounds, which possess a unique set of properties (e.g., narrow HOMO-LUMO gaps,⁴⁰ low-lying doubly excited electronic energy absorptions^{46,47} and electronic spin resonance (ESR) signals⁴⁸), has led to synthesis of various families of diradicaloids based on bisphenalenyls,^{41,44,49-51} zethrenes,⁵² indenofluorenes^{56,57} and closely related diindenoacenes⁵⁸⁻⁶⁵ among others. Through the study of these different classes of diradicals, a common theme has been unearthed, that the two concepts of antiaromaticity and diradical character are interrelated. In many cases antiaromatic molecules, once π -expanded, reveal a tendency to assume an aromatic, open shell resonance structure in the ground state to relieve the antiaromaticity of the conjugated, closed shell core.⁶⁶

Utilizing the indeno[1,2-*b*]fluorene framework, our group in recent years has aspired to tune both antiaromaticity (in benzene core molecules) and diradical character (naphthalene and larger aromatic cores) through two different approaches, either by changing the fusion bond order on both sides of the *s*-indacene core^{28,63,67} or by adding benzothiophene units in the same position (*anti* or *syn* to the apical carbon in the five-membered ring, e.g., **1-4** in Figure 6.1) to modulate electronic properties.^{27,60,62,68} These studies have provided key insights into what electronic factors can be altered to tune either the antiaromaticity (i.e., fusion bond order)^{27,28,67} and/or the diradical character (i.e., electronic repulsion factor and the transfer integral term)^{60,62,69} in a series of structurally related molecules. Such approaches have relied heavily on early synthetic modification to impart changes in the chemical connectivity to drive a concomitant changes in properties. These modifications are manifested either by π -extending the acene core requiring a change to the synthetic route very early on or through altering the outer fused rings that required synthetic changes during the key carbon-carbon bond forming steps; however, the amount of synthetic work needed to tune these properties was demanding, often requiring entirely new preparative routes.

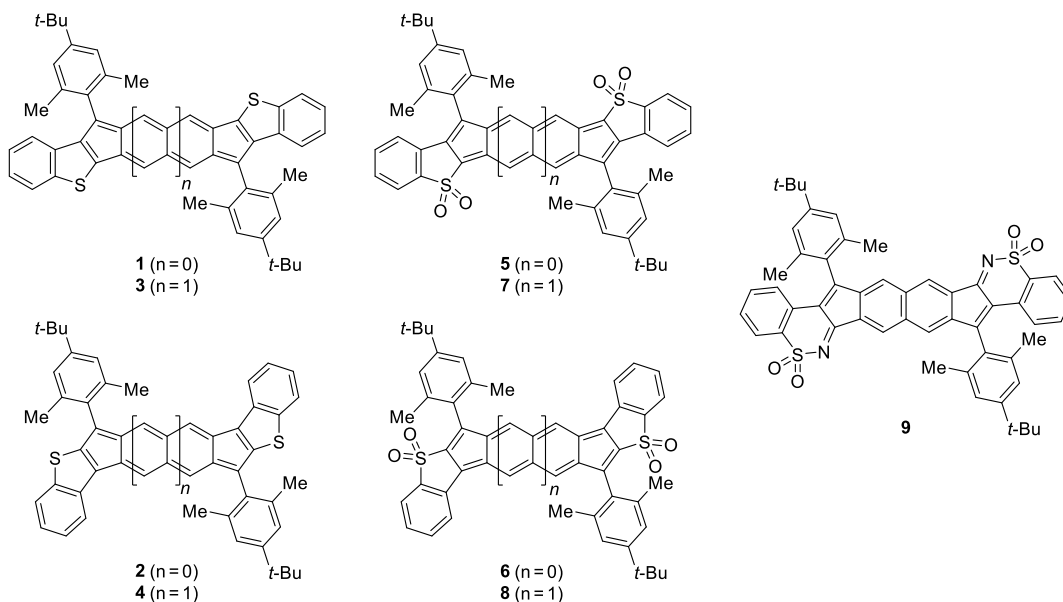
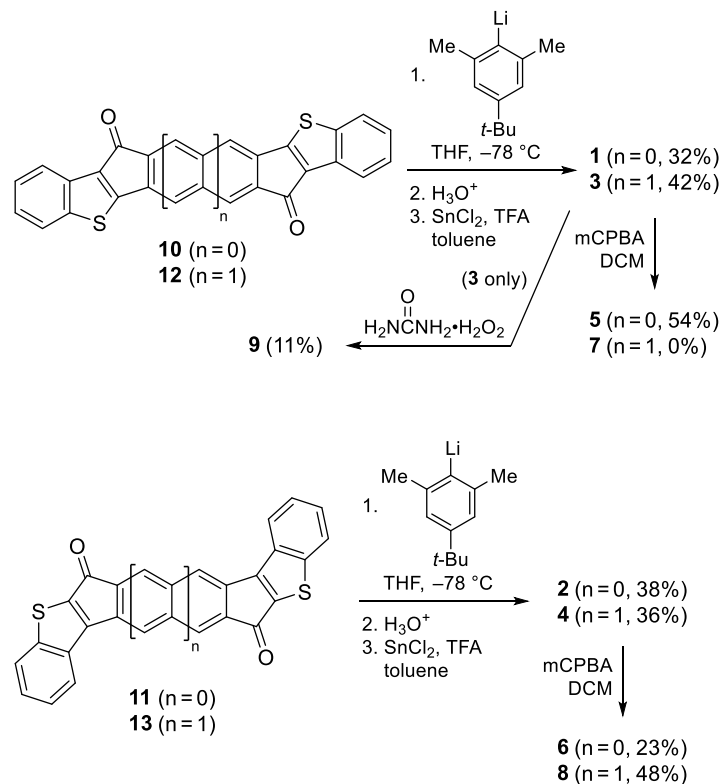


Figure 6.1 New IDBTs **1** and **2**, known IIDBTs **3** and **4**, their sulfone analogues **5-8**, and decomposition product **9**.

Our recent studies on indacenodibenzothiophenes^{27,68} (IDBTs, e.g. **1**, **2**) and indenoindenodibenzothiophenes^{60,62} (IIDBTs, e.g. **3**, **4**) provide a unique opportunity for late-stage modification of the electronics of our molecules, from electron-rich to electron-poor through the conversion of the sulfur atoms to fully oxidized sulfones (e.g., IDBT-S **5-6** and IIDBT-S **7-8**). A relevant report from the Campos group,⁷⁰ among others,⁷¹⁻⁷⁴ has shown that oxidation of sulfur in polythiophene lowers the LUMO energy level and thus affords an overall change in the properties of the bulk material. Herein we report the synthesis and detailed characterization of sulfones **5**, **6** and **8** and computationally corroborate that changing the oxidation state of the sulfur has profound effects on the antiaromaticity and diradical character of the molecules. This work looks to highlight the ability to impart overall large-scale electronic modification to the molecules, tuning the targeted properties, utilizing a non-arduous synthetic route.

6.3 Results and Discussion

Synthesis. Our initial efforts started with the known mesityl (2,4,6-trimethylphenyl) analogues of **1** and **2**.²⁷ While we successfully oxidized the former to **5-Mes** (see Supplementary Appendix E for details), oxidation of the latter afforded an insoluble and uncharacterizable violet solid. We then switched to 2,6-dimethyl-4-*t*-butylphenyl units (which we have coined *t*-Mes) on the apical carbons as these confer considerably improved solubility. Reacting 2,6-dimethyl-4-*t*-butylphenyllithium with diones **10** and **11** (Scheme 6.1) followed by an acidic aqueous workup gave intermediate diols (not shown) that were reductively dearomatized using SnCl₂ and catalytic trifluoroacetic acid (TFA) to furnish the fully conjugated IDBTs **1** and **2**, respectively. IIDBTs **3** and **4** were prepared analogously from diones **12** and **13** as previously reported.^{62,68} Oxidation of the fully conjugated scaffolds utilizing mCPBA successfully resulted in purple sulfones **5**, **6** and **8** in modest to moderate yields. Surprisingly, oxidation of *anti*-IIDBT **3** with mCPBA did not furnish sulfone **7** but rather an uncharacterizable orange solid whose absorption spectrum lacked the characteristic low energy bands >500 nm (Figure E.32), suggestive of a system with less than expected π -conjugation. We explored other oxidizing reagents such as H₂O₂, oxone, and urea-hydrogen peroxide (UHP). Only the reaction of **3** with UHP proceeded to afford a purple



Scheme 6.1 Synthesis of IDBTs **1**, **2** and IIDBT **3**, **4** and their conversion to the respective sulfones **5-8** along with formation of decomposition product **9**.

solid in low yield, which we initially believed to be the desired sulfone as the compound possessed low energy transitions out to $\sim 640\text{ nm}$ (Figure E.33) and an appropriate ^1H NMR spectrum (see Supplementary Appendix E); however, the structure obtained by X-ray diffraction (vide infra) revealed it to be molecule **9** as shown in Figure 6.1. This structure suggests that compound **7** likely was formed during the reaction but the oxidized ring hydrolyzed/cleaved (ArSO_2^- is a reasonable leaving group), urea next condensed onto the newly formed ketone carbonyls, and then system recycled in some manner to afford **9**. Regardless of how **9** is generated, we never observed direct evidence of **7**. Out of chemical curiosity, less π -conjugated *anti*-IDBT **1** was subjected to oxidation conditions using UHP, which furnished only a trace amount of an analogous sulfonamide (as detected by mass spectrometry). This outcome suggests that the *anti*-orientation of the pro-aromatic core of **7** is prone to degradation to regain naphthalene aromaticity as found in **9**, something we have not observed in any of our prior IIDBT studies.

NMR Spectroscopy and NICS-XY Scans. Because the central protons on the IDBTs are directly attached to the *s*-indacene core, one would expect these protons to be sensitive to the paratropic environment and experience an upfield chemical shift. Indeed this is the case—whereas the ¹H NMR chemical shift of the central six-membered ring protons of the parent indeno[1,2-*b*]fluorene is 6.85 ppm, these analogous protons in the previously reported Mes-substituted *anti*-IDBT and *syn*-IDBT appear at 6.11 and 6.06 ppm, respectively, in line with the claim of increased antiaromaticity of the *s*-indacene core of the IDBTs.²⁷ In the current study, substitution with *t*-Mes affords values of 6.09 and 6.06 ppm for **1** and **2**, respectively (Figure 6.2). In both cases, the *syn* derivative is slightly more upfield than the *anti* isomer, indicating the *syn* is slightly more paratropic, a result corroborated by NICS-XY scan calculations (vide infra).²⁷ Intriguingly, after sulfone formation this trend is reversed, the core singlet for *syn*-IDBT-S **6** appears at 6.91 ppm and for *anti*-IDBT-S **5** at 6.03 ppm, the latter result suggesting that the paratropic core of **5** is comparable to **1** and **2**.

Given the difficulty of assessing aromaticity/antiaromaticity based solely on relatively small changes of NMR chemical shifts, we explored computationally the ring currents of IDBT-S **5** and **6** using NICS-XY scans, as these allow us to explore areas of the molecule that possess both paratropic and diatropic ring currents within the same system.^{75,76} All calculations were performed with the unsubstituted structures to decrease computational cost as exclusion of the mesityl groups has been shown to have a negligible impact on the NICS-XY results.²⁸ Notably all the IDBT derivatives possess a paratropic *s*-indacene-like core (Figure 6.2, rings A and B). The NICS scans (Figure 6.2 bottom) replicate our prior studies that showed that the *syn*-IDBT core of **2** is nearly as antiaromatic (21-24 ppm, dark purple) as *s*-indacene itself (22-25 ppm, black), whereas the *anti*-IDBT core of **1** is slightly less paratropic (18-21 ppm, dark blue). In all cases the thiophene rings (C) appear to be atropic (0 to -1 ppm) regardless of sulfur oxidation state, and similarly the outer benzene rings (D) all possess strong aromaticity with minimal variation (-14 to -16 ppm). Interestingly, oxidation reverses the *syn/anti* ordering, where *syn*-IDBT-S **6** has weaker paratropicity (11-13 ppm, light purple) compared to IDBTs **1** and **2**, and *anti*-IDBT-S **5** shows comparable paratropicity (19-20 ppm, light blue) to **1**. In

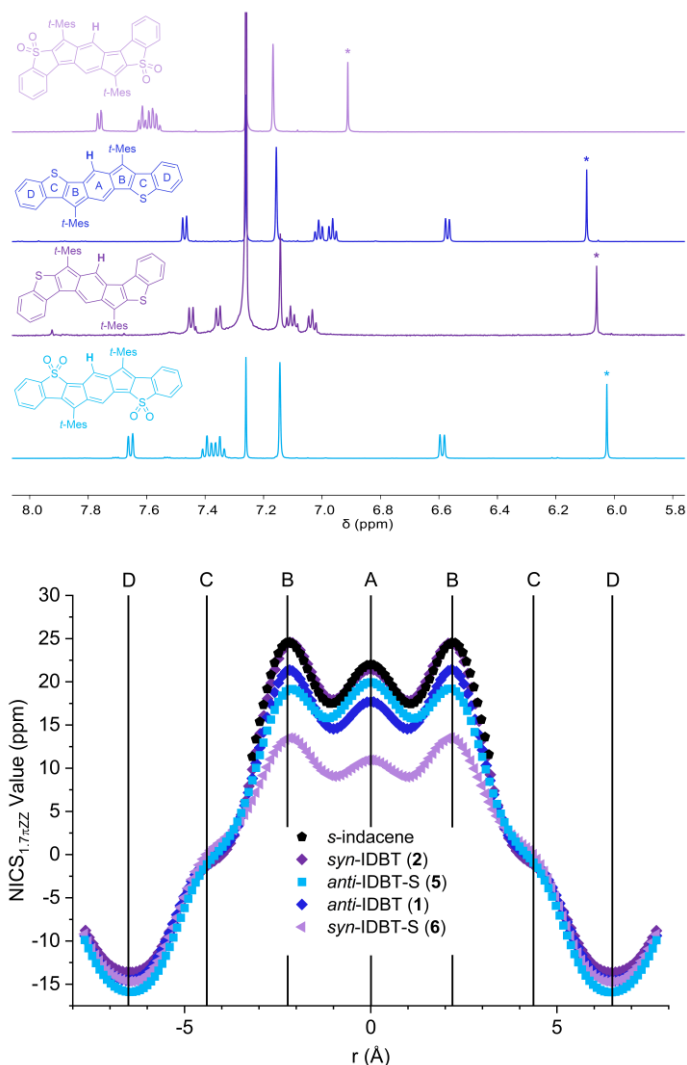


Figure 6.2 (Top) Proton NMR spectra of the aromatic region of IDBTs **1** and **2** and the corresponding sulfones **5** and **6**. The central proton (*) displayed in bold in the structures on the left can be used to roughly assess antiaromaticity. (Bottom) NICS-XY scans for IDBTs **1** and **2** and sulfones **5** and **6** along with the scan for the parent *s*-indacene, in order of most to least paratropic; for clarity the ring labels are shown above in the structure of **5**.

fact, the NICS values for ring A are essentially the same for **2** and **5**, which support their near identical chemical shifts in the aforementioned proton NMR experiments.

Further calculations suggest there are two competing effects that influence the antiaromatic characters of the parent IDBTs (**1** vs. **2**) and the corresponding sulfones (**5** vs. **6**)—a “Clar sextet-effect” and a “charge-effect”, respectively (vide infra). When a Clar sextet-effect dominates, the compound with more quinoidal character will have a smaller HOMO-LUMO energy gap (e.g., *syn*-IDBT **2**). When a charge-effect dominates,

the less charge-stabilized compound will have a smaller HOMO-LUMO gap (e.g., *anti*-IDBT-S **5**). A smaller HOMO-LUMO gap often translates to greater antiaromatic character, since the HOMO-LUMO gap is a denominator in the paramagnetic term of the equation used to compute magnetic shielding. Whether a Clar sextet-effect or charge-effect dominates depends on the electronegativity of the heteroatom(s).

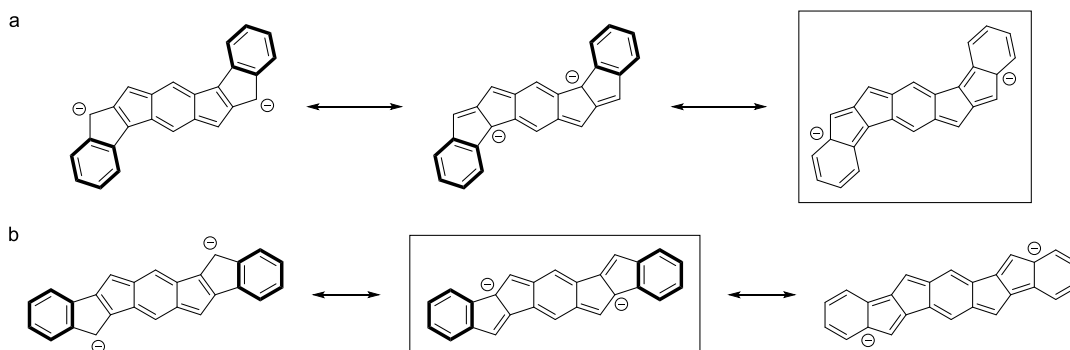


Figure 6.3 Selected resonance forms for the hydrocarbon dianion reference analogues of (a) *syn*-IDBT **2** and (b) *anti*-IDBT **1**; boxed structures are the dominant resonance forms recognized by NBO.

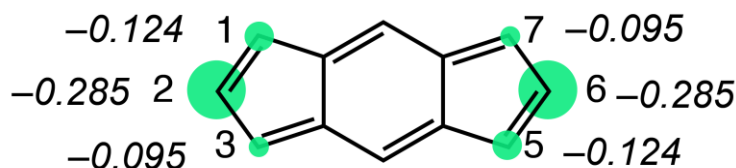


Figure 6.4 Natural population analyses (NPA) charges for *s*-indacene.

Calculations suggest that the stronger paratropicity of **2** (dark purple curve, Figure 6.2) vs. **1** (dark blue) is the result of a less aromatic resonance structure (i.e., a “Clar sextet-effect”). Computed natural bond orbital (NBO) analyses for the isoelectronic hydrocarbon “dianion” reference analogues of the benzothiophene-fused *s*-indacenes (i.e., *syn*- and *anti*-IDBT) show that the dominant resonance form of the *syn*-IDBT reference is a quinoidal resonance structure (boxed structure in Figure 6.3a and Figure E.22 for the NBO output), while that of the *anti*- reference displays two Clar sextets in the terminal benzenoid rings (boxed structure in Figure 6.3b and Figure E.23 for the NBO

output).⁷⁷ In concert, the computed NICS(1.7)_{πzz} values show a less negative value for **2** (−14 ppm) and a more negative value for **1** (−15 ppm) at the terminal benzene rings (ring D in Figure 6.2). The more paratropic *syn*-IDBT also has a smaller computed HOMO-LUMO gap (1.84 eV) compared to *anti*-IDBT (1.96 eV).

As shown experimentally, IDBT-S **5** and **6** display the opposite trend, i.e., a “charge-effect” dominates. Sulfone **5** (light blue trace in Figure 6.2) is significantly more paratropic than **6** (light purple) because the electronegative sulfone (SO₂) groups are placed at topologically disfavored positions, resulting in a narrower HOMO-LUMO gap and increased antiaromatic character. As shown in Figure 6.4, computed natural population analyses (NPA) charges for *s*-indacene are the most negative at carbons 2 and 6. Because of this charge distribution, fused ring arrangements that stabilize negative charges at carbons 2 and 6 will stabilize the *s*-indacene core. When SO₂ groups are fused to *s*-indacene in a *syn* arrangement, the electronegative SO₂ groups are placed at positions that help stabilize negative charges at carbons 2 and 6. For this reason, **6** exhibits a larger HOMO-LUMO gap (1.95 eV, Table E1) and decreased paratropicity. When SO₂ groups are fused to *s*-indacene in an *anti* arrangement, the SO₂ groups are connected to carbons 3 and 7 (the least negatively charged positions), and this stabilizes the *s*-indacene core to a lesser extent. As a result, *anti*-IDBT-S **5** exhibits a narrower HOMO-LUMO gap (1.65 eV), i.e., increased paratropicity. The charge-effect described here is akin to the rule of topological charge stabilization, first proposed by Gimarc to explain how the placement of heteroatoms in hydrocarbon frameworks affect the relative stabilities of the possible isomers.⁷⁸

It is worth noting that even though both Clar sextet-effects and charge-effects are present in the parent and sulfone compounds, differences in the antiaromatic characters of *syn* vs. *anti*-IDBT are dominated by the Clar sextet-effect, while the *syn*- vs. *anti*-sulfones set is influenced more so by the charge-effect because of the stronger electronegativity of the sulfones. To further illustrate the competing Clar sextet- and charge-effects, the NICS-XY scans of *syn*- and *anti*-IDT and *syn*- and *anti*-IDT-S were performed at the same level of theory (Figure E.16) The scans showed that without the terminal benzene rings (no Clar sextet-effect), both the IDT and IDT-S compounds show a more paratropic

anti- form due to a dominating charge-effect. It is also worth noting the more pronounced difference in paratropicity for the IDT-S pair (Figure E.16).

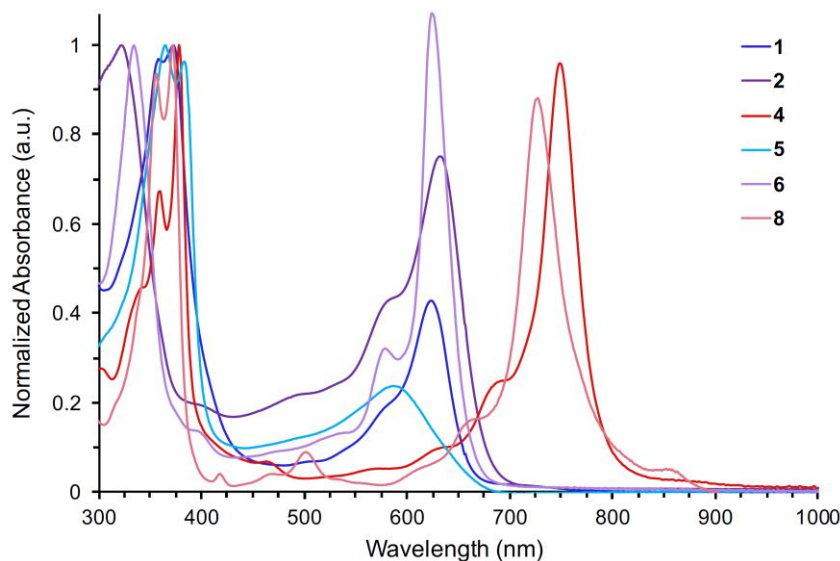


Figure 6.5 Electronic absorption spectra of the three stable sulfones **5**, **6**, and **8** and their parent thiophenes **1**, **2**, and **4** in CHCl_3 at room temperature. The spectrum of each sulfone is a similar color to the parent compound, with the sulfone having the lighter hue.

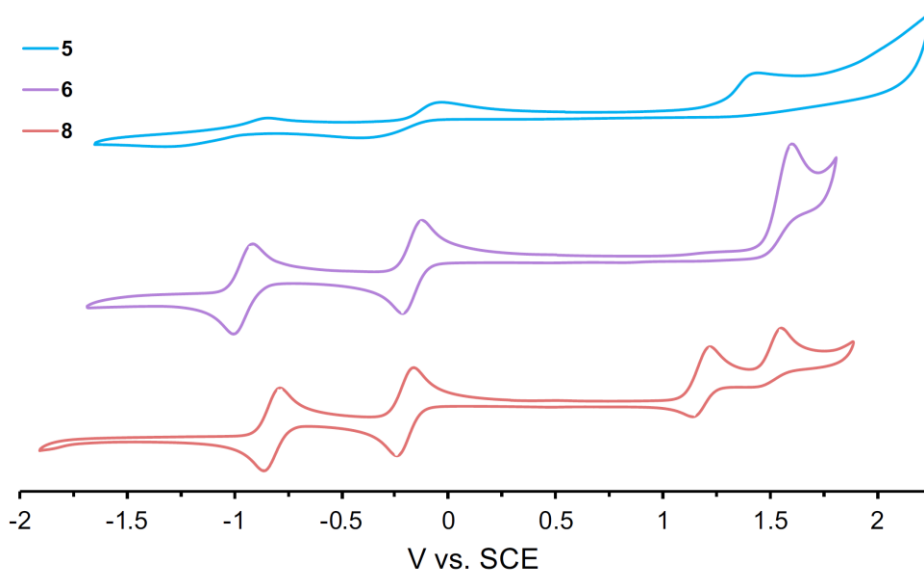
Electronic Absorption Spectroscopy. Sulfones **5**, **6** and **8** exhibit UV-Vis-NIR absorption spectra (Figure 6.5) very similar to their respective thiophene parents (**1**, **2**, **4**). All of the molecules possess strong absorptions in the range of 300-400 nm. Interestingly the main difference between the thiophene and sulfone compounds is displayed in the low energy absorptions, where all of the sulfones show a blue-shift of the main low energy absorption anywhere from 8 nm in compound **6** to as large as 37 nm in **5**. While the π -extended nature of the IIDBTs redshifts the low energy absorption appreciably (~ 100 nm), IIDBT-S **8** also is blue-shifted 24 nm compared to parent **4**, suggesting all three sulfones possess slightly larger optical energy gaps. Gratifyingly, the TD-DFT generated absorption spectra (Figures E.18-E.21) corroborate these changes for all sulfones; specifically, the calculations replicate that *anti*-**5** would display a greater blue shift in the low energy absorption than *syn*-**6**, a trend also predicted for the naphthalene series as well (*anti*-**7** vs. *syn*-**8**). Another interesting feature observed for compounds **4** and **8** is a weak absorption shoulder (852 and 866 nm, respectively) on the low energy

absorption due to a low-lying doubly excited electronic configuration, a common occurrence in molecules with appreciable open shell character (vide infra).^{46,47}

Electrochemistry. To further probe their electronic properties, cyclic voltammetry of sulfones **5/6/8** was carried out in CH₂Cl₂ (Figure 5.6). The redox behavior of the sulfones compared to their thiophene precursors are shown in Figures E.34-E.36, with the results compiled in Table 6.1. All of the sulfones undergo a reversible first reduction in solution along with a second reduction that is reversible for **6** and **8** and pseudo-reversible for **5**. IDBT-S **5** and **6** exhibit one irreversible oxidation, while IIDBT-S **8** displays one reversible oxidation followed by a second irreversible oxidation. E_{red}^1 values range from -0.17 to -0.22 V vs. SCE and E_{ox}^1 values range from 1.18 to 1.60 V vs. SCE. In our prior studies, comparison of the electrochemistry of parent IDBTs (**1** and **2**) showed that the *syn*-IDBT had the narrower HOMO-LUMO energy gap, in agreement with the fact that **2** was more antiaromatic.²⁷ Whereas the HOMO levels of **1** and **2** are comparable, **2** has a lower LUMO leading to the decreased energy gap. In the case of the IDBT-S, the trend is reversed—the LUMOs of **5** and **6** are essentially equal in energy but it is the higher in energy HOMO that leads to the decreased electrochemical energy gap in **5**. Given that HOMO-LUMO energy gaps generally narrow with increased antiaromaticity, this supports the finding that once oxidized **5** is the more antiaromatic of the two. These experimental observations are well reproduced by quantum chemical calculations (Table E1). Gratifyingly the electrochemical data for **8** matches DFT calculations well in that the HOMO-LUMO energy gap is calculated to be approximately 1.52 eV and the experimental value was 1.38 eV. As with the benzene-core sulfones the HOMO and LUMO energy levels experimentally and computationally are overall lower (more negative) for *syn*-IIDBT-S **8** when compared to the parent *syn*-IIDBT **4**. A general trend from these studies that all three sulfones possess overall lower energy HOMO and LUMO levels (HOMO < -5.8 eV, LUMO < -4.4 eV) relative to the parent thiophenes (HOMO < -5.3 eV, LUMO < -3.8 eV).

Table 6.1 Cyclic voltammetry data for thiophenes 1, 2, and 4 and sulfones 5, 6, and 8

cmpd	$E_{\text{red}2}$ (V)	$E_{\text{red}1}$ (V)	$E_{\text{ox}1}$ (V)	$E_{\text{ox}2}$ (V)	E_{HOMO} (eV)	E_{LUMO} (eV)	E_{gap} (eV)
1	-1.72	-0.87	0.84	1.32	-5.52	-3.81	1.71
5	-1.08	-0.22	1.44	–	-6.12	-4.46	1.67
2	-1.37	-0.75	0.86	1.57	-5.54	-3.93	1.61
6	-0.96	-0.17	1.60	–	-6.28	-4.51	1.77
4	-1.23	-0.67	0.66	1.09	-5.34	-4.01	1.33
8	-0.82	-0.20	1.18	1.55	-5.86	-4.48	1.38

**Figure 6.6** Cyclic voltammograms of **5**, **6** and **8**.

Solid-State Structures. To gain insight into the molecular structure of the electronically altered sulfones, single crystal X-ray diffraction (XRD) and subsequent bond length analysis of the structures was performed. Slow diffusion of CH_3CN into CHCl_3 gave deep violet crystals of **5-Mes** and **9**, whereas to attain strongly diffracting crystals for **6** and **8**, 3-5 mg of the target compound was dissolved in a 15:1 mixture of CHCl_3 and CH_3CN , which then slowly evaporated over several weeks to obtain suitable crystals for XRD.⁷⁸ The resultant structures as well as calculated geometries (Figures E.25-E.28) are shown in Figure 6.7. Whereas molecules of **5-Mes** pack roughly as 1D stacks with a distance of 3.51 Å between the average planes of the central fragments

(Figure E.39), **6**, **8** and **9** pack as isolated molecules with no close π - π contacts because of the orientation of the bulky *t*-Mes groups and/or the presence of solvent molecules (Figures E.41, E.43, E.45). As is typical of benzene- and naphthalene-based quinoidal systems, the molecules show distinct bond alternation about the antiaromatic core. Surprisingly, the bonding pattern in both the IDBT-S and IIDBT-S is flipped as a result of oxidation, as depicted in Figure 6.8. In fact, out of 50+ X-ray structures of our quinoidal molecules obtained over the past decade,²⁹ the three sulfones are the only molecules to have this flipped arrangement. Nonetheless, the experimental bond lengths (black numbers in Figure 6.7) of the hydrocarbon cores are all in relatively good agreement with the predicted values (<0.01 Å, blue numbers). All four structures possess bond lengths suggesting that two external six-membered rings behave as isolated benzenes, in line with the NICS-XY scans. The three sulfone structures all display asymmetric carbon-sulfur bond lengths on either side of the S atom where the shorter bond is from the sulfone to the core. Interestingly, the computations overestimate all of the C-S bond lengths by ~ 0.03 Å. The bond lengths for **9**, which are only experimental numbers, are typical of those found in a ring-fused naphthalene.

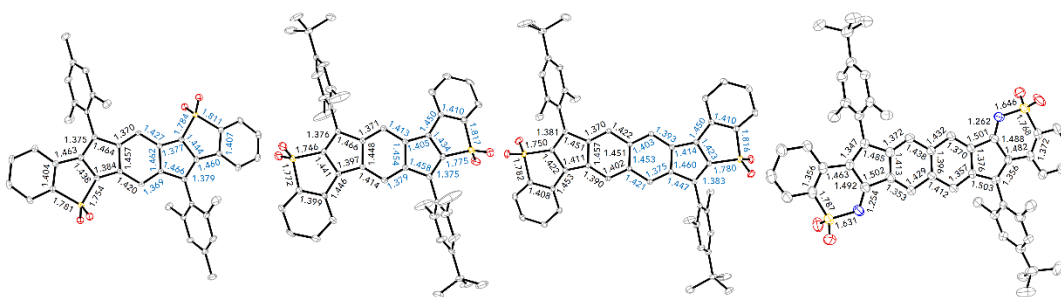


Figure 6.7. X-ray structures of (left to right) sulfone derivatives **5-Mes**, **6**, and **8** and decomposition product **9** with selected bond lengths (Å; experimental values in black, calculated values in blue); ellipsoids drawn at the 50% probability level. Experimental numbers for **6** represent the average value from two crystallographically independent molecules.

As depicted in Figure 6.8, the bonding alternation pattern in all three sulfones changes from the “normal” arrangement (left) to the “flipped” arrangement (right), and the computations corroborate these findings. Plunkett and co-workers discovered a similar bonding pattern reversal for an acenaphthylene-fused pentalene, but their

rationale, i.e., the [5]radialene orientation of the double bonds similar to C₆₀ and related “buckybowls”,²⁰ is clearly not applicable for our molecules. While calculations identified only a bond flipped structure for **6**, two minima structures were found for **5**—a higher energy structure with the normal bond alternation pattern and a flipped structure that is 1.5 kcal mol⁻¹ lower in energy.⁸⁰ NICS-XY scan calculations of **5** and its normal bonding pattern isomer **5*** provide a plausible explanation (Figure 6.8 bottom) for the bond-flipped behavior: whereas the NICS scan of **5** shows reduced paratropicity compared to *s*-indacene, the NICS scan of **5*** suggests that a normal bond alternation arrangement would afford a molecule with greater paratropicity than *s*-indacene. Since antiaromaticity is a destabilizing feature, the sulfones simply adopt a bond alternation pattern to minimize their paratropicity and thus maximize their overall stability. Computational reevaluation of the Plunkett group’s pentalene using NICS-XY scans (Figure E.17) reveals that flipping of the bond alternation pattern results in a significant reduction in paratropicity compared to normal pentalene bonding, a result consistent with the above arguments

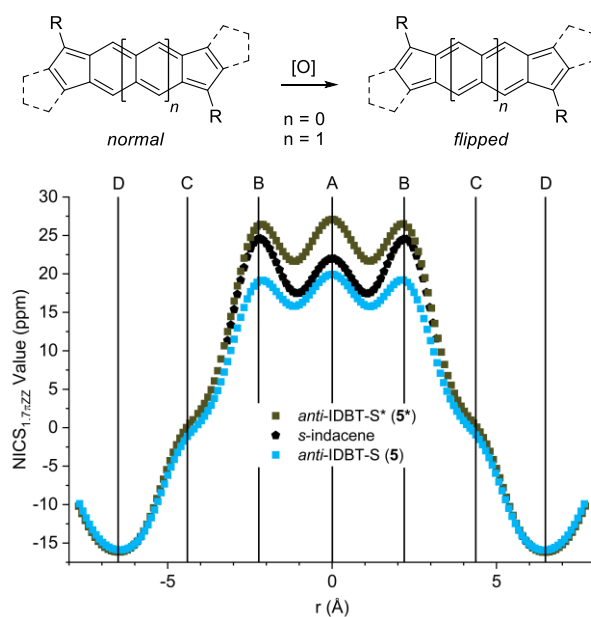


Figure 6.8 (Top) Generalized structures displaying the “normal” bonding pattern observed in most indeno[1,2-*b*]fluorene-based molecules and the “flipped” bonding pattern observed for sulfones **5**, **6** and **8**. (Bottom) NICS-XY scans of both *anti*-IDBT-S geometries where **5** is the observed bond-flipped orientation and **5*** is the normally observed bonding pattern.

Variable Temperature NMR. We recently disclosed the synthesis and characterization of IIDBTs **3** and **4**, which are rare examples of singlet ground-state diradicaloids that required heating to 100-150 °C in order to access their triplet spin state.^{60,62} The uniquely large singlet-triplet energy gaps (7-8 kcal mol⁻¹) that the IIDBTs display are in part explained by the electronic repulsion of the lone pairs on the sulfur atoms. If we were to remove participation of the sulfur lone pairs by changing them into sulfones as in **7** and **8**, we would expect an accompanying change in the singlet-triplet energy gap and the diradical character index y . As shown in Table E2, the computational results reveal that sulfone formation slightly decreases y (*anti* -0.012, *syn* -0.006) and increases ΔE_{ST} , more so for the *anti* isomers (**3**→**7**, $\Delta\Delta E_{ST}$ = 0.88 kcal mol⁻¹) than the *syn* isomers (**4**→**8**, $\Delta\Delta E_{ST}$ = 0.23 kcal mol⁻¹). These results are also in line with the linear (**3/7**) versus cross conjugation (**4/8**) arguments of the S atom with respect to the radical center accounting for the differences in IIDBT magnetic properties, i.e., cross conjugated **4/8** should be affected less than linearly conjugated **3/7**.

Although isolation of *anti*-IIDBT-S **7** proved elusive, we first explored the diradical nature of *syn*-sulfone **8** by variable temperature (VT) proton NMR spectroscopy. Based on its calculated ΔE_{ST} (-8.29 kcal mol⁻¹), one would expect the need for slightly higher temperatures to populate the triplet state when compared to *syn*-IIDBT **4** (-8.06 kcal mol⁻¹). Like its parent thiophene, sulfone **8** also displayed solubility issues at room temperature in either 1,1,2,2-tetrachloroethane-*d*₂ (Figure E.29) or 1,2-dichlorobenzene-*d*₄ (Figure E.30). As was the case with **4**, thermal broadening of the aromatic proton NMR signals of **8** (Figures 6.9 and E.31) began at 75 °C and resolution of the signals was almost lost by 125-130 °C. Interestingly, once the sample was cooled back to 25 °C, the solubility of **8** was greatly enhanced and the signals could be completely assigned. Like the computations, these qualitative results suggest that compounds **4** and **8** have very similar singlet-triplet energy gaps.

To experimentally examine the magnetic properties of the sole open-shell sulfone, superconducting quantum interference device (SQUID) magnetometry was performed on a sample of **8**. The magnetic properties of **8** were measured up to ~580 K, as the compound was shown by TGA to be stable at elevated temperatures (Figure E.37). The SQUID signal was subjected to the Bleaney-Bowers fitting⁸¹ from which the singlet-

triplet energy gap was calculated to be $-6.5 \text{ kcal mol}^{-1}$, the average of two sets of heating and cooling experiments. With changes of $<3\%$ between the heating and cooling runs, these results are indicative of the thermal resilience of **8** at high temperatures. Although somewhat lower than the calculated ΔE_{ST} ($-8.29 \text{ kcal mol}^{-1}$), the experimental value, much like in the case of IIDBTs **3** and **4**, support the hypothesis of an open shell molecule with a ground state singlet and an accessible triplet state only at elevated temperatures.

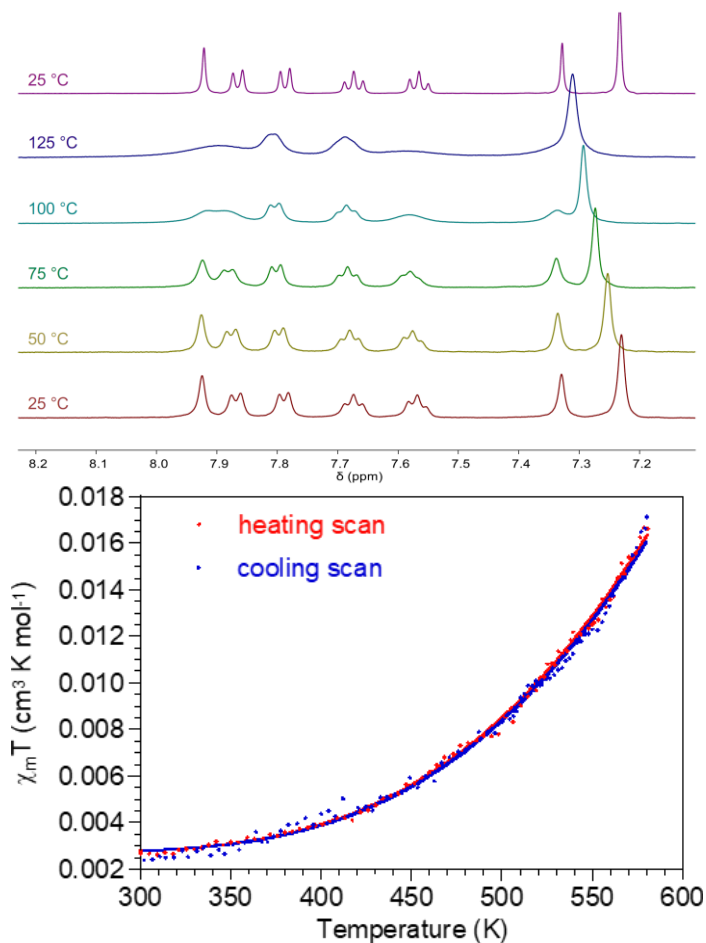


Figure 6.9 (Top) Variable temperature ^1H NMR spectra of the aromatic region of **8** in 1,1,2,2-tetrachloroethane- d_2 . (Bottom) SQUID magnetometry data for **8** in the solid state (circles) along with the corresponding Bleaney-Bower fits of the heating and cooling covers (solid lines).

6.4 Conclusions

A small family of benzothiophene-derived sulfones has been synthesized and fully characterized using a late stage modification approach. Through the use of a single chemical transformation, we are able to significantly alter the antiaromaticity in our IDBTs and the diradical character and related properties in *syn*-IIDBT. This work highlights the development of late stage modification methods to impart meaningful change in properties without time-consuming synthetic modification. These resulting changes in antiaromaticity are trackable through proton NMR spectroscopy, NICS-XY scan calculations, and electrochemistry. The CV data show that IDBT-S **5** is the first example of our thiophene-containing systems where the *anti*-derivative has a smaller electrochemical gap than the *syn*-isomer. The most significant change upon sulfone formation is flipping of the bond alternation pattern within the indacene core, as this relieves the potential destabilizing affects of enhanced paratropicity if the bond alternation were to retain a normal pattern. Notably, late stage modification has provided an additional way to tune the diradical character and singlet-triplet energy gap of our ever-expanding series of diradicaloids,^{58,60,62,63} garnering new hope for the implementation of diradicals into organic devices. Work is under way to develop additional late stage modification approaches to fine-tune antiaromaticity and diradical character and related properties in our indeno[1,2-*b*]fluorene-derived scaffolds, as well as to integrate some of these molecules into OFETs.

6.5 Experimental Section

6.5.1 General Experimental Details

General procedures. All air-sensitive manipulations were carried out under an inert nitrogen gas using standard Schlenk technique. For moisture sensitive reactions, THF and toluene were refluxed with Na benzophenone ketyl for 24 h prior to distillation and use. Silica gel (240-300 mesh) was used for column chromatography. All other reagents were purchased and used as received. NMR spectra were recorded on a Bruker Avance III HD 500 equipped with a Prodigy multinuclear cryoprobe (¹H: 500 MHz) or Bruker Avance III HD 600 equipped with a Prodigy multinuclear cryoprobe (¹H: 600 MHz, ¹³C: 151 MHz) NMR spectrometer at room temperature (unless otherwise noted).

^1H and ^{13}C NMR chemical shifts (δ) are expressed in ppm relative to the residual non-deuterated solvent reference (CDCl_3 : ^1H 7.26 ppm, ^{13}C 77.16 ppm; CD_2Cl_2 : ^1H 5.32 ppm, ^{13}C 53.84 ppm; $\text{DMSO}-d_6$: ^1H 2.50 ppm, ^{13}C 39.52 ppm). UV-Vis spectra were recorded on an Agilent Technologies Cary 60 UV-Vis spectrometer in HPLC grade CHCl_3 . 4-*tert*-Butyl-2,6-dimethylbromobenzene,¹ diones **10-11**,² diones **12-13**,³ and **1-Mes**² were prepared according to the literature.

6.5.2 Synthetic Details

General Procedure A: Preparation of Quinoidal Compounds 1-4. A flame-dried round bottom flask was charged with 4-*tert*-butyl-2,6-dimethylbromobenzene (6 equiv.) dissolved in dry THF that was then cooled to $-78\text{ }^\circ\text{C}$. Once at temperature, *n*-BuLi (5.5 equiv.) was added dropwise and the organolithiate was stirred at $-78\text{ }^\circ\text{C}$ for 1 h. Meanwhile in a separate flame-dried round bottom flask a suspension of dione (1 equiv.) in dry THF was also cooled to $-78\text{ }^\circ\text{C}$ to which the organolithiate was transferred via cannula. The reaction was gradually warmed to room temperature overnight. The reaction was quenched with sat. NH_4Cl solution and the organics were extracted with DCM (3x). The combined organic layer was then washed with H_2O and brine, dried (MgSO_4) and concentrated *in vacuo*. A short plug over SiO_2 purified the resultant diols which were carried onto the reductive dearomatization without further purification or characterization.

In a round-bottom flask the crude diol (1 equiv.) and anhydrous SnCl_2 (4 equiv.) were dissolved in dry toluene. Trifluoroacetic acid (3 drops, catalytic) was added to the mixture which was then stirred for 4 h. The reaction was monitored via TLC (9:1 hexanes/DCM). Once the reaction was complete, the mixture was concentrated to ~ 10 mL and then poured over a silica plug eluting with 1:1 hexanes/DCM to collect the crude reduced compounds. Column chromatography using an eluant of hexanes and DCM (see each compound for specific details) afforded the purified title compounds.

General Procedure B: Preparation of Sulfones. A flame-dried, foil wrapped round bottom flask equipped with a Claisen head was charged with compounds **1-4** (1 equiv.) and dry DCM. To this mCPBA (6 equiv.) was added in 3 portions over a 30 min period. After stirring at room temperature for 21 h, the reaction was quenched with a 10%

KOH solution and the organics were extracted using DCM (3x). The combined organic layers were washed with brine, dried (MgSO₄), and then concentrated to dryness. Column chromatography using a mixture of hexanes and DCM as eluant (see each compound for specific details) afforded the purified title compounds.

anti-IDBT (1). Following General Procedure A, the lithiate generated from 4-*tert*-butyl-2,6-dimethylbromobenzene (0.92 g, 3.80 mmol) in THF (10 mL) and *n*-BuLi (2.2 mL, 3.49 mmol) was added to dione **10**² (0.25 g, 0.63 mmol) in THF (20 mL) to produce the intermediate diol. A short SiO₂ plug using hexanes removed the non-polar impurities, followed by 1:3 DCM/hexanes to collect the first diastereomer and pure DCM to collect the second diastereomer.

Following General Procedure A, the diol mixture and SnCl₂ (0.30 g, 4 equiv.) were reacted in rigorously degassed and dry toluene (40 mL). After the initial plug, column chromatography on SiO₂ using 15% DCM/hexanes gave **1** (138 mg, 32% from dione) as a deep purple solid. ¹H NMR (600 MHz, CDCl₃) δ 7.47 (d, *J* = 7.9 Hz, 2H), 7.16 (s, 4H), 7.01 (t, *J* = 6.9 Hz, 2H), 6.96 (t, *J* = 7.5 Hz, 2H), 6.57 (dd, *J* = 8.0, 1.3 Hz, 2H), 6.09 (s, 2H), 2.36 (s, 12H), 1.39 (s, 18H). ¹³C NMR (151 MHz, CDCl₃) δ 150.91, 148.08, 147.56, 143.73, 143.04, 136.74, 136.02, 132.99, 131.53, 129.83, 125.91, 125.36, 124.37, 123.83, 123.51, 120.61, 34.42, 31.37, 20.92. HRMS (TOF ES⁺) (*m/z*) calculated for C₄₈H₄₅S₂ (M)⁺ 685.2963, found 685.2939.

anti-IDBT-sulfone (5). Following general procedure B, **1** (90 mg, 0.13 mmol) was reacted with mCPBA (135 mg, 0.79 mmol) in dry DCM (15 mL). After the basic aqueous work-up, the crude sulfone was purified by flash column chromatography using 45% DCM/hexanes as the eluant to give **5** (41 mg, 54%) as a vibrant purple solid with a blue sheen. ¹H NMR (500 MHz, CDCl₃) δ 7.66 (d, *J* = 8.2 Hz, 2H), 7.38 (t, *J* = 8.0 Hz, 2H), 7.35 (td, *J* = 7.5, 1.2 Hz, 2H), 7.14 (s, 4H), 6.59 (d, *J* = 7.5 Hz, 2H), 6.03 (s, 2H), 2.34 (s, 12H), 1.38 (s, 18H). ¹³C NMR (126 MHz, CDCl₃) δ 152.20, 146.56, 146.37, 144.90, 142.31, 140.70, 135.70, 133.47, 130.73, 130.70, 129.25, 127.99, 126.92, 125.01, 121.97, 121.78, 34.47, 31.20, 20.81. HRMS (TOF ES⁺) (*m/z*) calculated for C₄₈H₄₅O₄S₂ (M)⁺ 749.2759, found 749.2747.

anti-IDBT-sulfone (5-Mes). Following general procedure B, **1-Mes** (81 mg, 0.13 mmol) was reacted with mCPBA (135 mg, 0.79 mmol) in dry DCM (10 mL). After the

basic aqueous work-up, the crude sulfone was purified by flash column chromatography using 4:1 DCM/hexanes as the eluant (due to lower solubility of the mesityl groups) to give **5-Mes** (52 mg, 58%) as a deep purple solid. ^1H NMR (600 MHz, CDCl_3) δ 7.65 (d, $J = 7.6$ Hz, 2H), 7.39 (t, $J = 7.6$ Hz, 2H), 7.34 (t, $J = 7.7$ Hz, 2H), 6.97 (s, 4H), 6.59 (d, $J = 7.7$ Hz, 2H), 6.01 (s, 2H), 2.36 (s, 6H), 2.31 (s, 12H). ^{13}C NMR (151 MHz, CDCl_3) δ 146.65, 146.39, 145.17, 142.60, 140.89, 139.29, 136.37, 133.67, 130.94, 130.79, 129.53, 128.91, 128.13, 127.14, 122.10, 122.02, 21.31, 20.64. HRMS (METHOD) (m/z) calculated for $\text{C}_{42}\text{H}_{32}\text{O}_4\text{S}_2$ (M) $^+$ 664.1742, found 664.17xx.

syn-IDBT (2). Following General Procedure A, the lithiate generated from 4-*tert*-butyl-2,6-dimethylbromobenzene (0.92 g, 3.80 mmol) in THF (10 mL) and *n*-BuLi (2.2 mL, 3.49 mmol) was added to dione **11**² (0.25 g, 0.63 mmol) in THF (20 mL) to produce the intermediate diol. A short SiO_2 plug using hexanes removed non-polar impurities, followed by 30% DCM/hexanes to collect the first diastereomer and pure DCM to collect the second diastereomer.

Following General Procedure A, the diol mixture and SnCl_2 (0.39 g, 4 equiv.) were reacted in rigorously degassed and dry toluene (45 mL). After the initial plug using 1:9 DCM/hexanes, preparatory TLC (1:3 DCM/hexanes) afforded **2** (164 mg, 38% from the dione) as a teal solid. Due to the low solubility of the title compound (peaks are the same magnitude of the ^{13}C satellite peaks), the residual solvent peaks are greatly exaggerated. ^1H NMR (600 MHz, CDCl_3) δ 7.45 (d, $J = 8.1$ Hz, 2H), 7.36 (d, $J = 8.0$ Hz, 2H), 7.14 (s, 4H), 7.11 (t, $J = 7.2$ Hz, 4H), 7.04 (t, $J = 7.3$ Hz, 2H), 6.06 (s, 2H), 2.45 (s, 12H), 1.39 (s, 18H). ^{13}C NMR (151 MHz, CDCl_3) δ 151.16, 148.13, 147.05, 146.56, 140.93, 137.48, 136.05, 134.94, 133.35, 129.38, 125.17, 124.69, 124.40, 124.30, 123.93, 121.79, 34.46, 31.35, 20.98. HRMS (TOF ASAP⁺) (m/z) calculated for $\text{C}_{48}\text{H}_{45}\text{S}_2$ (M) $^+$ 685.2963, found 685.2931.

syn-IDBT-sulfone (6). Following General Procedure B, **2** (0.27 g, 0.40 mmol) was reacted with mCPBA (275 mg, 1.59 mmol) in dry DCM (40 mL). After the basic aqueous work-up, the crude sulfone was purified by flash column chromatography using 2:1 DCM/hexanes as the eluant to give **6** (72 mg, 23%) as a bluish-violet solid. ^1H NMR (600 MHz, CDCl_3) δ 7.76 (dd, $J = 7.2, 1.5$ Hz, 2H), 7.62 (td, $J = 6.6, 1.5$ Hz, 2H), 7.60–7.55 (m, 4H), 7.17 (s, 4H), 6.91 (s, 2H), 2.40 (s, 12H), 1.38 (s, 18H). ^{13}C NMR (151

MHz, CDCl₃) δ 152.31, 147.88, 147.35, 146.82, 143.46, 138.72, 136.66, 133.71, 132.62, 131.61, 128.93, 126.79, 125.88, 125.56, 125.09, 122.94, 34.92, 31.72, 21.15. HRMS (TOF ES⁺) (m/z) calculated for C₄₈H₄₅O₄S₂ (M)⁺ 749.2759, found 749.2749.

anti-IIDBT (3). Following General Procedure A, the lithiate generated from 4-*tert*-butyl-2,6-dimethylbromobenzene (0.61 g, 2.52 mmol) in THF (20 mL) and *n*-BuLi (1.5 mL, 2.36 mmol) was added to dione **12**³ (0.14 g, 0.32 mmol) in THF (20 mL) to produce the intermediate diol. A short SiO₂ plug using hexanes removed non-polar impurities, followed by 2:3 DCM/hexanes to collect the first diastereomer and pure DCM to collect the second diastereomer.

Following General Procedure A, the diol mixture and SnCl₂ (0.20 g, 4 equiv.) were reacted in rigorously degassed and dry toluene (40 mL). After the initial plug using 1:9 DCM/hexanes, the filtrate was concentrated. The solid was rinsed with cold MeCN (3x) and **3** was isolated as a deep purple solid (97 mg, 42% from the dione). NMR spectra and mass spectrum matched the data previously reported.³

anti-IIDBT-sulfonimide (9). Compound **3** (0.18 g, 0.25 mmol, 1 equiv.), urea-hydrogen peroxide (UHP) (0.24 g, 2.52 mmol, 10 equiv.) and phthalic anhydride (0.37 g, 2.52 mmol, 10 equiv.) were added to a flame-dried round bottom flask equipped with a reflux condenser under an N₂ atmosphere. Dry EtOAc (25 mL) was added and the reaction was heated to 90 °C for 24 h. The reaction was quenched with saturated Na₂SO₃ solution and then the organics were extracted with DCM (3x). The organics were washed sequentially with 1 M NaOH, H₂O and brine, dried (MgSO₄) and concentrated *in vacuo*. Purification by preparatory TLC (DCM) and collecting the vibrant purple band with an R_f of 0.5. furnished **9** (22 mg, 11%) as a purplish-red solid. ¹H NMR (600 MHz, CDCl₃) δ 8.09 (s, 2H), 8.05 (d, J = 7.8 Hz, 2H), 7.48 (t, J = 7.5 Hz, 2H), 7.33–7.27 (m, 6H), 7.13 (s, 2H), 6.94 (d, J = 8.2 Hz, 2H), 2.15 (s, 12H), 1.44 (s, 18H). ¹³C NMR (151 MHz, CDCl₃) δ 171.19, 157.87, 153.42, 142.35, 138.12, 134.60, 134.23, 133.18, 130.24, 128.46, 127.48, 126.37, 126.10, 125.12, 124.90, 120.90, 35.10, 31.73, 20.46. MS (ES⁺) (m/z) calculated for C₅₂H₄₆N₂O₄S₂ (M)⁺ 826.3, found 826.3.

syn-IIDBT (4). Following General Procedure A, the lithiate generated from 4-*tert*-butyl-2,6-dimethylbromobenzene (0.82 g, 3.37 mmol) in THF (10 mL) and *n*-BuLi (1.9 mL, 3.09 mmol) was added to dione **13**³ (0.25 g, 0.56 mmol) in THF (20 mL) to

produce the intermediate diol. A short SiO₂ plug using hexanes removed non-polar impurities, followed by 45% DCM/hexanes to collect the first diastereomer and pure EtOAc to collect the second diastereomer.

Following General Procedure A, the diol mixture and SnCl₂ (0.39 g, 4 equiv.) were reacted in rigorously degassed and dry toluene (45 mL). After the initial plug using 1:9 DCM/hexanes, preparatory TLC of the crude material using 1:3 DCM/hexanes as eluant gave **4** (149 mg, 36% from the dione) as a green solid. NMR spectra and mass spectrum matched the previously reported compound.³

***syn*-IIDBT-sulfone (8)**. Following General Procedure B, **4** (0.11 g, 0.15 mmol) was reacted with mCPBA (210 mg, 1.21 mmol) in dry DCM (20 mL). After the basic aqueous work-up, the crude sulfone was purified by flash column chromatography using 2:1 DCM/hexanes as the eluant to give **8** (58 mg, 48%) as a greyish-purple solid. (¹H NMR (500 MHz, CDCl₃) δ 7.83 (s, 2H), 7.76–7.73 (m (overlapping dd), 4H), 7.58 (td, *J* = 7.7, 1.1 Hz, 2H), 7.48 (t, *J* = 7.4 Hz, 2H), 7.24 (s, 2H), 7.16 (s, 4H), 2.29 (s, 12H), 1.38 (s, 18H). ¹³C NMR (151 MHz, CDCl₃) δ 152.13, 145.83, 142.26, 142.11, 141.40, 140.14, 136.85, 136.52, 135.41, 133.82, 131.05, 130.17, 130.04, 127.40, 127.05, 124.96, 124.00, 123.03, 34.90, 31.73, 21.03. HRMS (TOF ES⁺) (*m/z*) calculated for C₅₂H₄₆O₄S₂ (M)⁺ 798.2838, found 798.2831.

6.6 Bridge to Chapter VII

In the work highlighted in this chapter we showed how we could alter the diradical character and antiaromaticity of our indeno[1,2-*b*]fluorene derivatives. For the benzene cored IDBT series we observed significant and trackable changes to the antiaromaticity of the sulfonated derivatives traced computationally to a sigma-effect that the electron withdrawing sulfone unit introduces. The study of changes in the naphthalene cored IIDBTs were hampered due to the unstable nature of the *anti*-IIDBT sulfone not enabling a study of both the *syn* and *anti* derivatives. However, it was found that we were able to change the singlet-triplet energy gap of our *syn*-IIDBT diradical by approximately 1.5 kcal mol⁻¹ through oxidation of the sulfur to the sulfone. In the next chapter we focus on the conclusions and outlooks of the various ways that we have been able to control the single-triplet energy gap and what consequences this has for meaningful application.

CHAPTER VII

CONCLUSIONS AND OUTLOOK

Over the last five years the Haley lab has had a profound run of publishing important, thought-provoking work in the field of organic carbon based diradicals and has had a large impact on the development of the field. As demonstrated by the studies above we are aiming to produce real, synthesizable open-shell compounds with moderate to good stability, based on exploiting the key electronic structure concepts such a U and t_{ab} that control diradical properties (y and ΔE_{ST}) according to the two-electron two-site model. Structure property connections and a deep understanding of these studies are mandatory for the rational design of diradicals with tailored singlet-triplet energy gap. A fundamental understanding of the inherit electronic and magnetic properties of open shell diradicals is essential so that these properties can be modified to match the needs of industry. Simply put, tuning of the singlet-triplet energy gap to match application is key. It is well documented that there are many posited uses for diradicals in both electronic and magnetic applications. But above all else the development of practical diradicals, those with intermediate y values, where the singlet-triplet energy gap can be tailored to be operational at room temperature will be paramount to their use in common place organic electronics.

APPENDIX A:

SUPPLEMENTARY INFORMATION FOR CHAPTER II

Appendix A is the supplementary information for Chapter II of this dissertation. It includes characterization spectra, further experimental data, and computational details.

NMR Spectra

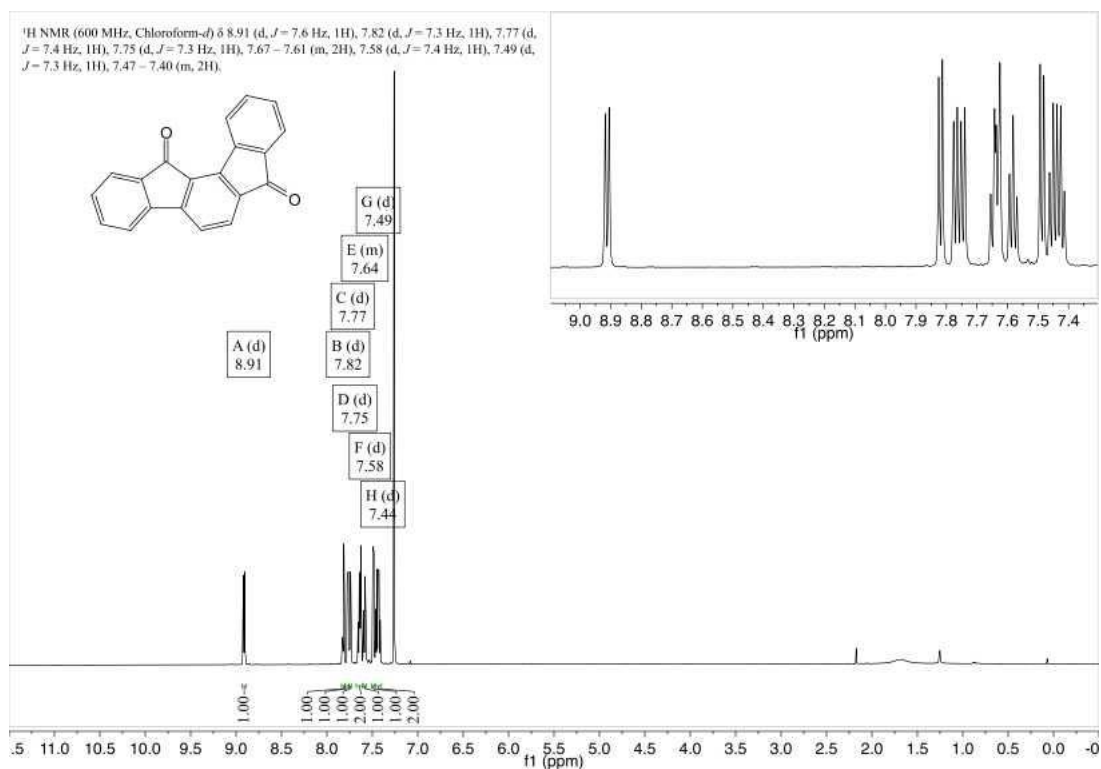


Figure A.1 ¹H NMR (600 MHz, CDCl₃) spectrum of indeno[1,2-*a*]fluorene-7,12-dione.

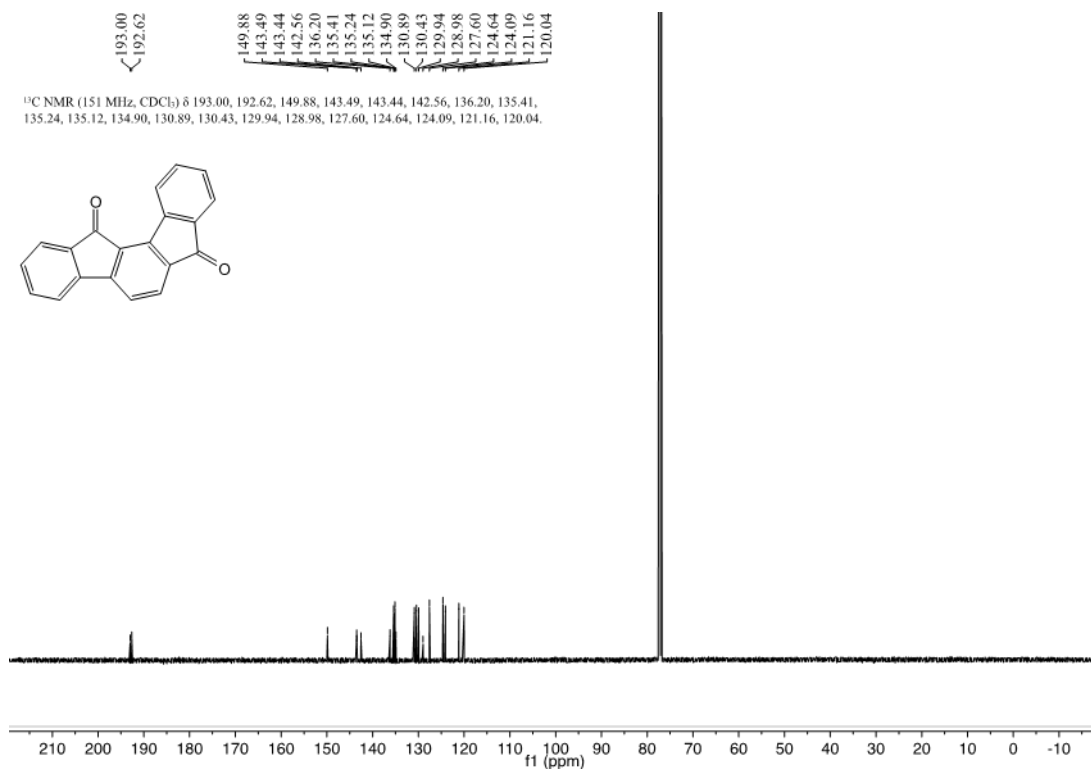


Figure A.2 ¹³C NMR (151 MHz, CDCl₃) spectrum of indeno[1,2-*a*]-7,12-dione.

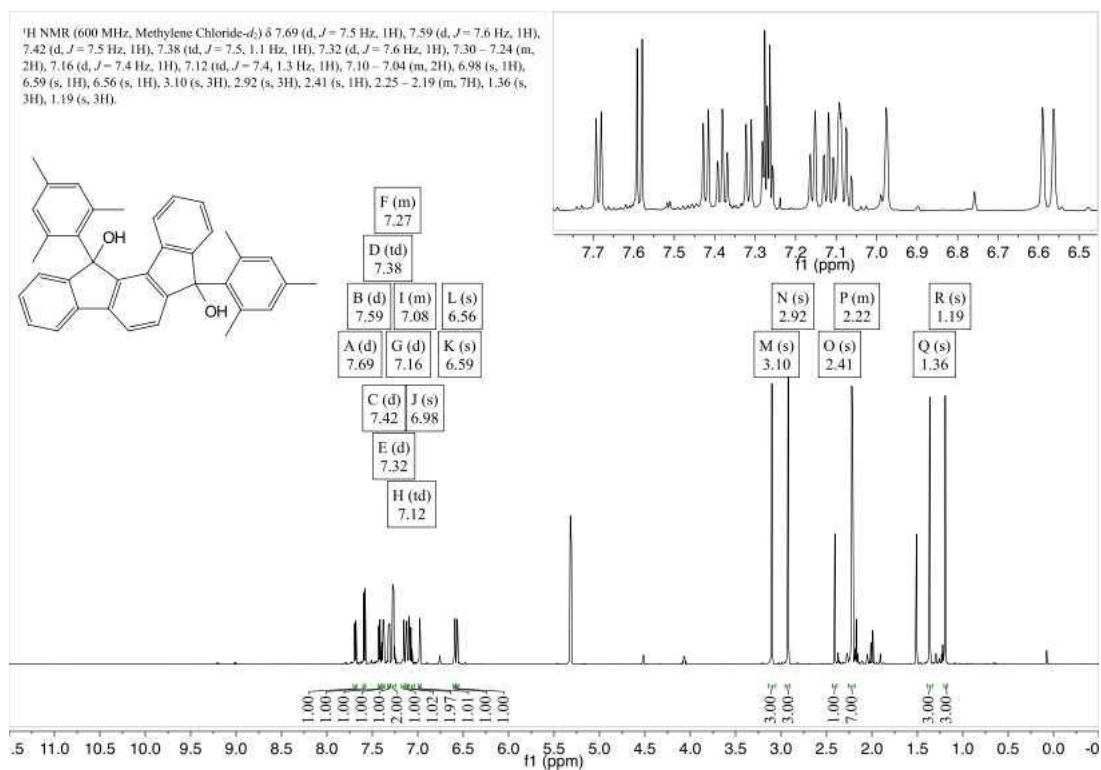


Figure A.3 ¹H NMR (600 MHz, CD₂Cl₂) spectrum of 7,12-Dimesitylindeno[1,2-*a*]fluorene-7,12-diol (8, first diastereomer)

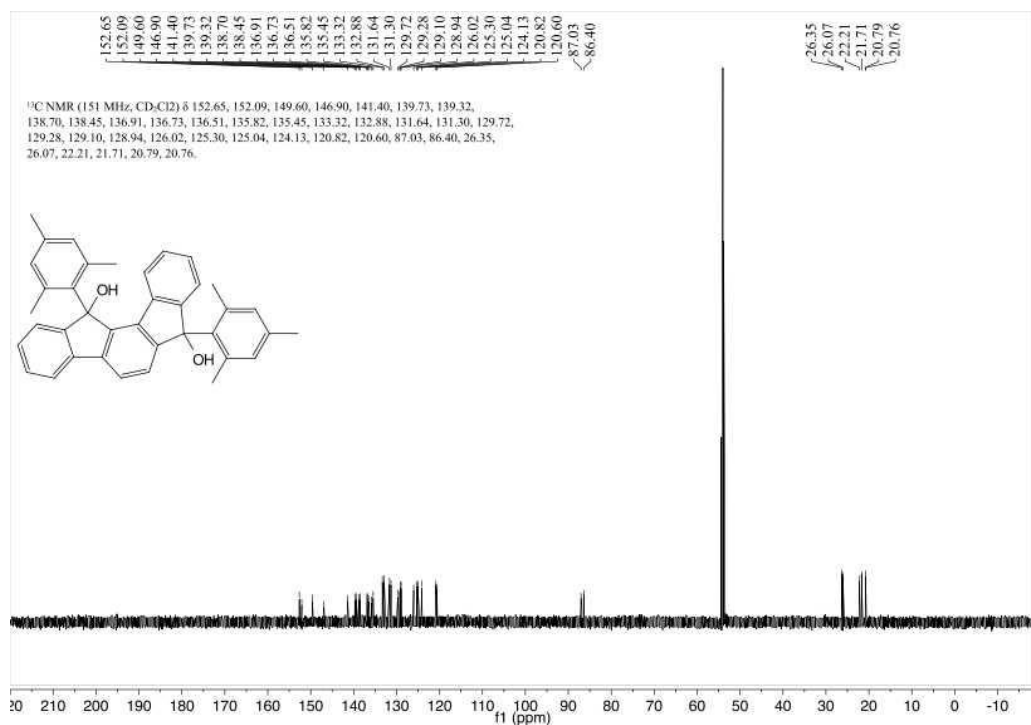


Figure A.4 ¹³C NMR (151 MHz, CD₂Cl₂) spectrum of 7,12-Dimesitylindeno[1,2-*a*]fluorene-7,12-diol (8, first diastereomer).

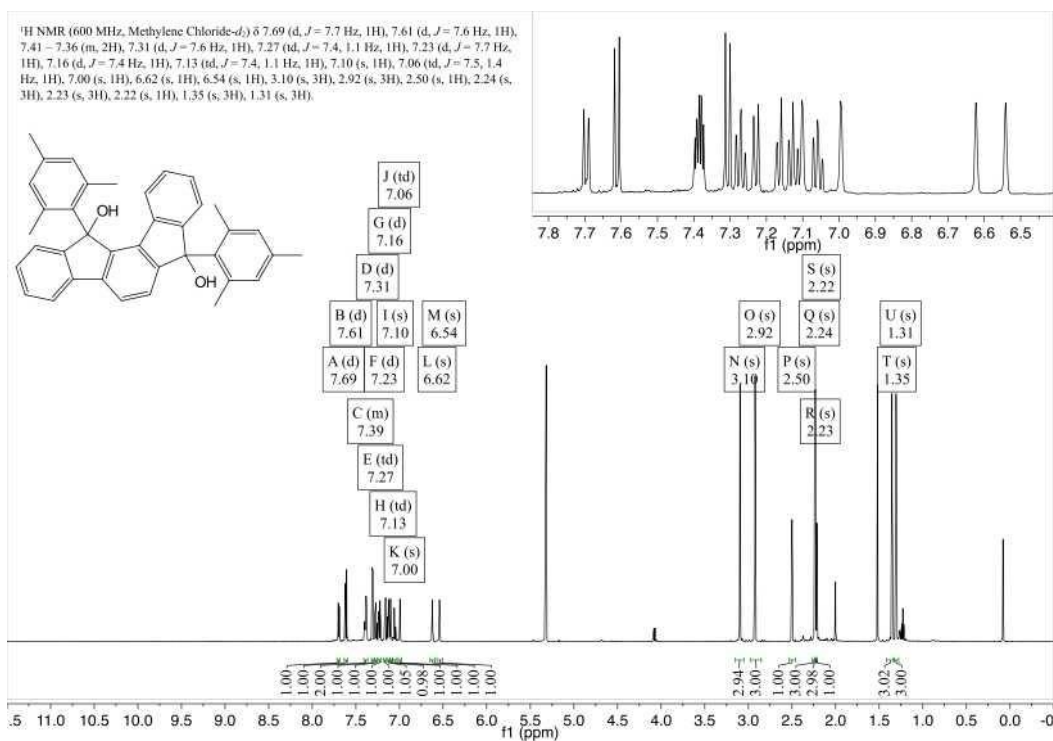


Figure A.5 ¹H NMR (600 MHz, CD₂Cl₂) spectrum of 7,12-Dimesitylindeno[1,2-*a*]fluorene-7,12-diol (8, second diastereomer)

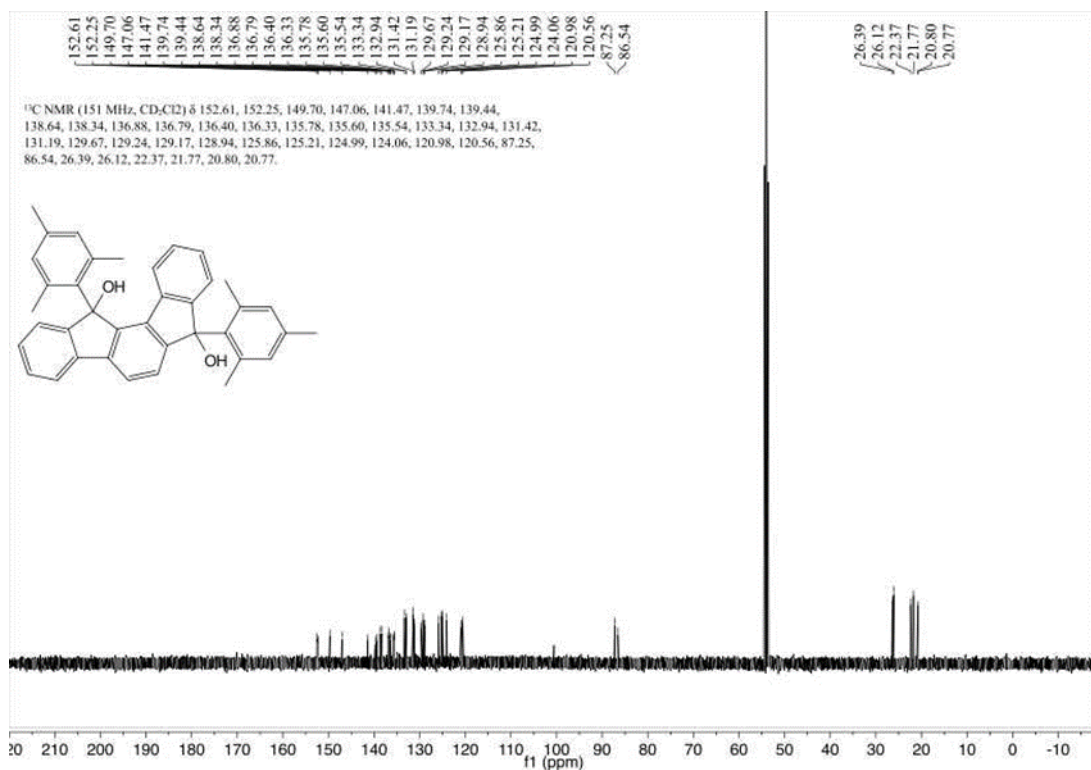


Figure A.6 ¹³C NMR (151 MHz, CD₂Cl₂) spectrum of 7,12-Dimesitylindeno[1,2-*a*]fluorene-7,12-diol (8, second diastereomer).

¹H NMR (400 MHz, THF-*d*₈) δ 7.73 (d, *J* = 9.2 Hz, 1H), 7.71 (d, *J* = 9.2 Hz, 1H), 6.94 (s, 2H), 6.89 (s, 2H), 6.82–6.71 (m, 3H), 6.63 (t, *J* = 6.7 Hz, 1H), 6.54–6.43 (m, 3H), 6.03 (t, *J* = 8.0 Hz, 1H), 2.41 (s, 3H), 2.31 (s, 3H), 2.10 (s, 6H), 2.00 (s, 6H).

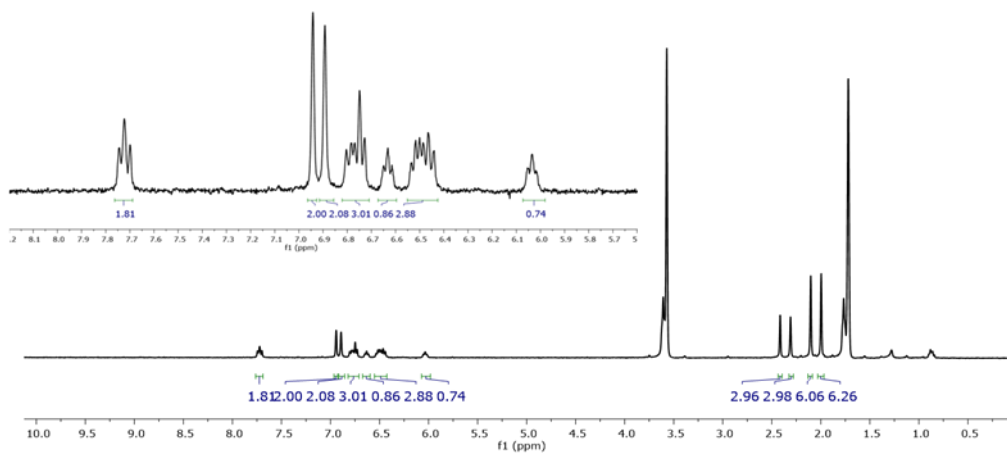


Figure A.7 ¹H NMR (400 MHz, THF-*d*₈) spectrum of the metal and ligand complex: [Cs₂²⁺(THF)₂(6²⁻)] – ¹H NMR

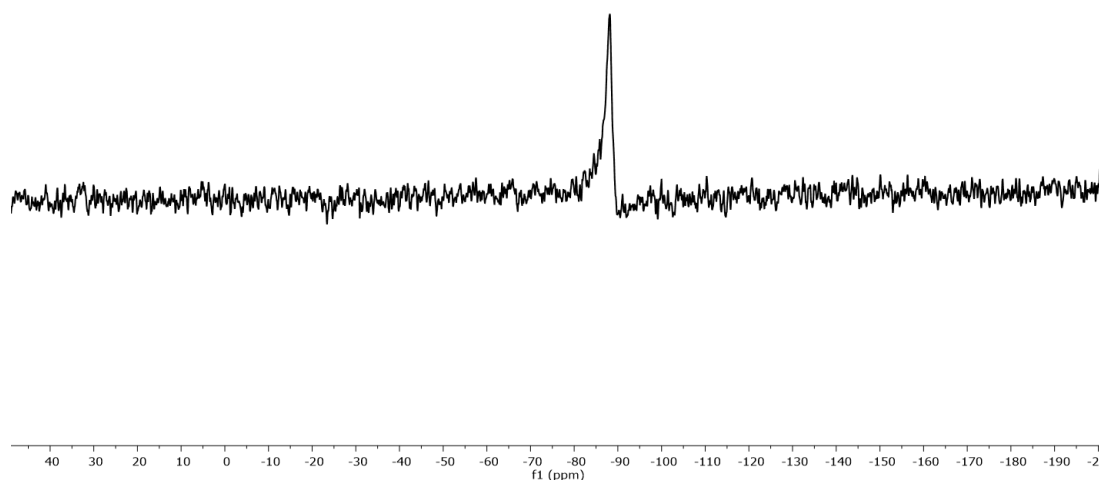


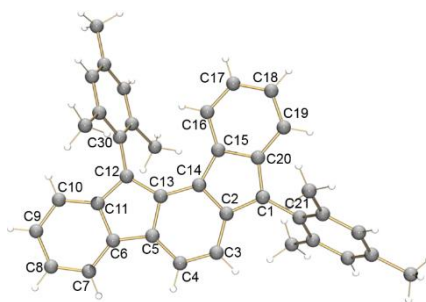
Figure A.8 ^{133}Cs NMR spectrum of the metal and ligand complex: $[\text{Cs}_2^{2+}(\text{THF})_2(6^{2-})]$

Computational Information

Table A1. Diradical character indices y for the five parent IF regioisomers **1-5** calculated at the PUHF/6-311G*//SF-CL-TDDFT B3LYP/6-311G* level of approximation.

Compound	y [-]
1	0.80
2	0.26
3	0.29
4	0.65
5	0.25

Table A2. C–C bond lengths (Å) of dimesityl[1,2-*a*]IF **6** optimized for the singlet (S) and triplet (T) states at several levels along with numbering scheme.



Bond	Bond length (Å)				Bond	Bond length (Å)			
	6-like (S) ^a y = 0.64	6'-like (S) ^b y = 0.99	6'-like (T) ^b	6''-like (S) ^a y = 0.59		6-like (S)	6'-like (S)	6'-like (T)	6''-like (S)
C1–C2	1.460	1.433	1.422	1.377	C9–C10	1.405	1.392	1.394	1.363
C1–C20	1.381	1.429	1.438	1.467	C10–C11	1.388	1.403	1.400	1.434
C1–C21	1.484	1.482	1.483	1.483	C11–C12	1.471	1.436	1.444	1.383
C2–C3	1.369	1.396	1.405	1.433	C12–C13	1.392	1.451	1.439	1.474
C2–C14	1.455	1.447	1.446	1.473	C12–C30	1.482	1.482	1.483	1.485
C3–C4	1.429	1.396	1.393	1.362	C13–C14	1.440	1.404	1.411	1.374
C4–C5	1.362	1.386	1.389	1.422	C14–C15	1.411	1.468	1.471	1.489
C5–C6	1.468	1.453	1.455	1.390	C15–C16	1.422	1.393	1.392	1.383
C5–C13	1.475	1.450	1.452	1.477	C15–C20	1.475	1.437	1.433	1.421
C6–C7	1.382	1.390	1.389	1.424	C16–C17	1.371	1.399	1.401	1.410
C6–C11	1.414	1.427	1.423	1.467	C17–C18	1.435	1.400	1.396	1.386
C7–C8	1.407	1.398	1.399	1.366	C18–C19	1.363	1.390	1.394	1.405
C8–C9	1.390	1.403	1.400	1.442	C19–C20	1.431	1.402	1.398	1.385

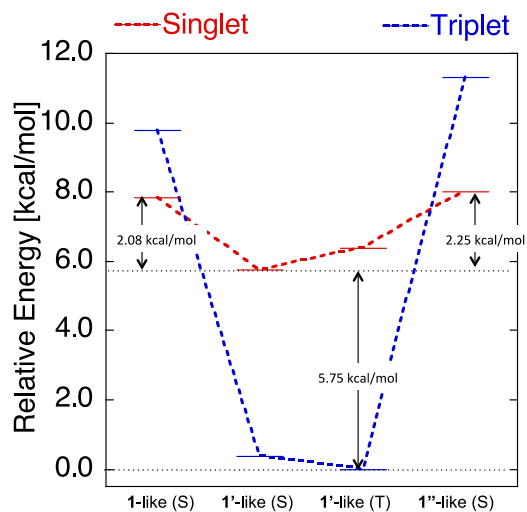


Figure A.9 Relative energies of singlet (S) and triplet (T) states for the parent [1,2-*a*]IF **1** optimized at the RB3LYP/6-311G* [1-like (S) and 1''-like (S)] and the UB3LYP/6-311G* [1'-like (S) and 1'-like (T)] levels. Single point calculations are performed at the SF-NC-TDDFT PBE50/6-311G* level.

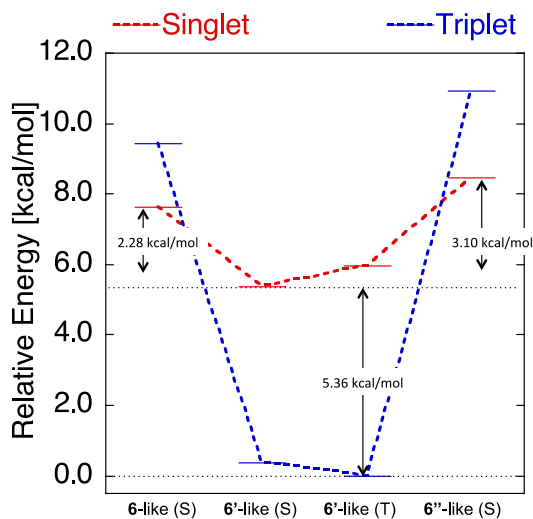


Figure A.10 Relative energies of singlet (S) and triplet (T) states for dimesityl[1,2-*a*]IF **6** optimized at the RB3LYP/6-311G* [6-like (S) and 6''-like (S)] and the UB3LYP/6-311G* [6'-like (S) and 6'-like (T)] levels. Single point calculations are performed at the SF-NC-TDDFT PBE50/6-311G* level.

Calculation results of S-T gap for **6** with mesityl groups

Since the adiabatic ΔE_{S-T} gap of the parent [1,2-*a*]IF for the UB3LYP optimized **1'**-like structure is close to that for the SF-CL-TDDFT optimized structures, we further examined the adiabatic S-T energy gap of the [1,2-*a*]IF with mesityl groups, i.e., **6**, by using the UB3LYP optimized structures (Table S3). The y value for **6** is estimated to be 0.99 at the PUHF/6-311G**// UB3LYP/6-311G* level, which is very close to that of the parent [1,2-*a*]IF **1** (0.97) estimated at the same level. Figure S3 shows the odd (unpaired) electron density map, showing a spatial contribution of the diradical character index y , for **6** in the singlet and triplet states, where odd electrons are primarily distributed on the five-membered rings for both spin states. The adiabatic ΔE_{S-T} gap for the UB3LYP optimized structures of **6** is $-5.36 \text{ kcal mol}^{-1}$ (Figure S2), which is close to that of the parent [1,2-*a*]IF obtained at the same level (Figure S1); thus, the effect of the mesityl groups on the ΔE_{S-T} gap is expected to be small. Therefore, [1,2-*a*]IF **6** is predicted to be a ground state triplet.

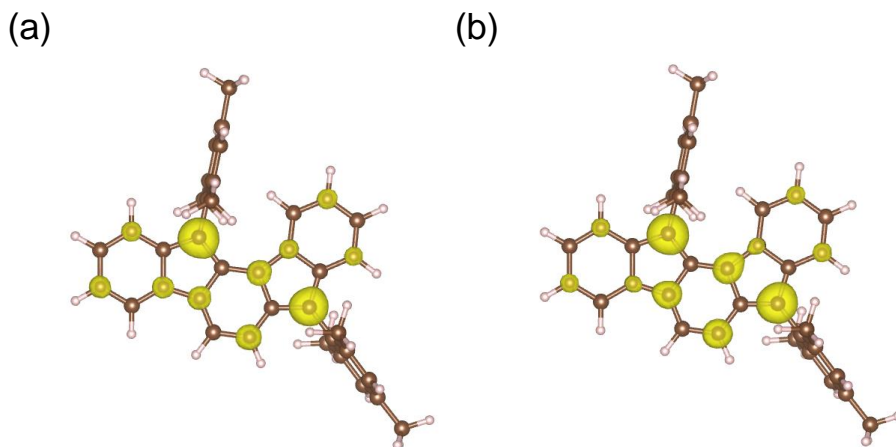


Figure A.11. Odd electron density maps with the isosurface value of 0.005 au for singlet (a) and triplet (b) states of [1,2-*a*]IF **6** calculated at the PUHF/6-311G**// UB3LYP/6-311G* level.

Calculated Electronic Absorption Spectrum

Theoretically simulated UV-vis spectrum for triplet **6** at the TD-UB3LYP/6-311G**/UB3LYP/6-311G* level is as follows. Although some peaks are slightly shifted, theoretically simulated result is in good agreement with experimental result. Weak bands around 600-700 nm are assigned as $129\beta \rightarrow 131\beta$ and $129\beta \rightarrow 130\beta$ transitions (please see Figure A.13 on the next page).

Table A3. Excitation properties (excitation wavelength λ and oscillator strength f) of triplet **6** calculated at the TD-UB3LYP/6-311G* level.

Number	λ (nm)	f (--)	Transitions	
1	660.55	0.0073	$129\beta \rightarrow 131\beta$	0.90619
2	636.30	0.0042	$129\beta \rightarrow 130\beta$	0.93351
3	531.34	0.0382	$128\beta \rightarrow 130\beta$	0.81268
4	487.85	0.0903	$128\beta \rightarrow 131\beta$	0.83805
11	409.63	0.0637	$131\alpha \rightarrow 132\alpha$	0.79192
22	332.97	0.5511	$130\alpha \rightarrow 133\alpha$	0.63243
			$131\alpha \rightarrow 133\alpha$	0.40401

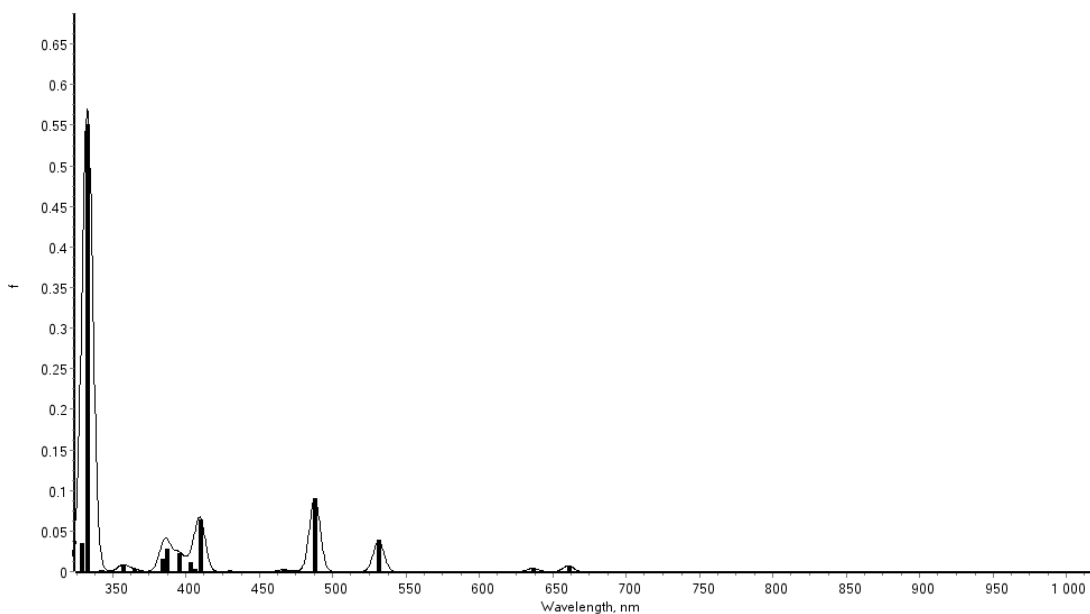


Figure A.12 Theoretically simulated UV-vis spectrum for triplet **6** at the TD-UB3LYP/6-311G**/ UB3LYP/6-311G* level; vertical axis corresponds to the oscillator strength.

Calculated Frontier Molecular Orbitals

The calculated ΔE between the SOMO (α -131: -4.851 eV) and SUMO (β -130: -3.034 eV) levels is 1.817 eV, which corresponds relatively well to the electrochemically determined E_{gap} .

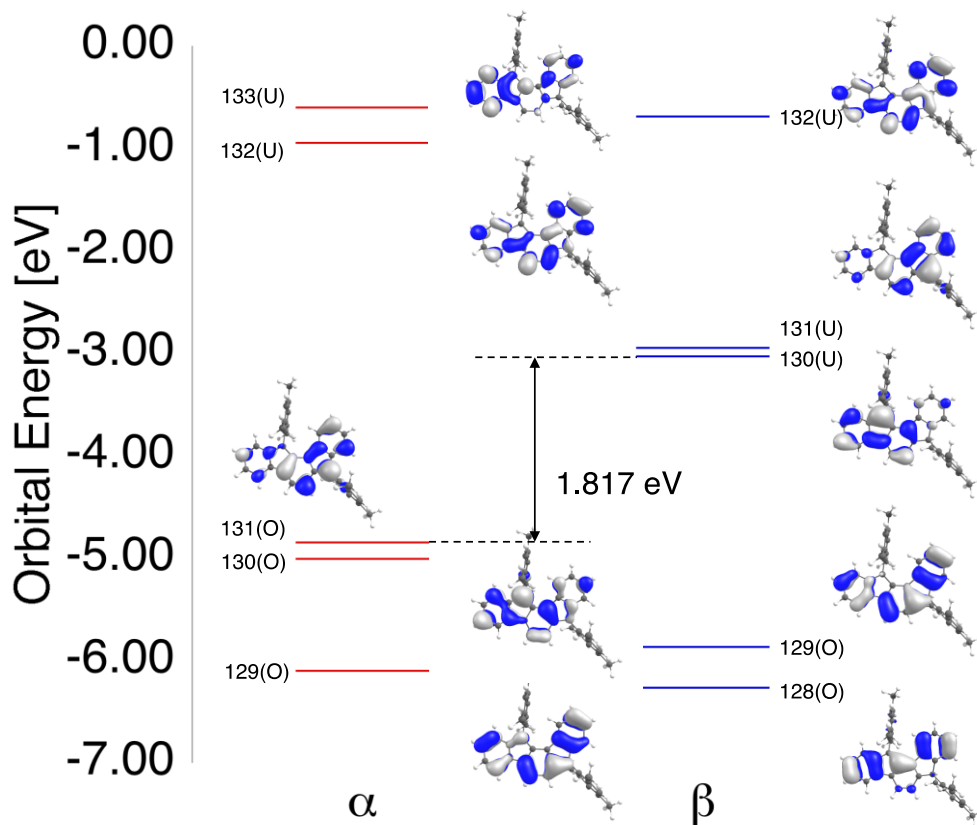


Figure A.13 Frontier MO diagram for triplet **6** calculated at the UB3LYP/6 - 311G*//UB3LYP/6-311G* level.

Additional Spectroscopy

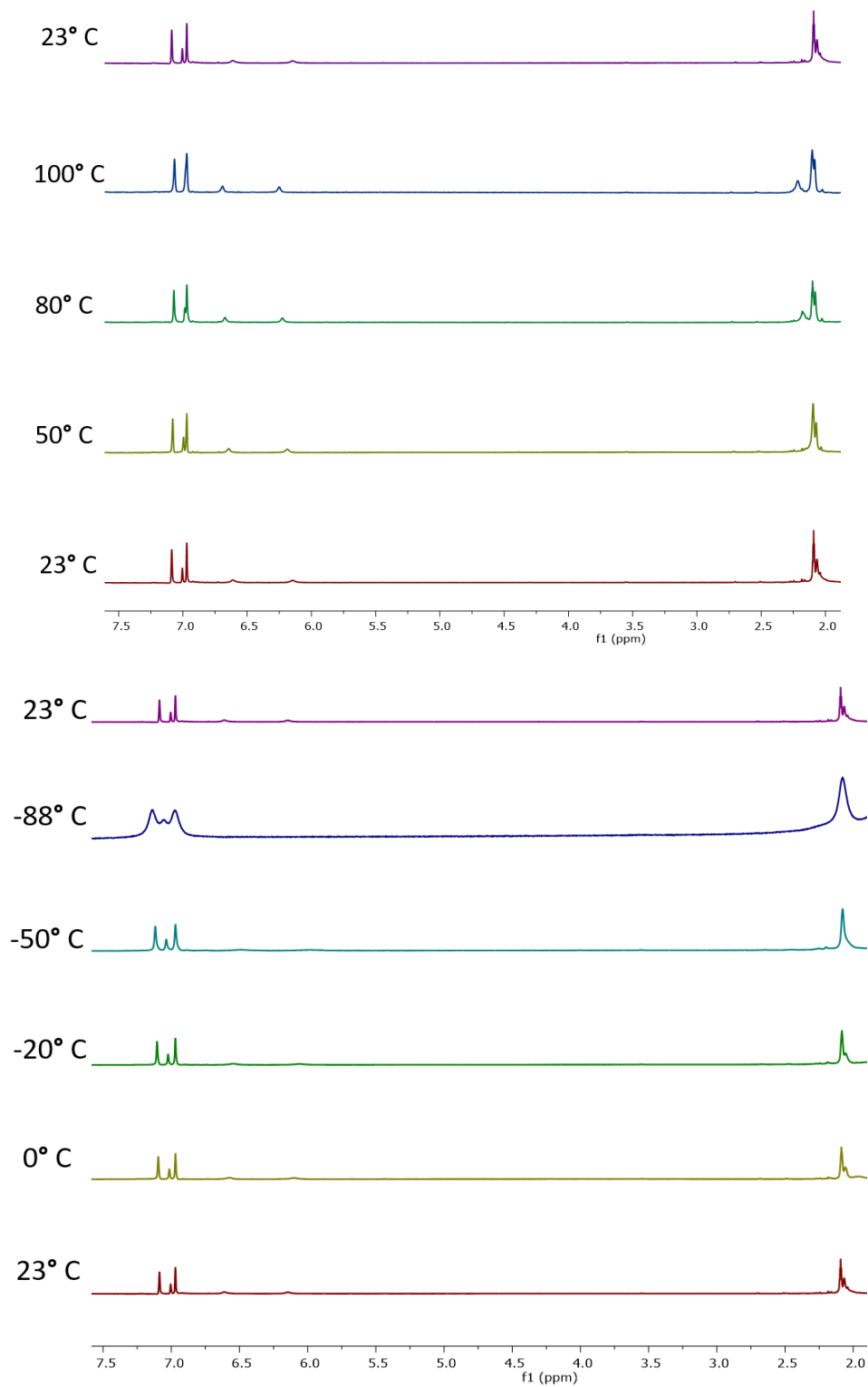
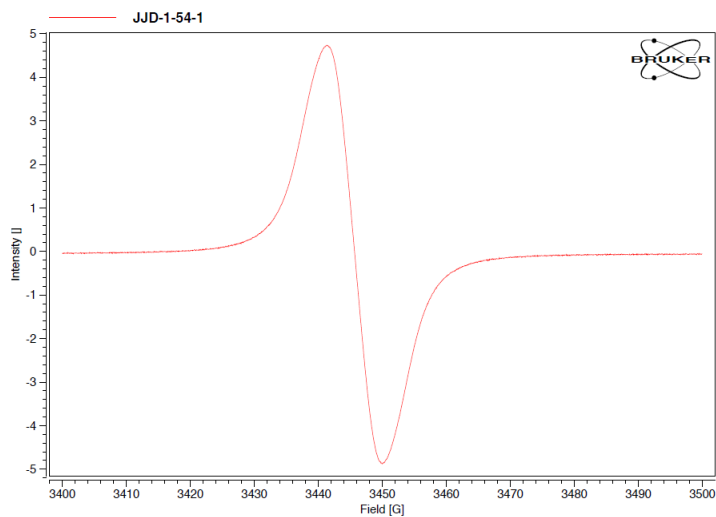


Figure A.14 High temperature (top) and low temperature (bottom) ¹H NMR spectra of **6** in 1,2-C₆H₄Cl₂.

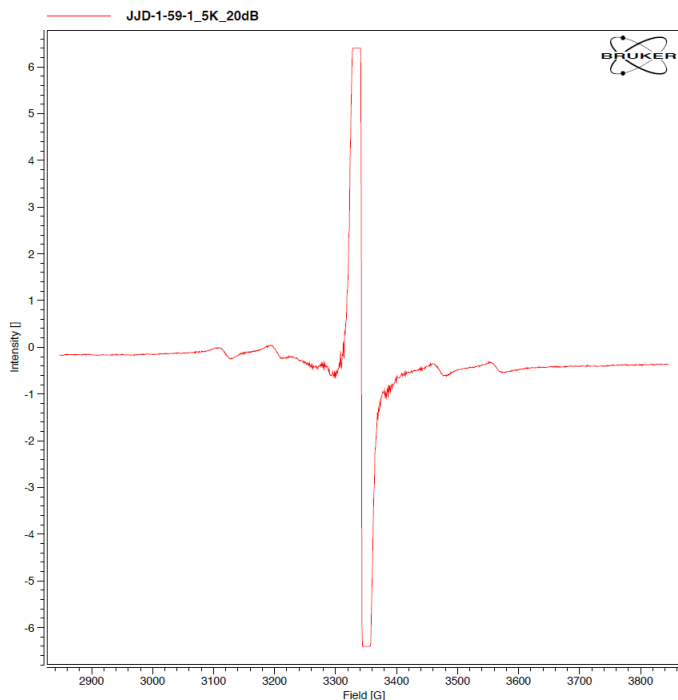


```

TITLE          JJD-1-54-1
FILE NAME      JJD-1-54-1
FILE PATH      /home/ch613/xoprFiles/Data/Haley/Just
DATASET TYPE   Experimental 1D Real, Intensity(Field)
AXIS STRUCTURE Field: indexed
AXIS DATA FORMAT Intensity: double
                Field: double
AXIS RANGE     Field [G]: 3400 to 3499.95, 2048 pts
                width 99.9512, center 3449.98
  
```

```

-----
AVAILABLE PARAMETERS
Operator       ch613
Date           08/31/16
Time           21:24:01
State of Aggregation C
Averaged Scans 10
Sampling Time [s] 0.01
Field Mod. Amplitude [T] 0.0001
Field Mod. Frequency [Hz] 100000
Microwave Frequency [Hz] 9.679141e+09
Microwave Power [W] 0.0002167
Receiver Gain  60
Receiver Time Constant [s] 0.00128
Receiver Phase [deg] 0.0
Receiver Harmonic 1
Receiver Offset [%FS] 0.0
  
```



```

TITLE          JJD-1-59-1_5K_20dB
FILE NAME      JJD-1-59-1_5K_20dB
FILE PATH      /home/ch613/xoprFiles/Data/Haley/Justin/
DATASET TYPE   Experimental 1D Real, Intensity(Field)
AXIS STRUCTURE Field: indexed
AXIS DATA FORMAT Intensity: double
                Field: double
AXIS RANGE     Field [G]: 2847 to 3846.02, 1024 pts
                width 999.023, center 3346.51
  
```

```

-----
AVAILABLE PARAMETERS
Operator       ch613
Date           09/17/16
Time           23:25:56
State of Aggregation C
Averaged Scans 10
Sampling Time [s] 0.0293
Field Mod. Amplitude [T] 0.001
Field Mod. Frequency [Hz] 100000
Microwave Frequency [Hz] 9.385414e+09
Microwave Power [W] 0.002167
Receiver Gain  60
Receiver Time Constant [s] 0.00128
Receiver Phase [deg] 0.0
Receiver Harmonic 1
Receiver Offset [%FS] 0.0
  
```

Figure A.15 Room temperature (top) and 5K (bottom) ESR spectra of **6**. For the latter spectrum, the microwave frequency and power used experimentally were 9.385 GHz and 2.167 mW, respectively. The experimentally determined zero-field splitting parameter $|D| = \sim 22$ mT. The g value is ~ 2.005 , which is appropriate for an organic radical.

All electrochemical experiments were conducted with traditional 3-electrode geometry using a Biologic SP-50 potentiostat. Electrolyte solutions (0.1 M) were prepared from HPLC grade CH_2Cl_2 and anhydrous Bu_4NBF_4 . The stock solution was degassed via freeze-pump-thaw (3x) cycles. The working electrode was a glassy carbon electrode (3-mm diameter), with a Pt-coil counter electrode and a Ag wire pseudo reference. The ferrocene/ferrocenium (Fc/Fc^+) couple was used as an internal standard following each experiment. Potential values were re-referenced to SCE using a value of 0.46 (V vs. SCE) for the Fc/Fc^+ couple in CH_2Cl_2 . When necessary, potentials were re-referenced to NHE using $\text{SCE} = -0.24$ (V vs. NHE). LUMO and HOMO levels were approximated using $\text{SCE} = -4.68$ eV vs. vacuum. CV experiments were conducted in a N_2 -filled drybox at sweep rates of 50 (reported), 75, 100 and 125 mV s^{-1} . All scan rates show quasi-reversible kinetics with no alteration of peak splitting with scan rate. $E_{1/2}$ values were calculated assuming $E_{1/2} \approx E^{0'} = (E_{\text{anodic}} + E_{\text{cathodic}})/2$ based on these observations for reversible couples; for irreversible couples the $E^{0'}$ value is estimated as the potential at peak current. $E_{a,c}$ peak splitting of the Fc/Fc^+ couple was similar to that of the analyte (~ 100 mV). The anodic peak current increased linearly with the square root of the scan rate in the range of 50–125 mV s^{-1} , indicating a diffusion-controlled process. Analyte concentrations were ca. 1–5 mM.

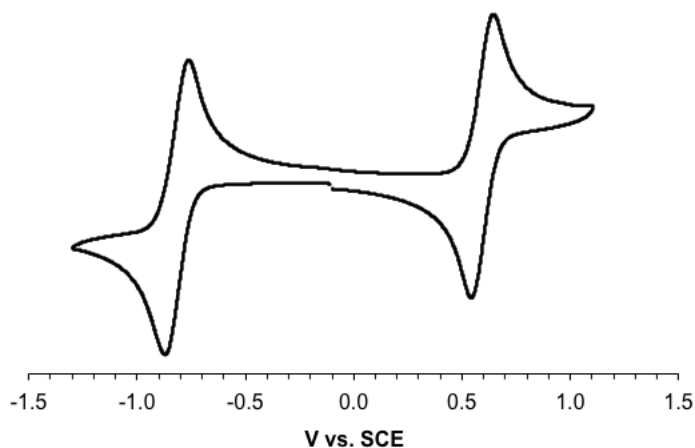


Figure A.16. Cyclic voltammogram of [1,2-*a*]IF **6** isolated from the reduction of diol **8**.

X-ray Diffraction Details

General x-ray data collection. Data collection for $[\text{Cs}_2^{2+}(\text{THF})_2(\mathbf{6}^{2-})]$ was performed on a Bruker D8 VENTURE X-ray diffractometer with PHOTON 100 CMOS shutterless mode detector equipped with a Mo-target X-ray tube ($\lambda = 0.71073 \text{ \AA}$) at $T = 100(2) \text{ K}$. Data reduction and integration were performed with the Bruker software package SAINT (version 8.38A). Data were corrected for absorption effects using the empirical methods as implemented in SADABS (version 2016/2). The structure was solved by SHELXT^[7] and refined by full-matrix least-squares procedures using the Bruker SHELXTL (version 2016/6) software package. All non-hydrogen atoms (including those in disordered parts) were refined anisotropically. The H-atoms were also included at calculated positions and refined as riders, with $U_{\text{iso}}(\text{H}) = 1.2 U_{\text{eq}}(\text{C})$ and $U_{\text{iso}}(\text{H}) = 1.5 U_{\text{eq}}(\text{C})$ for methyl groups. One of two THF molecules coordinated to cesium cation was found to be disordered and was modeled with two orientations with relative occupancies of 0.56:0.44. The geometries of the disordered parts were restrained to be similar using SAME restraint. The anisotropic displacement parameters of the solvent THF molecule in the direction of the bonds were restrained to be equal with a standard uncertainty of 0.004 \AA^2 using RIGU restraint. They were also restrained to have the same U_{ij} components, with a standard uncertainty of 0.01 \AA^2 using SIMU restraint. ORTEP plots and the solid state packing are shown in Figures A.17 and A.18, respectively.

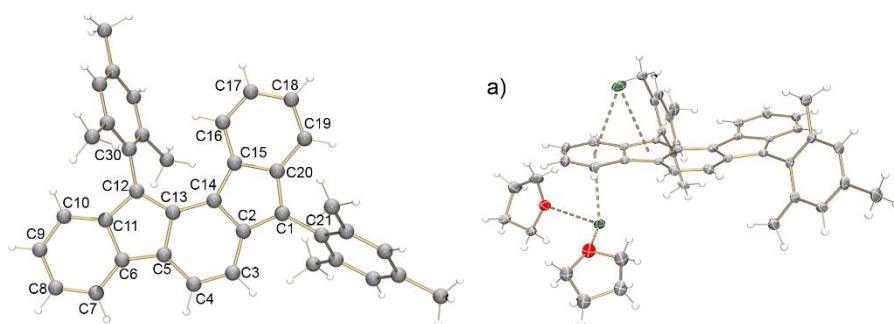


Figure A.17 ORTEP drawings of the $\mathbf{6}^{2-}$ core in $[\text{Cs}_2^{2+}(\text{THF})_2(\mathbf{6}^{2-})]$ (b) and the asymmetric unit (a) drawn with thermal ellipsoids at the 40% probability level. Color scheme used: Cs green, O red, C grey, H white.

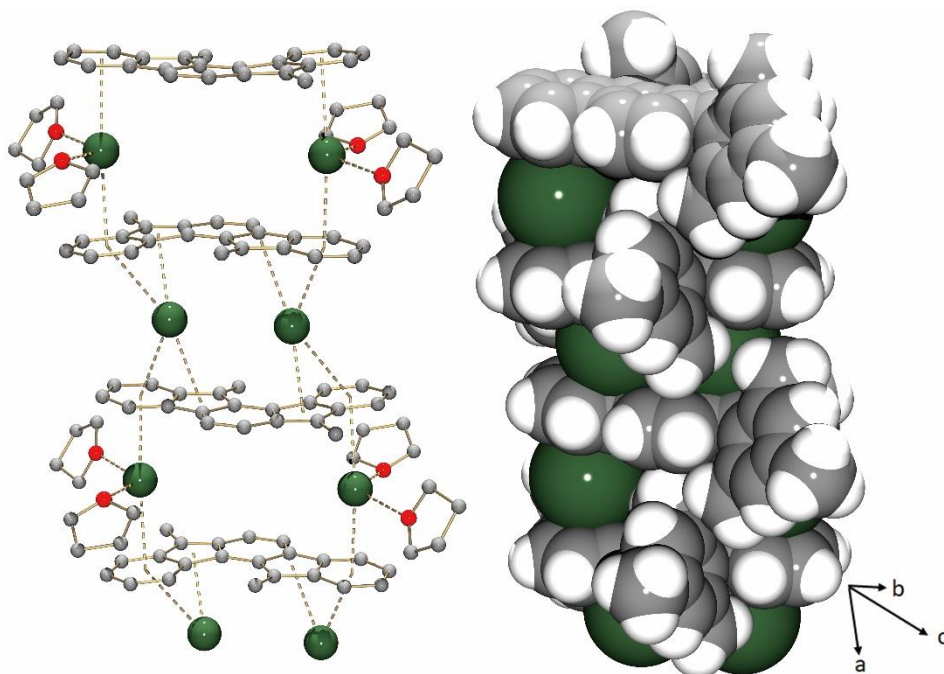


Figure A.18 Solid state packing of $[\text{Cs}_2^{2+}(\text{THF})_2(\mathbf{6}^{2-})]$, ball-and-stick (H-atoms and mesityl groups are removed for clarity, left) and space-filling model (THF molecules are omitted, right).

APPENDIX B:

SUPPLEMENTARY INFORMATION FOR CHAPTER III

Appendix B is the supplementary information for Chapter III of this dissertation. It includes characterization spectra, further experimental data, and computational details.

NMR Spectra

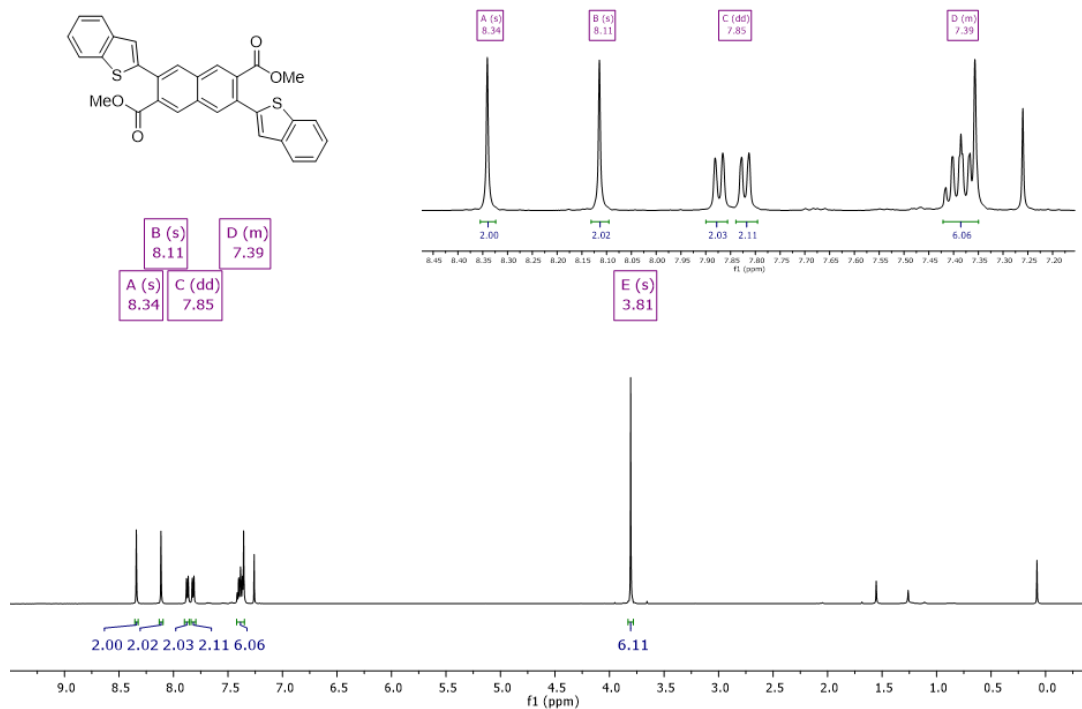


Figure B.1 ^1H NMR (500 MHz, CDCl_3) spectrum of diester 13.

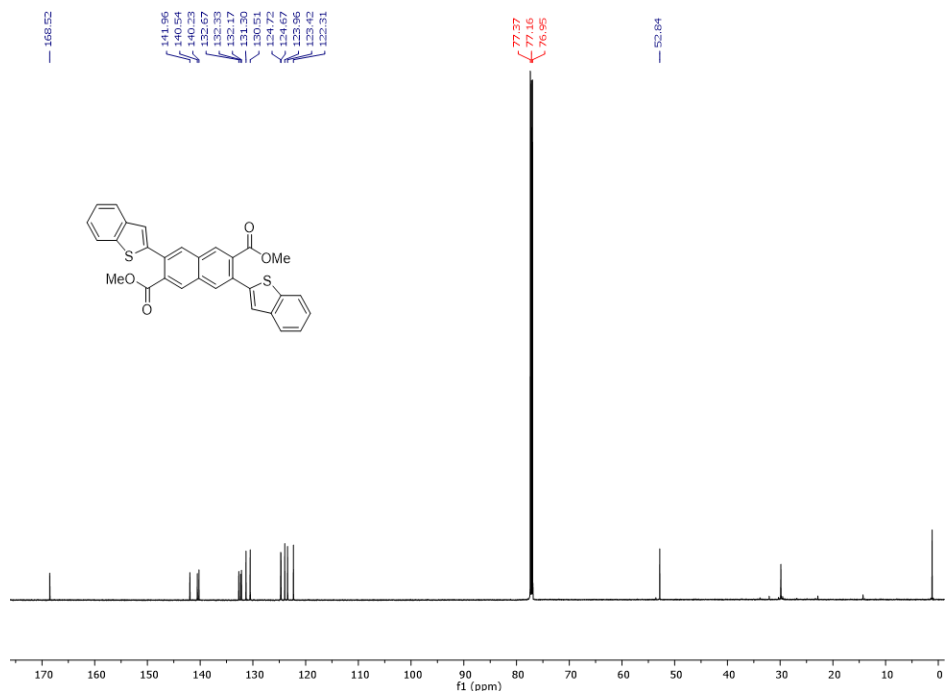


Figure B.2 ^{13}C NMR (151 MHz, CDCl_3) spectrum of diester 13.

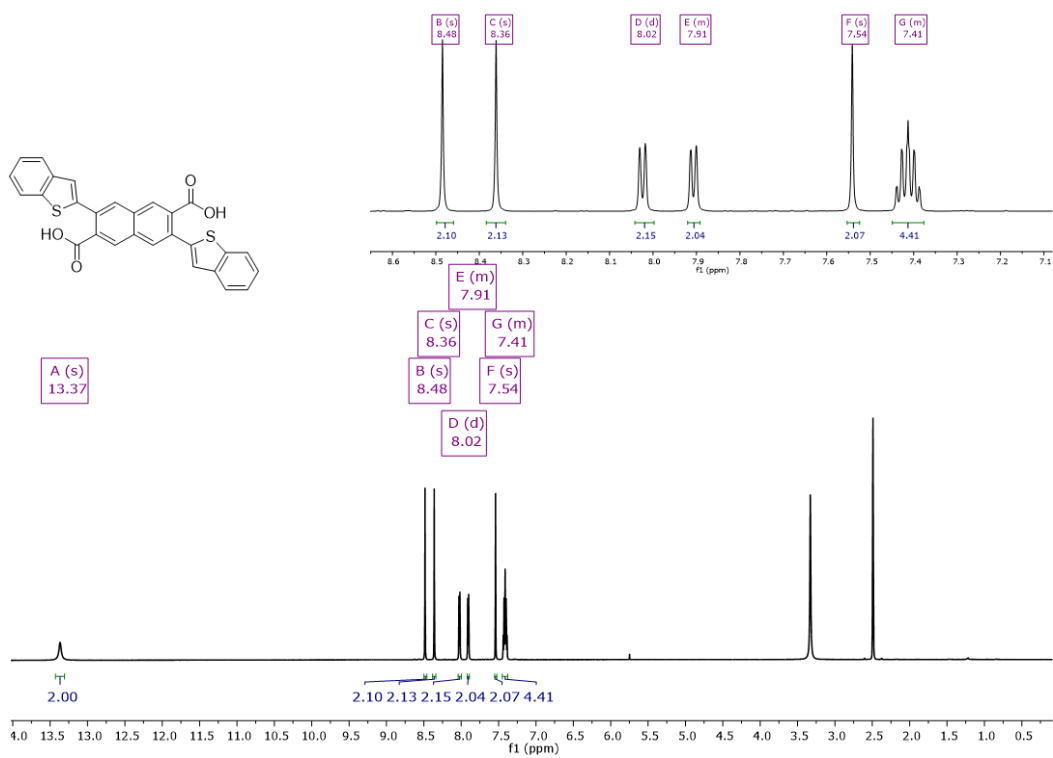


Figure B.3 ^1H NMR (600 MHz, $\text{DMSO}-d_6$) spectrum of the intermediate diacid.

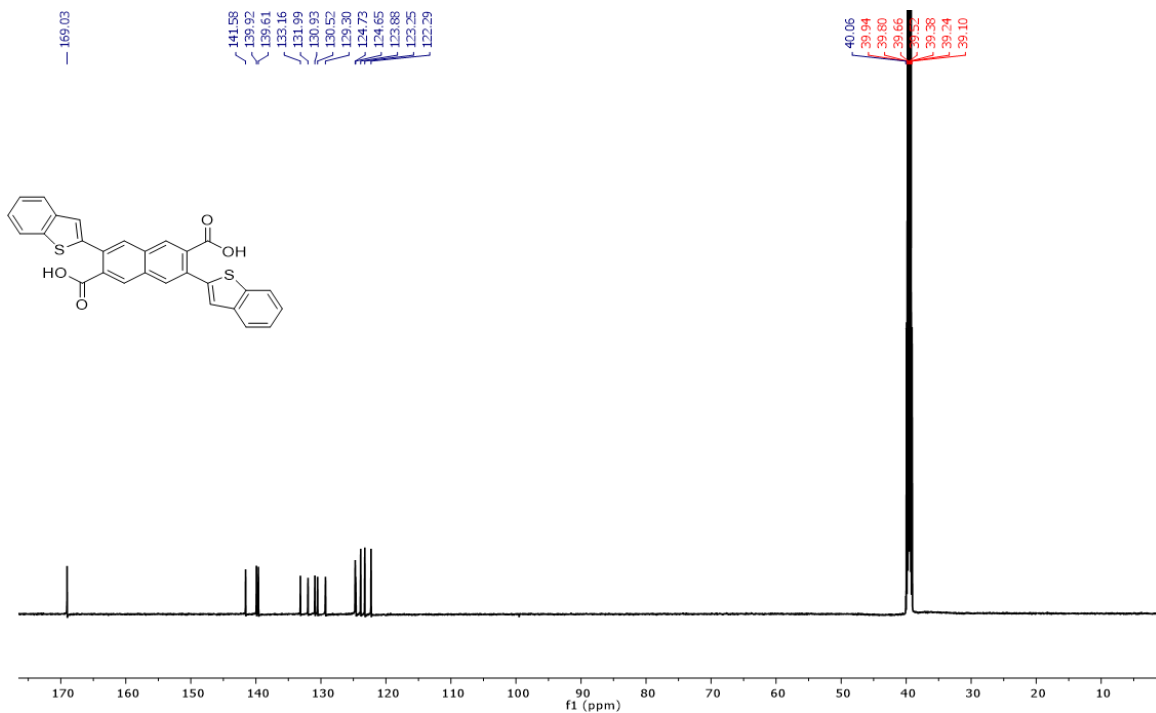


Figure B.4 ^{13}C NMR (151 MHz, $\text{DMSO}-d_6$) spectrum of the intermediate diacid.

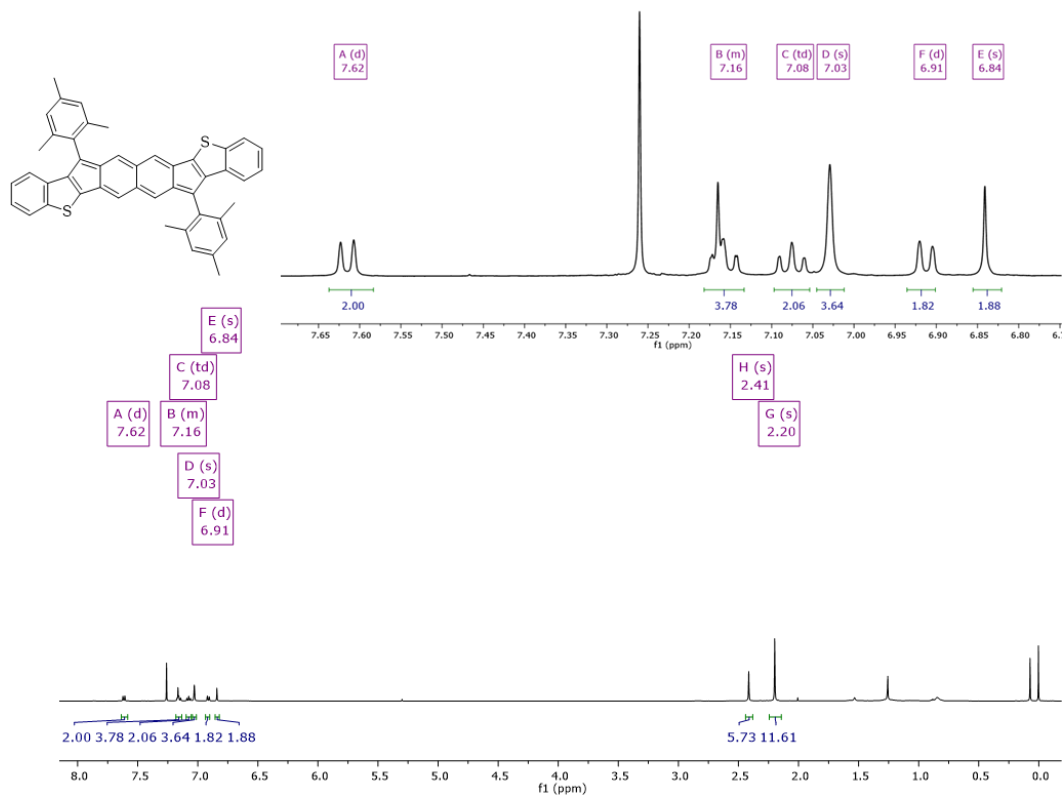


Figure B.5 ^1H NMR (500 MHz, CDCl_3) spectrum of the IIDBT 10a.

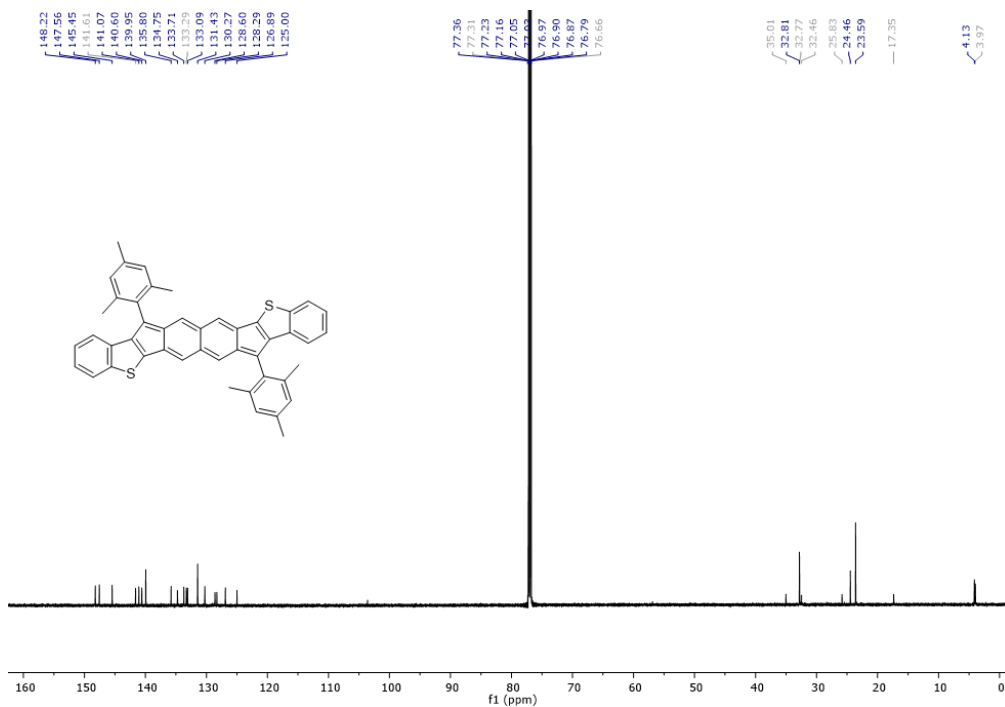


Figure B.6 ¹³C NMR (151 MHz, CDCl₃) spectrum of the IIDBT 10a.

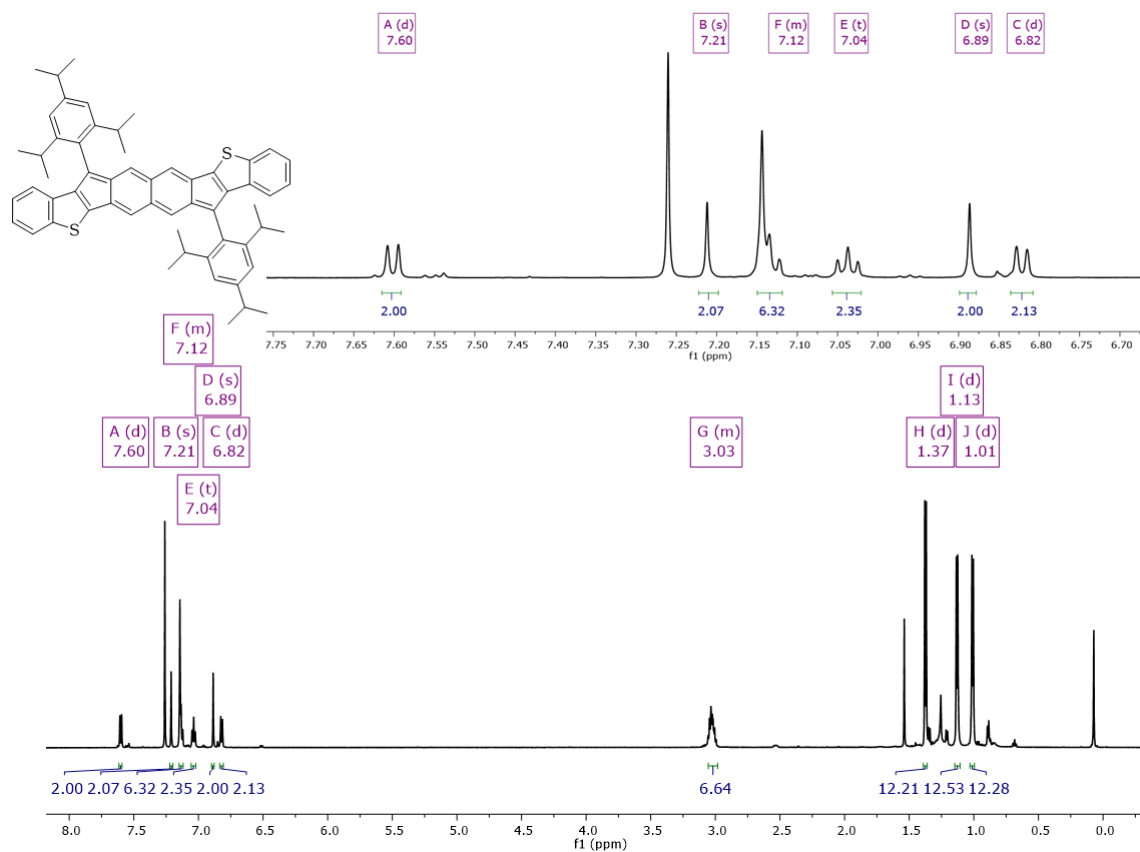


Figure B.7 ¹H NMR (500 MHz, CDCl₃) spectrum of the IIDBT 10b.

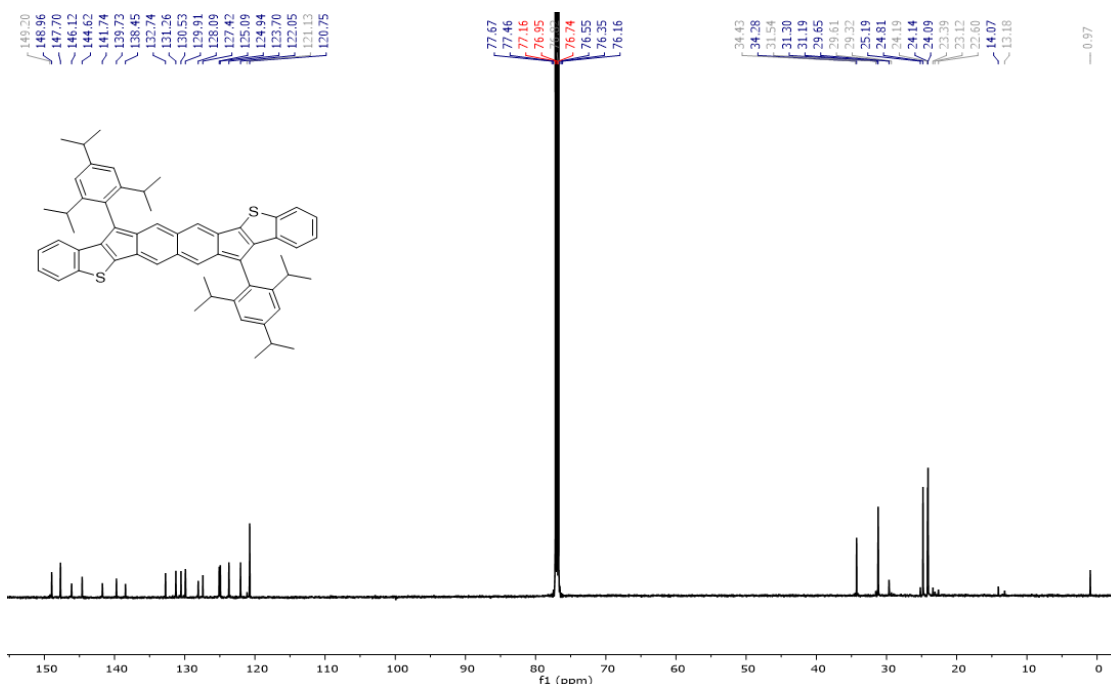


Figure B.8 ¹³C NMR (151 MHz, CDCl₃) spectrum of the IIDBT 10b.

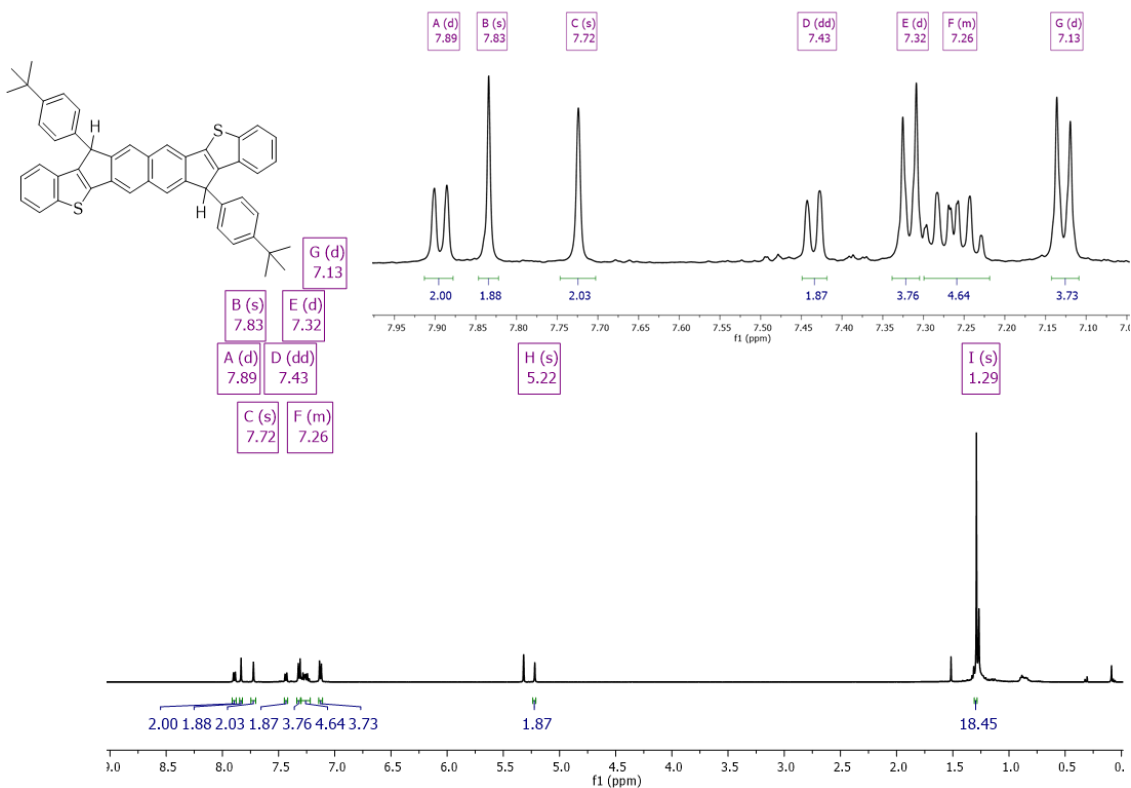


Figure B.9 ¹H NMR (500 MHz, CD₂Cl₂) spectrum of dihydro-IIDBT 10cH₂.

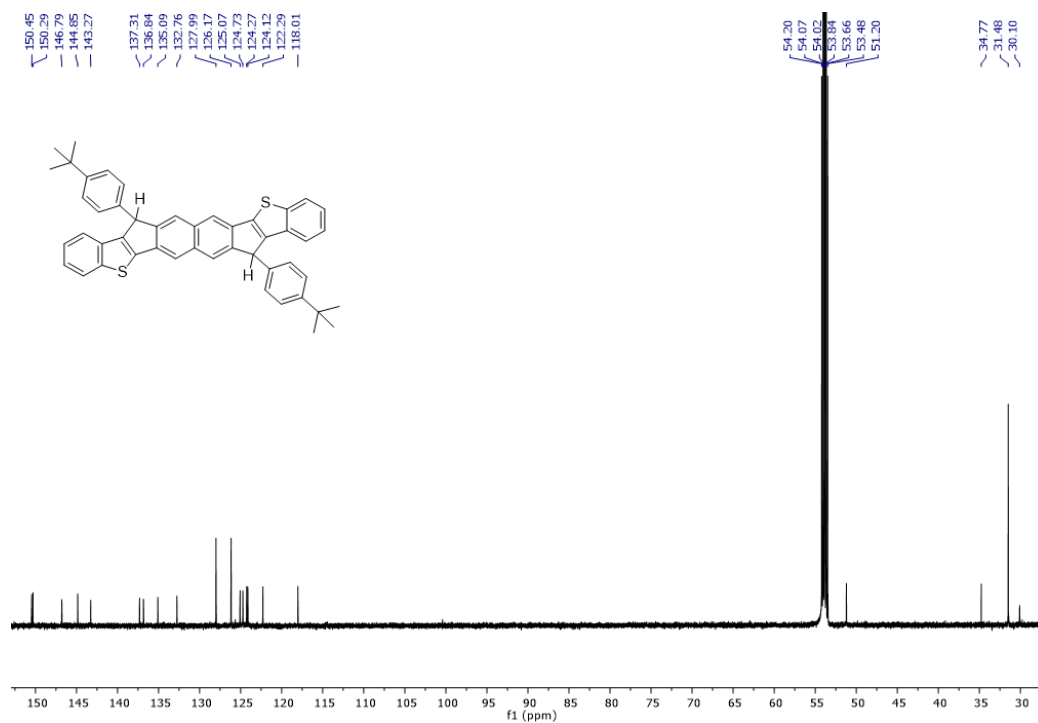


Figure B.10 ¹³C NMR (151 MHz, CD₂Cl₂) spectrum of dihydro-IIDBT 10cH₂.

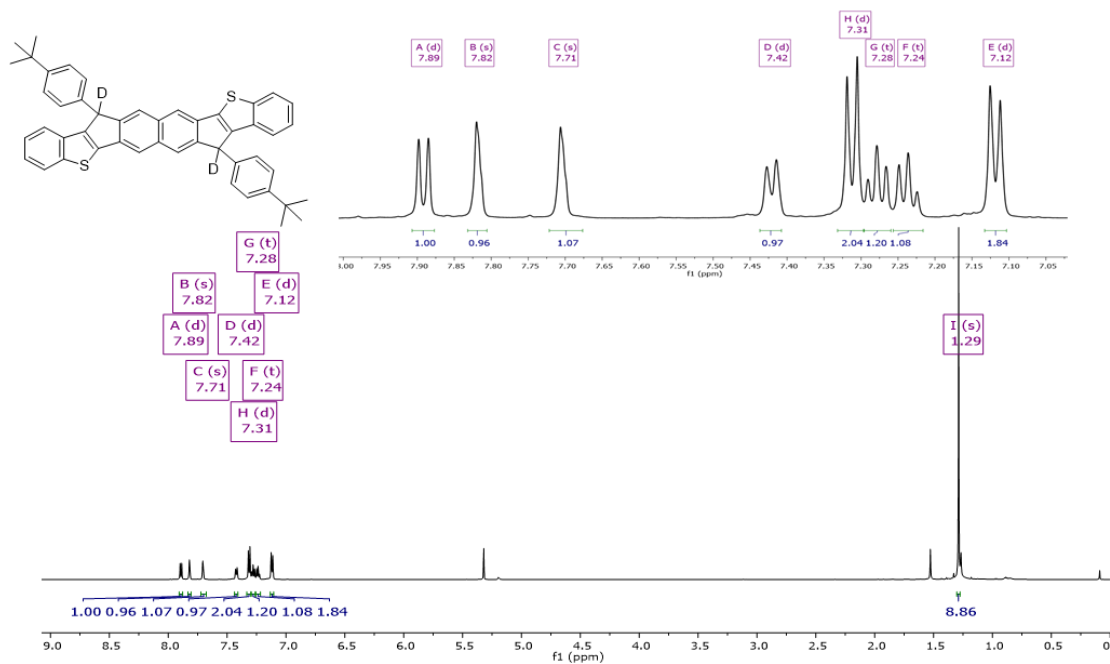


Figure B.11 ¹H NMR (600 MHz, CD₂Cl₂) spectrum of dideutero-IIDBT 10cD₂, the product of radical reactivity with Bu₃SnD.

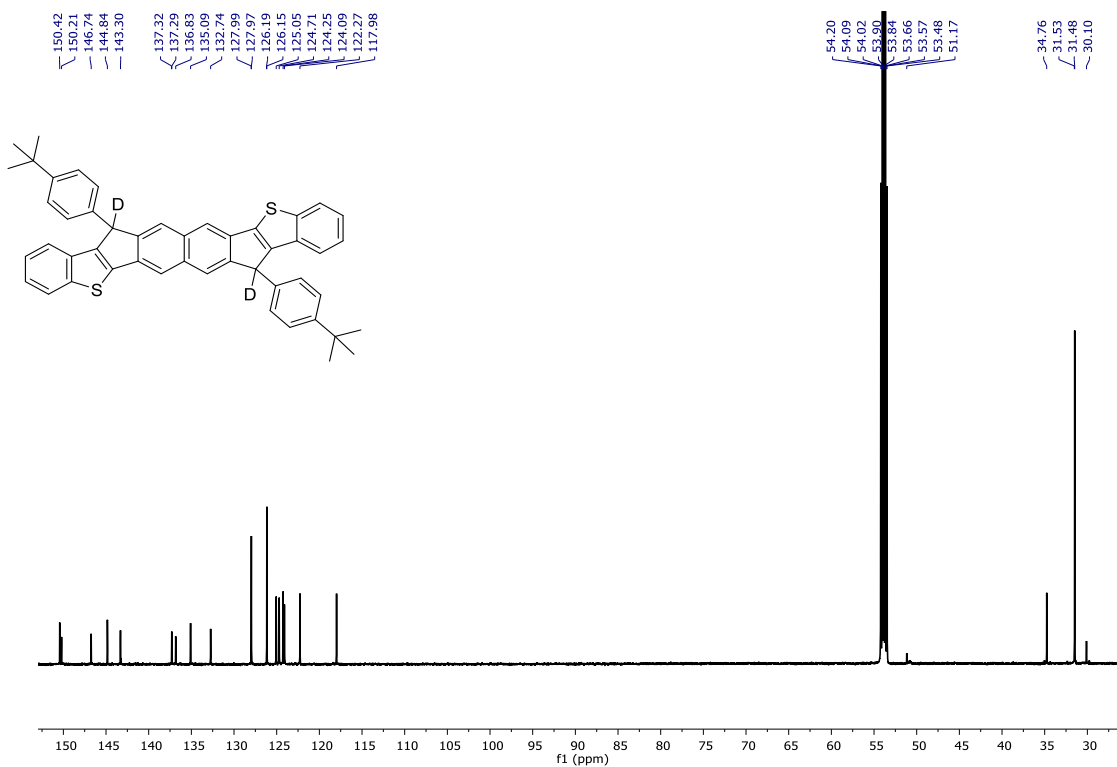


Figure B.12 ¹³C NMR (151 MHz, CD₂Cl₂) spectrum of dideutero-IIDBT 10cD₂, the product of radical reactivity with Bu₃SnD.

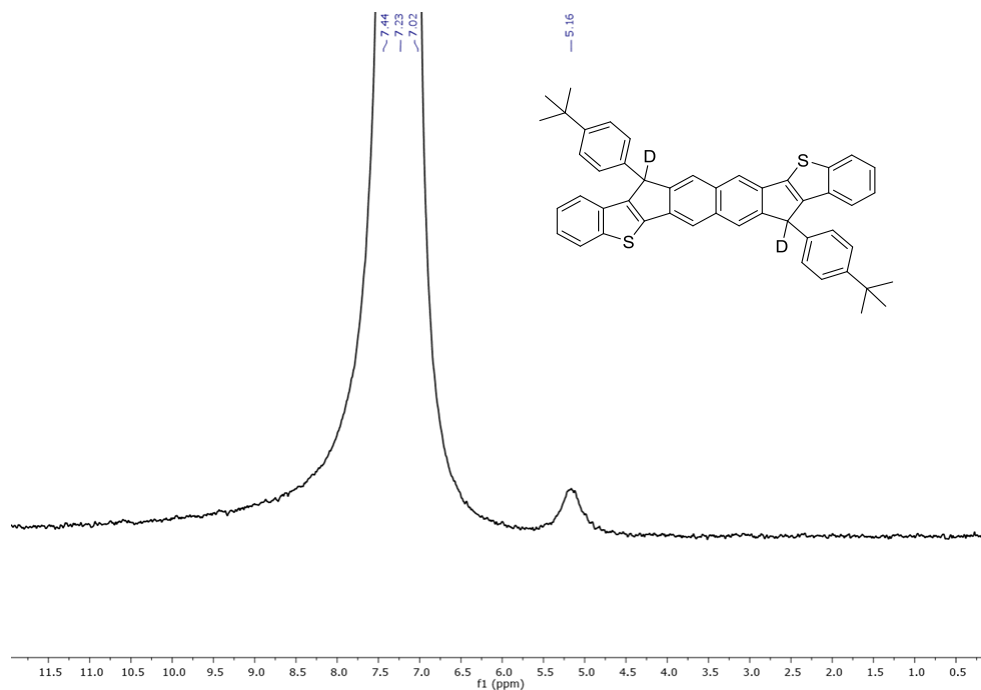


Figure B.13 ²D NMR (600 MHz, CD₂Cl₂) spectrum of dideutero-IIDBT 10cD₂, the product of radical reactivity with Bu₃SnD.

Computational Information

Table B1. Theoretically Estimated y and ΔE_{S-T} Values of Compounds 6-11. Zero-point vibration energy correction was estimated from the frequency analysis at the R(U)B3LYP/6-311G* level of approximation.

Compound	y for singlet state (-)	adiabatic ΔE_{S-T} (kcal mol ⁻¹)
6	0.30	-19.4
7	0.49	-10.3
8	0.62	-5.4
9	0.41	-15.8
10	0.61	-8.8
11	0.74	-4.4

Table B2. Physical Parameters calculated by the CASCI (2,2) method using the MOs obtained by tuned-LC-RBLYP/6-311G(d) calculation.

	7	10
$ t_{ab} $ (eV)	1.163	1.031
$f_{ST}(y)$ (-)	-0.894	-0.655
$U/2$ (eV)	1.446	1.563
$(U/2)f_{ST}(y)$ (eV)	-1.293	-1.025
$2K_{ab}$ (eV)	0.082	0.165

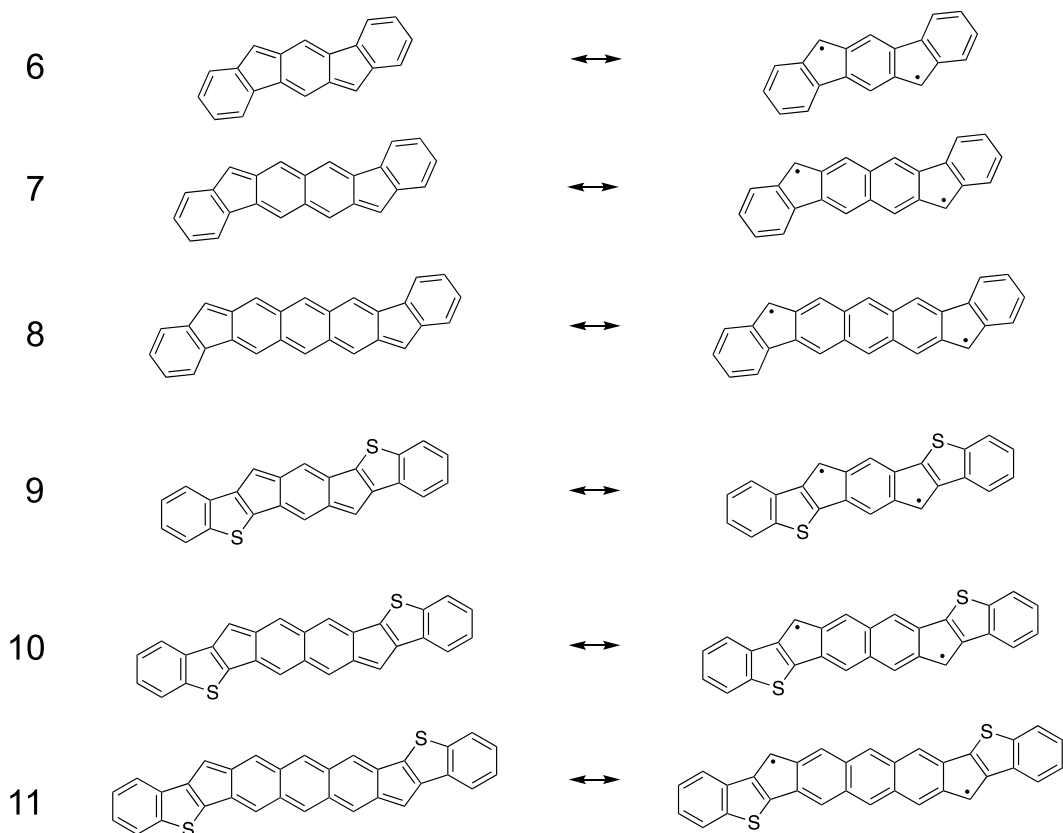
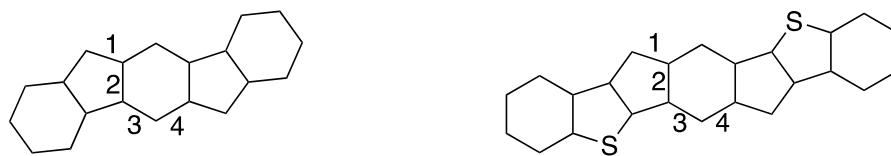
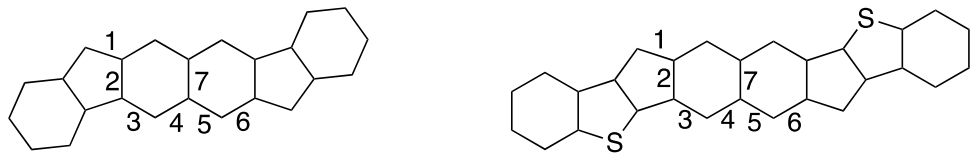


Figure B.14 Possible CS and OS forms in the resonance structures of **6-11**.

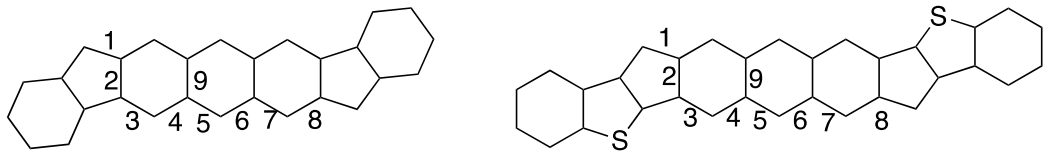
Table B3. Comparison of bond lengths (Å) of selected bonds between **6** and **9**.



6			9		
Bond	RB3LYP	Expt.	Bond	RB3LYP	Expt.
1	1.381	1.380	1	1.410	1.409
2	1.466	1.467	2	1.460	1.457
3	1.360	1.356	3	1.378	1.377
4	1.434	1.433	4	1.412	1.412

Table B4. Comparison of bond lengths (\AA) of selected bonds between **7** and **10**.


7				10			
Bond	RB3LYP	UB3LYP	Expt.	Bond	RB3LYP	UB3LYP	Expt.
1	1.389	1.397	–	1	1.419	1.430	1.424
2	1.462	1.458	–	2	1.465	1.461	1.463
3	1.357	1.360	–	3	1.375	1.375	1.364
4	1.441	1.438	–	4	1.420	1.420	1.420
5	1.381	1.387	–	5	1.403	1.410	1.398
6	1.417	1.411	–	6	1.392	1.387	1.387
7	1.465	1.460	–	7	1.456	1.451	1.457

Table B5. Comparison of bond lengths [\AA] of selected bonds between **8** and **11**.


8				11			
Bond	RB3LYP	UB3LYP	Expt.	Bond	RB3LYP	UB3LYP	Expt.
1	1.393	1.412	1.400	1	1.419	1.435	–
2	1.465	1.460	1.460	2	1.474	1.469	–
3	1.357	1.360	1.359	3	1.373	1.371	–
4	1.441	1.437	1.447	4	1.422	1.426	–
5	1.376	1.387	1.402	5	1.393	1.396	–
6	1.425	1.413	1.446	6	1.406	1.402	–
7	1.388	1.406	1.399	7	1.408	1.420	–
8	1.411	1.397	1.416	8	1.388	1.379	–
9	1.461	1.453	1.461	9	1.457	1.451	–

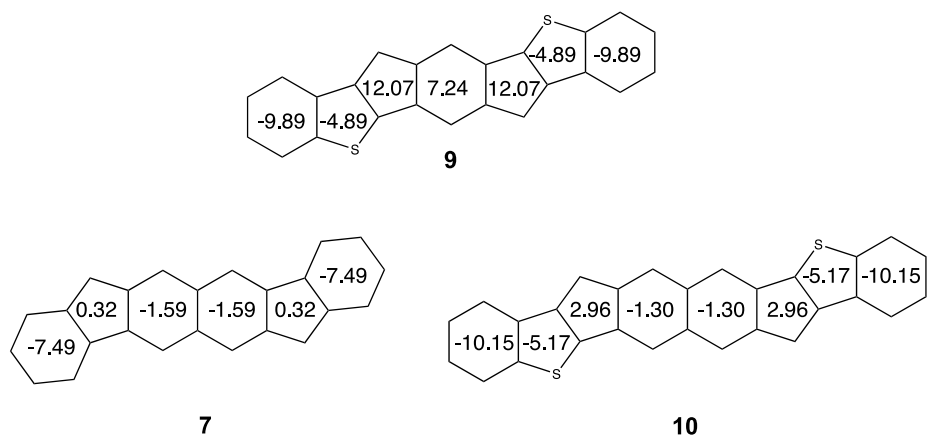


Figure B.15 NICS(1) [ppm] on each ring calculated at the UB3LYP/6-311G(d) level of approximation.

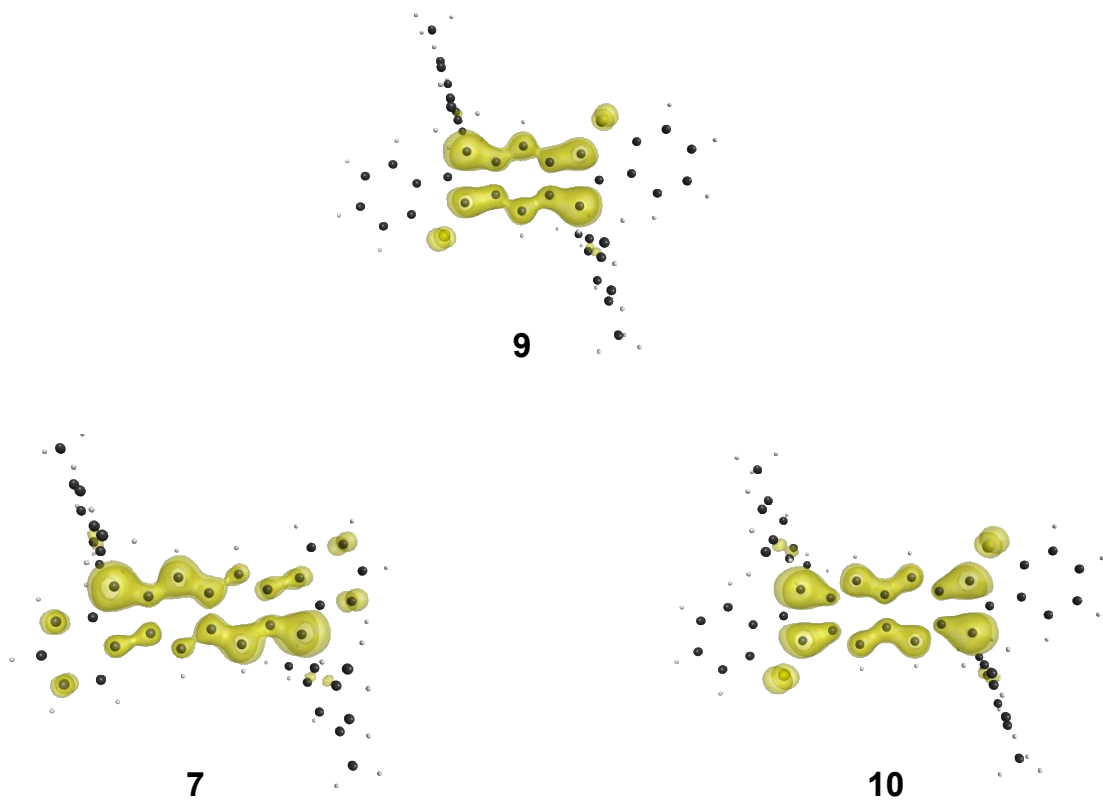


Figure B.16 Odd-electron density maps for 7, 9 and 10 calculated at the LC-UBLYP/6-311G(d) level of approximation. Yellow mesh represents the isosurface of odd-electron density with the contour value of 0.001 a.u.

Table B6. Singlet–Triplet gap (ΔE_{S-T}) and Each Physical Parameter Calculated by the CASCI(2,2) Method Using the UNOs Obtained by UHF/6-311G(d) calculation.

	6	7	8	9	10	11
ΔE_{S-T} (eV)	-1.726	-1.029	-0.686	-1.071	-0.532	-0.323
y (-) ^{a)}	0.130	0.237	0.325	0.249	0.420	0.524
$ t_{ab} $ (eV)	1.531	1.146	0.910	-1.255	0.876	0.669
$f_{ST}(y)$ (-)	-1.030	-0.547	-0.356	-0.515	-0.228	-0.137
$\frac{U}{2} = K_{gu}^M$ (eV)	1.733	1.943	1.989	2.204	2.459	2.472
$(U/2)f_{ST}(y)$ (eV)	-1.786	-1.063	-0.707	-1.136	-0.560	-0.339
J_{gg}^M (eV)	5.602	4.924	4.441	5.930	5.202	4.685
J_{uu}^M (eV)	5.630	4.940	4.444	5.900	5.173	4.649
J_{gu}^M (eV)	5.556	4.899	4.421	5.851	5.160	4.651
$2K_{ab}$ (eV)	0.060	0.033	0.021	0.064	0.028	0.016

^{a)} Note that the theoretical occupation numbers of NOs, therefrom y is calculated, depend on the method of calculations.

Additional Spectroscopy

Approximately 10 mg of IIDBT **10a** was dissolved in 1,1,2,2-tetrachloroethane- d_2 and transferred to a J-Young tube. The solution was degassed by 4 freeze-pump-thaw cycles. Spectra were acquired in a Varian Inova 500 MHz spectrometer that was heated to 50, 75, 100, 125, then 25 °C (Fig. B.17).

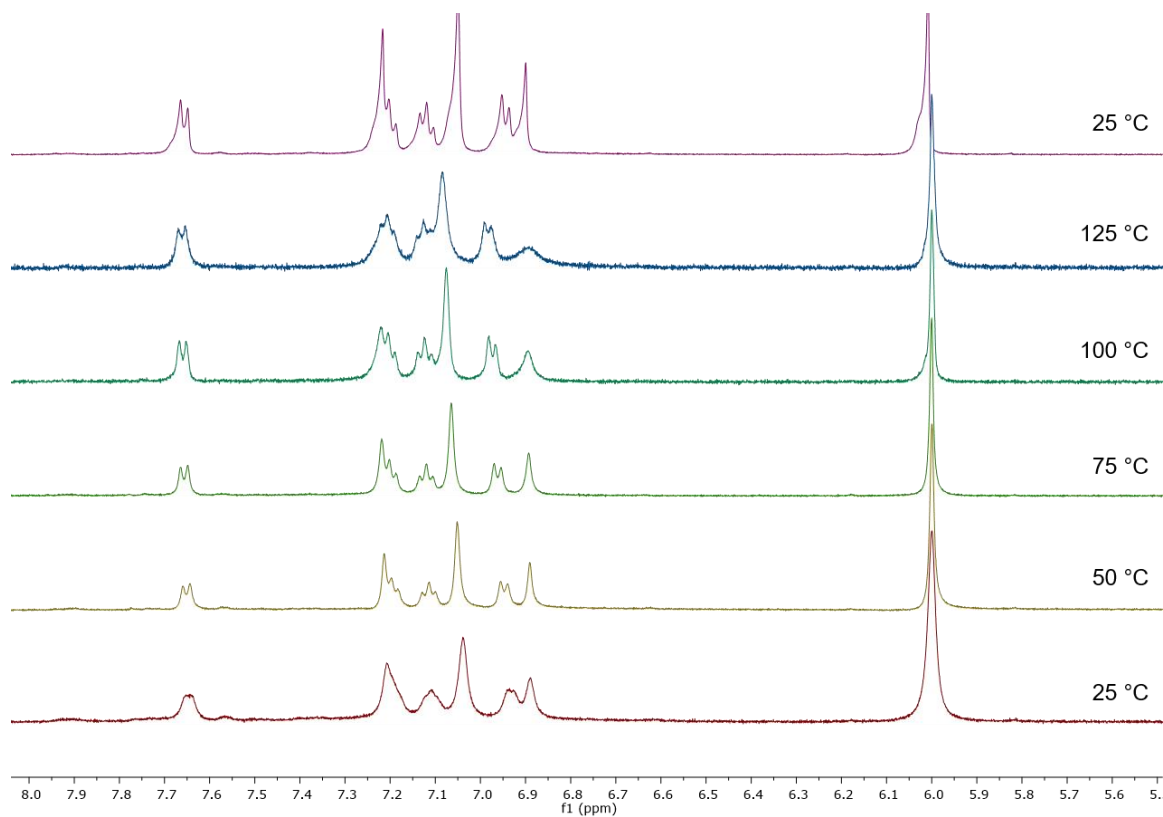


Figure B.17 VT ^1H NMR spectra of the aromatic region of IIDBT **10a** in 1,1,2,2-tetrachloroethane- d_2 .

Cyclic voltammetry (CV) for the two compounds was carried out in a three compartment electrochemical cell in CH_2Cl_2 with 0.1 M TBAPF_6 using a Pt wire as working electrode and a Pt gauze as counter-electrode and a Ag wire as pseudo-reference electrode and the data tested versus the Fc/Fc^+ couple. The temperature was kept at 298 K. The exact concentrations of the samples are unknown (approx. 10^{-4} M). The cyclic voltammograms are shown below in Supplementary Fig B.18.

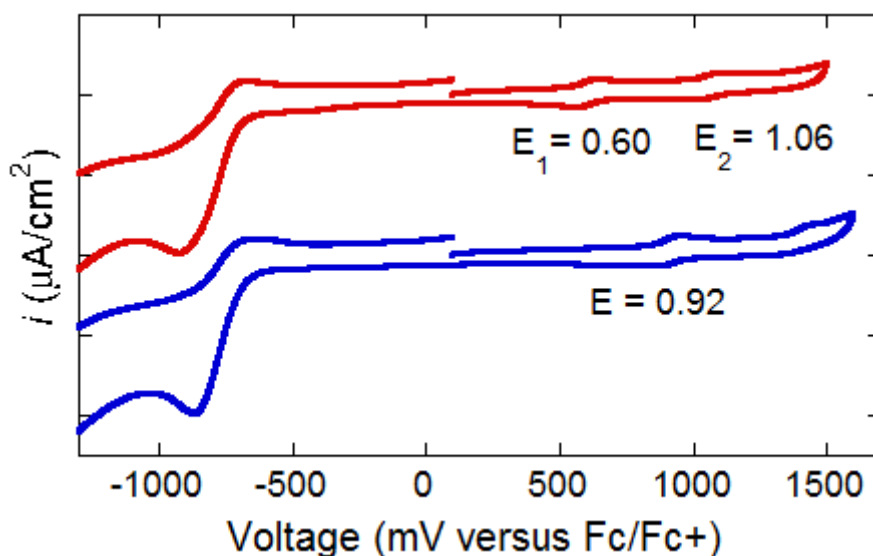


Figure B.18 CVs of **9** (blue) and **10b** (red).

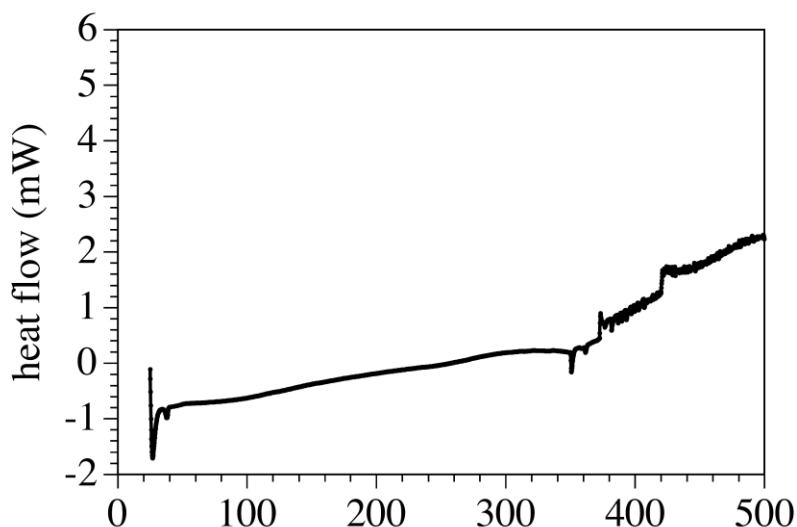


Figure B.19 DCS measurement of 10a in an oxygen-free dry N_2 flow in the temperature range 25-500 $^{\circ}\text{C}$ (298-773 K).

X-ray Diffraction Details

General x-ray data collection. Diffraction intensities for **10b** were collected at 173 K on a Bruker Apex2 CCD diffractometer using CuK α radiation, $\lambda=1.54178$ Å. Space group was determined based on intensity statistics. Absorption correction was applied by SADABS. Structure was solved by direct methods and Fourier techniques and refined on F^2 using full matrix least-squares procedures. All non-H atoms were refined with anisotropic thermal parameters. H atoms were refined in calculated positions in a rigid group model. Solvent molecule, CH₃CN, fills out an empty space in the packing and is highly disordered over three or four positions. Some of these positions are related by an inversion center. This solvent molecule was treated by SQUEEZE; the correction of the X-ray data by SQUEEZE was 51 electron/cell; the expected number of electrons is 44 electrons/cell. Crystals of **10b** were very thin plates and did not provide visible reflections at high angles. Even using a strong *Incoatec I μ S* Cu source it was possible to collect diffraction data only up to $2\theta_{\max} = 101.25^\circ$. Nonetheless the collected data provide an appropriate number of measured reflections: 2737 reflections per 271 refined parameters. All calculations were performed by the Bruker SHELXL-2014 package.

5.2 Crystallographic data for 10b. C₆₂H₆₄N₂S₂, C₅₈H₅₈S₂•2(CH₃CN), M = 901.26, 0.12 × 0.09 × 0.01 mm, T = 173(2) K, Triclinic, space group *P*-1, $a = 9.0360(6)$ Å, $b = 10.7067(7)$ Å, $c = 14.4033(10)$ Å, $\alpha = 77.940(4)^\circ$, $\beta = 85.741(5)^\circ$, $\gamma = 74.769(4)^\circ$, $V = 1314.56(16)$ Å³, $Z = 1$, $D_c = 1.138$ Mg/m³, $\mu(\text{Cu}) = 1.210$ mm⁻¹, $F(000) = 964$, $2\theta_{\max} = 101.25^\circ$, 9539 reflections, 2737 independent reflections [$R_{\text{int}} = 0.0436$], $R1 = 0.0545$, $wR2 = 0.1503$ and $\text{GOF} = 1.068$ for 2737 reflections (271 parameters) with $I > 2\sigma(I)$, $R1 = 0.0755$, $wR2 = 0.1593$ and $\text{GOF} = 1.068$ for all reflections, max/min residual electron density $+0.337/-0.166$ eÅ⁻³. CCDC-1589136 contains the supplementary crystallographic data for this compound. The data can be obtained free of charge from the Cambridge Crystallographic Data Centre via www.ccdc.cam.ac.uk/data_request/cif.

APPENDIX C:

SUPPLEMENTARY INFORMATION FOR CHAPTER IV

Appendix C is the supplementary information for Chapter IV of this dissertation. It includes characterization spectra, further experimental data, and computational details.

NMR Spectra

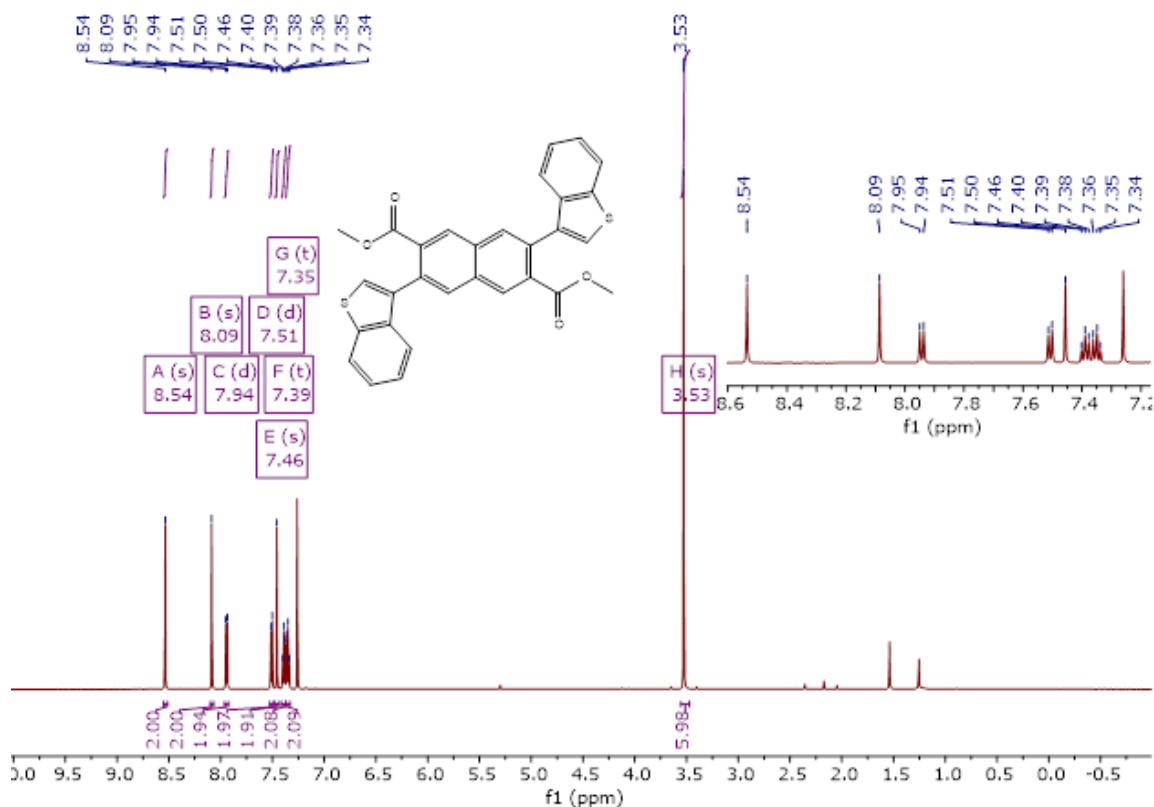


Figure C.1 ¹H NMR (500 MHz, CDCl₃) spectrum of dibenzothiophene-diester 4.

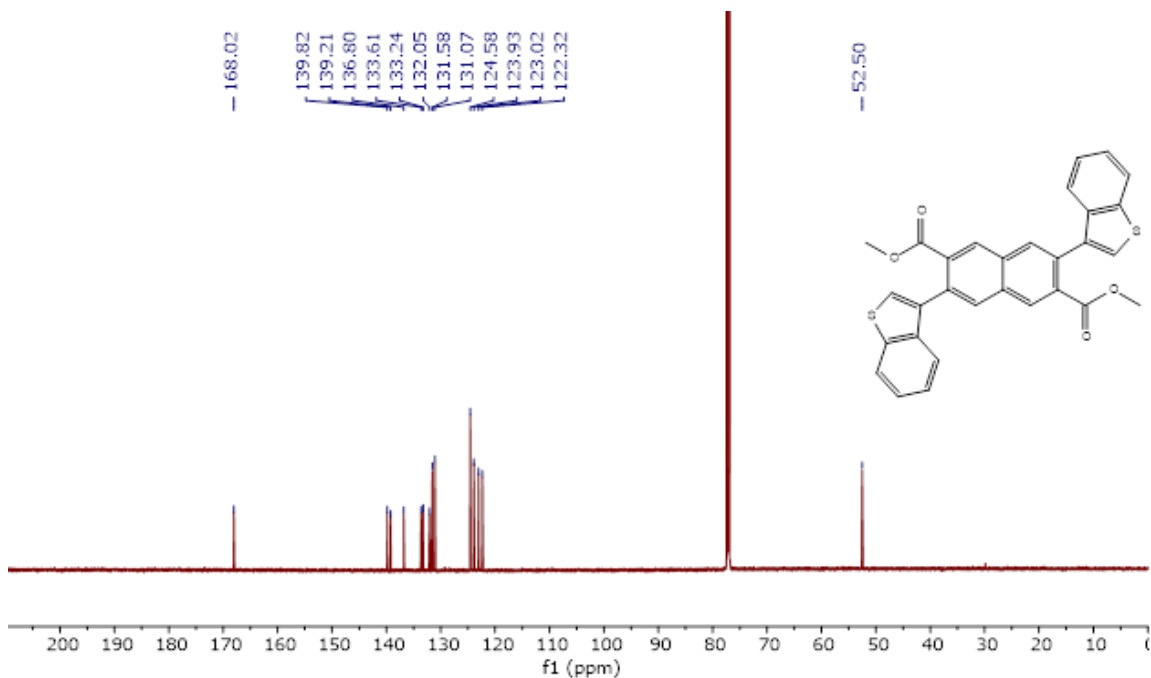


Figure C.2 ^{13}C NMR (151 MHz, CDCl_3) spectrum of dibenzothiophene-diester 4.

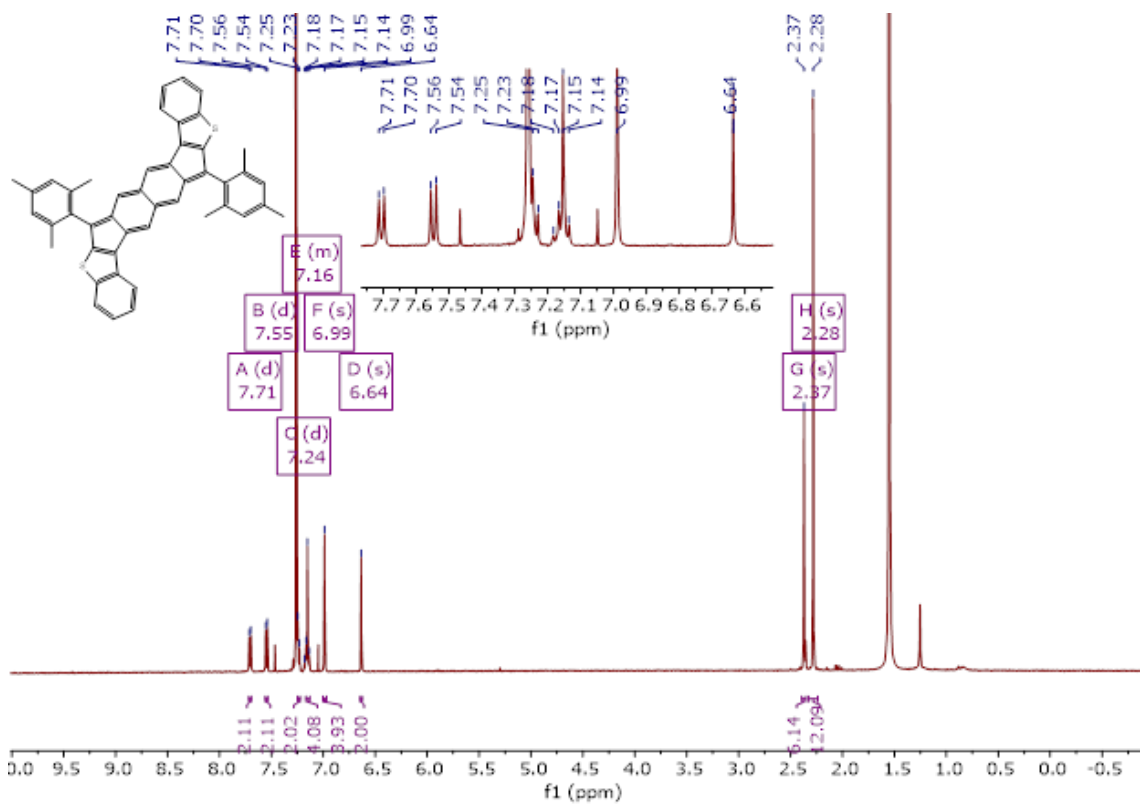


Figure C.3 ^1H NMR (500 MHz, CDCl_3) spectrum of *syn*-IIDBT with mesityl groups

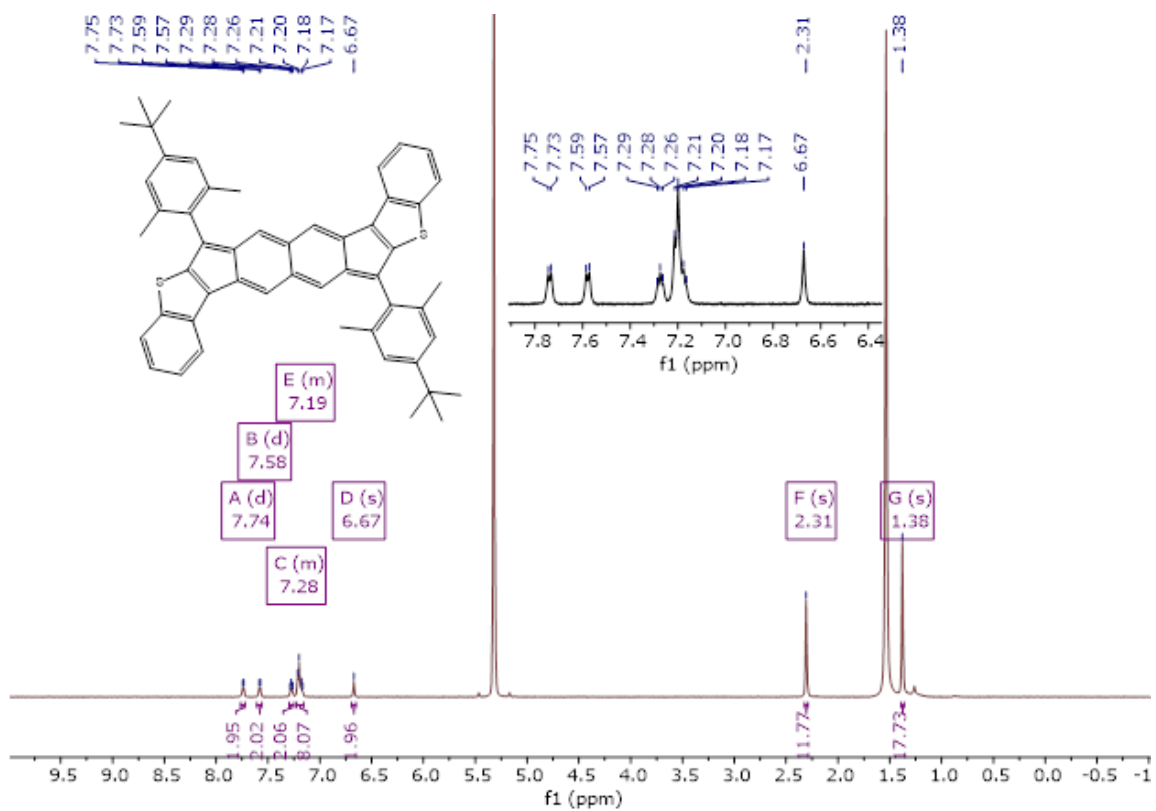


Figure C.4 ¹H NMR (600 MHz, CD₂Cl₂) spectrum of 2 with tert-butyl-mesityl groups.

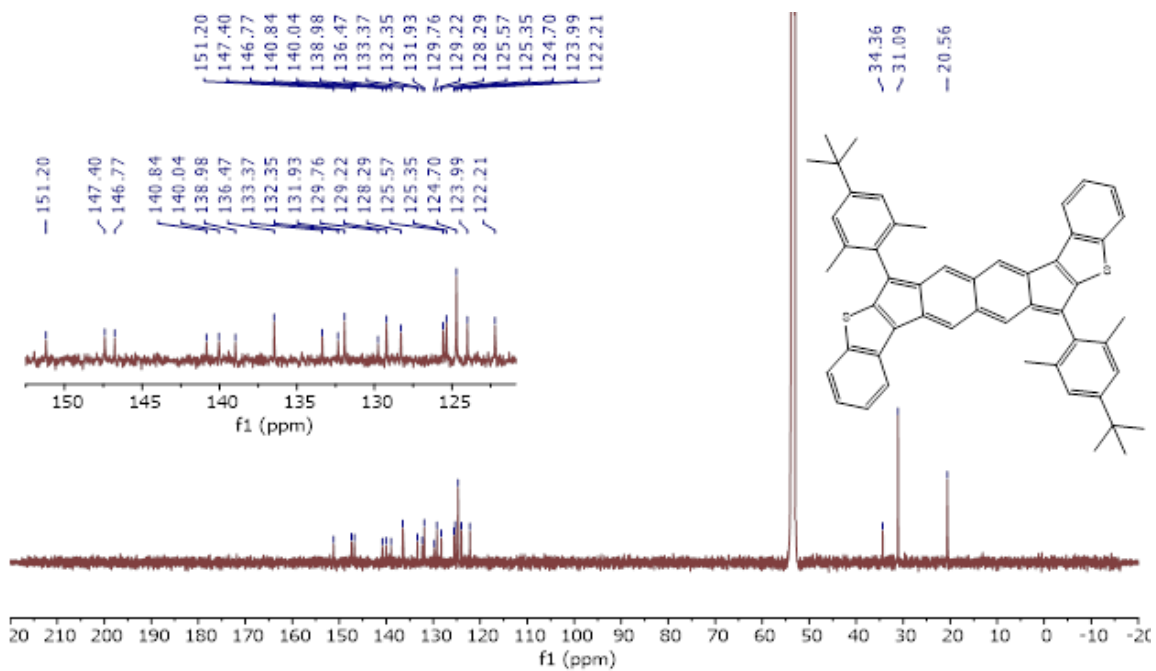


Figure C.5 ¹³C NMR (151 MHz, CD₂Cl₂) spectrum of 2 with tert-butyl-mesityl groups.

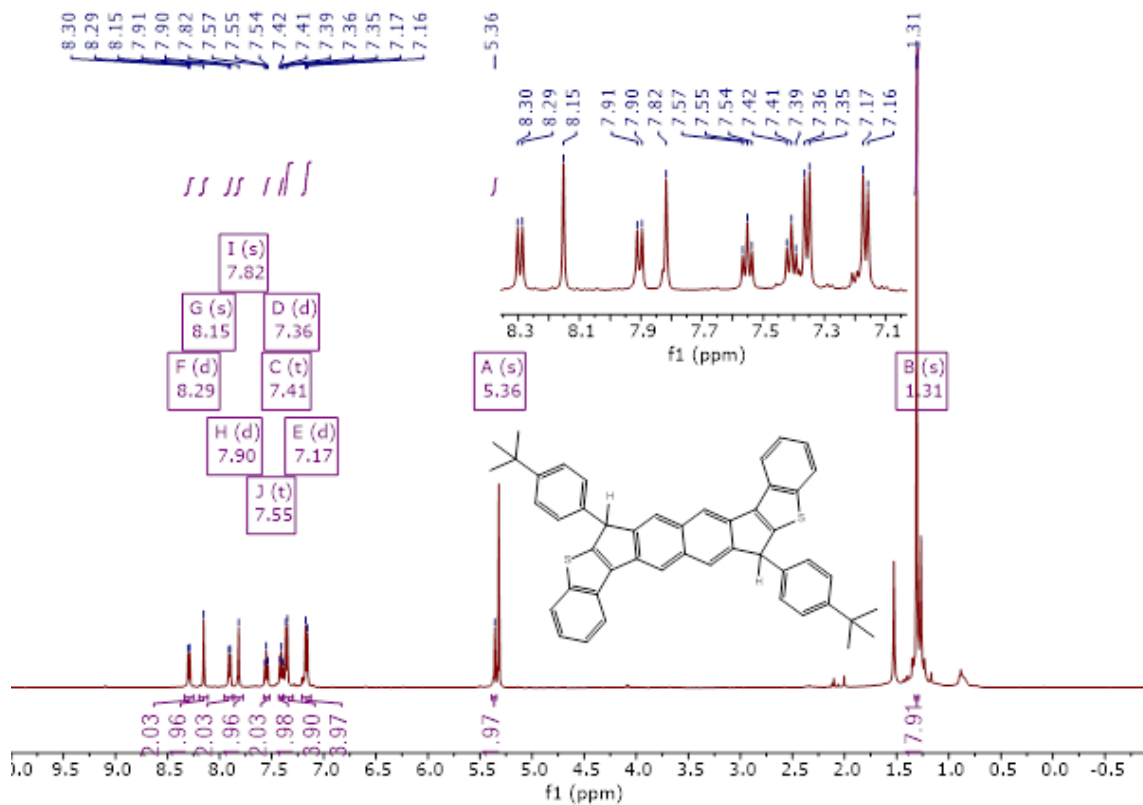


Figure C.6 ¹H NMR (500 MHz, CD₂Cl₂) spectrum of DihydroIIDBT (2cH₂).

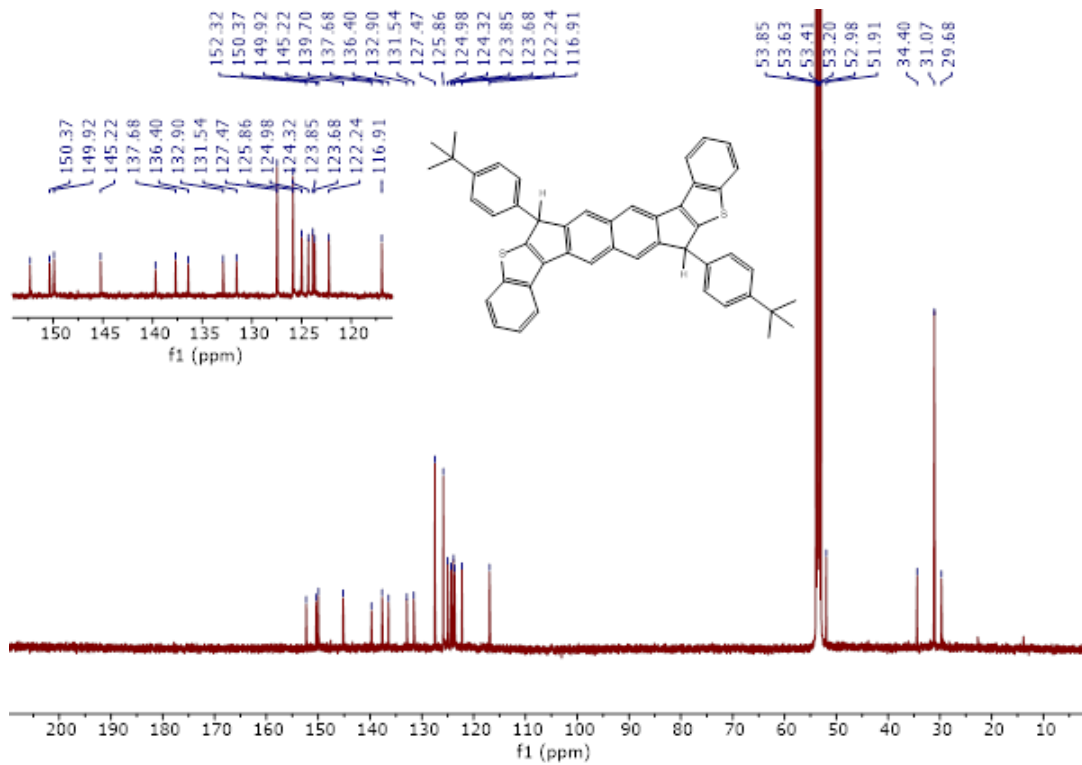


Figure C.7 ¹³C NMR (151 MHz, CD₂Cl₂) spectrum of DihydroIIDBT (2cH₂).

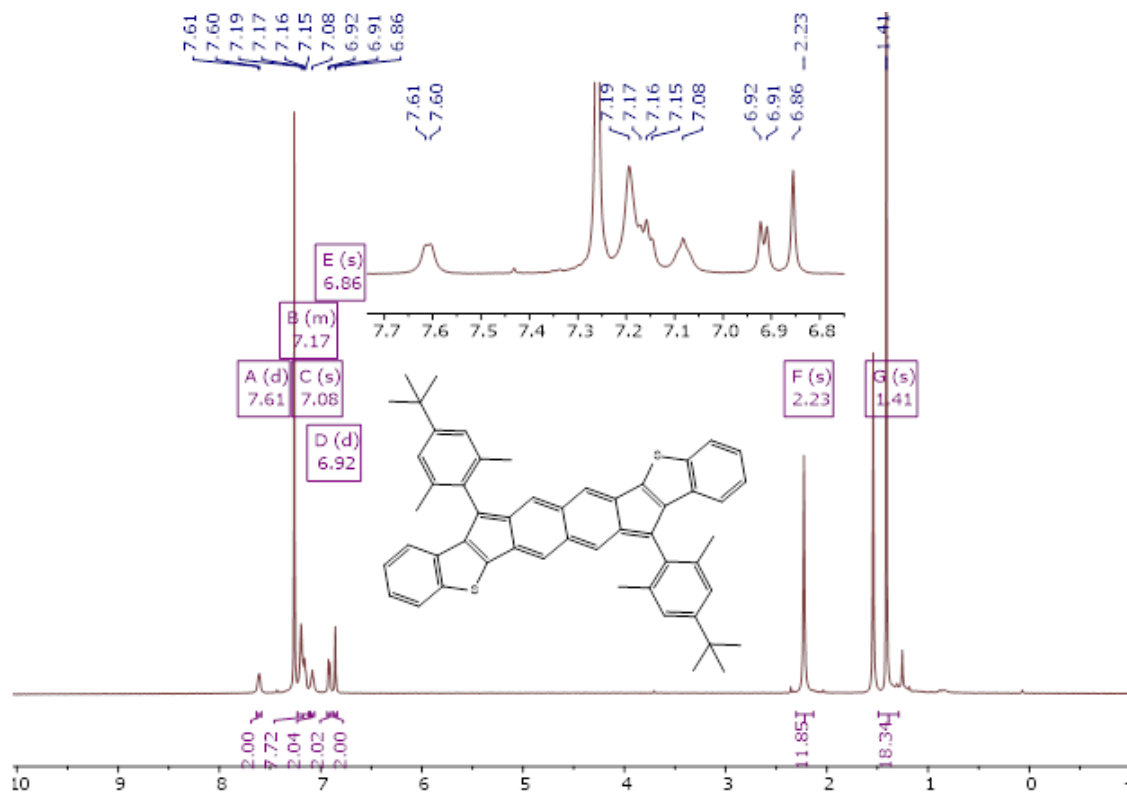


Figure C.8 ^1H NMR (500 MHz, CD_2Cl_2) spectrum of *anti*-IIDBT 1b.

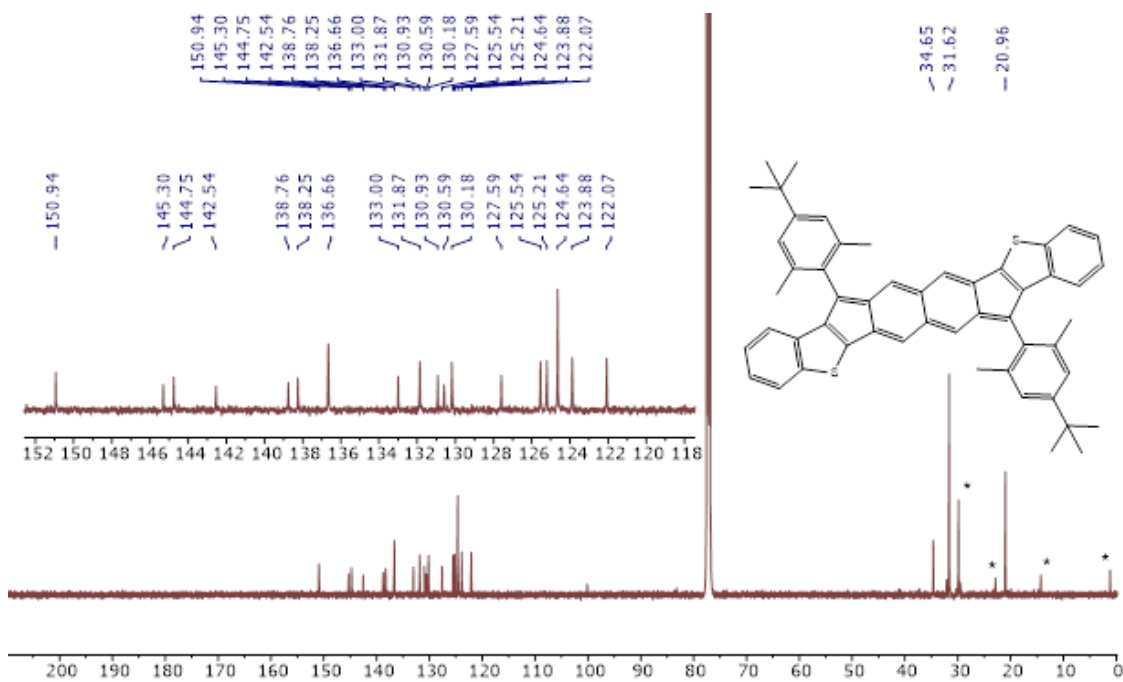


Figure C.9 ^{13}C NMR (151 MHz, CD_2Cl_2) spectrum of *anti*-IIDBT 1b.

Computational Information

Computational Details. Geometry optimization and frequency analysis for the singlet and triplet states were performed at the RB3LYP and UB3LYP levels, respectively, using the 6-311G* basis set. Vertical and adiabatic ΔE_{ST} values were evaluated at the spin-flip non-collinear (SF-NC-)TDDFT PBE5050/6-311G* level, where zero-point vibrational energy (ZPVE) corrections for the singlet and triplet states were estimated from the results of the frequency analysis calculations at the RB3LYP and UB3LYP levels, respectively. Excitation energies were evaluated at the TD-UB3LYP/6-311G* level. CASCI(2,2) calculations for the estimations of VCI parameters were performed using the molecular orbitals obtained at the tuned-LC-RBLYP/6-311G* level, where an optimal range-separating parameter μ for each system was determined by IP-tuning scheme for N -electron system. These calculations were performed using Gaussian 09 (geometry optimization and excitation energy), GAMESS-US (CASCI), and Q-Chem 4.2 (ΔE_{ST}) program packages. Diradical characters y were evaluated at the PUHF/6-311G* [denoted as $y(\text{PUHF})$] and tuned-LC-RBLYP-CASCI(2,2)/6-311G* [denoted as $y(\text{CASCI})$] levels.

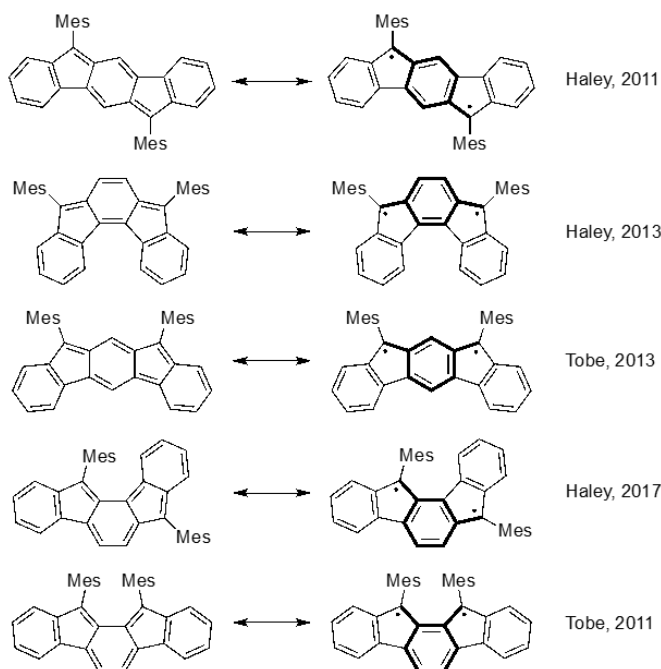


Figure C.10 Quinoidal and diradical resonance forms of the five regioisomeric indenofluorenes.

Table C1. Summary of calculation results for **1a** and **1s**.

	1a	2a
y (PUHF) [-]	0.613	0.658
Vertical ΔE_{ST} [kcal mol ⁻¹]	-11.65	-11.09
Adiabatic ΔE_{ST} [kcal mol ⁻¹]	-9.37	-8.84
Adiabatic ΔE_{ST} (+ZPVE) [kcal mol ⁻¹]	-8.77	-8.06
Tuned value of μ [bohr ⁻¹]	0.1444	0.1434
y (CASCI) [-]	0.203	0.210
Vertical ΔE_{ST} (CASCI) [kcal mol ⁻¹]	-19.8	-17.5
$ t_{ab} $ [eV]	1.031	0.905
$f_{ST}(y)$ [-]	-0.655	-0.632
$U/2 = K_{gu}^M$ [eV]	1.563	1.404
$(U/2)f_{ST}(y)$ [eV]	-1.025	-0.887
J_{gg}^M [eV]	4.417	4.225
J_{uu}^M [eV]	4.755	4.394
J_{gu}^M [eV]	4.420	4.179
$2K_{ab}$ [eV]	0.165	0.130

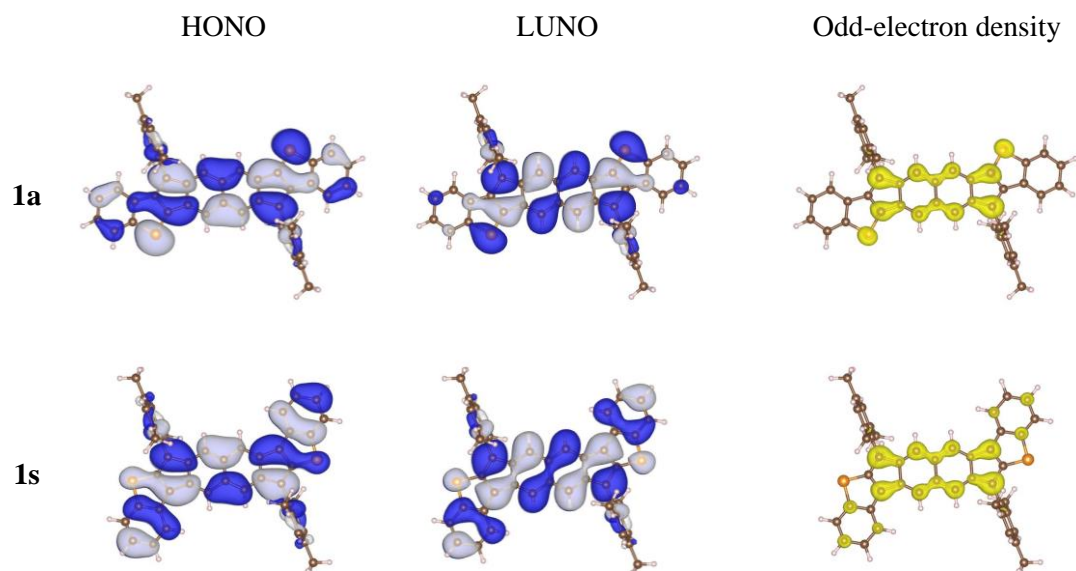


Figure C.11 Spatial distributions of natural orbitals (NOs) and odd-electron density calculated at the tuned-LC-RBLYP-CASCI(2,2)/6-311G* level. White and blue meshes for NO maps represent the isosurfaces with the contour values of ± 0.01 a.u. Yellow mesh for odd-electron density maps represents the isosurface with the contour value of 0.0005 a.u.

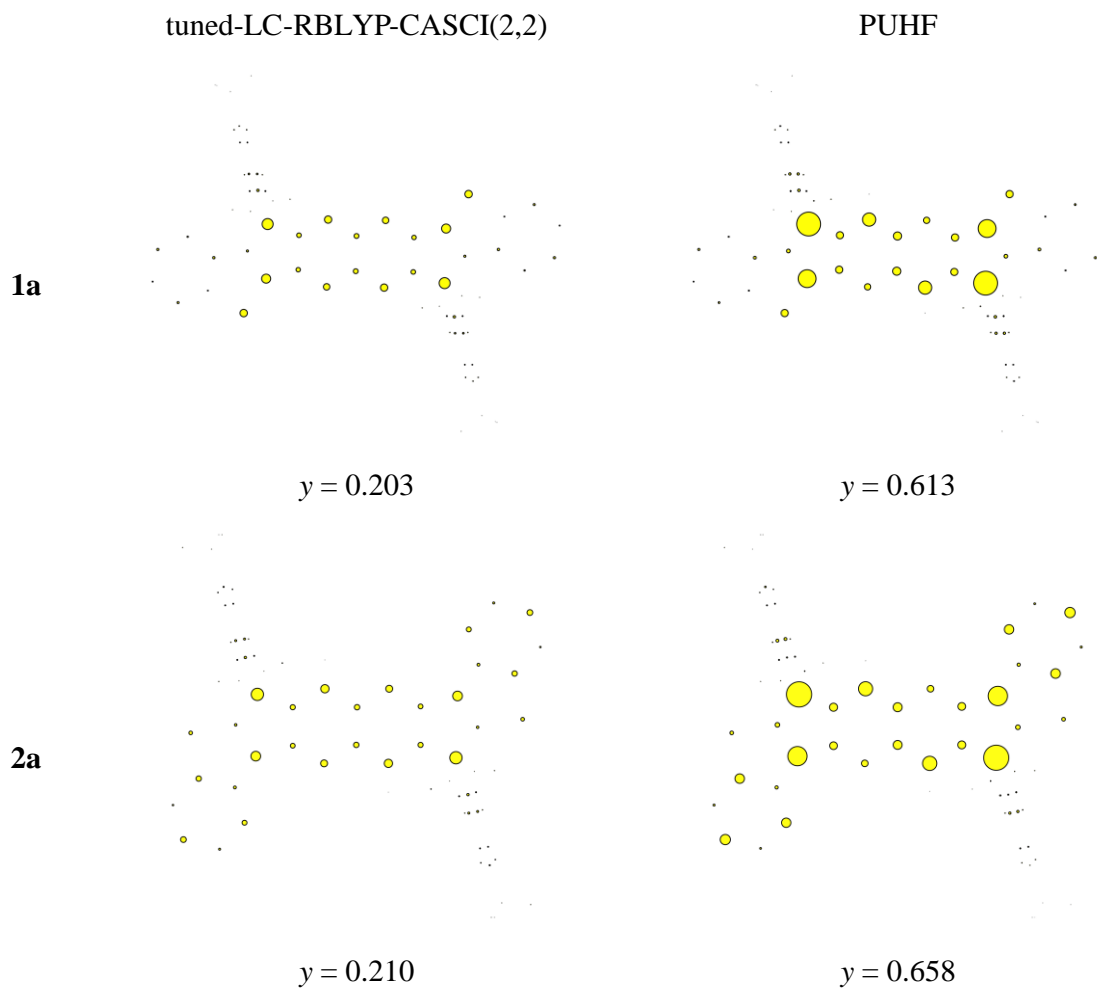
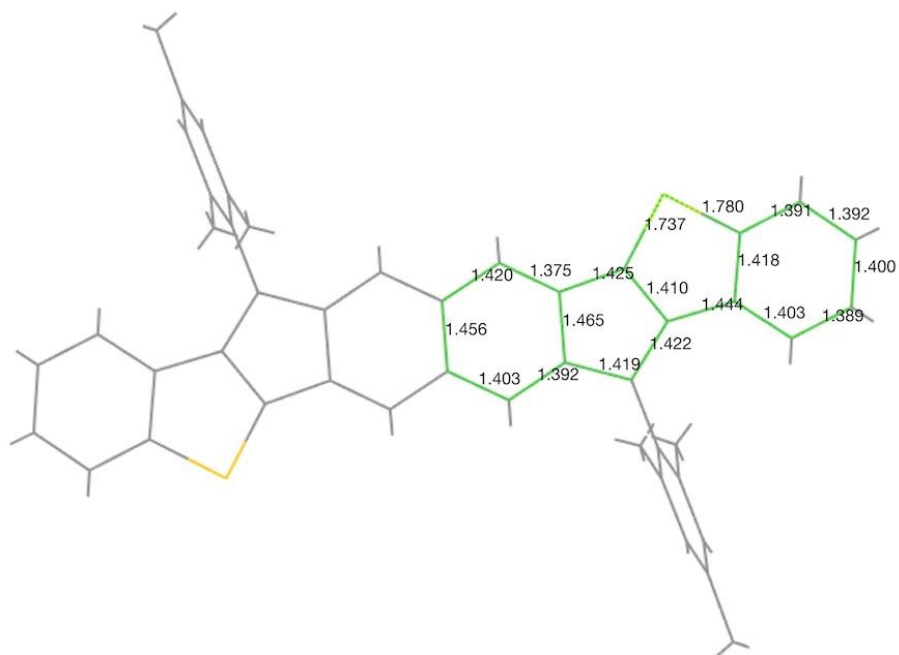


Figure C.12 Mulliken population analysis for the odd-electron density calculated at the tuned-LC-RBLYP-CASCI(2,2)/6-311G* and PUHF/6-311G* levels. Note that the sum of odd-electron populations (odd-electron number) corresponds to $2y$ at the given level of approximation.

1a



2a

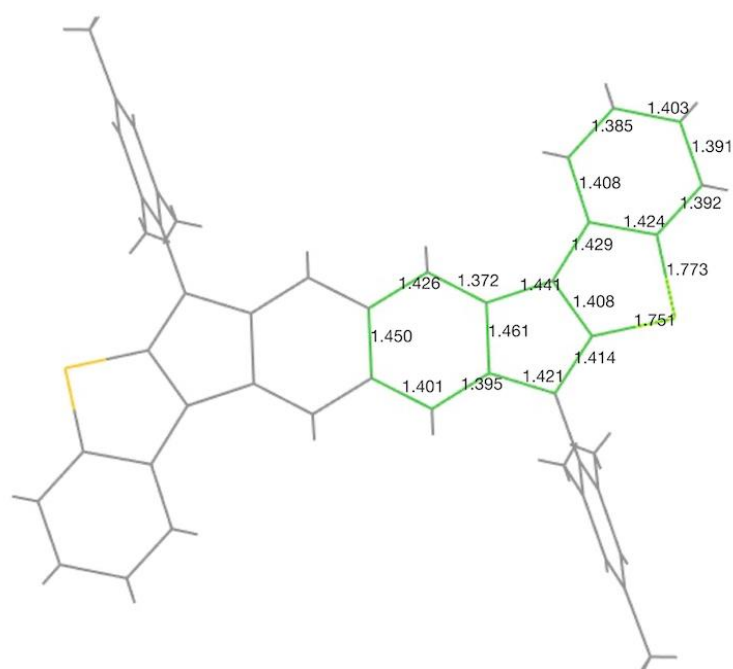


Figure C.13 Selected bond lengths (Å) for the singlet state calculated at the RB3LYP/6-311G* level.

SQUID measurements. Magnetic susceptibility measurements were performed with a Quantum Design MPMS-XL-7 SQUID susceptometer equipped with a sample space oven reaching a maximum temperature of 800 K. The magnetic measurements were performed in the 300-700 K temperature range with an applied field of 1 T using a sample space oven with the samples inserted in a 1.5 mm diameter aluminium foil cylinder. The sample masses used for the magnetic measurements are 11.665, 3.868 and 1.469 mg for **2a**, **1b** and **2b**, respectively. The susceptibility data were corrected for the same sample holder previously measured using the same conditions and for the diamagnetic contributions of the compound as deduced by using Pascal's constant tables. The magnetic measurements were fitted using the classical Bleaney-Bowers model for an antiferromagnetic $S = \frac{1}{2}$ dimer. This model reproduces satisfactorily the magnetic properties of **2a** with $g = 2.0(1)$, $J = -3479$ K and a paramagnetic $S = \frac{1}{2}$ impurity (ρ) of *ca.* 0.6% with a regression factor, $R = 0.99877$ (the Hamiltonian is written as $H = -JS_1S_2$). This J value corresponds to a ΔE_{ST} of *ca.* -6.9 kcal mol⁻¹.

Compounds **1b** and **2b** were measured in the heating and cooling scans in order to verify stability. The magnetic measurements of **1b** and **2b** were also fitted to the classical Bleaney-Bowers model. This model for **1b** gives (solid lines in Figure C.14): $g = 2.0(1)$, $J = -4141$ K and $\rho \approx 0.1\%$ in the heating scan ($R = 0.9991$) and $g = 2.0(1)$, $J = -4227$ K and $\rho \approx 0.1\%$ in the cooling scan ($R = 0.9985$). These J values correspond to ΔE_{ST} of *ca.* -8.2 and -8.4 kcal mol⁻¹, for the heating and cooling scans, respectively. For **2b** we obtain (solid lines in Figure C.15): $g = 2.0(1)$, $J = -3652$ K and $\rho \approx 0.1\%$ in the heating scan ($R = 0.9994$) and $g = 2.0(1)$, $J = -3533$ K and $\rho \approx 0.2\%$ in the cooling scan ($R = 0.9979$). These J values correspond to ΔE_{ST} of *ca.* -7.2 and -7.0 kcal mol⁻¹, for the heating and cooling scans, respectively.

In all cases the paramagnetic impurities may come from a small fraction of mono-radical present in the sample. Given the low magnetic signal, the J value obtained presents an uncertainty of around 10%, as this error corresponds to the error in the $\chi_m T$ values (and, therefore in the g values that are directly related to them). For the estimated ΔE_{ST} values

from the fit to the Bleaney-Bowers model, however, the ΔE_{ST} value mainly depends on the curvature of the plot as T increases; thus, the error in ΔE_{ST} can be evaluated to be around $0.2 \text{ kcal mol}^{-1}$, which is more like 2-3%.

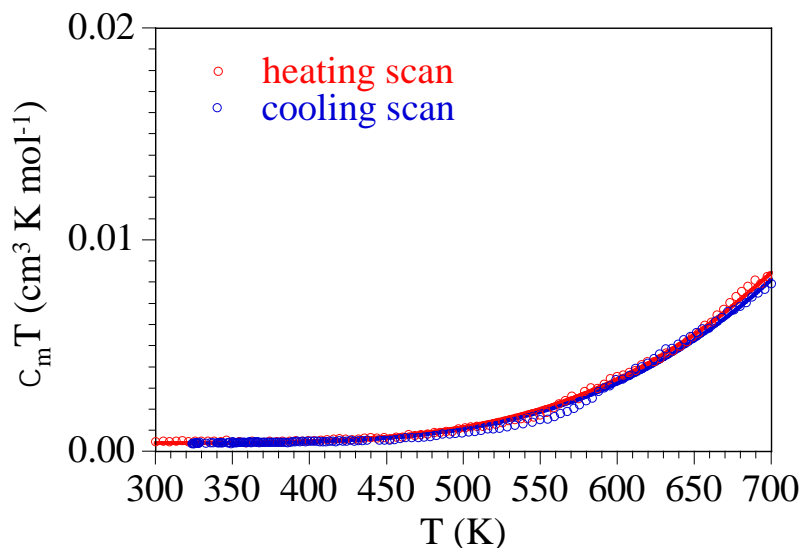


Figure C.14 Variable temperature SQUID measurement of *anti*-IIDBT **1b** in the heating (red points) and cooling scans (blue points). Solid lines are the best fit to the Bleaney-Bowers dimer model.

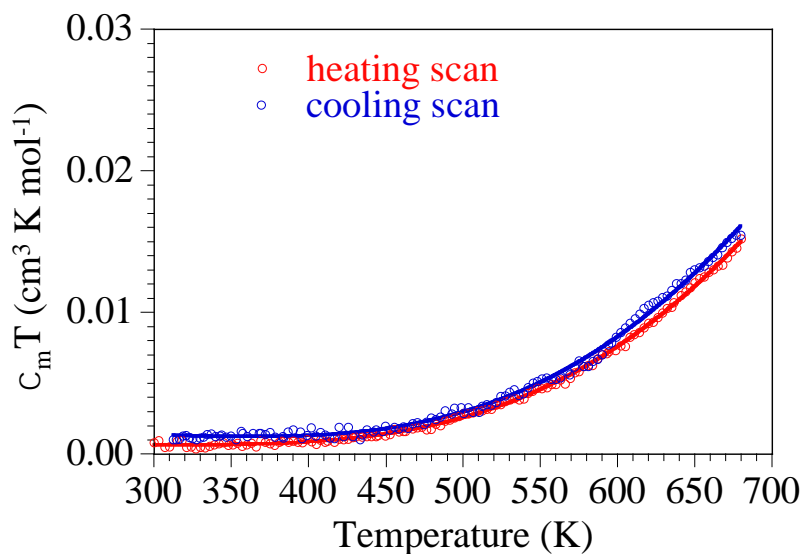


Figure C.15 Variable temperature SQUID measurement of *syn*-IIDBT **2b** in the heating (red points) and cooling scans (blue points). Solid lines are the best fit to the Bleaney-Bowers dimer model

TGA measurements. Thermogravimetric Analysis (TGA) was performed from 25-1000 °C on samples of **1a-1b** and **2a-2b** using a TGA Q500 V6.7 Build 203 instrument. The measurements were performed under an oxygen-free dry N₂ flow.

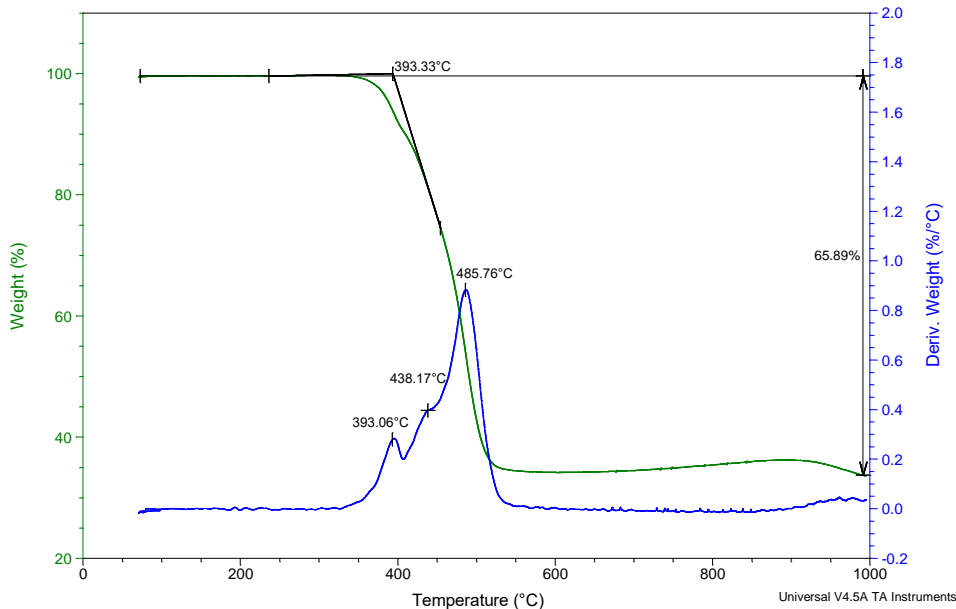


Figure C.16 TGA plot for *anti*-IIDBT **1a**.

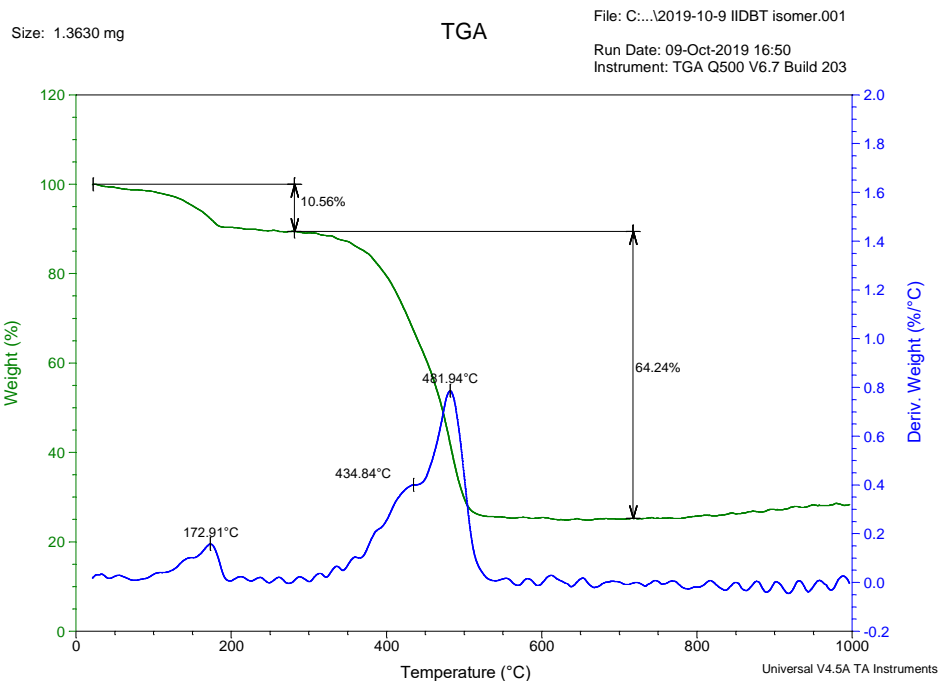


Figure C.17 TGA plot for *anti*-IIDBT **1b**. The small, initial weight loss corresponds to 1,2-dichlorobenzene solvent.

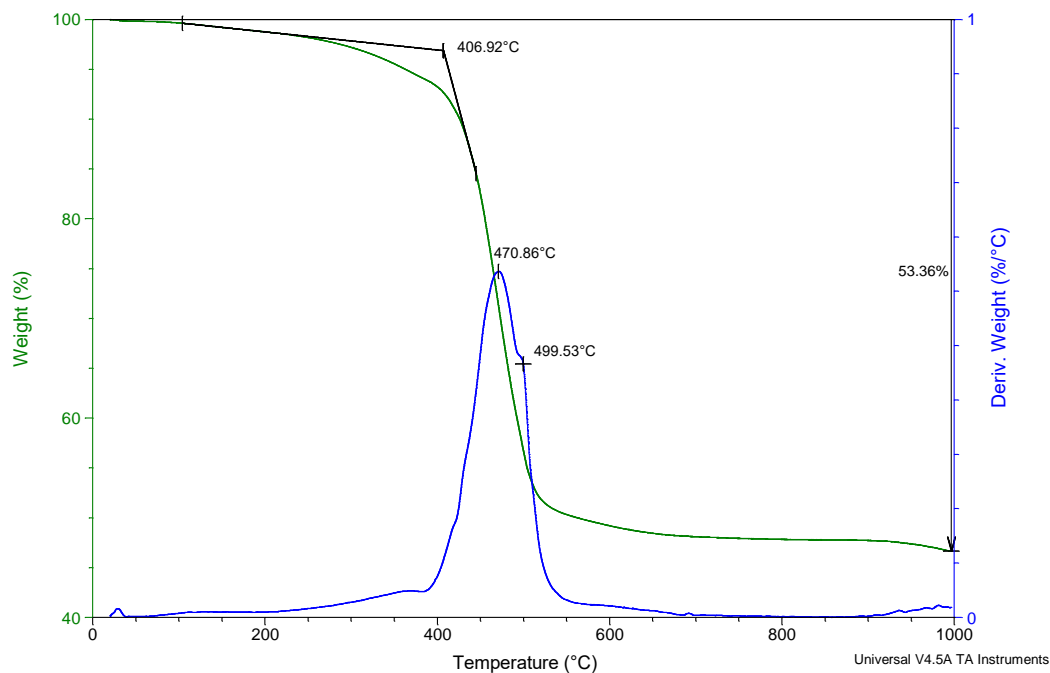


Figure C.18 TGA plot for *syn*-IIDBT 2a.

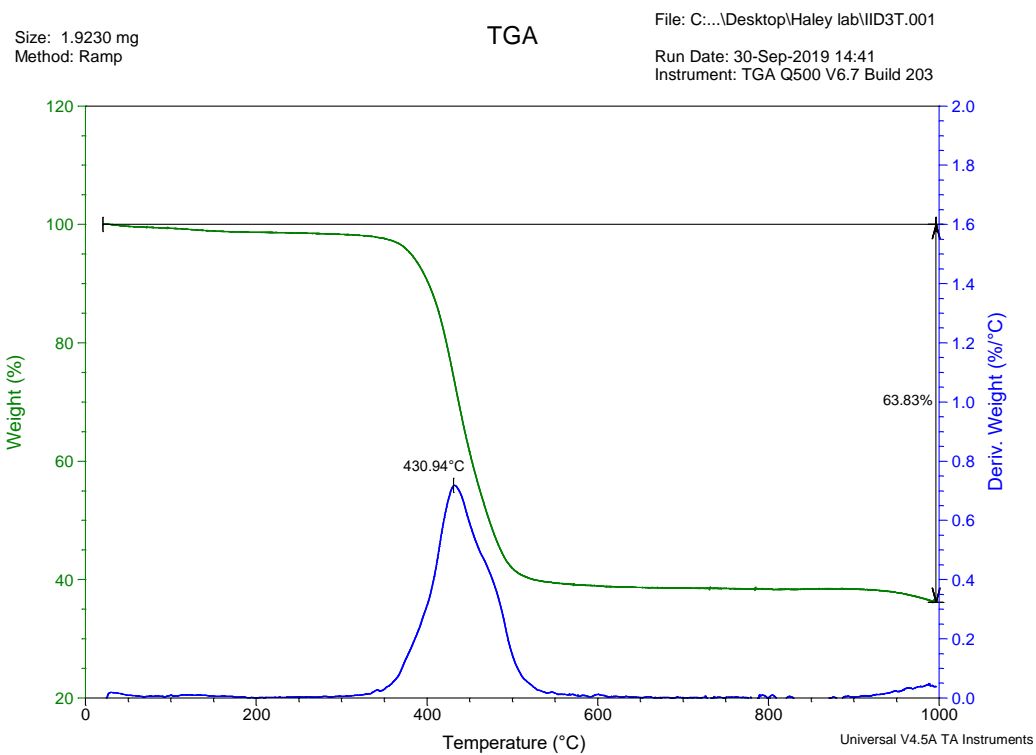


Figure C.19 TGA plot for *syn*-IIDBT 2b.

X-ray Diffraction Details

General Details for X-ray Structures. Diffraction intensities for **1d** were collected at 173 K on a Bruker Apex2 CCD diffractometer using CuK α radiation, $\lambda = 1.54178 \text{ \AA}$. Space group was determined based on intensity statistics. Absorption correction was applied by SADABS. Structure was solved by direct methods and Fourier techniques and refined on F^2 using full matrix least-squares procedures. All non-H atoms were refined with anisotropic thermal parameters. H atoms in all structures were refined in calculated positions in a rigid group model. Solvent molecule, CH₃CN, is highly disordered over three or four positions. Some of these positions are related by an inversion center. This solvent molecule was treated by SQUEEZE. The correction of the X-ray data by SQUEEZE was 51 electron/cell; the expected number of electrons is 44 electrons/cell. Crystals of **1d** were very thin plates that did not provide visible reflections at high angles. Even using a strong *Incoatec I μ S* Cu source it was possible to collect diffraction data only up to $2\theta_{\max} = 101.25^\circ$. The collected data provide 2737 reflections per 271 refined parameters. All calculations were performed by the Bruker SHELXL-2014 package. X-ray diffraction data for **2b** were collected on a Rigaku XtaLAB Synergy diffractometer coupled to a Rigaku Hypix detector with Cu K α radiation ($\lambda = 1.54184 \text{ \AA}$), from a PhotonJet micro-focus X-ray source at 200 K. The diffraction images were processed and scaled using the CrysAlisPro software. The structures were solved through intrinsic phasing using SHELXT¹³ and refined against F^2 on all data by full-matrix least squares with SHELXL¹⁵ following established refinement strategies.¹⁶ All non-hydrogen atoms were refined anisotropically. All hydrogen atoms bound to carbon were included in the model at geometrically calculated positions and refined using a riding model. The isotropic displacement parameters of all hydrogen atoms were fixed to 1.2 times the U_{eq} value of the atoms they are linked to (1.5 times for Me groups).

Crystallographic Data for 1d. C₆₂H₆₄N₂S₂, C₅₈H₅₈S₂•2(CH₃CN), M = 901.27, 0.12 x 0.09 x 0.01 mm, T = 173(2) K, Triclinic, space group *P*-1, $a = 9.0360(6) \text{ \AA}$, $b = 10.7067(7) \text{ \AA}$, $c = 14.4033(10) \text{ \AA}$, $\alpha = 77.940(4)^\circ$, $\beta = 85.741(5)^\circ$, $\gamma = 74.769(4)^\circ$, $V = 1314.56(16) \text{ \AA}^3$, $Z = 1$, $D_c = 1.138 \text{ Mg/m}^3$, $\mu(\text{Cu}) = 1.210 \text{ mm}^{-1}$, $F(000) = 482$, $2\theta_{\max} = 101.25^\circ$, 9539 reflections, 2737 independent reflections [$R_{\text{int}} = 0.0436$], $R1 = 0.0545$, $wR2 = 0.1503$ and

GOF = 1.068 for 2737 reflections (271 parameters) with $I > 2\sigma(I)$, $R1 = 0.0755$, $wR2 = 0.1593$ and GOF = 1.068 for all reflections, max/min residual electron density $+0.337/-0.166 \text{ e}\text{\AA}^{-3}$. CCDC 1589136.

Crystallographic Data for 2b. $C_{54}H_{48}Cl_6S_2$, $C_{52}H_{46}S_2 \cdot 2(CHCl_3)$, $M = 973.74$, $0.185 \times 0.073 \times 0.037 \text{ mm}^3$, $T = 200.00(10) \text{ K}$, Monoclinic, space group $P2_1/c$, $a = 8.11560(10) \text{ \AA}$, $b = 9.97380(10) \text{ \AA}$, $c = 29.2458(3) \text{ \AA}$, $\alpha = 90^\circ$, $\beta = 94.8550(10)^\circ$, $\gamma = 90^\circ$, $V = 2358.76(4) \text{ \AA}^3$, $Z = 2$, $D_c = 1.371 \text{ Mg/m}^3$, $\mu(\text{Cu}) = 4.432 \text{ mm}^{-1}$, $F(000) = 1012$, $2\theta_{\text{max}} = 67.723^\circ$, 29112 reflections, 4271 independent reflections [$R(\text{int}) = 0.0397$], $R1 = 0.0847$, $wR2 = 0.2315$ and GOF = 1.041 for all reflections, max/min residual electron density $+1.232/-0.929 \text{ e}\text{\AA}^{-3}$. CCDC 1949404.

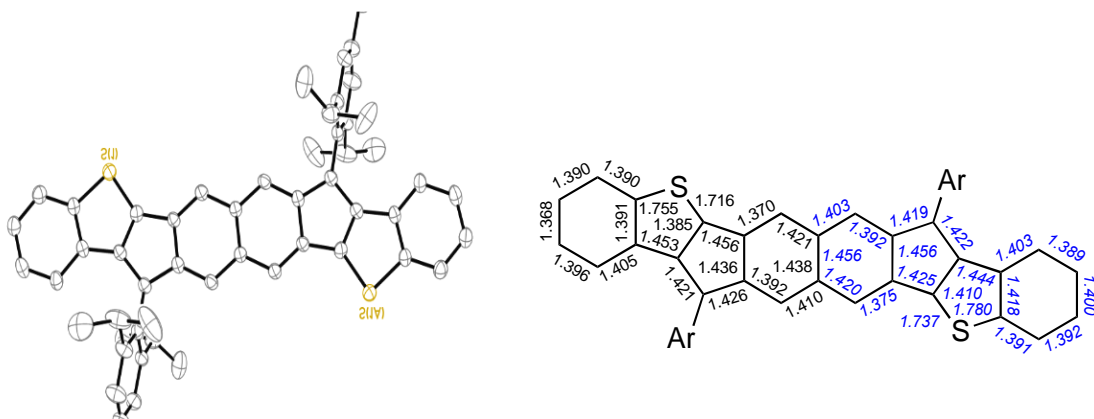


Figure C.20 (left) Molecular structure of **1d** with the ellipsoids drawn with 50% probability level; hydrogens are omitted for clarity. (right) Experimental (black) bond lengths for the core motif of **1d** along with the calculated (blue) values for **1a**.

APPENDIX D:

SUPPLEMENTARY INFORMATION FOR CHAPTER V

Appendix D is the supplementary information for Chapter V of this dissertation. It includes characterization spectra, further experimental data, and computational details.

NMR Spectra

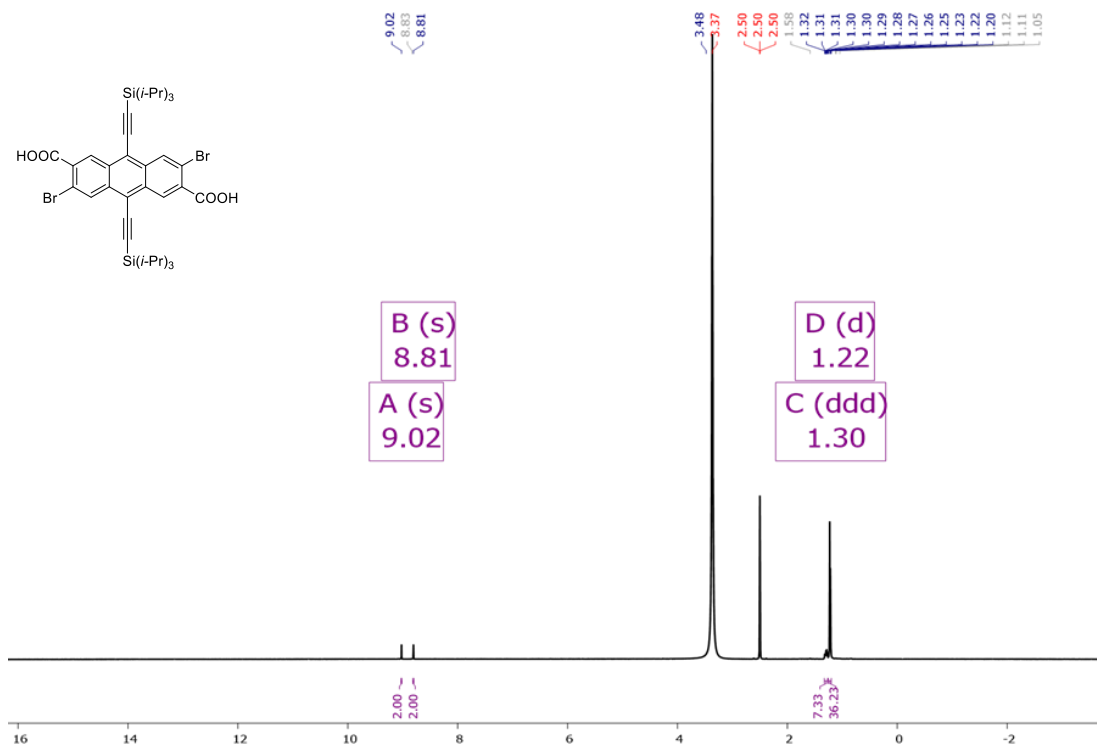


Figure D.1 ¹H NMR (600 MHz, DMSO-*d*₆) spectrum of dibromo-diacid-anthracene (15).

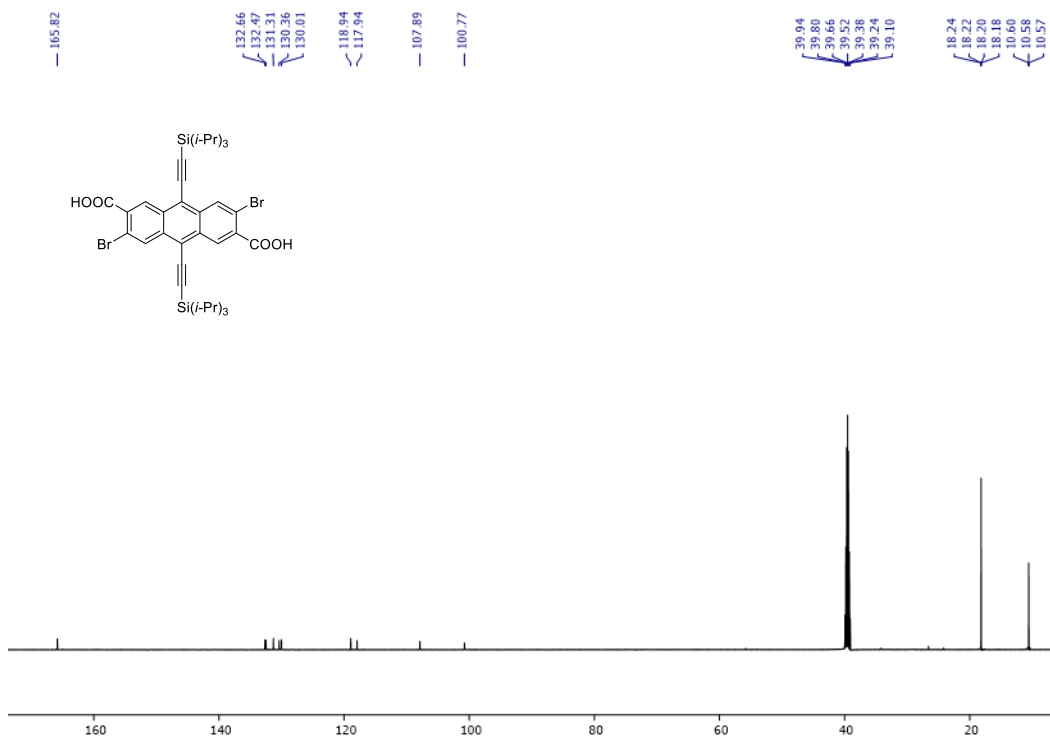


Figure D.2 ^{13}C NMR (151 MHz, $\text{DMSO-}d_6$) spectrum of dibromo-diacid-anthracene (15)

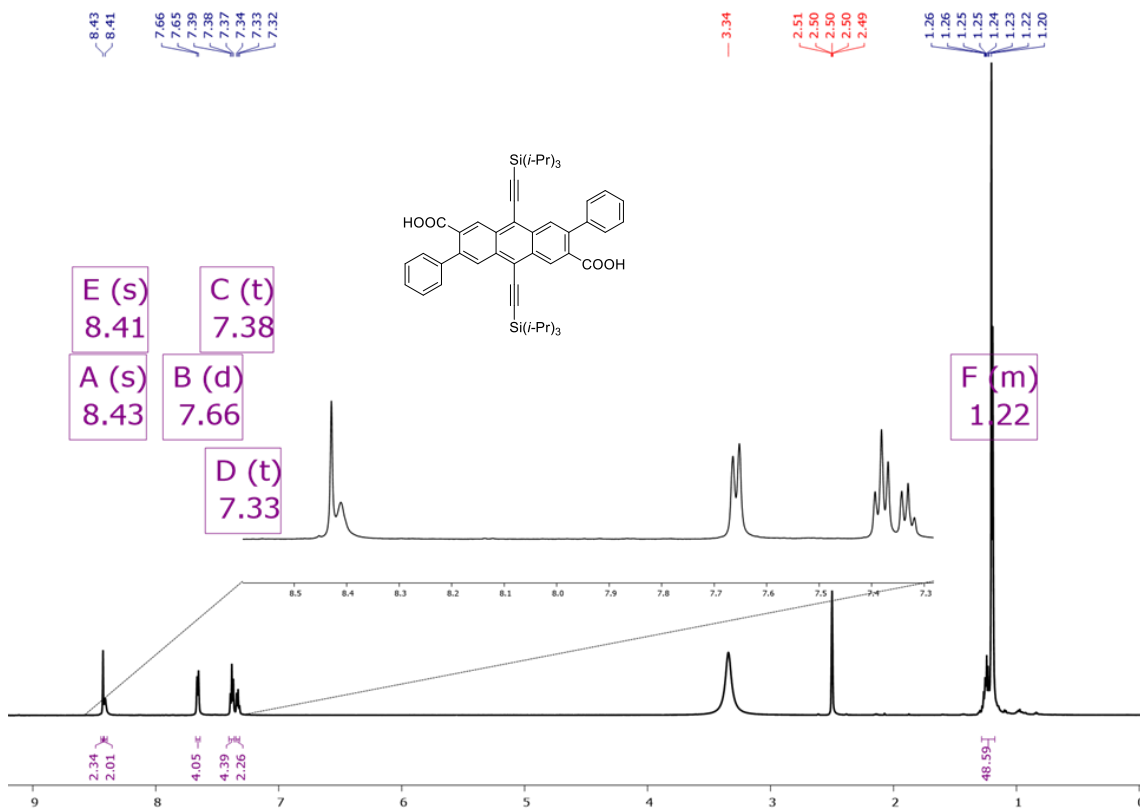


Figure D.3 ^1H NMR (600 MHz, $\text{DMSO-}d_6$) spectrum of the cross coupled product (16).

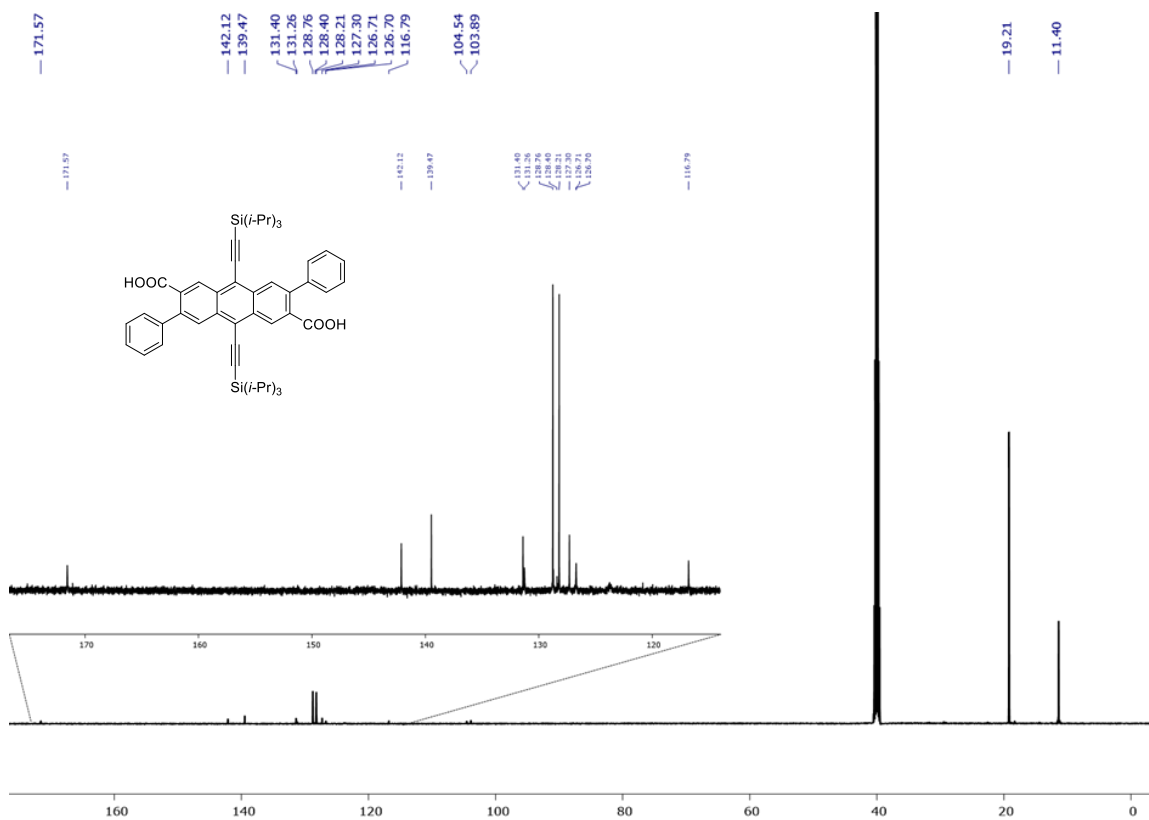


Figure D.4 ^{13}C NMR (151 MHz, $\text{DMSO-}d_6$) spectrum of the cross coupled product (16).

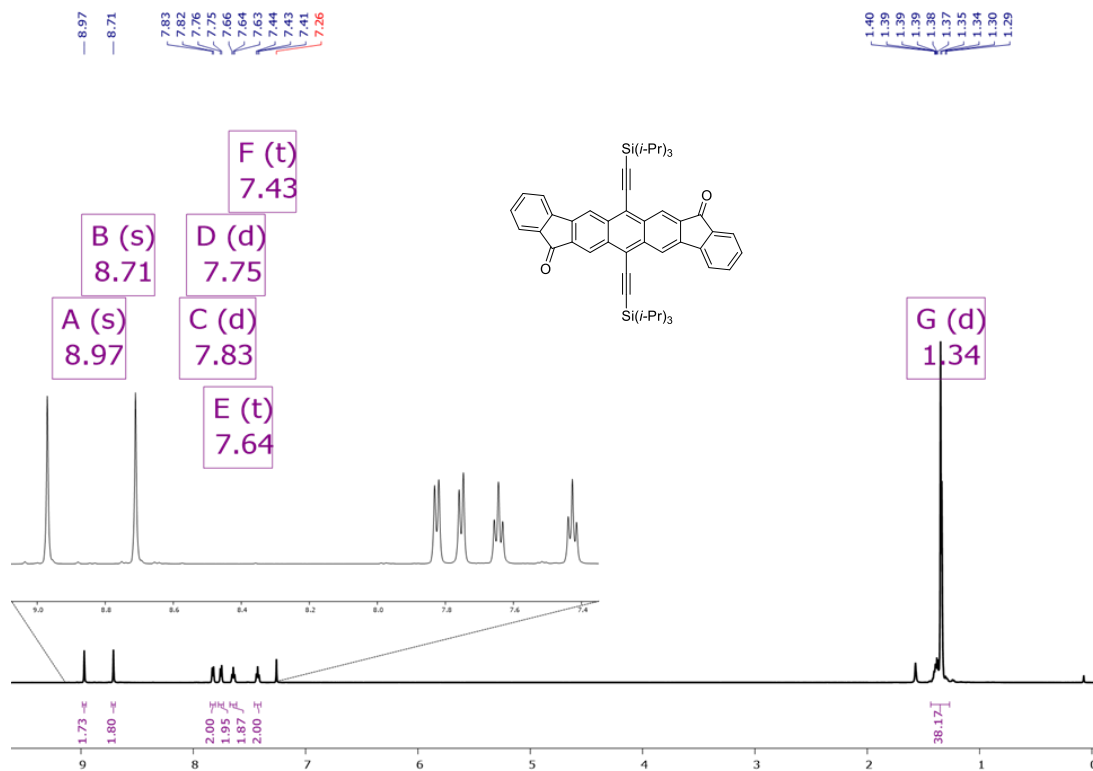


Figure D.5 ^1H NMR (600 MHz, CDCl_3) spectrum of the DIAn dione (17).

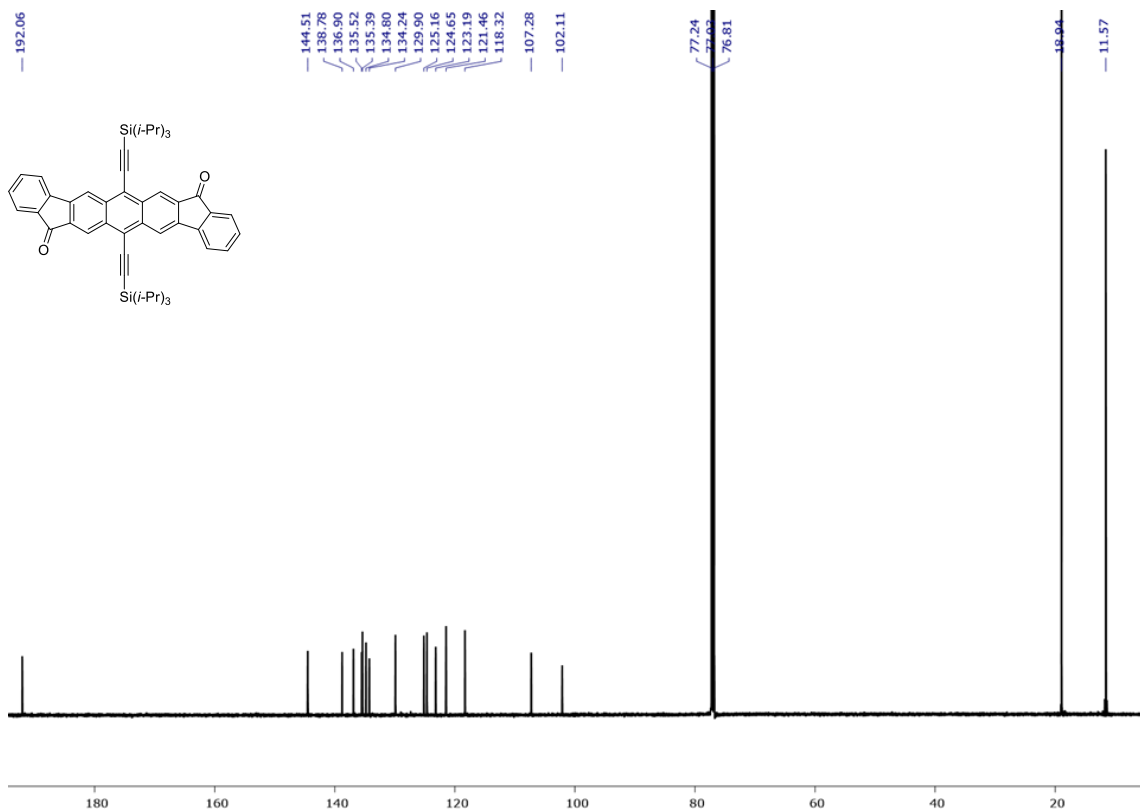


Figure D.6 ^{13}C NMR (151 MHz, CDCl_3) spectrum of the DIAn dione (17).

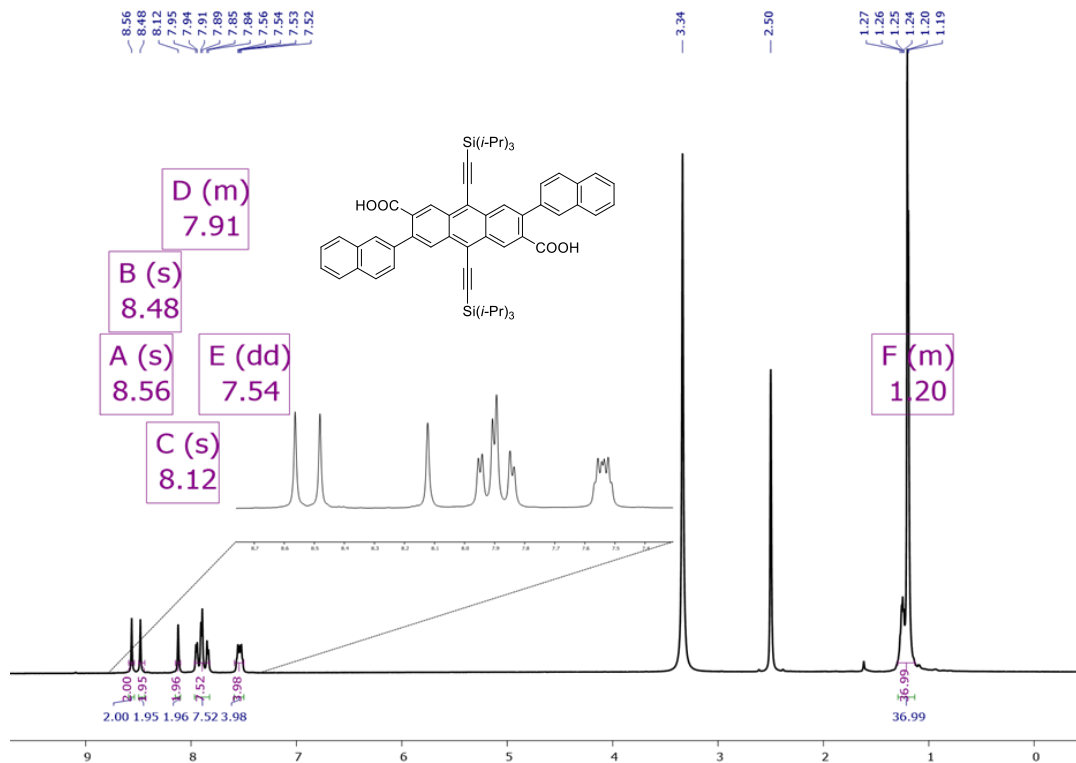


Figure D.7 ^1H NMR (600 MHz, CDCl_3) spectrum of the anti-DB cross coupling (18).

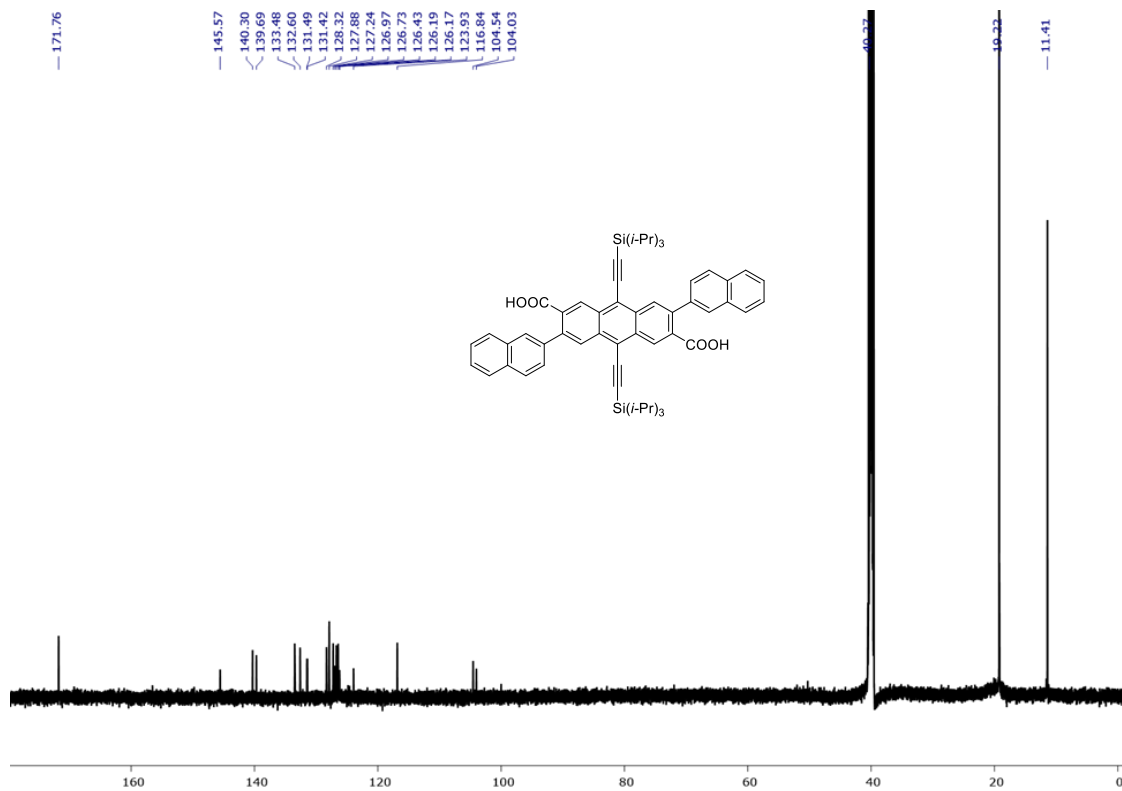


Figure D.8 ^{13}C NMR (151 MHz, CDCl_3) spectrum of the anti-DB cross coupling (18).

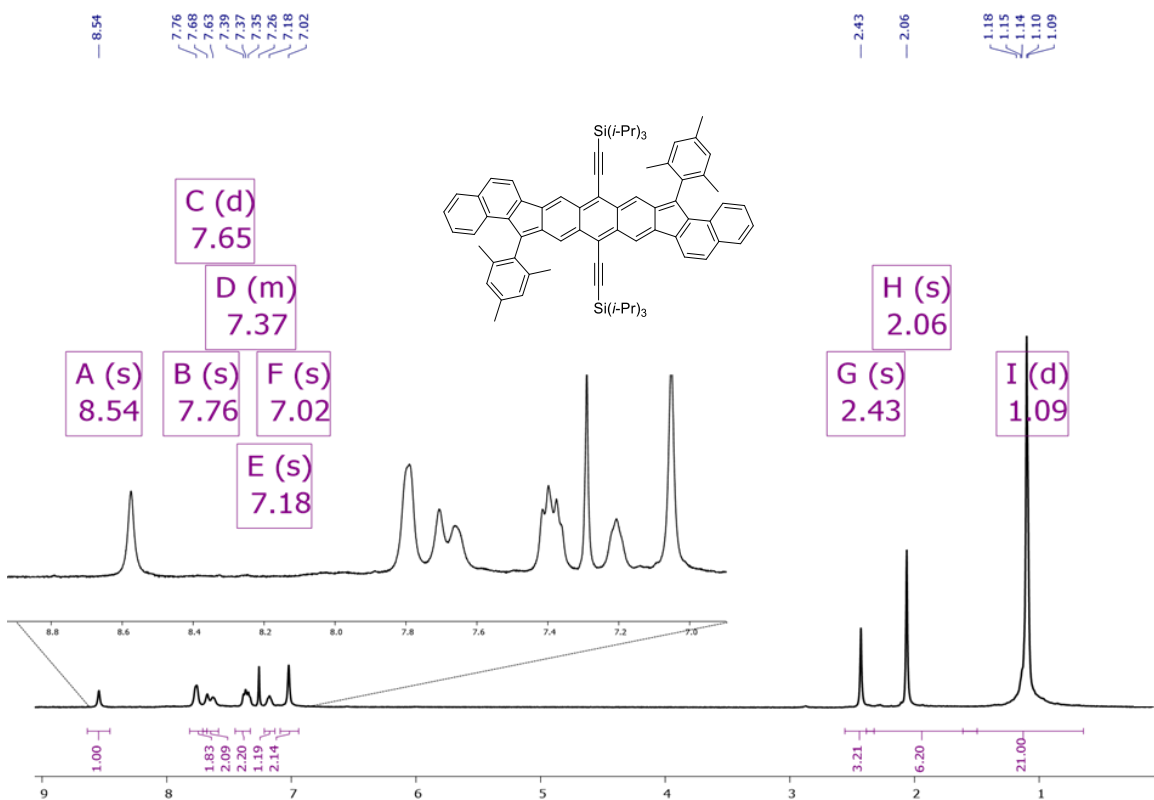


Figure D.9 ^1H NMR (500 MHz, CDCl_3) spectrum of the final Anti-DB-DIAN (12).

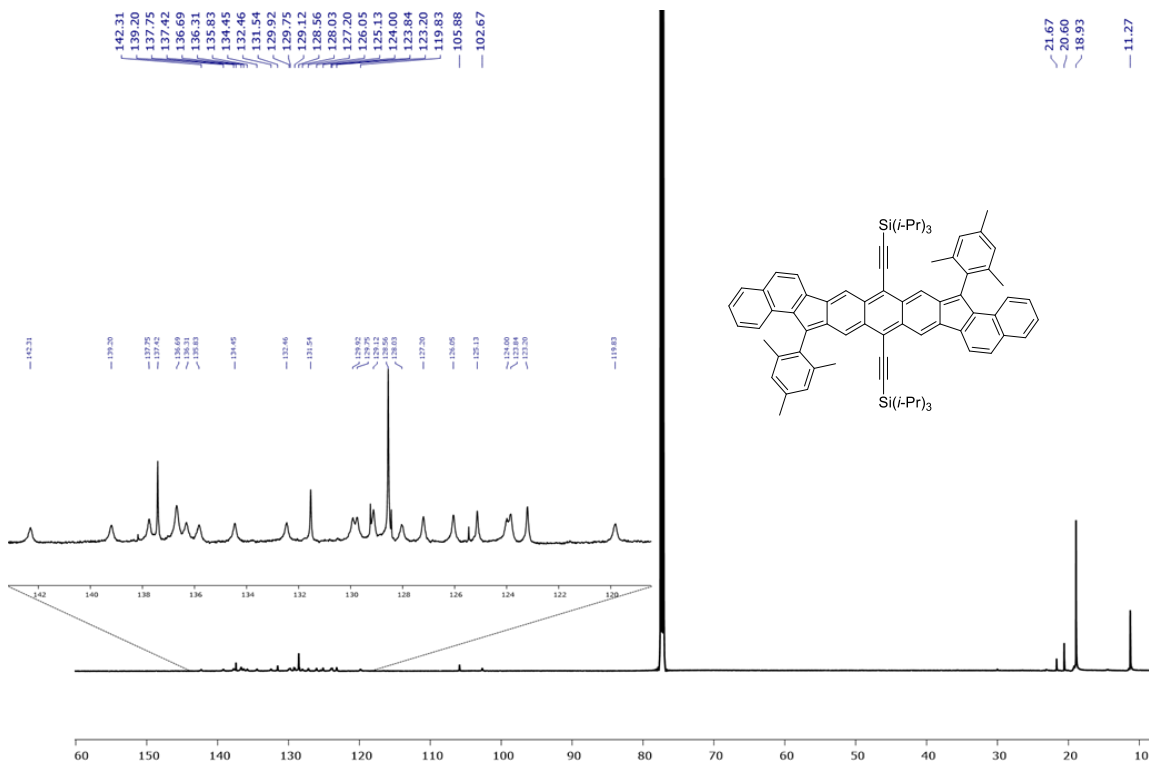


Figure D.10 ^{13}C NMR (151 MHz, CDCl_3) spectrum of the final Anti-DB-DIAN (12).

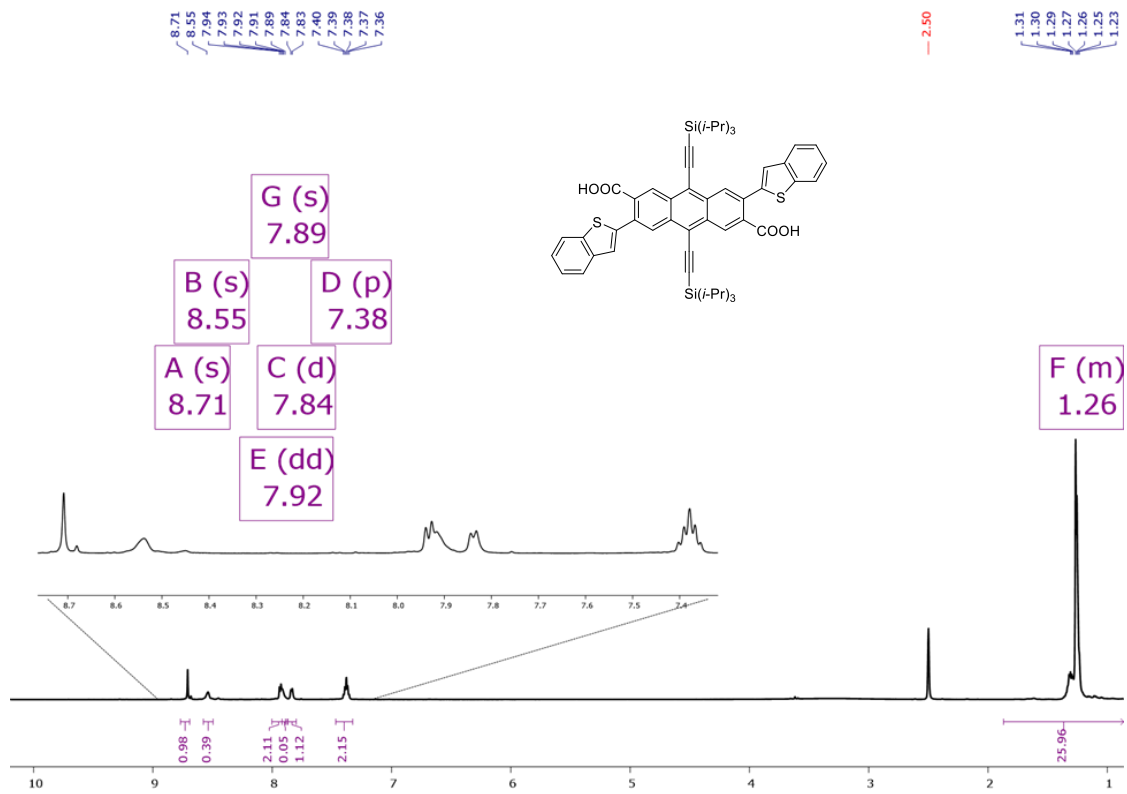


Figure D.11 ^1H NMR (600 MHz, $\text{DMSO-}d_6$) spectrum of the BT-DIAN coupling (20).

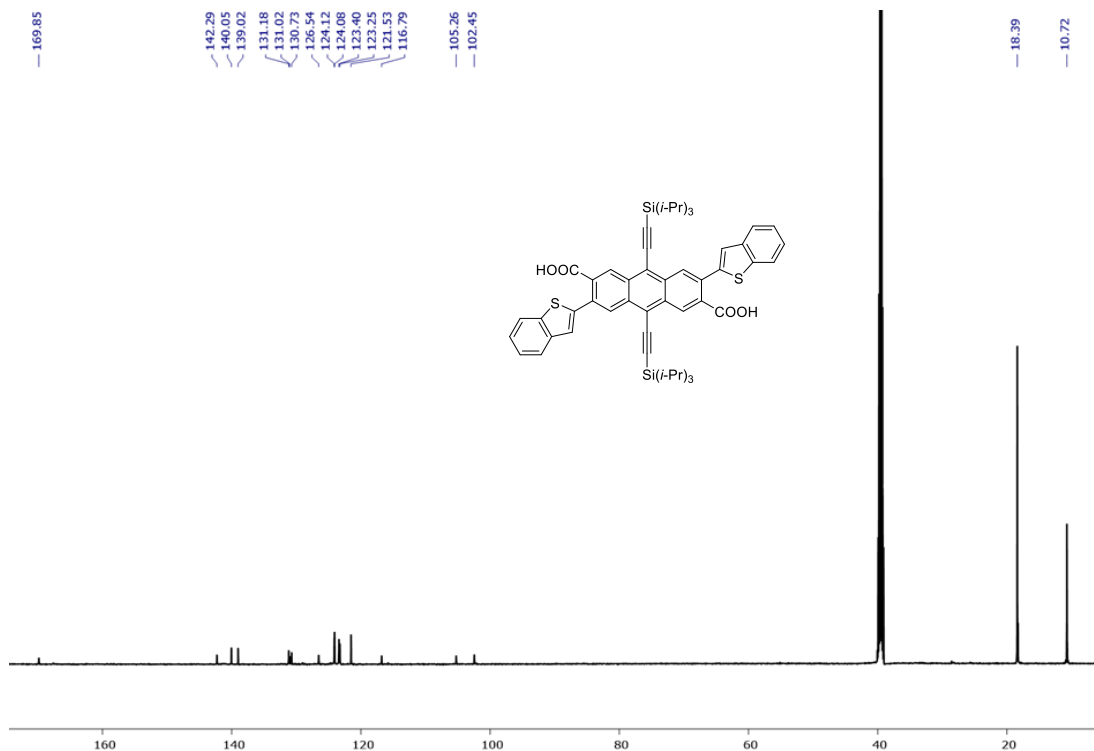


Figure D.12 ^{13}C NMR (151 MHz, $\text{DMSO-}d_6$) spectrum of the BT-DIAN coupling (20).

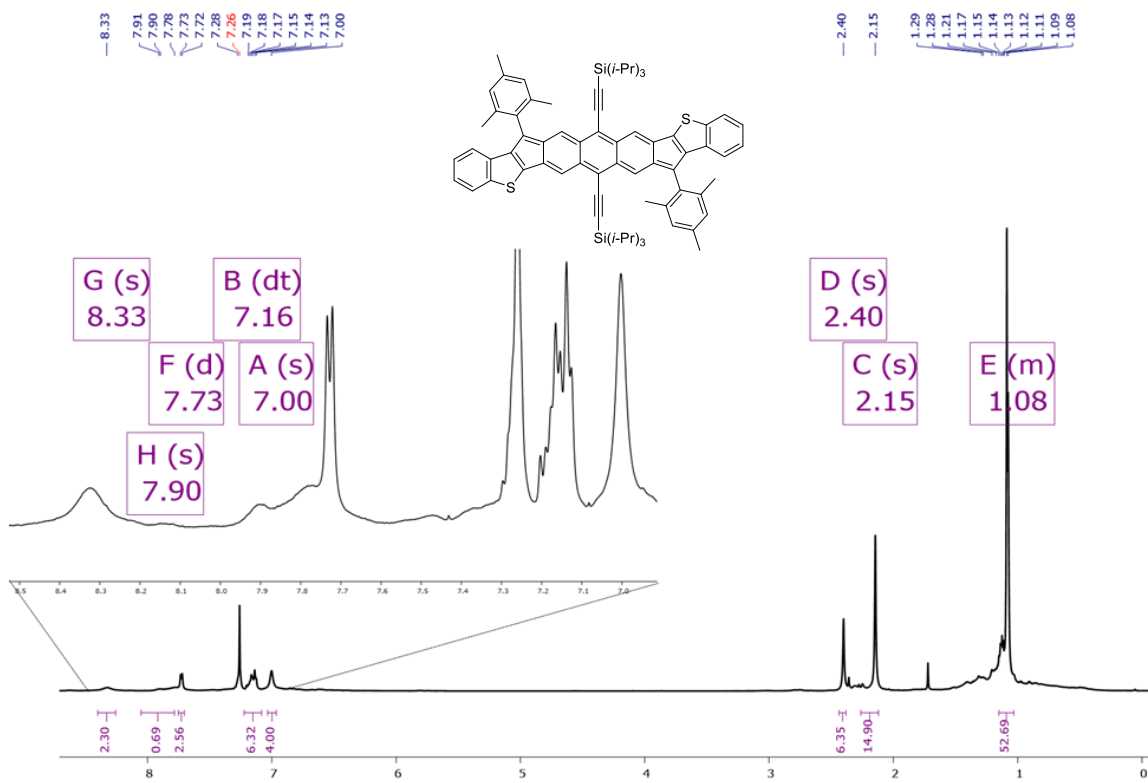


Figure D.13 ^1H NMR (600 MHz CDCl_3) spectrum of the final BT-DIAN (13). Aromatic resonances are not sharp due the strong diradical character of 13.

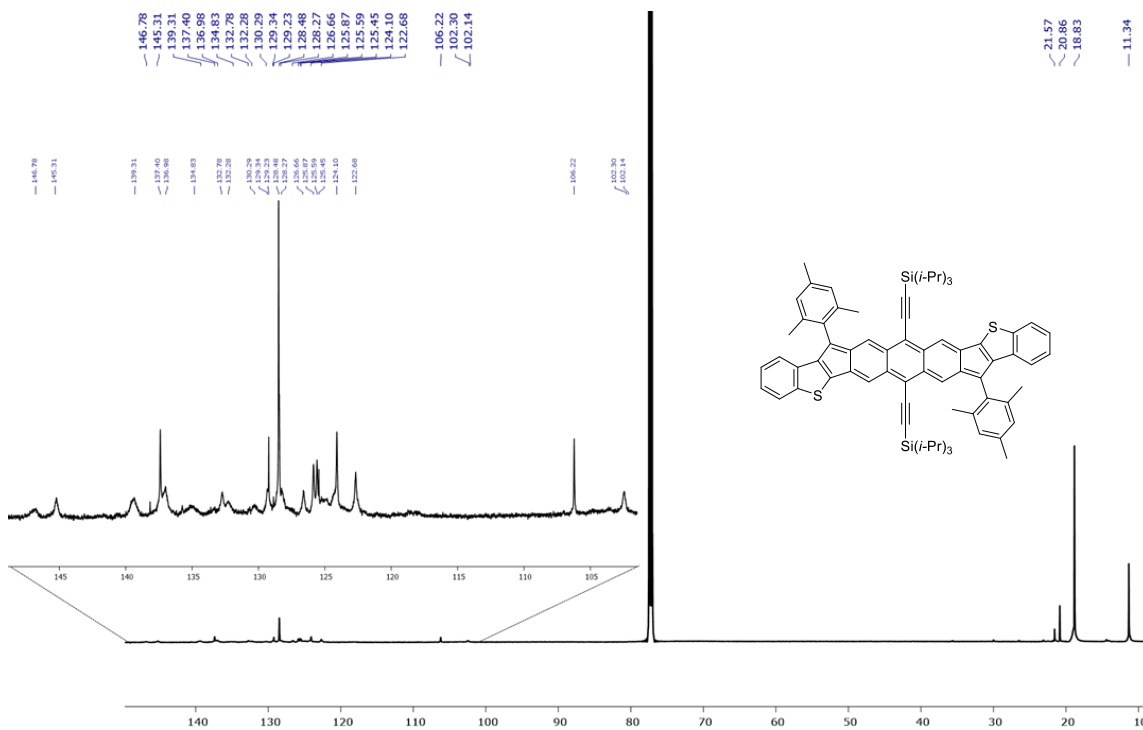


Figure D.14 ^{13}C NMR (151 MHz CDCl_3) spectrum of the final BT-DIAn (13).

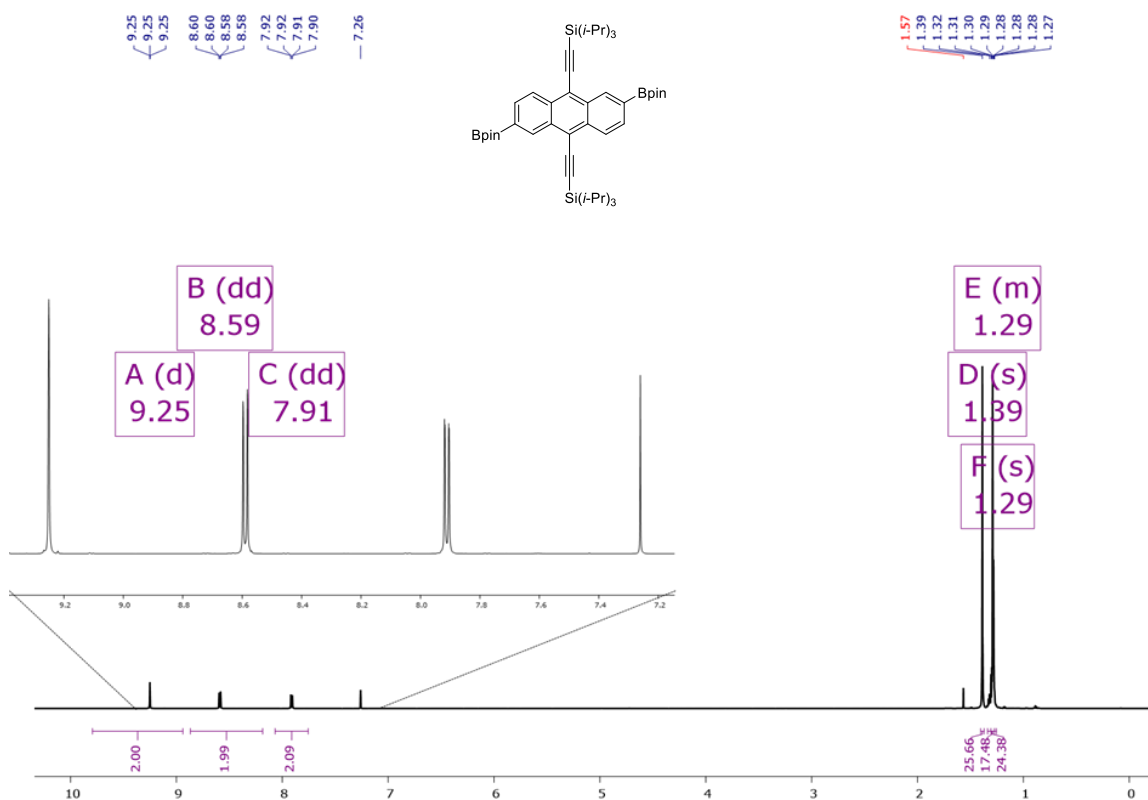


Figure D.15 ^1H NMR (600 MHz CDCl_3) spectrum of diborylated-TIPS-anthracene (22).

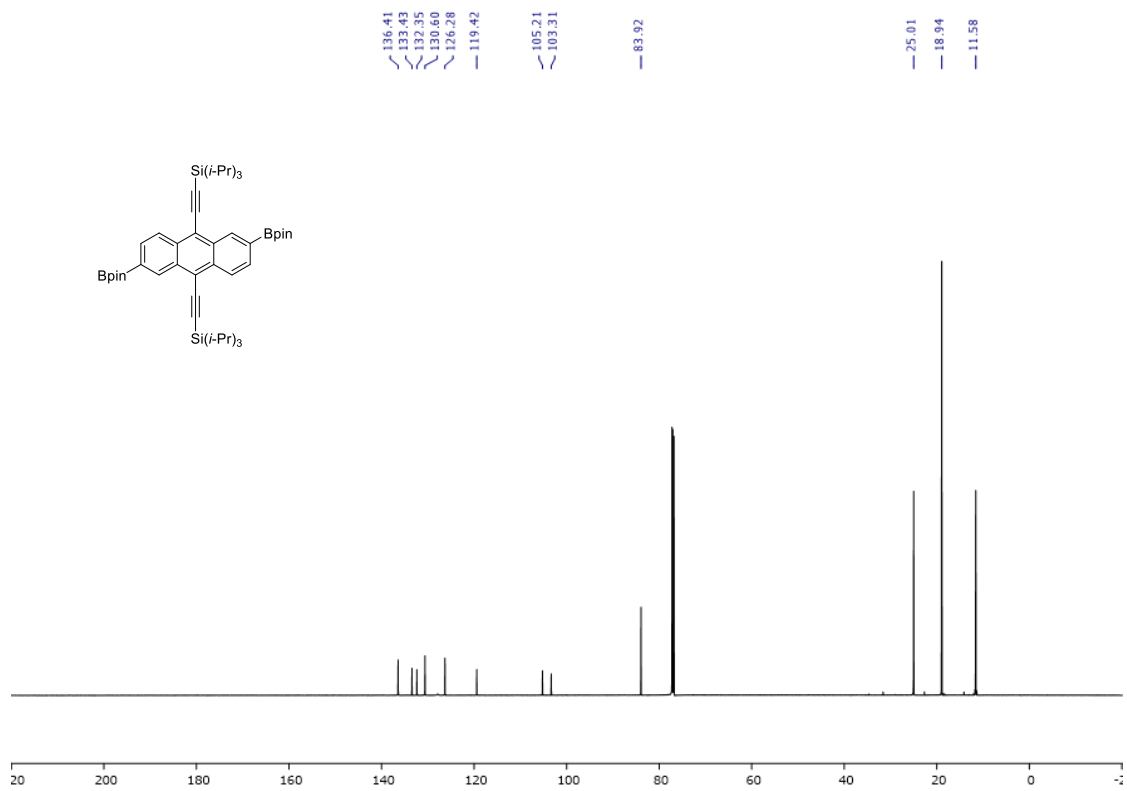


Figure D.16 ^{13}C NMR (151 MHz CDCl_3) spectrum of diborylated-TIPS-anthracene (22).

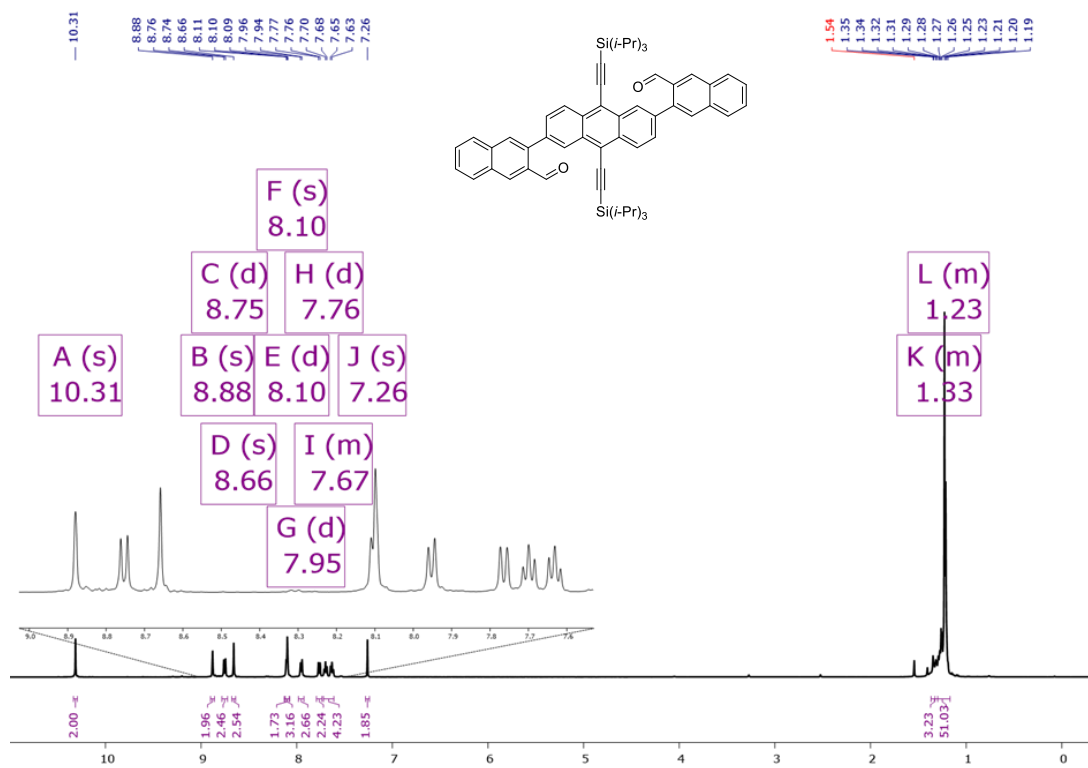


Figure D.17 ^1H NMR (500 MHz CDCl_3) spectrum of linear-dialdehyde (24).

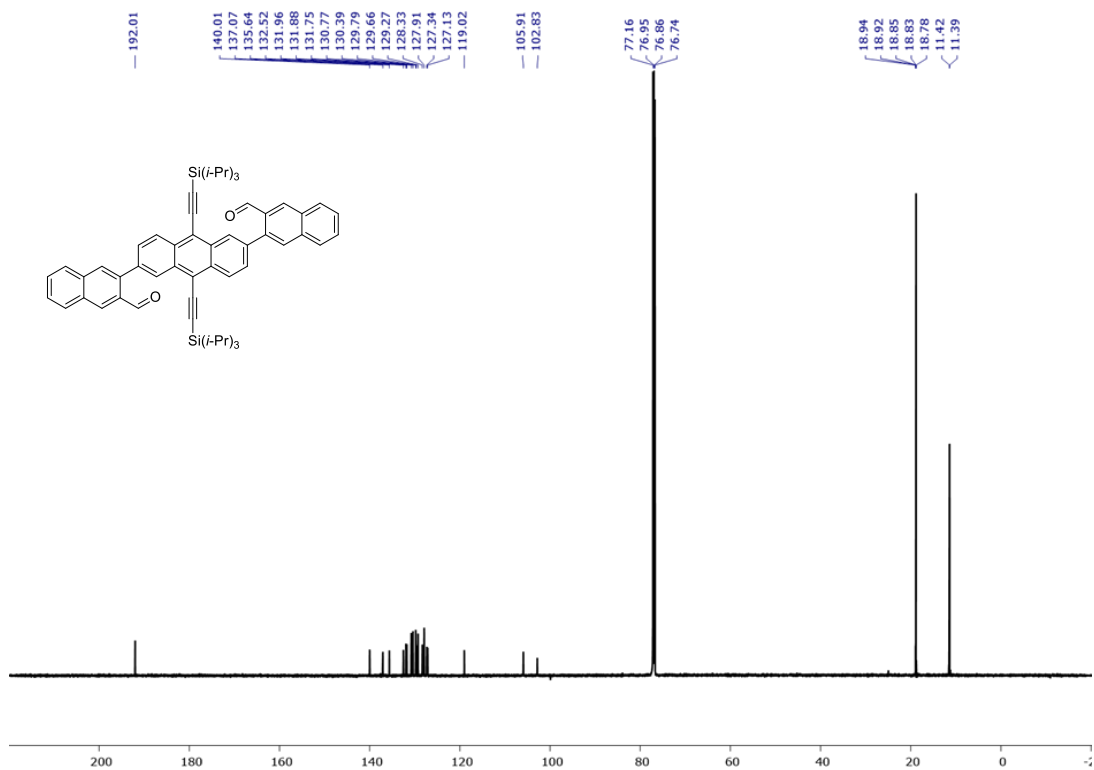


Figure D.18 ^{13}C NMR (151 MHz CDCl_3) spectrum of linear-dialdehyde (24).

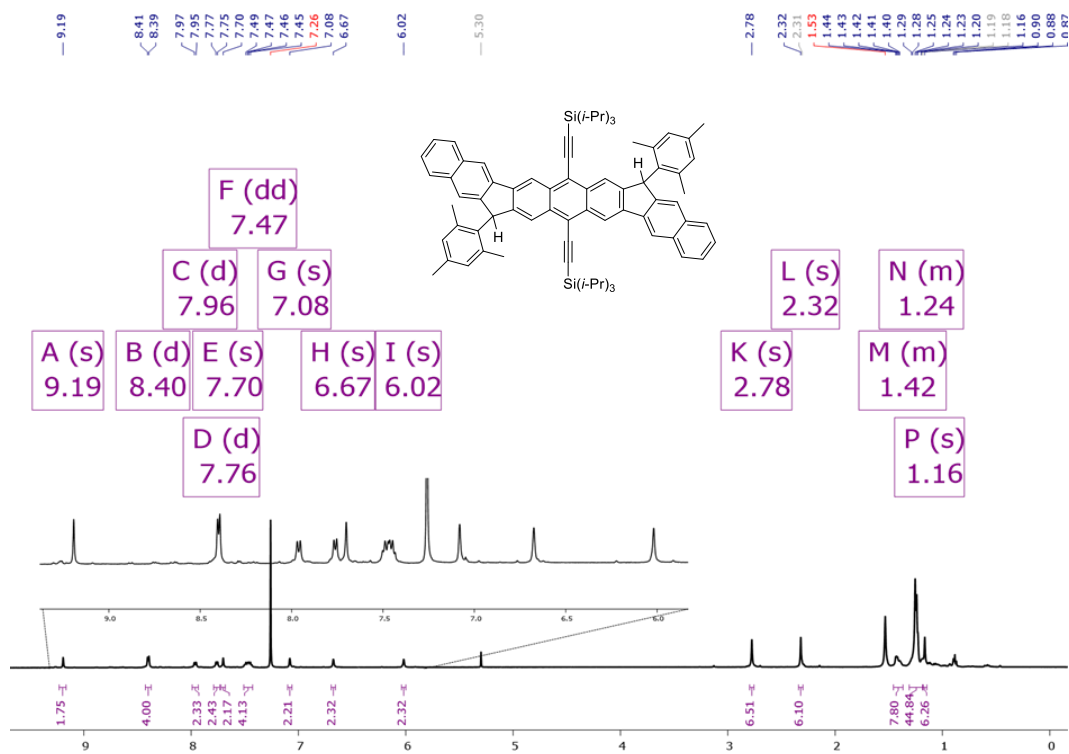


Figure D.19 ^1H NMR (500 MHz CDCl_3) spectrum of the dihydro-linear DIAn (25).

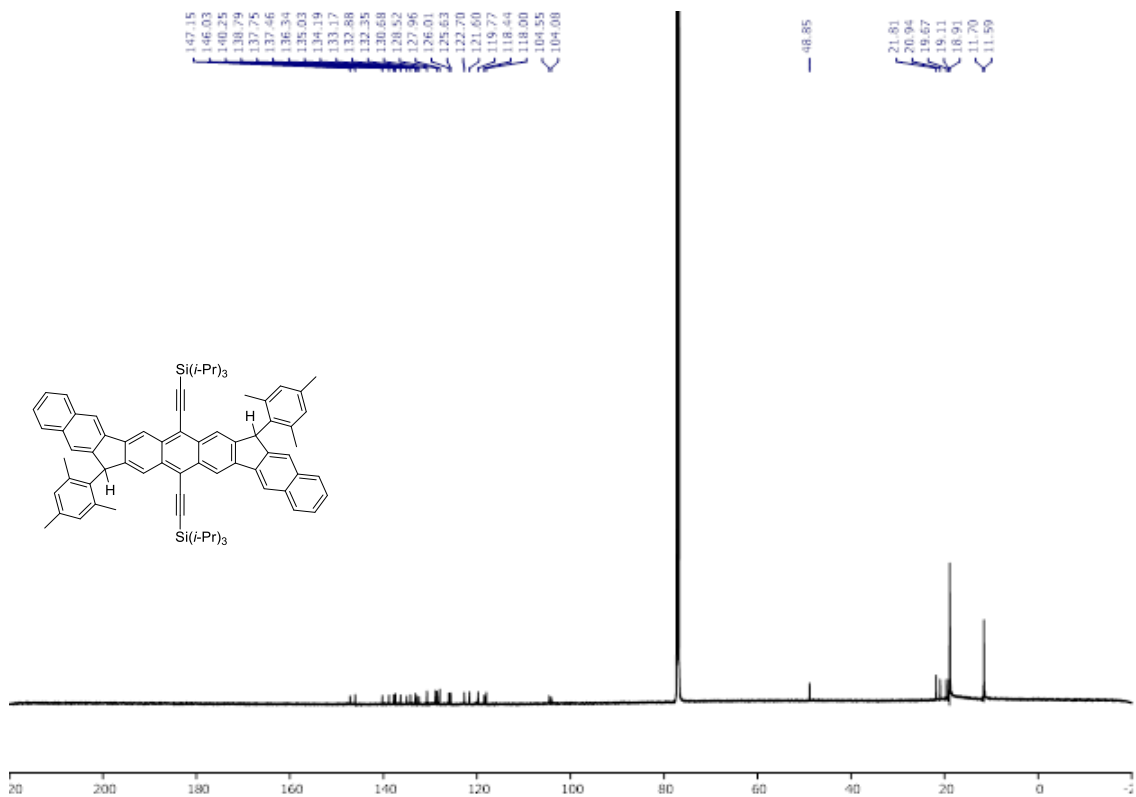


Figure D.20 ^{13}C NMR (151 MHz CDCl_3) spectrum of the dihydro-linear DIAn (25).

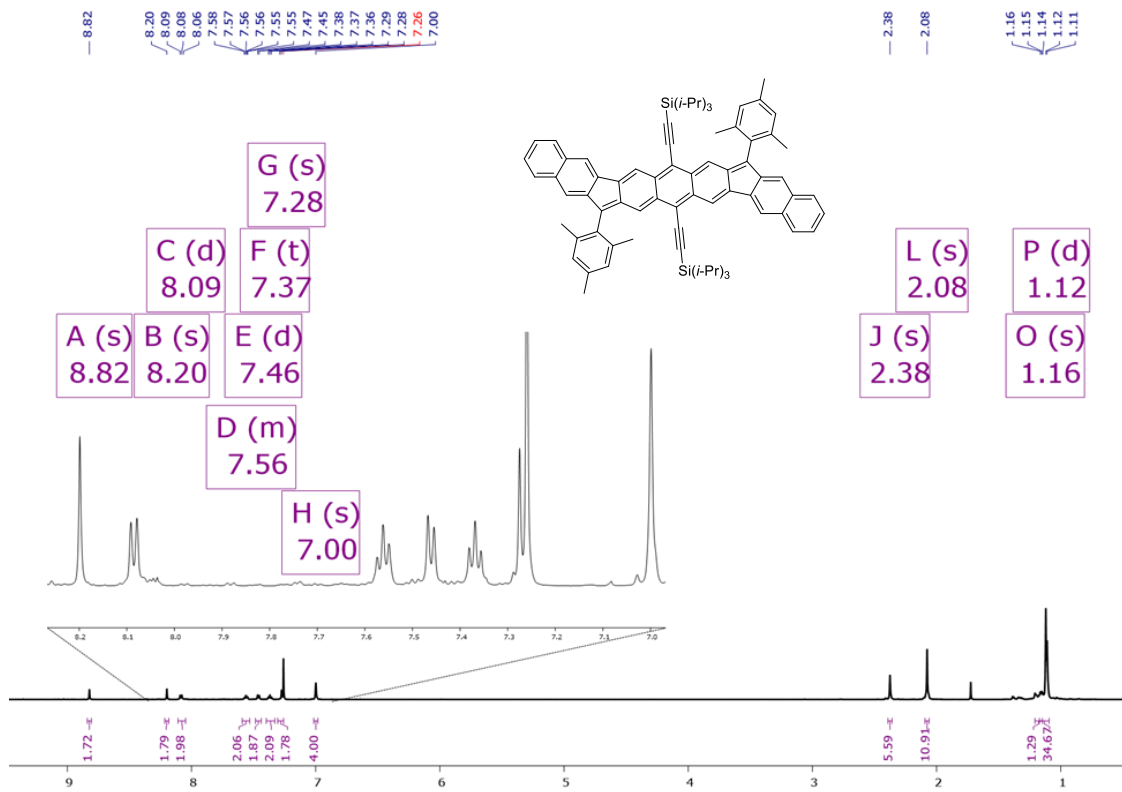


Figure D.21 ^1H NMR (600 MHz CDCl_3) spectrum of the final linear-DB- DIAn (10).

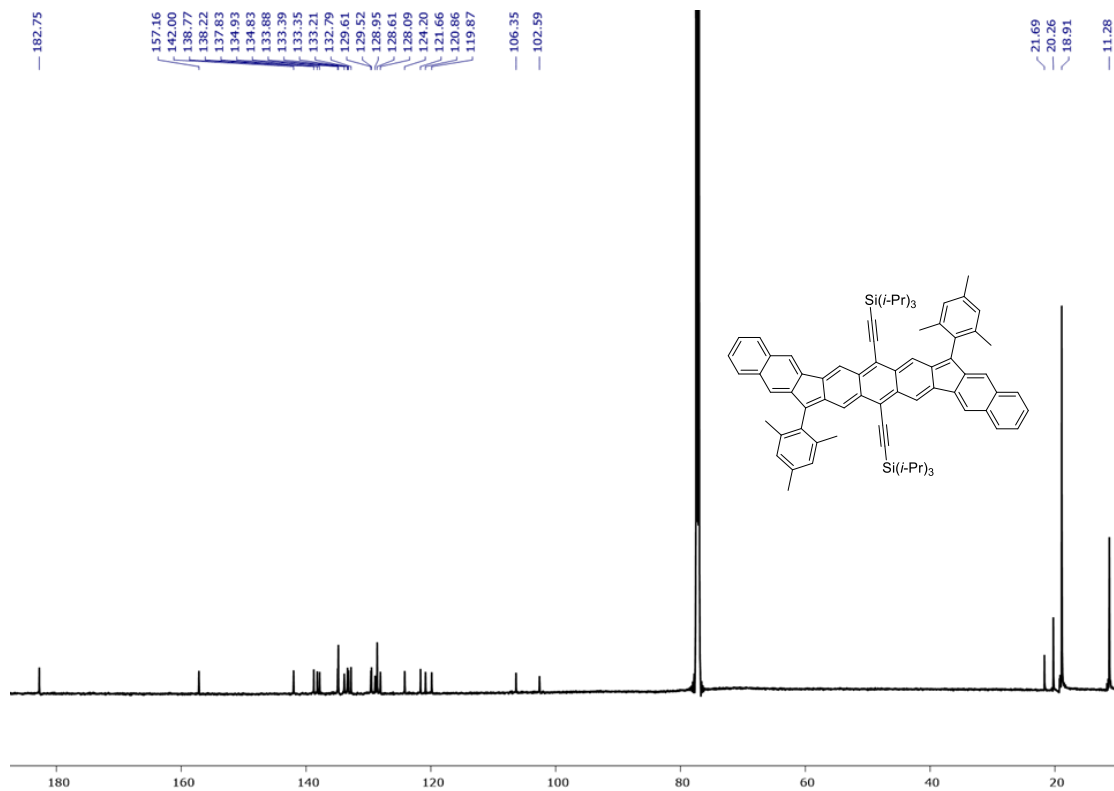


Figure D.22 ^{13}C NMR (151 MHz CDCl_3) spectrum of the final linear-DB-DIAN (10).

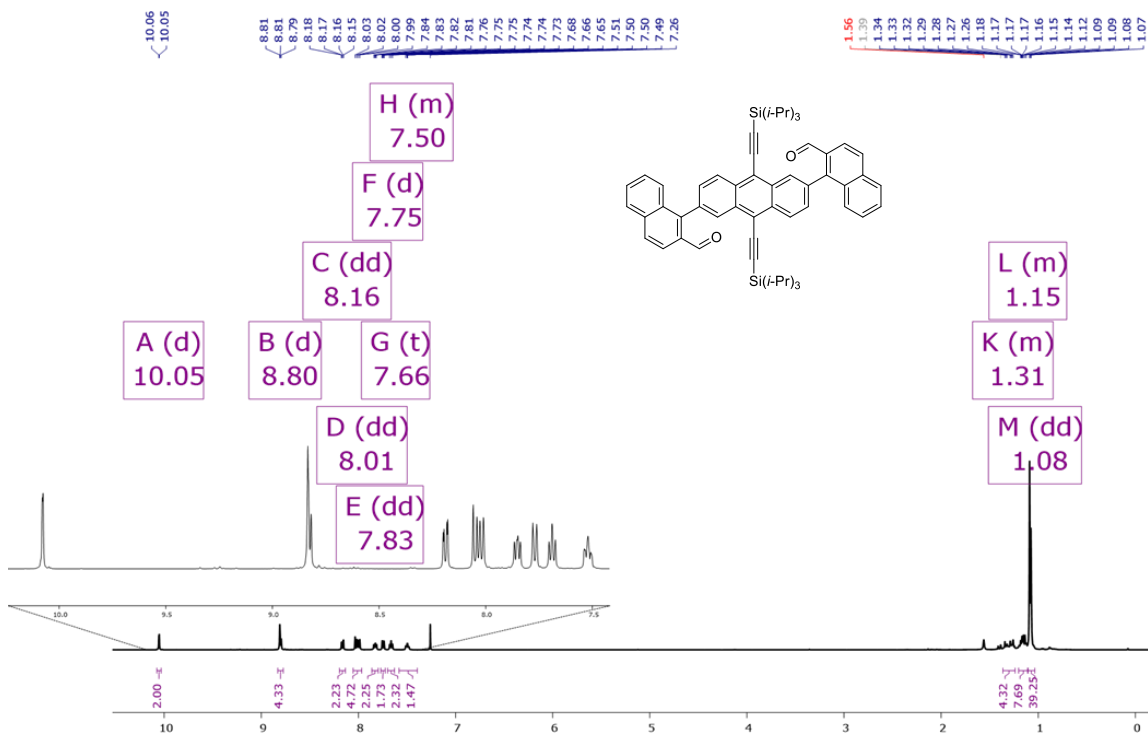


Figure D.23 ^1H NMR (500 MHz CDCl_3) spectrum of the *syn*-dialdehyde (27)

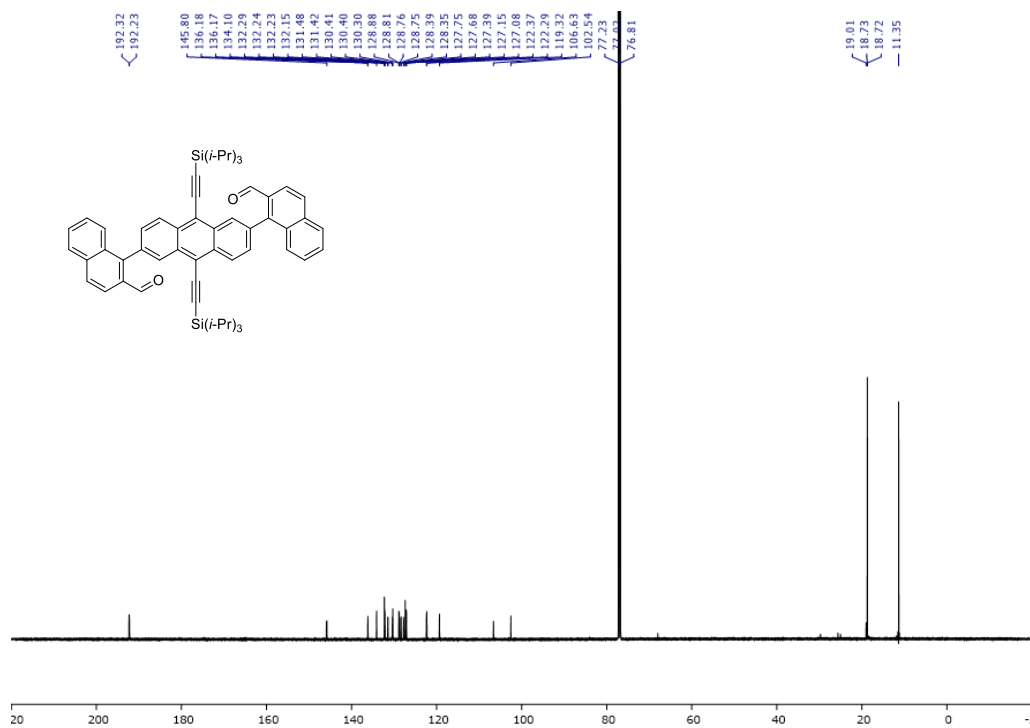


Figure D.24 ^{13}C NMR (151 MHz CDCl_3) spectrum of the *syn*-dialdehyde (27).

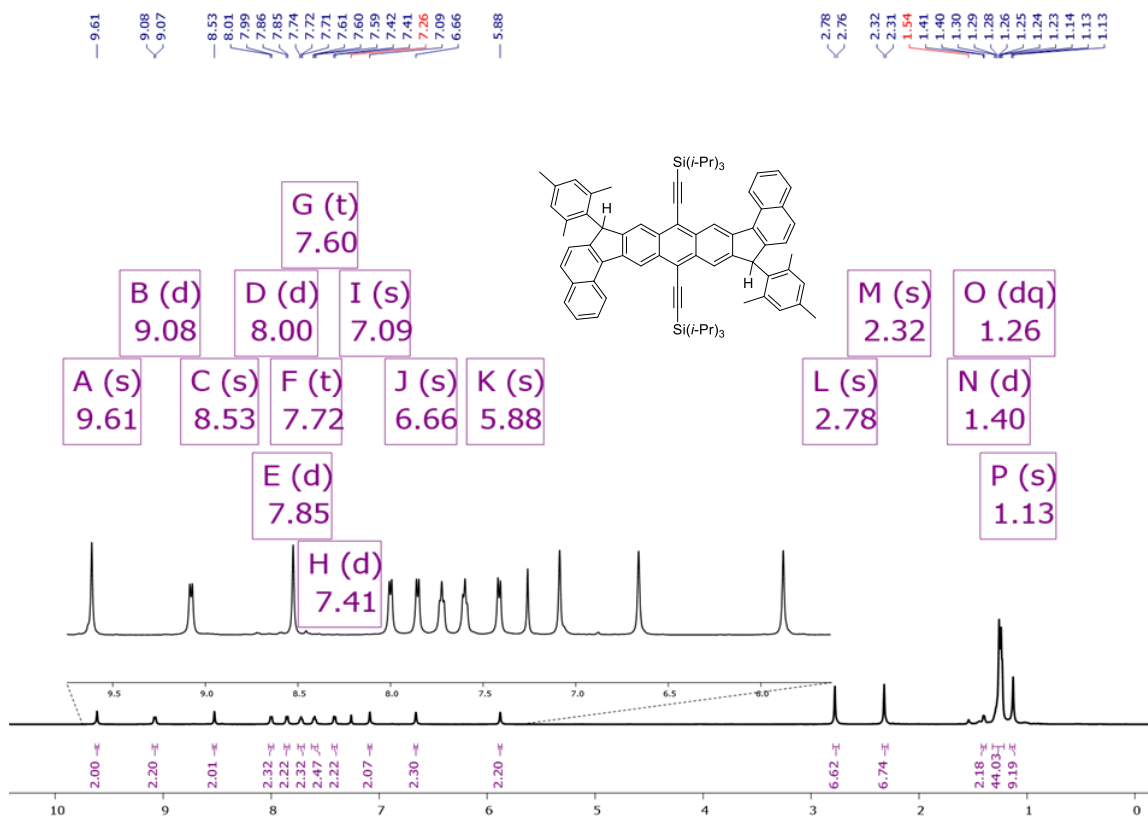


Figure D.25 ^1H NMR (600 MHz CDCl_3) spectrum of the *syn*-DB-DIAn-dihydro (28).

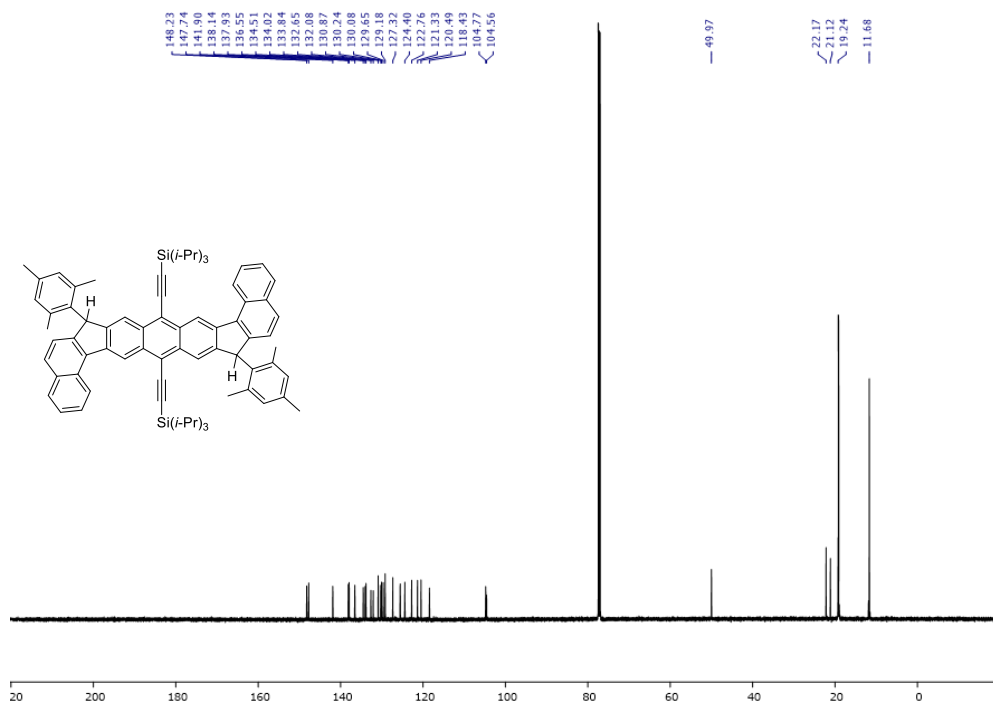


Figure D.26 ^{13}C NMR (151 MHz CDCl_3) spectrum of the *syn*-DB-DIAN-dihydro (28).

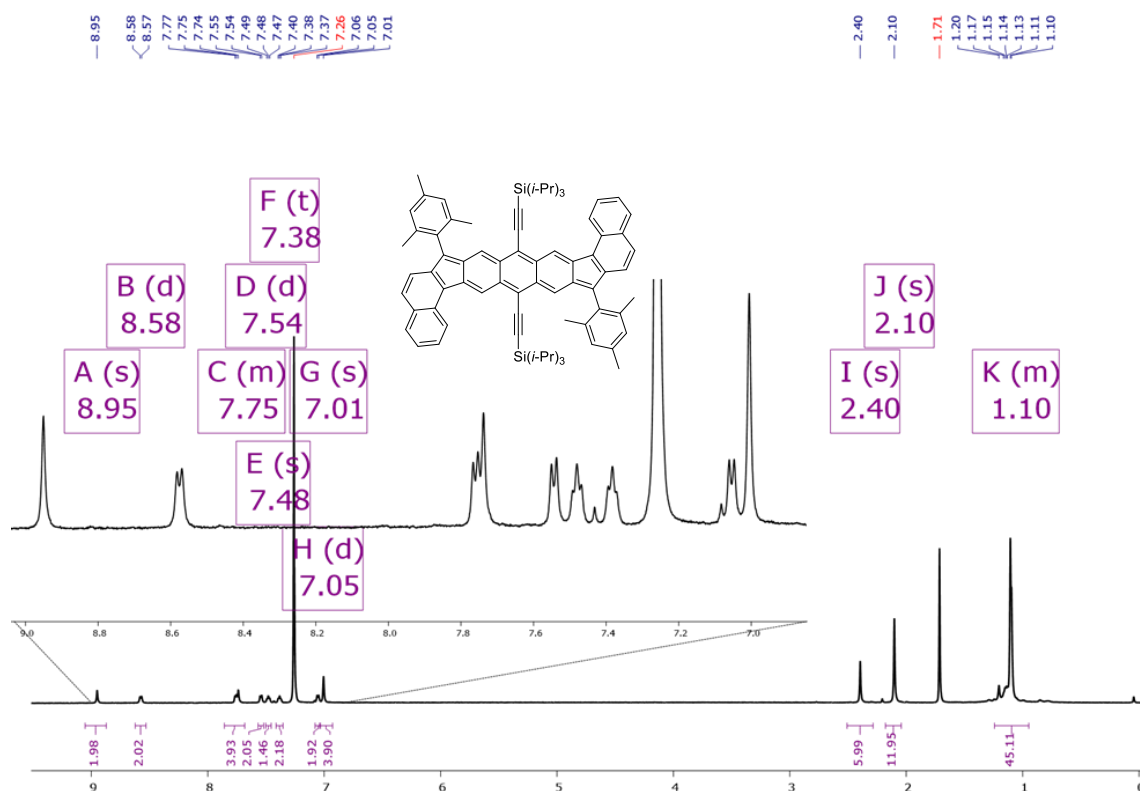


Figure D.27 ^1H NMR (600 MHz CDCl_3) spectrum of the final *syn*-DB-DIAN. Insolubility lead to the inability to collect a ^{13}C spectrum.

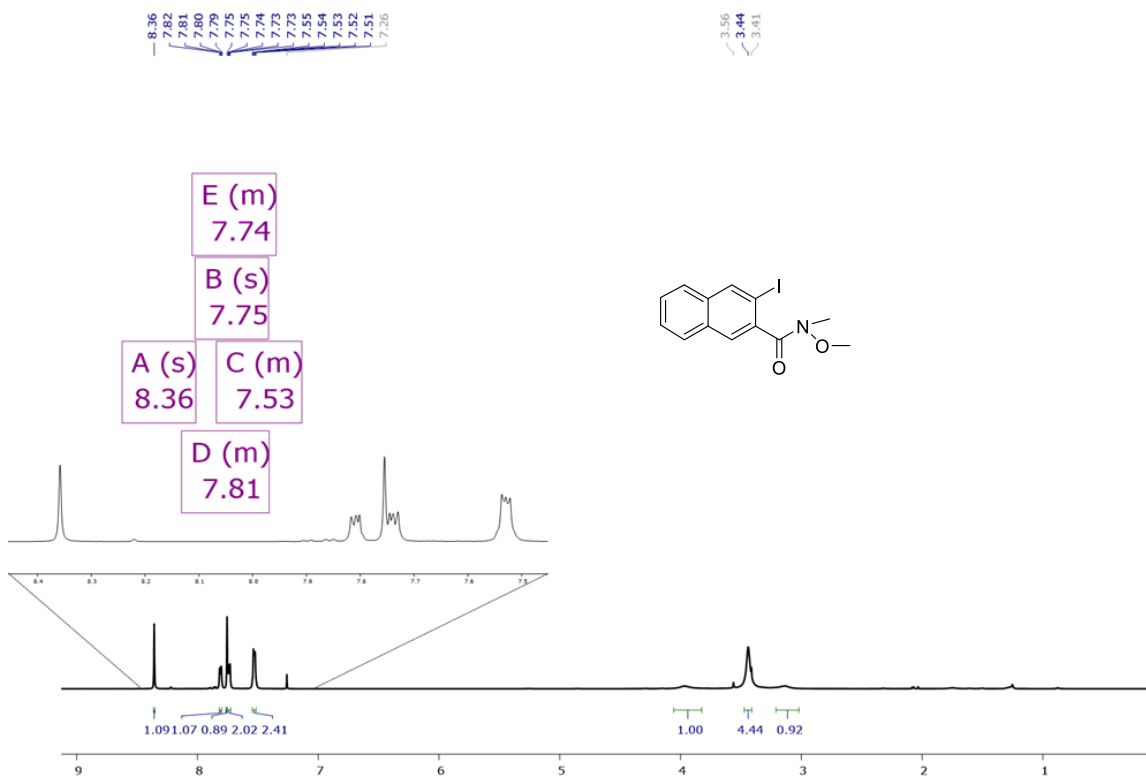


Figure D.28 ¹H NMR (600 MHz CDCl₃) spectrum of the Weinreb Amide intermediate.

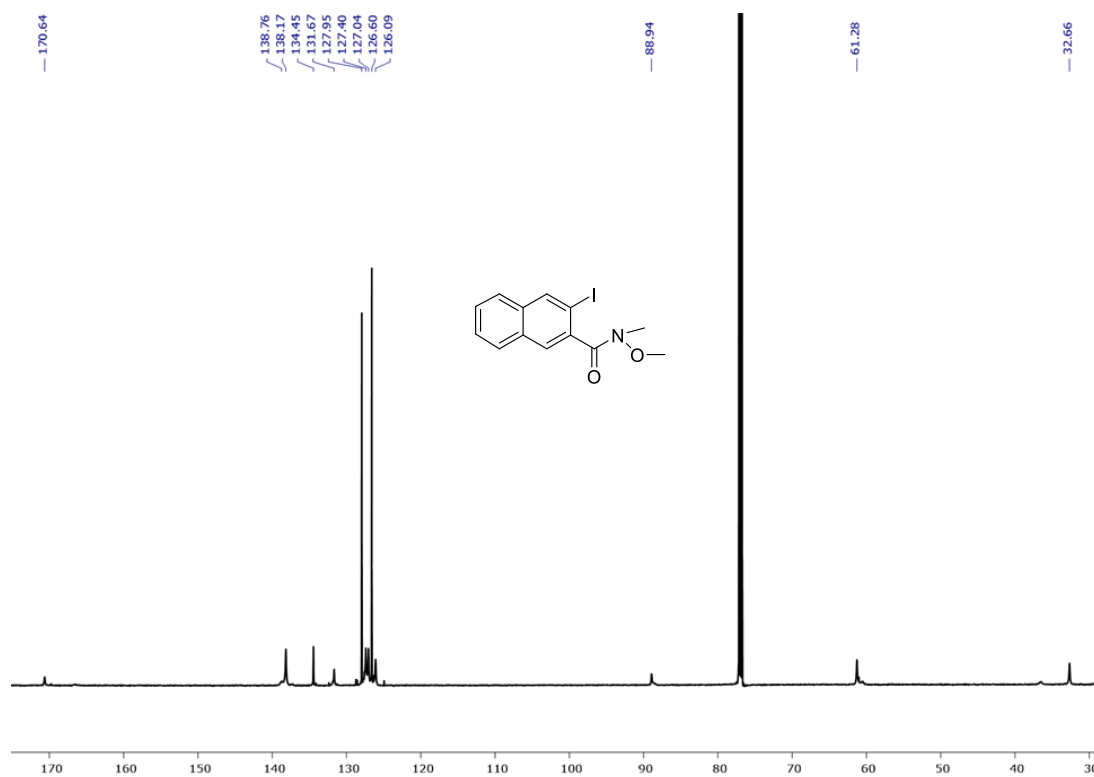


Figure D.29 ¹³C NMR (151 MHz CDCl₃) spectrum of the Weinreb Amide intermediate.

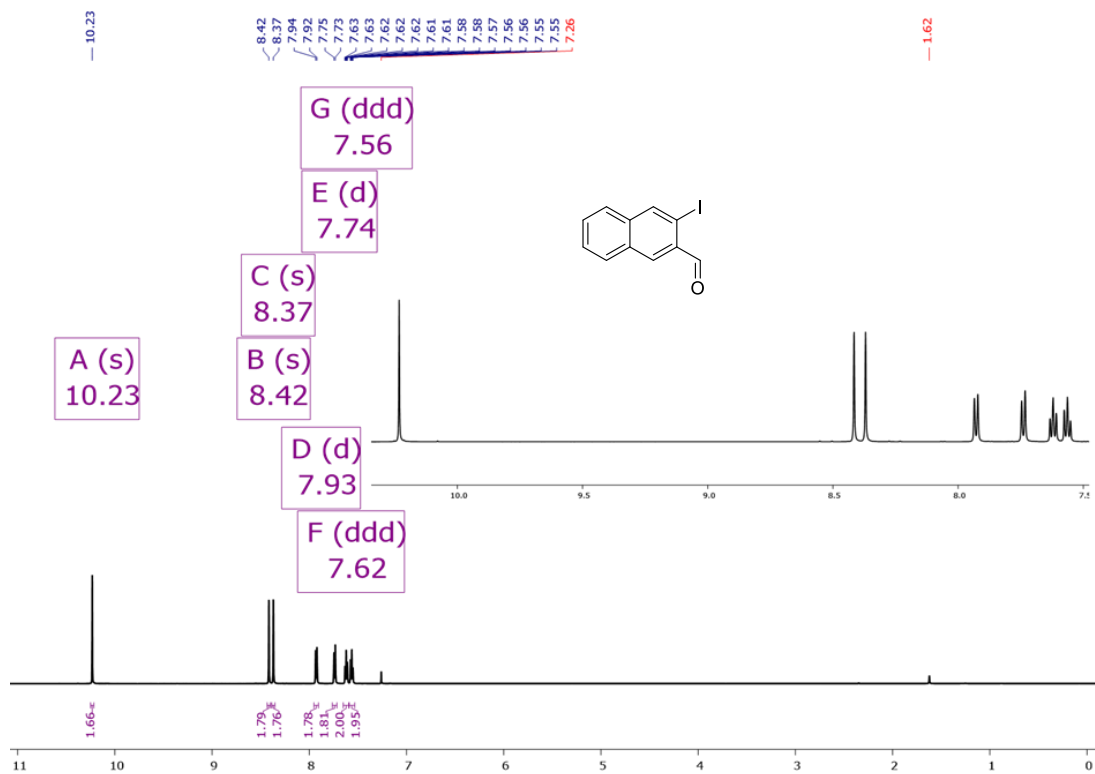


Figure D.30 ^1H NMR (600 MHz CDCl_3) spectrum of 3-iodo-2-naphthaldehyde.

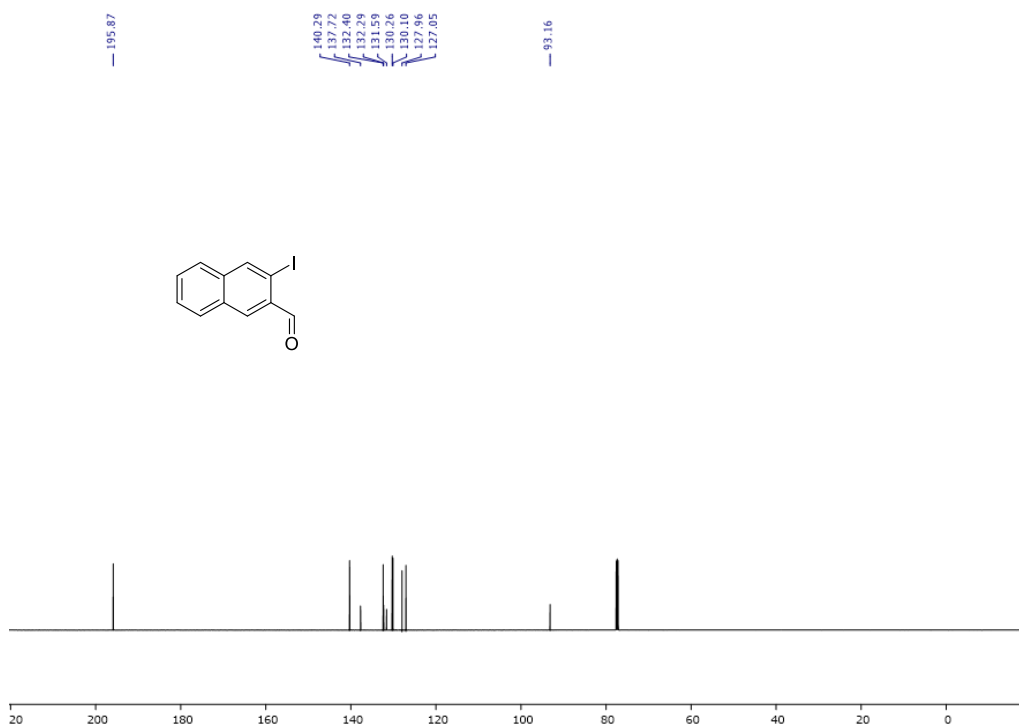


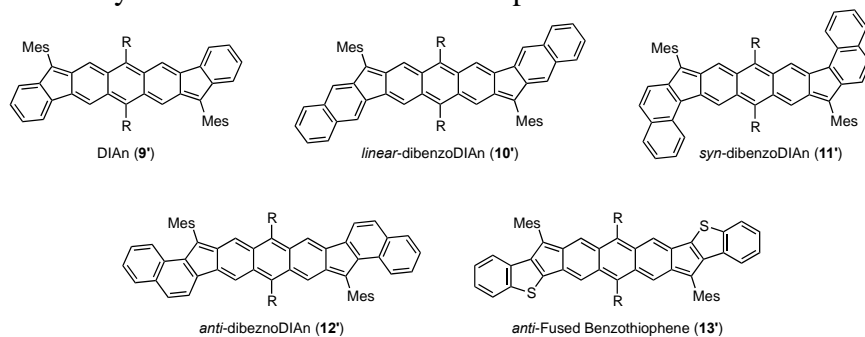
Figure D.31 ^{13}C NMR (151 MHz CDCl_3) spectrum of 3-iodo-2-naphthaldehyde.

Computational Information

General. Geometry optimization and frequency analysis for the singlet and triplet states were performed at the RB3LYP and UB3LYP levels, respectively, using the 6-311G* basis set. Vertical and adiabatic ΔE_{ST} values were evaluated at the spin-flip non-collinear (SF-NC)-TDDFT PBE50/6-311G* level, where ZPVE corrections for the singlet and triplet states were estimated from the results of the frequency analysis calculations at the RB3LYP and UB3LYP levels, respectively. CASCI(2,2) calculations for the estimations of VCI parameters were performed using the molecular orbitals obtained at the (tuned-)LC-RBLYP/6-311G* level, where optimal range-separating parameters μ were determined by so-called IP-tuning scheme for N -electron system. Diradical characters y and corresponding odd-electron density maps were evaluated at the PUHF/6-311G* [denoted as $y(\text{PUHF})$] and tuned-LC-RBLYP-CASCI(2,2)/6-311G* [denoted as $y(\text{CASCI})$] levels. These calculation methods were reported to be useful for analyzing experimental geometries, electronic structures and magnetic properties of open-shell hydrocarbons with intermediate and large diradical characters. Nucleus-independent chemical shift (NICS(1)) values and anisotropy of induced current density (AICD) plots were evaluated at the GIAO- and CSGT-LC-UBLYP/6-311G* level where the same IP-tuned values of μ as the LC-RBLYP-CASCI calculations were employed. SF-TDDFT and CASCI were performed using Q-Chem 4.2 and GAMESS-US program packages, respectively. The remaining calculations were done using Gaussian 09 rev. D01 package.

Table D1. Summary of calculation results for compounds **9-13** when R = H.

	9'	10'	11'	12'	13'
y (PUHF) [-]	0.615	0.625	0.675	0.701	0.725
Vertical ΔE_{ST} [kcal mol ⁻¹]	-11.42	-11.77	-9.60	-8.47	-6.97
Adiabatic ΔE_{ST} [kcal mol ⁻¹]	-6.47	-6.48	-6.00	-5.31	-5.11
Experimental ΔE_{ST} [kcal mol ⁻¹]	-4.2	-4.8	-3.8	-3.2	-3.4
Adiabatic ΔE_{ST} (+ZPVE) [kcal mol ⁻¹]	-5.42	-5.27	-4.99	-4.46	-4.37
Tuned value of μ [bohr ⁻¹]	0.1469	0.1352	0.1356	0.1349	0.1376
y (CASCI) [-]	0.206	0.193	0.223	0.236	0.273
Vertical ΔE_{ST} (CASCI) [kcal mol ⁻¹]	-20.05	-20.73	-16.64	-15.11	-13.25
$ t_{ab} $ [eV]	0.957	0.941	0.865	0.825	0.834
$f_{ST}(y)$ [-]	-0.647	-0.692	-0.589	-0.550	-0.458
$U/2 = K_{gu}^M$ [eV]	1.463	1.379	1.401	1.393	1.573
$(U/2)f_{ST}(y)$ [eV]	-0.946	-0.954	-0.824	-0.767	-0.720
J_{gg}^M [eV]	4.172	3.871	4.013	3.865	4.055
J_{uu}^M [eV]	4.231	4.060	4.092	4.021	4.233
J_{gu}^M [eV]	4.125	3.911	3.950	3.831	3.999
$2K_{ab}$ [eV]	0.077	0.055	0.103	0.112	0.145

Table D2. Summary of calculation results for compounds **9-13** when R = CCSiMe₃.

	9'	10'	11'	12'	13'
y (PUHF) [-]	0.623	0.638	0.686	0.711	0.815
Vertical ΔE_{ST} [kcal mol ⁻¹]	-10.56	-11.09	-8.59	-7.52	-5.78
Adiabatic ΔE_{ST} [kcal mol ⁻¹]	-5.83	-6.15	-5.04	-4.31	-3.98
Adiabatic ΔE_{ST} (+ZPVE) [kcal mol ⁻¹]	-4.71	-5.09	-4.16	-3.45	-3.41
Experimental ΔE_{ST} [kcal mol ⁻¹]	-4.2	-4.8	-3.8	-3.2	-3.4
Tuned value of μ [bohr ⁻¹]	0.1348	0.1258	0.1261	0.1254	0.1276
y (CASCI) [-]	0.213	0.198	0.235	0.250	0.298
Vertical ΔE_{ST} (CASCI) [kcal mol ⁻¹]	-19.14	-20.03	-15.57	-14.05	-11.66
$ t_{ab} $ [eV]	0.916	0.905	0.818	0.781	0.774
$f_{ST}(y)$ [-]	-0.621	-0.674	-0.554	-0.513	-0.404
$U/2 = K_{gu}^M$ [eV]	1.435	1.348	1.378	1.377	1.572
$(U/2)f_{ST}(y)$ [eV]	-0.891	-0.909	-0.762	-0.706	-0.635
J_{gg}^M [eV]	4.082	3.772	3.954	3.822	4.042
J_{uu}^M [eV]	4.048	3.902	3.915	3.854	4.036
J_{gu}^M [eV]	4.004	3.797	3.847	3.741	3.910
$2K_{ab}$ [eV]	1.435	0.041	0.087	0.096	1.572

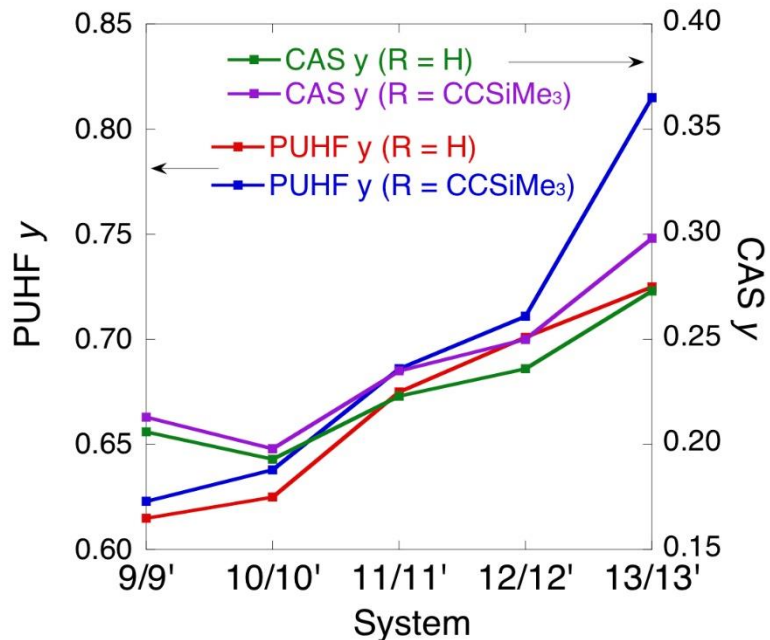


Figure D.32 Comparison of calculated y values.

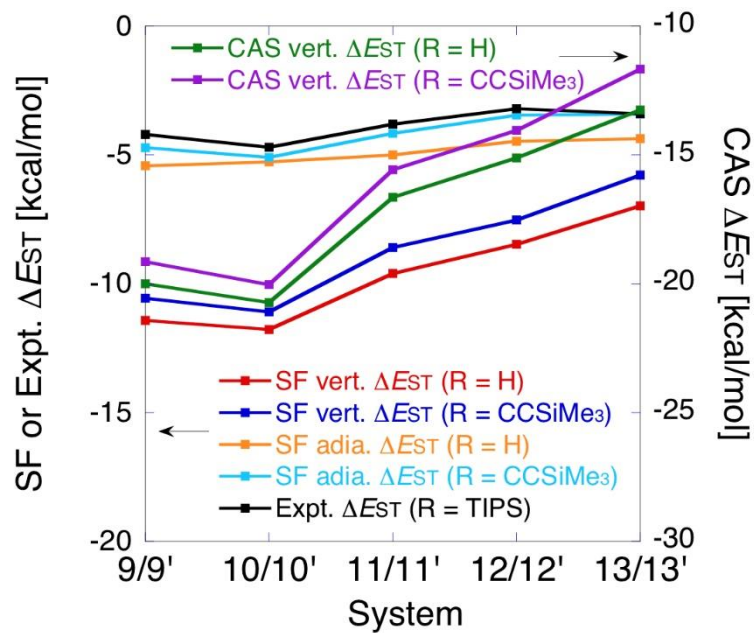
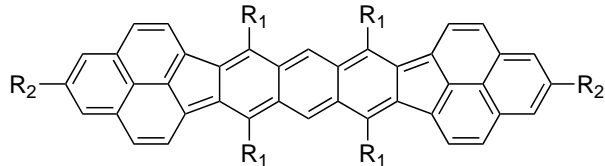


Figure D.33 Comparison of calculated and experimental ΔE_{ST} gaps.

Table D3. Summary of calculation results for bisphenalenyl-fused anthracene derivatives (BPLA).



	$R_1 = R_2 = H$	$R_1 = Ph / R_2 = H$	$R_1 = Ph / R_2 = t-Bu$
y (PUHF) [-]	0.887	0.888	0.883
Vertical ΔE_{ST} [kcal mol ⁻¹]	-2.81	-2.77	-2.75
Adiabatic ΔE_{ST} [kcal mol ⁻¹]	-1.81	-1.83	-1.80
Adiabatic ΔE_{ST} (+ZPVE) [kcal mol ⁻¹]	-1.02	-1.13	-1.10
Tuned value of μ [bohr ⁻¹]	0.1558	0.1406	0.1328
y (CASCI) [-]	0.445	0.439	0.441
Vertical ΔE_{ST} (CASCI) [kcal mol ⁻¹]	-4.72	-4.95	-4.91
$ t_{ab} $ [eV]	0.468	0.469	0.467
$f_{ST}(y)$ [-]	-0.202	-0.208	-0.206
$U/2 = K_{gu}^M$ [eV]	1.401	1.382	1.385
$(U/2)f_{ST}(y)$ [eV]	-0.283	-0.288	-0.285
J_{gg}^M [eV]	3.303	3.271	3.261
J_{uu}^M [eV]	3.327	3.288	3.275
J_{gu}^M [eV]	3.237	3.206	3.196
$2K_{ab}$ [eV]	0.079	0.074	0.072

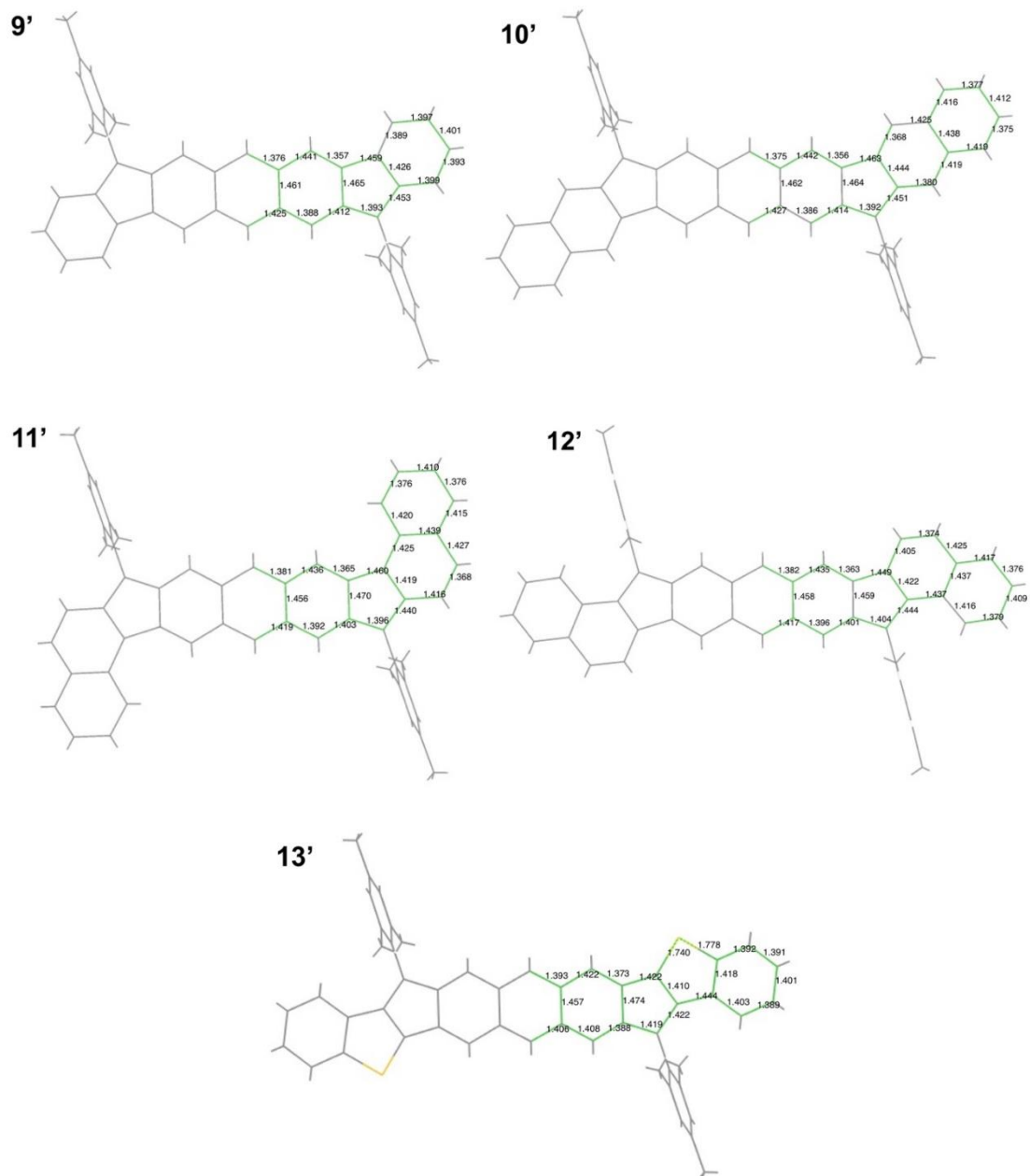


Figure D.34 Selected bond lengths (Å) of **9'-13'** (R = H) in the singlet state calculated at the RB3LYP/6-311G* level.

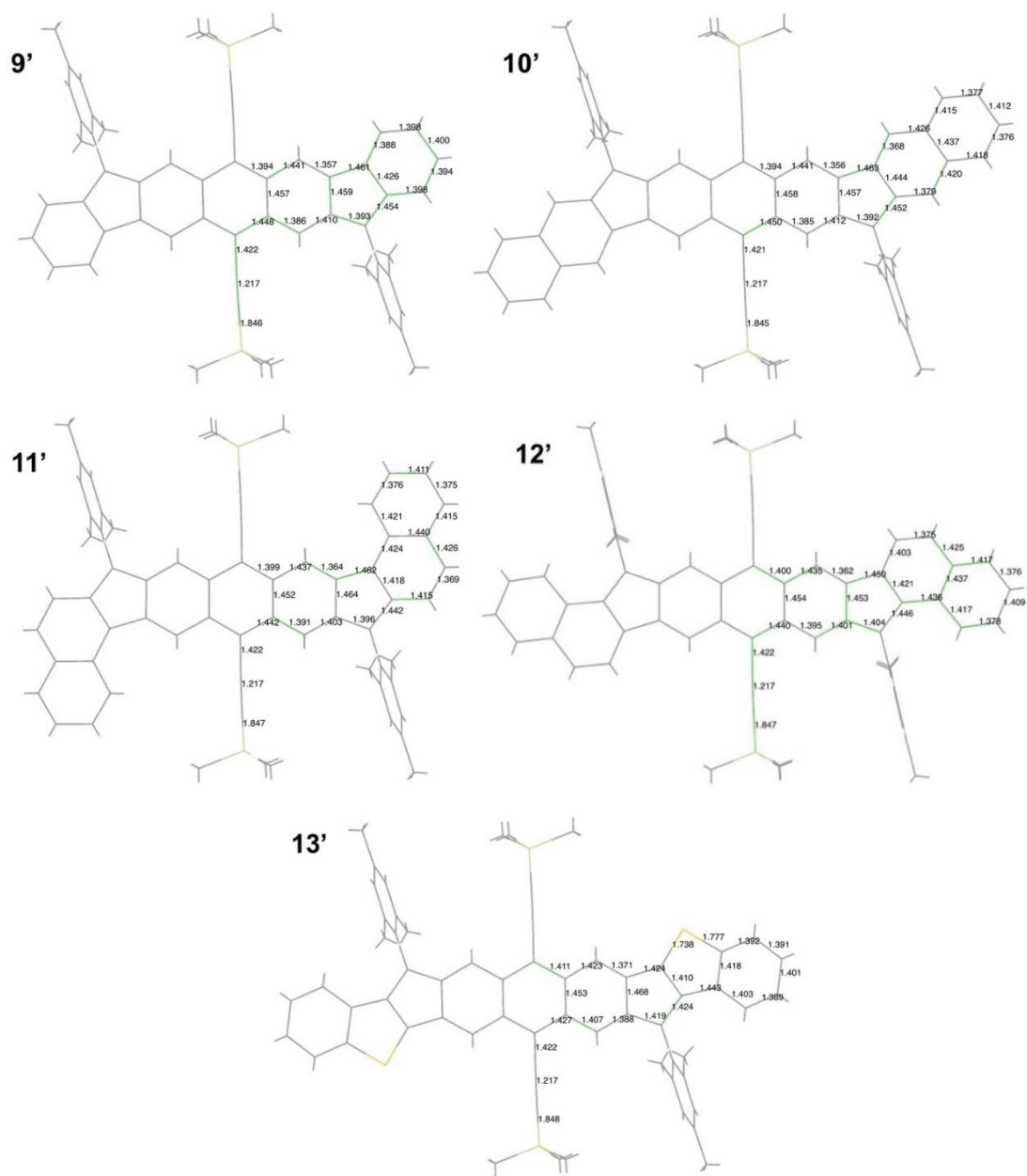


Figure D.35 Selected bond lengths (Å) of **9'-13'** (R = CCSiMe₃) in the singlet state calculated at the RB3LYP/6-311G* level.

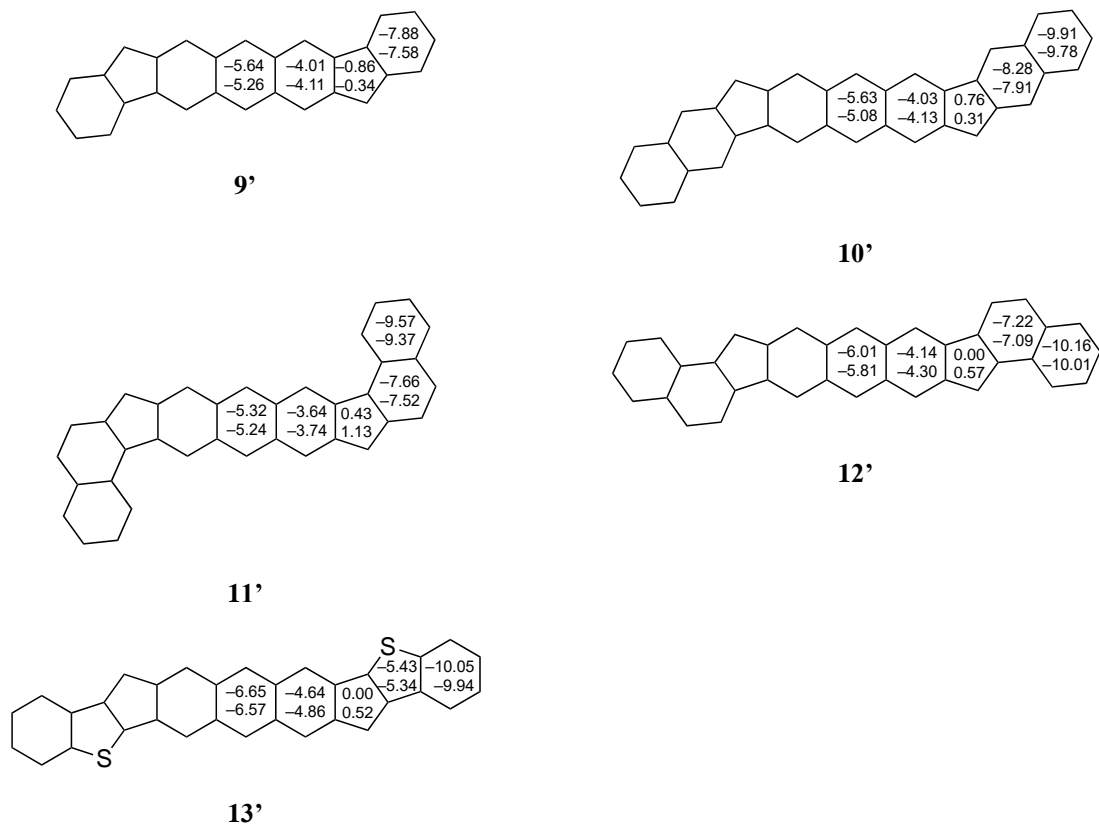


Figure D.36 NICS(1) values [ppm] of **9'**-**13'** calculated at the GIAO-LC-UBLYP/6-311G* using the tuned values of μ obtained at the LC-RBLYP level. Upper and lower values in each ring correspond to the results of R = H and R = CCSiMe₃, respectively.

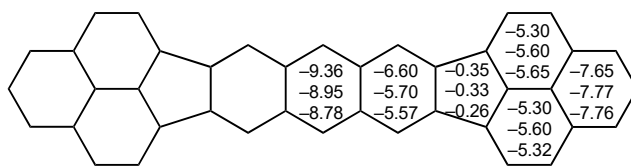


Figure D.37 NICS(1) values [ppm] of diphenalenyl derivatives (BPLA) calculated at the GIAO-LC-UBLYP/6-311G* using the tuned values of μ obtained at the LC-RBLYP level. Upper, middle and lower values in each ring correspond to the results of R₁ = R₂ = H, R₁ = Ph / R₂ = H and R₁ = Ph / R₂ = *t*-Bu, respectively.

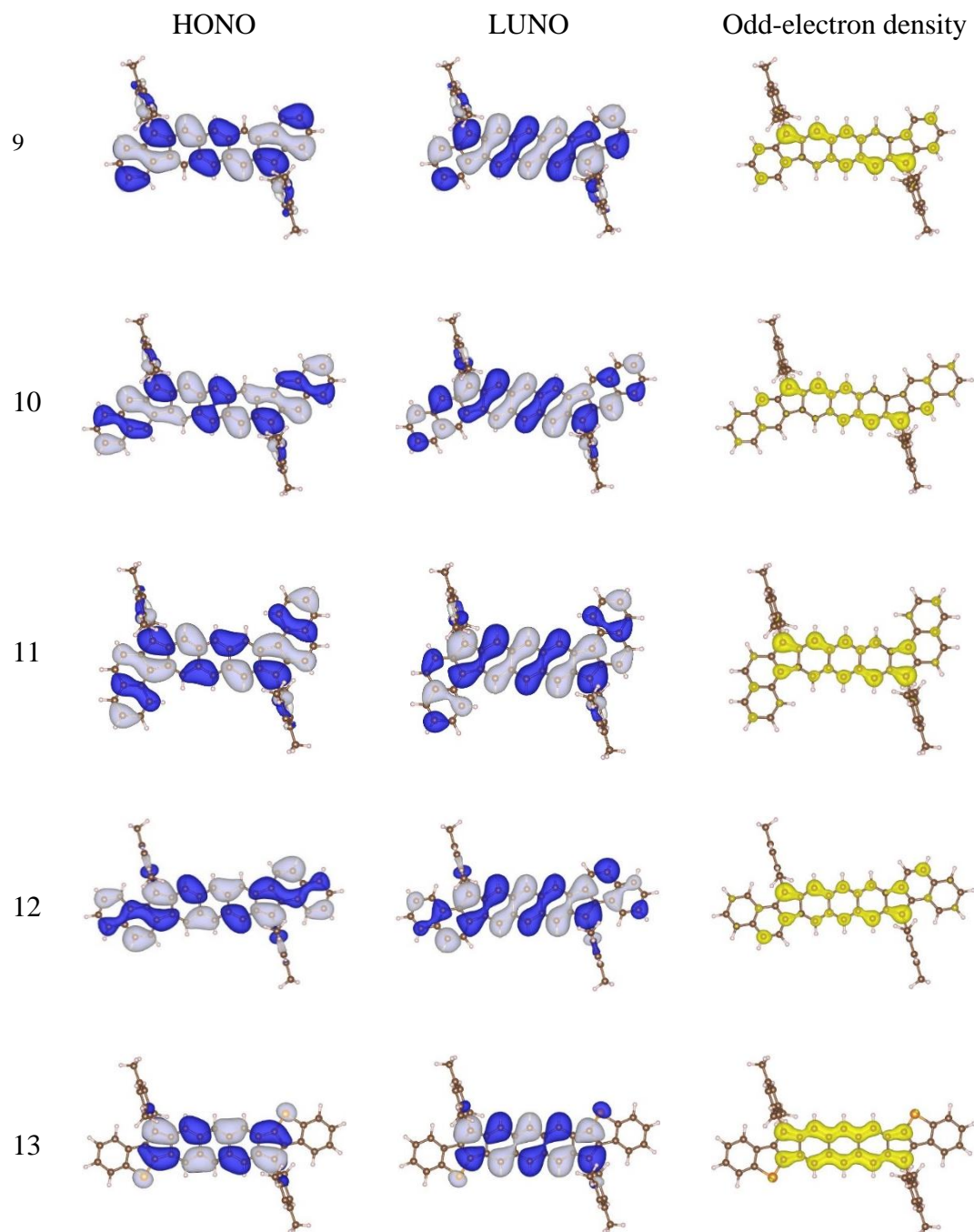


Figure D.38 Spatial distributions of HONO, LUNO and odd-electron density for **9'-13'** with R = H calculated at the tuned-LC-RBLYP-CASCI(2,2)/6-311G* level. Blue/white surfaces of NO maps represent the isosurfaces with the contour values of +0.01/-0.01 a.u. Yellow surface of odd-electron density map represents the isosurface with the contour value of 0.0005 a.u

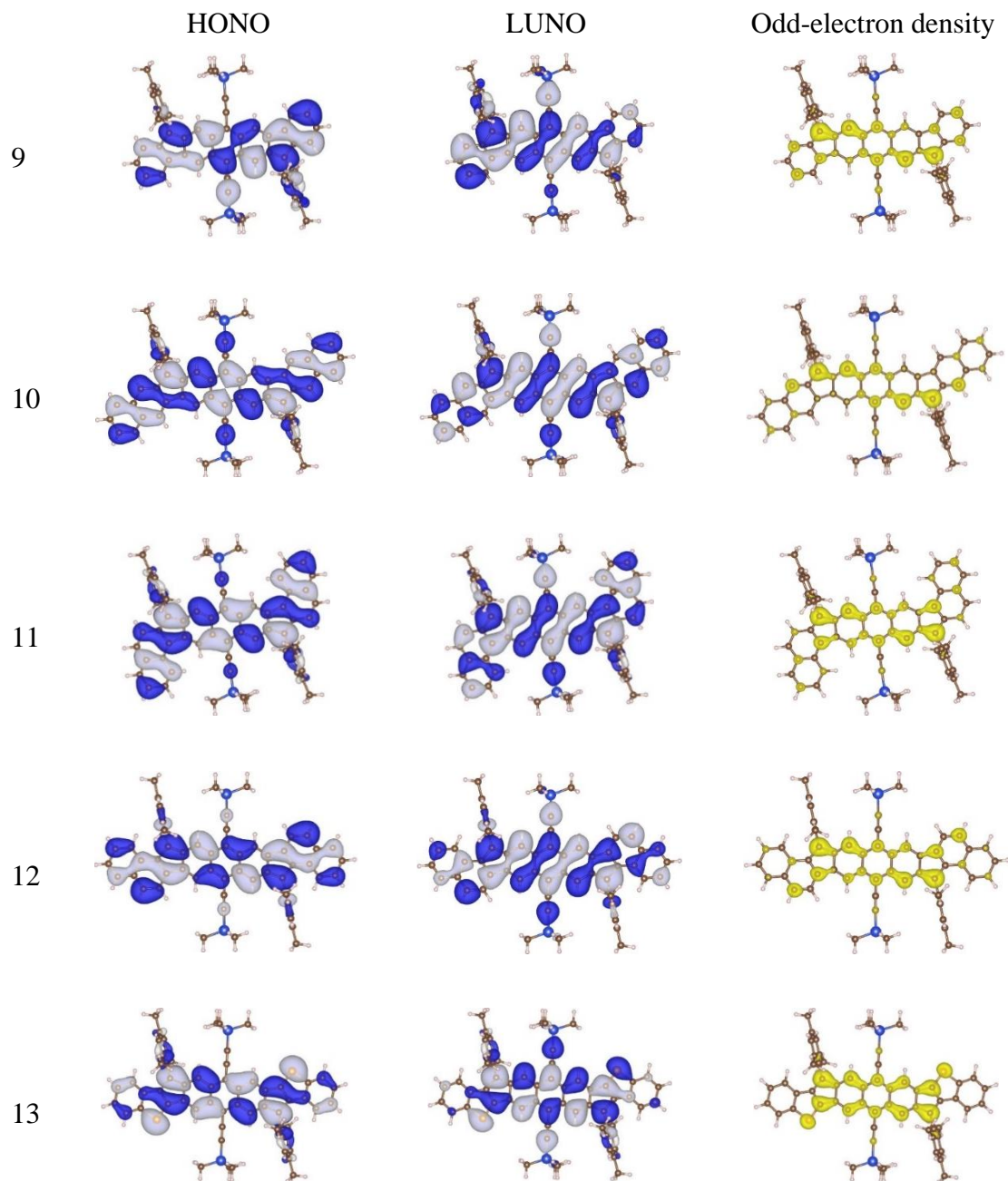


Figure D.39 Spatial distributions of HONO, LUNO and odd-electron density for 9'-13' with R = CCSiMe₃ calculated at the tuned-LC-RBLYP-CASCI(2,2)/6-311G* level. Blue/white surfaces of NO maps represent the isosurfaces with the contour values of +0.01/-0.01 a.u. Yellow surface of odd-electron density map represents the isosurface with the contour value of 0.0005 a.u.

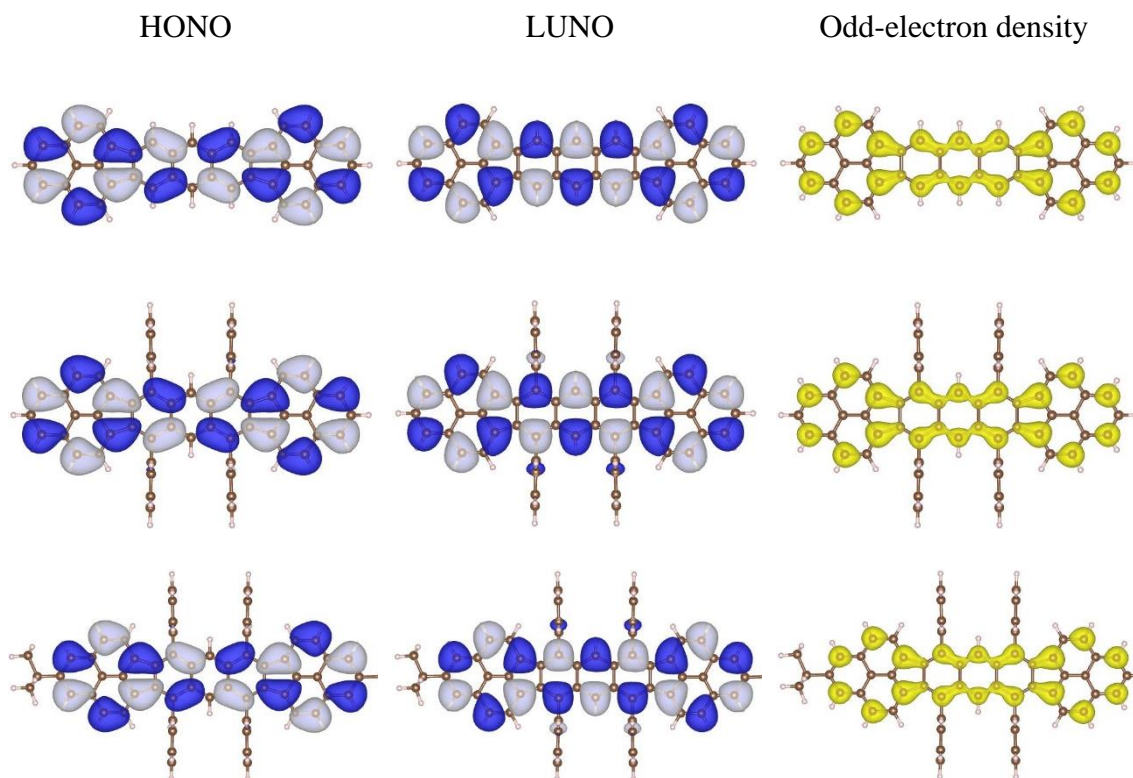


Figure D.40 Spatial distributions of HONO, LUNO and odd-electron density for derivatives of BPLA with $R_1 = R_2 = H$ (upper), $R_1 = Ph/R_2 = H$ (middle) and $R_1 = Ph/R_2 = t\text{-Bu}$ (lower) calculated at the tuned-LC-RBLYP-CASCI(2,2)/6-311G* level. Blue/white surfaces of NO maps represent the isosurfaces with the contour values of $+0.01/-0.01$ a.u. Yellow surface of odd-electron density map represents the isosurface with the contour value of 0.0005 a.u.

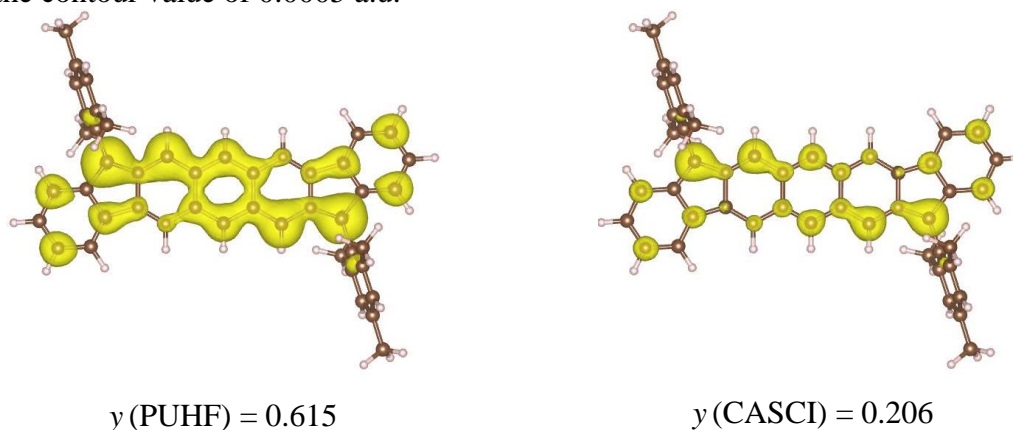


Figure D.41 Comparison of odd-electron density maps for **9'** with $R = H$ calculated at the PUHF/6-311G* and tuned-LC-RBLYP-CASCI(2,2)/6-311G* levels. Yellow surface of odd-electron density map represents the isosurface with the contour value of 0.0005 a.u.

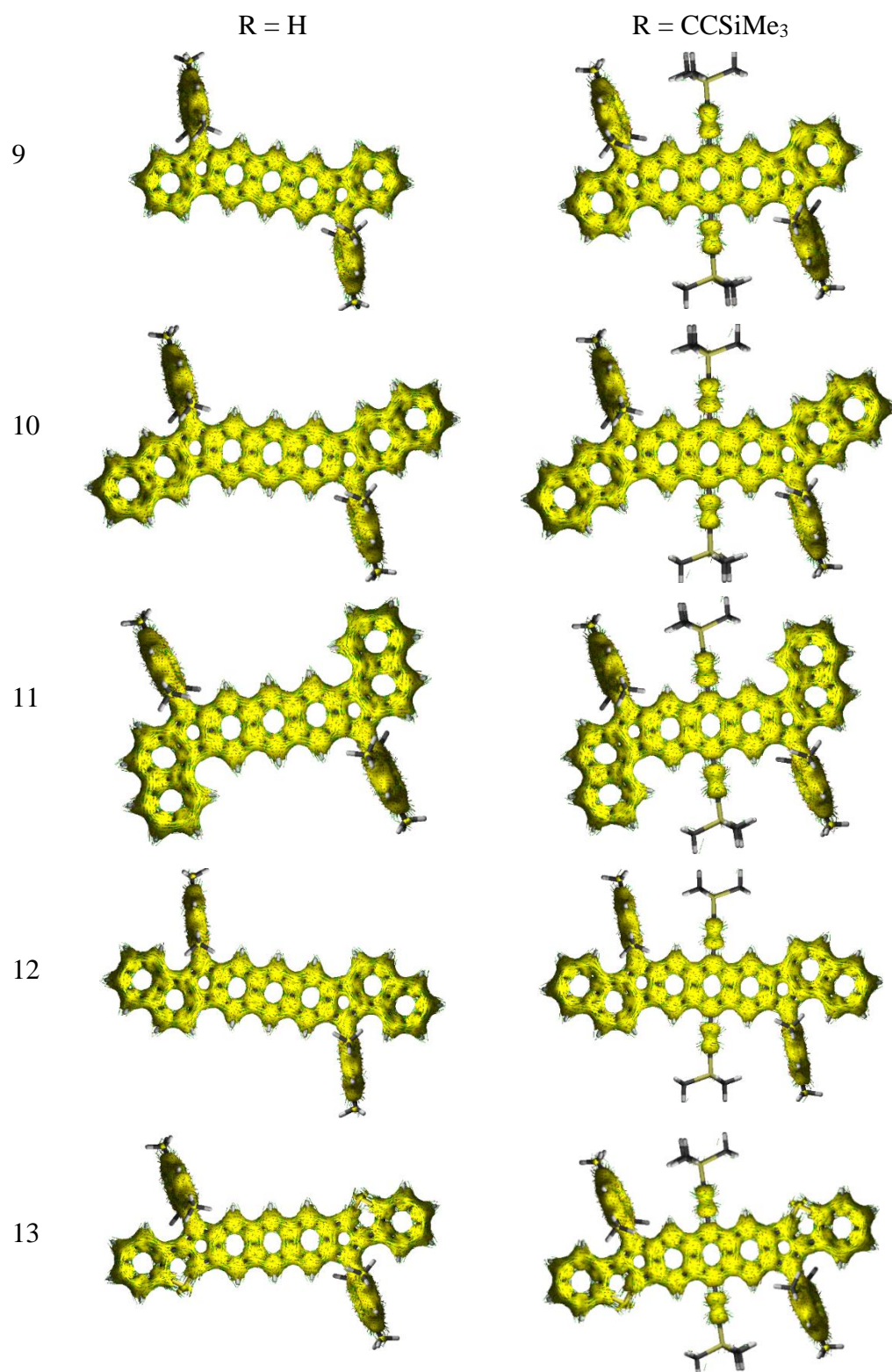
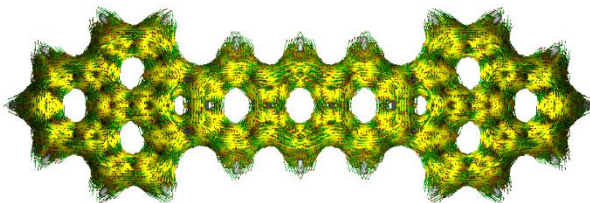
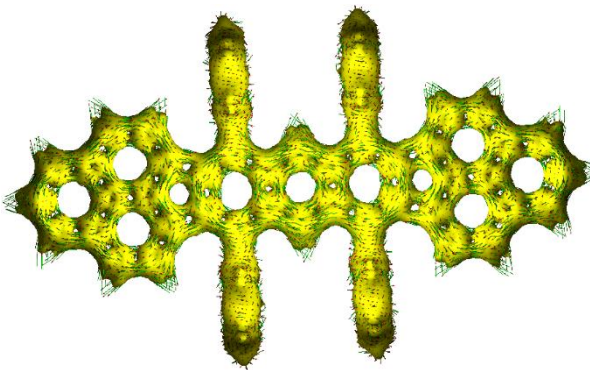


Figure D.42 Anisotropy of induced current density (AICD) maps for **9'**-**13'** calculated at the CSGT-LC-UBLYP/6-311G* using the tuned values of μ obtained at the LC-RBLYP level.

$R_1 = R_2 = H$



$R_1 = Ph / R_2 = H$



$R_1 = Ph / R_2 = t-$
Bu

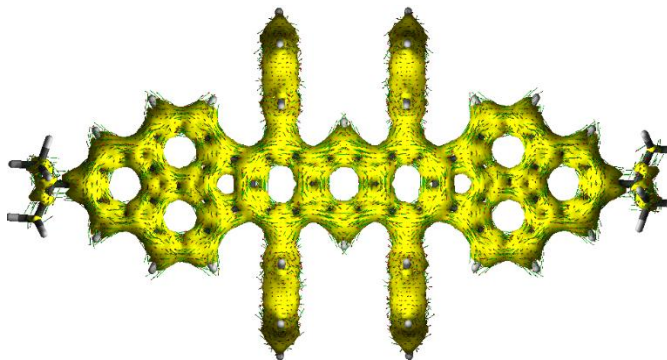


Figure D.43 Anisotropy of induced current density (AICD) maps for derivatives of BPLA calculated at the CSGT-LC-UBLYP/6-311G* using the tuned values of μ obtained at the LC-RBLYP level.

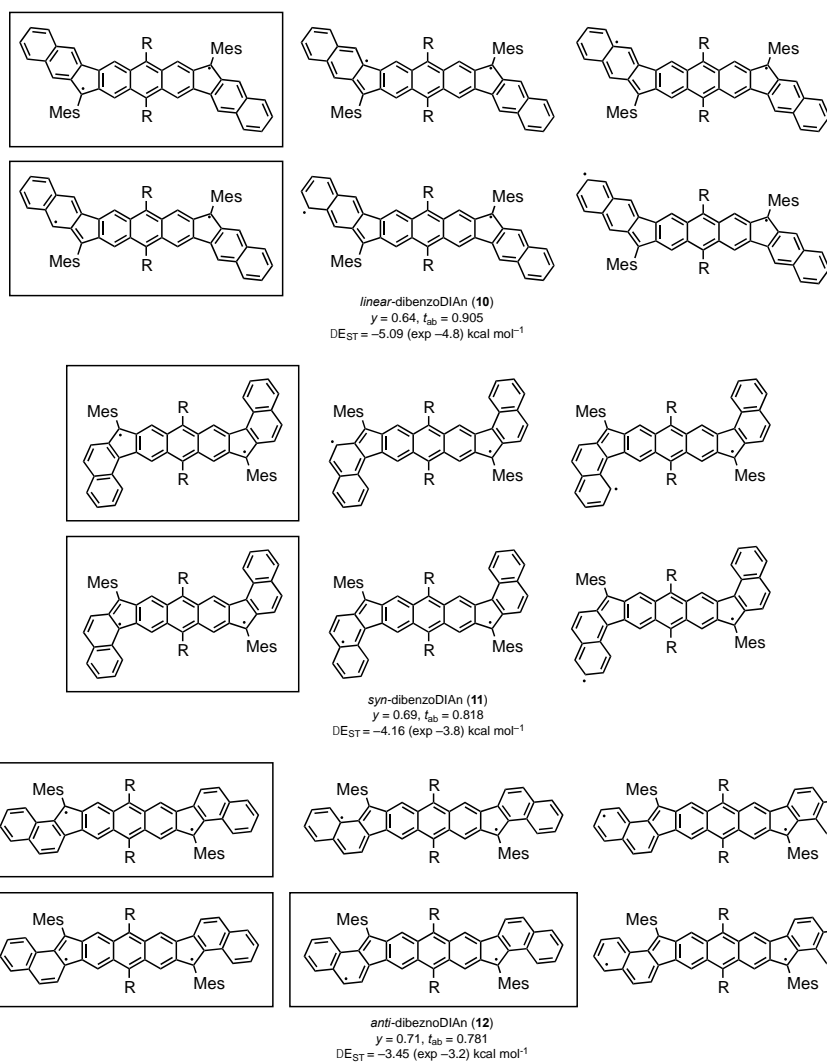


Figure D.44 Shown above are the main diradical resonance forms that can be written in **10-12**. Since all three isomers contain the same number of Clar sextets in the open shell form (three), one must examine radical stability as it is delocalized into the appended rings. In **10** and **11** only two resonance forms preserve aromaticity in the external naphthalene, whereas three resonance forms for **12** retain the aromaticity in the external naphthalene; thus, **12** should be the most diradical of the three constitutional isomers, and its calculated y value reflects this. Deciding between **10** and **11** is trickier since both have only two preferred resonance forms. For **10** the forms are triply benzylic (top) and singly benzylic/singly allylic (bottom) versus triply benzylic (top) and doubly benzylic/singly allylic (bottom) for **11**; thus, **11** should be more open shell than **10**, and again the calculated y values reflect this. The above analysis is very qualitative, which supports the need for the detailed, quantitative computational analysis reported herein.

Calculated Raman band assignments. It is well known that DFT calculations on singlet diradicals do not provide reliable Raman spectra (the BS symmetry approach works well for relative energies but the wavefunction and geometric properties are not good, and by extrapolation, Raman intensities (and spectra) are unreliable). Therefore, we cannot support our assignment and discussion based on the theoretical Raman spectra of **10-13**. In order to solve this, we have carried out quantum chemical calculations at the B3LYP/6-31G** level for **25** and **28**, which are the dihydrogenated analogues of **10** and **11**, respectively, and are closed-shell structure on which theoretical Raman spectra at the B3LYP/6-31G** level work very well. We take the case of **25** as an example to proceed with the full explanation of the assignment procedure. Figure D.45 and D.46 shows the theoretical and experimental Raman spectra of **25** indicating that the theoretical spectrum reproduces very well the experimental vibrational Raman fingerprint. This assures to make an accurate assignment of the main bands based on the theoretical vibrational eigenvectors (see Figure D.47).

Based on these eigenvectors, only the theoretical bands at 1624 cm^{-1} (experimentally 1629 cm^{-1}) and that at 1516 cm^{-1} (experimentally 1540 cm^{-1}) correspond to motions mostly containing CC stretching vibrations of the central anthracene. On the other hand, the two bands at 1583 cm^{-1} (experimentally at 1583 cm^{-1}) and 1562 cm^{-1} (experimentally at 1565 cm^{-1}) are due mostly to CC stretching modes of the external naphthalenes.

Obviously, vibrational mixing of the CC stretching modes of the two aromatic groups (naphthalene and anthracene) unavoidably occurs. This mixing is expected to be stronger in the case of **25** as the two groups are similarly aromatic. However, this mixing between vibrations of analogue aromatic groups will be smaller or minimal in the case of diradical compound **10** (diradical equivalent of **25**) as the central anthracene is partially quinoidal. Assuming that the number of CC skeletal normal modes in **10** and **25** should be equals in this $1700\text{-}1500\text{ cm}^{-1}$ region, a one-to-one correspondence between the Raman bands of the two compounds can be made such as proposed in Figure D.47 (arrows). From this correspondence, the band at 1581 cm^{-1} of **10** can be ascribed to an anthracene-based CC stretching, or $\nu_{\text{anth}}(\text{CC})$. Following the same procedure, the band to be assigned in **11** as the $\nu_{\text{anthra}}(\text{CC})$ Raman band is that at 1589 cm^{-1} . For **12** there is no dihydrogenated

compound available, so the assignment relies on the trend with **10** and **11** such as shown in Figure 6B on the main manuscript.

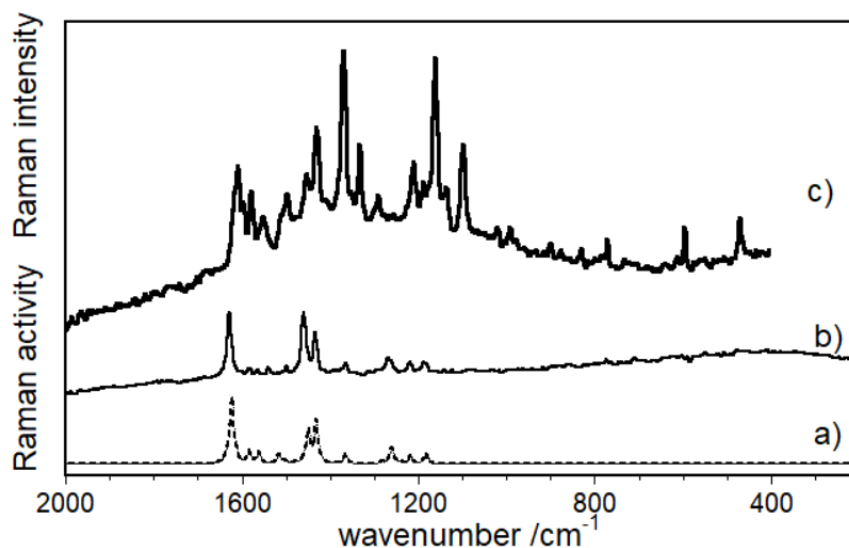


Figure D.45 Comparison of the B3LYP/6-31G** theoretical spectrum of **25** (a) and its experimental one (b) together with the Raman spectrum of **10** (c).

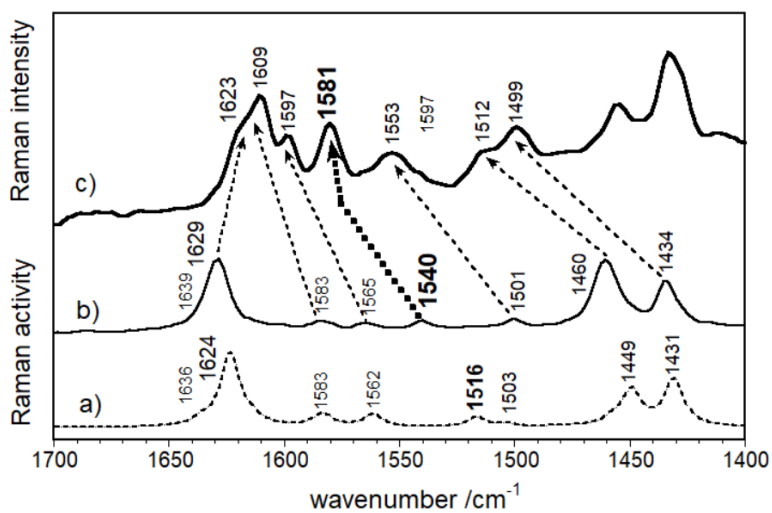


Figure D.46 Band correlation between the B3LYP/6-31G** theoretical spectrum of **25** (a) and its experimental one (b) and between the Raman bands of **25** (b) and **10** (c).

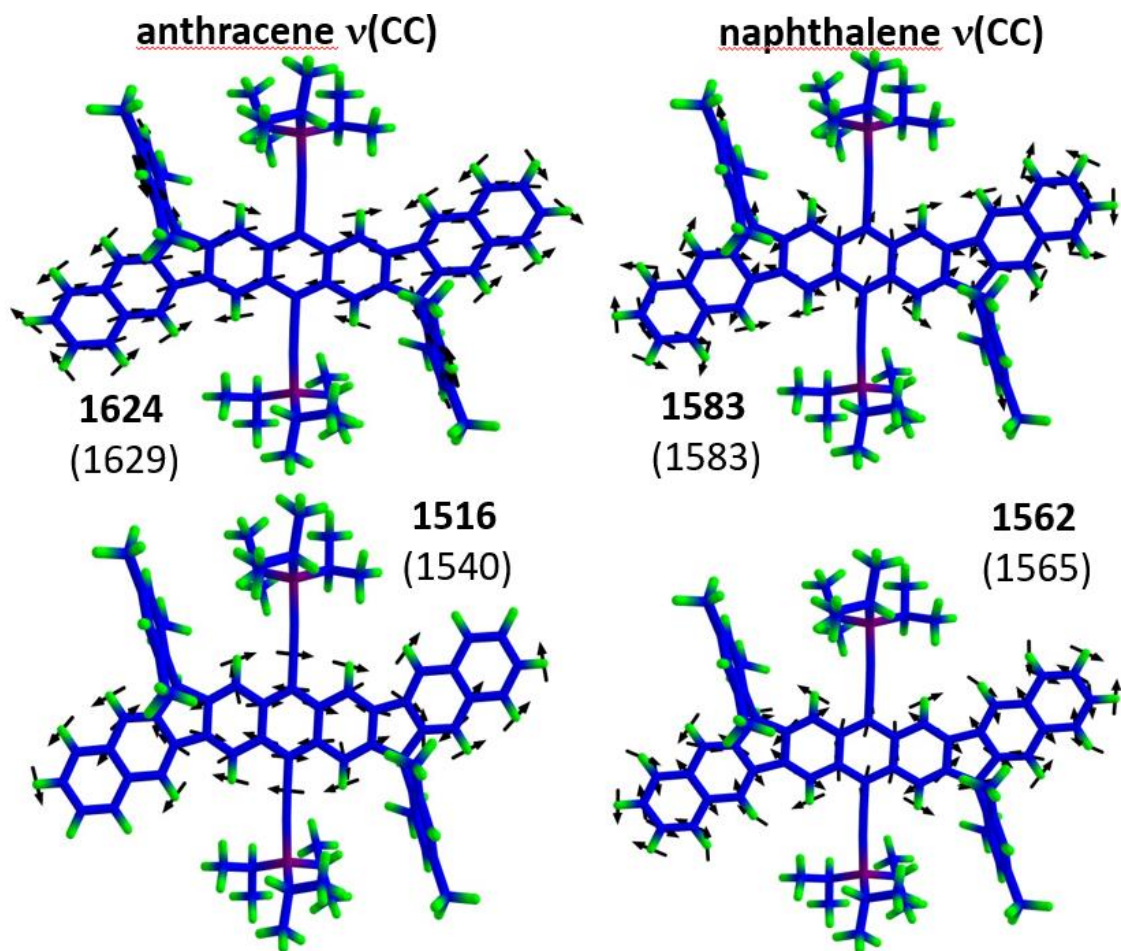


Figure D.47 B3LYP/6-31G** vibrational eigenvectors associated with the main Raman bands in the region of 1650-1500 cm^{-1} of the theoretical spectrum of **25**.

Additional Spectroscopy

VT NMR. Approximately 10 mg of each new **DIAn** derivative was dissolved in CDCl_3 and placed in an NMR tube. The spectra were acquired on a Varian Inova 500 MHz spectrometer that was cooled to 0, -15, -30, -45, -55, followed by warming back to 25 °C to reacquire a room temperature spectrum. Additionally, *anti*-DB-DIAn (**12**) was cooled in $\text{THF-}d_8$ to try and get complete resolution of the aromatic signals at -100 °C. The *linear*-DB-DIAn (**10**) also required a second VT-NMR experiment where the sample was heated in $(\text{CDCl}_2)_2$ to 140 °C to begin to populate the triplet state.

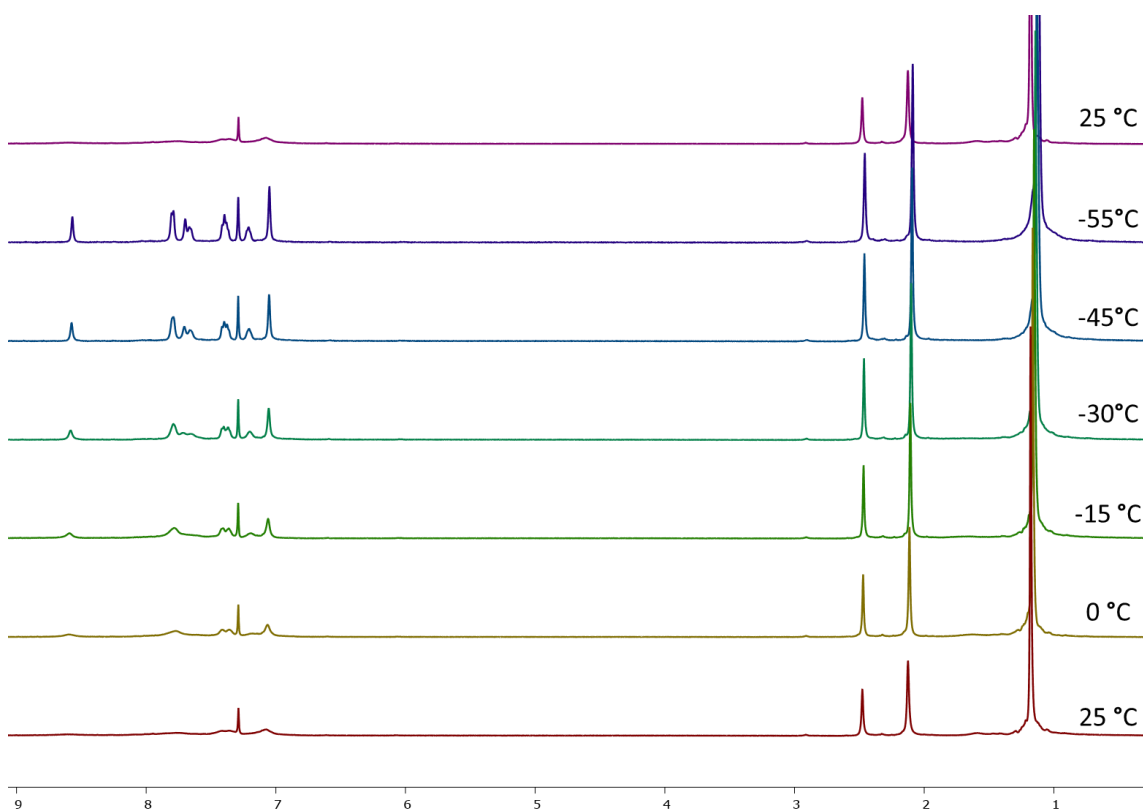


Figure D.48 VT ^1H NMR full spectra of *anti*-DB-DIAn (**12**) in CDCl_3 showing thermal depopulation of the paramagnetic triplet state at low temperatures.

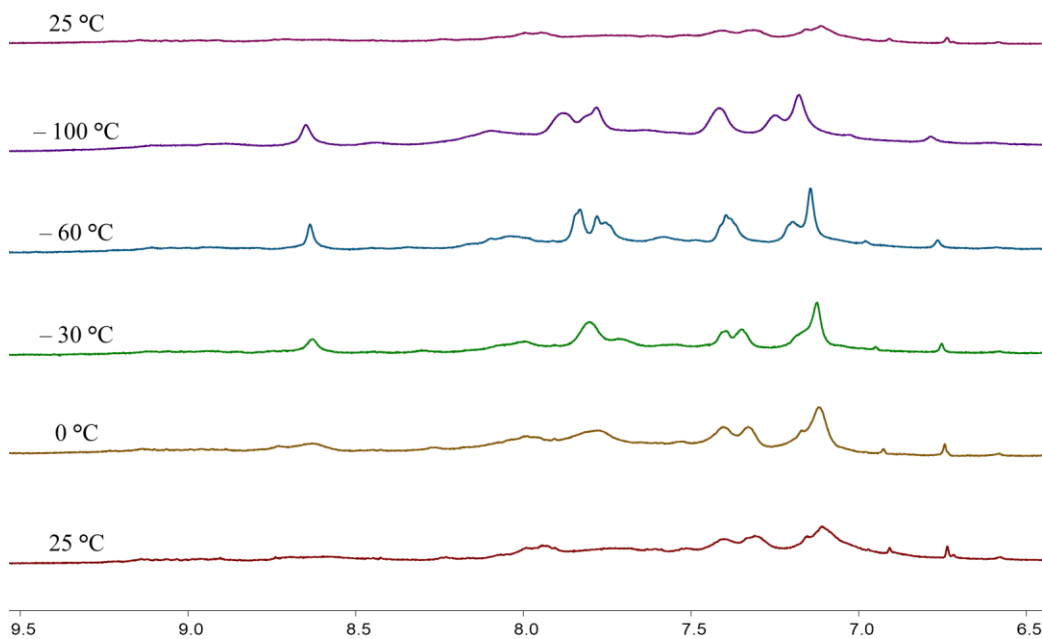


Figure D.49 VT ^1H NMR spectra of the aromatic region of *anti*-DB-DIAN (**12**) in $\text{THF-}d_8$ showing thermal depopulation of the paramagnetic triplet state at extremely low temperatures.

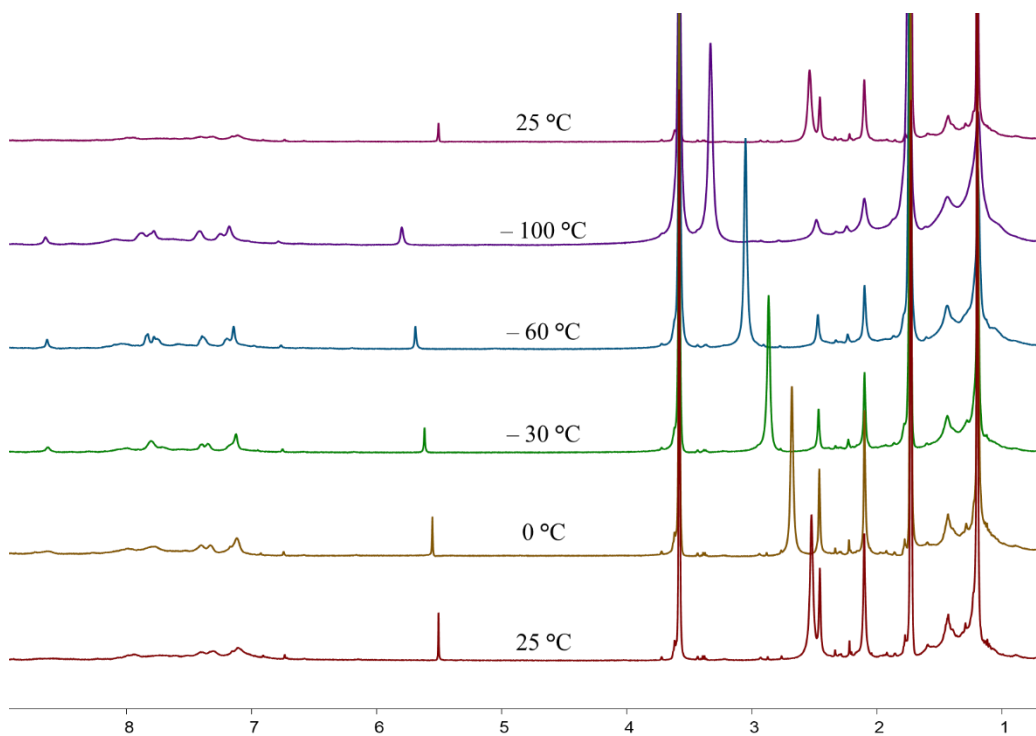


Figure D.50 VT ^1H NMR full spectra of *anti*-DB-DIAN (**12**) in $\text{THF-}d_8$ showing thermal depopulation of the paramagnetic triplet state at extremely low temperatures.

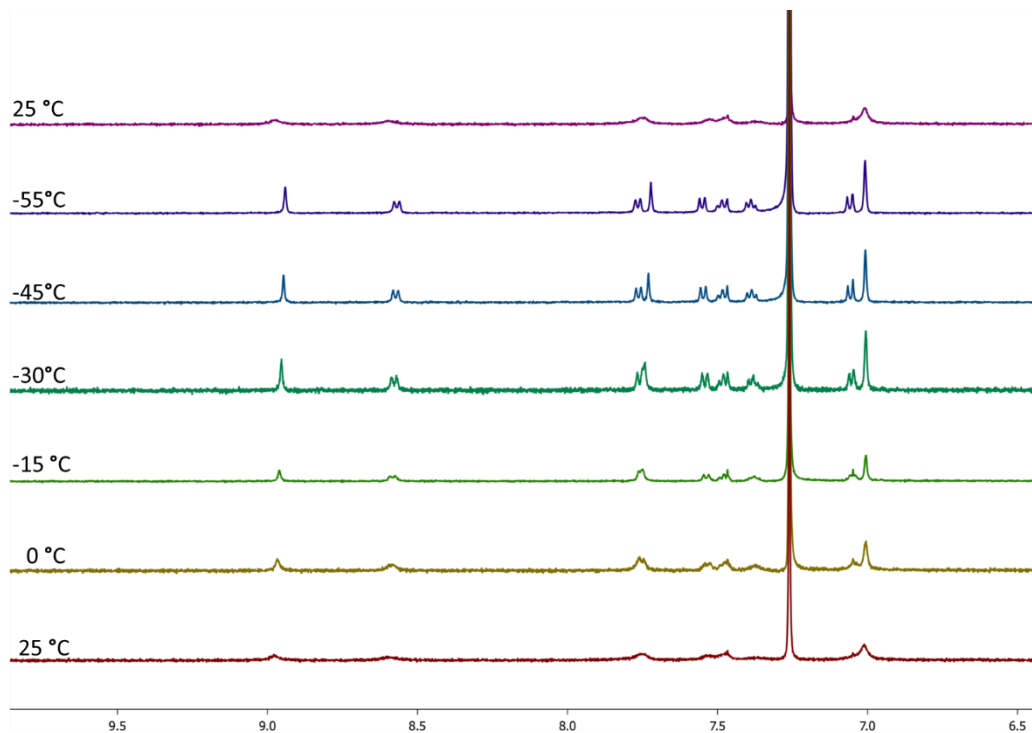


Figure D.51 VT ¹H NMR spectra of the aromatic region of *syn*-DB-DIAN (**11**) in CDCl₃ showing thermal depopulation of the paramagnetic triplet state at low temperatures.

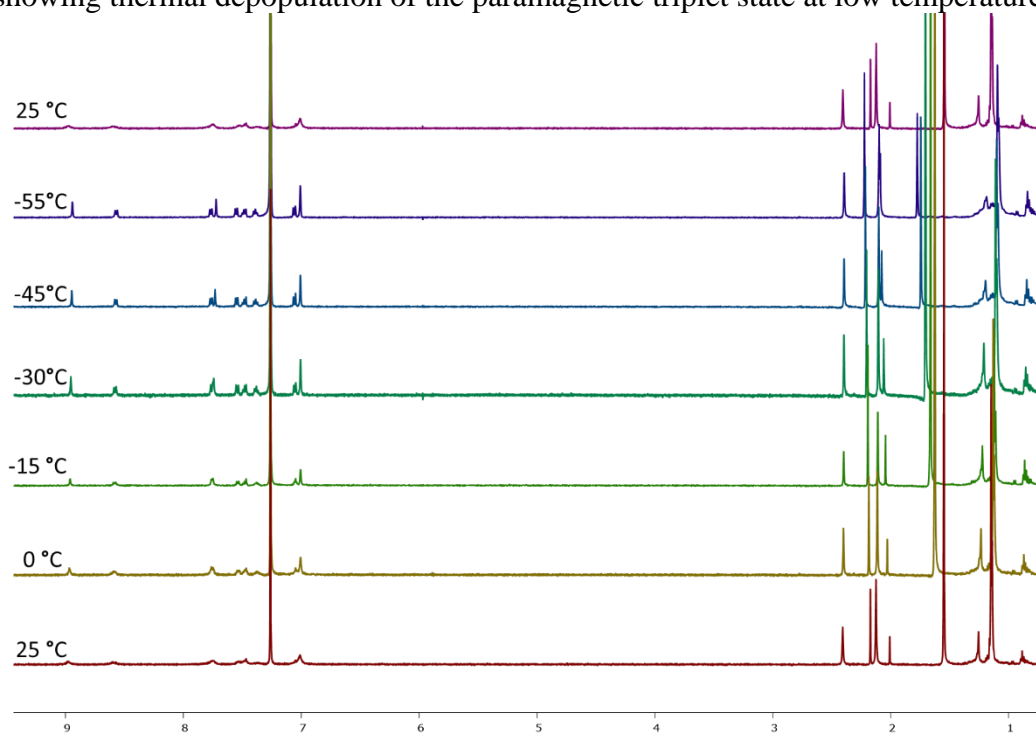


Figure D.52 VT ¹H NMR full spectra of *syn*-DB-DIAN (**11**) in CDCl₃ showing thermal depopulation of the paramagnetic triplet state at low temperatures.

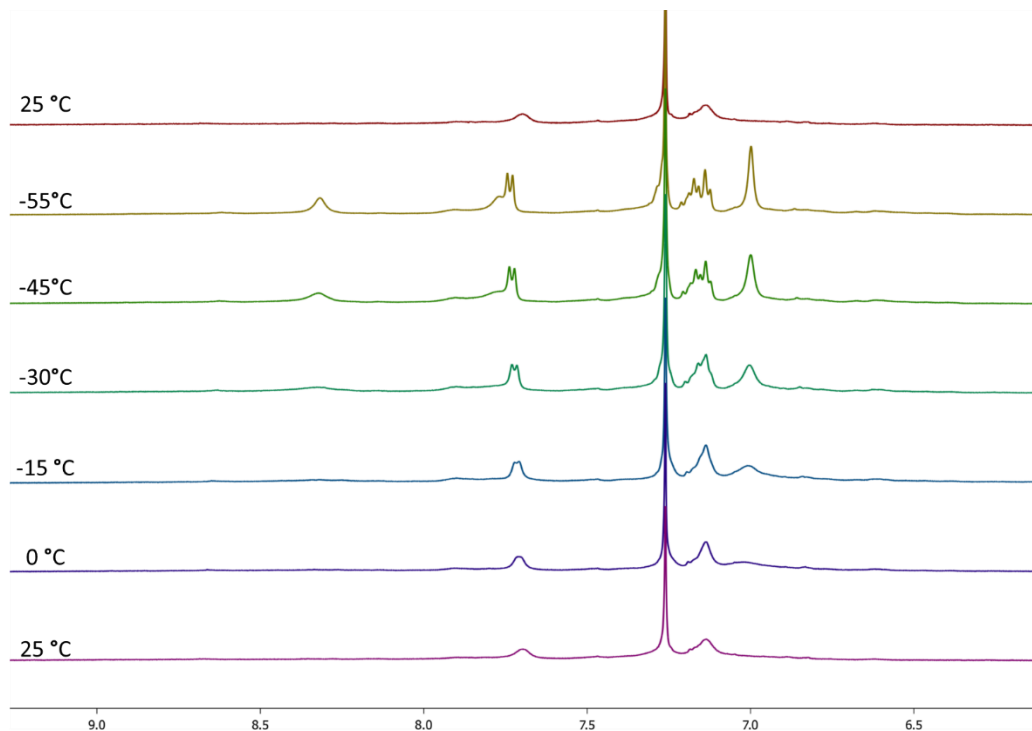


Figure D.53 VT ^1H NMR spectra of the aromatic region of BT-DIAN (**13**) in CDCl_3 showing thermal depopulation of the paramagnetic triplet state at low temperatures.

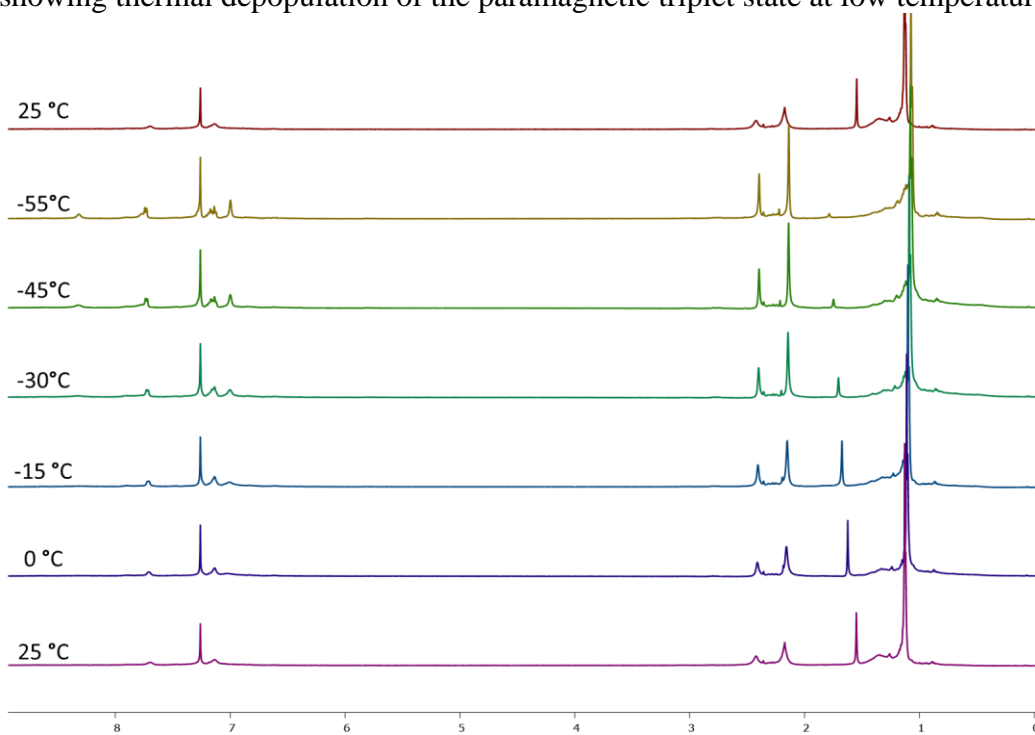


Figure D.54 VT ^1H NMR full spectra of BT-DIAN (**13**) in CDCl_3 showing thermal depopulation of the paramagnetic triplet state at low temperatures.

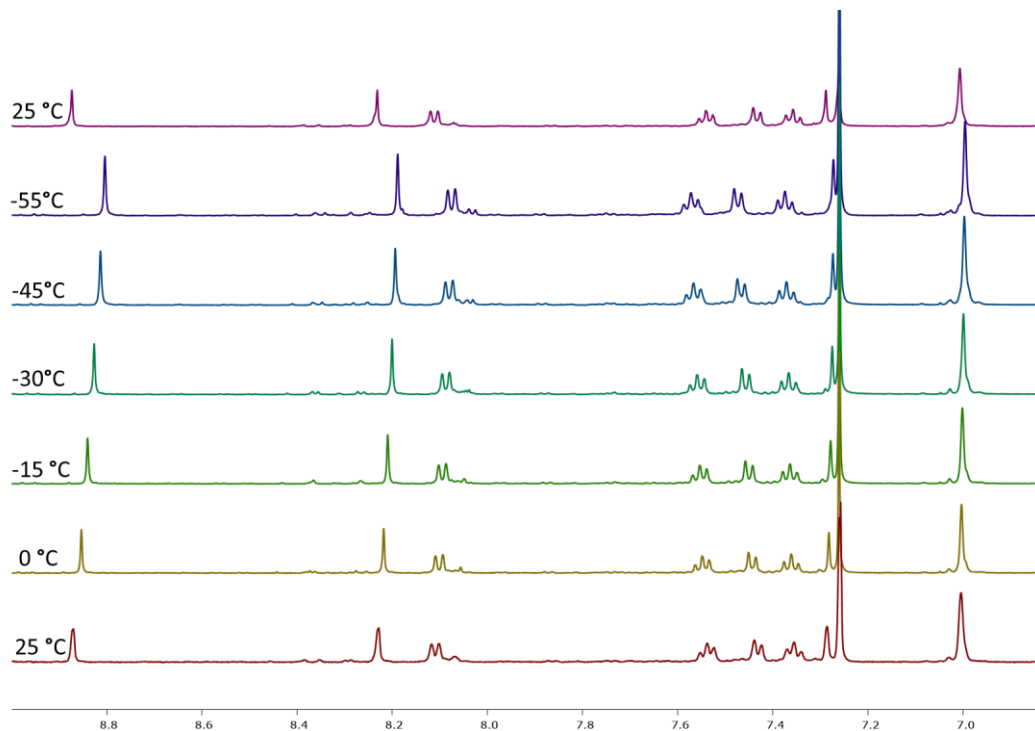


Figure D.55 VT ^1H NMR spectra of the aromatic region of *linear*-DB-DIAN (**10**) in CDCl_3 showing no thermal depopulation of the paramagnetic triplet state at low temperature.

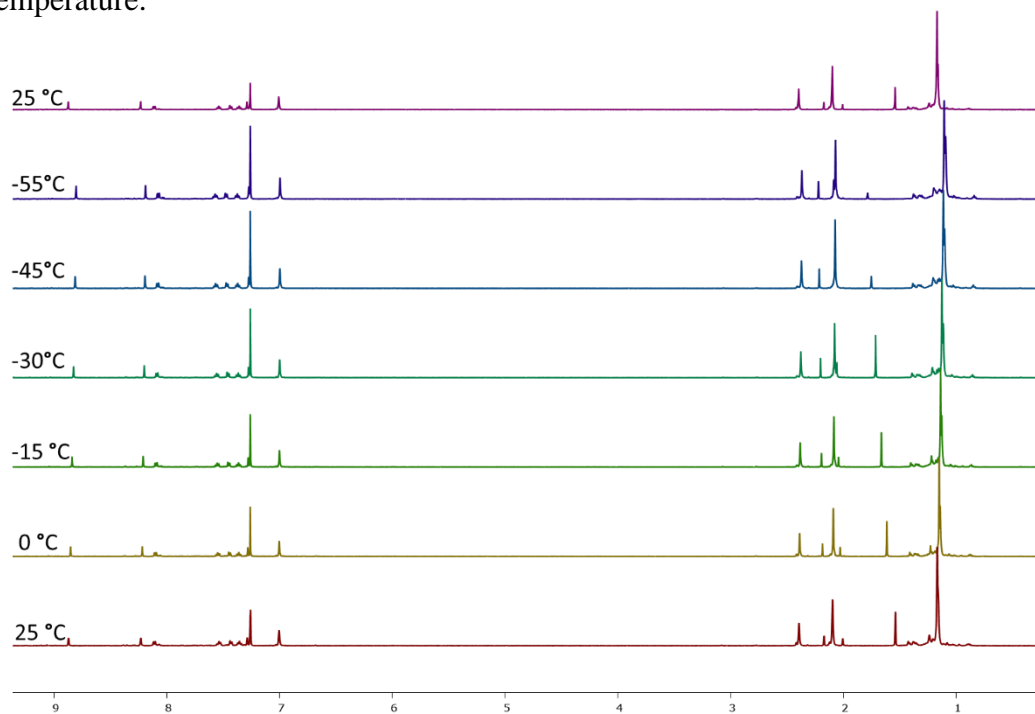


Figure D.56 VT ^1H NMR full spectra *linear*-DB-DIAN (**10**) in CDCl_3 showing no thermal depopulation of the paramagnetic triplet state at low temperatures.

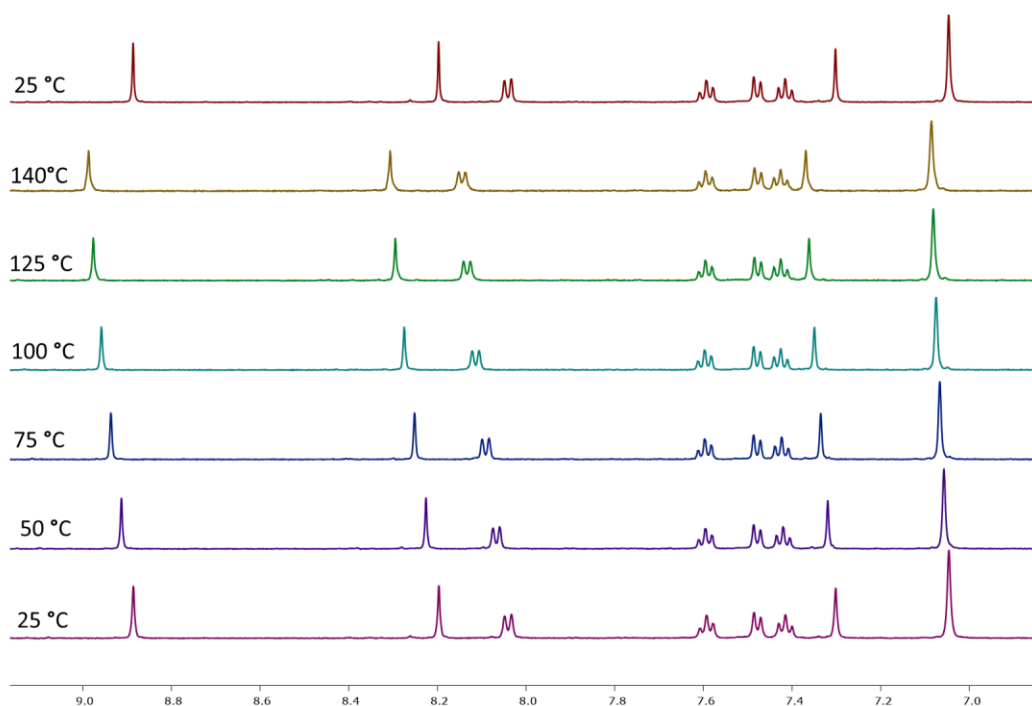


Figure D.57 VT ^1H NMR spectra of the aromatic region of *linear*-DB-DIAN (**10**) in $(\text{CDCl}_2)_2$ showing slight thermal population of the paramagnetic triplet state at high temperatures.

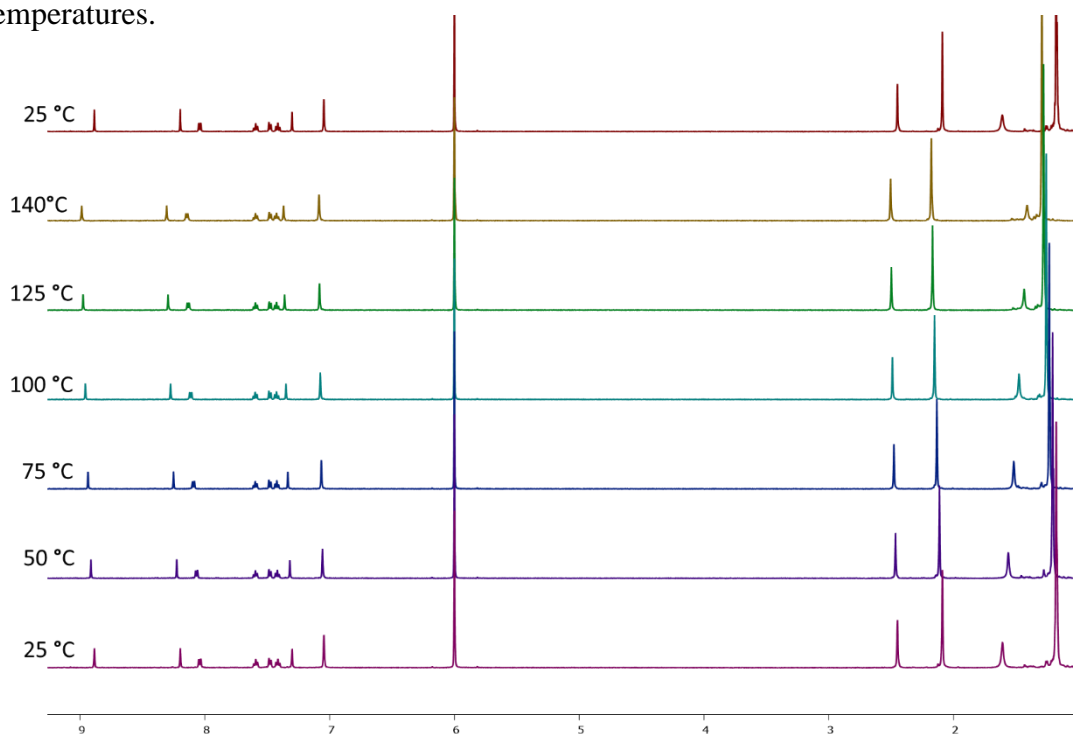


Figure D.58 VT ^1H NMR full spectra of *linear*-DB-DIAN (**10**) in $(\text{CDCl}_2)_2$ showing slight thermal population of the paramagnetic triplet state at high temperatures up to 140 $^\circ\text{C}$.

Compound Half-life Determinations. A 10^{-5} M stock solution of each DIAn derivative (prepared by dissolving **10-13** in HPLC-grade CH_2Cl_2) was added to a cuvette with 2 mL of CH_2Cl_2 until the high wavelength absorbance reach 1 a.u. All these operations were performed with non-degassed solvents and were conducted on the bench-top. The cuvette was sealed with a Teflon cap and left on the bench top for continual measurement.

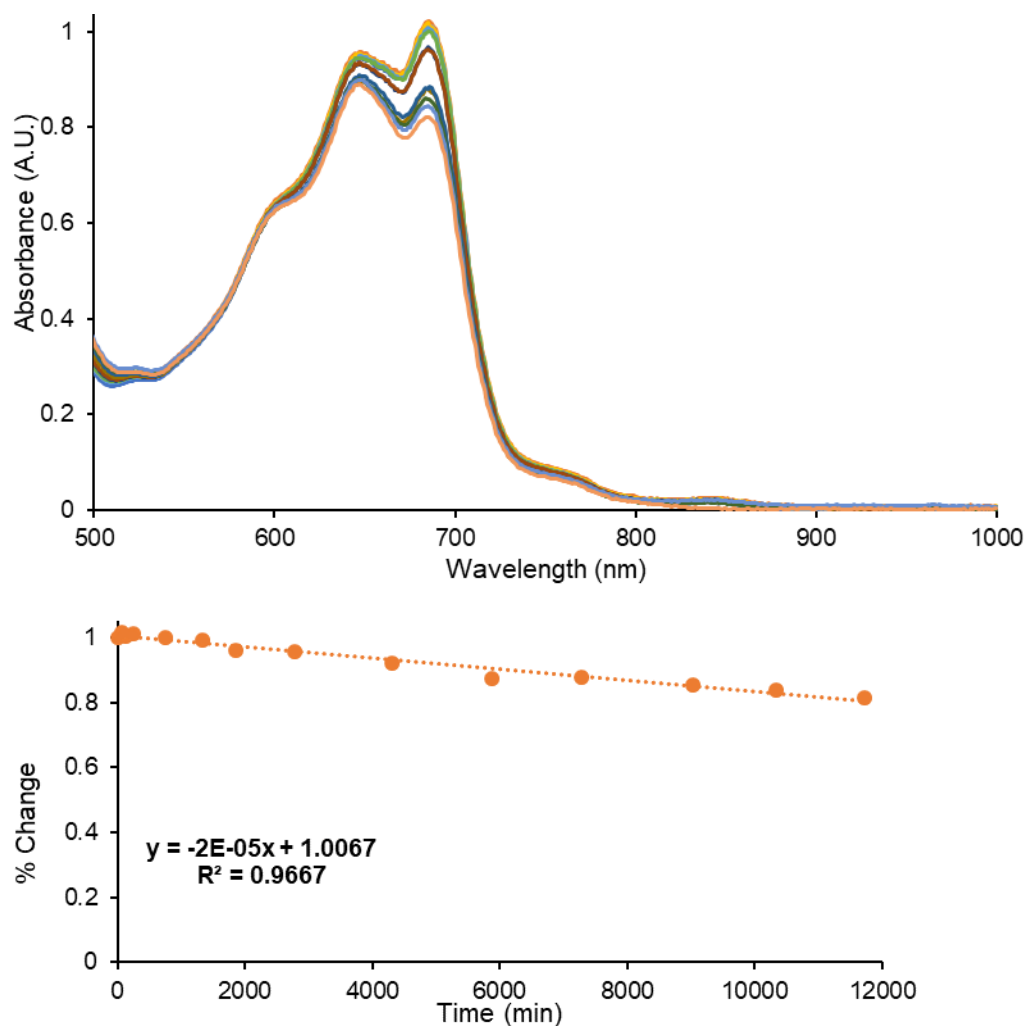


Figure D.59 Top: Decomposition of compound **10**, where the visual trend of minor decomposition over time can be seen. Absorbance spectra were collected over an eight-day period, taken at $t = 0, 1, 2, 4, 12, 22, 31, 46, 56, 71, 98, 121, 150, 172$ and 195 h. Bottom: Graph of the % change vs. time for *linear-DB-DIAn 10* and linear regression analysis to obtain the equation of a line. Extrapolation to % change = 0.5 gives a half-life of ~ 20 days.

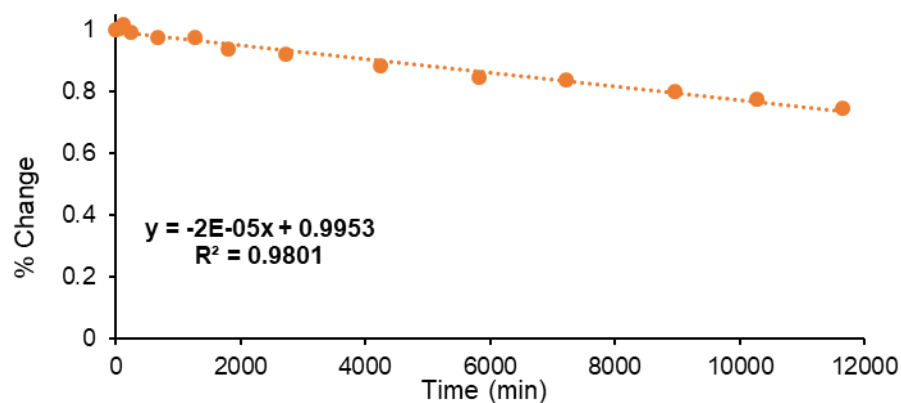
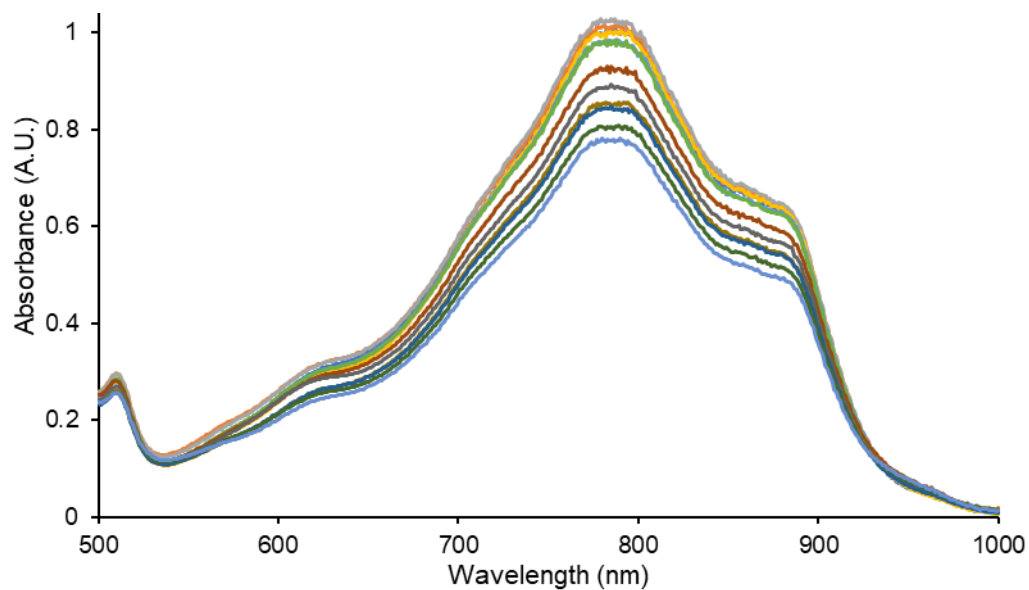


Figure D.60 Top: Decomposition of compound **11**, where the visual trend of intermediate decomposition over time can be observed. Absorbance spectra were collected over an eight-day period, taken at $t = 0, 1, 2, 4, 12, 22, 31, 46, 56, 71, 98, 121, 150, 172$ and 196 h. Bottom: Graph of the % change vs. time for *syn*-DB-DIAN **11** and linear regression analysis to get the equation of a line. Extrapolation to % change = 0.5 gives a half-life of ~15.5 days.

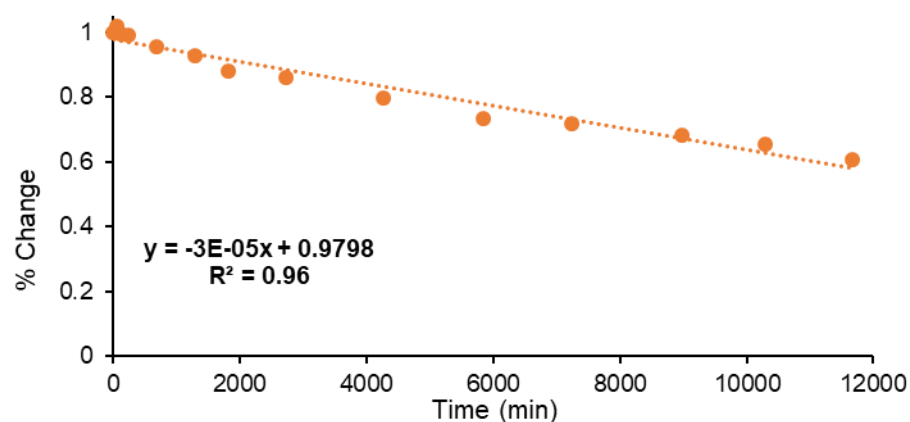
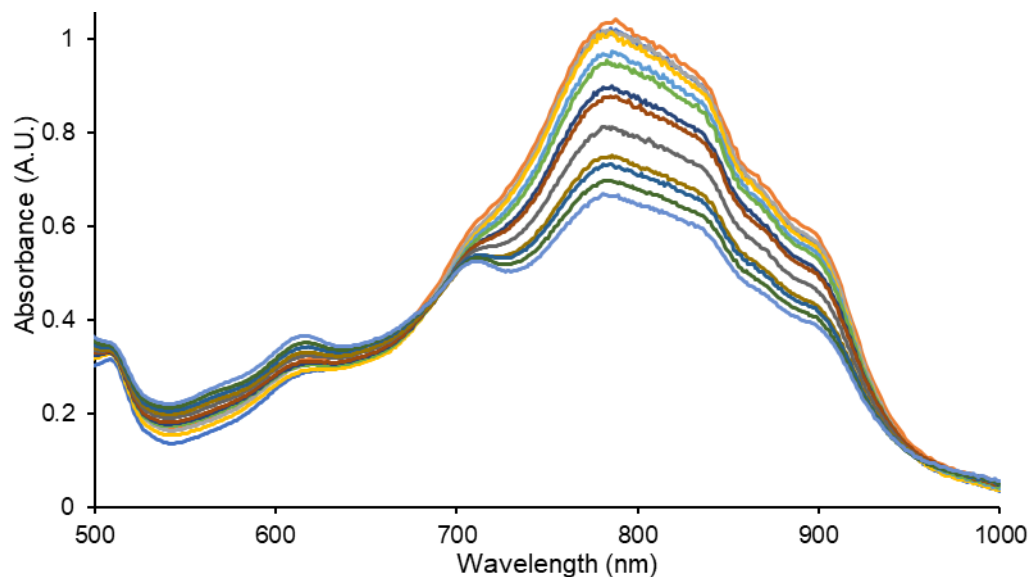


Figure D.61 Top: Decomposition of compound **12**, where the visual trend of intermediate decomposition over time can be seen here. Absorbance spectra were collected over an eight-day period, taken at $t = 0, 1, 2, 4, 11, 22, 31, 46, 56, 71, 98, 121, 150, 172$ and 195 h. Bottom: Graph of the % change vs. time for *anti*-DB-DIA n **12** and linear regression analysis to get the equation of a line. Extrapolation to % change = 0.5 gives a half-life of ~ 9.75 days.

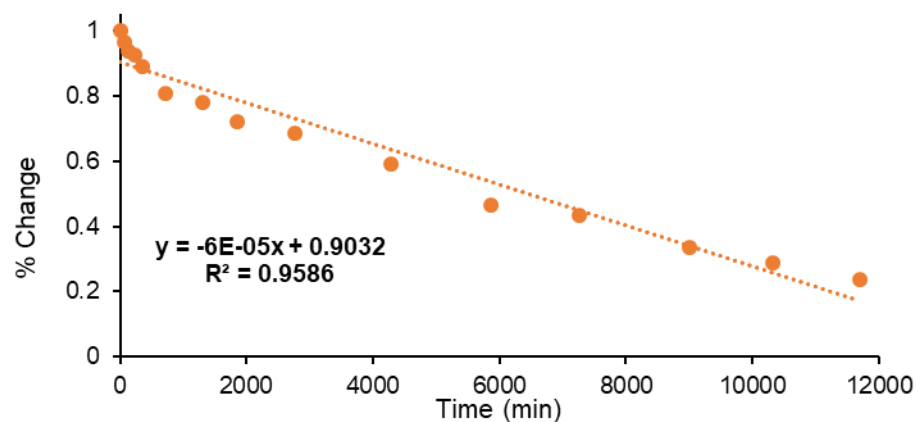
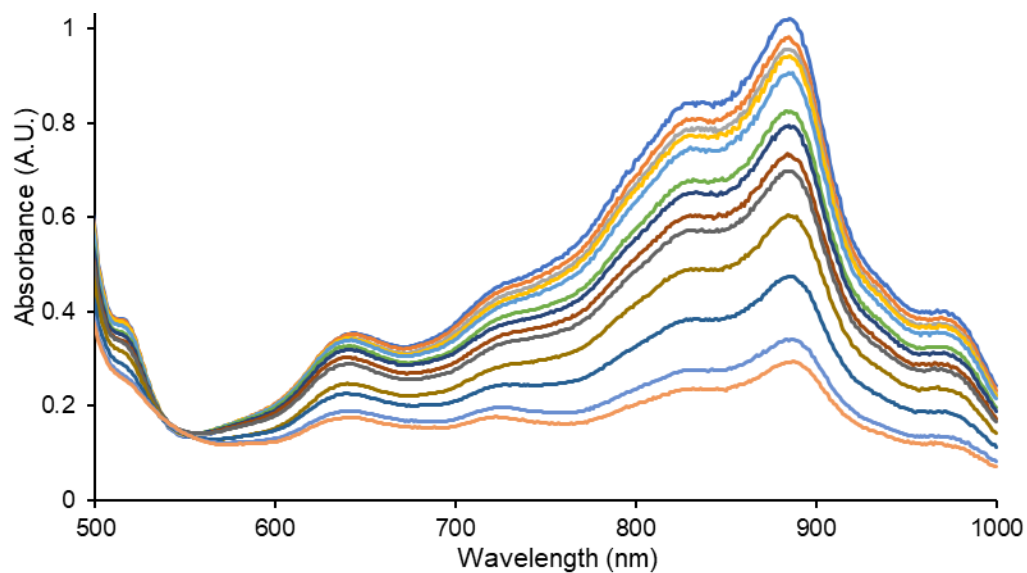


Figure D.62 Top: Decomposition of compound **13**, where the visual trend of rapid decomposition over time can be seen. Absorbance spectra were collected over an eight-day period, taken at $t = 0, 1, 2, 4, 6, 12, 22, 31, 46, 56, 71, 98, 121, 150, 172$ and 195 h. Bottom: Graph of the % change vs. time for BT-DIAN **13** and linear regression analysis to get the equation of a line. Extrapolation to % change = 0.5 gives a half-life of ~ 4.5 days.

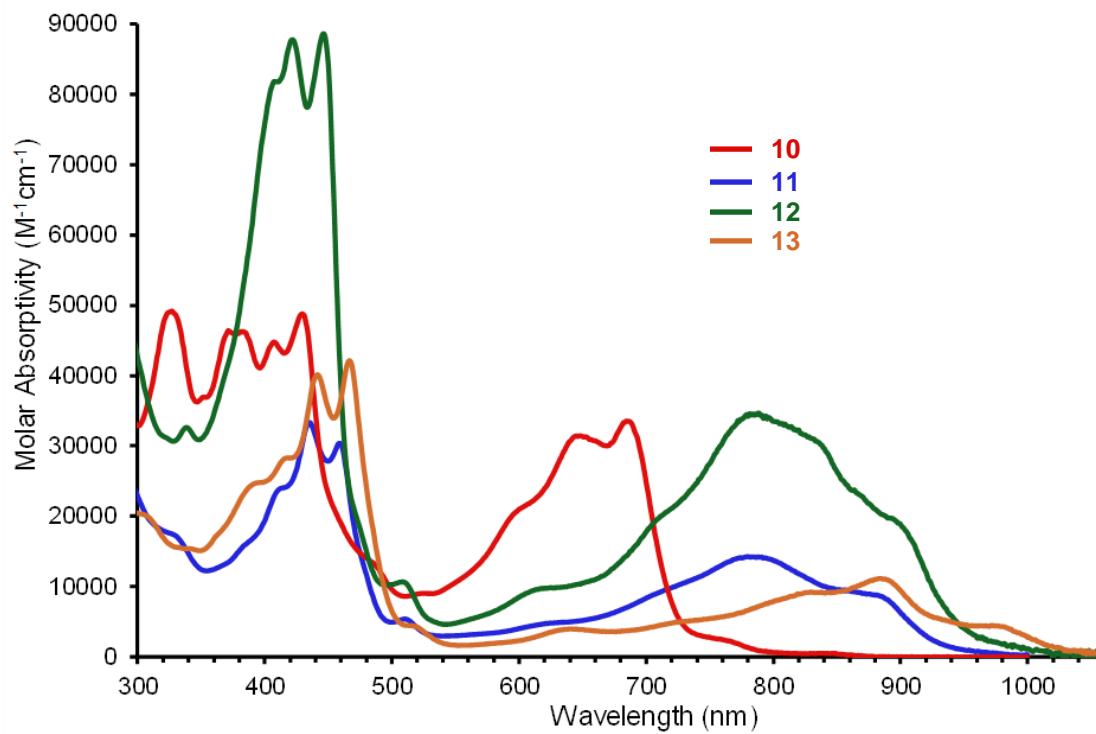


Figure D.63 Plot of wavelength vs. molar absorptivity for all four new DIAn derivatives 10-13.

SQUID. Magnetic susceptibility measurements were performed with a Quantum Design MPMS-XL-7 SQUID susceptometer. The magnetic measurements were performed in the 10-400 K temperature range with an applied field of 1 T using a sample space oven with the samples inserted in a 1.5 mm diameter aluminium foil cylinder. The sample masses used for the magnetic measurements are 13.304, 2.739, 17.918 and 16.501 mg for **10**, **11**, **12** and **13**, respectively. The susceptibility data were corrected for the same sample holder previously measured using the same conditions and for the diamagnetic contributions of the compound as deduced by using Pascal's constant tables. The magnetic measurements were fitted using the classical Bleaney-Bowers model for an antiferromagnetic $S = \frac{1}{2}$ dimer plus a monomeric $S = \frac{1}{2}$ impurity. This model reproduces satisfactorily the magnetic properties of compounds **10-13** with the following parameters:

compound	mass (mg)	g	J (K)	ρ (%)	R	calc. ΔE_{ST} (kcal mol ⁻¹)	exp. ΔE_{ST} (kcal mol ⁻¹)
10	13.304	2.0(1)	-2433	1.5	0.99332	-5.09	-4.83
11	2.739	2.0(1)	-1932	1.4	0.97294	-4.16	-3.84
12	17.918	2.0(1)	-1633	4.5	0.99332	-3.45	-3.25
13	16.501	2.0(1)	-1701	2.3	0.99835	-3.41	-3.38

In all cases the paramagnetic impurities may come from a small fraction of mono-radical present in the sample. Given the low magnetic signal, the g value obtained presents an uncertainty of around 10%, as this error corresponds to the error in the $\chi_m T$ values (and, therefore in the g values that are directly related to them). For the estimated ΔE_{ST} values from the fit to the Bleaney-Bowers model, however, since the ΔE_{ST} value mainly depends on the curvature of the plot as T increases, the error in ΔE_{ST} can be evaluated to be around 0.2 kcal mol⁻¹, which represents around 4-6% of the estimated value.

CV Measurements. Electrochemical experiments have been conducted in CH₂Cl₂ at 10⁻⁴-10⁻⁵ M concentrations of **10-13** at room temperature using 0.1 M Bu₄NPF₄ as the supporting electrolyte. Cyclic voltammetry covering the anodic and cathodic parts was performed at a scan rate of 100 mV s⁻¹, which are shown in Figure D.64 together with Table D4 that summarizes the main values. Glassy carbon was used as the working electrode and a Pt wire was the auxiliary electrode against a pseudo-reference electrode of Ag/0.001M AgNO₃/0.1M Bu₄NPF₄. All redox potentials provided are referenced to the Fc/Fc⁺ pair.

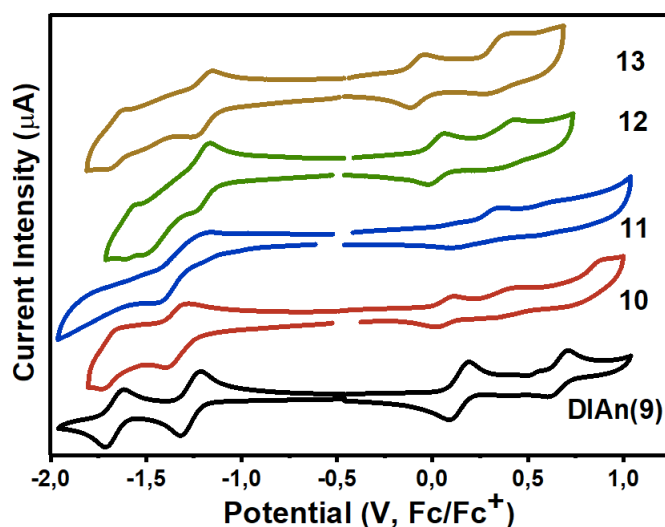


Figure D.64 Cyclic voltammograms of compounds **10-13** together with the CV data of DIAn **9** for comparison.

Table D4. Redox potentials (V) for compounds **9-13** analyzed by cyclic voltammetry and the corresponding CV and optically-determined energy gaps (eV).

Compound	E ¹ _{red} (V)	E ² _{red} (V)	E ¹ _{oxd} (V)	E ² _{oxd} (V)	E ³ _{oxd} (V)	CV E _{gap} (eV)	Opt. E _{gap} (eV)
DIAn 9 ³	-1.27	-1.65	0.14	0.66	—	1.41	1.38
10	-1.13	-1.65	0.11	0.42	1.31	1.24	1.45
11	-1.31	—	0.13	0.59	—	1.44	1.25
12	-1.20	-1.58	0.03	0.39	—	1.23	1.20
13	-1.21	-1.67	-0.08	0.34	—	1.13	1.17

X-ray Diffraction Details

General. X-ray diffraction intensities for **10–13** and **17** were collected at 173 K on a Bruker Apex2 DUO CCD diffractometer using CuK α radiation, $\lambda = 1.54178 \text{ \AA}$. Space groups were determined based on systematic absences (**10**, **11** and **13**) and intensity statistics (**12** and **17**). Absorption corrections were applied by SADABS. Structures were solved by direct methods and Fourier techniques and refined on F^2 using full matrix least-squares procedures. All non-H atoms were refined with anisotropic thermal parameters. All H atoms were refined in calculated positions in a rigid group model. The structures of **11** and **13** have two and one solvent CHCl $_3$ molecules, respectively, disordered over two positions. The structures of **12** and **13** have three and two symmetrically independent molecules, respectively. All calculations were performed by the Bruker SHELXL package.

Crystallographic Data for **10**: C $_{76}$ H $_{80}$ Si $_2$, M = 1049.58, 0.23 x 0.05 x 0.01 mm, T = 173 K, Monoclinic, space group $P2_1/n$, $a = 8.9079(3) \text{ \AA}$, $b = 17.7241(7) \text{ \AA}$, $c = 19.6818(8) \text{ \AA}$, $\beta = 93.694(3)^\circ$, $V = 3101.0(2) \text{ \AA}^3$, $Z = 2$, $D_c = 1.124 \text{ Mg/m}^3$, $\mu(\text{Cu}) = 0.827 \text{ mm}^{-1}$, $F(000) = 1128$, $2\theta_{\text{max}} = 133.28^\circ$, 20406 reflections, 5426 independent reflections [$R_{\text{int}} = 0.0472$], $R1 = 0.0497$, $wR2 = 0.1337$ and GOF = 1.064 for 5426 reflections (352 parameters) with $I > 2\sigma(I)$, $R1 = 0.0643$, $wR2 = 0.1444$ and GOF = 1.064 for all reflections, max/min residual electron density +0.394/−0.230 $\text{e}\text{\AA}^{-3}$. CCDC 1949613.

Crystallographic Data for **11**: C $_{78}$ H $_{82}$ Cl $_6$ Si $_2$, M = 1288.31, 0.07 x 0.05 x 0.05 mm, T = 173 K, Monoclinic, space group $P2_1/c$, $a = 17.4631(5) \text{ \AA}$, $b = 11.2063(4) \text{ \AA}$, $c = 17.8838(5) \text{ \AA}$, $\beta = 92.013(2)^\circ$, $V = 3497.64(19) \text{ \AA}^3$, $Z = 2$, $D_c = 1.223 \text{ Mg/m}^3$, $\mu(\text{Cu}) = 2.885 \text{ mm}^{-1}$, $F(000) = 1360$, $2\theta_{\text{max}} = 133.47^\circ$, 28944 reflections, 6178 independent reflections [$R_{\text{int}} = 0.0546$], $R1 = 0.0578$, $wR2 = 0.1601$ and GOF = 1.057 for 6178 reflections (416 parameters) with $I > 2\sigma(I)$, $R1 = 0.0677$, $wR2 = 0.1704$ and GOF = 1.057 for all reflections, max/min residual electron density +0.791/−0.522 $\text{e}\text{\AA}^{-3}$. CCDC 1949612.

Crystallographic Data for **12**: C $_{76}$ H $_{80}$ Si $_2$, M = 1049.58, 0.10 x 0.09 x 0.01 mm, T = 176 K, Triclinic, space group $P-1$, $a = 12.4587(4) \text{ \AA}$, $b = 18.8918(5) \text{ \AA}$, $c = 21.9325(7) \text{ \AA}$, $\alpha = 70.816(2)^\circ$, $\beta = 73.513(2)^\circ$, $\gamma = 89.561(2)^\circ$, $V = 4654.1(3) \text{ \AA}^3$, $Z = 3$, $D_c = 1.123 \text{ Mg/m}^3$, $\mu(\text{Cu}) = 0.827 \text{ mm}^{-1}$, $F(000) = 1692$, $2\theta_{\text{max}} = 133.50^\circ$, 58587 reflections, 16392

independent reflections [$R_{\text{int}} = 0.0720$], $R1 = 0.0846$, $wR2 = 0.2329$ and $\text{GOF} = 1.029$ for 16392 reflections (1054 parameters) with $I > 2\sigma(I)$, $R1 = 0.1154$, $wR2 = 0.2581$ and $\text{GOF} = 1.029$ for all reflections, max/min residual electron density $+0.632/-0.430 \text{ e}\text{\AA}^{-3}$. CCDC 1949614.

Crystallographic Data for **13**: $\text{C}_{73}\text{H}_{77}\text{Cl}_3\text{S}_2\text{Si}_2$, $M = 1180.99$, $0.17 \times 0.11 \times 0.02 \text{ mm}$, $T = 173 \text{ K}$, Monoclinic, space group $P2_1/n$, $a = 16.014(3) \text{ \AA}$, $b = 24.460(4) \text{ \AA}$, $c = 18.439(3) \text{ \AA}$, $\beta = 114.320(9)^\circ$, $V = 6581.7(19) \text{ \AA}^3$, $Z = 4$, $D_c = 1.192 \text{ Mg/m}^3$, $\mu(\text{Cu}) = 2.505 \text{ mm}^{-1}$, $F(000) = 2504$, $2\theta_{\text{max}} = 133.35^\circ$, 41542 reflections, 11396 independent reflections [$R_{\text{int}} = 0.0954$], $R1 = 0.0676$, $wR2 = 0.1850$ and $\text{GOF} = 1.114$ for 11396 reflections (758 parameters) with $I > 2\sigma(I)$, $R1 = 0.1038$, $wR2 = 0.2188$ and $\text{GOF} = 1.115$ for all reflections, max/min residual electron density $+0.516/-0.554 \text{ e}\text{\AA}^{-3}$. CCDC 1964314.

Crystallographic Data for **17**: $\text{C}_{50}\text{H}_{54}\text{O}_2\text{Si}_2$, $M = 743.11$, $0.21 \times 0.16 \times 0.11 \text{ mm}$, $T = 173 \text{ K}$, Triclinic, space group $P-1$, $a = 7.9361(2) \text{ \AA}$, $b = 8.6174(2) \text{ \AA}$, $c = 15.7838(4) \text{ \AA}$, $\alpha = 75.621(2)^\circ$, $\beta = 89.016(2)^\circ$, $\gamma = 85.925(2)^\circ$, $V = 1042.97(5) \text{ \AA}^3$, $Z = 1$, $D_c = 1.183 \text{ Mg/m}^3$, $\mu(\text{Cu}) = 1.062 \text{ mm}^{-1}$, $F(000) = 398$, $2\theta_{\text{max}} = 133.47^\circ$, 10894 reflections, 3572 independent reflections [$R_{\text{int}} = 0.0347$], $R1 = 0.0510$, $wR2 = 0.1376$ and $\text{GOF} = 1.078$ for 3572 reflections (244 parameters) with $I > 2\sigma(I)$, $R1 = 0.0588$, $wR2 = 0.1458$ and $\text{GOF} = 1.078$ for all reflections, max/min residual electron density $+0.425/-0.282 \text{ e}\text{\AA}^{-3}$. CCDC 1949611.

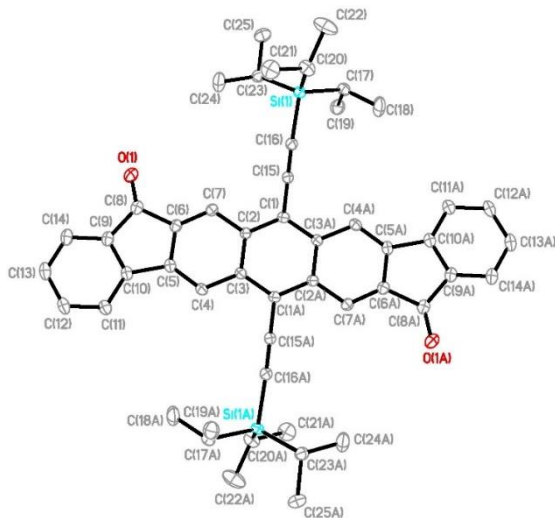


Figure D.65 Molecular structure of DIAn-dione **17** with atom labelling; ellipsoids drawn at the 50% probability level.

APPENDIX E:

SUPPLEMENTARY INFORMATION FOR CHAPTER VI

Appendix E is the supplementary information for Chapter VI of this dissertation. It includes characterization spectra, further experimental data, and computational details.

NMR Spectra

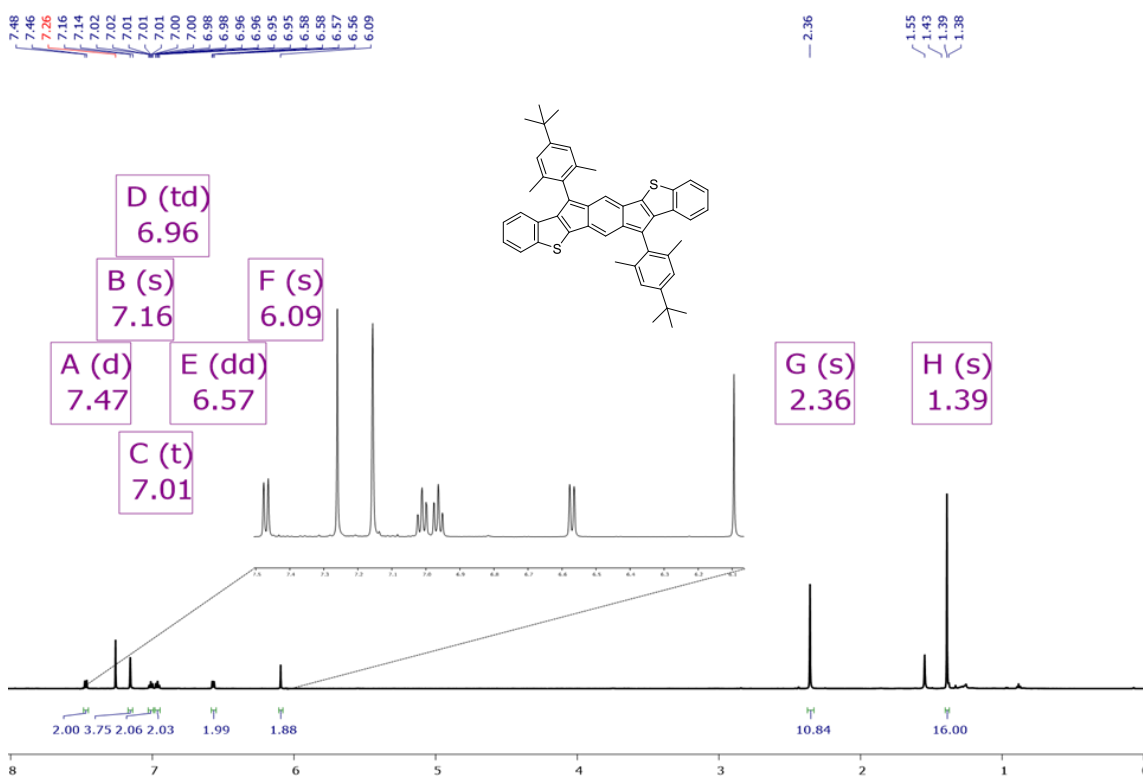


Figure E.1 ^1H NMR (600 MHz, CDCl_3) spectrum of *anti*-IDBT (1).

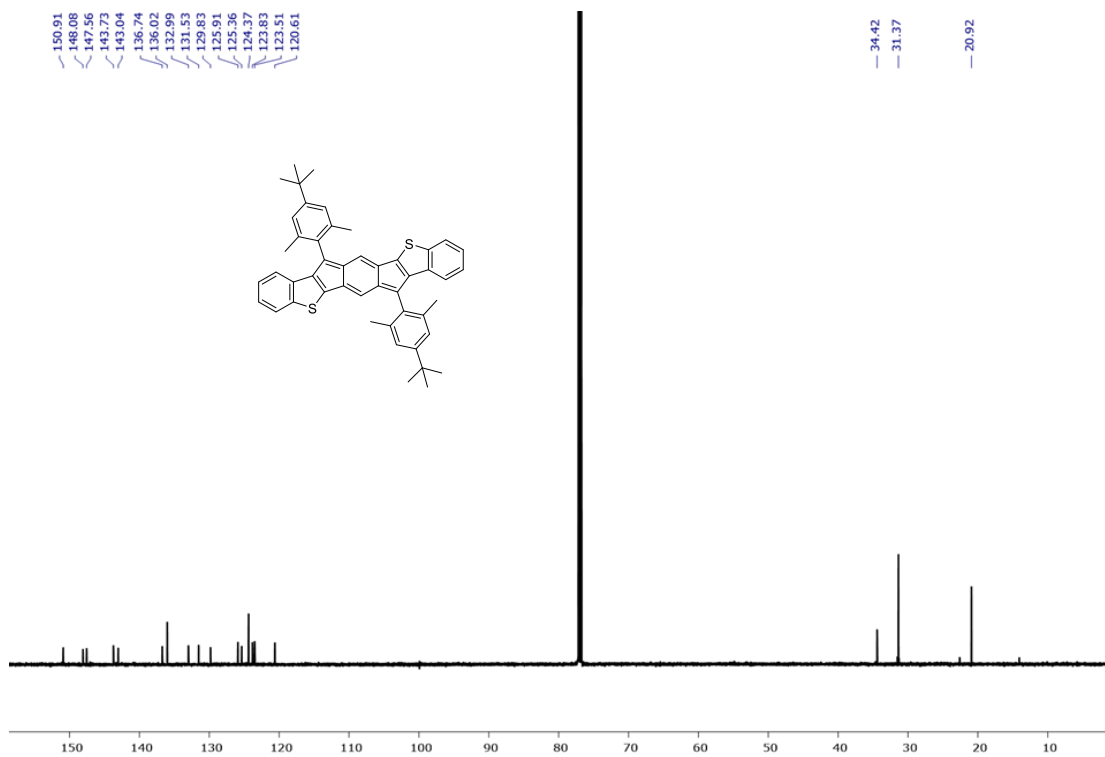


Figure E.2 ¹³C NMR (151 MHz, CDCl₃) spectrum of *anti*-IDBT (1).

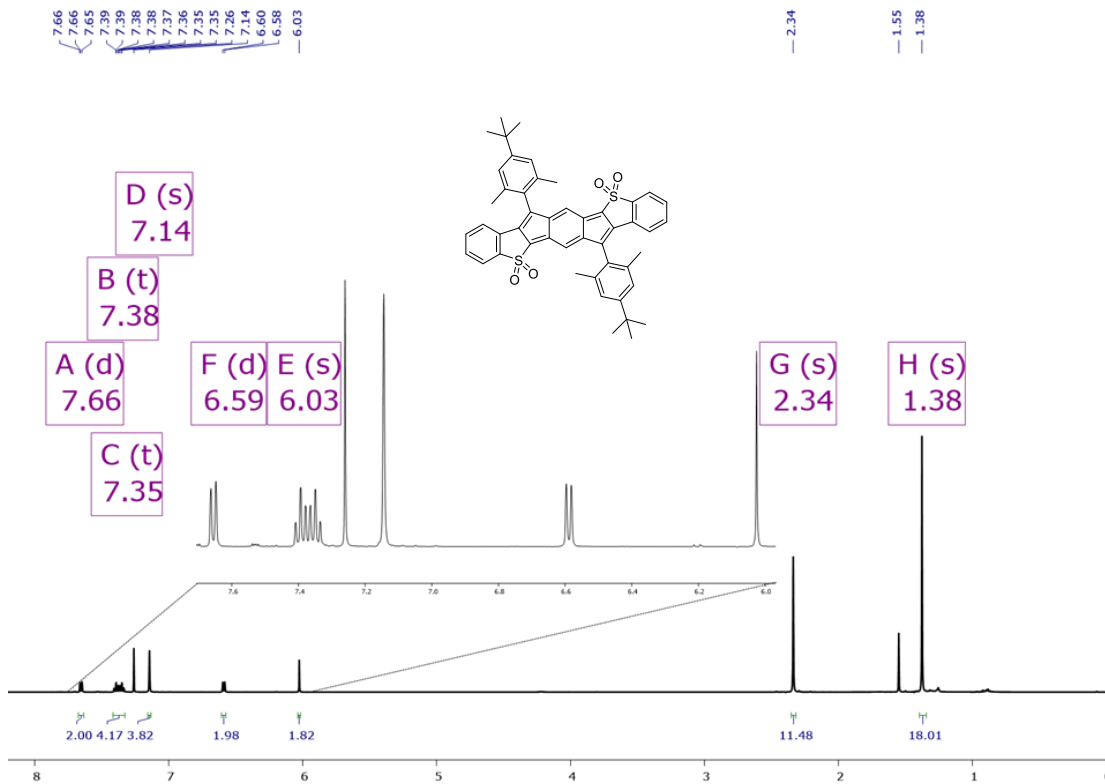


Figure E.3 ¹H NMR (500 MHz, CDCl₃) spectrum of *anti*-IDBT-sulfone (5).

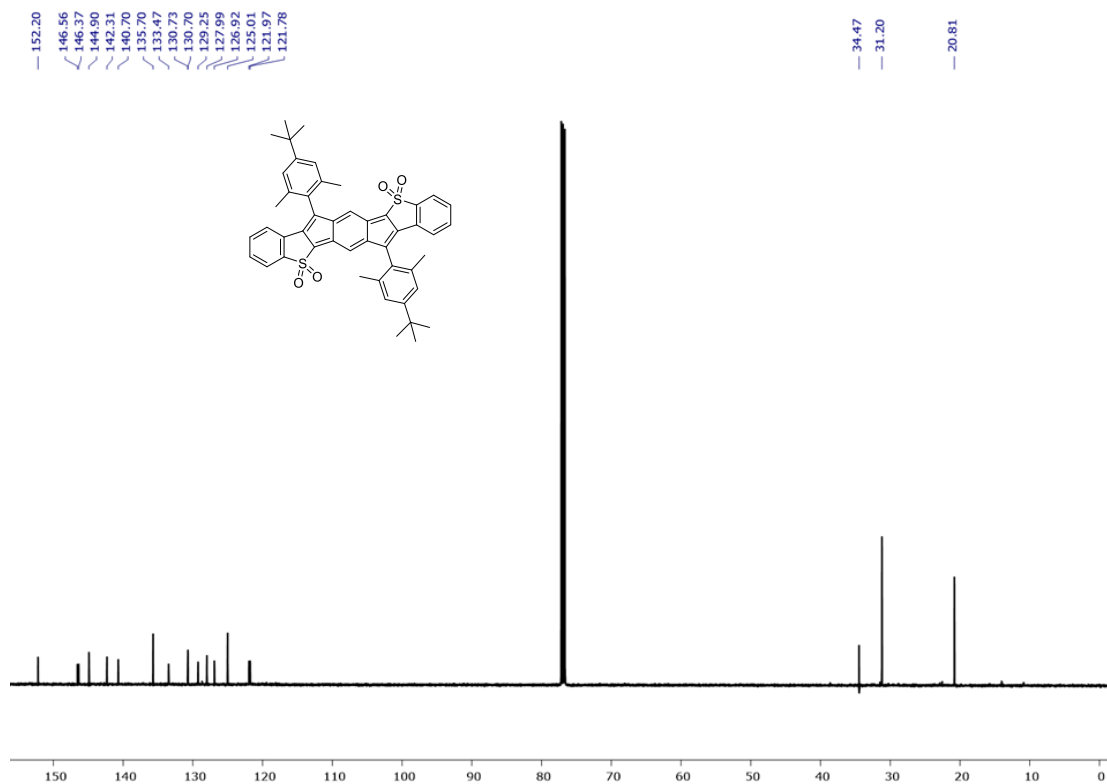


Figure E.4 ¹³C NMR (151 MHz, CDCl₃) spectrum of *anti*-IDBT-sulfone (5).

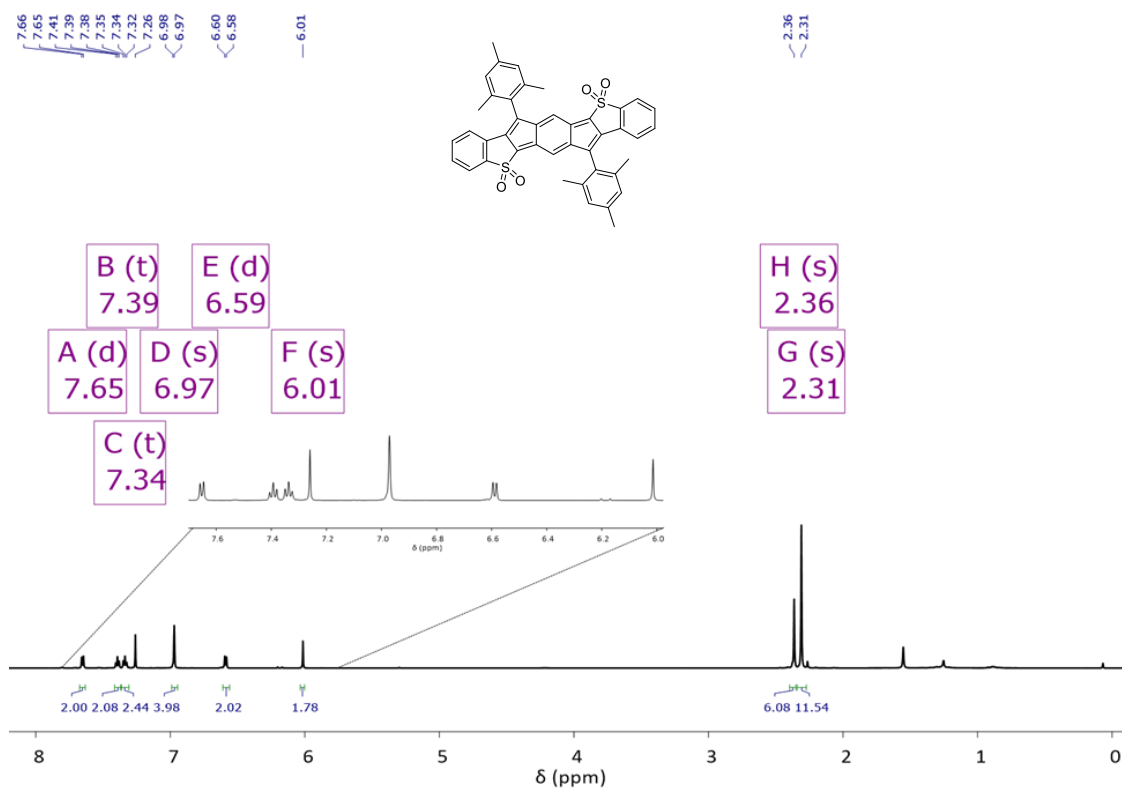


Figure E.5 ¹H NMR (600 MHz, CDCl₃) spectrum of Mes-*anti*-IDBT-sulfone (5Mes).

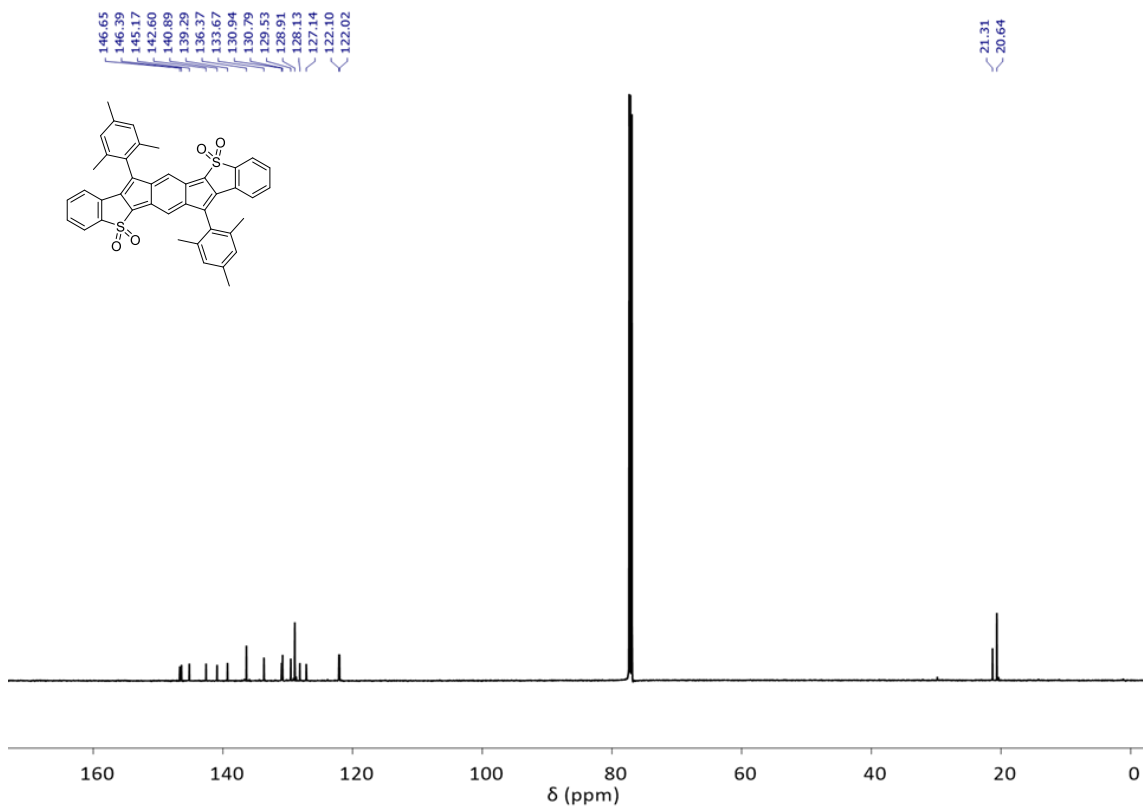


Figure E.6 ^{13}C NMR (151 MHz, CDCl_3) spectrum of Mes-anti-IDBT-sulfone (5Mes).

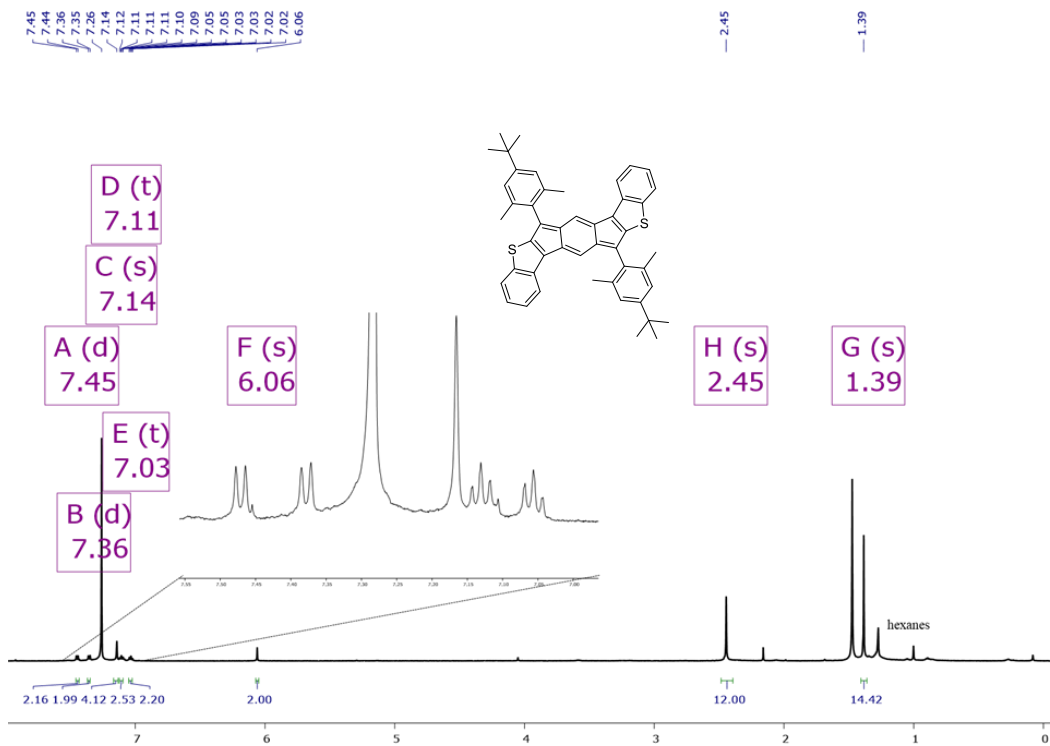


Figure E.7 ^1H NMR (600 MHz, CDCl_3) spectrum of *syn*-IDBT (2).

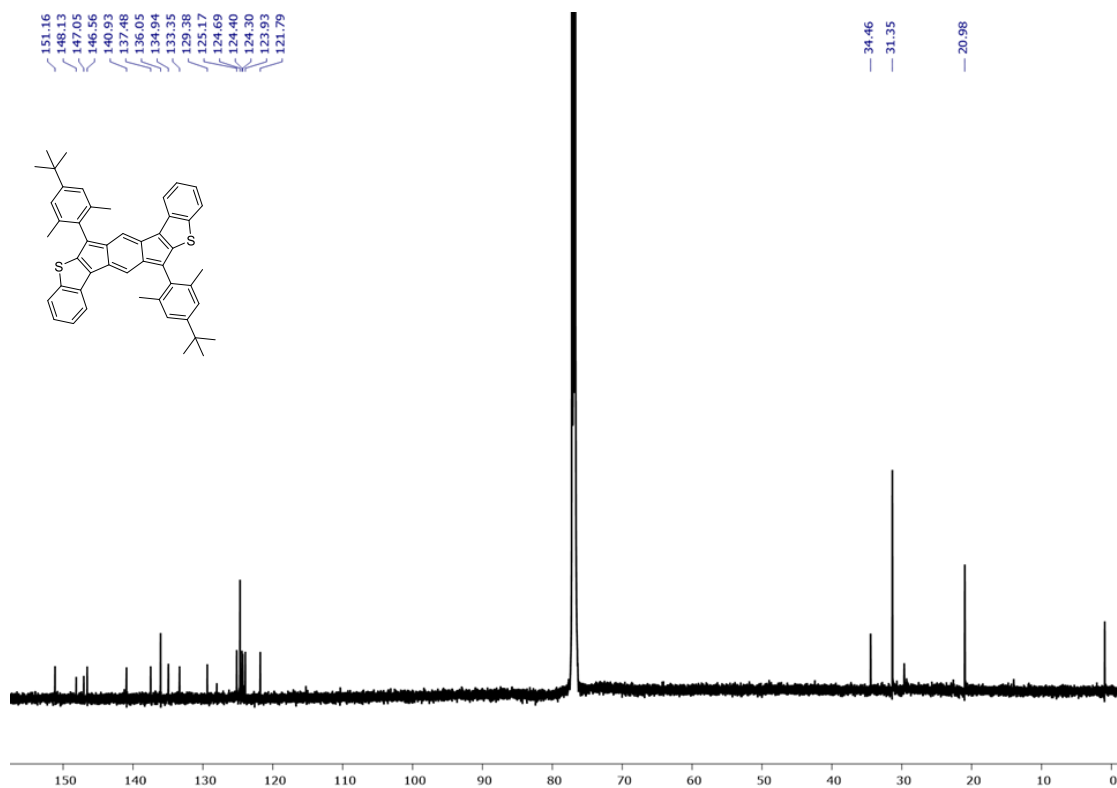


Figure E.8 ^{13}C NMR (151 MHz, CDCl_3) spectrum of *syn*-IDBT (2).

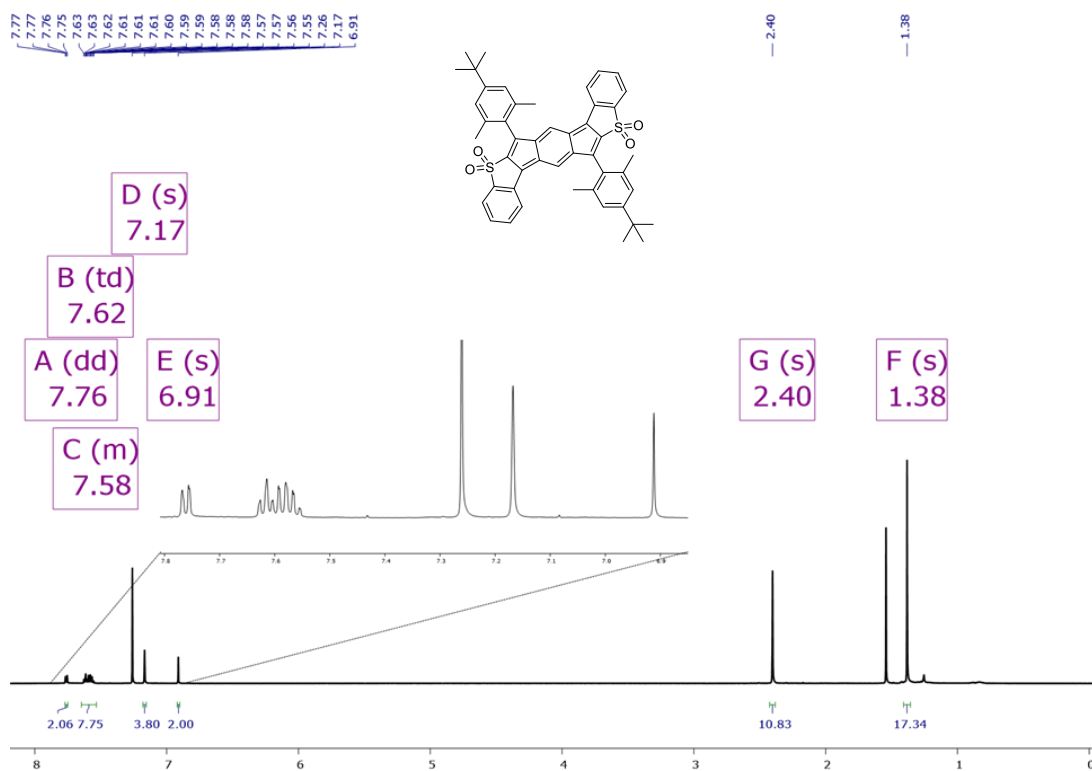


Figure E.9 ^1H NMR (600 MHz, CDCl_3) spectrum of *syn*-IDBT-sulfone (6).

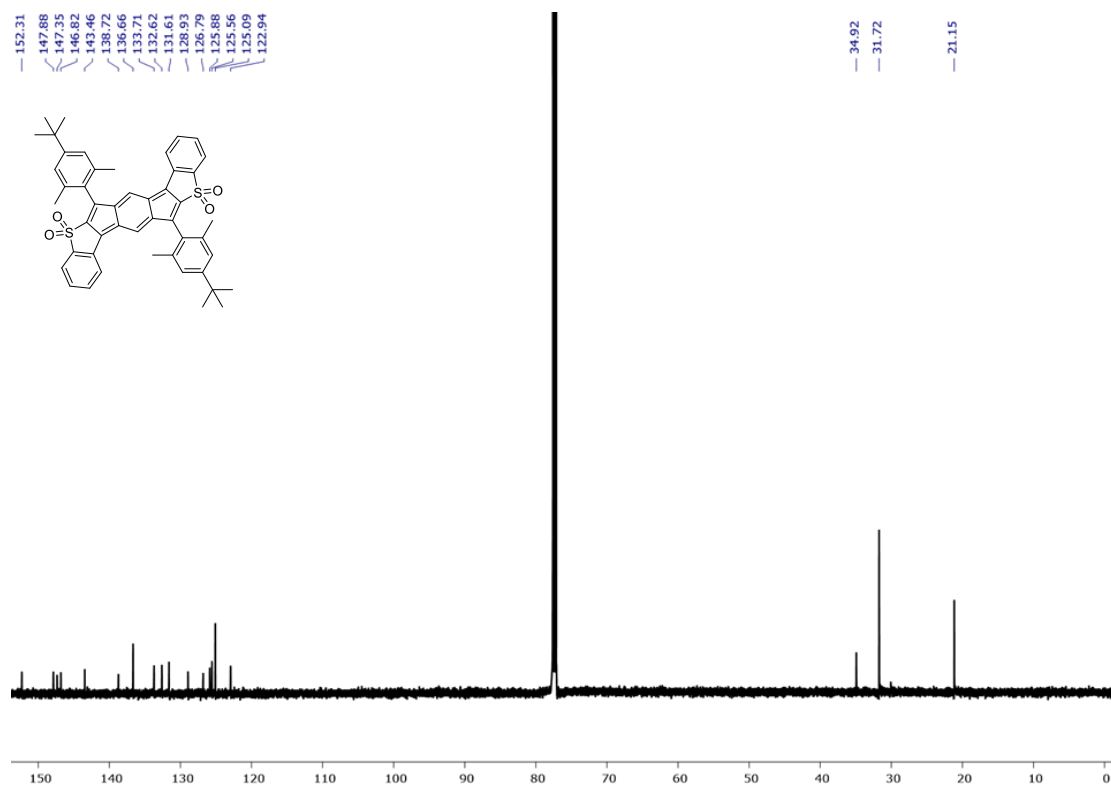


Figure E.10 ^{13}C NMR (151 MHz, CDCl_3) spectrum of *syn*-IDBT-sulfone (6).

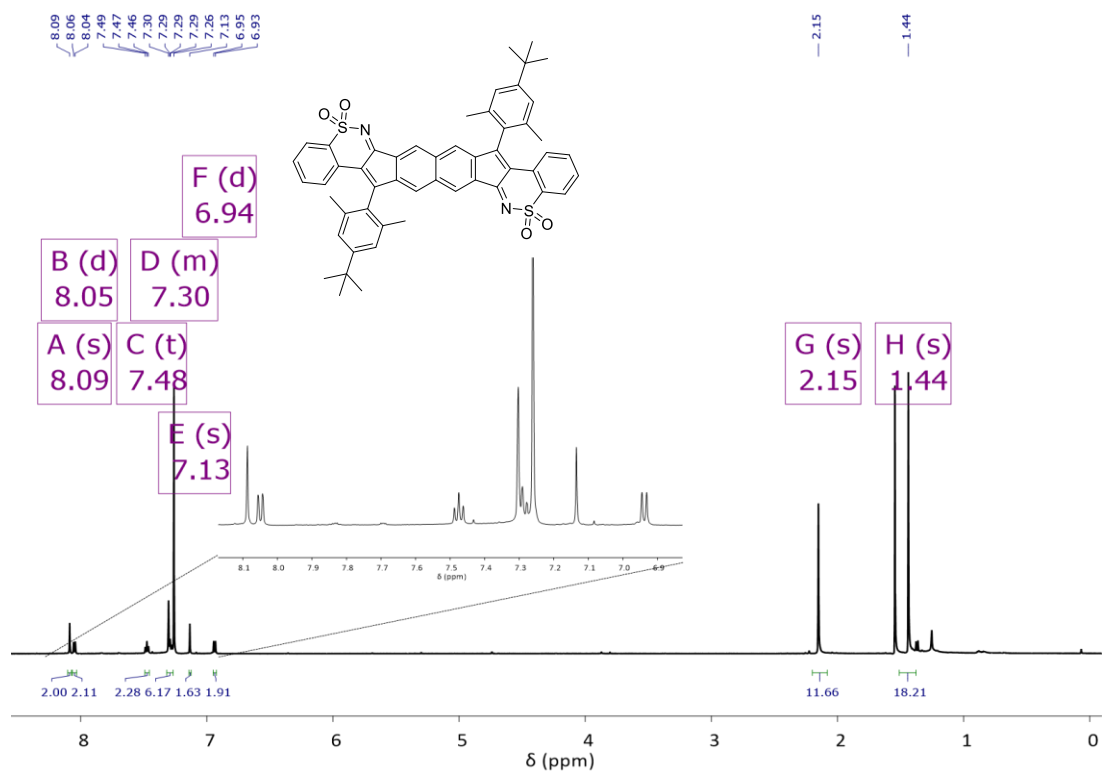


Figure E.11 ^1H NMR (600 MHz, CDCl_3) spectrum of the sulfonimide decomposition product (9).

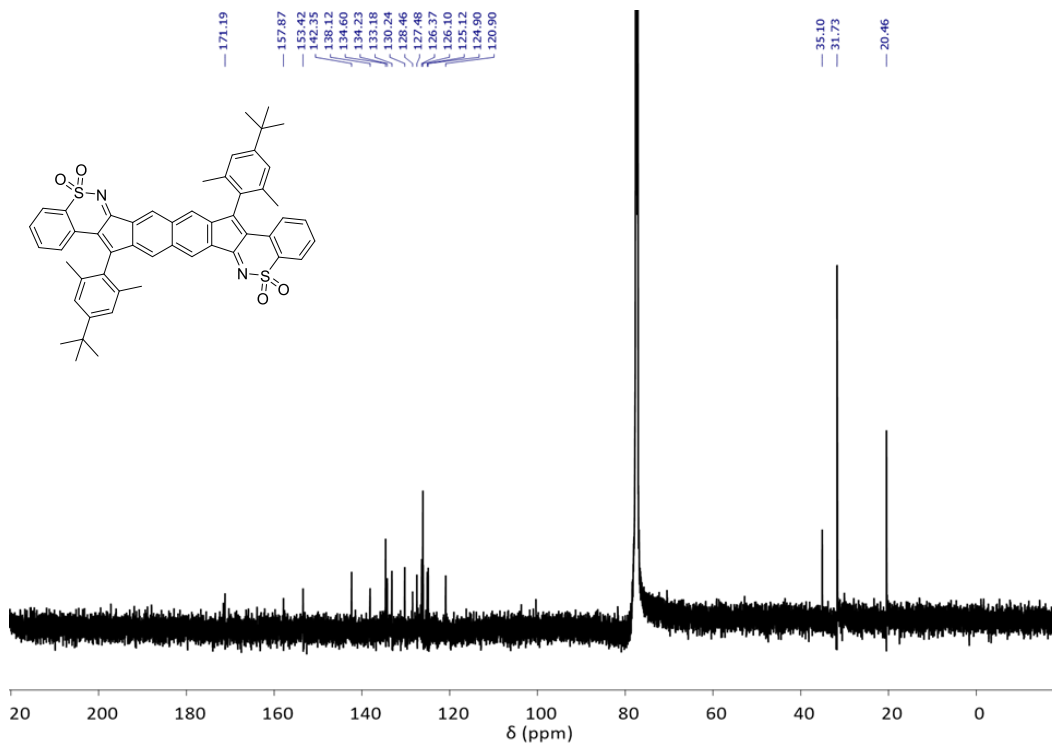


Figure E.12 ^{13}C NMR (151 MHz, CDCl_3) spectrum of the sulfonimide decomposition product (9).

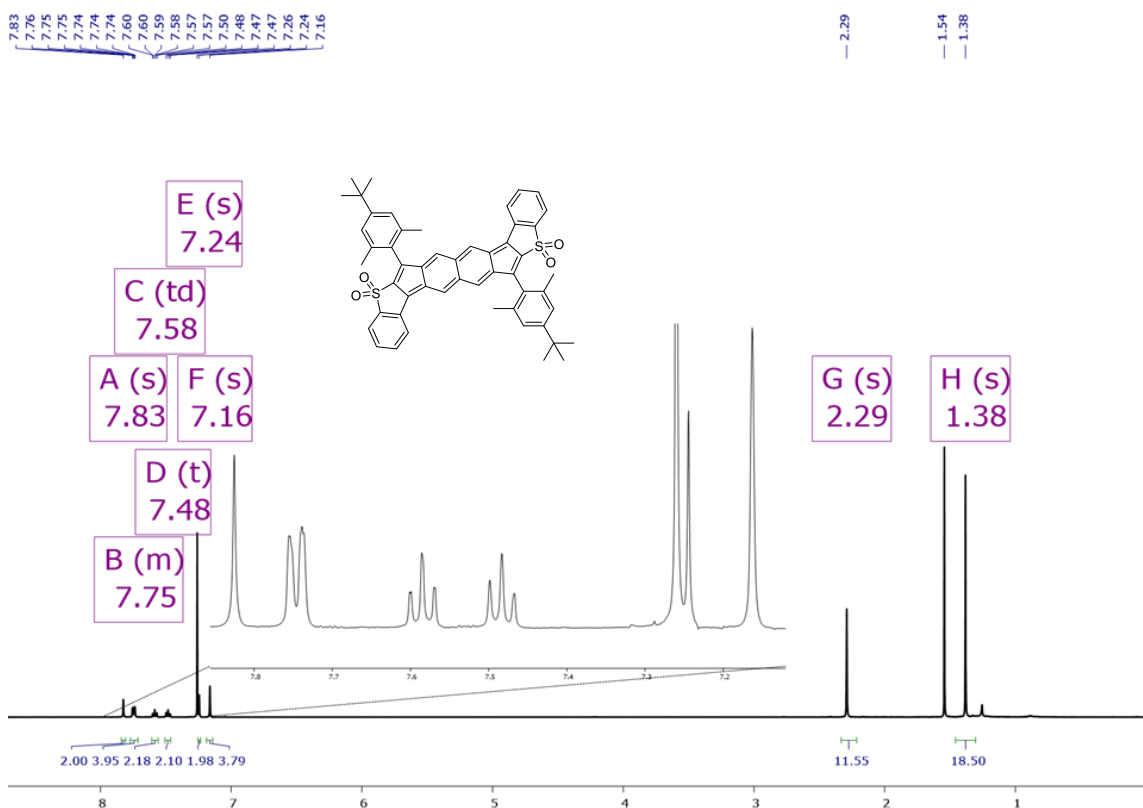


Figure E.13 ^1H NMR (500 MHz, CDCl_3) spectrum of *syn*-IIDBT-sulfone (8).

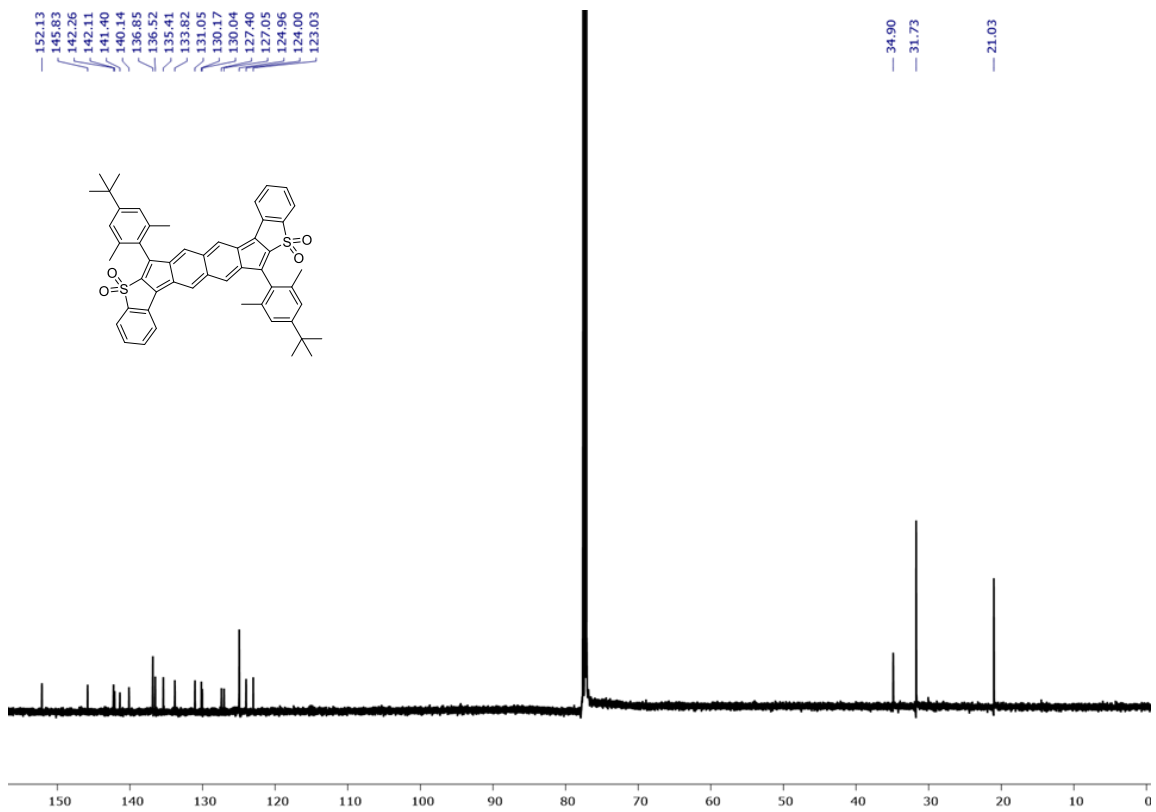


Figure E.14 ¹³C NMR (151 MHz, CDCl₃) spectrum of *syn*-IIDBT-sulfone (8).

Computational Information

NICS-XY scan details. All calculations related to the NICS-XY scans were performed using Gaussian 09. Geometries were optimized using B3LYP/6-311++G** level of theory and the structures were verified to be minima by frequency calculation. NICS-XY scans were carried out with the Aroma package at the B3LYP/6-311++G** level of theory using the sigma-only model. For the sake of computational efficiency calculations were performed on the hydrocarbon parent molecules for each compound. Previous computational studies in our group have shown that due to their nearly orthogonal orientation relative to the plane of the indacene core, removal of the pendant aryl groups on the apical carbons has little to no effect on NICS-XY scan calculations.

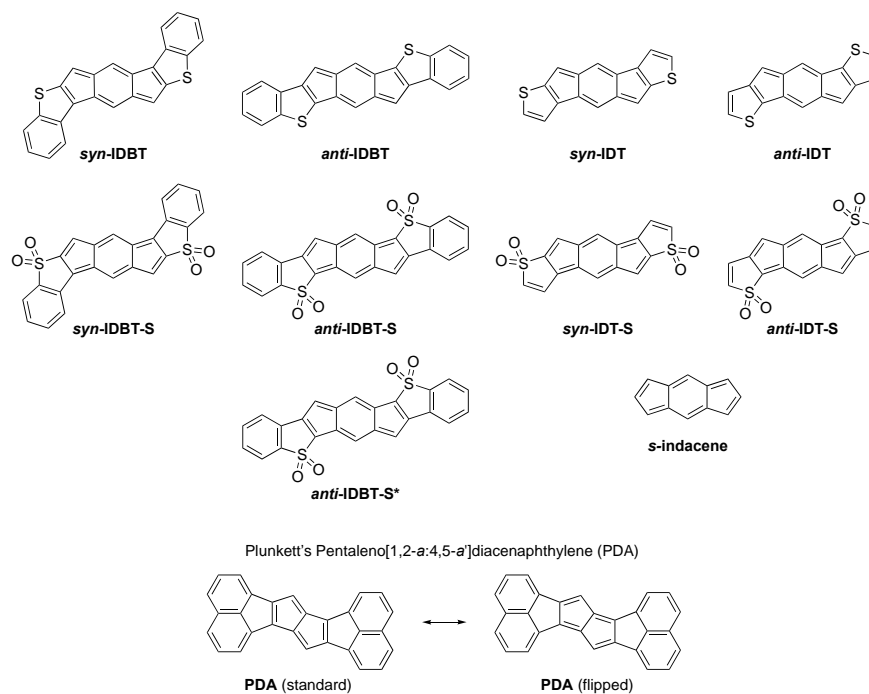


Figure E.15 Simplified structures used for the NICS-XY scan calculations.

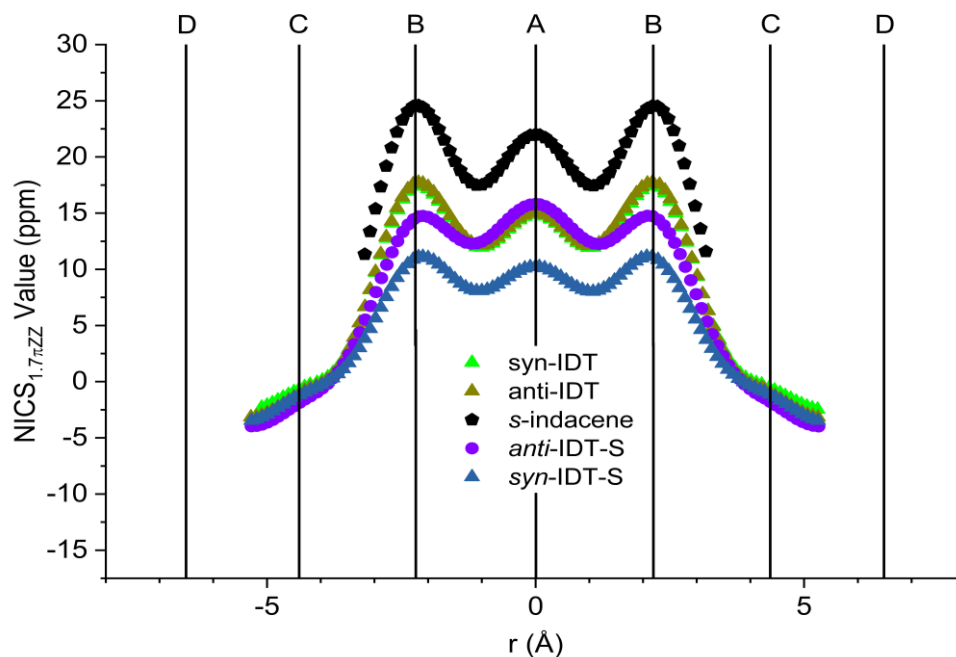


Figure E.16 NICS-XY scans of IDTs and IDT-sulfones

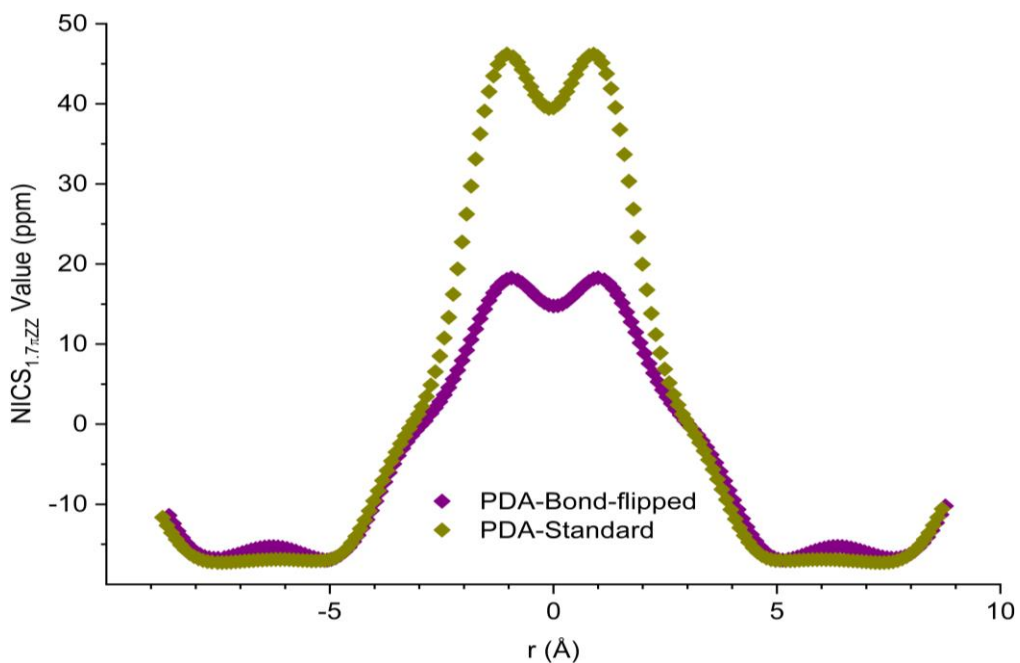


Figure E.17 NICS-XY scans (left) of **PDA** with standard bond alternation vs. **PDA** with flipped bond alternation along with a depiction of the scan pathway (right). Like the sulfones, the observed bonding pattern is due to the minimization of paratropicity in the pentalene core of the PDAs. It is worth noting that the “standard” geometry is 10.8 kcal mol⁻¹ higher in energy than the “flipped” geometry.

Calculated HOMO/LUMO Energy Levels with TD-DFT Calculations for Predicted**UV-Vis:** The same geometries used above for the NICS-XY scans were used to predict

UV-vis spectra and calculate optical energy gaps for the IDBTs and IDBT sulfones.

Optical values were calculated with TD-B3LYP/6-311++G** for the IDBTs and IDBT-

sulfones, and with TD-B3LYP/6-311+G* for the IIDBTs and IIDBT-sulfones. HOMO-

LUMO levels were generated using B3LYP/6-311++G** for the IDBTs and IDBT-

sulfones, and using B3LYP/6-311+G* for the IIDBTs and IIDBT-sulfones.

Table E1. Calculated optical data and HOMO-LUMO energy gaps for compounds **1-8**.

	λ_{\max} (nm)	f	configuration	Optical Gap (eV)	HOMO (eV)	LUMO (eV)	E_{gap} (eV)
<i>anti</i> -IDBT (1)	597	0.3685	HOMO-1→LUMO (93%)	2.05	-5.297	-3.336	1.961
<i>anti</i> -IDBT-S (5)	550	0.1528	HOMO-1→LUMO (75%)	2.20	-6.179	-4.339	1.840
<i>syn</i> -IDBT (2)	608	0.5578	HOMO-1→LUMO (94%)	1.99	-5.292	-3.455	1.837
<i>syn</i> -IDBT-S (6)	603	0.7178	HOMO→LUMO (99%)	2.04	-6.347	-4.393	1.954
<i>anti</i> -IIDBT (3)	702	0.5576	HOMO→LUMO (95%)	1.78	-4.983	-3.378	1.605
<i>anti</i> -IIDBT-S (7)	639	0.4487	HOMO→LUMO (93%)	1.94	-6.198	-4.387	1.811
<i>syn</i> -IIDBT (4)	730	0.7576	HOMO→LUMO (100%)	1.71	-5.100	-3.572	1.528
<i>syn</i> -IIDBT-S (8)	716	0.8410	HOMO→LUMO (100%)	1.75	-5.888	-4.368	1.520

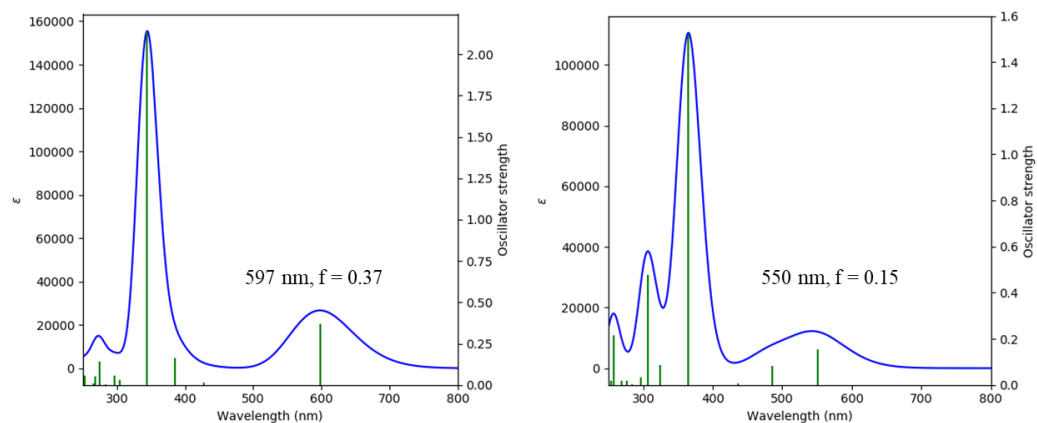


Figure E.18 TD-DFT predicted UV-Vis spectra for (left) *anti*-IDBT (**1**) and for (right) *anti*-IDBT-sulfone (**5**) calculated at the B3LYP/6-311++G* level of theory.

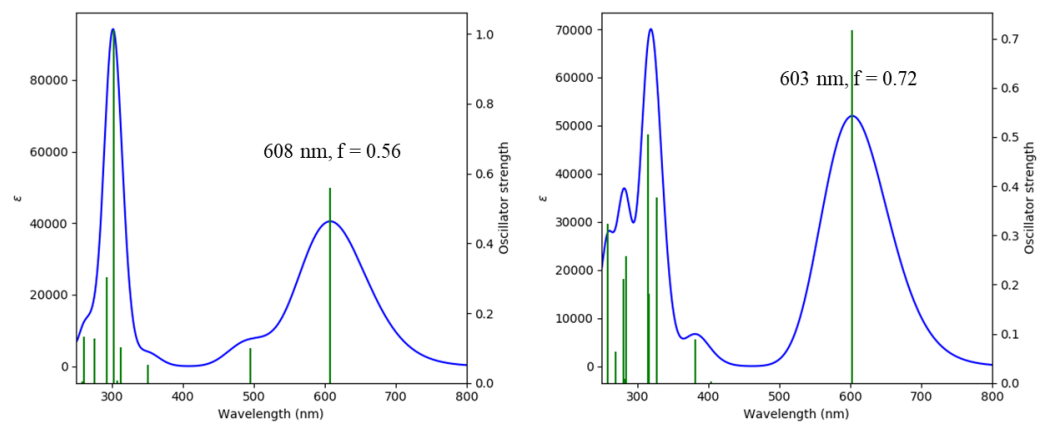


Figure E.19 TD-DFT predicted UV-Vis spectra for (left) *syn*-IDBT (**2**) and for (right) *syn*-IDBT-sulfone (**6**) calculated at the B3LYP/6-311++G* level of theory.

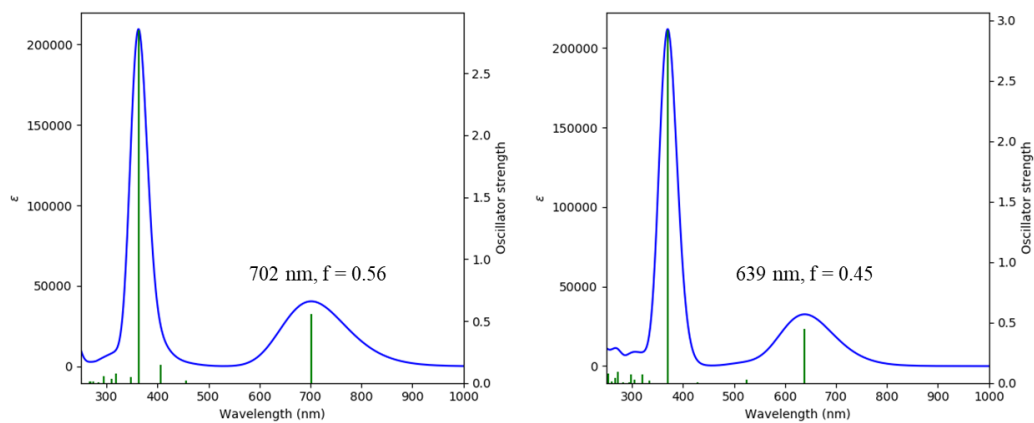


Figure E.20 TD-DFT predicted UV-Vis spectra for (left) *anti*-IIDBT (**3**) and for (right) *anti*-IIDBT-sulfone (**7**) calculated at the TD-U3LYP/6-311+G* level of theory.

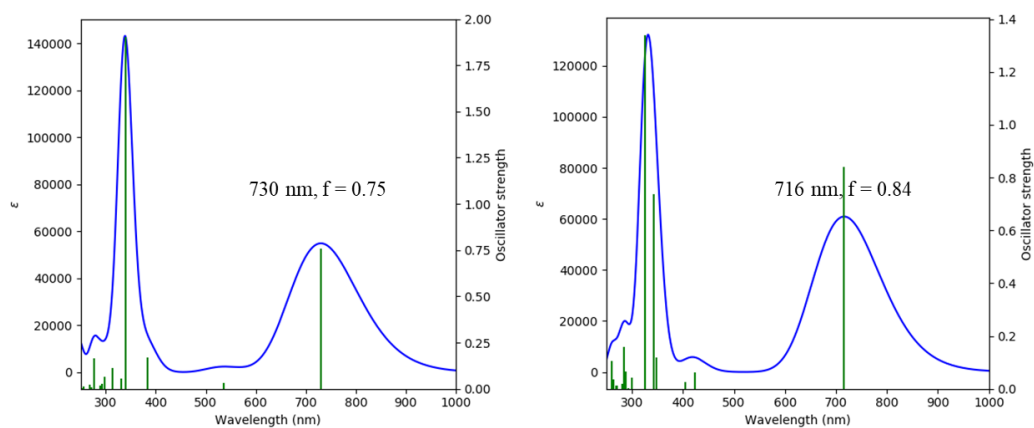
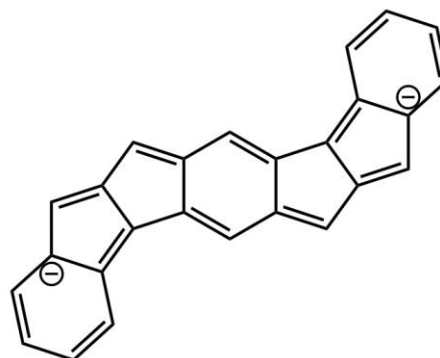
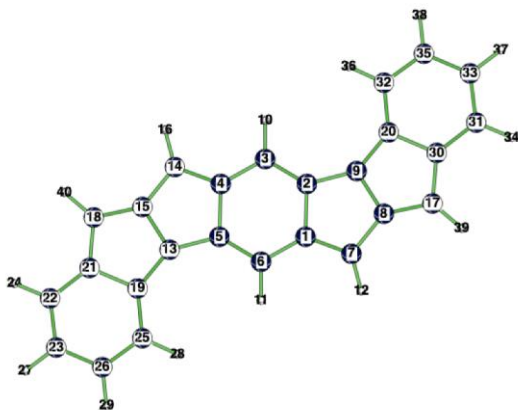


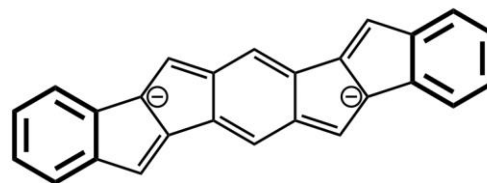
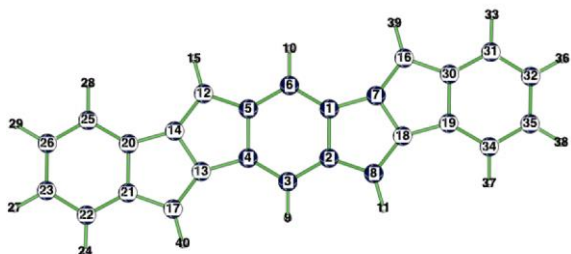
Figure E.21 TD-DFT predicted UV-Vis spectra for (left) *syn*-IIDBT (**4**) and for (right) *syn*-IIDBT-sulfone (**8**) calculated at the TD-U3LYP/6-311+G* level of theory.

Clar Sextet-Effects in *syn*- and *anti*-IDBT Fused *s*-Indacenes. Geometries for the dianion hydrocarbon reference compounds that are isoelectronic with the benzothiophene-fused *s*-indacenes (i.e., *syn*-IDBT **2** and *anti*-IDBT **1**) were optimized at B3LYP/6-311++G(d,p) using the Gaussian16 program. Vibrational frequency analyses verified the nature of the stationary points. Natural Lewis structure (NLS) analyses were performed at the same level of theory using the NBO 7.0 program to identify the major Lewis structures of the dianion hydrocarbon references and illustrate the “Clar sextet-effect”. The NLS procedure finds and prints out a representation of the best possible Lewis structure for a given molecular wavefunction. According to the recognized Lewis structure, atom numbers specified in the “LONE” string indicate the locations of lone pairs, and the pairs of atom numbers specified in the “BOND” string indicate the locations of single (S) and double (D) bonds. The NLS-recognized Lewis structures for the *syn*-IDBT dianion reference (Figure E.22, note absence of Clar sextets in the suggested Lewis structure) and the *anti*-IDBT dianion reference (Figure E.23, note two Clar sextets in the suggested Lewis structure) are shown below.



```
LONE 21 1 30 1 END
BOND S 1 2 S 1 6 D 1 7 D 2 3 S 2 9 S 3 4 S 3 10 S 4 5 D 4 14 D 5 6 S 5 13 S 6 11
S 7 8 S 7 12 S 8 9 D 8 17 D 9 20 S 13 15 D 13 19 S 14 15 S 14 16 D 15 18 S 17 30
S 17 39 S 18 21 S 18 40 S 19 21 S 19 25 S 20 30 S 20 32 S 21 22 D 22 23 S 22 24
S 23 26 S 23 27 D 25 26 S 25 28 S 26 29 S 30 31 D 31 33 S 31 34 D 32 35 S 32 36
S 33 35 S 33 37 S 35 38 END
```

Figure E.22 NLS output string, atom numbering, and Lewis structure for the isoelectronic dianion hydrocarbon reference structure of *syn*-IDBT **2**. Note the absence of formal Clar sextets in the NLS-recognized Lewis structure.



```
LONE 14 1 18 1 END
BOND S 1 2 D 1 6 S 1 7 S 2 3 D 2 8 D 3 4 S 3 9 S 4 5 S 4 13 S 5 6 D 5 12 S 6 10
D 7 16 S 7 18 S 8 11 S 8 18 S 12 14 S 12 15 S 13 14 D 13 17 S 14 20 S 16 30
S 16 39 S 17 21 S 17 40 S 18 19 S 19 30 D 19 34 S 20 21 D 20 25 D 21 22 S 22 23
S 22 24 D 23 26 S 23 27 S 25 26 S 25 28 S 26 29 D 30 31 S 31 32 S 31 33 D 32 35
S 32 36 S 34 35 S 34 37 S 35 38 END
```

Figure E.23 NLS output string, atom numbering, and Lewis structure for the isoelectronic dianion hydrocarbon reference of *anti*-IDBT **1**. Note two Clar sextets in the NLS-recognized Lewis structure.

Charge-Effects in IDT and IDT-S Fused *s*-Indacenes. When the two terminal benzene rings of IDBT and IDBT-S are removed, both thiophene (IDT) and thiophene-dioxide (IDT-S) fused *s*-indacenes exhibit a more paratropic *anti*-isomer. In these systems, the “Clar sextet-effect,” arising from differences in the dominant resonance forms of the outer benzenoid rings is absent, and a “charge-effect” (i.e., topological charge stabilization) dominates. Computed NPA charges for the *s*-indacene core show that carbons 2 and 6 display the most negative charges (see Figure 6.4 in the main text). In the *syn*-forms, the S and SO₂ groups stabilize negative charges at carbons 2 and 6, resulting in larger HOMO-LUMO gaps (S: 2.29 eV, SO₂: 2.27 eV) and decreased paratropicity. In the *anti*-forms, the S and SO₂ groups destabilize charges at carbons 2 and 6, resulting in smaller HOMO-LUMO gaps (S: 1.35 eV, SO₂: 1.28 eV) and increased paratropicity.

Geometries for IDT and IDT-S were optimized at B3LYP/6-311++G(d,p) using the Gaussian16 program. Optimized Cartesian coordinates are included in Section 7.1 of the SI. Natural Population Analyses (NPA) analyses were performed at the same level of theory using the NBO 7.0 program as implemented in Gaussian16. HOMO-LUMO gaps were computed as vertical excitation energies from the HOMO to the LUMO orbitals at TD-B3LYP/6-311++G(d,p).

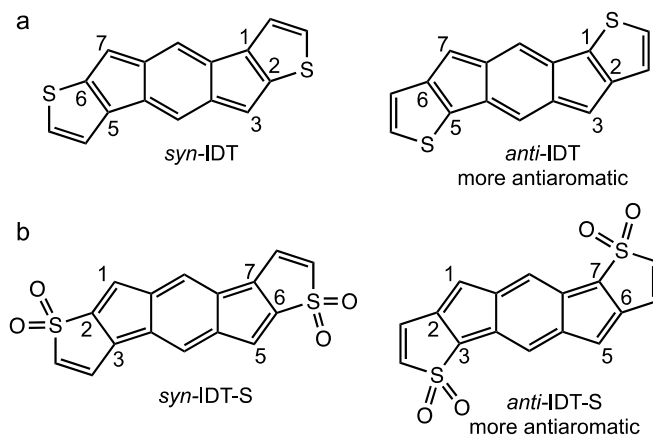


Figure E.24 Structures for (a) IDT (shown in “normal” bonding pattern) and (b) IDT-S (shown in “flipped” bonding pattern). Both systems show a more paratropic *anti*-form, as expected by a “charge-effect” (i.e., topological charge stabilization; see Figure S25). Electronegative groups stabilize the *s*-indacene core when attached to positions 2 and 6 (*syn*-), and destabilize the *s*-indacene core when attached to positions 1 and 5 or 3 and 7 (*anti*-).

Optimized geometries and calculated γ and ΔE_{ST} values: Geometry optimization and frequency analysis calculations for the singlet and triplet states were performed at the RB3LYP and UB3LYP levels, respectively, using the 6-311G* basis set. Vertical and adiabatic ΔE_{ST} values were evaluated at the SF-NC-TDDFT PBE50/6-311G* level, where zero-point vibrational energy (ZPVE) corrections for the singlet and triplet states were estimated from the results of the frequency analysis calculations at the RB3LYP and UB3LYP levels, respectively. Diradical character γ for the singlet state was evaluated at the PUHF/6-311G* level. Quantum chemical calculations were performed using Gaussian 09 and Q-Chem 5 program packages. Calculation results were visualized using DrawMol package.

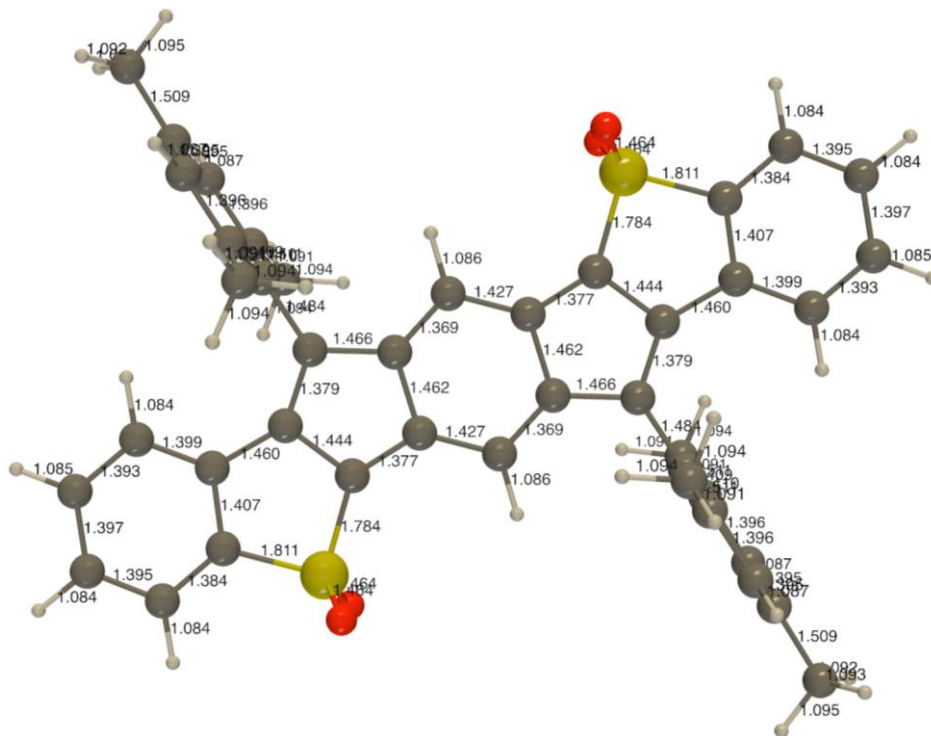


Figure E.25 Optimized geometry of *anti*-IDBT-sulfone **5**.

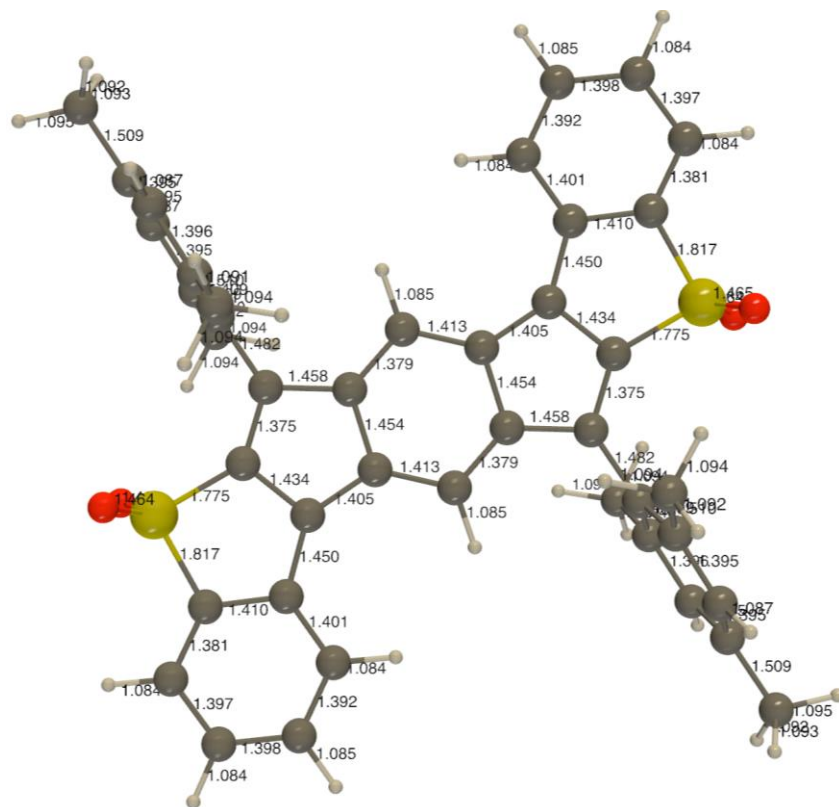


Figure E.26 Optimized geometry of *syn*-IDBT-sulfone **6**.

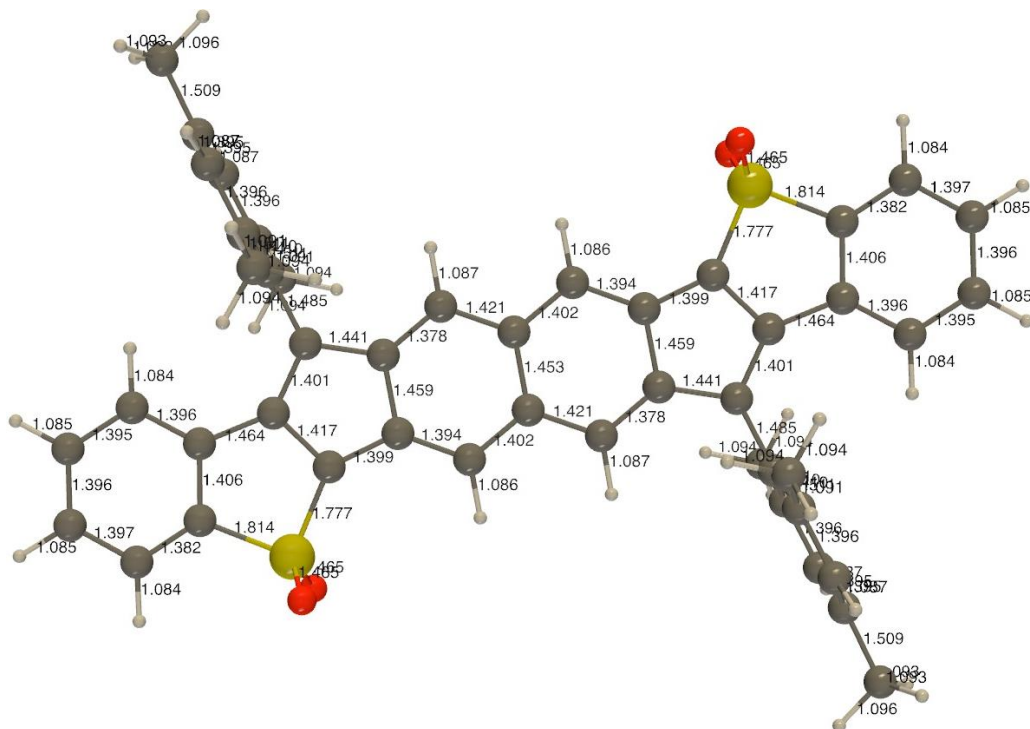


Figure E.27 Optimized geometry of *anti*-IDBT-sulfone **7**.

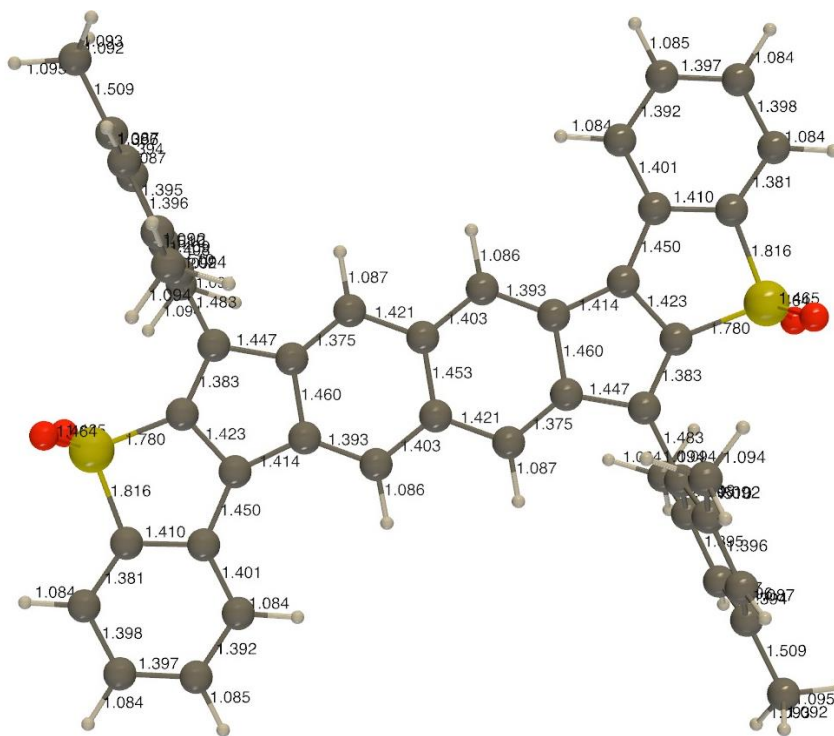


Figure E.28 Optimized geometry of *syn*-IIDBT-sulfone **8**.

Table E2. Summary of calculation results.

	IIDBT		IIDBT-sulfone	
	<i>anti</i> (3)	<i>syn</i> (4)	<i>anti</i> (7)	<i>syn</i> (8)
y (PUHF) [-]	0.613	0.658	0.601	0.652
Vert. ΔE_{ST} (kcal mol ⁻¹)	-11.65	-11.09	-13.59	-11.26
Adia. ΔE_{ST} (kcal mol ⁻¹)	-9.37	-8.84	-10.72	-9.33
Adia. ΔE_{ST} (+ZPVE) (kcal mol ⁻¹)	-8.77	-8.06	-9.65	-8.29
ΔE_{ST} (exp) (kcal mol ⁻¹)	-8.3	-7.1	n.a.	-6.5

Additional Spectroscopy

Additional Variable Temperature NMR spectra. Approximately 5 mg of *syn*-IIDBT-sulfone (**8**) was placed in an NMR tube with different NMR solvents and the spectra were collected at different temperatures. The spectra were acquired on a Bruker 500 MHz spectrometer that was heated to the maximum temperature range of each NMR solvent.

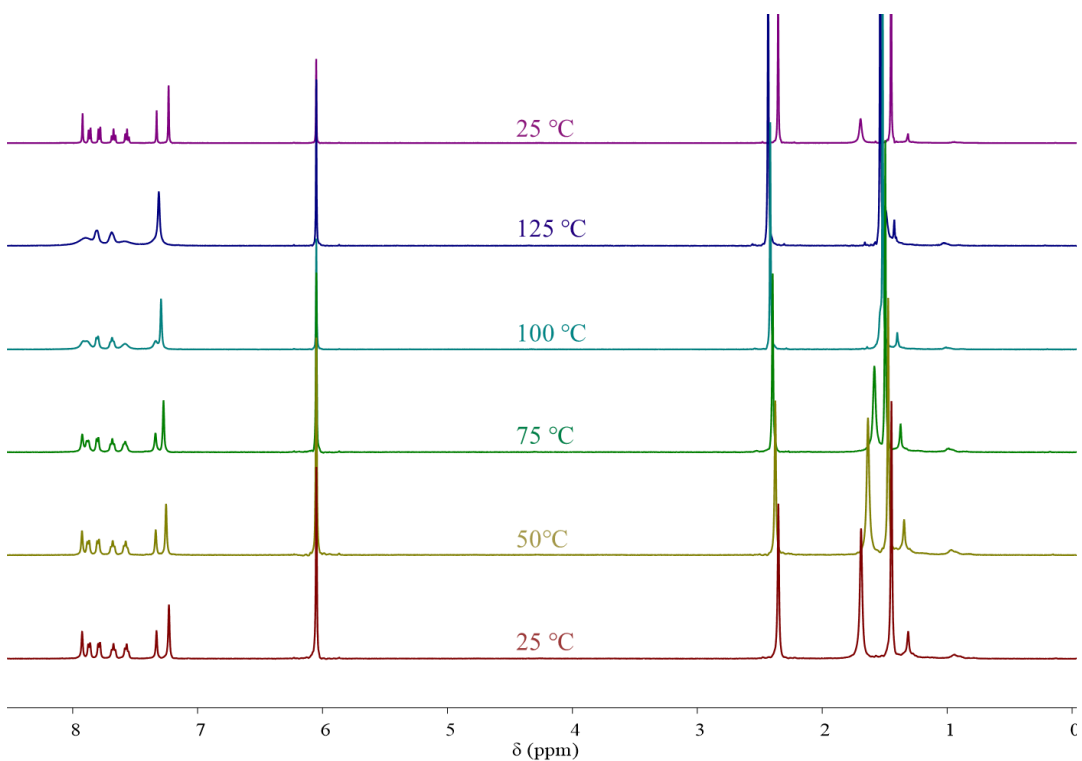


Figure E.29 VT ^1H NMR full spectra of **8** in 1,1,2,2-tetrachloroethane- d_2 showing thermal population of the paramagnetic triplet state at elevated temperatures.

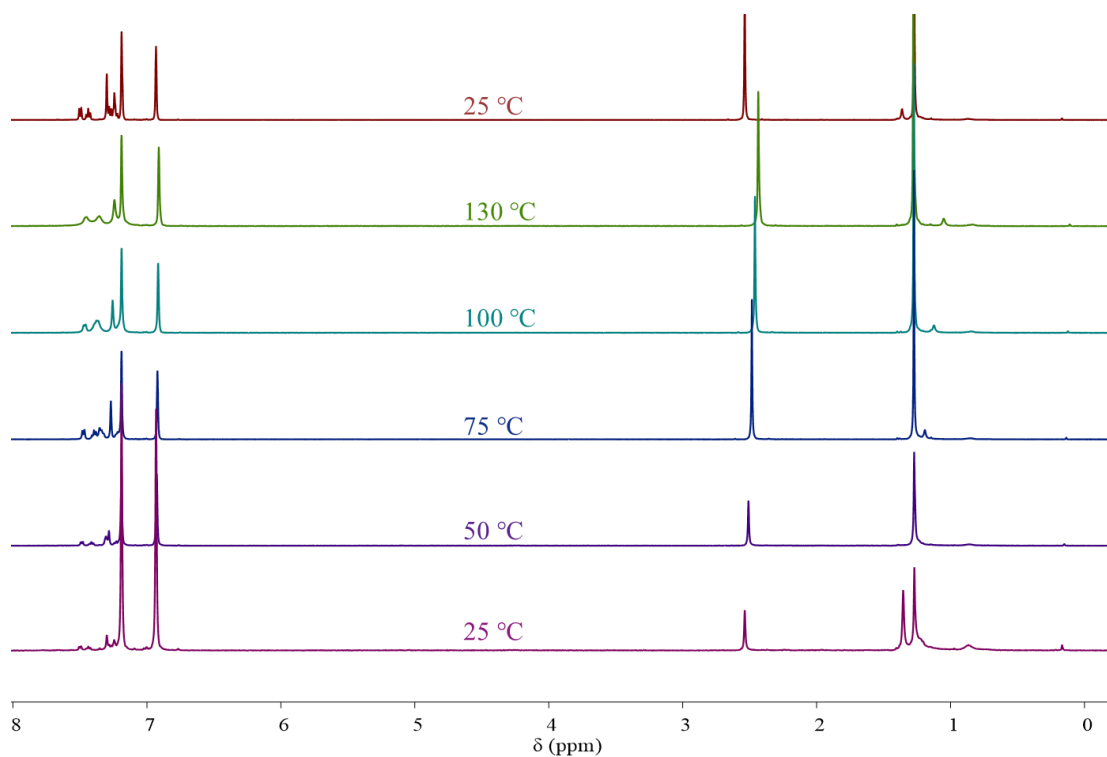


Figure E.30 VT ^1H NMR full spectra of **8** in 1,2-dichlorobenzene- d_4 showing thermal population of the paramagnetic triplet state at elevated temperatures.

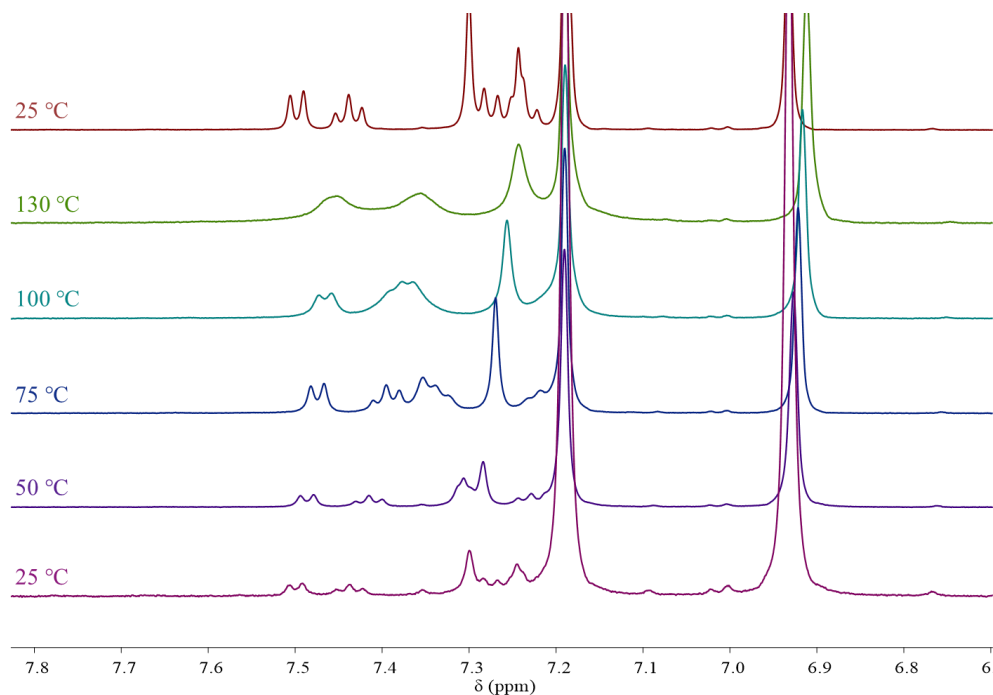


Figure E.31 VT ^1H NMR of the aromatic region of **8** in 1,2-dichlorobenzene- d_4 showing thermal population of the paramagnetic triplet state at elevated temperatures.

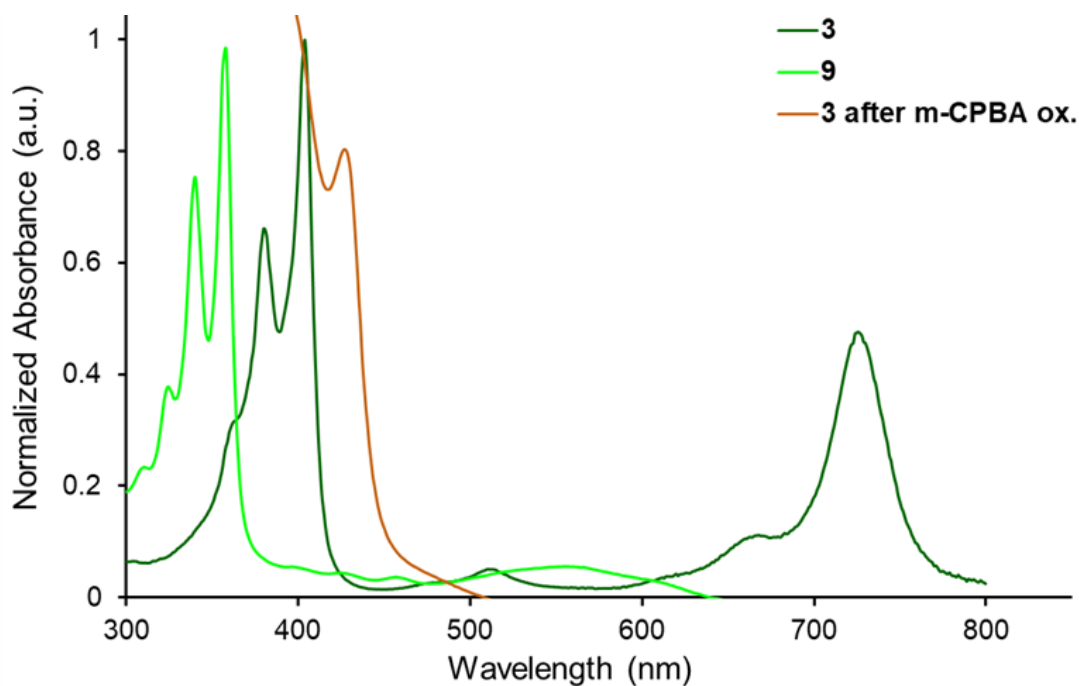


Figure E.32 Electronic absorption spectra for *anti*-IIDBT (**3**), the sulfonamide side product **9** from the reaction of **3** with UHP, and the orange colored decomposition product that was the result of the unsuccessful oxidation of **3** with mCPBA.

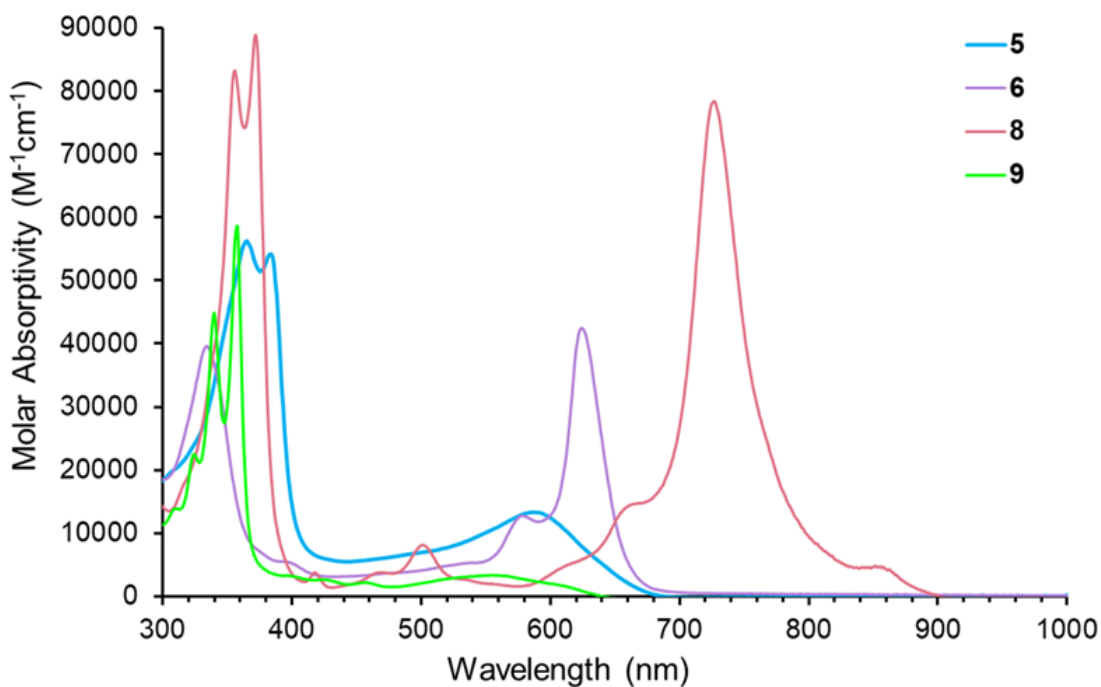


Figure E.33 Plot of wavelength vs. molar absorptivity for the three successfully synthesized sulfone compounds (**5**, **6**, **8**), and the sulfonamide side product **9**.

5. Cyclic Voltammetry

CV Measurements. All electrochemical experiments were conducted with traditional 3-electrode geometry using a Biologic SP-50 potentiostat. Electrolyte solutions (0.1 M) were prepared from anhydrous, degassed HPLC grade CH_2Cl_2 and anhydrous Bu_4NPF_6 . The working electrode was a glassy carbon electrode (3-mm diameter), with a Pt-coil counter electrode and a Ag wire pseudo reference. The ferrocene/ferrocenium (Fc/Fc^+) couple was used as an internal standard following each experiment. Potential values were re-referenced to SCE using a value of 0.46 (V vs. SCE) for the Fc/Fc^+ couple in CH_2Cl_2 . LUMO and HOMO levels were approximated using $\text{SCE} = -4.68 \text{ eV vs. vacuum}$. CV experiments were conducted in a three-neck flask that had been evacuated and backfilled with nitrogen for three cycles using standard Schlenk-line technique. Voltammograms were recorded at a sweep rates of 50 mV s^{-1} . $E_{1/2}$ values were calculated assuming $E_{1/2} \approx E_o' = (E_{\text{anodic}} + E_{\text{cathodic}})/2$ based on these observations for reversible couples; for irreversible couples the E_o' value is estimated as the potential at peak current. Analyte concentrations were ca. 1-5 mM.

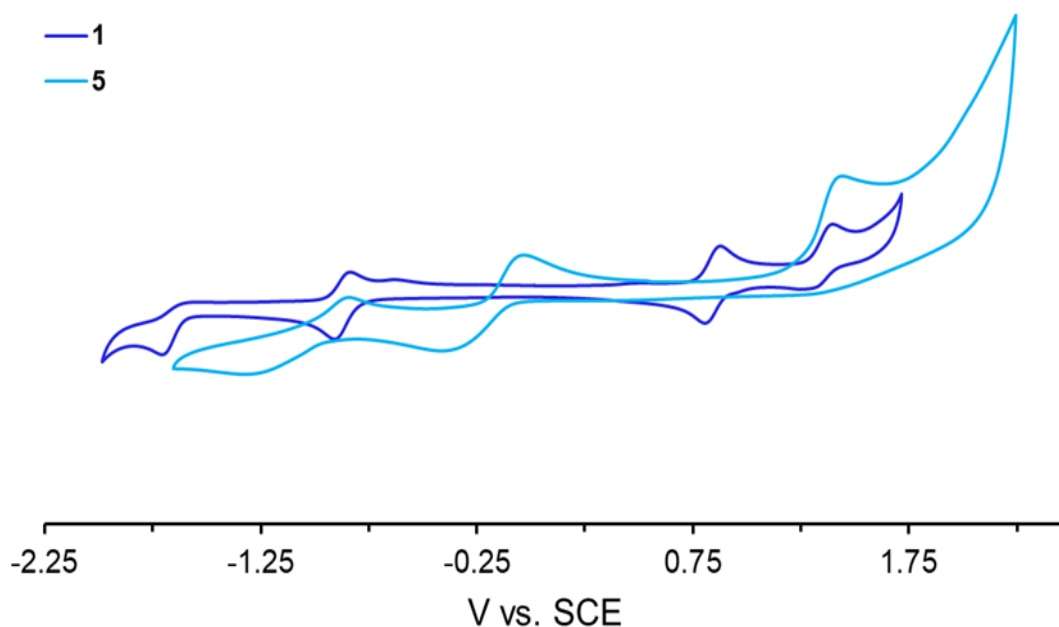


Figure E.34 Cyclic voltammograms of **1** and **5**.

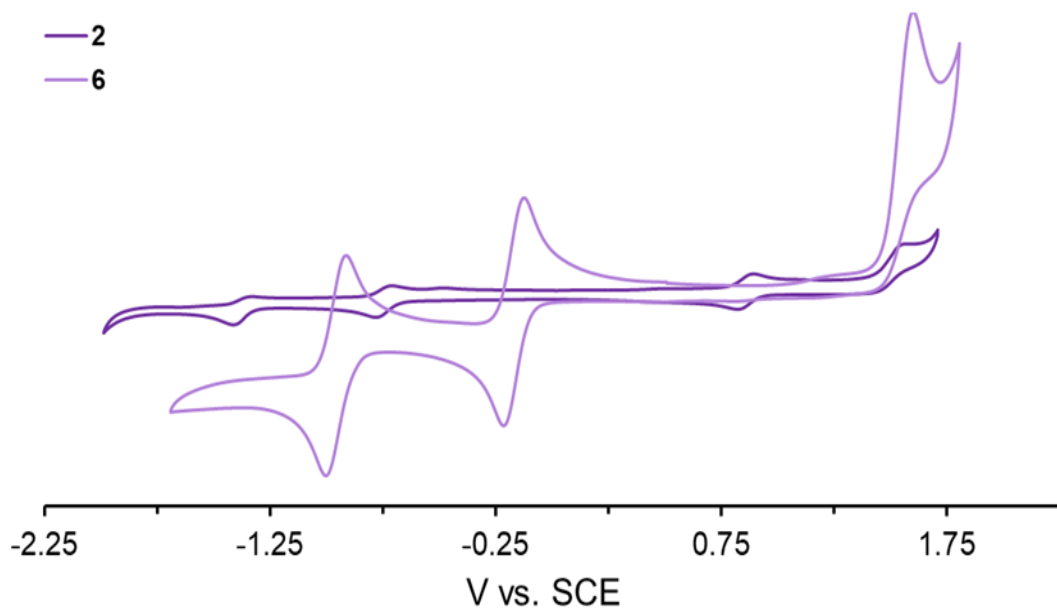


Figure E.35 Cyclic voltammograms of **2** and **6**.

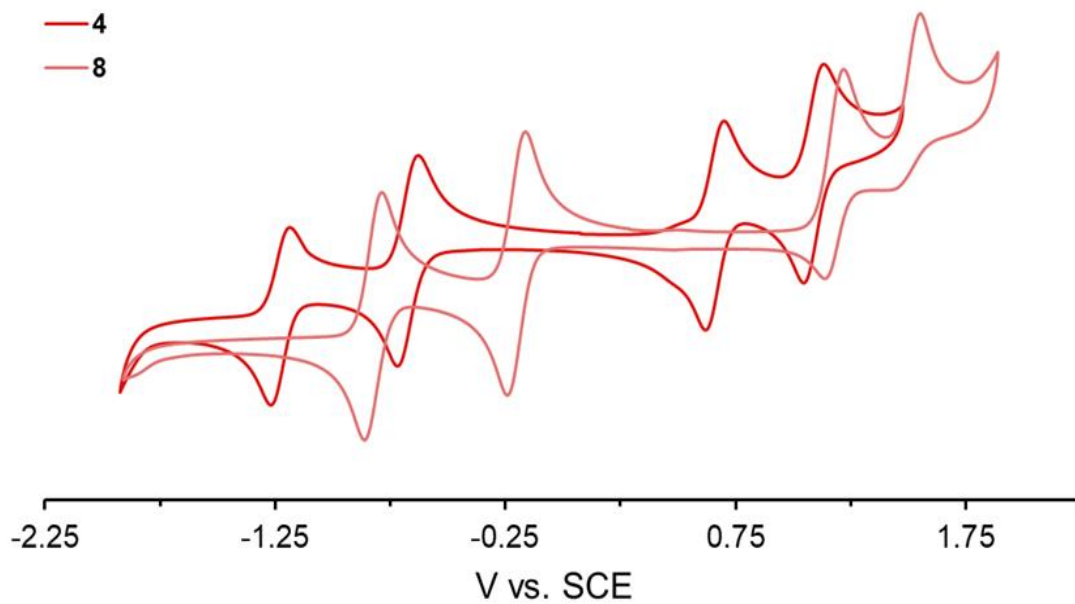


Figure E.36 Cyclic voltammograms of **4** and **8**.

SQUID Details and TGA Analysis: Magnetic susceptibility measurements were performed with a Quantum Design MPMS-XL-5 SQUID susceptometer in the 300-580 K temperature range with an applied field of 0.5 T using a sample space oven with the sample ($m = 4.528$ mg) inserted in a 1.5 mm diameter aluminum foil cylinder. The susceptibility data were corrected for the same sample holder previously measured using the same conditions and for the diamagnetic contributions of the compound as deduced by using Pascal's constant tables. The magnetic measurements were fitted using the classical Bleaney-Bowers model for an antiferromagnetic $S = \frac{1}{2}$ dimer plus a monomeric $S = \frac{1}{2}$ impurity.

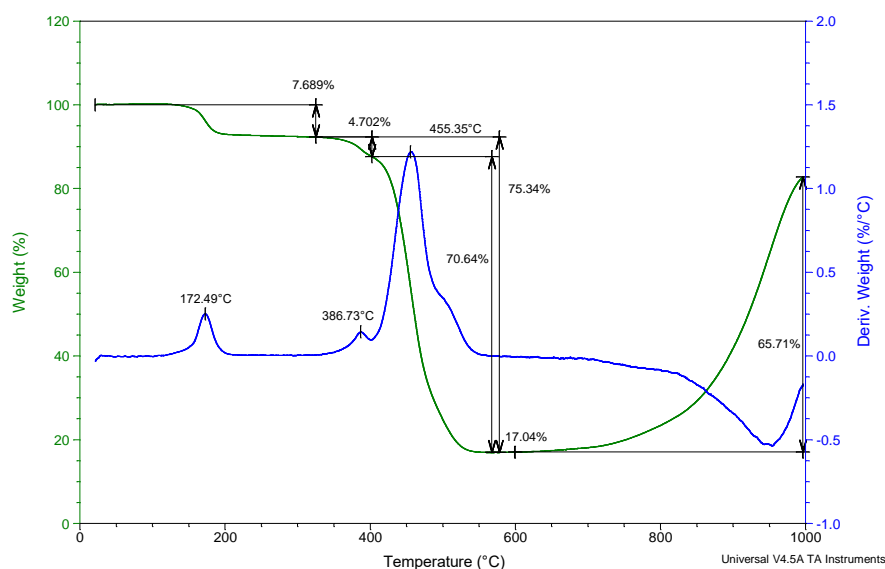


Figure E.37 TGA data for *syn*-IIDBT-S 8. Weight loss at ~170 °C corresponds to loss of residual 1,2-dichlorobenzene solvent. (or possibly loss of a *t*-butyl group)

X-ray Diffraction Details

General. Diffraction intensities were collected at 173 K on a Bruker Apex2 CCD diffractometer using CuK α ($\lambda = 1.54178 \text{ \AA}$, **5-Mes** and **9**) or MoK α ($\lambda = 0.71073 \text{ \AA}$, **6**) radiation. Space groups were determined based on systematic absences (**9**) and intensity statistics (**5-Mes** and **6**). Absorption corrections were applied by SADABS. Structures were solved by direct methods and Fourier techniques and refined on F^2 using full matrix least-squares procedures. All non-H atoms were refined with anisotropic thermal parameters. H atoms in all structures were refined in calculated positions in a rigid group model. One of two solvent molecules CHCl₃ in **9** and a mixture of solvent molecules CH₂Cl₂/CHCl₃/CH₃CN in **6** are highly disordered in a general position and around an inversion center, respectively. These disordered solvent molecules were treated by SQUEEZE. The corrections of the X-ray data by SQUEEZE are 232 and 208 electron/cell; the required values are 232 electron/cell for four CHCl₃ in **9**. The disordered solvent molecules in **6** were not resolved and they have not been included into the final formula of the compound given in the CIF file. Thermal parameters for terminal *t*-Bu groups in **6** and **9** are significantly elongated. The crystal structure of **9** was treated as a racemic twin; the Flack parameter is 0.28(3). X-ray diffraction for crystals of **9** at high angles is very weak due to strong disorder in the structure. As a result the structure of **9** is not very precisely determined. All calculations were performed by the Bruker SHELXL-2014 package. Low-temperature X-ray diffraction data for **8** were collected on a Rigaku XtaLAB Synergy diffractometer coupled to a Rigaku Hypix detector with Cu K α radiation ($\lambda = 1.54184 \text{ \AA}$) from a PhotonJet micro-focus X-ray source at 100 K. The diffraction images were processed and scaled using the CrysAlisPro software. The structures were solved through intrinsic phasing using SHELXT and refined against F^2 on all data by full-matrix least squares with SHELXL following established refinement strategies. All non-hydrogen atoms were refined anisotropically. All hydrogen atoms bound to carbon were included in the model at geometrically calculated positions and refined using a riding model. The isotropic displacement parameters of all hydrogen atoms were fixed to 1.2 times the U_{eq} value of the atoms they are linked to.

Crystallographic Data for 5-Mes: $C_{43}H_{33}Cl_3O_4S_2$, $M = 784.16$, $0.06 \times 0.04 \times 0.02$ mm, $T = 173(2)$ K, Triclinic, space group $P-1$, $a = 8.1459(3)$ Å, $b = 9.0608(4)$ Å, $c = 13.562(5)$ Å, $\alpha = 75.860(2)^\circ$, $\beta = 73.582(2)^\circ$, $\gamma = 84.176(2)^\circ$, $V = 930.52(6)$ Å³, $Z = 1$, $Z' = 0.5$, $D_c = 1.399$ Mg/m³, $\mu(\text{Cu}) = 3.628$ mm⁻¹, $F(000) = 406$, $2\theta_{\text{max}} = 133.05^\circ$, 8785 reflections, 3229 independent reflections [$R_{\text{int}} = 0.0463$], $R1 = 0.0530$, $wR2 = 0.1387$ and $\text{GOF} = 1.077$ for 3229 reflections (255 parameters) with $I > 2\sigma(I)$, $R1 = 0.0566$, $wR2 = 0.1411$ and $\text{GOF} = 1.077$ for all reflections, max/min residual electron density $+0.662/-0.451$ eÅ⁻³. CCDC 1995028.

Crystallographic Data for 6: $C_{48}H_{44}O_4S_2$, $M = 748.95$, $0.06 \times 0.03 \times 0.01$ mm, $T = 173(2)$ K, Triclinic, space group $P-1$, $a = 13.0977(14)$ Å, $b = 15.0775(16)$ Å, $c = 15.4634(15)$ Å, $\alpha = 115.901(3)^\circ$, $\beta = 94.740(3)^\circ$, $\gamma = 112.307(3)^\circ$, $V = 2425.5(4)$ Å³, $Z = 2$, $Z' = 1$, $D_c = 1.025$ Mg/m³, $\mu(\text{Mo}) = 0.146$ mm⁻¹, $F(000) = 792$, $2\theta_{\text{max}} = 56.32^\circ$, 17634 reflections, 8491 independent reflections [$R_{\text{int}} = 0.0485$], $R1 = 0.0848$, $wR2 = 0.2035$ and $\text{GOF} = 1.002$ for 8491 reflections (487 parameters) with $I > 2\sigma(I)$, $R1 = 0.1468$, $wR2 = 0.2237$ and $\text{GOF} = 1.002$ for all reflections, max/min residual electron density $+0.465/-0.389$ eÅ⁻³. CCDC 1995030.

Crystallographic Data for 8: $C_{56}H_{52}N_2O_4S_2$, $C_{52}H_{46}O_4S_2 \cdot 2(\text{CH}_3\text{CN})$, $M = 881.11$, $0.136 \times 0.058 \times 0.047$ mm³, $T = 100.00(2)$ K, Triclinic, space group $P-1$, $a = 7.62440(10)$ Å, $b = 10.3907(2)$ Å, $c = 15.0797(3)$ Å, $\alpha = 92.525(2)^\circ$, $\beta = 97.786(2)^\circ$, $\gamma = 98.462(2)^\circ$, $V = 1168.26(4)$ Å³, $Z = 1$, $D_c = 1.252$ Mg/m³, $\mu(\text{Cu}) = 1.418$ mm⁻¹, $F(000) = 466$, $2\theta_{\text{max}} = 74.503^\circ$, 24859 reflections, 4765 independent reflections [$R_{\text{int}} = 0.0318$], $R1 = 0.0470$, $wR2 = 0.1063$ and $\text{GOF} = 1.020$ for all reflections, max/min residual electron density $+0.397/-0.464$ eÅ⁻³. CCDC 1994473.

Crystallographic Data for 9: $C_{54}H_{48}Cl_6N_2O_4S_2$, $M = 1065.76$, $0.14 \times 0.06 \times 0.02$ mm, $T = 173(2)$ K, Monoclinic, space group Cc , $a = 11.949(3)$ Å, $b = 25.877(6)$ Å, $c = 16.528(5)$ Å, $\beta = 98.21(2)^\circ$, $V = 5058(2)$ Å³, $Z = 4$, $Z' = 0.5$, $D_c = 1.400$ Mg/m³, $\mu(\text{Cu}) = 4.257$ mm⁻¹, $F(000) = 2208$, $2\theta_{\text{max}} = 135.86^\circ$, 17136 reflections, 6906 independent reflections [$R_{\text{int}} = 0.0827$], $R1 = 0.0719$, $wR2 = 0.1746$ and $\text{GOF} = 1.052$ for 6906 reflections (578 parameters) with $I > 2\sigma(I)$, $R1 = 0.0972$, $wR2 = 0.2030$ and $\text{GOF} = 1.052$ for all reflections, Flack = $0.28(3)$, max/min residual electron density $+0.277/-0.348$ eÅ⁻³. CCDC 1995029.

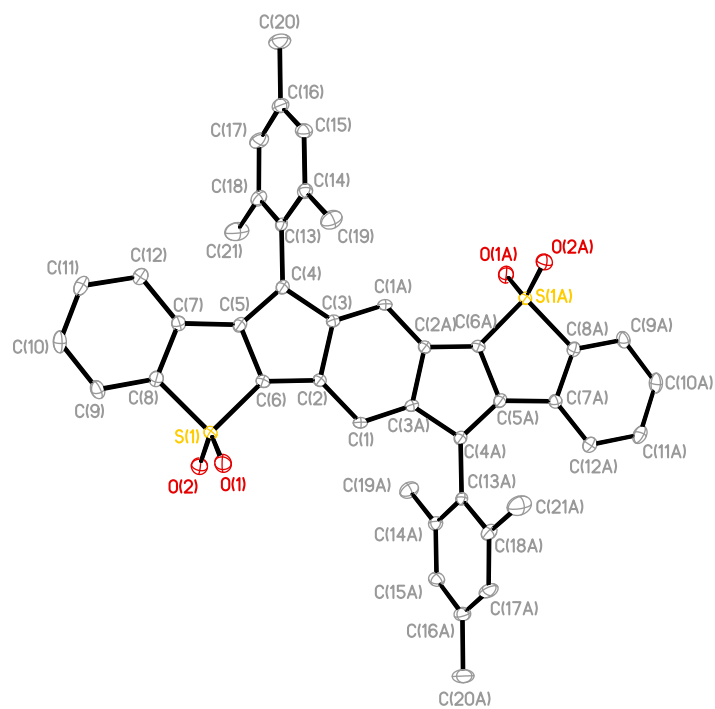


Figure E.38 Molecular structure of IDBT-S 5-Mes.

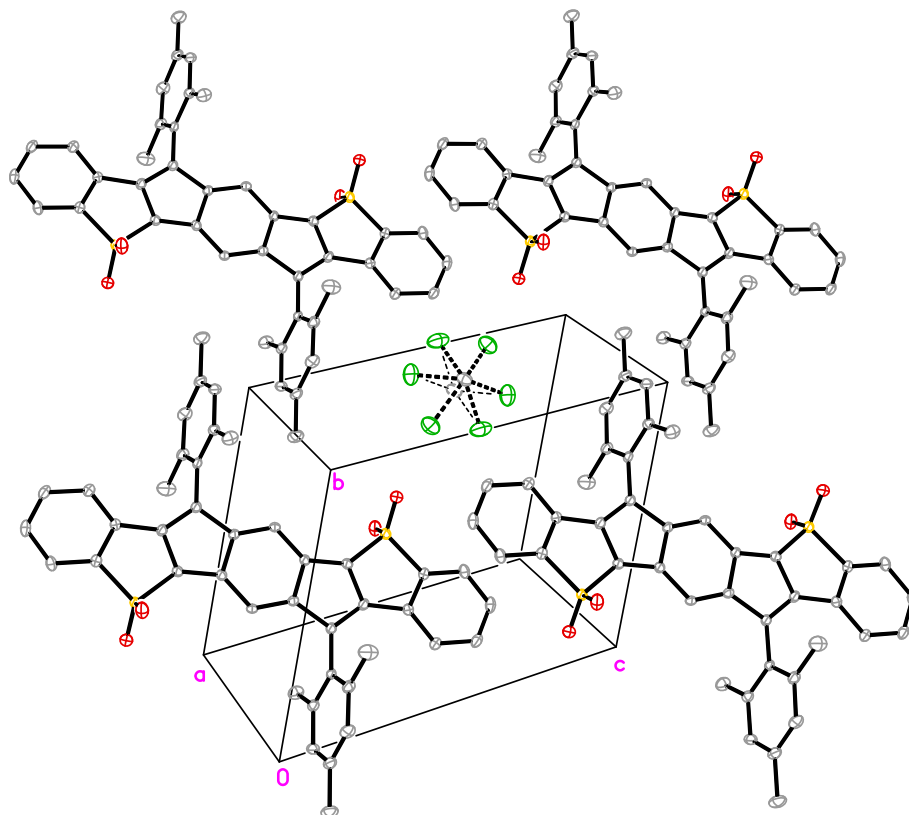


Figure E.39 Molecular packing of IDBT-S 5-Mes with disordered solvent molecule.

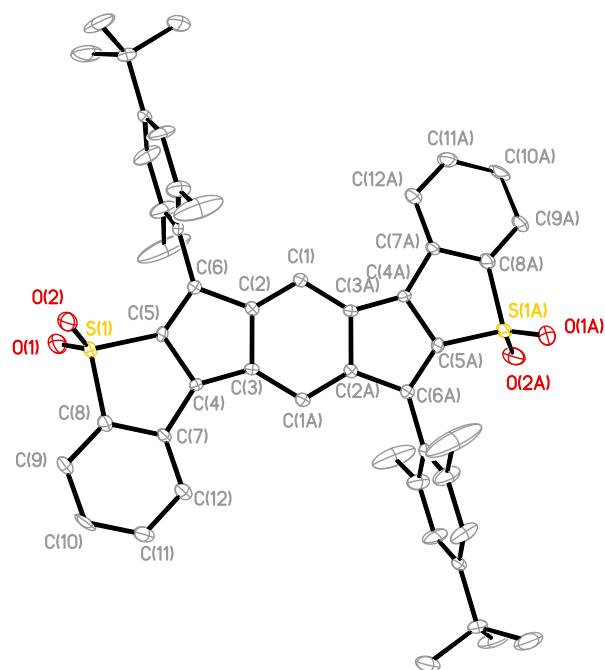


Figure E.40 Molecular structure of IDBT-S 6.

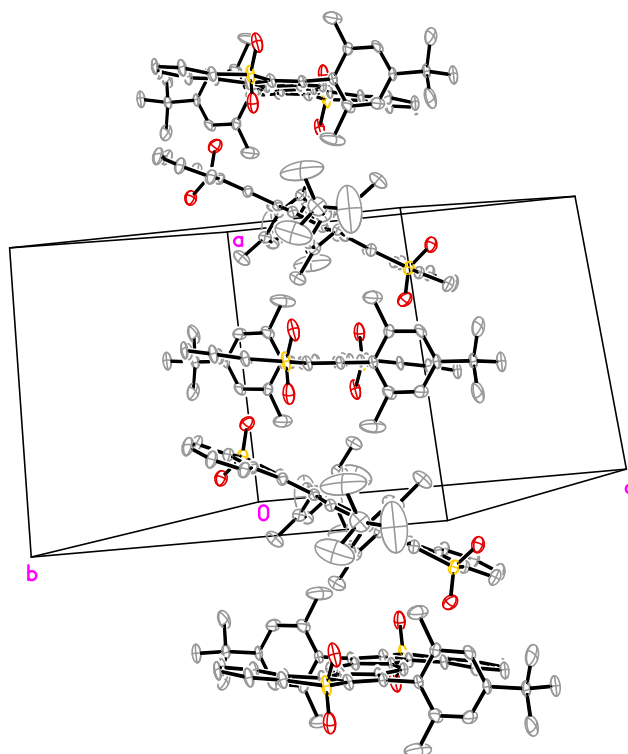


Figure E.41 Molecular packing of IDBT-S 6.

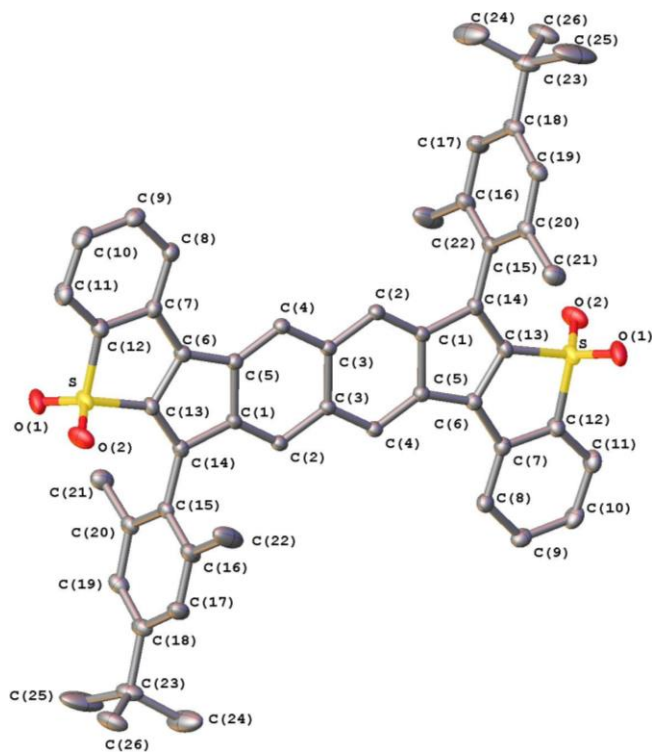


Figure E.42 Molecular structure of IDBT-S 8.

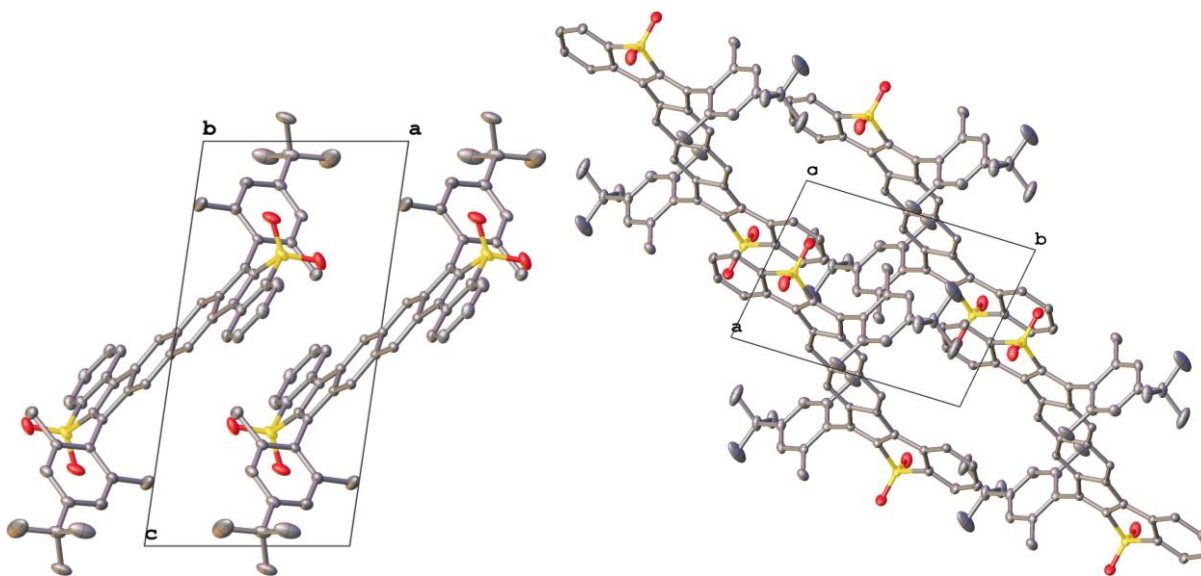


Figure E.43 Molecular packing of IDBT-S 8.

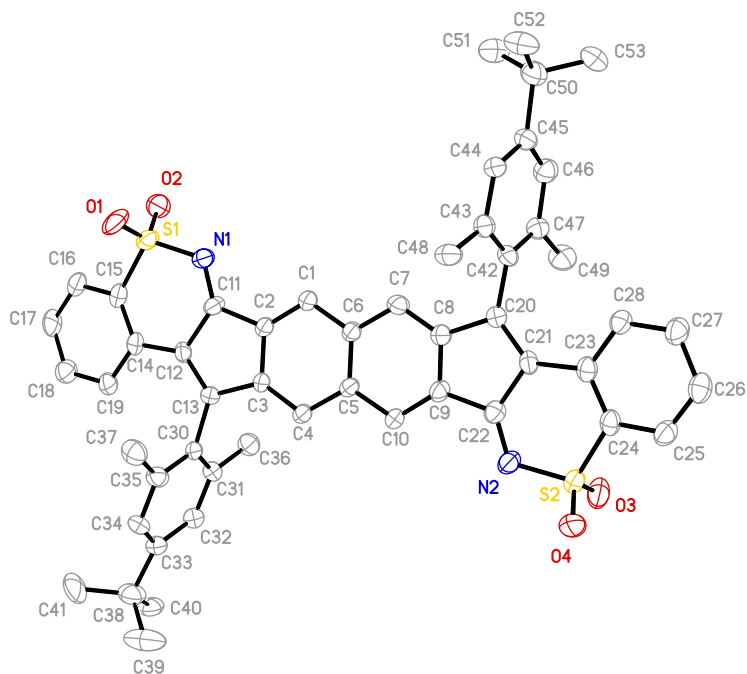


Figure E.44 Molecular structure of decomposition product **9**.

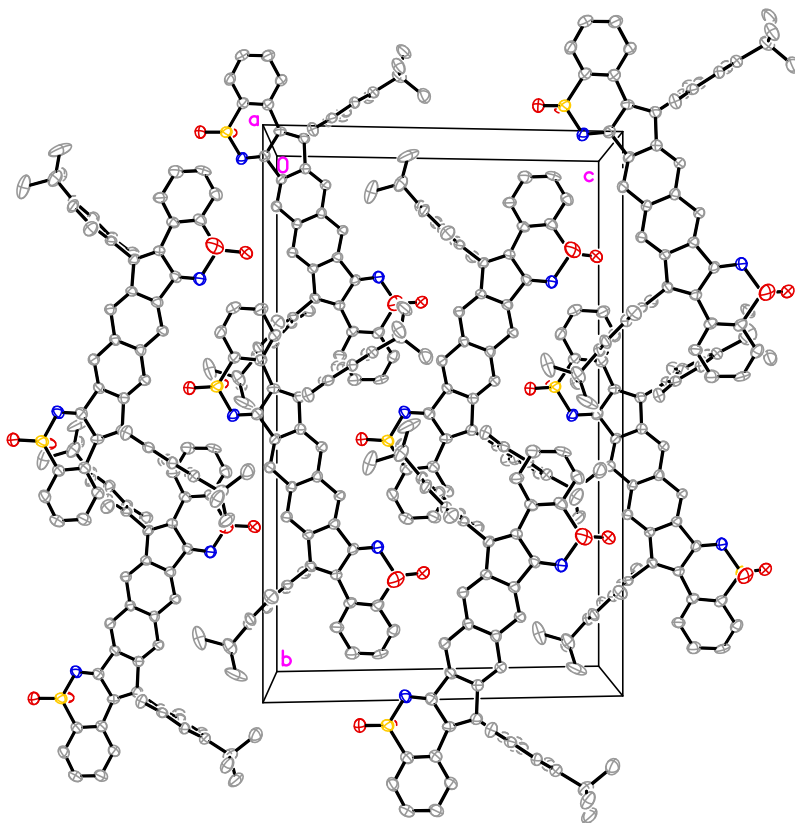


Figure E.45 Molecular packing of decomposition product **9**.

REFERENCES CITED

Chapter I.

1. G. E. Rudebusch, J. L. Zafra, K. Jorner, K. Fukuda, J. L. Marshall, I. Arrechea-Marcos, G. L. Espejo, R. Ponce Ortiz, C. J. Gómez-García, L. N. Zakharov, M. Nakano, J. Casado, M. M. Haley, *Nat. Chem.* **2016**, *8*, 753.
2. C. K. Frederickson, B. D. Rose, M. M. Haley, *Acc. Chem. Res.* **2017**, *50*, 977.
3. M. Abe, *Chem Rev.* **2013**, *113*, 7011.
4. a) T. Kubo, *Chem. Lett.* **2015**, *44*, 111; b) M. Nakano, *Top. Curr. Chem.* **2017**, *375*, 73.
5. A. E. Tschitschibabin, *Ber. Btsch. Chem. Ges.* **1907**, *40*, 1810.
6. E. Clar, *Polycyclic Hydrocarbons*, Vol. 1 and 2, John Wiley, New York **1964**.
7. a) Z. Sun, S. Lee, K. H. Park, X. Zhu, W. Zhang, B. Zheng, P. Hu, Z. Zeng, S. Das, Y. Li, C. Chi, R.-W. Li, K.-W. Huang, J. Ding, D. Kim, J. Wu. *J. Am. Chem. Soc.* **2013**, *135*, 18229; b) Z. Zeng, X. Shi, C. Chi, J. T. López Navarrete, J. Casado, J. Wu, *Chem. Soc. Rev.* **2015**, *44*, 6578; c) T. Y. Gopalakrishna, W. Zeng, X. Lu, J. Wu, *Chem. Commun.* **2018**, *54*, 2186.
8. a) K. Yamaguchi, *Chem. Phys. Lett.* **1975**, *33*, 330; b) D. Döhnert, J. Koutecky, *J. Am. Chem. Soc.* **1980**, *102*, 1789.
9. P. Karafiloglou *J. Chem. Educ.* **1989**, *66*, 816.
10. a) J. J. Dressler, Z. Zhou, J. L. Marshall, R. Kishi, S. Takamuku, Z. Wei, S. N. Spisak, M. Nakano, M. A. Petrukhina, M. M. Haley, *Angew. Chem. Int. Ed.* **2017**, *56*, 15363; b) Z. Zeng, Y. M. Sung, N. Bao, D. Tan, R. Lee, J. L. Zafra, B. S. Lee, M. Ishida, J. Ding, J. T. López Navarrete, Y. Li, W. Zeng, D. Kim, K.-W. Huang, R. D. Webster, J. Casado, J. Wu. *J. Am. Chem. Soc.* **2012**, *134*, 14513.
11. J. J. Dressler, M. Teraoka, G. L. Espejo, R. Kishi, S. Takamuku, C. J. Gómez-García, L. N. Zakharov, M. Nakano, J. Casado, M. M. Haley, *Nat. Chem.* **2018**, *10*, 1134.
12. a) P. Hu, J. Wu, *Can. J. Chem.* **2017**, *95*, 223; b) W. Zeng, Z. Sun, T. S. Heng, T. P. Gonçalves, T. Y. Gopalakrishna, K. W. Huang, J. Ding, J. Wu, *Angew. Chem. Int. Ed.* **2016**, *55*, 8615; c) Y. Li, W. K. Heng, B. S. Lee, N. Aratani, J. L. Zafra, N. Bao, R. Lee, Y. M. Sung, Z. Sun, K. W. Huang, R. D. Webster, J. T. Lopez Navarrete, D. Kim, A. Osuka, J. Ding, J. Wu. *J. Am. Chem. Soc.* **2012**, *134*, 14913.
13. a) A. Konishi, Y. Hirao, J. Kurata, T. Kubo, M. Nakano, K. Kamada *Pure Appl. Chem.* **2014**, *86*, 497; b) A. Konishi, Y. Hirao, K. Matsumoto, H. Kurata, R. Kishi, Y. Shigeta, M. Nakano, K. Tokunaga, K. Kamada, T. Kubo, *J. Am. Chem. Soc.* **2013**, *135*, 1430.

14. a) T. Kubo, A. Shimizu, M. Sakamoto, M. Uruichi, K. Yakushi, M. Nakano, D. Shiomi, K. Sato, T. Takui, Y. Morita, K. Nakasuji, *Angew. Chem. Int. Ed.* **2005**, *44*, 6564; b) A. Shimizu, Y. Hirao, K. Matsumoto, H. Kurata, T. Kubo, M. Uruichi, K. Yakushi, *Chem. Commun.* **2012**, *48*, 5629; c) T. Kubo, M. Sakamoto, M. Akabane, Y. Fujiwara, K. Yamamoto, M. Akita, K. Inoue, T. Takui, K. Nakasuji, *Angew. Chem. Int. Ed.* **2004**, *43*, 6474;
15. a) J. Casado, *Top. Curr. Chem.* **2017**, *375*, 209 ; b) Z. Zeng, M. Ishida, J. L. Zafra, X. Zhu, Y. M. Sung, N. Bao, R. D. Webster, B. S. Lee, R. Li, W. Zeng, Y. Li, C. Chi, J. T. Lopez Navarrete, J. Ding, J. Casado, D. Kim, J. Wu, *J. Am. Chem. Soc.* **2013**, *135*, 6363; c) Z. Zeng, J. Wu, *Chem. Rec.* **2015**, *15*, 322.
16. a) M. Bendikov, H. M. Duong, K. Starkey, K. N. Houk, E. A. Carter, F. Wudl, *J. Am. Chem. Soc.* **2004**, *126*, 7416; b) B. Purushothaman, M. Bruzek, S. R. Parkin, A.-F. Miller, J. E. Anthony, *Angew. Chem. Int. Ed.* **2011**, *50*, 7013; c) S. Dong, T. Y. Gopalakrishna, Y. Han, H. Phan, T. Tao, Y. Ni, G. Liu, C. Chi, *J. Am. Chem. Soc.* **2019**, *141*, 62; d) S. N. Intorp, M. Hodecker, M. Müller, O. Tverskoy, M. Rosenkranz, E. Dmitrieva, A. A. Popov, F. Rominger, J. Freudenberg, A. Dreuw, U. H. F. Bunz, *Angew. Chem. Int. Ed.* **2020**, accepted (DOI 10.1002/anie.201915977).
17. A. Shimizu, R. Kishi, M. Nakano, D. Shiomi, K. Sato, T. Takui, I. Hisaki, M. Miyata, Y. Tobe, *Angew. Chem. Int. Ed.* **2013**, *52*, 6076.
18. a) G. E. Rudebusch, G. L. Espejo, J. L. Zafra, M. Pena-Alvarez, S. N. Spisak, K. Fukuda, Z. Wei, M. Nakano, M. A. Petrukhina, J. Casado, M. M. Haley, *J. Am. Chem. Soc.* **2016**, *138*, 12648; b) H. Miyoshi, M. Miki, S. Hirano, A. Shimizu, R. Kishi, K. Fukuda, D. Shiomi, K. Sato, T. Takui, I. Hisaki, M. Nakano, Y. Tobe, *J. Org. Chem.* **2017**, *82*, 1380; c) J. E. Barker, J. J. Dressler, A. Cárdenas Valdivia, R. Kishi, E. T. Strand, L. N. Zakharov, S. N. MacMillan, C. J. Gómez-García, M. Nakano, J. Casado, M. M. Haley, *J. Am. Chem. Soc.* **2020**, *3*, 1548; d) J. J. Dressler, A. Cárdenas Valdivia, R. Kishi, G. E. Rudebusch, A. M. Ventura, B. E. Chastain, C. J. Gómez-García, L. N. Zakharov, M. Nakano, J. Casado, M. M. Haley, *Chem* **2020**, *6*,
19. Z. Sun, Q. Ye, C. Chi, J. Wu, *Chem. Soc. Rev.* **2012**, *41*, 7857.
20. a) P. Ravat, T. Šolomek, P. Ribar, M. Juriček, *Synlett* **2016**, *27*, 1613; b) S. Di Motta, F. Negri, D. Fazzi, C. Castiglioni, E. V. Canesi, *J. Phys. Chem. Lett.* **2010**, *1*, 3334.
21. A. Shimizu, T. Kubo, M. Uruichi, K. Yakushi, M. Nakano, D. Shiomi, K. Sato, T. Takui, Y. Hirao, K. Matsumoto, H. Kurata, Y. Morita, K. Nakasuji, *J. Am. Chem. Soc.* **2010**, *132*, 14421.
22. K. Kamada, K. Ohta, T. Kubo, A. Shimizu, Y. Morita, K. Nakasuji, R. Kishi, S. Ohta, S. Furukawa, H. Takahashi, M. Nakano, *Angew. Chem. Int. Ed.* **2007**, *46*, 3544.
23. Y. Morita, S. Suzuki, K. Sato, T. Takui, *Nat. Chem.* **2011**, *3*, 197.

24. Y. Morita, S. Nishida, T. Murata, M. Moriguchi, A. Ueda, M. Satoh, K. Arifuku, K. Sato, T. Takui, *Nat. Mater.* **2011**, *10*, 947.
25. a) M. Nakano, R. Kishi, T. Nitta, T. Kubo, K. Nakasuji, K. Kamada, K. Ohta, B. Champagne, E. Botek, K. Yamaguchi, *J. Phys. Chem. A* **2005**, *109*, 885; b) M. Nakano, R. Kishi, S. Ohta, H. Takahashi, T. Kubo, K. Kamada, K. Ohta, E. Botek, B. Champagne, *Phys. Rev. Lett.* **2007**, *99*, 033001; c) M. Nakano, B. Champagne, *J. Phys. Chem. Lett.* **2015**, *6*, 3236; d) X. Hu, W. Wang, D. Wang, Y. Zheng, *J. Mater. Chem. C* **2018**, *6*, 11232.
26. a) T. Minami, M. Nakano, *J. Phys. Chem. Lett.* **2012**, *3*, 145; b) M. B. Smith, J. Michl, *Annu. Rev. Phys. Chem.* **2013**, *64*, 361; c) O. Varnavski, N. Abeyasinghe, J. Aragón, J. J. Serrano-Pérez, E. Ortí, J. T. López Navarrete, K. Takimiya, D. Casanova, J. Casado, T. Goodson, *J. Phys. Chem. Lett.* **2015**, *6*, 1375; d) S. Ito, T. Minami, M. Nakano, *J. Phys. Chem. C* **2012**, *116*, 19729.
27. H. Koike, M. Chikamatsu, R. Azumi, J. Tsutsumi, K. Ogawa, W. Yamane, T. Nishiuchi, T. Kubo, T. Hasegawa, K. Kanai, *Adv. Funct. Mater.* **2016**, *26*, 277.
28. Y. Ni, S. Lee, M. Son, N. Aratani, M. Ishida, A. Samanta, H. Yamada, Y.-T. Chang, H. Furuta, D. Kim, J. Wu, *Angew. Chem. Int. Ed.* **2016**, *55*, 2815.
29. T. Ullrich, P. Pinter, J. Messelberger, P. Haines, R. Kaur, M. M. Hansmann, D. Munz, D. M. Guldi, *Angew. Chem. Int. Ed.* **2020**, DOI 10.1002/anie.202001286.
30. B. D. Rose, C. L. Vonnegut, L. N. Zakharov, M. M. Haley, *Org. Lett.* **2012**, *14*, 2426.
31. D. T. Chase, A. G. Fix, S. J. Kang, B. D. Rose, C. D. Weber, Y. Zhong, L. N. Zakharov, M. C. Lonergan, C. Nuckolls, M. M. Haley, *J. Am. Chem. Soc.* **2012**, *134*, 10349.
32. A.-C. Knall, R. S. Ashraf, M. Nikolka, C. B. Nielsen, B. Purushothaman, A. Sadhanala, M. Hurhangee, K. Broch, D. J. Harkin, J. Novák, M. Neophytou, P. Hayoz, H. Sirringhaus, I. McCulloch, *Adv. Funct. Mater.* **2016**, *26*, 6961.
33. J. E. Barker, C. K. Frederickson, M. H. Jones, L. N. Zakharov, M. M. Haley, *Org. Lett.* **2017**, *19*, 5312.
34. G. E. Rudebusch, L. N. Zakharov, M. M. Haley, unpublished studies.
35. B. Bleaney, K. D. Bowers, *Proc. R. Soc. Lond. A* **1952**, *214*, 451.
36. It is worth noting that the magnetic behavior of DIAN was examined using ESR. While a thermal dependence was observed for the signal representative of the triplet state, the results were more qualitative in the ESR case, highlighting our preference for SQUID magnetometry.
37. Y.-C., Hsieh, C.-F. Wu, Y.-T. Chen, C.-T. Fang, C.-S. Wang, C.-H. Li, L.-Y. Chen, M.-J., Cheng, C.-C., Chueh, P.-T. Chou, Y.-T., Wu, *J. Am. Chem. Soc.* **2018**, *43*, 14357.

38. D. Hibi, K. Kitabayashi, K. Fujita, T. Takashi, Y. Tobe, *J. Org. Chem.* **2016**, *81*, 3735.
39. J. Ma, J. Liu, M. Baumgarten, Y. Fu, Y.-Z., Tan, K. S. Schellhammer, F. Ortmann, G. Cuniberti, H. Komber, R. Berger, K. Mullen, X. Feng, *Angew. Chem. Int. Ed.* **2017**, *56*, 3280.
40. M. A. Majewski, P. J. Chmielewski, A. Chien, Y. H. Tadeusz Lis, M. Witwicki, D. Kim, P. M. Zimmermna, M. Stepien, *Chem. Sci.* **2019**, *10*, 3413.
41. R.-Q. Lu, S. Wu, L.-L. Yang, W.-B. Gao, H. Qu, X.-Y. Wang, J.-B., Chen, C. Tang, H.-Y. Shi, X.-Y. Cao, *Angew. Chem. Int. Ed.* **2019**, *58*, 7600.

Chapter II.

1. a) *Organic Light Emitting Devices: Synthesis, Properties and Applications*, K. Mullen, U. Scherf, Eds.; Wiley-VCH: Weinheim, **2006**; b) *Carbon-Rich Compounds: From Molecules to Materials*, M. M. Haley, R. R. Tykwinski, Eds.; Wiley-VCH: Weinheim, **2006**; c) *Functional Organic Materials*, T. J. Muller, U. H. F. Bunz, Eds.; Wiley-VCH: Weinheim, **2007**.
2. a) M. Bendikov, F. Wudl, D. F. Perepichka, *Chem. Rev.* **2004**, *104*, 491-4946; b) J. E. Anthony, *Chem. Rev.* **2006**, *106*, 5028-5048; c) J. E. Anthony, *Angew. Chem. Int. Ed.* **2008**, *47*, 452-483; *Angew. Chem.* **2008**, *120*, 460-492.
3. a) J. E. Anthony, A. Facchetti, M. Heeney, S. R. Marder, X. Zhan, *Adv. Mater.* **2010** *22*, 3876-3892; b) J. Cao, G. London, O. Dumele, M. von Wantoch Rekowski, N. Trapp, L. Ruhlmann, C. Boudon, A. Stanger, F. Diederich, *J. Am. Chem. Soc.* **2015**, *137*, 7178-7188; c) Z. Jin, Y. C. Teo, N. G. Zulaybar, M. D. Smith, Y. Xia, *J. Am. Chem. Soc.* **2017**, *139*, 1806-1809.
4. a) C. K. Frederickson, B. D. Rose and M. M. Haley, *Acc. Chem. Res.* **2017**, *50*, 977-987; b) A. G. Fix, D. T. Chase, M. M. Haley, *Top. Curr. Chem.* **2014**, *349*, 159-195.
5. a) Y. Tobe, *Chem. Rec.* **2015**, *15*, 86-96; b) A. Shimizu, S. Nobusue, H. Miyoshi, Y. Tobe, *Pure Appl. Chem.* **2014**, *86*, 517-528.
6. Inter alia: a) J. Nishida, S. Tsukaguchi, Y. Yamashita, *Chem. Eur. J.* **2012**, *18*, 8964-8970; b) K. Sbagoud, M. Mamada, J. Marrot, S. Tokito, A. Yassar, M. Frigoli, *M. Chem. Sci.* **2015**, *6*, 3402-3409; c) P. Hu, S. Lee, T. S. Heng, N. Aratani, T. P. Goncalves, Q. Qi, X. Shi, H. Yamada, K.-W. Huang, J. Ding, D. Kim, J. Wu, *J. Am. Chem. Soc.* **2016**, *138*, 1065-1077. d) Y.-C. Loh, H.-C. Ting, Y.-Z. Li, Y.-H. Li, S.-W. Liu, K.-W. Huang, K.-T. Wong, *Org. Chem. Front.* **2017**, *4*, 675-681.

7. a) G. E. Rudebusch, M. M. Haley, in *Polycyclic Arenes and Heteroarenes: Synthesis, Properties and Applications*, Q. Miao, Ed.; Wiley-VCH: Weinheim, **2015**, pp. 37-60; b) J. L. Marshall, M. M. Haley, in *Organic Redox Systems: Synthesis, Properties and Applications*, T. Nishinaga, Ed.; John Wiley & Sons: New York, **2016**, pp. 311-358; c) K. N. Plunkett, *Synlett* **2013**, *24*, 898-902.
8. a) D. T. Chase, A. G. Fix, S. J. Kang, B. D. Rose, C. D. Weber, Y. Zhong, L. N. Zakharov, M. C. Lonergan, C. Nuckolls, M. M. Haley, *J. Am. Chem. Soc.* **2012**, *134*, 10349-10352; b) G. E. Rudebusch, J. L. Zafra, K. Jorner, K. Fukuda, J. L. Marshall, I. Arrechea-Marcos, G. L. Espejo, R. P. Ortiz, C. J. Gómez-García, L. N. Zakharov, M. Nakano, H. Ottosson, J. Casado, M. M. Haley, *Nat. Chem.* **2016**, *8*, 753-759; c) J. L. Marshall, K. Uchida, C. K. Frederickson, C. Schutt, A. M. Zeidell, K. P. Goetz, T. W. Finn, K. Jarolimek, L. N. Zakharov, C. Risko, R. Herges, O. D. Jurchescu, M. M. Haley, *Chem. Sci.* **2016**, *7*, 5547-5558.
9. a) C. K. Frederickson, L. N. Zakharov, M. M. Haley, *J. Am. Chem. Soc.* **2016**, *138*, 16827-16838; b) G. E. Rudebusch, G. L. Espejo, J. L. Zafra, M. Pena-Alvarez, S. N. Spisak, K. Fukuda, Z. Wei, M. Nakano, M. A. Petrukhina, J. Casado, M. M. Haley, *J. Am. Chem. Soc.* **2016**, *138*, 12648-12654; c) X. Fu, D. Zhao, *Org. Lett.* **2015**, *17*, 5694-5697; d) B. D. Rose, N. J. Sumner, A. S. Filatov, S. J. Peters, L. N. Zakharov, M. A. Petrukhina, M. M. Haley, *J. Am. Chem. Soc.* **2014**, *136*, 9181-9189.
10. Inter alia: a) M. Abe, *Chem. Rev.* **2013**, *113*, 7011-7088; b) T. Kubo, *Chem. Lett.* **2015**, *44*, 111-122; c) M. Nakano, B. Champagne, *J. Phys. Chem. Lett.* **2015**, *6*, 3 236-3256; d) M. Nakano, *Chem. Rec.* **2017**, *17*, 27-62; e) M. Nakano, *Top. Curr. Chem.* **2017**, *375*, 47-113; f) K. Fukuda, T. Nagami, J. Y. Fujiyoshi, M. Nakano, *J. Phys. Chem. A* **2015**, *119*, 10620-10627; g) Z. Zeng, X. Shi, C. Chi, J. T. López Navarrete, J. Casado, J. Wu, *Chem. Soc. Rev.* **2015**, *44*, 6578-6596.
11. a) K. Yamaguchi, *Chem. Phys. Lett.* **1975**, *33*, 330-335; b) M. Nakano, *Excitation Energies and Properties of Open-Shell Singlet Molecules*, Springer: Heidelberg, Germany **2014**.
12. First reported, stable examples: a) [1,2-*b*]IF: D. T. Chase, B. D. Rose, S. P. McClintock, L. N. Zakharov, M. M. Haley, *Angew. Chem. Int. Ed.* **2011**, *50*, 1127-1130; *Angew. Chem.* **2011**, *123*, 1159-1162; b) [2,1-*a*]IF: A. Shimizu, Y. Tobe, *Angew. Chem. Int. Ed.* **2011**, *50*, 6906-6910; *Angew. Chem.* **2011**, *123*, 7038-7042; c) [2,1-*b*]IF: A. Shimizu, R. Kishi, M. Nakano, D. Shiomi, K. Sato, T. Takui, I. Hisaki, M. Miyata, Y. Tobe, *Angew. Chem. Int. Ed.* **2013**, *52*, 6076-6079; *Angew. Chem.* **2013**, *125*, 6192-6195; d) [2,1-*c*]IF: A. G. Fix, P. E. Deal, C. L. Vonnegut, B. D. Rose, L. N. Zakharov, M. M. Haley, *Org. Lett.* **2013**, *15*, 1362-1365.
13. To fairly compare diradical character of regioisomers **1-5**, we re-calculated all five y values using the projected unrestricted Hartree-Fock (PUHF) method with the 6-311G* basis set. Geometry optimization for the IF regioisomers was performed at the spin-flip-collinear-time-dependent density functional theory (SF-CL-TDDFT) BHandHLYP/6-311G* level.

14. a) E. Clar, *Polycyclic Hydrocarbons*, Academic: London, **1964**; b) R. G. Harvey, *Polycyclic Aromatic Hydrocarbons*, Wiley-VCH: New York, **1997**.
15. Other examples of the [1,2-*a*]IF topology do exist where the apical carbon of each five-membered ring is sp^3 -hybridized. This subtle but important difference results in dramatically different properties of the molecules; see: M. Romain, D. Tondelier, B. Geffroy, O. Jeannin, E. Jacques, J. Rault-Berthelot, C. Poriel, *Chem. Eur. J.* **2015**, *21*, 9426-9439, and references therein.
16. M. J. Frisch et al., *Gaussian 09, Revision D.01* (Gaussian, Inc., **2009**).
17. a) Y. Shao, M. Head-Gordon, A. I. Krylov, *J. Chem. Phys.* **2003**, *118*, 4807-4818; b) F. Wang, T. Ziegler, *J. Chem. Phys.* **2004**, *121*, 12191-12196; c) F. Wang, T. Ziegler, *J. Chem. Phys.* **2005**, *122*, 074109-1-9; d) F. Wang, T. Ziegler, *Int. J. Quantum Chem.* **2006**, *106*, 2545-2550.
18. a) Y. Shao et al., *Mol. Phys.* **2015**, *113*, 184-215; b) M. W. Schmidt, K. K. Baldridge, J. A. Boatz, S. T. Elbert, M. S. Gordon, J. H. Jensen, S. Koseki, N. Matsunaga, K. A. Nguyen, S. Su, T. L. Windus, M. Dupuis, J. A. Montgomery, *J. Comput. Chem.* **1993**, *14*, 1347-1363.
19. N. C. Baird, *J. Am. Chem. Soc.* **1972**, *94*, 4941-4948.
20. M. Rosenberg, C. Dahlstrand, K. Kilså, H. Ottosson, *Chem. Rev.* **2014**, *114*, 5379-5425.
21. a) P. v. R. Schleyer, C. Maerker, A. Dransfeld, H. Jiao, N. J. R. van Eikema Hommes, *J. Am. Chem. Soc.* **1996**, *118*, 6317-6318; b) H. Fallah-Bagher-Shaidaei, C. S. Wannere, C. Corminboeuf, R. Puchta, P. v. R. Schleyer, *Org. Lett.* **2006**, *8*, 863-866.
22. a) R. Herges, D. Geuenich, *J. Phys. Chem. A* **2001**, *105*, 3214-3220; b) D. Geuenich, K. Hess, F. Köhler, R. Herges, *Chem. Rev.* **2005**, *105*, 3758-3772.
23. L. Chardonens, R. Ritter, *Helv. Chim. Acta* **1955**, *38*, 393-396.
24. CCDC 1571038 contains the supplementary crystallographic data for this paper. These data are provided free of charge by The Cambridge Crystallographic Data Centre.
25. a) S. N. Spisak, A. V. Zabula, A. S. Filatov, A. Yu. Rogachev, M. A. Petrukhina, *Angew. Chem. Int. Ed.* **2011**, *50*, 8090-8094; *Angew. Chem.* **2011**, *123*, 8240-8244; b) N. J. Sumner, S. N. Spisak, A. S. Filatov, A. Yu. Rogachev, A. V. Zabula, M. A. Petrukhina, *Organometallics* **2014**, *33*, 2874-2878; c) S. N. Spisak, Z. Wei, A. Yu. Rogachev, T. Amaya, T. Hirao, M. A. Petrukhina, *Angew. Chem. Int. Ed.* **2017**, *56*, 2582-2587; *Angew. Chem.* **2017**, *129*, 2626-2631.

Chapter III.

1. Tschitschibabin, A. E. Über einige phenylierte Derivate des p,p-Ditolyls. *Chem. Ber.* **40**, 1810-1819 (1907).

2. Gopalakrishna, T. Y., Zeng, W., Lu, X. & Wu, J. From open-shell singlet diradicaloids to polyradicaloids. *Chem. Commun.* **54**, 2186–2199 (2018).
3. Di Motta, S., Negri, F., Fazzi, D., Castiglioni, C. & Canesi, E. V. Biradicaloid and polyenic character of quinoidal oligothiophenes revealed by the presence of a low-lying double-exciton state. *J. Phys. Chem. Lett.* **1**, 3334–3339 (2010).
4. Rudebusch, G. E. *et al.* Diindeno-fusion of an anthracene as a design strategy for stable organic biradicals. *Nat. Chem.* **8**, 753–759 (2016).
5. Morita, Y., Suzuki, S., Sato, K. & Takui, T. Synthetic organic spin chemistry for structurally well-defined open-shell graphene fragments. *Nat. Chem.* **3**, 197–204 (2011).
6. Morita, Y. *et al.* Organic tailored batteries materials using stable open-shell molecules with degenerate frontier orbitals. *Nat. Mater.* **10**, 947–951 (2011).
7. Nakano, M. *et al.* Second hyperpolarizability (γ) of singlet diradical system: dependence of γ on the diradical character. *J. Phys. Chem. A* **109**, 885–891 (2005).
8. Nakano, M. *et al.* Relationship between third-order nonlinear optical properties and magnetic interactions in open-shell systems: a new paradigm for nonlinear optics. *Phys. Rev. Lett.* **99**, 033001 (2007).
9. Nakano, M. & Champagne, B. Theoretical design of open-shell singlet molecular systems for nonlinear optics. *J. Phys. Chem. Lett.* **6**, 3236–3256 (2015).
10. Minami, T. & Nakano, M. Diradical character view of singlet fission. *J. Phys. Chem. Lett.* **3**, 145–150 (2012).
11. Smith, M. B. & Michl, J. Recent advances in singlet fission. *Annu. Rev. Phys. Chem.* **64**, 361–386 (2013).
12. Varnavski, O. *et al.* High yield ultrafast intramolecular singlet exciton fission in a quinoidal bithiophene. *J. Phys. Chem. Lett.* **6**, 1375–1384 (2015).
13. Hu, P. & Wu, J. Modern zethrene chemistry. *Can. J. Chem.* **95**, 223–233 (2017).
14. Zeng, W. *et al.* Super-heptazethrene. *Angew. Chem. Int. Ed.* **55**, 8615–8619 (2016).
15. Sun, Z. *et al.* Dibenzohaptazethrene isomers with different biradical characters: an exercise of Clar's aromatic sextet rule in singlet biradicaloids. *J. Am. Chem. Soc.* **135**, 18229–18236 (2013).
16. Li, Y. *et al.* Kinetically blocked heptazethrene and octazethrene: closed-shell or open-shell in the ground state? *J. Am. Chem. Soc.* **134**, 14913–14922 (2012).
17. Konishi, A., Hirao, Y., Kurata, H., Kubo, T. & Nakano, M. Anthenes: model systems for understanding the edge state of graphene nanoribbons. *Pure Appl. Chem.* **86**, 497–595 (2014).

18. Konishi, A. *et al.* Synthesis and characterization of quarteranthenes: elucidating the characteristics of the edge state of graphene nanoribbons at the molecular level. *J. Am. Chem. Soc.* **135**, 1430–1437 (2013).
19. Kubo, T. *et al.* Four-stage amphoteric redox properties and biradicaloid character of tetra-*tert*-butyldicyclopenta[*b*; *d*]thieno[1,2,3-*cd*;5,6,7-*c'* *d'*]diphenalene. *Angew. Chem. Int. Ed.* **43**, 6474–5479 (2004).
20. Shimizu, A. *et al.* Alternating covalent bonding interactions in a one-dimensional chain of a phenalenyl-based singlet biradical molecule having Kekulé structures. *J. Am. Chem. Soc.* **132**, 14421–14428 (2010).
21. Shimizu, A. *et al.* Aromaticity and π -bond covalency: prominent intermolecular covalent bonding interaction of a Kekulé hydrocarbon with very significant singlet biradical character. *Chem. Commun.* **48**, 5629–5631 (2012).
22. Frederickson, C. K., Rose, B. D. & Haley, M. M. Explorations of the indenofluorenes and expanded quinoidal analogues. *Acc. Chem. Res.* **50**, 977–987 (2017).
23. Chase, D. T. *et al.* 6,12-Diarylindeno[1,2-*b*]fluorenes: synthesis photophysics, and ambipolar OFETs. *J. Am. Chem. Soc.* **134**, 10349–10352 (2012).
24. Shimizu, A. *et al.* Indeno[2,1-*b*]fluorene: a 20- π -electron hydrocarbon with very low-energy light absorption. *Angew. Chem. Int. Ed.* **52**, 6076–6079 (2013).
25. Young, B. S. *et al.* Synthesis and properties of fully-conjugated indacenedithiophenes. *Chem. Sci.* **5**, 1008–1014 (2014).
26. Marshall, J. L. *et al.* Indacenodibenzothiophenes: synthesis, optoelectronic properties and materials applications of molecules with strong antiaromatic character. *Chem. Sci.* **7**, 5547–5558 (2016).
27. Miyoshi, H. *et al.* Fluoreno[2,3-*b*]fluorene vs. indeno[2,1-*b*]fluorene: unusual relationship between the number of π electrons and excitation energy in *m*-quinodimethane-type singlet diradicaloids. *J. Org. Chem.* **82**, 1380–1388 (2017).
28. Barker, J. E., Frederickson, C. K., Jones, M. H., Zakharov, L. N. & Haley, M. M. Synthesis and properties of quinoidal fluorenofluorenes. *Org. Lett.* **19**, 5312–5315 (2017).
29. Casado, J. Para-quinodimethanes: A unified review of the quinoidal-versus-aromatic competition and its implications. *Top. Curr. Chem.* **375**, 73 (2017).
30. Zeng, Z. & Wu, J. Stable π -extended *p*-quinodimethanes: synthesis and tunable ground states. *Chem. Rec.* **15**, 322–328 (2015).
31. Zeng, Z. *et al.* Pushing extended *p*-quinodimethanes to the limit: stable tetracyano-oligo(*N*-annulated perylene)quinodimethanes with tunable ground states. *J. Am. Chem. Soc.* **135**, 6363–6371 (2013).

32. Bendikov, M. *et al.* Oligoacenes: theoretical predictions of open-shell diradical ground states. *J. Am. Chem. Soc.* **126**, 7416–7417 (2004).
33. Jiang, D. E. & Dai, S. Electronic ground state of higher acenes. *J. Phys. Chem.* **112**, 332–335 (2008).
34. Purushothaman, B., Bruzek, M., Parkin, S. R., Miller, A. & Anthony, J. E. Synthesis and structural characterization of crystalline nonacenes. *Angew. Chem. Int. Ed.* **50**, 7013–7017 (2011).
35. Kubo, T. Recent progress in quinoidal singlet biradical molecules. *Chem. Lett.* **4**, 111–122 (2015).
36. Sun, Z., Zeng, Z. & Wu, J. Extended zethrenes, *p*-quinodimethanes and periacenes with a biradical ground state. *Acc. Chem. Res.* **47**, 2582–2591 (2014).
37. Abe, M. Diradicals. *Chem. Rev.* **113**, 7011–7088 (2013).
38. Nakano, M. Electronic structure of open-shell singlet molecules: diradical character viewpoint. *Top. Curr. Chem.* **375**, 47 (2017).
39. Zeng, Z. *et al.* Pro-aromatic and anti-aromatic π -conjugated molecules: an irresistible wish to become diradicals. *Chem. Soc. Rev.* **44**, 6578–6596 (2015).
40. Clar, E. *The Aromatic Sextet*, Wiley; London, UK, 1972.
41. Yamaguchi, K. The electronic structure of biradicals in the unrestricted Hartree-Fock approximation. *Chem. Phys. Lett.* **33**, 330–335 (1975).
42. Zeng, W. *et al.* Phenalenyl-fused porphyrins with different ground states. *Chem. Sci.* **6**, 2427–2433 (2015).
43. Shi, X. *et al.* Benzo-thia-fused [*n*]thienoacenequinodimethanes with small to moderate diradical characters: the role of pro-aromaticity *versus* antiaromaticity. *Chem. Sci.* **7**, 3036–3046 (2016).
44. Frisch, M. J. *et al.* Gaussian 09, Revision B.01, Gaussian, Inc., Wallingford, CT, 2009.
45. Fukuda, K., Nagami, T., Fujiyoshi, J. & Nakano, M. Interplay between open-shell character, aromaticity, and second hyperpolarizabilities in indenofluorenes. *J. Phys. Chem. A* **119**, 10620–10627 (2015).
46. Bernard, Y. A., Shao, Y. & Krylov, A. I. General formulation of spin-flip time-dependent density functional theory using non-collinear kernels: theory, implementation, and benchmarks. *J. Chem. Phys.* **136**, 204103–1–17 (2012).
47. Shao, Y. *et al.* Advances in molecular quantum chemistry contained the Q-chem 4 program package. *Mol. Phys.* **113**, 184–215 (2014).
48. Knall, A. *et al.* Naphthacenodithiophene based polymers- new members of the acenodithiophene family exhibiting high mobility and power conversion efficiency. *Adv. Funct. Mater.* **26**, 6961–6969 (2016).

49. Nakagawa, H., Kawai, S., Nakashima, T. & Kawai, T. Synthesis of photochemical reaction of photochromic terarylene having a leaving methoxy group. *Org. Lett.* **11**, 1475–1478 (2009).
50. Schleyer, P. v. R. *et al.* Dissected nucleus-independent chemical shift analysis of π -aromaticity and antiaromaticity. *Org. Lett.* **3**, 2465–2468 (2001).

Chapter IV.

1. Clar, E. *Polycyclic Hydrocarbons, Vols. 1 and 2*; John Wiley: New York, 1964.
2. Dediu, V. A.; Hueso, L. E.; Bergenti, I.; Taliani, C. Spin route to organic electronics. *Nat. Mater.* **2009**, *8*, 707–716.
3. Abe, M., Diradicals. *Chem. Rev.* **2013**, *113*, 7011–7088.
4. (a) Muhammad, S.; Nakano, M.; Al-Sehemi, A. G.; Kitagawa, Y.; Irfan, A.; Chaudhry, A. R.; Kishi, R.; Ito, S.; Yoneda, K.; Fukuda, K. Role of a singlet diradical character in carbon nanomaterials: a novel hot spot for efficient nonlinear optical materials. *Nanoscale* **2016**, *8*, 17998–18020. (b) Nakano, M. Open-Shell-Character-Based Molecular Design Principles: Applications to Nonlinear Optics and Singlet Fission. *Chem. Rec.* **2017**, *17*, 27–62. (c) Huang, Y.; Egap, E. Open-shell organic semiconductors: An emerging class of materials with novel properties. *Polym. J.* **2018**, *50*, 603–614.
5. (a) Zeng, Z.; Shi, X.; Chi, C.; Lopez Navarrete, J. T.; Casado, J.; Wu, J. Pro-aromatic and anti-aromatic π -conjugated molecules: an irresistible wish to be diradicals. *Chem. Soc. Rev.* **2015**, *44*, 6578–6596. (b) Shi, X.; Chi, C. Heterocyclic Quinodimethanes. *Top. Curr. Chem.* **2017**, *375*, 169–207. (c) Casado, J. Para-Quinodimethanes: A Unified Review of the Quinoidal-Versus-Aromatic Competition and its Implications. *Top. Curr. Chem.* **2017**, *375*, 209–248. (d) Tobe, Y. Quinodimethanes Incorporated in Non-Benzenoid Aromatic or Antiaromatic Frameworks. *Top. Curr. Chem.* **2017**, *375*, 107–168. (e) Gopalakrishna, T. Y.; Zeng, W.; Lu, X.; Wu, J. From open-shell singlet diradicaloids to polyradicaloids. *Chem. Commun.* **2018**, *54*, 2186–2199.
6. (a) Nakano, M.; Kishi, R.; Ohta, S.; Takahashi, H.; Kubo, T.; Kamada, K.; Ohta, K.; Botek, E.; Champagne, B. Relationship between Third-Order Nonlinear Optical Properties and Magnetic Interactions in Open-Shell Systems: A New Paradigm for Nonlinear Optics. *Phys. Rev. Lett.* **2007**, *99*, 033001-1–033001-4. (b) Nakano, M.; Champagne, B. Diradical character dependences of the first and second hyperpolarizabilities of asymmetric open-shell singlet systems. *J. Chem. Phys.* **2013**, *138*, 244306-1–244306-13.

7. (a) Nakano, M.; Minami, T.; Yoneda, K.; Muhammad, S.; Kishi, R.; Shigeta, Y.; Kubo, T.; Rougier, L.; Champagne, B.; Kamada, K.; Ohta, K. Giant Enhancement of the Second Hyperpolarizabilities of Open-Shell Singlet Polyaromatic Diphenalenyl Diradicaloids by an External Electric Field and Donor-Acceptor Substitution. *J. Phys. Chem. Lett.* **2011**, *2*, 1094–1098. (b) Zeng, Z.; Ishida, M.; Zafra, J. L.; Zhu, X.; Sung, Y. M.; Bao, N.; Webster, R. D.; Lee, B. S.; Li, R.-W.; Zeng, W.; Li, Y.; Chi, C.; López Navarrete, J. T.; Ding, J.; Casado, J.; Kim, D.; Wu, J. Pushing Extended *p*-Quinodimethanes to the Limit: Stable Tetracyano-oligo(*N*-annulated perylene)quinodimethanes with Tunable Ground States. *J. Am. Chem. Soc.* **2013**, *135*, 6363–6371. (c) Zeng, Z.; Lee, S.; Zafra, J. L.; Ishida, M.; Bao, N.; Webster, R. D.; López Navarrete, J. T.; Ding, J.; Casado, J.; Kim, D.-H.; Wu, J. Turning on the biradical state of tetracyano-perylene and quaterylenequinodimethanes by incorporation of additional thiophene rings. *Chem. Sci.* **2014**, *5*, 3072–3080. (d) Zeng, Z.; Lee, S.; Son, M.; Fukuda, K.; Mayorga Burrezo, P.; Zhu, X.; Qi, Q.; Li, R.-W.; López Navarrete, J. T.; Ding, J.; Casado, J.; Nakano, M.; Kim, D.; Wu, J. Push-Pull Type Oligo(*N*-annulated perylene)quinodimethanes: Chain Length and Solvent-Dependent Ground States and Physical Properties. *J. Am. Chem. Soc.* **2015**, *137*, 8572–8583.
8. Zeng, Z.; Sung, Y. M.; Bao, N.; Tan, D.; Lee, R.; Zafra, J. L.; Lee, B. S.; Ishida, M.; Ding, J.; López Navarrete, J. T.; Li, Y.; Zeng, W.; Kim, D.; Huang, K.-W.; Webster, R. D.; Casado, J.; Wu, J. Stable Tetrabenzo-Chichibabin's Hydrocarbons: Tunable Ground State and Unusual Transition between Their Closed-Shell and Open-Shell Resonance Forms. *J. Am. Chem. Soc.* **2012**, *134*, 14513–14525.
9. Dressler, J. J.; Teraoka, M.; Espejo, G. L.; Kishi, R.; Takamuku, S.; Gómez-García, C. J.; Zakharov, L. N.; Nakano, M.; Casado, J.; Haley, M. M. Thiophene and its sulfur inhibit indenoindenodibenzothiophene diradicals from low-energy lying thermal triplets. *Nat. Chem.* **2018**, *10*, 1134–1140.
10. Examples of quinoidal/diradicaloid constitutional isomers, *inter alia*: (a) Tukada, H. *p*-Phenylene-2,2'-bis(1,1:3,3-di-2,2'-biphenyl-enepropenyl): A Stable Non-Kekule Molecule as a Ground-State Singlet. *J. Am. Chem. Soc.* **1991**, *113*, 8991–8992. (b) Tukada, H.; Mutai, K. A Stable Triplet Non-Kekulé Molecule; *m*-Phenylene-2,2'-bis(1,1:3,3-di-2,2'-biphenylenepropenyl). *Tetrahedron Lett.* **1992**, *33*, 6665–6668. (c) Kubo, T.; Sakamoto, M.; Nakasuji, K. Biradicaloid Character of Phenalenyl-Based Aromatic Compounds with a Small HOMO–LUMO Gap. *Polyhedron* **2005**, *24*, 2522–2527. (d) Sun, Z.; Lee, S.; Hyung, K.; Zhu, X.; Zhang, W.; Zheng, B.; Hu, P.; Zeng, Z.; Das, S.; Li, Y.; Chi, C.; Li, R.W.; Huang, K.W.; Ding, J.; Kim, D.; Wu, J. Dibenzoheptazethrene Isomers with Different Biradical Characters: An Exercise of Clar's Sextets Rule in Singlet Biradicaloids. *J. Am. Chem. Soc.* **2013**, *135*, 18229–18236. (e) Hu, P.; Lee, S.; Park, K. H.; Das, S.; Heng, T. S.; Gonçalves, T. P.; Huang, K.-W.; Ding, J.; Kim, D.; Wu, J. Octazethrene and Its Isomer with Different Diradical Characters and Chemical Reactivity: The Role of the Bridge Structure. *J. Org. Chem.* **2016**, *81*, 2911–2919.

11. (a) Chase, D. T.; Rose, B. D.; McClintock, S. P.; Zakharov, L. N.; Haley, M. M. Indeno[1,2-*b*]fluorenes: Fully conjugated Antiaromatic Analogues of Acenes. *Angew. Chem., Int. Ed.* **2011**, *50*, 1127–1130. (b) Shimizu, A.; Tobe, Y. Indeno[2,1-*a*]fluorene: An Air-stable Orthoquinodimethane Derivative. *Angew. Chem., Int. Ed.* **2011**, *50*, 6906–6910. (c) Fix, A. G.; Deal, P. E.; Vonnegut, C. L.; Rose, B. D.; Zakharov, L. N.; Haley, M. M. Indeno[2,1-*c*]fluorene: A New Electron-Accepting Scaffold for Organic Electronics. *Org. Lett.* **2013**, *15*, 1362–1365. (d) Shimizu, A.; Kishi, R.; Nakano, M.; Shiomi, D.; Sato, K.; Takui, T.; Hisaki, I.; Miyata, M.; Tobe, Y. Indeno[2,1-*b*]fluorene: A 20- π -Electron Hydrocarbon with Very Low-Energy Light Absorption. *Angew. Chem. Int. Ed.* **2013**, *52*, 6076–6079. (e) Dressler, J. J.; Zhou, Z.; Marshall, J. L.; Kishi, R.; Takamuku, S.; Wei, Z.; Spisak, S. N.; Nakano, M.; Petrukhina, M. A.; Haley, M. M. Synthesis of the Unknown Indeno[1,2-*a*]fluorene Regioisomer: Crystallographic Characterization of Its Dianion. *Angew. Chem., Int. Ed.* **2017**, *56*, 15363–15367.
12. (a) Tobe, Y. Non-Alternant Non-Benzenoid Aromatic Compounds: Past, Present, and Future. *Chem. Rec.* **2015**, *15*, 86–96; (b) Frederickson, C. K.; Rose, B. D.; Haley, M. M. Explorations of the Indenofluorenes and Expanded Quinoidal Analogues. *Acc. Chem. Res.* **2017**, *50*, 977–987.
13. Nakano, M. Electronic Structure of Open-Shell Singlet Molecules: Diradical Character Viewpoint. *Top. Curr. Chem.* **2017**, *375*, 1–67.
14. *Inter alia*: (a) Gilroy, J. B.; McKinnon, S. D. J.; Kennepohl, P.; Zsombor, M. S.; Ferguson, M. J.; Thompson, L. K.; Hicks, R. G. Probing Electronic Communication in Stable Benzene-Bridged Verdazyl Diradicals. *J. Org. Chem.* **2007**, *72*, 8062–8069. (b) Caneschi, A.; Chiesi, P.; David, L.; Ferraro, F.; Gatteschi, D.; Sessoli, R. Crystal Structure and Magnetic Properties of Two Nitronyl Nitroxide Biradicals and of Their Copper(II) Complexes. *Inorg. Chem.* **1993**, *32*, 1445–1453.
15. (a) Hubbard, J. Electron correlations in narrow energy bands. *Proc. R. Soc. A* **1963**, *276*, 238–257. (b) Fazekas, P. *Lecture Notes on Electron Correlation and Magnetism*; World Scientific: Singapore, 1999.
16. Gebhard, F. *The Mott Metal-Insulator Transition, Models and Methods*; Springer: Heidelberg, Germany, 1997.
17. Knall, A.-C.; Ashraf, R. S.; Nikolka, M.; Nielsen, C. B.; Purushothaman, B.; Sadhanala, A.; Hurhangee, M.; Broch, K.; Harkin, D. J.; Novák, J.; Neophytou, M.; Hayoz, P.; Sirringhaus, H.; McCulloch, I. Naphthacenodithiophene Based Polymers—New Members of the Acenodithiophene Family Exhibiting High Mobility and Power Conversion Efficiency. *Adv. Funct. Mater.* **2016**, *26*, 6961–6969.
18. Nakagawa, H.; Kawai, S.; Nakashima, T.; Kawai, T. Synthesis and Photochemical Reactions of Photochromic Terarylene Having a Leaving Methoxy Group. *Org. Lett.* **2009**, *11*, 1475–1478.

19. Kubo, T.; Shimizu, A.; Sakamoto, M.; Uruichi, M.; Yakushi, K.; Nakano, M.; Shiomi, D.; Sato, K.; Takui, T.; Morita, Y.; Nakasuji, K. Synthesis, Intermolecular Interaction, and Semiconductive Behavior of a Delocalized Singlet Biradical Hydrocarbon. *Angew. Chem., Int. Ed.* **2005**, *44*, 6564–6568.
20. Shimizu, A.; Kubo, T.; Uruichi, M.; Yakushi, K.; Nakano, M.; Shiomi, D.; Sato, K.; Takui, T.; Hirao, Y.; Matsumoto, K.; Kurata, H.; Morita, Y.; Nakasuji, K. Alternating Covalent Bonding Interactions in a One-Dimensional Chain of a Phenalenyl-Based Singlet Biradical Molecule Having Kekulé Structures. *J. Am. Chem. Soc.* **2010**, *132*, 14421–14428.
21. Bleaney, B.; Bowers, K. D. Anomalous Paramagnetism of Copper Acetate. *Proc. R. Soc. Lond. A.* **1952**, *214*, 451–465.
22. Shimizu, A.; Hirao, Y.; Matsumoto, K.; Kurata, H.; Kubo, T.; Uruichi, M.; Yakushi, K. Aromaticity and π -bond covalency: prominent intermolecular covalent bonding interaction of a Kekulé hydrocarbon with very significant singlet biradical character. *Chem. Commun.* **2012**, *48*, 5629–5631.

Chapter V.

1. For a review, see Gopalakrishna, T.Y., Zeng, W., Xuefeng, L., and Wu, J. (2018) From open-shell singlet diradicaloids to polyradicaloids. *Chem. Commun.* *54*, 2186–2199.
2. Morita, Y., Suzuki, S., Sato, K., and Takui, T. (2011) Synthetic organic spin chemistry for structurally well-defined open-shell graphene fragments. *Nature Chem.* *3*, 197–204.
3. Morita, Y., Nishida, S., Murata, T., Moriguchi, M., Ueda, A., Satoh, M., Arifuku, K., Sato, K., and Takui, T. (2011) Organic tailored batteries materials using stable open-shell molecules with degenerate frontier orbitals. *Nat. Mater.* *10*, 947–951.
4. Nakano, M., Kishi, R., Nitta, T., Kubo, T., Nakasuji, K., Kamada, K., Ohta, K., Champagne, B., Botek, E., and Yamaguchi, K. (2005) Second Hyperpolarizability (γ) of Singlet Diradical System: Dependence of γ on the Diradical Character. *J. Phys. Chem. A* *109*, 885–891.
5. Nakano, M., Kishi, R., Ohta, S., Takahashi, H., Kubo, T., Kamada, K., Ohta, K., Botek, E., and Champagne, B. (2007) Relationship between Third-Order Nonlinear Optical Properties and Magnetic Interactions in Open-Shell Systems: A New Paradigm for Nonlinear Optics. *Phys. Rev. Lett.* *99*, 033001(1)–033001(4).
6. Nakano, M. and Champagne, B. (2015) Theoretical Design of Open-Shell Singlet Molecular Systems for Nonlinear Optics *J. Phys. Chem. Lett.* *6*, 3236–3256.
7. Hu, X., Wang, W., Wang, D., and Zheng, Y. (2018) The electronic applications of stable diradicaloids: present and future. *J. Mater. Chem. C* *6*, 11232–11242.

8. Minami, T. and Nakano, M. (2012) Diradical Character View of Singlet Fission. *J. Phys. Chem. Lett.* *3*, 145–150.
9. Smith, M.B. and Michl, J. Recent advances in singlet fission. *Annu. Rev. Phys. Chem.* **2013**, *64*, 361–386.
10. Varnavski, O., Abeyasinghe, N., Arago, J., Serrano-Perez, J.J., Orti, E., Lopez-Navarrete, J.T., Takimiya, K., Casanova, D., Casado, J., and Goodson III, T. (2015) High Yield Ultrafast Intramolecular Singlet Exciton Fission in a Quinoidal Bithiophene. *J. Phys. Chem. Lett.* *6*, 1375–1384.
11. Kioke, H., Chikamatsu, M., Azumi, R., Tsutsumi, J., Ogawa, K., Yamane, W., Nishiuchi, T., Kubo, K., Hasegawa, T., and Kanai, K. (2016) Stable Delocalized Singlet Biradical Hydrocarbon for Organic Field-Effect Transistors. *Adv. Funct. Mater.* *13*, 277–283.
12. Ni, Y., Lee, S., Aratani, N., Ishida, M., Samanta, A., Yamada, H., Chang, Y.T., Furuta, H., Kim, D., and Wu, J. (2016) A Diradical Approach towards BODIPY-Based Dyes with Intense Near-Infrared Absorption around $\lambda = 1100$ nm. *Angew. Chem. Int. Ed.* *55*, 2815–2819.
13. Thiele, J. and Balhorn, H. (1904) Ueber einen chinoiden Kohlenwasserstoff. *Chem. Ber.* *37*, 1463–1470.
14. Tschitschibabin, A.E. (1907) Über einige phenylierte Derivate des *p,p*-Ditolyls. *Chem. Ber.* *40*, 1810–1819.
15. For a review, see Abe, M. (2013) Diradicals. *Chem. Rev.* *113*, 7011–7088.
16. Kubo, T., Shimizu, A., Sakamoto, M., Uruichi, M., Yakushi, K., Nakano, M., Shiomi, D., Sato, K., Takui, T., Morita, Y., and Nakasuji, K. (2005) Synthesis, Intermolecular Interaction, and Semiconductive Behavior of a Delocalized Singlet Biradical Hydrocarbon. *Angew. Chem. Int. Ed.* *44*, 6564–6568.
17. Shimizu, A., Kubo, T., Uruichi, M., Yakushi, K., Nakano, M., Shiomi, D., Sato, K., Takui, T., Hirao, Y., Matsumoto, K., Kurata, H., Morita, Y., and Nakasuji, K. (2010) Alternating Covalent Bonding Interactions in a One-Dimensional Chain of a Phenalenyl-Based Singlet Biradical Molecule Having Kekulé Structures. *J. Am. Chem. Soc.* *132*, 14421–14428.
18. Shimizu, A., Hirao, Y., Matsumoto, K., Kurata, H., Kubo, T., Uruichi, M., and Yakushi, K. (2012) Aromaticity and π -bond covalency: prominent intermolecular covalent bonding interaction of a Kekulé hydrocarbon with very significant singlet biradical character. *Chem. Commun.* *48*, 5629–5631.
19. Kubo, T., Sakamoto, M., Akabane, M., Fujiwara, Y., Yamamoto, K., Akita, M., Inoue, K., Takui, T., and Nakasuji, K. (2004) Four-Stage Amphoteric Redox Properties and Biradicaloid Character of Tetra-*tert*-butyldicyclopenta[*b;d*]thieno[1,2,3-*cd*;5,6,7-*c'd'*]diphenalene. *Angew. Chem. Int. Ed.* *43*, 6474–6479.

20. For a review, see Casado, J. (2017) Para-Quinodimethanes: A Unified Review of the Quinoidal-Versus-Aromatic Competition and its Implications. *Top. Curr. Chem.* *375*, 209–248.
21. Zeng, Z. and Wu, J. (2015) Stable π -Extended *p*-Quinodimethanes: Synthesis and Tunable Ground States. *Chem. Rec.* *15*, 322–328.
22. Zeng, Z., Ishida, M., Zafra, J.L., Zhu, X., Sung, Y.M., Bao, N., Webster, R.D., Lee, B.S., Li, R., Zeng, W., Li, Y., Chi, C., Lopez-Navarrete, J.T., Ding, J., Casado, J., Kim, D., and Wu, J. (2013) Pushing Extended *p*-Quinodimethanes to the Limit: Stable Tetracyano-oligo(*N*-annulated perylene)quinodimethanes with Tunable Ground States. *J. Am. Chem. Soc.* *135*, 6363–6371.
23. Chase, D.T., Fix, A.G., Kang, S.J., Rose, B.D., Weber, C.D., Zhong, Y., Zakharov, L.N., Lonergan, M.C., Nuckolls, C., and Haley, M.M. (2012) 6,12-Diarylindeno[1,2-*b*]fluorenes: Syntheses, Photophysics, and Ambipolar OFETs. *J. Am. Chem. Soc.* *134*, 10349–10352.
24. Shimizu, A., Kishi, R., Nakano, M., Shiomi, D., Sato, K., Takui, T., Hisaki, I., Miyata, M., and Tobe, Y. (2013) Indeno[2,1-*b*]fluorene: A 20- π -Electron Hydrocarbon with Very Low-Energy Light Absorption. *Angew. Chem. Int. Ed.* *52*, 6076–6079.
25. Dressler, J.J., Zhou, Z., Marshall, J.L., Kishi, R., Takamuku, S., Wei, Z., Spisak, S.N., Nakano, M., Petrukhina, M.A., and Haley, M.M. (2017) Synthesis of the Unknown Indeno[1,2-*a*]fluorene Regioisomer: Crystallographic Characterization of Its Dianion. *Angew. Chem. Int. Ed.* *56*, 15363–15367.
26. For a review see Frederickson, C.K., Rose, B.D., and Haley, M.M. (2017) Explorations of the Indenofluorenes and Expanded Quinoidal Analogues. *Acc. Chem. Res.* *50*, 977–987.
27. Rudebusch, G.E., Zafra, J.L., Jorner, K., Fukuda, K., Marshall, J.L., Arrechea-Marcos, I., Espejo, G.L., Ortiz, R.P., Gomez-García, C.J., Zakharov, L.N., Nakano, M., Ottosson, H., Casado, J., and Haley, M.M. (2016) Diindeno-fusion of an anthracene as a design strategy for stable organic biradicals. *Nat. Chem.* *8*, 753–759.
28. Rudebusch, G.E., Espejo, G.Z., Zafra, J.L., Pena-Alvarez, M., Spisak, S.N., Fukuda, K., Wei, Z., Nakano, M., Petrukhina, M.A., Casado, J., and Haley, M.M. (2016) A Biradical Balancing Act: Redox Amphoterism in a Diindenoanthracene Derivative Results from Quinoidal Acceptor and Aromatic Donor Motifs. *J. Am. Chem. Soc.* *138*, 12648–12654.
29. Marshall, J.L., Uchida, K., Frederickson, C.F., Schutt, C., Zeidell, A.M., Goetz, K.P., Finn, T.W., Jarolimek, K., Zakharov, L.N., Risko, C., Herges, R., Jurchescu, O.D., and Haley, M.M. (2016) Indacenodibenzothiophenes: synthesis, optoelectronic properties and materials applications of molecules with strong antiaromatic character. *Chem. Sci.* *7*, 5547–5558.

30. Miyoshi, H., Miki, M., Hirano, S., Shimizu, A., Kishi, R., Fukuda, K., Shiomi, D., Sato, K., Takui, T., Hisaki, I., Nakano, M., and Tobe, Y. (2017) Fluoreno[2,3-*b*]fluorene vs Indeno[2,1-*b*]fluorene: Unusual Relationship between the Number of π Electrons and Excitation Energy in *m*-Quinodimethane-Type Singlet Diradicaloids. *J. Org. Chem.* *82*, 1380–1388.
31. Barker, J.E., Frederickson, C.K., Jones, M.H., Zakharov, L.N., and Haley, M.M. (2017) Synthesis and Properties of Quinoidal Fluorenofluorenes. *Org. Lett.* *19*, 5312–5315.
32. Frederickson, C.K., Barker, J.E., Dressler, J.J., Zhou, Z., Hanks, E.R., Bard, J.P., Zakharov, L.N., Petrukhina, M.A., and Haley, M.M. (2018) Synthesis and Characterization of a Fluorescent Dianthracenoindacene. *Synlett* *29*, 2562–2566.
33. Dressler, J.J., Teraoka, M., Espejo, G.L., Kishi, R., Takamuku, S., Gómez-García, C.J., Zakharov, L.N., Nakano, M., Casado, J., and Haley, M.M. (2018) Thiophene and its sulfur inhibit indenoindenodibenzothiophene diradicals from low-energy lying thermal triplets. *Nat. Chem.* *10*, 1134–1140.
34. For a review, see Hu, P. and Wu, J. (2017) Modern zethrene chemistry. *Can. J. Chem.* *95*, 223–233.
35. Zeng, W., Sun, Z., Heng, T.S., Goncalves, T.P., Gopalakrishna, T.Y., Huang, K.-W., Ding, J., and Wu, J. (2016) Super-heptazethrene. *Angew. Chem. Int. Ed.* *55*, 8615–8619.
36. Sun, Z., Lee, S., Park, K.H., Zhu, Z., Zhang, W., Zheng, B., Hu, P., Zeng, Z., Das, S., Li, Y., Chi, C., Li, R.-W., Huang, K.-W., Ding, J., Kim, D., and Wu, J. (2013) Dibenzoheptazethrene Isomers with Different Biradical Characters: An Exercise of Clar's Aromatic Sextet Rule in Singlet Biradicaloids. *J. Am. Chem. Soc.* *135*, 18229–18236.
37. Li, Y., Heng, W.K., Lee, B.S., Aratani, N., Zafra, J.L., Bao, N., Lee, R., Sung, Y.M., Sun, Z., Huang, K.W., Webster, R.D., Lopez-Navarrete, J.T., Kim, D., Osuka, A., Casado, J., Ding, J., and Wu, J. (2012) Kinetically Blocked Stable Heptazethrene and Octazethrene: Closed-Shell or Open-Shell in the Ground State? *J. Am. Chem. Soc.* *134*, 14913–14922.
38. For a review see Konishi, A., Hirao, Y., Kurata, H., Kubo, T., Nakano, M., and Kamada, K. (2014) Anthenes: Model systems for understanding the edge state of graphene nanoribbons. *Pure Appl. Chem.* *86*, 497–505.
39. Konishi, A., Hirao, Y., Matsumoto, K., Kurata, H., Kishi, R., Shigeta, Y., Nakano, M., Tokunaga, K., Kamada, K., and Kubo, T. (2013) Synthesis and Characterization of Quarteranthene: Elucidating the Characteristics of the Edge State of Graphene Nanoribbons at the Molecular Level. *J. Am. Chem. Soc.* *135*, 1430-1437.
40. Bendikov, M., Duong, H.M., Starkey, K., Houk, K.N., Carter, E.A., and Wudl, F. (2004) Oligoacenes: Theoretical Prediction of Open-Shell Singlet Diradical Ground States. *J. Am. Chem. Soc.* *126*, 7416–7417.

41. Purushothaman, B., Bruzek, M., Parkin, S.R., Miller, A.-F., and Anthony, J.E. (2011) Synthesis and Structural Characterization of Crystalline Nonacenes. *Angew. Chem. Int. Ed.* *50*, 7013–7017.
42. Dong, S., Gopalakrishna, T., Han, Y., Phan, H., Tao, T., Ni, Y., Liu, G., and Chi, C. (2019) Extended Bis(anthraoxa)quinodimethanes with Nine and Ten Consecutively Fused Six-Membered Rings: Neutral Diradicaloids and Charged Diradical Dianions/Dications. *J. Am. Chem. Soc.* *141*, 62–66.
43. Kubo, T. (2015) Recent Progress in Quinoidal Singlet Biradical Molecules. *Chem. Lett.* *44*, 111–122.
44. Sun, Z., Zeng, Z., and Wu, J. (2014) Zethrenes, Extended *p*-Quinodimethanes, and Periacenes with a Singlet Biradical Ground State. *Acc. Chem. Res.* *47*, 2582–2591.
45. Zeng, Z., Shi, X., Chi, C., Lopez Navarrete, J. T., Casado, J., and Wu, J. (2015) Pro-aromatic and anti-aromatic π -conjugated molecules: an irresistible wish to be diradicals. *Chem. Soc. Rev.* *44*, 6578–6596.
46. Ravat, P., Solomek, T., Ribar, P., and Juricek, M. (2016) Biradicaloid with a Twist: Lowering the Singlet–Triplet Gap. *Synlett* *27*, 1613–1617.
47. Di Motta, S., Negri, F., Fazzi, D., Castiglioni, C., and Canesi, E. V. (2010) Biradicaloid and Polyenic Character of Quinoidal Oligothiophenes Revealed by the Presence of a Low-Lying Double-Exciton State. *J. Phys. Chem. Lett.* *1*, 3334–3339.
48. Sun, Z., Ye, Q., Chi, C., and Wu, J. (2012) Low band gap polycyclic hydrocarbons: from closed-shell near infrared dyes and semiconductors to open-shell radicals. *Chem. Soc. Rev.* *41*, 7857–7889.
49. Lu, R.-Q., Wu, S., Yang, L.-L., Gao, W.-B., Qu, H., Wang, X.-Y., Chen, J.-B., Tang, C., Shi, H.-Y., and Cao, X.-Y. (2019) Stable Diindeno-Fused Corannulene Regioisomers with Open-Shell Singlet Ground States and Large Diradical Characters. *Angew. Chem. Int. Ed.* *58*, 7600–7605.
50. Zeng, W., Phan, H., Heng, T.S., Gopalakrishna, T.Y., Aratani, N., Zeng, Z., Yamada, H., Ding, J., and Wu, J. (2017) Rylene Ribbons with Unusual Diradical Character. *Chem* *2*, 81–92.
51. Yamaguchi, K. (1975) The electronic structures of biradicals in the unrestricted Hartree-Fock approximation. *Chem. Phys. Lett.* *33*, 330–335.
52. Frederickson, C.K., Zakharov, L.N., and Haley, M.M. (2016) Modulating Paratropicity Strength in Diareno-Fused Antiaromatics. *J. Am. Chem. Soc.* *138*, 16827–16838.
53. Motomura, S., Nakano, M., Fukui, H., Yoneda, K., Kubo, T., Carion, R., and Champagne, B. (2011) Size dependences of the diradical character and the second hyperpolarizabilities in dicyclopenta-fused acenes: relationships with their aromaticity/antiaromaticity. *Phys. Chem. Chem. Phys.* *13*, 20575–20583.

54. Barker, J.E., Dressler, J.J., Valdivia, A.C., Kishi, R., Strand, E.T., Zakharov, L.N., MacMillan, S.N., Gómez-García, C.J., Nakano, M., Casado, J., and Haley, M.M. (2020) Molecule Isomerism Modulates the Diradical Properties of Stable Singlet Diradicaloids. *J. Am. Chem. Soc.* *142*, 1548–1555.
55. Shao, Y., Head-Gordon, M., and Krylov, A.I. (2003) The Spin–Flip Approach within Time-Dependent Density Functional Theory: Theory and Applications to Diradicals. *J. Chem. Phys.* *118*, 4807–4818.
56. Wang, F. and Ziegler, T. (2006) Use of Noncollinear Exchange–Correlation Potentials in Multiplet Resolutions by Time-Dependent Density Functional Theory. *Int. J. Quantum Chem.* *106*, 2545–2550.
57. Iikura, H., Tsuneda, T., Yanai, T., and Hirao, K. (2001) A Long-Range Correction Scheme for Generalized-Gradient-Approximation Exchange Functionals. *J. Chem. Phys.* *115*, 3540–3544.
58. Stein, T., Eisenberg, H., Kronik, L., and Baer, R. (2010) Fundamental Gaps in Finite Systems from Eigenvalues of a Generalized Kohn-Sham Method. *Phys. Rev. Lett.* *105*, 266802–1-4.
59. Park, J.-H., Chung, D.S., Park, J.-W., Ahn, T., Kong, H., Jung, Y.K., Lee, J., Yi, M.H., Park, C.E., Kwon, S.-K., and Shim, H.-K. (2007) Soluble and Easily Crystallized Anthracene Derivatives: Precursors of Solution-Processable Semiconducting Molecules. *Org. Lett.* *9*, 2573–2576.
60. Nakagawa, H., Kawai, S., Nakashima, T., and Kawai, T. (2009) Synthesis and Photochemical Reactions of Photochromic Terarylene Having a Leaving Methoxy Group. *Org. Lett.* *11*, 1475–1478.
61. It is worth noting that we did explore use of other low-melting NMR solvents; however, **12** proved to be less soluble and/or precipitated from solution at very cold temperatures.
62. We repeated the x-ray determination of **11** with a crystal from a different batch of material yet obtained essentially the same bond length values.
63. Bleaney, B. and Bowers, K.D. (1952) Anomalous paramagnetism of copper acetate. *Proc. R. Soc. Lond. A* *214*, 451–465.

Chapter VI.

1. Giri, G.; Verploegen, E.; Mannsfeld, S. C. B.; Atahan-Evrenk, S.; Kim, D. H.; Lee, S. Y.; Bercerril, H. A.; Aspuru-Guzik, A.; Toney, M. F.; Bao, Z. Tuning Charge Transport in Solution-Sheared Organic Semiconductors Using Lattice S train. *Nature* **2011**, *480*, 504–508.
2. Payne, M. M.; Parkin, S. R.; Anthony, J. E. Functionalized Higher Acenes: Hexacene and Heptacene. *J. Am. Chem. Soc.* **2005**, *127*, 8028–8029.

3. Fudickar, W.; Linker, T. Why Triple Bonds Protect Acenes from Oxidation and Decomposition. *J. Am. Chem. Soc.* **2012**, *134*, 15071–15082.
4. Anthony, J. E. The Larger Acenes: Versatile Organic Semiconductors. *Angew. Chem. Int.* **2008**, *47*, 452–483.
5. Zade, S. S.; Zamoshchik, N.; Reddy, A. R.; Fridman-Marueli, G.; Sheberla, D.; Bendikov, M. Products and Mechanism of Acene Dimerization. A Computational Study. *J. Am. Chem. Soc.* **2011**, *133*, 10803–10816.
6. Schleyer, P. v. R.; Manoharan, M.; Jiao, H.; Stahl, F. The Acenes: Is There a Relationship between Aromatic Stabilization and Reactivity? *Org. Lett.* **2001**, *3*, 3643–3646.
7. Chen, W.; Yu., F.; Xu, Q.; Zhou, G.; Zhang, Q. Recent Progress in High Linearly Fused Polycyclic Conjugated Hydrocarbons (PCHs, $n > 6$) with Well-Defined Structures. *Adv. Sci.* **2020**, 1903766 (DOI: 10.1002/advs.20190376)
8. Breslow, R.; Brown, J.; Gajewski, J. J. Antiaromaticity of Cyclopropenyl Anions. *J. Am. Chem. Soc.* **1967**, *89*, 4383–4390.
9. Breslow, R. Antiaromaticity. *Acc. Chem. Res.* **1973**, *6*, 393–398.
10. Krygowski, T. M.; Cyranski, M. K.; Czarnocki, Z.; Häfelinger, G.; Katritzky, A. R. Aromaticity: A Theoretical Concept of Immense Practical Importance. *Tetrahedron* **2000**, *56*, 1783–1791.
11. Wiberg, K. B. Antiaromaticity in Monocyclic Conjugated Carbon Rings. *Chem Rev.* **2001**, *101*, 1317–1332.
12. Chen, Z.; Wannere, C. S.; Corminboeuf, C.; Puchta, R.; Schleyer, P. v. R. Nucleus-Independent Chemical Shifts (NICS) as an Aromaticity Criterion. *Chem Rev.* **2005**, *105*, 3842–3888.
13. Mills, N. S.; Llagostera, K. B. Summation of Nucleus Independent Chemical Shifts as a Measure of Aromaticity. *J. Org. Chem.* **2007**, *72*, 9163–9169.
14. Shen, J.; Yuan, D.; Qiao, Y.; Shen, X.; Zhang, Z.; Zhong, Y.; Yi, Y.; Zhu, X. Diaceno[*a,e*]Pentalenes from Homoannulations of *o*-Alkynylaryliodides Utilizing a Unique Pd(OAc)₂/n-Bu₄NOAc Catalytic Combination. *Org. Lett.* **2014**, *16*, 4924–4927.
15. Kawase, T.; Fujiwara, T.; Kitamura, C.; Konishi, A.; Hirao, Y.; Matsumoto, K.; Kurata, H.; Kubo, T.; Shinamura, S.; Mori, H.; Miyazaki, E.; Takimiya, K. Dinaphthopentalenes: Pentalene Derivatives for Organic Thin-Film Transistors. *Angew. Chem. Int. Ed.* **2010**, *49*, 7728–7732.
16. Dai, G.; Chang, J.; Shi, X.; Zhang, W.; Zheng, B.; Huang, K.-W.; Chi, C. Thienoacene-Fused Pentalenes: Syntheses, Structures, Physical Properties and Applications for Organic Field-Effect Transistors. *Chem. Eur. J.* **2015**, *21*, 2019–2028.

17. Oshima, H.; Fukazawa, A.; Yamaguchi, S. Facile Synthesis of Polycyclic Pentalenes with Enhanced Hückel Antiaromaticity. *Angew. Chem. Int. Ed.* **2017**, *56*, 3270–3274.
18. Konishi, A.; Okada, Y.; Nakano, M.; Sugisaki, K.; Sato, K.; Takui, T.; Yasuda, M. Synthesis and Characterization of Dibenzo[*a,f*]pentalene: Harmonization of the Antiaromatic and Singlet Biradical Character. *J. Am. Chem. Soc.* **2017**, *139*, 15248–15287.
19. Kato, S.; Kuwako, S.; Takahashi, N.; Kijima, T.; Nakamura, Y. Benzo- and Naphthopentalenes: Syntheses, Structures, and Properties. *J. Org. Chem.* **2016**, *81*, 7700–7710.
20. Yuan, B.; Zhuang, J.; Kirmess, K. M.; Bridgmohan, C. N.; Whalley, A. C.; Wang, L.; Plunkett, K. N. Pentaleno[1,2-*a*:4,5']diacenaphthylenes: Uniquely Stabilized Pentalene Derivatives. *J. Org. Chem.* **2016**, *81*, 8312–8318.
21. Cao, J.; London, G.; Dumele, O.; von Wantoch Rekowski, M.; Trapp, N.; Ruhlmann, L.; Boudon, C.; Stanger, A.; Diederich, F. The Impact of Antiaromatic Subunits in $[4n+2]$ π -Systems: Bispentalenes with $[4n+2]$ π -Electron Perimeters and Antiaromatic Character. *J. Am. Chem. Soc.* **2015**, *137*, 7178–7188.
22. Dai, G.; Chang, J.; Zhang, W.; Bai, S.; Huang, K.-W.; Xu, J.; Chi, C. Dianthraceno[*a,e*]pentalenes: Synthesis, Crystallographic Structures and Applications in Organic Field-Effect Transistors. *Chem. Commun.* **2015**, *51*, 23955–26900.
23. Wang, J.; Chu, M.; Fan, J.-X.; Lau, T.-K.; Ren, A.-M.; Lu, X.; Miao, Q. Crystal Engineering of Biphenylene-Containing Acenes for High-Mobility Organic Semiconductors. *J. Am. Chem. Soc.* **2019**, *141*, 3589–3596.
24. Jin, Z.; Teo, Y. C.; Teat, S. J.; Xia, Y. Regioselective Synthesis of [3]Naphthylenes and Tuning of Their Antiaromaticity. *J. Am. Chem. Soc.* **2017**, *139*, 15933–15939.
25. Jin, Z.; Yao, Z.-F.; Barker, K. P.; Pei, J.; Xia, Y. Dinaphthobenzo[1,2:4,5]dicyclobutadiene: Antiaromatic and Orthogonally Tunable Electronics and Packing. *Angew. Chem. Int. Ed.* **2019**, *58*, 2034–2039.
26. Teo, Y. C.; Jin, Z.; Xia, Y. Synthesis of Cyclobutadienoid-Fused Phenazines with Strongly Modulated Degrees of Antiaromaticity. *Org. Lett.* **2018**, *20*, 3300–3304.
27. Marshall, J. L.; Uchida, K.; Frederickson, C. K.; Schütt, C.; Zeidell, A. M.; Goetz, K. P.; Finn, T. W.; Jarolimek, K.; Zakharov, L. N.; Risko, C.; Herges, R.; Jurchescu, O. D.; Haley, M. M. Indacenodibenzothiophenes: Synthesis, Optoelectronic Properties and Materials Applications of Molecules with Strong Antiaromatic Character. *Chem. Sci.* **2016**, *7*, 5547–5558.
28. Frederickson, C. K.; Zakharov, L. N.; Haley, M. M. Modulating Paratropicity Strength in Diareno-Fused Antiaromatics. *J. Am. Chem. Soc.* **2016**, *138*, 16827–16838.

29. Frederickson, C. K.; Rose, B. D.; Haley, M. M. Explorations of the Indenofluorenes and Expanded Quinoidal Analogues. *Acc. Chem. Res.* **2017**, *50*, 977–987.
30. Melidonie, J.; Liu, J.; Fu, Y.; Weigand, J. J.; Berger, R.; Feng, X. Pyrene-Fused *s*-Indacene. *J. Org. Chem.* **2018**, *83*, 6633–6639.
31. Broløs, L.; Kilde, M. D.; Hammerich, O.; Nielsen, M. B. Toward Redox-Active Indenofluorene-Extended Tetrathiafulvalene Oligomers—Synthesis and Studies of Dimeric Scaffolds. *J. Org. Chem.* **2020**, *85*, 3277–3286.
32. Ie, Y.; Sato, C.; Yamamoto, K.; Nitani, M.; Aso, Y. A Thiazole-Fused Antiaromatic Compound Containing an *s*-Indacene Chromophore with a High Electron Affinity. *Chem. Lett.* **2018**, *47*, 1534–1537.
33. Jiang, Q.; Tao, T.; Phan, H.; Han, Y.; Gopalakrishna, T. Y.; Heng, T. S.; Li, G.; Yuan, L.; Ding, J.; Chi, C. Diazuleno-*s*-Indacene Diradicaloids: Syntheses, Properties, and Local (Anti)Aromaticity Shift from Neutral to Dicationic State. *Angew. Chem. Int. Ed.* **2018**, *57*, 16737–16741.
34. Breslow, R.; Schneebeli, S. T. Structure-Property Relationships in Molecular Wires. *Tetrahedron* **2011**, *67*, 10171–10178.
35. Breslow, R.; Foss, F. W. Charge Transport in Nanoscale Aromatic and Antiaromatic Systems. *J. Phys. Condens. Matter* **2008**, *20*, 374104.
36. Chen, W.; Li, H.; Widawsky, J. R.; Appayee, C.; Venkataraman, L.; Breslow, R. Aromaticity Decreases Single-Molecule Junction Conductance. *J. Am. Chem. Soc.* **2014**, *136*, 918–920.
37. Mahendran, A.; Gopinath, P.; Breslow, R. Single Molecule Conductance of Aromatic, Nonaromatic, and Partially Antiaromatic Systems. *Tetrahedron Lett.* **2015**, *56*, 4833–4835.
38. Zeidell, A. M.; Jennings, L.; Frederickson, C. K.; Ai, Q.; Dressler, J. J.; Zakharov, L. N.; Risko, C.; Haley, M. M.; Jurchescu, O. D. Organic Semiconductors Derived from Dinaphtho-Fused *s*-Indacenes: How Molecular Structure and Film Morphology Influence Thin-Film Transistor Performance. *Chem. Mater.* **2019**, *31*, 6962–6970.
39. Liu, C.; Xu, S.; Zhu, W.; Zhu, X.; Hu, W.; Li, Z.; Wang, Z. Diaceno[*a,e*]pentalenes: An Excellent Molecular Platform for High-Performance Organic Semiconductors. *Chem. Eur. J.* **2015**, *21*, 17016–17022.
40. Gopalakrishna, T. Y.; Zeng, W.; Lu, X.; Wu, J. From Open-Shell Singlet Diradicaloids to Polyradicaloids. *Chem. Commun.* **2018**, *54*, 2186–2199.
41. Koike, H.; Chikamatsu, M.; Azumi, R.; Tsutsumi, J.; Ogawa, K.; Yamane, W.; Nishiuchi, T.; Kubo, T.; Hasegawa, T.; Kanai, K. Stable Delocalized Singlet Biradical Hydrocarbon for Organic Field-Effect Transistors. *Adv. Funct. Mater.* **2016**, *26*, 277–283.

42. Morita, Y.; Suzuki, S.; Sato, K.; Takui, T. Synthetic Organic Spin Chemistry for Structurally Well-Defined Open-Shell Graphene Fragments. *Nat. Chem.* **2011**, *3*, 197–204.
43. Morita, Y.; Nishida, S.; Murata, T.; Moriguchi, M.; Ueda, A.; Satoh, M.; Arifuku, K.; Sato, K.; Takui, T. Organic Tailored Batteries Materials Using Stable Open-Shell Molecules with Degenerate Frontier Orbitals. *Nat. Mater.* **2011**, *10*, 947–951.
44. Smith, M. B.; Michl, J. Recent Advances in Singlet Fission. *Annu. Rev. Phys. Chem.* **2013**, *64*, 361–386.
45. Minami, T.; Nakano, M. Diradical Character View of Singlet Fission. *J. Phys. Chem. Lett.* **2012**, *3*, 145–150.
46. Ravat, P.; Šolomek, T.; Ribar, P.; Juriček, M. Biradicaloid with a Twist: Lowering the Singlet-Triplet Gap. *Synlett* **2016**, *27*, 1613–1617.
47. Di Motta, S.; Negri, F.; Fazzi, D.; Castiglioni, C.; Canesi, E. V. Biradicaloid and Polyenic Character of Quinoidal Oligothiophenes Revealed by the Presence of a Low-Lying Double-Exciton State. *J. Phys. Chem. Lett.* **2010**, *1*, 3334–3339.
48. Abe, M. Diradicals. *Chem Rev.* **2013**, *113*, 7011–7088.
49. Kubo, T.; Shimizu, A.; Sakamoto, M.; Uruichi, M.; Yakushi, K.; Nakano, M.; Shiomi, D.; Sato, K.; Takui, T.; Morita, Y.; Nakasuji, K. Synthesis, Intermolecular Interaction, and Semiconductive Behavior of a Delocalized Singlet Biradical Hydrocarbon. *Angew. Chem. Int. Ed.* **2005**, *44*, 6564–6568.
50. Shimizu, A.; Kubo, T.; Uruichi, M.; Yakushi, K.; Nakano, M.; Shiomi, D.; Sato, K.; Takui, T.; Hirao, Y.; Matsumoto, K.; Kurata, H.; Morita, Y.; Nakasuji, K. Alternating Covalent Bonding Interactions in a One-Dimensional Chain of a Phenalenyl-Based Singlet Biradical Molecule Having Kekulé Structures. *J. Am. Chem. Soc.* **2010**, *132*, 14421–14428.
51. Shimizu, A.; Hirao, Y.; Matsumoto, K.; Kurata, H.; Kubo, T.; Uruichi, M.; Yakushi, K. Aromaticity and π -Bond Covalency: Prominent Intermolecular Covalent Bonding Interaction of a Kekulé Hydrocarbon with Very Significant Singlet Biradical Character. *Chem. Commun.* **2012**, *48*, 5629–5631.
52. Hu, P.; Wu, J. Modern Zethrene Chemistry. *Can. J. Chem.* **2017**, *95*, 223–233.
53. Zeng, W.; Sun, Z.; Heng, T. S.; Gonçalves, T. P.; Gopalakrishna, T. Y.; Huang, K. W.; Ding, J.; Wu, J. Super-Heptazethrene. *Angew. Chem. Int. Ed.* **2016**, *55*, 8615–8619.
54. Sun, Z.; Lee, S.; Park, K. H.; Zhu, X.; Zhang, W.; Zheng, B.; Hu, P.; Zeng, Z.; Das, S.; Li, Y.; Chi, C.; Li, R. W.; Huang, K. W.; Ding, J.; Kim, D.; Wu, J. Dibenzoheptazethrene Isomers with Different Biradical Characters: An Exercise of Clar's Aromatic Sextet Rule in Singlet Biradicaloids. *J. Am. Chem. Soc.* **2013**, *135*, 18229–18236.

55. Li, Y.; Heng, W. K.; Lee, B. S.; Aratani, N.; Zafra, J. L.; Bao, N.; Lee, R.; Sung, Y. M.; Sun, Z.; Huang, K. W.; Webster, R. D.; Lopez-Navarrete, J. T.; Kim, D.; Osuka, A.; Casado, J.; Ding, J.; Wu, J. Kinetically Blocked Stable Heptazethrene and Octazethrene: Closed-Shell or Open-Shell in the Ground State? *J. Am. Chem. Soc.* **2012**, *134*, 14913–14922.
56. Shimizu, A.; Kishi, R.; Nakano, M.; Shiomi, D.; Sato, K.; Takui, T.; Hisaki, I.; Miyata, M.; Tobe, Y. Indeno[2,1-*b*]fluorene: A 20- π -Electron Hydrocarbon with Very Low-Energy Light Absorption. *Angew. Chem. Int. Ed.* **2013**, *52*, 6076–6079.
57. Dressler, J. J.; Zhou, Z.; Marshall, J. L.; Kishi, R.; Takamuku, S.; Wei, Z.; Spisak, S. N.; Nakano, M.; Petrukhina, M. A.; Haley, M. M. Synthesis of the Unknown Indeno[1,2-*a*]fluorene Regioisomer: Crystallographic Characterization of Its Dianion. *Angew. Chem. Int. Ed.* **2017**, *56*, 15363–15367.
58. Rudebusch, G. E.; Zafra, J. L.; Jorner, K.; Fukuda, K.; Marshall, J. L.; Arrechea-Marcos, I.; Espejo, G. L.; Ponce Ortiz, R.; Gómez-García, C. J.; Zakharov, L. N.; Nakano, M.; Ottosson, H.; Casado, J.; Haley, M. M. Diindeno-Fusion of an Anthracene as a Design Strategy for Stable Organic Biradicals. *Nat. Chem.* **2016**, *8*, 753–759.
59. Miyoshi, H.; Miki, M.; Hirano, S.; Shimizu, A.; Kishi, R.; Fukuda, K.; Shiomi, D.; Sato, K.; Takui, T.; Hisaki, I.; Nakano, M.; Tobe, Y. Fluoreno[2,3-*b*]fluorene vs Indeno[2,1-*b*]fluorene: Unusual Relationship between the Number of π Electrons and Excitation Energy in *m*-Quinodimethane-Type Singlet Diradicaloids. *J. Org. Chem.* **2017**, *82*, 1380–1388.
60. Dressler, J. J.; Teraoka, M.; Espejo, G. L.; Kishi, R.; Takamuku, S.; Gómez-García, C. J.; Zakharov, L. N.; Nakano, M.; Casado, J.; Haley, M. M. Thiophene and Its Sulfur Inhibit Indenoindenodibenzothiophene Diradicals from Low-Energy Lying Thermal Triplets. *Nat. Chem.* **2018**, *10*, 1134–1140.
61. Hacker, A. S.; Pavano, M.; Wood, J. E.; Hashimoto, H.; D'Ambrosio, K. M.; Frederickson, C. K.; Zafra, J. L.; Gómez-García, C. J.; Postils, V.; McDonald, A. R.; Casanova, D.; Frantz, D. K.; Casado, J. Fluoreno[2,1-*a*]fluorene: an *ortho*-naphthoquinodimethane-based system with partial diradical character. *Chem. Commun.* **2019**, *55*, 14186–14189.
62. Barker, J. E.; Dressler, J. J.; Cárdenas Valdivia, A.; Kishi, R.; Strand, E. T.; Zakharov, L. N.; MacMillan, S. N.; Gómez-García, C. J.; Nakano, M.; Casado, J.; Haley, M. M. Molecule Isomerism Modulates the Diradical Properties of Stable Singlet Diradicaloids. *J. Am. Chem. Soc.* **2020**, *142*, 1548–1555.
63. Dressler, J. J.; Cárdenas Valdivia, A.; Kishi, R.; Rudebusch, G. E.; Ventura, A. M.; Chastain, B. E.; Gómez-García, C. J.; Zakharov, L. N.; Nakano, M.; Casado, J.; Haley, M. M. Diindenoanthracene Diradicaloids Enable Rational, Incremental Tuning of Their Singlet-Triplet Energy Gaps. *Chem* **2020**, *6*, in press (DOI: 10.1016/j.chempr.2020.02.010).

64. Majewski, M. A.; Chmielewski, P. J.; Chien, A.; Hong, Y.; Lis, T.; Witwicki, M.; Kim, D.; Zimmerman, P. M.; Stępień, M. 5,10-Dimesityldiindeno[1,2-*a*:2',1'-*i*]phenanthrene: A Stable Biradicaloid Derived from Chichibabin's Hydrocarbon. *Chem. Sci.* **2019**, *10*, 3413–3420.
65. Lu, R.-Q.; Wu, S.; Yang, L.-L.; Gao, W.-B.; Qu, H.; Wang, X.-Y.; Chen, J.-B.; Tang, C.; Shi, H.-Y.; Cao, X.-Y. Stable Diindeno-Fused Corannulene Regioisomers with Open-Shell Singlet Ground States and Large Diradical Characters. *Angew. Chem. Int. Ed.* **2019**, *58*, 7600–7605.
66. Zeng, Z.; Shi, X.; Chi, C.; López Navarrete, J. T.; Casado, J.; Wu, J. Pro-Aromatic and Anti-Aromatic π -Conjugated Molecules: An Irresistible Wish to Be Diradicals. *Chem. Soc. Rev.* **2015**, *44*, 6578–6596.
67. Frederickson, C. K.; Barker, J. E.; Dressler, J. J.; Zhou, Z.; Hanks, E. R.; Bard, J. P.; Zakharov, L. N.; Petrukhina, M. A.; Haley, M. M. Synthesis and Characterization of a Fluorescent Dianthracenoindacene. *Synlett* **2018**, *29*, 2562–2566.
68. Young, B. S.; Chase, D. T.; Marshall, J. L.; Vonnegut, C. L.; Zakharov, L. N.; Haley, M. M. Synthesis and Properties of Fully-Conjugated Indacenedithiophenes. *Chem. Sci.* **2014**, *5*, 1008–1014.
69. Nieman, R.; Silva, N. J.; Aquino, A. J. A.; Haley, M. M.; Lischka, H. The Interplay of Biradicaloid Character and Singlet/Triplet Energy Splitting for *cis*-/*trans*-Diindenoacenes and Related Benzothiophene-Capped Oligomers as Revealed by Extended Multireference Calculations. *J. Org. Chem.* **2020**, *85*, 3664–3675.
70. Wei, S.; Xia, J.; Dell, E. J.; Jiang, Y.; Song, R.; Lee, H.; Rodenbough, P.; Briseno, A. L.; Campos, L. M. Bandgap Engineering through Controlled Oxidation of Polythiophenes. *Angew. Chem. Int. Ed.* **2014**, *53*, 1832–1836.
71. Pappenfus, T. M.; Seidenkranz, D. T.; Lovander, M. D.; Beck, T. L.; Karels, B. J.; Ogawa, K.; Janzen, D. E. Synthesis and Electronic Properties of Oxidized Benzo[1,2-*b*:4,5-*b'*]dithiophenes. *J. Org. Chem.* **2014**, *79*, 9408–9412.
72. Liu, G.; Zhang, H.; Huang, Y.; Han, Z.; Liu, G.; Liu, Y.; Dong, X. Q.; Zhang, X. Efficient Synthesis of Chiral 2,3-Dihydrobenzo[*b*]thiophene 1,1-Dioxides via Rh-Catalyzed Hydrogenation. *Chem. Sci.* **2019**, *10*, 2507–2512.
73. Barbarella, G.; Pudova, O.; Arbizzani, C.; Mastragostino, M.; Bongini, A. Oligothiophene-S,S-Dioxides: A New Class of Thiophene-Based Materials. *J. Am. Chem. Soc.* **1998**, *63*, 1742–1745.
74. Dell, E. J.; Campos, L. M. The Preparation of Thiophene-S,S-Dioxides and Their Role in Organic Electronics. *J. Mater. Chem.* **2012**, *22*, 12945–12952.
75. Gershoni-Poranne, R.; Stanger, A. The NICS-XY-Scan: Identification of Local and Global Ring Currents in Multi-Ring Systems. *Chem. Eur. J.* **2014**, *20*, 5673–5688.

76. Stanger, A. Nucleus-Independent Chemical Shifts (NICS): Distance Dependence and Revised Criteria for Aromaticity and Antiaromaticity. *J. Org. Chem.* **2006**, *71*, 883–893.
77. Even though NBO recognizes the resonance forms we draw for the dianion reference molecules, NRT analyses (which would give us the relative weights for a few of the most important resonance forms) would not finish because of a very large number (1000+) of potential resonance forms.
78. Gimarc, B. M. Topological Charge Stabilization. *J. Am. Chem. Soc.* **1983**, *105*, 1979–1984.
79. Despite multiple efforts, we were unable to obtain a suitable structure for **5** with the *t*-Mes groups. Regardless, our prior studies have shown that use of different bulky aryl groups attached to the apical carbons has minimal effect on the molecular geometry of the π -expanded conjugated system; see reference 62.
80. It is worth noting that no bond-flipped minima structures were found for **1** or **2** as both prefer a “normal” bonding pattern.
81. Bleaney, B.; Bowers, K. D. Anomalous Paramagnetism of Copper Acetate. *Proc. R. Socl. Lond. A* **1952**, *214*, 451–465.